

Modern world heat transfer problems: Role of nanofluids and fractional order approaches

Edited by

Adnan, Umar Khan and Ilyas Khan

Published in

Frontiers in Energy Research



FRONTIERS EBOOK COPYRIGHT STATEMENT

The copyright in the text of individual articles in this ebook is the property of their respective authors or their respective institutions or funders. The copyright in graphics and images within each article may be subject to copyright of other parties. In both cases this is subject to a license granted to Frontiers.

The compilation of articles constituting this ebook is the property of Frontiers.

Each article within this ebook, and the ebook itself, are published under the most recent version of the Creative Commons CC-BY licence. The version current at the date of publication of this ebook is CC-BY 4.0. If the CC-BY licence is updated, the licence granted by Frontiers is automatically updated to the new version.

When exercising any right under the CC-BY licence, Frontiers must be attributed as the original publisher of the article or ebook, as applicable.

Authors have the responsibility of ensuring that any graphics or other materials which are the property of others may be included in the CC-BY licence, but this should be checked before relying on the CC-BY licence to reproduce those materials. Any copyright notices relating to those materials must be complied with.

Copyright and source acknowledgement notices may not be removed and must be displayed in any copy, derivative work or partial copy which includes the elements in question.

All copyright, and all rights therein, are protected by national and international copyright laws. The above represents a summary only. For further information please read Frontiers' Conditions for Website Use and Copyright Statement, and the applicable CC-BY licence.

ISSN 1664-8714
ISBN 978-2-83251-292-0
DOI 10.3389/978-2-83251-292-0

About Frontiers

Frontiers is more than just an open access publisher of scholarly articles: it is a pioneering approach to the world of academia, radically improving the way scholarly research is managed. The grand vision of Frontiers is a world where all people have an equal opportunity to seek, share and generate knowledge. Frontiers provides immediate and permanent online open access to all its publications, but this alone is not enough to realize our grand goals.

Frontiers journal series

The Frontiers journal series is a multi-tier and interdisciplinary set of open-access, online journals, promising a paradigm shift from the current review, selection and dissemination processes in academic publishing. All Frontiers journals are driven by researchers for researchers; therefore, they constitute a service to the scholarly community. At the same time, the *Frontiers journal series* operates on a revolutionary invention, the tiered publishing system, initially addressing specific communities of scholars, and gradually climbing up to broader public understanding, thus serving the interests of the lay society, too.

Dedication to quality

Each Frontiers article is a landmark of the highest quality, thanks to genuinely collaborative interactions between authors and review editors, who include some of the world's best academicians. Research must be certified by peers before entering a stream of knowledge that may eventually reach the public - and shape society; therefore, Frontiers only applies the most rigorous and unbiased reviews. Frontiers revolutionizes research publishing by freely delivering the most outstanding research, evaluated with no bias from both the academic and social point of view. By applying the most advanced information technologies, Frontiers is catapulting scholarly publishing into a new generation.

What are Frontiers Research Topics?

Frontiers Research Topics are very popular trademarks of the *Frontiers journals series*: they are collections of at least ten articles, all centered on a particular subject. With their unique mix of varied contributions from Original Research to Review Articles, Frontiers Research Topics unify the most influential researchers, the latest key findings and historical advances in a hot research area.

Find out more on how to host your own Frontiers Research Topic or contribute to one as an author by contacting the Frontiers editorial office: frontiersin.org/about/contact

Modern world heat transfer problems: Role of nanofluids and fractional order approaches

Topic editors

Adnan — Mohi-ud-Din Islamic University, Pakistan

Umar Khan — Hazara University, Pakistan

Ilyas Khan — Majmaah University, Saudi Arabia

Citation

Adnan, Khan, U., Khan, I., eds. (2023). *Modern world heat transfer problems: Role of nanofluids and fractional order approaches*. Lausanne: Frontiers Media SA.
doi: 10.3389/978-2-83251-292-0

Table of contents

- 05 **MHD williamson nanofluid flow in the rheology of thermal radiation, joule heating, and chemical reaction using the Levenberg–Marquardt neural network algorithm**
Aatif Ali, N. Ameer Ahammad, Elsayed Tag-Eldin, Fehmi Gamaoun, Yousef Ibrahim Daradkeh and Mansour F. Yassen
- 28 **Numerical simulation of ternary nanofluid flow with multiple slip and thermal jump conditions**
Saad Alshahrani, N. Ameer Ahammad, Muhammad Bilal, Mohamed E. Ghoneim, Aatif Ali, Mansour F. Yassen and Elsayed Tag-Eldin
- 37 **Suction effect on MHD flow of Brinkman-type fluid with heat absorption and first-order chemical reaction**
Shao-Wen Yao, Mushtaq Ahmad, Mustafa Inc, Ikhlaiq Ahmad, Muhammad Imran Asjad and Mudassar Nazar
- 48 **Numerical analysis of thermal transportation in nanodiamond and silver-based nanofluid using the Cattaneo–Christov heat flux model**
Samina Zuhra, Waseem Sikander, Mohamed Abdelghany Elkotb, E. M. Tag-Eldin, Sana Gul Khattak and Mansour F. Yassen
- 61 **Thermal characteristics of kerosene oil-based hybrid nanofluids (Ag-MnZnFe₂O₄): A comprehensive study**
Sohail Ahmad, Kashif Ali, Tahir Haider, Wasim Jamshed, El Sayed M. Tag El Din and Syed M. Hussain
- 70 **Analysis of fractional MHD convective flow with CTNs' nanoparticles and radiative heat flux in human blood**
Maryam Aleem, Mustafa Inc, Shahzad Sarwar, Muhammad Imran Asjad and A. S. A. Alsubaie
- 87 **Newtonian heating effect in pulsating magnetohydrodynamic nanofluid flow through a constricted channel: A numerical study**
Amjad Ali, Zainab Bukhari, Muhammad Amjad, Sohail Ahmad, El. Sayed M. Tag El. Din and Syed M. Hussain
- 106 **Mathematical analysis of casson fluid flow with energy and mass transfer under the influence of activation energy from a non-coaxially spinning disc**
M. M. Alqarni, Muhammad Bilal, Reem Allogmany, Elsayed Tag-Eldin, Mohamed E. Ghoneim and Mansour F. Yassen
- 116 **The radiative flow of the thin-film Maxwell hybrid nanofluids on an inclined plane in a porous space**
Taza Gul, Safyan Mukhtar, Wajdi Alghamdi, Elsayed Tag Eldin, Mansour F. Yassen and Kamel Guedri

- 128 **Thermal examination for the micropolar gold–blood nanofluid flow through a permeable channel subject to gyrotactic microorganisms**
Arshad Khan, Maryam Ahmed Alyami, Wajdi Alghamdi, M. M. Alqarni, Mansour F. Yassen and Elsayed Tag Eldin
- 143 **Dynamics of MHD second-grade nanofluid flow with activation energy across a curved stretching surface**
Srinivas C. Reddy, Kanayo Kenneth Asogwa, Mansour F. Yassen, Adnan, Zahoor Iqbal, Sayed M-Eldin, Bagh Ali and Swarnalatha KM
- 155 **Energy and mass transport through hybrid nanofluid flow passing over an extended cylinder with the magnetic dipole using a computational approach**
M. Riaz Khan, N. Ameer Ahammad, Sharifah E. Alhazmi, Aatif Ali, Mostafa A. H. Abdelmohimen, Reem Allogmany, Elsayed Tag-Eldin and Mansour F. Yassen
- 169 **Entropy generation investigation of MHD $Ag-$ and $Au-H_2O$ nanofluid above an exponential porous stretchable surface with thermal radiation and stagnation point flow**
I. Rashid, T. Zubair, M. I. Asjad and J. Awrejcewicz
- 181 **Quadratic regression estimation of hybridized nanoliquid flow using Galerkin finite element technique considering shape of nano solid particles**
Mustafa Mutiur Rahman, Wasim Jamshed, Suriya Uma Devi. S, Rabha W. Ibrahim, Amjad Ali Pasha, Basma Souayeh, Rabia Safdar, Mohamed R. Eid, Syed M. Hussain and El Sayed M. Tag El Din
- 199 **Thermal energy development in magnetohydrodynamic flow utilizing titanium dioxide, copper oxide and aluminum oxide nanoparticles: Thermal dispersion and heat generating formularization**
Muhammad Bilal Hafeez, Marek Krawczuk, Wasim Jamshed, El Sayed M. Tag El Din, Hamiden Abd El-Wahed Khalifa and Fayza Abdel Aziz ElSeabee
- 212 **Radiative couple stress Casson hybrid nanofluid flow over an inclined stretching surface due to nonlinear convection and slip boundaries**
Taza Gul, Safyan Mukhtar, Wajdi Alghamdi, Zehba Raizah, Sharifah E. Alhazmi and ElSayed Tag ElDin
- 224 **Energy transport features of Oldroyd-B nanofluid flow over bidirectional stretching surface subject to Cattaneo–Christov heat and mass fluxes**
Arafat Hussain, Zahoor Iqbal, Mostafa A. H. Abdelmohimen, Kamel Guedri, Elsayed Tag-eldin and Mansour F. Yassen
- 236 **Applying the natural transform iterative technique for fractional high-dimension equations of acoustic waves**
Laiq Zada, Nasir Ali, Rashid Nawaz, Wasim Jamshed, Mohamed R. Eid, El Sayed M. Tag El Din, Hamiden Abd El- Wahed Khalifa and Fayza Abdel Aziz ElSeabee



OPEN ACCESS

EDITED BY

Umar Khan,
Hazara University, Pakistan

REVIEWED BY

Zulqurnain Sabir,
United Arab Emirates University, United
Arab Emirates
Samina Zuhra,
Abasyn University, Pakistan

*CORRESPONDENCE

Aatif Ali,
atifkh98@gmail.com
Mansour F. Yassen,
mf.ali@psau.edu.sa

SPECIALTY SECTION

This article was submitted to Process
and Energy Systems Engineering,
a section of the journal
Frontiers in Energy Research

RECEIVED 09 June 2022

ACCEPTED 08 July 2022

PUBLISHED 11 August 2022

CITATION

Ali A, Ahammad NA, Tag-Eldin E,
Gamaoun F, Daradkeh YI and Yassen MF
(2022), MHD williamson nanofluid flow
in the rheology of thermal radiation,
joule heating, and chemical reaction
using the Levenberg–Marquardt neural
network algorithm.
Front. Energy Res. 10:965603.
doi: 10.3389/fenrg.2022.965603

COPYRIGHT

© 2022 Ali, Ahammad, Tag-Eldin,
Gamaoun, Daradkeh and Yassen. This is
an open-access article distributed
under the terms of the [Creative
Commons Attribution License \(CC BY\)](#).
The use, distribution or reproduction in
other forums is permitted, provided the
original author(s) and the copyright
owner(s) are credited and that the
original publication in this journal is
cited, in accordance with accepted
academic practice. No use, distribution
or reproduction is permitted which does
not comply with these terms.

MHD williamson nanofluid flow in the rheology of thermal radiation, joule heating, and chemical reaction using the Levenberg–Marquardt neural network algorithm

Aatif Ali^{1*}, N. Ameer Ahammad², Elsayed Tag-Eldin³,
Fehmi Gamaoun⁴, Yousef Ibrahim Daradkeh⁵ and
Mansour F. Yassen^{6,7*}

¹Department of Mathematics, Abdul Wali Khan University Mardan, Khyber Pakhtunkhwa, Pakistan, ²Department of Mathematics, Faculty of Science, University of Tabuk, Tabuk, Saudi Arabia, ³Faculty of Engineering and Technology, Future University in Egypt, New Cairo, Egypt, ⁴Department of Mechanical Engineering, College of Engineering, King Khalid University, Abha, Saudi Arabia, ⁵Department of Computer Engineering and Networks, College of Engineering at Wadi Addawasir, Prince Sattam Bin Abdulaziz University, Al-Kharj, Saudi Arabia, ⁶Department of Mathematics, College of Science and Humanities in Al-Aflaj, Prince Sattam Bin Abdulaziz University, Al-Aflaj, Saudi Arabia, ⁷Department of Mathematics, Faculty of Science, Damietta University, Damietta, Egypt

Various studies have been conducted on the topic of predicting the thermal conductivity of nanofluids. Here, the thermal conductivity of nanofluids is determined using artificial neural networks since this approach is rapid and accurate, as well as cost-effective. To forecast the thermal conductivity of magnetohydrodynamic Williamson nanofluids flow through a vertical sheet, a feed-forward neural network with various numbers of neurons has been evaluated, and the best network based on the performance is selected. The fluid model incorporates the effects of Joule heating, heat generation absorption, thermal radiation, and a chemical reaction (MHD-WNF-HGA). A combination of heat radiation and reactive species improves the energy and solute profiles. The magnetic Reynolds number is assumed to be so small; therefore, the generated magnetic field has no effect. A postulate of similarity variables is used to convert the physical model in the form of nonlinear partial differential equations to an ordinary differential equation system. A supervised Levenberg–Marquardt backpropagation algorithm possesses a multilayer perceptron that is used for training the network, which is one of the top algorithms in machine learning. The bvp4c numerical technique is adopted to build the datasets for the construction of continuous neural network mapping. Flow, energy, and concentration profiles of the fluidic flow are constructed by adjusting several physical quantities such as the Williamson parameter, thermal radiation parameter, magnetic parameter, Eckert number, Darcy number, Brownian motion, and thermophoresis parameter. Analytical techniques such as error histogram graphs and regression-based statistical graphs are used to examine the accuracy of a suggested method. It has been found that the Levenberg–Marquardt backpropagation neural network

mappings' derivation, convergence, authentication, and consistency have been proven. Furthermore, thermal radiation assists the energy distribution to increase smoothly. Fluid velocity drops with the Williamson parameter, whereas thermophoresis impact enhances the strength of the nanofluid density.

KEYWORDS

nanofluid, Williamson fluid, stretched surface, Levenberg–Marquardt technique, backpropagation neural networks, artificial intelligence

1 Introduction

Energy is a crucial physical property that must be transferred for any system to perform work. Work and heat may be used for energy transmission (Incropera et al., 1996). It is feasible for heat to transfer from one system to another when their temperatures vary (Cengel and Boles, 2015). Heat transfer is a subfield of physics concerned with the transmission of thermal (heat) energy. Heat transfer applications are encountered on a daily basis in the form of the human body's constant heat output and its usage of clothing to adjust its internal temperature in reaction to external conditions (Cengel and Heat, 2003). In addition, heat transmission is used to regulate the temperature in our buildings and is necessary for cooking and drying. It is also used to control the temperature of car radiators and electrical equipment (Zhao et al., 2016). Heat transfer is used by solar thermal collectors (González et al., 2021) and thermal control components (Okonkwo et al., 2021) to convert solar energy into heat and power. Several of these components must quickly distribute heat in order for the system to work at its maximum effectiveness and efficiency (Okonkwo et al., 2018). Low gate size necessitates enhanced heat control. Generally, the smaller the gadget must be, the higher is the demand for efficient cooling technologies. Therefore, the improvement of heat transfer is a key priority in the area of thermal engineering. Different strategies are arising aim to enhance the heat transfer coefficient among working fluids and their contact surfaces (Das et al., 2006; Meseguer et al., 2012). The research development of heat transfer fluids has resulted from the enhancement of the thermal characteristics of these fluids by the inclusion of nanoscale particles. The dispersion of these solid particles in the host fluid improves the fluid's energy transmission, resulting in enhanced thermal conductivity and heat transfer qualities. First of all, microscaled particles have been suspended in a fluid for more than a century by Maxwell (Choi et al., 1995). Research into fluid dispersion has been hampered by erosion and clogging caused by microparticles that settle quickly in the liquid. Colloidal dispersion in fids may now be studied in more detail due to the advent of nanoparticles. Later, the term “nanofluid” was coined in 1995 by Choi and Eastman (Maxwell, 1881). By incorporating a modest volumetric quantity of ultrafine nanomaterials into fluids, researchers have come up with many ideas for enhancing thermal efficiency and convective heat transfer. The thermal characteristics of fluids are

improved when nanoparticles are scattered in them. Additionally, there are many features involved in the stability of nanofluids such as, Brownian motion, host fluid layer, particle's nanolayers, and lower pumping power relative to pure liquids. The effect of different nanoparticles made of conducting materials on the improvement of thermal transfer is investigated in the research studies by Sheikholeslami et al. (2019a); Sheikholeslami et al. (2019b); Goodarzi et al. (2019); Sajid and Ali (2019); Alhowaity et al. (2022a); Alsallami et al. (2022); Elattar et al. (2022). Aluminum oxide nanoparticles in base fluid nanofluids past a sensor surface is studied by Mahdi et al. (2019). Three-dimensional magnetohydrodynamic squeezing flow of aluminum nanoparticle base in water type nanofluid is shown in the study by Khan et al. (2020). The rheological model through hybrid nanofluid flow is proposed in the study by Al-Mubaddel et al. (2022). Freezing temperature is studied in aluminum oxide nanofluid magnetic flow with a radiative effect in the study by AdnanKhan and Ahmed (2022). Nanofluids flow with a variety of forces and characteristics, which have been studied for the rate of heat transfer are in the research studies by Khan et al. (2019a); Shah et al. (2019); Ahmed et al. (2020); Khan et al. (2021a); Ashraf et al. (2022); Alhowaity et al. (2022b).

Non-Newtonian fluid models have been the subject of many experiments and theoretical studies cause of the wide variety of biological and industrial processes where they are applicable. Many industrial applications, such as emulsification, lubrication, nuclear fuel slurries, biofluids in cells and polymerization, and therapeutic fluid is in consideration of non-Newtonian fluids rather than Newtonian fluid theory. Many rheological models have been developed based on non-Newtonian fluids' varied rheological characteristics such as power law model, Jeffery fluid model, Carreau model, Ellis–Sisko–Williamson model, cross-model, and other fluid models are the existing models. Among all, the Williamson fluid model is a basic model that may replicate the viscoelastic shear-thinning features of non-Newtonian fluids. Williamson (1929) established this idea in 1929, and he provided the experimental data. It is expected that the functional viscosity in the Williamson fluid model would decrease endlessly as the shear rate increases, which is nothing more than an infinite viscosity at rest (zero fluid motion) and zero-valued viscosity as the shear rate approaches infinity. In terms of fluid properties, Williamson nanofluid may be classified

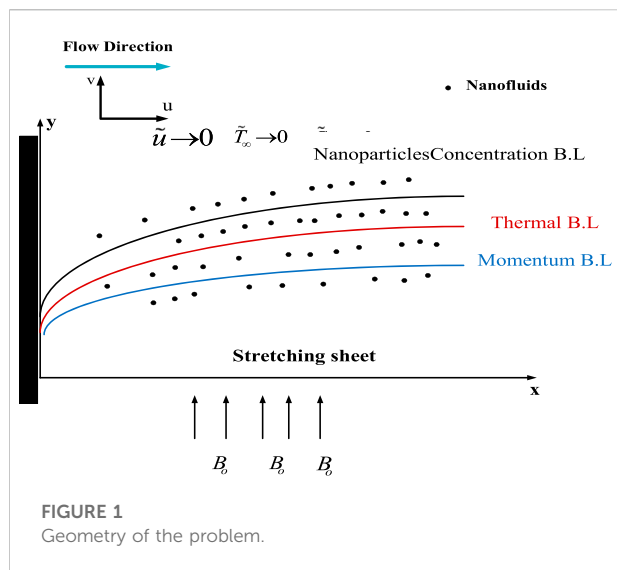
as visco-inelastic. When it came to investigating the issue of boundary layer flow over a flat surface, Blasius (1950), Sakiadis (1961), and others first looked into the theoretical aspects of approximation and precise methods. Few recent Williamson fluid research studies have been published in the study by Acharya et al. (2019); Khan et al. (2019b); Hamid and Khan (2019); Ibrahim and Gamachu (2019); Rasool et al. (2019); Zaman and Gul (2019); Pandya et al. (2020); Subbarayudu et al. (2020). Thermal radiation is the process through which the heat of a material induces the emission of electromagnetic waves (variation of its internal energy). It is one of the three ways different kinds of organisms may trade their own energy storage. The kind of radiation emitted might vary from ultraviolet to far-field infrared depending on the temperature of the substance. Every component of the body emits and absorbs thermal radiation continuously, and the absorbed radiation may have originated from a vast distance away. Each of these components transmits and receives heat in a manner that is directly influenced by their molecular structure. Connected to a body's capability to transfer and store heat is its ability to radiate heat from its surface (specific temperatures). The two most important characteristics of thermal energy storage systems are heat transport performance and energy storage density. Nanotechnology may be effective for speeding both the melting and solidification of phase transition materials. Copper/water nanofluid is taken in a flat tube and numerically investigated for thermal transportation (She and Fan, 2018). Flow and energy transportation of metal oxide host water nanofluid is presented in the study by Ahmed et al. (2021) which is used in the PV/T system. For cooling purpose, the fluid is analyzed in the review of heat transfer science (Yang and Liu, 2018). MWCNT/water and Fe_3O_4 /water-type hybrid nanofluids are studied to analyze the convective heat transfer and pumping power through perpendicular rib tabulators (Irandoost Shahrestani et al., 2021). Three-dimensional magnetic hybrid nanofluid along with chemical reaction and thermal radiation is passed an inclined rotating sheet is presented in the study by Umar et al. (2020). Numerical approach Lobatto IIIA is used to analyze heat transport of nanofluid in three-dimensional magnetic flow in the study by Ayub et al. (2021a). Similarly, the energy transport of magnetic Carreau nanofluid has been studied by Ayub et al. (2022) using the infinite rate of shear viscosity condition. The nanofluid magnetic dipole flow is studied by Shah et al. (2022) under the effect of binary reaction and heat transportation through a cylindrical channel. The cubic autocatalytic chemical reaction has been studied for the unsteady cross nanofluid through a melting sheet in the study by Shah et al. (2021a). All the literature focused on enhancing thermal transportation using nanofluid in different circumstances and forces which is indeed the great demand of the advanced industry. Nanofluid with thermal radiation specification has been studied by Ayub et al. (2021b), Kumar et al. (2021), Raja et al. (2022), Khan et al. (2018), Raja et al. (2021), and Khan et al. (2021b). Artificial

neural networks (ANNs) are computer networks that replicate the central nervous system by stimulating nerve cells or neurons. These have a self-organizing characteristic that aids them in solving a variety of issues, making them very convenient to use in computing and algorithmic kinds. Complex challenges, particularly nonanalytical, nonlinear, and nonstationary, may be solved with ANNs because of their ability to ease high-level programming in their crude mimicry of a biological network, which can be used to handle a wide range of problems. The experimental study is carried out using artificial neural networks strategies, to simulate energy and exergy of the evacuated solar-tubes is performed in the study by Sadeghi et al. (2020), thermal conductivity model nanofluid-based study is carried out in the study by Pare and Ghosh (2021), non-Newtonian hybrid nanofluid is taken to predict the dynamic viscosity (Toghraie et al., 2020), and statistical tools applied for thermos-physical properties of nanofluid (Esfe et al., 2022). The third-grade nanofluidic model along with convective conditions has been taken through a stretchable surface which is further solved by neural technique in the study by Shoaib et al. (2021). Furthermore, ANNs are important to forecast the findings of theoretical and numerical approximation studies of nanofluidic models (Sheikholeslami et al., 2019c; Sabir et al., 2022; Zuhra et al., 2022). Levenberg–Marquardt backpropagation neural network has been applied for the computational purpose of the nanofluid model (Vakili et al., 2016; Shah et al., 2021b; Shoaib et al., 2021; Umar et al., 2021; Botmart et al., 2022).

There have been several studies on the thermophysical characteristics of nanofluids, as mentioned earlier. ANNs, on the other hand, have been widely used in nanofluid-based thermal systems because of their ability to solve complicated problems at a lower cost and time. This research focuses on the ANN technique named Levenberg–Marquardt algorithm-based backpropagation to predict the physical parameters of Williamson nanofluids flow under the effects of Joule heating and thermal radiation.

Procedural study is highlighted as follows,

- Williamson nanofluid is occupied in two-dimensional, magnetic flow stream that passes past a stretching surface in a porous medium.
- Thermal radiation force, mass diffusion, energy transfer, heat generation/absorption, and Joule heat are imposed in a fluid.
- Self-similar transformation is adopted to convert the physical model into a nonlinear differential system that has physical nondimensional variations to be computed.
- The Bvp4c technique is used to find the numerical solutions in the form of a dataset. Which is further furnished through the neural network process for analysis.
- In the NN process, the fitness functions are taken, that is, multiple responses are converted to a single response.



- > Designed backpropagation based neural networks by providing training and testing datasets. Levenberg–Marquardt algorithm is adapted to speed up the training.
- > The significance of the LMB-NN technique is illustrated through statistical tools such as mean square error, error histograms, correlation, and regression fitting graphs.
- > The analysis of variations that are Williamson parameter, Brownian motion, Prandtl number, thermophoresis, heat generation, Darcy number, Eckert number, and chemical reaction parameter velocity and temperature field are illustrated in the graphic structure.

In the remaining, a physical description of the flow model is presented in Section 2. Section 3 discusses the Levenberg–Marquardt strategy and step-by-step procedure in detail. Section 4 presents the findings of the proposed model *via* graphs and tables and discussion on each one. At last, a brief summary of the model *via* the ANN technique is presented.

2 Flow model and its mathematical construction

Let us consider a mathematical model for incompressible two-dimensional Williamson nanofluid past a stretched surface. [Figure 1](#) depicts the design of the problem with Cartesian coordinates (x, y) followed by velocity components (u, v) with fluid flow arrangement. To observe mass diffusion and heat transfer, the interface of the applied magnetization field with dynamic viscosity and a porous medium are used. The transfer of heat is augmented by supposing the thermophysical characteristics of heat generation/absorption and Joule heating with a velocity of

$\tilde{U}_w(x) = \tilde{B}x$ with \tilde{B} is the extending parameter. The basic equations of the law of conservation of mass, momentum, heat, and nanoparticles concentration associated with the abovementioned stated assumptions are as follows (Bouslimi et al., 2021).

The governing equations of the flow model are as follows.

2.1 Continuity equation

The law of conservation of mass for continuity equation in vectorial form can be written as follows:

$$\tilde{\nabla}.\vec{q}=0, \quad (1)$$

where \vec{q} is denoted as the flow velocity vector, and $\vec{\nabla}$ is known as the differential operator.

2.2 Momentum equation

According to Navier–Stokes’ equation, for the equilibrium of linear-momentum,

$$\rho_f \left[\frac{\partial \vec{\hat{q}}}{\partial t} + (\vec{\hat{q}} \cdot \vec{\nabla}) \vec{\hat{q}} \right] + \frac{\mu}{K} \vec{\hat{q}} = \vec{F}_e + \vec{\nabla} \cdot \vec{S}. \quad (2)$$

2.3 Energy equation

The constitutive equation provides the following energy efficiency for heat conduction without the impact of viscous dissipation.

$$(\rho c_p)_f \left[\frac{\partial \bar{T}}{\partial t} + (\bar{q} \cdot \bar{\nabla}) \bar{T} \right] + \bar{q} \cdot \bar{q}' = (\rho c_p)_p \left[\frac{\partial \bar{T}}{\partial \tau_\infty} (\bar{\nabla} \bar{T} \cdot \bar{\nabla} \bar{T}) + \bar{D}_B (\bar{\nabla} \bar{C} \cdot \bar{\nabla} \bar{T}) \right] + \bar{\nabla} \cdot (k \bar{\nabla} \bar{T}) + Q(\bar{T} - \bar{T}_\infty) + J_h. \quad (3)$$

2.4 Conservation equation of the nanoparticle concentration

The nanoparticle concentration volume fraction equation in the occurrence of a homogeneous chemical reaction becomes

$$\frac{\partial \tilde{C}}{\partial \tilde{t}} + (\vec{q} \cdot \vec{\nabla}) \tilde{C} + R^* (\tilde{C} - \tilde{C}_\infty) = \frac{\tilde{D}_T}{\tilde{T}_\infty} \tilde{\nabla}^2 \tilde{T} + \tilde{D}_B \tilde{\nabla}^2 \tilde{C}. \quad (4)$$

The Cauchy stress tensor (\tilde{S}) for the Williamson nanofluid is defined as (Alhowaity et al., 2022b)

$$\tilde{S} = \bar{\tau} - \tilde{P}\bar{I}, \quad (5)$$

$$\bar{\tau} = \left(\frac{\mu_0 - \mu_\infty}{1 - \Gamma \dot{\gamma}} + \mu_\infty \right) \bar{A}_1, \quad (6)$$

where $(\mu_0, \mu_\infty) \rightarrow$ limiting viscosity at zero and at an infinite shear rate, respectively, $\bar{\tau} \rightarrow$ extra stress tensor, $\bar{I} \rightarrow$ unit tensor, $(\Gamma > 0) \rightarrow$ time constant, $\bar{A}_1 \rightarrow$ first Rivlin–Erickson tensor, $\bar{P} \rightarrow$ pressure, and $\dot{\gamma} \rightarrow$ is defined as:

$$\pi = \text{trace}(\bar{A}_1)^2, \dot{\gamma} = \sqrt{\frac{\pi}{2}}. \quad (7)$$

Here, it is considered the case for $\Gamma \dot{\gamma} < 1$ and $\mu_\infty = 0$; thus, Eq. 6 can be transformed into the following form:

$$\bar{\tau} = \left(\frac{\mu_0}{1 - \Gamma \dot{\gamma}} \right) \bar{A}_1 = \mu_0 (1 + \Gamma \dot{\gamma}) \bar{A}_1. \quad (8)$$

According to Eq. 8, the binomial expression may be used. The two-dimensional boundary layer equations for the flow may be stated as follows:

$$\frac{\partial \tilde{u}}{\partial x} + \frac{\partial \tilde{v}}{\partial y} = 0, \quad (9)$$

$$\frac{\partial \tilde{u}}{\partial x} \tilde{u} + \frac{\partial \tilde{u}}{\partial y} \tilde{v} + \frac{\nu}{K} \tilde{u} + \frac{\tilde{\sigma} \tilde{B}_0^2}{\tilde{\rho}} \tilde{u} = \nu \frac{\partial^2 \tilde{u}}{\partial y^2} + \sqrt{2} \nu \Gamma \frac{\partial^2 \tilde{u}}{\partial y^2} \frac{\partial \tilde{u}}{\partial y}, \quad (10)$$

$$\frac{\partial \tilde{T}}{\partial x} \tilde{u} + \frac{\partial \tilde{T}}{\partial y} \tilde{v} + \frac{1}{(\tilde{\rho} \tilde{c}_p)_f} \frac{\partial \tilde{q}_r}{\partial y} = \alpha \frac{\partial^2 \tilde{T}}{\partial y^2} + \frac{(\tilde{\rho} \tilde{c}_p)_p}{(\tilde{\rho} \tilde{c}_p)_f} \left[\tilde{D}_T \left(\frac{\partial \tilde{T}}{\partial y} \right)^2 + \tilde{D}_B \left(\frac{\partial \tilde{C}}{\partial y} \frac{\partial \tilde{T}}{\partial y} \right) \right] + \frac{Q}{(\tilde{\rho} \tilde{c}_p)_f} (\tilde{T} - \tilde{T}_\infty) + \frac{\tilde{\sigma} \tilde{B}_0^2(t)}{(\tilde{\rho} \tilde{c}_p)_f} \tilde{u}^2, \quad (11)$$

$$\frac{\partial \tilde{C}}{\partial x} \tilde{u} + \frac{\partial \tilde{C}}{\partial y} \tilde{v} + R^* (\tilde{C} - \tilde{C}_\infty) = \frac{\tilde{D}_T}{\tilde{T}_\infty} \frac{\partial^2 \tilde{T}}{\partial y^2} + \tilde{D}_B \frac{\partial^2 \tilde{C}}{\partial y^2}. \quad (12)$$

Also, the following nomenclature is used: $(\tilde{u}, \tilde{v}) \rightarrow$ velocity components, $\alpha \rightarrow$ thermal diffusivity, $\tilde{\rho} \rightarrow$ density of the fluid, $\nu \rightarrow$ kinematic viscosity of the fluid, $\tilde{B}_0 \rightarrow$ uniform magnetic field, $(\tilde{T}, \tilde{T}_\infty) \rightarrow$ fluid and ambient fluid temperature, respectively, $\tilde{D}_B \rightarrow$ coefficient of Brownian diffusion, $\tilde{D}_T \rightarrow$ thermophoretic diffusivity, $\tilde{\sigma} \rightarrow$ electrical-conductivity, $\tilde{c}_p \rightarrow$ specific thermal at fixed pressure, $R^* \rightarrow$ reaction rate of constructive/destructive, $(\tilde{C}) \rightarrow$ concentration nanoparticles, and \tilde{C}_∞ is ambient nanoparticle concentration.

Nonlinear thermal radiation and Joule heating are connected in the energy equation. In the energy equation, the viscous dissipation is expected to be very little that it may be ignored. Homogeneous chemical processes have an effect on concentration equations.

The corresponding boundary conditions for the present fluidic problem are given as follows:

$$\text{At } \hat{y} = 0: \tilde{u} = \tilde{U}_w(x), \tilde{v} = 0, \tilde{T} = \tilde{T}_w, \tilde{D}_B \frac{\partial \tilde{C}}{\partial y} + \frac{\tilde{D}_T}{\tilde{T}_\infty} \frac{\partial \tilde{T}}{\partial y}, \quad (13)$$

$$\text{As } \hat{y} \rightarrow \infty: \tilde{u} \rightarrow 0, \tilde{v} \rightarrow 0, \tilde{T} \rightarrow \tilde{T}_\infty, \tilde{C} \rightarrow \tilde{C}_\infty, \quad (14)$$

where $\tilde{U}_w(x) = \tilde{B}x \rightarrow$ stretching surface velocity, $(\tilde{B} > 0) \rightarrow$ stretching rate, and $\tilde{q}_r \rightarrow$ radiation heat flux and is defined as follows:

$$\tilde{q}_r = -\frac{\partial \tilde{T}^4}{\partial \hat{y}} \frac{4\tilde{\sigma}^*}{3k^*} = -\frac{16\tilde{\sigma}^*}{3k^*} \tilde{T}^3 \frac{\partial \tilde{T}}{\partial \hat{y}}, \quad (15)$$

$$\therefore \frac{1}{(\tilde{\rho} \tilde{c}_p)_f} \frac{\partial}{\partial \hat{y}} \left(\tilde{q}_r \right) = \frac{1}{(\tilde{\rho} \tilde{c}_p)_f} \frac{\partial}{\partial \hat{y}} \left(-\frac{\partial \tilde{T}^4}{\partial \hat{y}} \frac{4\tilde{\sigma}^*}{3k^*} \right) = -\frac{16\tilde{\sigma}^*}{3k^* (\tilde{\rho} \tilde{c}_p)_f} \frac{\partial}{\partial \hat{y}} \left(\tilde{T}^3 \frac{\partial \tilde{T}}{\partial \hat{y}} \right). \quad (16)$$

By substituting Eqs 15 and 16 in Eq. 11, we obtain

$$\frac{\partial \tilde{T}}{\partial x} \tilde{u} + \frac{\partial \tilde{T}}{\partial y} \tilde{v} = \alpha \frac{\partial^2 \tilde{T}}{\partial y^2} + \frac{(\tilde{\rho} \tilde{c}_p)_p}{(\tilde{\rho} \tilde{c}_p)_f} \left[\tilde{D}_T \left(\frac{\partial \tilde{T}}{\partial y} \right)^2 + \tilde{D}_B \left(\frac{\partial \tilde{C}}{\partial y} \frac{\partial \tilde{T}}{\partial y} \right) \right] + \frac{16\tilde{\sigma}^*}{3k^* (\tilde{\rho} \tilde{c}_p)_f} \frac{\partial}{\partial \hat{y}} \left(\tilde{T}^3 \frac{\partial \tilde{T}}{\partial \hat{y}} \right) + \frac{Q}{(\tilde{\rho} \tilde{c}_p)_f} (\tilde{T} - \tilde{T}_\infty) + \frac{\tilde{\sigma} \tilde{B}_0^2(t)}{(\tilde{\rho} \tilde{c}_p)_f} \tilde{u}^2. \quad (17)$$

The nondimensional variables and similarity transformations listed as follows are introduced as

$$\left. \begin{aligned} \eta = y \sqrt{\frac{\tilde{U}_w(x)}{\nu x}}, \tilde{u} = \tilde{B}x f'(\eta), \tilde{v} = -(\tilde{B}\nu)^{\frac{1}{2}} f(\eta), \\ \theta(\eta) = \frac{\tilde{T} - \tilde{T}_\infty}{\tilde{T}_w - \tilde{T}_\infty}, \quad \phi(\eta) = \frac{\tilde{C} - \tilde{C}_\infty}{\tilde{C}_w - \tilde{C}_\infty}, \end{aligned} \right\} \quad (18)$$

The equation of continuity is identically satisfied by using Eq. 18 and Eqs 10, 12, 17, coupled with Eqs 13, 14; assume the form of ordinary differential equations shown as follows:

$$f'''(\eta) (1 + \lambda f''(\eta)) + f''(\eta) f(\eta) - f'(\eta) (f'(\eta) - M - Da) = 0, \quad (19)$$

$$\begin{aligned} \theta''(\eta) + (M \circ Ec f(\eta) + Nb \phi(\eta) + Nt \theta'(\eta)) \theta'(\eta) \\ + \text{Pr} \left(R \left((1 + (\theta_w - 1) \theta(\eta))^3 \right) \theta'(\eta) \right)' \\ + Ec \circ M (f(\eta))^2 + S \theta(\eta) = 0, \end{aligned} \quad (20)$$

$$\phi''(\eta) + \left(Nt / Nb \right) \theta''(\eta) + Le (f(\eta) \phi'(\eta) - \gamma \phi(\eta)) = 0, \quad (21)$$

where the boundary conditions (13–14) after transforming into nondimensional form are given as

$$f(0) = 0, f'(0) = 1, Nt \theta'(0) + Nb \phi'(0) = 0, \theta(0) = 1, \quad (22)$$

$$f'(\infty) \rightarrow 0, \theta(\infty) \rightarrow 0, \phi(\infty) \rightarrow 0. \quad (23)$$

With the nondimensional parameters given as $(M = \frac{\tilde{\sigma} \tilde{B}_0^2}{(\tilde{\rho} \tilde{c}_p)_f}) \rightarrow$ magnetic field parameter, $(R = \frac{16\tilde{\sigma}^* \tilde{T}_\infty^3}{3k^*}) \rightarrow$ nonlinear thermal radiation parameter, $(\text{Pr} = \frac{\mu}{\alpha}) \rightarrow$ Prandtl number, $(Nb = \frac{(\tilde{\rho} \tilde{c}_p)_p \tilde{D}_B \tilde{C}_\infty}{(\tilde{\rho} \tilde{c}_p)_f \nu}) \rightarrow$ Brownian motion parameter, $(Nt = \frac{(\tilde{\rho} \tilde{c}_p)_p \tilde{D}_T (\tilde{T}_w - \tilde{T}_\infty)}{(\tilde{\rho} \tilde{c}_p)_f \nu \tilde{T}_\infty}) \rightarrow$ thermophoresis parameter, $(S = \frac{Q}{\tilde{D}_B \tilde{B}}) \rightarrow$ heat generation ($S > 0$) or absorption parameter ($S < 0$), $(Le = \frac{\nu}{\tilde{D}_B}) \rightarrow$ Lewis number, $(Da = \frac{\mu}{\rho} \tilde{B} K) \rightarrow$ Darcy number, $(Ec = \frac{\tilde{U}_w^2(x)}{\tilde{c}_p (\tilde{T}_w - \tilde{T}_\infty)}) \rightarrow$ Eckert number, $(\lambda = \Gamma x \sqrt{2\tilde{B}^3/\nu}) \rightarrow$ non-Newtonian Williamson parameter, and $(\gamma = \frac{R^*}{\tilde{B}}) \rightarrow$ chemical reaction parameter. Also, expressions for Nu_x and Cf_x are shown as follows:

$$Nu_x = \frac{x\tilde{q}_w}{k_f}(\tilde{T}_w - \tilde{T}_\infty), \quad (24)$$

$$Cf_x = \frac{\tau_w}{\tilde{\rho}\tilde{U}_w^2(x)}. \quad (25)$$

The Sherwood number Sh_x , which represents a nondimensional mass flow, is currently zero. Here, \tilde{q}_w indicates heat flux, and τ_w denotes shear stress of the wall along a stretching surface, respectively, and their mathematical expressions are given as follows:

$$\tilde{q}_w = -\alpha\left(\frac{\partial\tilde{T}}{\partial y}\right)_{y=0} + (\tilde{q}_r)_y, \quad (26)$$

$$\tilde{\tau}_w = \tilde{\mu}_f\left(1 + \frac{\Gamma}{2}\frac{\partial\tilde{u}}{\partial y}\right)\frac{\partial\tilde{u}}{\partial y}\bigg|_{y=0}. \quad (27)$$

The dimensionless formulation of Eqs 24 and 25 after substituting Eqs 26 and 27 are as follows:

$$\frac{Nu_x}{\sqrt{Re_x}} = -(1 + R\theta_w^3)\theta'(0), \quad (28)$$

$$C_{fx}\sqrt{Re_x} = \left(1 + \frac{\lambda}{2}f''(0)\right)f''(0), \quad (29)$$

where $\sqrt{Re_x}$ is the Reynolds number relative to the stretching velocity $\tilde{U}_w(x)$.

3 Design methodology/neural network modeling

Machine learning algorithms (MLAs) have been created to handle real-world problems arising in various fields of science, engineering, and mathematics. Depending on the training approach, these MLAs can be divided into three categories.

- Reinforcement learning algorithms (RLAs)
- Unsupervised learning algorithms (ULAs)
- Supervised learning algorithms (SLAs)

The supervised learning algorithm (SLA) is quite similar to how a human learns, by considering the fact that humans solve exercise problems or datasets to obtain new knowledge. The current study employs SLA in which adjustments of weights are constructed based on the comparison and correlation with some target output. For weight adjustment, a teaching signal is fed into the neural networks (NNs) which are called a training sample or training dataset. In SLA, the correct output is what the model is alleged to provide for the given input. Errors are backpropagated through the scheme, allowing the scheme to adjust the weights that supervise the neural networks (NNs).

The brief deliberation of the results for the propose Levenberg–Marquardt learning algorithm for backpropagated neural networks (LMLA-BPNNs) subjected to the Joule's heating effect of MHD Williamson nanofluid flow through a porous medium in the rheology of nonlinear thermal radiation and chemical reaction with variable heat generation/absorption (MHD-WNF-HGA) has been evaluated in this part. The partial differential equations (PDEs) prescribing MHD-WNF-HGA are converted to set ordinary differential equations (ODEs) by employing appropriate transformation. The set of differential Eqs 19–21 contains a detailed mathematical strategy for reproducing results employing a numerical scheme, and the fluidic problem MHD-WNF-HGA is tackled down with the help of “bvp4c” built-in function by MATLAB software for nine variants where higher order nondimensional system of ODEs are transformed to first-order ODEs.

$$f'''(\eta) = \frac{((f'(\eta) - M - Da)f'(\eta) - f(\eta)f''(\eta))}{(1 + \lambda f''(\eta))}, \quad (30)$$

$$\theta''(\eta) = -\frac{\Pr\left(\frac{3R(\theta_w - 1)(1 + (\theta_w - 1)\theta(\eta))^2(\theta'(\eta))^2 + S\theta(\eta) + Nb\theta'(\eta)\phi(\eta) + f(\eta)\theta'(\eta) + Nt(\theta'(\eta))^2 + M \circ Ec(f(\eta))^2}{(1 + \Pr \circ R(1 + (\theta_w - 1)\theta(\eta))^3)}\right)}{(1 + \Pr \circ R(1 + (\theta_w - 1)\theta(\eta))^3)}, \quad (31)$$

$$\phi''(\eta) = -\left(\left(Nt/Nb\right)\theta''(\eta) + Le(f(\eta)\phi'(\eta) - \gamma\phi(\eta))\right), \quad (32)$$

$$f(\eta) = X_1,$$

$$f'(\eta) = X_2,$$

$$f''(\eta) = X_3,$$

$$X'_3 = \frac{(X_2 - M - Da)X_2 - X_1X_3}{(1 + \lambda f''X_3)},$$

$$\theta(\eta) = X_4,$$

$$\theta'(\eta) = X_5,$$

$$X'_5 = -\frac{\Pr\left(\frac{3R(\theta_w - 1)(1 + (\theta_w - 1)X_4)^2(X_5)^2 + SX_4 + NbX_4X_6 + X_1X_5 + Nt(X_5)^2 + M \circ Ec(X_1)^2}{(1 + \Pr \circ R(1 + (\theta_w - 1)X_4)^3)}\right)}{(1 + \Pr \circ R(1 + (\theta_w - 1)X_4)^3)},$$

$$\phi(\eta) = X_6,$$

$$\phi'(\eta) = X_7,$$

$$X'_7 = -\left(\left(Nt/Nb\right)X'_5 + Le(X_1X_7 - \gamma X_6)\right). \quad (33)$$

With the boundary conditions,

$$\begin{aligned} X_a(1) = 0, X_a(2) = 1, X_a(4) = 1, NtX_a(5) + NbX_a(7) = 0, \\ X_b(2) = 0, X_b(4) = 0, X_b(6) = 0. \end{aligned} \quad (34)$$

Taking both into account,

$$f'''(\eta) = X'_3, \theta''(\eta) = X'_5, \phi''(\eta) = X'_7. \quad (35)$$

The dataset formation in the form of a numerical solution by employing “bvp4c” built-in function using MATLAB by variation of magnetic field quantity (M), non-Newtonian Williamson parameter (λ), nonlinear thermal radiation parameter (R), Darcy number (Da), heat generation/absorption parameter (S), ratio-temperature (θ_w),

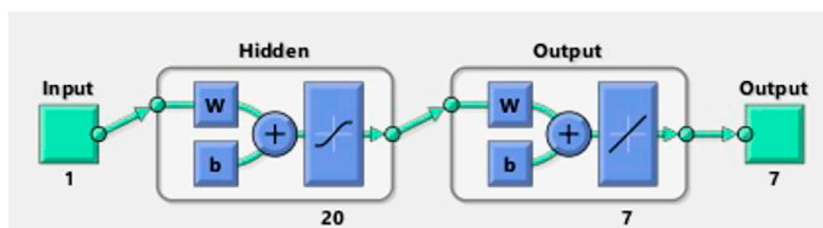


FIGURE 2
Neural networks for MHD-WNF-HGA.

thermophoresis parameter (Nt), chemical reaction parameter (γ), and Lewis number (Le). The transformed set of Eqs 19–21 which characterize the fluidic model representing MHD-WNF-HGA, the suggested LMLA-BPNN solver is accomplished by exerting neural network (NN) toolbox in MATLAB software by operating “nftool”, a built-in function. LMLA-BPNN receives knowledge via learning and stored that knowledge within interneuron connections “strengths”, which is expressed in the form of numerical values called “weights” which has a two-layered structure (input layer, hidden layer, and output layer). The output signal values for a newly testing input signal values are computed using these weights.

The “input layer” presents a pattern to the network, which then interconnects with one or more than one “hidden layer” where the actual computing is carried out via a system of weighted “connections”. The hidden layers then connect to an “output layer,” where the result is displayed as output. The artificial neural networks (ANNs) architecture is composed of 20 highly processing elements (neurons) interconnected in a parallel way to solve the fluidic problem with a sigmoid activation function. The sigmoid activation function is an S-shaped nonlinearly smooth function having input values ranging from +1 to 0, as illustrated in Figure 2. However, Figure 3 shows the block architecture of the process flow. The aim of determining the approximated solution of the proposed LMLA-BPNN is the reference dataset for training, validation, and testing purposes. The validity, reliability, and convergence of the LMLA-BPNN based on a comprehensive study of regression analysis, accuracy assessments, and histogram analysis supervised for the MHD-WNF-HGA fluidic model, which is sufficiently detailed graphically and numerically in Table 1.

For flow, energy, and nanoparticle concentration distribution of MHD-WNF-HGA, the reference dataset is built up that comprises nine scenarios with cases of LMLA-BPNN. The bvp4c built-in function technique is in collaboration with LMLA-BPNN for η between 0 and 10 having equidistance of 0.01 s used in all processes of each case. The acquired datasets are determined as reference outcomes in terms of $(f', \theta, \phi(\eta))$. Table 1 displays the numerical solutions of LMLA-BPNN for

variants of $(f', \theta, \phi(\eta))$ for MHD-WNF-HGA in terms of MSE, that is, training data (determine model parameters), validation data (yardstick to overfitting), testing data (final scoring of the model) and production (predict output), backpropagated networks, time taken, and total iterations/epochs, for all the scenarios connected with MHD-WNF-HGA.

4 Result interpretation

The designed LMLA-BPNN outcomes for the MHD-WNF-HGA fluid model have been illustrated in Figures 4–13 for various positions (scenarios) of I–IX. Figures 4A–13A is interpreting convergence of training data, validation data, and trying data progression through the epochs index for finding the cases of M , Da , and λ for $f'(\eta)$; the case of R , S , and θ_w for $\theta(\eta)$; and finally, the cases of Nt , γ , and Le $\phi(\eta)$. The magnificent validation performance attained at epochs 578, 239, 111, 141, 379, 401, 480, 110, and 218 with mean squared error (MSE) almost 2.2485×10^{-10} , 8.2744×10^{-9} , 2.3708×10^{-9} , 4.6156×10^{-9} , 1.1175×10^{-9} , 1.1155×10^{-8} , 1.8823×10^{-9} , 1.2153×10^{-9} , and 3.2418×10^{-10} in times 12, 05, 02, 03, 06, 10, 09, 03 and 05 s, respectively. It is estimated that the influence of all the obtained lines is smooth and leads to the stability point, indicating that the performance is perfect and ideal. According to the relative Table 1 and figures, the performance approach will be better by lowering MSE values. The smaller the MSE values, the more effective and precise the performance of the given approach is likely to be. Figures 4B–13B reveals the authenticity that LMLA-BPNN is precise, accurate, and efficiently convergent for solving the cases of M , Da , and λ for $f'(\eta)$; the case of R , S , and θ_w for $\theta(\eta)$; and finally, the cases of Nt , γ , and Le $\phi(\eta)$. Figures 4B–13B demonstrates the gradient and Mu values for all the scenarios in the time duration for the training in recognizing another vector. The process is updating constantly during training. The training is terminated based on the number of validations checks and on the magnitude of the gradient. As the training approaches to a minimum level of performance, gradient will become very small. The training

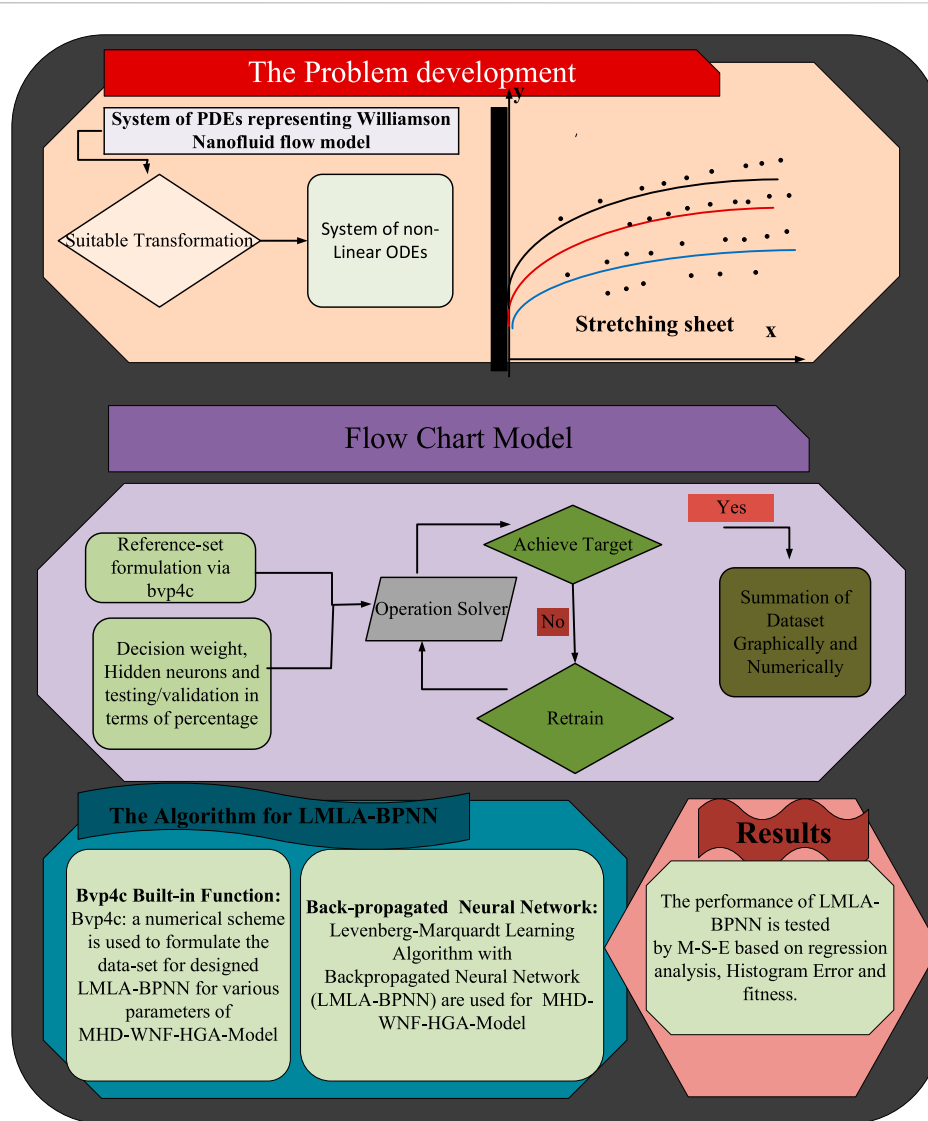


FIGURE 3
Flow architecture of the MHD-WNF-HGA model.

will stop if the magnitude of the gradient become less than 1.0×10^{-5} . μ is the adaptive parameter of LMLA-BPNN, which is directly influenced on error convergence. The associated values of gradient are 9.9774×10^{-8} , 1.9235×10^{-7} , 7.0696×10^{-8} , 9.875×10^{-8} , 9.997×10^{-8} , 9.9587×10^{-8} , 9.9421×10^{-8} , 4.7068×10^{-8} , and 9.9582×10^{-8} , while μ is 1×10^{-9} , 1×10^{-9} , 1×10^{-9} , 1×10^{-9} , 1×10^{-9} , 1×10^{-8} , 1×10^{-8} , 1×10^{-9} , and 1×10^{-10} with epoch 578, 239, 111, 141, 379, 401, 480, 110, and 218, respectively. Result interpretation shows that enhancing the epoch can cause a reduction in μ and gradient values.

Figures 4C–13C represent the fitness analysis graphs for the proposed fluidic and the error occurred due to the variations of targeted solutions and reference solutions. The graphical

representation indicates that the target result overlays the reference outlines of the LMLA-BPNN solver for all four cases with scenarios, indicating that the framework for the neural network (NN) design validates the accuracy of the solution.

After neural network training, the error histogram analysis plotted in Figures 4D–13D describes the distribution of error calculated from the zero axes. The error analysis and error values clarify the difference between the expected values and the targeted values. For six different scenarios of the LMLA-BPNN model, the average value of the error bin almost contrasts with the zero-line error adjoining. The average error bin comparing baseline line error which has surrounding errors for six different circumstances of the MHD-WNF-HGA model is -5.1×10^{-07} , 6.39×10^{-06} , 1.47×10^{-05} , -1.1×10^{-05} ,

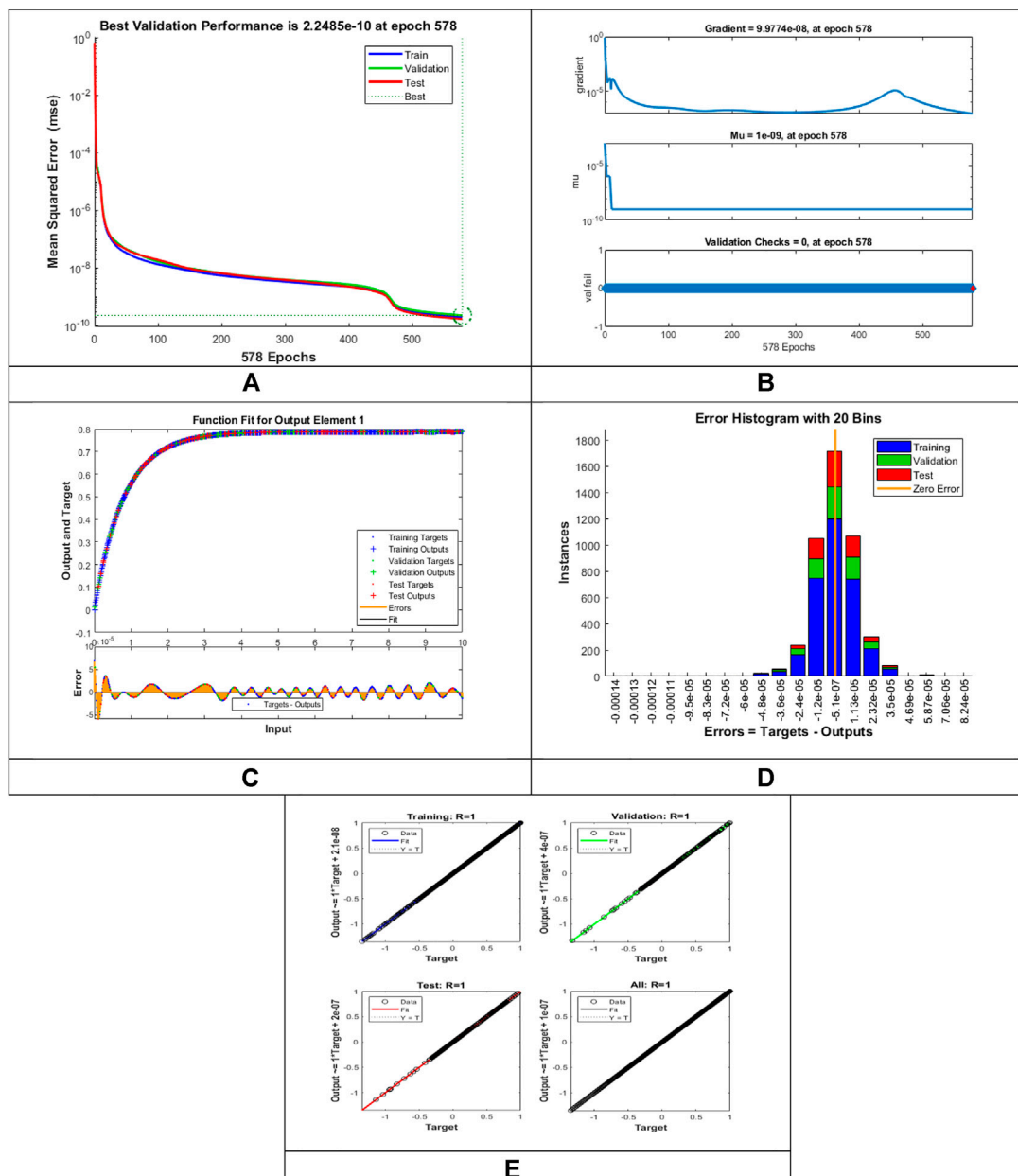


FIGURE 4

Pictorial illustration for the LMLA-BPNN base on variants of M vs $f'(\eta)$ for MHD-WNF-HGA. (A) M-S-E demonstration, (B) transition state analysis, (C) curve fitting, (D) error histogram, and (E) regression analysis.

1.08×10^{-05} , 8.17×10^{-06} , 1.85×10^{-05} , 5.71×10^{-06} , and 3.06×10^{-06} . According to the error histogram analysis, the maximum number of error values collapse over the zero-line, indicating that LMLA-BPNN is an accurate algorithm for all the cases of each scenario. The network is next validated by creating a regression plot, which depicts the relationship between the network, outputs, and the target values. The network outputs and the target values would be exactly equal if the training is

perfect. The results are shown in Figures 5E–13E. The three axes demonstrate the testing, validation, and training of the data. The perfect result-output = targets is shown in each axis of the dashed line. The solid line demonstrates the best fit linear regression line between the output values and target values, and the values of R indicate their relationship. During this computation, the regression analysis $R = 1$ indicates an exact linear relationship between the values of output and target

TABLE 1 LMLA-BPBB's outcomes for scenario I of MHD-WNF-HGA.

| Scenario | Training | Validation | Testing | Performance | Gradient | Mu | Epoch | Time(s) |
|----------|---------------------------|---------------------------|---------------------------|------------------------|-----------------------|------------------------|-------|---------|
| 1 | 1.95310×10^{-10} | 2.24846×10^{-10} | 1.69148×10^{-10} | 1.95×10^{-10} | 9.98×10^{-8} | 1.00×10^{-9} | 578 | 12 |
| 2 | 5.54977×10^{-9} | 8.27443×10^{-9} | 7.44496×10^{-9} | 5.27×10^{-9} | 1.92×10^{-7} | 1.00×10^{-9} | 245 | 05 |
| 3 | 1.86162×10^{-9} | 2.37081×10^{-9} | 1.46306×10^{-9} | 1.86×10^{-9} | 7.07×10^{-8} | 1.00×10^{-9} | 111 | 02 |
| 4 | 4.53775×10^{-9} | 4.61556×10^{-9} | 4.45013×10^{-9} | 4.54×10^{-9} | 9.87×10^{-8} | 1.00×10^{-9} | 141 | 03 |
| 5 | 8.33608×10^{-10} | 1.11751×10^{-9} | 1.04017×10^{-9} | 8.34×10^{-10} | 1.00×10^{-7} | 1.00×10^{-9} | 379 | 06 |
| 6 | 9.43417×10^{-9} | 1.11549×10^{-8} | 1.10602×10^{-8} | 9.43×10^{-9} | 9.96×10^{-8} | 1.00×10^{-8} | 401 | 10 |
| 7 | 1.50954×10^{-9} | 1.88233×10^{-9} | 2.10328×10^{-9} | 1.51×10^{-9} | 9.94×10^{-8} | 1.00×10^{-8} | 480 | 09 |
| 8 | 1.20551×10^{-9} | 1.21534×10^{-9} | 2.02206×10^{-9} | 1.21×10^{-9} | 4.71×10^{-8} | 1.00×10^{-9} | 110 | 03 |
| 9 | 2.70529×10^{-10} | 3.24184×10^{-10} | 3.08943×10^{-10} | 2.71×10^{-10} | 9.96×10^{-8} | 1.00×10^{-10} | 218 | 05 |

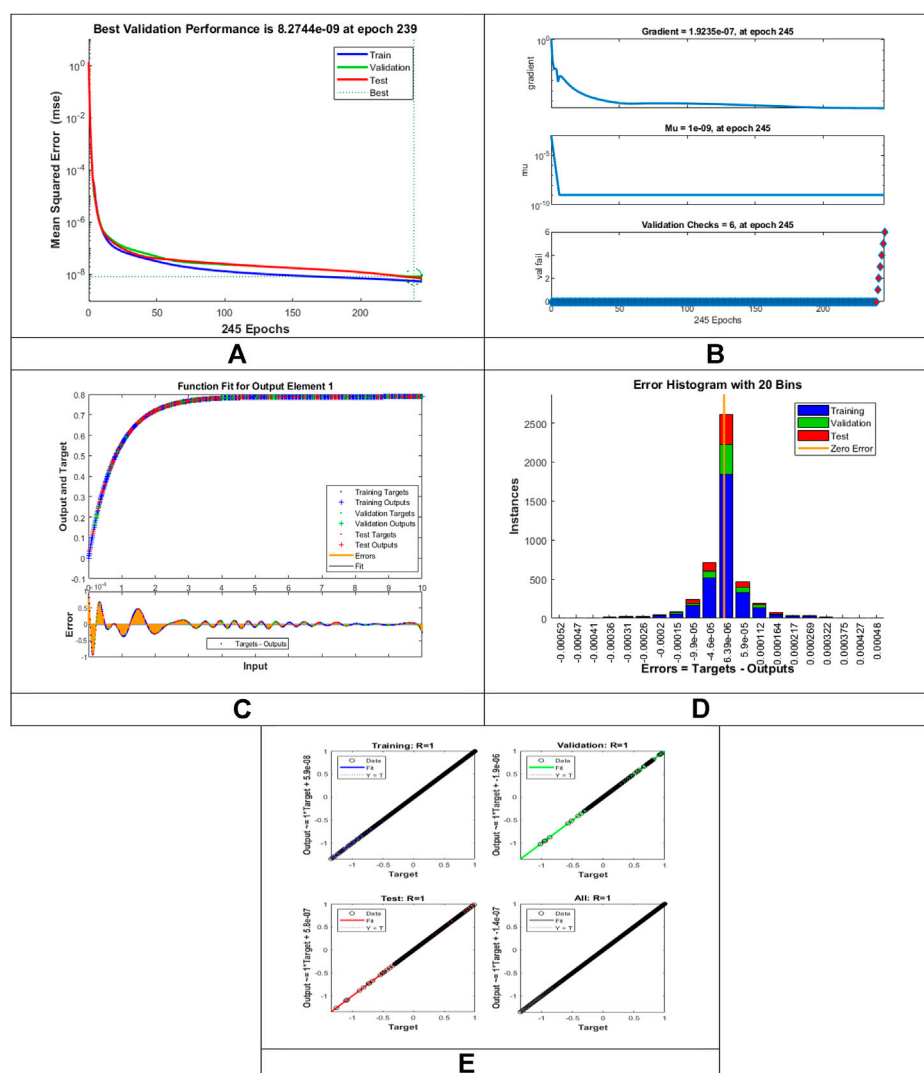


FIGURE 5

Pictorial illustration for the LMLA-BPNN base on variants of Da vs $f'(\eta)$ MHD-WNF-HGA. (A) M-S-E demonstration, (B) transition state analysis, (C) curve fitting, (D) error histogram, and (E) regression-analysis.

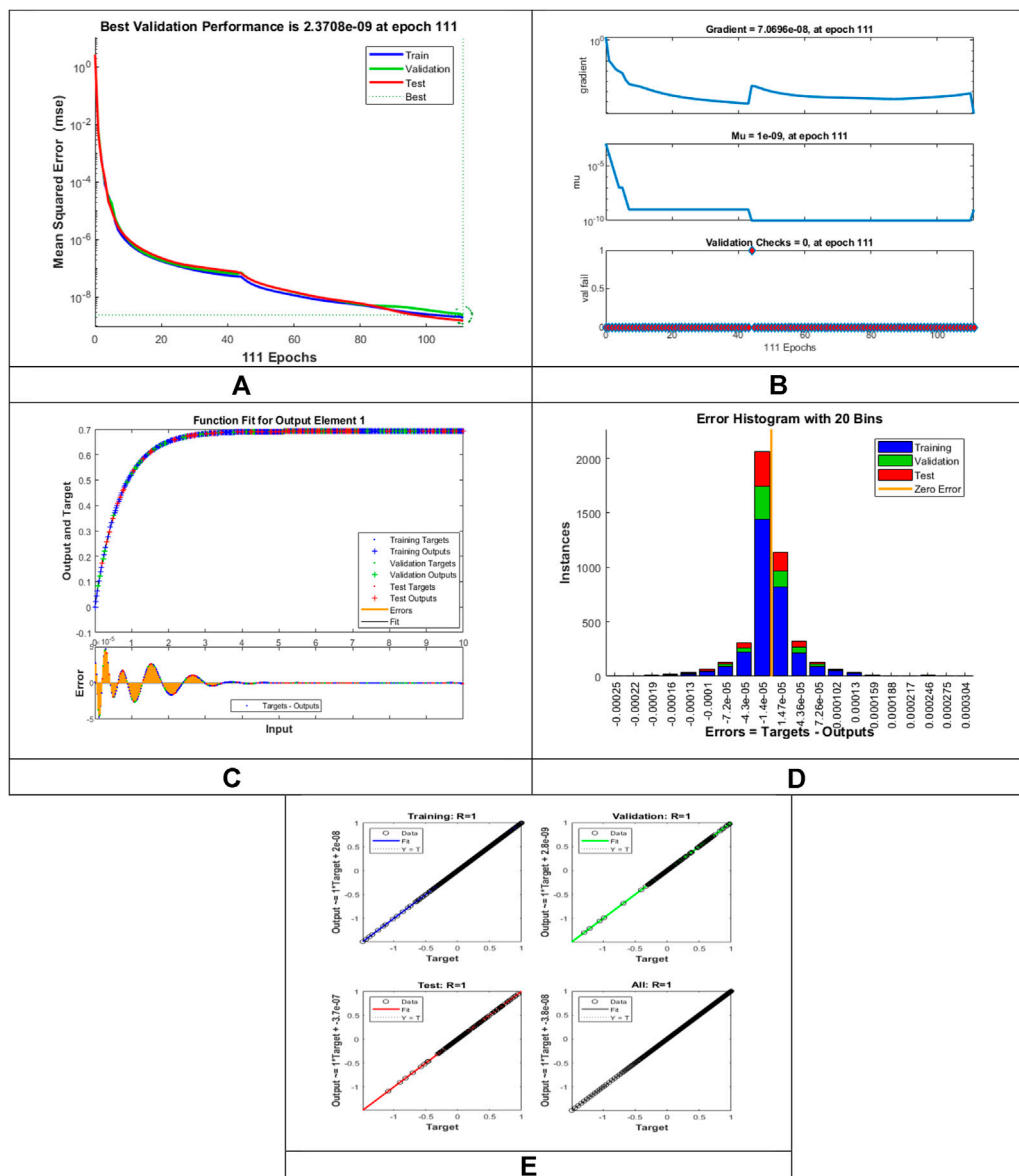


FIGURE 6

Pictorial illustration for the LMLA-BPNN base on variants of λ vs $f'(\eta)$ for MHD-WNF-HGA. (A) M-S-E demonstration, (B) transition state analysis, (C) curve fitting, (D) error histogram, and (E) regression analysis.

values, which explains the effectiveness of LMLA-BPNN resolves the MHD-WNF-HGA fluidic model.

4.1 Velocity distributions

In the rheology of thermal radiation and chemical reaction with varying heat generation/absorption, the present work analyzes the Joule heating impact of MHD Williamson nanofluid flow through a porous layer. This research

compares the effects of applied magnetic field, nonlinear thermal radiation, and heat generation/absorption. The system of partial differential equations (PDEs) is changed into a system of ordinary differential equations (ODEs) using the appropriate transformation to set an important nondimensional parameter arising in the physical fluid model and solved numerically by applying the “bvp4c” technique in MATLAB software to obtain the dataset. The numerical computation is performed for various nondimensional parameters, namely, non-Newtonian Williamson parameter (λ), nonlinear thermal radiation

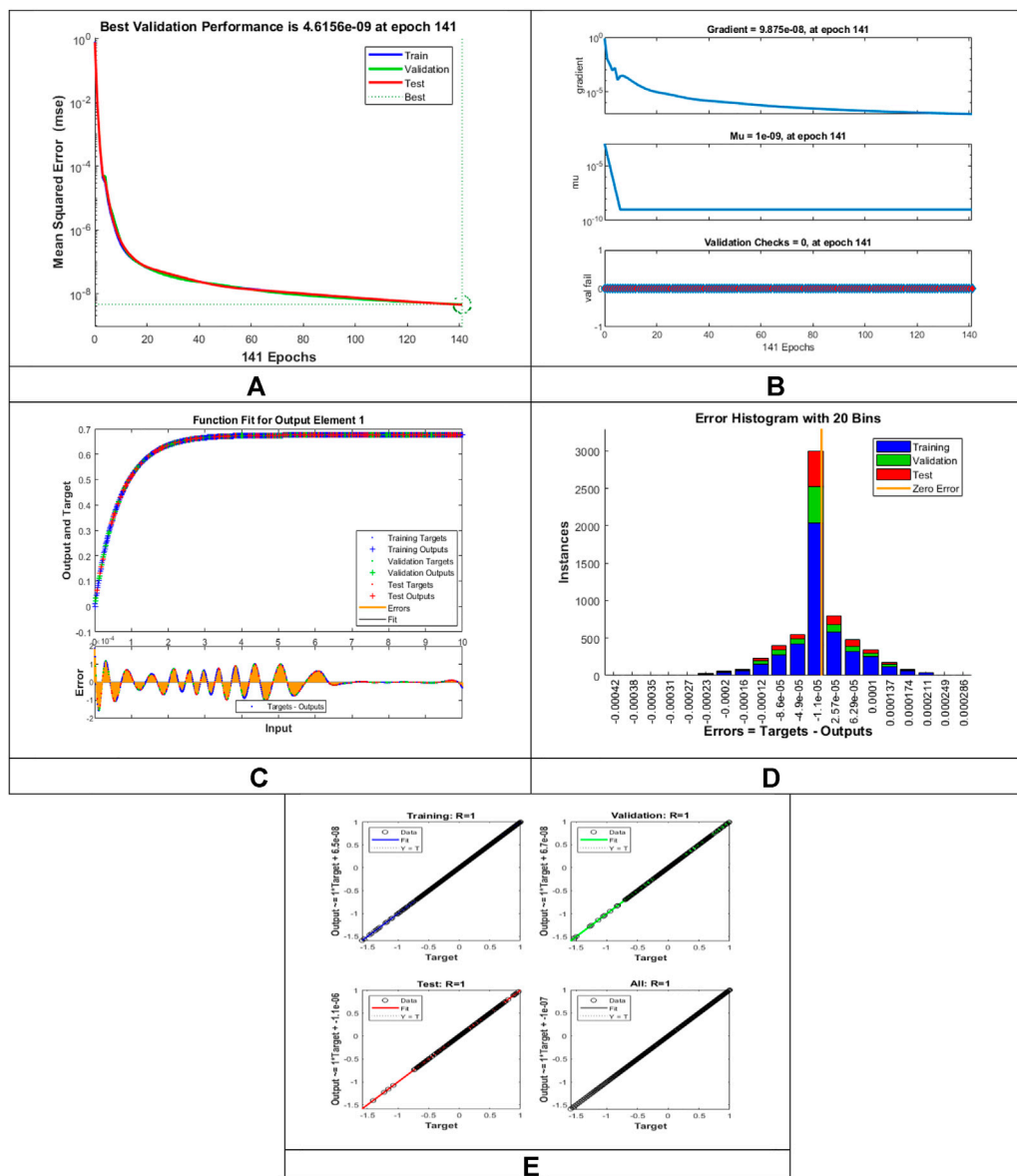


FIGURE 7

Pictorial illustration for the LMLA-BPNN base on variants of R vs $\theta(\eta)$ for MHD-WNF-HGA. (A) M-S-E demonstration, (B) transition state analysis, (C) curve fitting, (D) error histogram, and (E) regression analysis.

parameter (R), Eckert number (Ec), ratio temperature (θ_w), Darcy number (Da), magnetic field parameter (M), Brownian motion parameter (Nb), heat generation/absorption parameter (S), thermophoresis parameter (Nt), Lewis number (Le), Prandtl number (Pr), and chemical reaction parameter (γ). For computation purpose, we have assumed default values for the physical quantities in all cases (unless, otherwise specified) as follows: $R = M = Da = Nt = Nb = 0.5$, $\lambda = 0.3$, $\gamma = Le = 1.0$, $Pr = 5.0$, and $S = -0.1$. The computational values of the diverse thermophysical properties are considered for fluid

profiles, that is, momentum ($f'(\eta)$), temperature ($\theta(\eta)$), and concentration ($\phi(\eta)$) for magnetohydrodynamic (MHD) Williamson nanofluid flow over a stretching sheet, which is displayed in Figures 13–15. For numerical calculations, we used specific numerical values for parameters as shown in Table 2. The numerical finding of all the physical quantities with respect to flow distribution, energy distribution, and concentration distribution of nanoparticles along with their reference solution has been displayed with the help of graphical figures to obtain a good insight into the physical

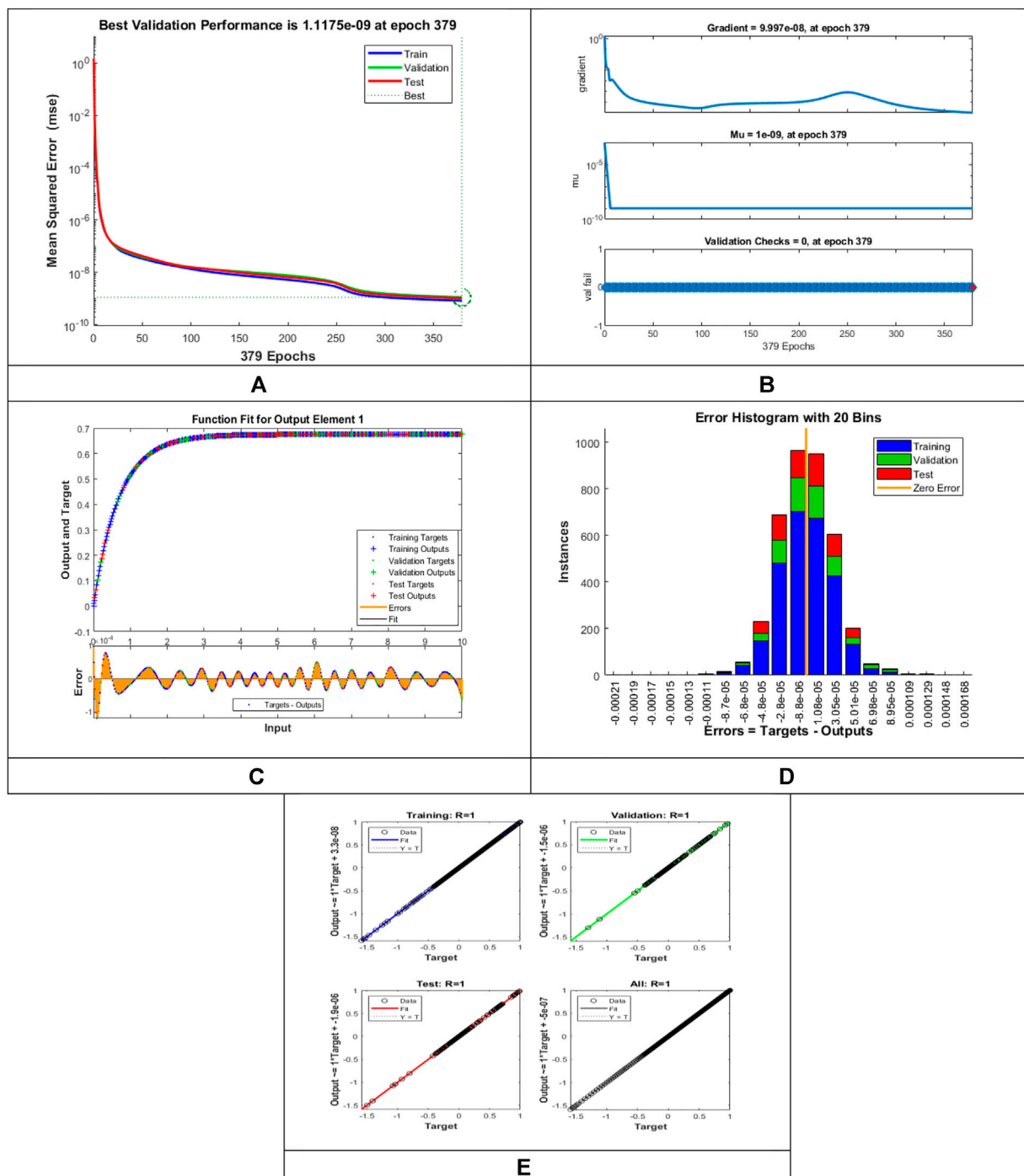


FIGURE 8

Pictorial illustration for the LMLA-BPNN base on variants of S vs $\theta(\eta)$ for MHD-WNF-HGA. (A) M-S-E demonstration, (B) transition state analysis, (C) curve fitting, (D) error histogram, and (E) regression analysis.

problem. The relative analysis of velocity distribution $f(\eta)$ with reference solution is displayed for magnetic field quantity (M), non-Newtonian Williamson quantity (λ), and Darcy number (Da) in Figures 13A,C,E, respectively. A single surface's flow rate

is completely controlled by the velocity distribution. Velocity distribution plays a significant representation to analyze the occurrence of the flow rate of the fluid. Conversely, when external forces are applied to a flowing fluid, the behavior of

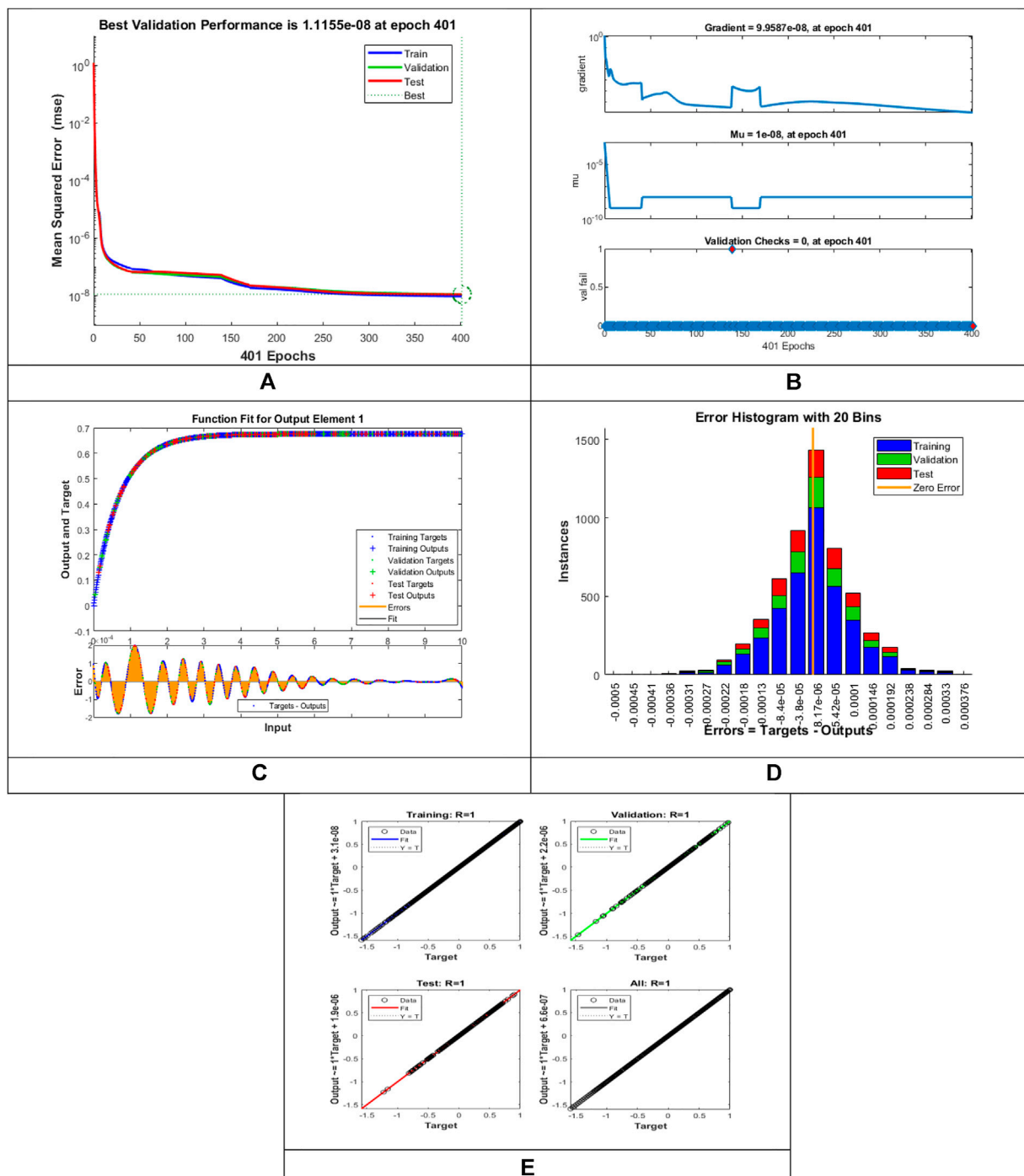


FIGURE 9

Pictorial illustration for the LMLA-BPNN base on variants of θ_w vs $\theta(\eta)$ for MHD-WNF-HGA. (A) M-S-E demonstration, (B) transition state analysis, (C) curve fitting, (D) error histogram, and (E) regression analysis.

the fluid changes, and one of these external forces is the magnetic force. Figure 13A displays the consequence of the influence of magnetic field (M) on the flow profile $f'(\eta)$ of the fluid. It is observed that impact in this sense is lowered strongly due to an

inverse relationship between velocity profile and magnetic field parameter. So by enhancing the influence of magnetic quantity means a decline in the flow speed of the fluid. When a magnetic field is used to influence a moving fluid, the particles of fluid

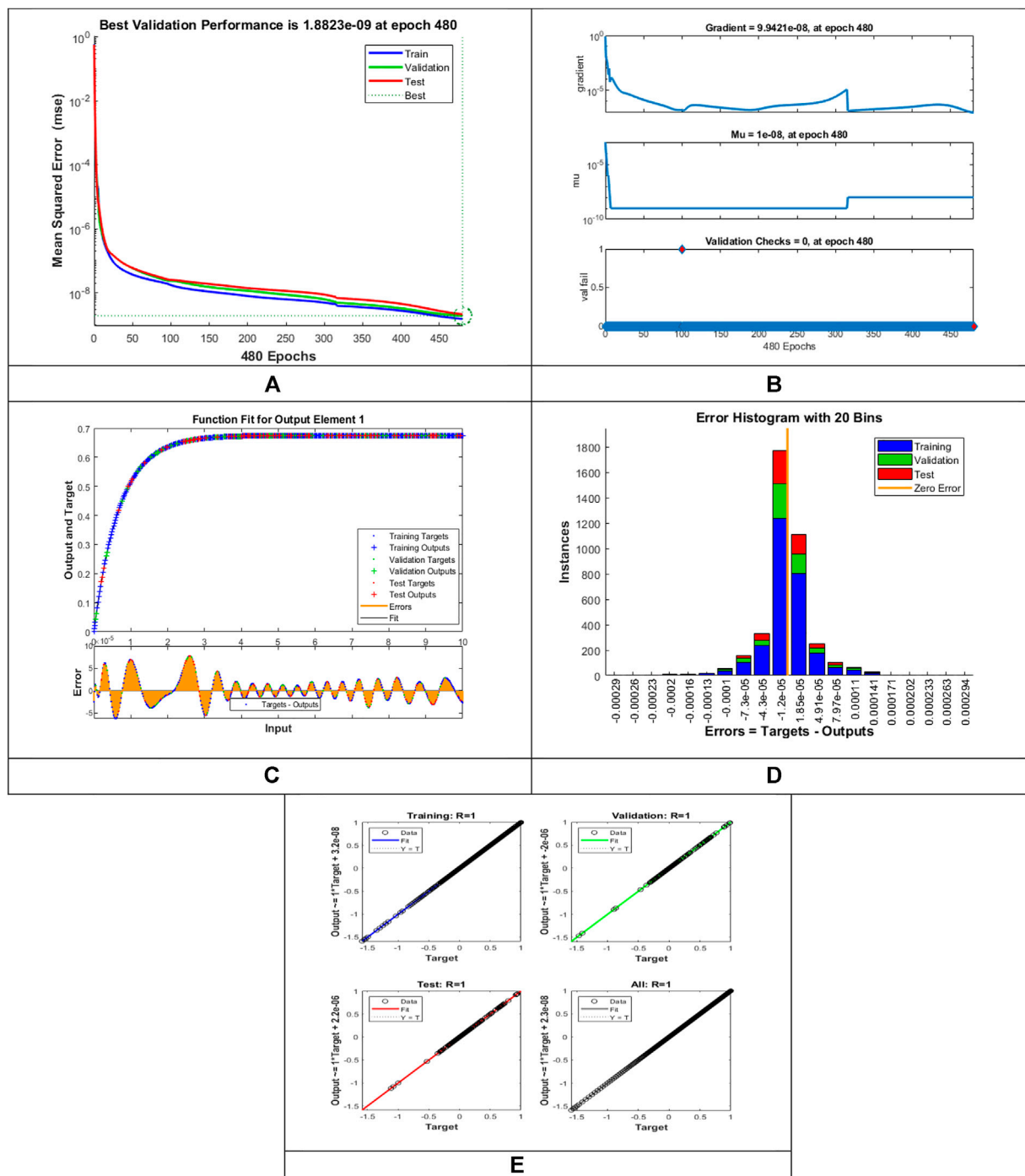


FIGURE 10

Pictorial illustration for the LMLA-BPNN base on variants of Nt vs $\phi(\eta)$ for MHD-WNF-HGA. (A) M-S-E demonstration, (B) transition state analysis, (C) curve fitting, (D) error histogram, and (E) regression analysis.

stimulated causes a countervailing force called a resistive force, which slows and resists the motion of these fluids. Furthermore, this force is upright to both the magnetic field vector and the

velocity vector which give rise to the resistive force, known as the Lorentz force generated in the direction of the fluid flow. As a result of the applied magnetic field, the Lorentz force emerges,

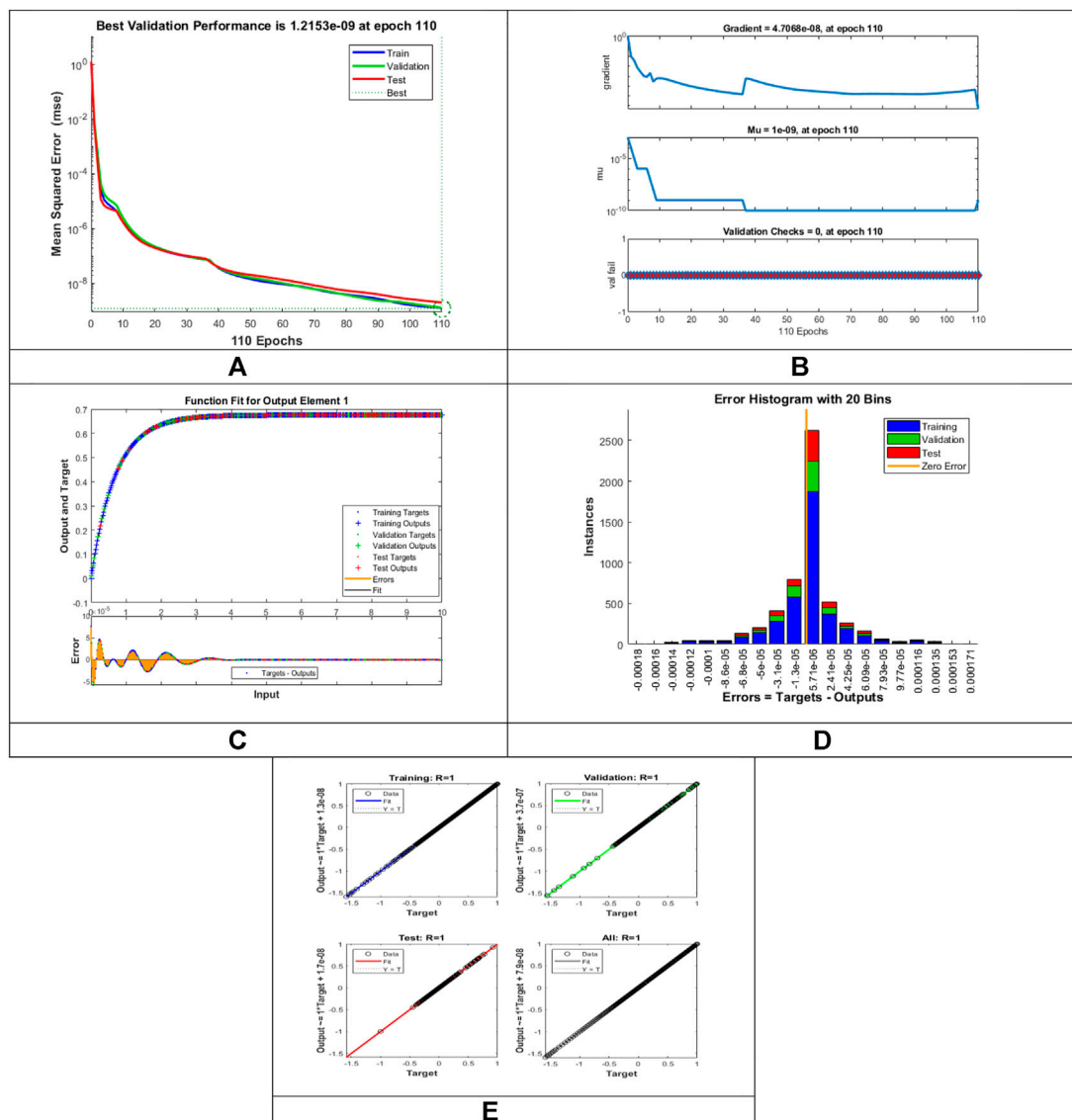


FIGURE 11

Pictorial illustration for the LMLA-BPNN base on variants of γ vs $\phi(\eta)$ for MHD-WNF-HGA. (A) M-S-E demonstration, (B) transition state analysis, (C) curve fitting, (D) error histogram, and (E) regression analysis.

opposing the flow and reducing fluid viscosity. The existence of a magnetic field causes a drag force, which causes to lower down the motion of the fluid. Figure 13C presents the impact of Darcy number (Da) on velocity distribution. It is illustrated from the figure that the influence of larger values of (Da) causes a decrease in velocity distribution. Physically, the porous media with a network of tiny voids known as pores that are disrupted by the fluids as it travels through this medium. Simultaneously, the porosity of a porous medium affects the permeability of the fluid through it. In addition, the higher the Darcy number (Da), the larger the conflict of the porosity in

permeable media which leads to the movement of fluid on one hand, and the fluid viscosity on the other hand, resulting a decline in fluid velocity. The association between the non-Newtonian Williamson parameter (λ) and the velocity distribution is shown in Figure 13E. A rise in a non-Newtonian Williamson parameter (λ) allows retardation in the velocity distribution $f'(\eta)$ which reduces the movement of fluid velocity. The absolute error (AE) analysis is shown in Figures 13B,D,F for (M), (Da), and (λ) to verify the correctness criterion. The numeric output of AE for (ε) lies in the range $10^{-8} - 10^{-3}$, $10^{-8} - 10^{-4}$, and $10^{-8} - 10^{-1}$ for (M), (Da), and

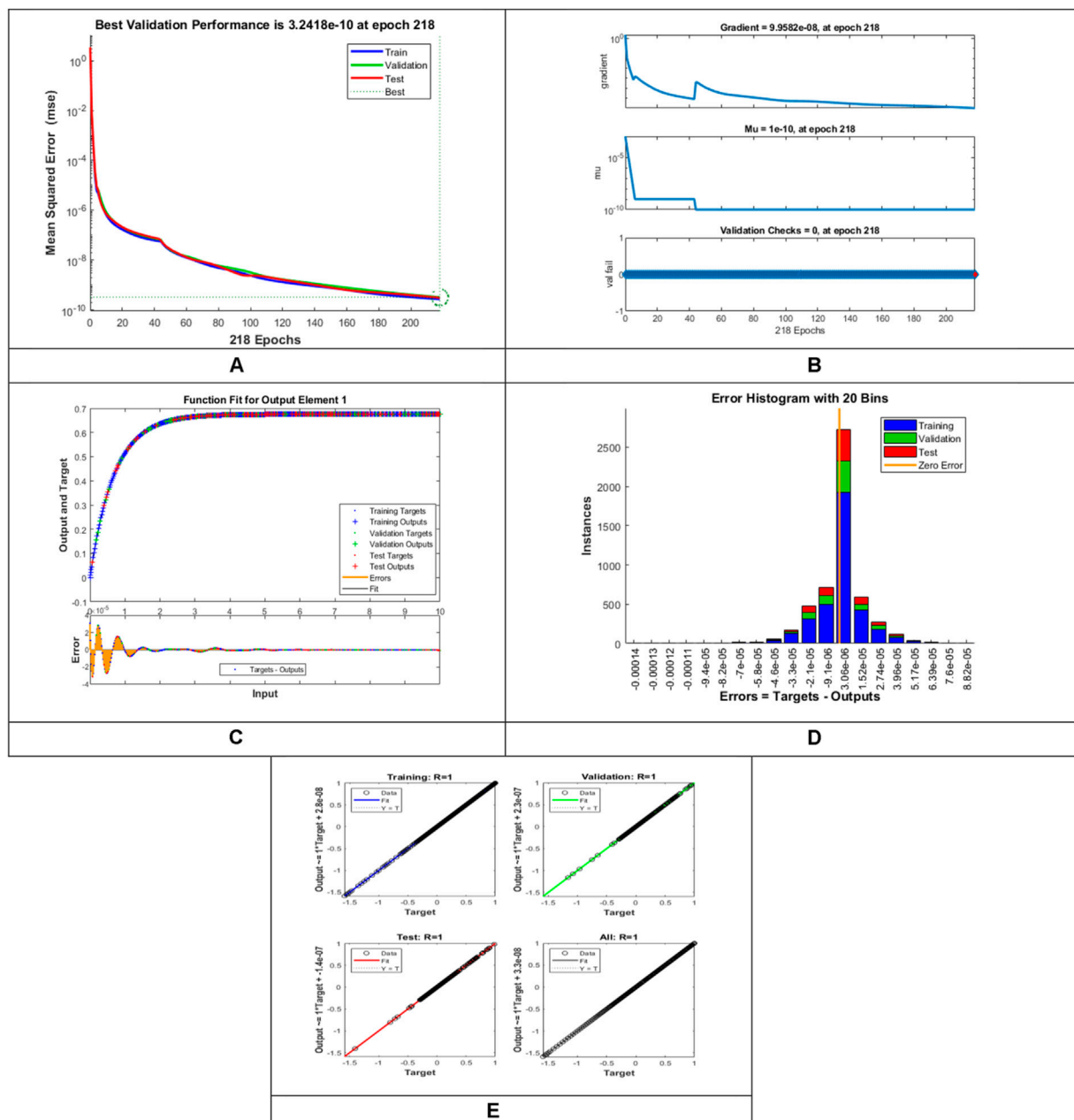


FIGURE 12

Pictorial illustration for the LMLA-BPNN base on variants of Le vs $\phi(\eta)$ for MHD-WNF-HGA. (A) M-S-E demonstration, (B) transition state analysis, (C) curve fitting, (D) error histogram, (E) and regression analysis.

(λ) with respect to $f'(\eta)$, respectively. The absolute error numeric result with the reference outputs shows the satisfactory accuracy criteria.

4.2 Temperature distributions

Fluid temperature distribution $\theta(\eta)$ has a considerable influence on the behavior of fluids and the impact on the

particles within the fluid. Figures 14A,C,E show the comparison with a reference solution for various values of nonlinear thermal radiation parameter (R), heat generation/absorption parameter (S), and ratio temperature (θ_w). Figure 14A exemplifies the differences in temperature distribution $\theta(\eta)$ with altered values of nonlinear thermal radiation parameter (R). The temperature profile increased with upsurging values of the nonlinear thermal radiation parameter. The heat transfer rate inside the flow regime is

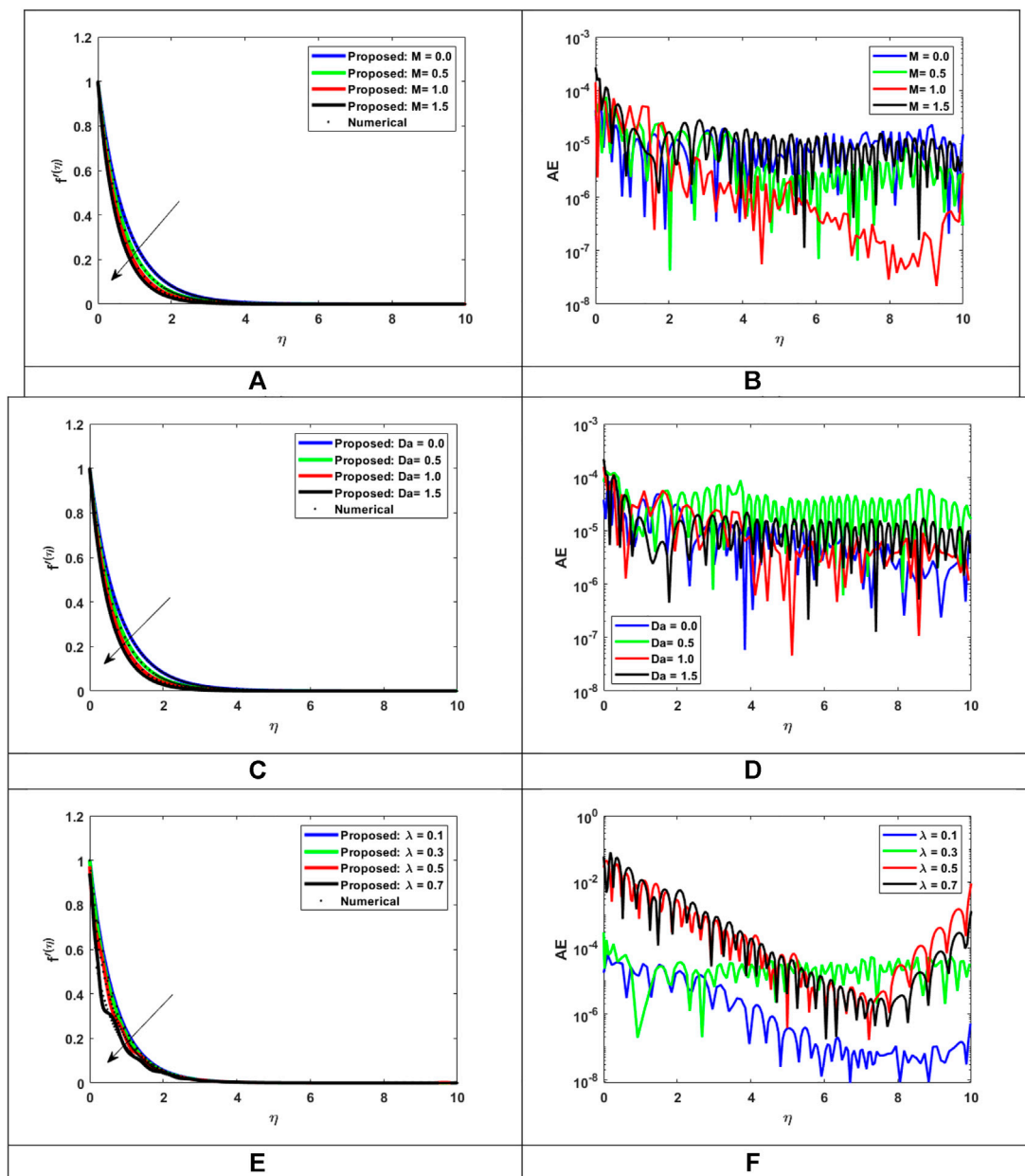


FIGURE 13

Assessment of LMLA-BPNN with reference dataset of MHD-WNF-HGA. (A) Variation of M for $f'(\eta)$, (B) AE for MHD-WNF-HGA, (C) Variation of Da for $f'(\eta)$, (D) AE for MHD-WNF-HGA, (E) Variation of λ for $f'(\eta)$, (F) AE for MHD-WNF-HGA.

higher and it works to simulate the fluid flow. The nonlinear thermal radiation parameter has three physical effects on the heat transmission of the nanofluid. First, the temperature of the boundary layer is raised on a regular basis. Second, the flow regime's nanoparticles acquire thermal energy, enhancing thermal diffusion and heat transmission within the fluid owing to the thermal conductivity of the nanoparticles.

Finally, it aims to improve the thermal transfer techniques of nanofluids, specifically the thermal transfer method by load and by conduction. Figure 14C shows fluid temperature distribution $\theta(\eta)$ with different values of heat generation/absorption parameter (S). Due to the rise in numerical values of the generation/absorption parameter, a huge rise in the fluid heat transfer is seen. There is a physical increase in

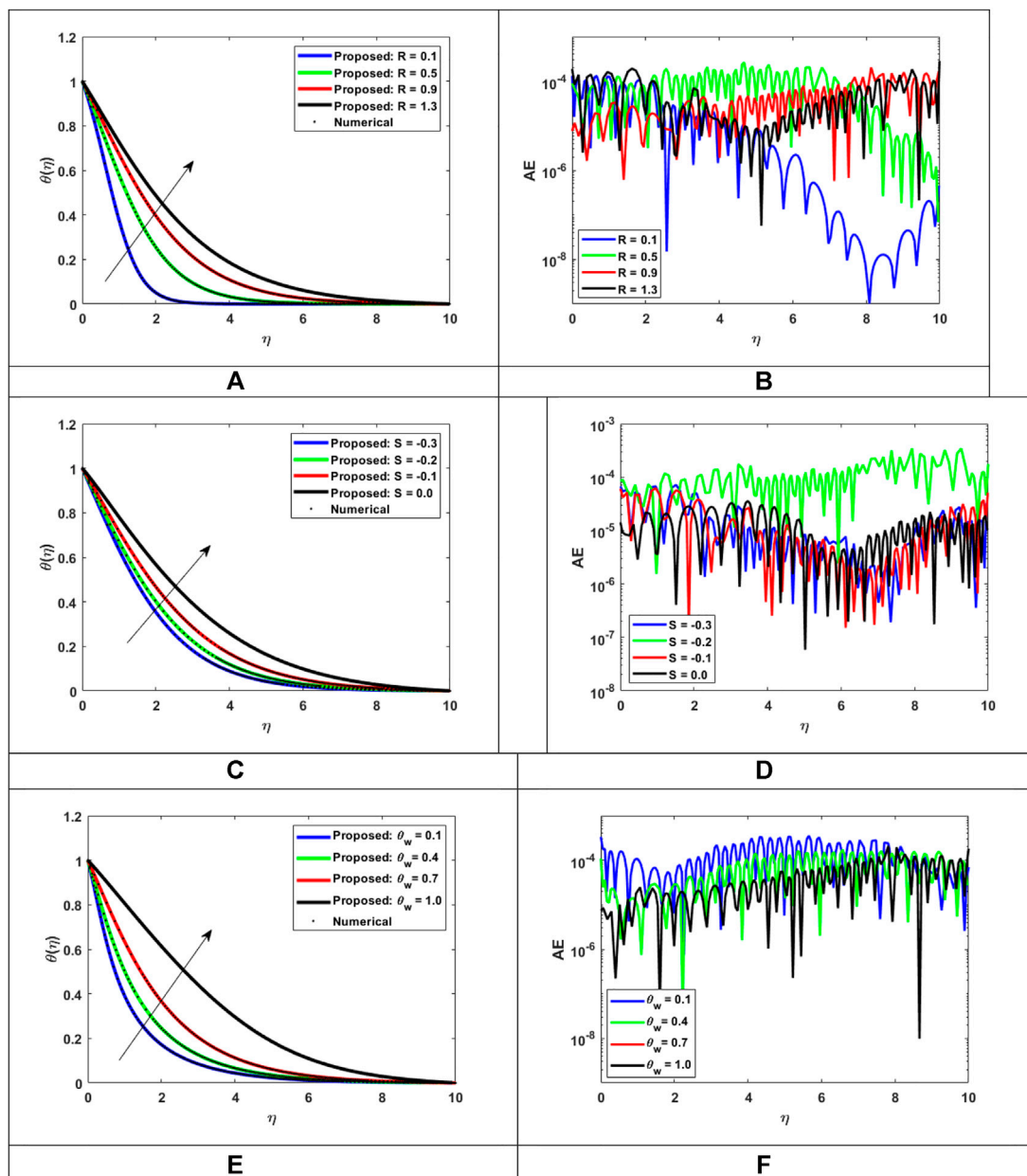


FIGURE 14

Assessment of LMLA-BPNN along the reference dataset of MHD-WNF-HGA. (A) Variation of R for $\theta(\eta)$, (B) AE for MHD-WNF-HGA, (C) Variation of S for $\theta(\eta)$, (D) AE for MHD-WNF-HGA, (E) Variation of θ_w for $\theta(\eta)$, (F) with AE for MHD-WNF-HGA.

the thermal dispersion and transfer of the fluids when heat is generated, which raises the temperature of the fluids. Also, with an increase in the heat source type ($S > 0$) values, the thickness of the boundary layer and the fluid temperature are likewise upsurges, while an opposite behavior occurs in the case of the heat absorption type ($S < 0$). However, when moving upward from the state of heat absorption to

generation, there is reformation in boundary layer thickness and thermal diffusion. Figure 14E investigates the disparities in temperature distribution $\theta(\eta)$ with improved values of the ratio temperature parameter (θ_w). The temperature profile increased with the enhancing ratio temperature parameter (θ_w). This effect enhances the temperature of the boundary layer and increases its thickness. The absolute error tool is

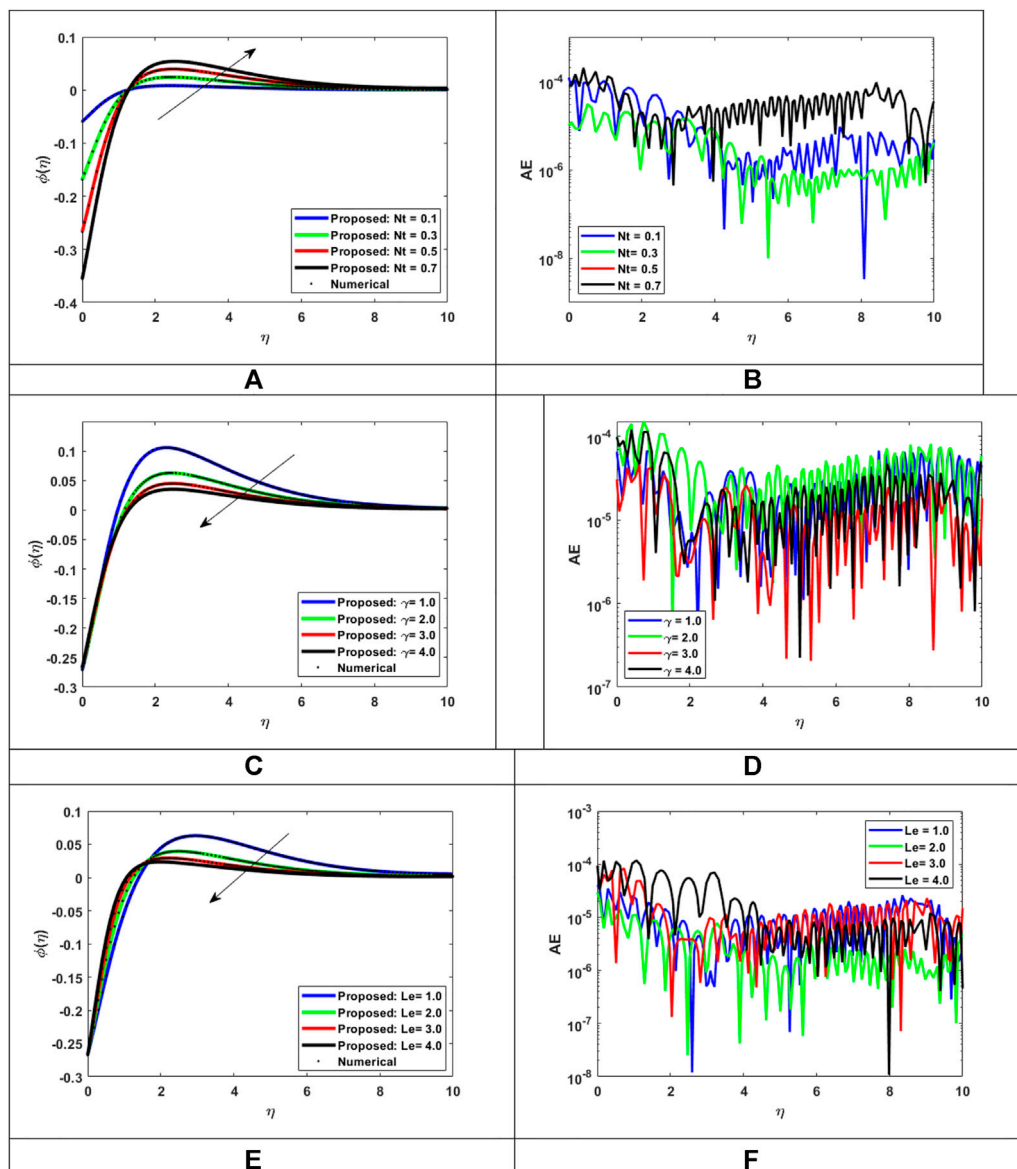


FIGURE 15

Assessment of LMLA-BPNN along the reference dataset of MHD-WNF-HGA. (A) Variation of N_t for $\phi(\eta)$, (B) AE for MHD-WNF-HGA, (C) Variation of γ for $\phi(\eta)$, (D) AE for MHD-WNF-HGA, (E) variation of Le for $\phi(\eta)$, (F) AE for MHD-WNF-HGA.

TABLE 2 Variant of MHD-WNF-HGA.

Physical quantities of our interest-based scenarios

| Case | S-I | S-II | S-III | S-IV | S-V | S-VI | S-VII | S-VIII | S-IX |
|----------|-----------|------------|-----------------|-----------|------------|------------------|------------|----------------|----------------|
| Case I | $M = 0.0$ | $Da = 0.0$ | $\lambda = 0.1$ | $R = 0.1$ | $S = -0.3$ | $\theta_w = 0.1$ | $Nt = 0.1$ | $\gamma = 1.0$ | $\gamma = 1.0$ |
| Case II | $M = 0.5$ | $Da = 0.5$ | $\lambda = 0.3$ | $R = 0.5$ | $S = -0.2$ | $\theta_w = 0.4$ | $Nt = 0.3$ | $\gamma = 2.5$ | $\gamma = 2.5$ |
| Case III | $M = 1.0$ | $Da = 1.0$ | $\lambda = 0.5$ | $R = 0.9$ | $S = -0.1$ | $\theta_w = 0.7$ | $Nt = 0.5$ | $\gamma = 3.0$ | $\gamma = 3.0$ |
| Case IV | $M = 1.5$ | $Da = 1.5$ | $\lambda = 0.7$ | $R = 1.3$ | $S = 0.0$ | $\theta_w = 1.0$ | $Nt = 0.7$ | $\gamma = 4.0$ | $\gamma = 4.0$ |

S stands for scenario.

shown in Figures 14B,D,E for (R) , (S) , and (θ_w) to check the accuracy criteria, respectively. The values of AE are in the ranges $10^{-9} - 10^{-4}$, $10^{-7} - 10^{-3}$, and $10^{-7} - 10^{-3}$ for $\theta(\eta)$. The absolute error numeric result with the reference outputs shows the satisfactory accuracy criteria.

4.3 Concentration of nanoparticle distribution

To examine the physical properties of the concentration of nanoparticles within the fluids, it is important to study the nomenclature and application of the fluids. The effectiveness and intensity of thermal and electrical conductivity, for instance, are correlated with the concentration of nanoparticles while studying fluid behavior. The relative analysis of nanoparticles concentration distribution $\phi(\eta)$ with reference result is illustrated in Figures 15B,D,E for (Nt) , (γ) , and (Le) . Figure 15A investigates the effect of the thermophoresis parameter (Nt) with respect to the concentration of nanoparticle distribution $\phi(\eta)$ within the flow regime of the fluid. As the thermophoresis parameter increases, the concentration of nanoparticle distribution enhances, the rate of heat transfer in the boundary layer increases, provoking particle deposition away from the fluid regime and therefore enhancing the concentration of the nanofluid particles. The effect of the chemical reaction parameter (γ) and Lewis number (Le) on the concentration of nanoparticles distribution $\phi(\eta)$ is illustrated in Figures 15C,E, respectively. A significant decrease is observed with the rise in the chemical reaction parameter (γ) and Lewis number (Le) . The absolute error (AE) analysis of (Nt) , (γ) , and (Le) on nanoparticle concentration distribution $\phi(\eta)$ are shown in Figures 11B,D,F to check the accuracy criteria, respectively. The AE values lies between $10^{-8} - 10^{-3}$, $10^{-7} - 10^{-3}$, and $10^{-8} - 10^{-3}$ for $\phi(\eta)$. The absolute error numeric result with the reference outputs shows the satisfactory accuracy criteria.

5 Conclusion

This research used the Levenberg–Marquardt neural network technique with backpropagation to solve the magnetohydrodynamic Williamson nanofluid flow through a stretched surface under the effects of nonlinear thermal radiation, Joule heating, heat generation/absorption, and chemical reaction (MHD-WNF-HGA). The solution of a mathematical model exhibiting (MHD-WNF-HGA) was examined with the adjustment of certain circumstances (scenarios). The bvp4c approach is used to build the dataset for the MHD-WNF-HGA model, which contains deviations from a variety of physical measurements such as the Williamson parameter, thermal radiation parameter, magnetic parameter, Eckert number, Darcy number, Brownian motion,

and thermophoresis parameter. The MHD-WNF-HGA reference dataset is made up of various versions, with LMLA-BPNN training, testing, and validation accounting for 80, 10, and 10% of the dataset, respectively.

The important findings of the present investigations are as follows.

- Fluid flow speed drops when magnetic force and Darcy law are applied to the flow. Also, Williamson fluid velocity is high for the lower values but as the values rise, the velocity drop with speed.
- The temperature distribution elevates with the help of the thermal radiation parameter, heat generation absorption parameter, and temperature ration parameter.
- The thermophoresis effect enhances the strength of nanofluid concentration, while the chemical reaction quantity and Lewis number weaken the concentration strength.

Furthermore

- The mean square error is anticipated to be in the average range of 10^{-5} for LMLA-BPNN when comparing the reference solution to the suggested data, which shows the close agreement between both.

Data availability statement

The original contributions presented in the study are included in the article/Supplementary Material; further inquiries can be directed to the corresponding authors.

Author contributions

All authors listed have made a substantial, direct, and intellectual contribution to the work and approved it for publication.

Acknowledgments

The author would like to extend his appreciation to the Deanship of Scientific Research at King Khalid University, Saudi Arabia, for funding this work through the Research Group Program under the grant No. RGP.2/12/43.

Conflict of interest

The authors declare that the research was conducted in the absence of any commercial or financial relationships that could be construed as a potential conflict of interest.

Publisher's note

All claims expressed in this article are solely those of the authors and do not necessarily represent those of their affiliated

organizations, or those of the publisher, the editors, and the reviewers. Any product that may be evaluated in this article, or claim that may be made by its manufacturer, is not guaranteed or endorsed by the publisher.

References

- Acharya, N., Das, K., and Kundu, P. K. (2019). Influence of multiple slips and chemical reaction on radiative MHD Williamson nanofluid flow in porous medium: A computational framework. *Multidiscip. Model. Mater. Struct.* 15 (3), 630–658. doi:10.1108/MMMS-08-2018-0152
- AdnanKhan, U., and Ahmed, N. (2022). Thermal enhancement and entropy investigation in dissipative ZnO-SAE50 under thermal radiation: A computational paradigm. *Waves Random Complex Media*, 1–16. doi:10.1080/17455030.2022.2053243
- Ahmed, N., Khan, U., Mohyud-Din, S. T., Khan, I., Murtaza, R., Hussain, I., et al. (2020). A novel investigation and hidden effects of MHD and thermal radiations in viscous dissipative nanofluid flow models. *Front. Phys.* 8, 75. doi:10.3389/fphy.2020.00075
- Ahmed, S., Ahshan, K. H., Mondal, M., Alam, N., and Hossain, S. (2021). Application of metal oxides-based nanofluids in PV/T systems: A review. *Front. Energy*, 1–32. doi:10.1007/s11708-021-0758-8
- Al-Mubaddel, F. S., Allehiany, F. M., Nofal, T. A., Alam, M. M., Ali, A., Asamoah, J. K. K., et al. (2022). Rheological model for generalized energy and mass transfer through hybrid nanofluid flow comprised of magnetized cobalt ferrite nanoparticles. *J. Nanomater.* 2022, 1–11. doi:10.1155/2022/7120982
- Alhowaity, A., Bilal, M., Hamam, H., Alqarni, M. M., Mukdasai, K., Ali, A., et al. (2022a). Non-Fourier energy transmission in power-law hybrid nanofluid flow over a moving sheet. *Sci. Rep.* 12 (1), 10406. doi:10.1038/s41598-022-14720-x
- Alhowaity, A., Hamam, H., Bilal, M., and Ali, A. (2022b). "Numerical study of Williamson hybrid nanofluid flow with thermal characteristics past over an extending surface," in *Heat transfer* (United States: Wiley Online Library). doi:10.1002/htj.22616
- Alsallami, S. A., Zahir, H., Muhammad, T., Hayat, A. U., Khan, M. R., and Ali, A. (2022). Numerical simulation of Marangoni Maxwell nanofluid flow with Arrhenius activation energy and entropy anatomization over a rotating disk. *Waves Random Complex Media*, 1–19. doi:10.1080/17455030.2022.2045385
- Ashraf, W., Khan, U., Al-Johani, A. S., Ahmed, N., Mohyud-Din, S. T., Khan, I., et al. (2022). Impact of freezing temperature (T_f) of Al_2O_3 and molecular diameter (H_2O)_d on thermal enhancement in magnetized and radiative nanofluid with mixed convection. *Sci. Rep.* 12, 703. doi:10.1038/s41598-021-04587-9
- Ayub, A., Darvesh, A., Altamirano, G. C., and Sabir, Z. (2021). Nanoscale energy transport of inclined magnetized 3D hybrid nanofluid with Lobatto IIIA scheme. *Heat. Transf.* 50 (7), 6465–6490. doi:10.1002/htj.22188
- Ayub, A., Sabir, Z., Le, D. N., and Aly, A. A. (2021). Nanoscale heat and mass transport of magnetized 3-D chemically radiative hybrid nanofluid with orthogonal/inclined magnetic field along rotating sheet. *Case Stud. Therm. Eng.* 26, 101193. doi:10.1016/j.csite.2021.101193
- Ayub, A., Sabir, Z., Shah, S. Z. H., Mahmoud, S. R., Algarni, A., Sadat, R., et al. (2022). Aspects of infinite shear rate viscosity and heat transport of magnetized Carreau nanofluid. *Eur. Phys. J. Plus* 137 (2), 247. doi:10.1140/epjp/s13360-022-02410-6
- Blasius, H. (1950). The boundary layers in fluids with little friction. *Zeitschrift für hermost und hermo*, 56(NACA-TM-1256).
- Botmart, T., Sabir, Z., Raja, M. A. Z., Weera, W., Sadat, R., Ali, M. R., et al. (2022). A numerical study of the fractional order dynamical nonlinear susceptible infected and quarantine differential model using the stochastic numerical approach. *Fractal Fract.* 6 (3), 139. doi:10.3390/fractalfract6030139
- Bouslimi, J., Omri, M., Mohamed, R. A., Mahmoud, K. H., Abo-Dahab, S. M., Soliman, M. S., et al. (2021). MHD Williamson nanofluid flow over a stretching sheet through a porous medium under effects of joule heating, nonlinear thermal radiation, heat generation/absorption, and chemical reaction. *Adv. Math. Phys.* 2021, 1–16. doi:10.1155/2021/9950993
- Cengel, Y. A., and Boles, M. A. (2015). *Gas-vapor mixtures and air-conditioning. Thermodynamics and engineering approach*. 8th ed. New York, NY, USA: McGraw-Hill, 725–729.
- Cengel, Y., and Heat, T. M. (2003). *A practical approach*. New York, NY, USA: McGraw-Hill.
- Choi, S. U. S., Singer, D. A., and Wang, H. P. (1995). Developments and applications of non-Newtonian flows. *Asme Fed.* 66, 99–105.
- Das, S. K., Choi, S. U., and Patel, H. E. (2006). Heat transfer in nanofluids—A review. *Heat. Transf. Eng.* 27 (10), 3–19. doi:10.1080/01457630600904593
- Elattar, S., Helmi, M. M., Elkotb, M. A., El-Shorbagy, M. A., Abdelrahman, A., Bilal, M., et al. (2022). Computational assessment of hybrid nanofluid flow with the influence of hall current and chemical reaction over a slender stretching surface. *Alexandria Eng. J.* 61 (12), 10319–10331. doi:10.1016/j.aej.2022.03.054
- Esfe, M. H., Kamyab, M. H., and Toghraie, D. (2022). Statistical review of studies on the estimation of thermophysical properties of nanofluids using artificial neural network (ANN). *Powder Technol.* 400 (5), 117210. doi:10.1016/j.powtec.2022.117210
- González, A., Ruz, O., and Castillo, E. (2021). Numerical study of the fluid dynamics and heat transfer for shear-thinning nanofluids in a micro pin-fin heat sink. *Case Stud. Therm. Eng.* 28, 101635. doi:10.1016/j.csite.2021.101635
- Goodarzi, H., Akbari, O. A., Sarafraz, M. M., Karchegani, M. M., Safaei, M. R., Sheikh Shabani, G. A., et al. (2019). Numerical simulation of natural convection heat transfer of nanofluid with Cu, MWCNT, and Al_2O_3 nanoparticles in a cavity with different aspect ratios. *J. Therm. Sci. Eng. Appl.* 11 (6), 061020. doi:10.1115/1.4043809
- Hamid, A., and Khan, M. (2019). Multiple solutions for MHD transient flow of Williamson nanofluids with convective heat transport. *J. Taiwan Inst. Chem. Eng.* 103, 126–137. doi:10.1016/j.jtice.2019.07.001
- Ibrahim, W., and Gamachu, D. (2019). Nonlinear convection flow of Williamson nanofluid past a radially stretching surface. *AIP Adv.* 9 (8), 085026. doi:10.1063/1.5113688
- Incropera, F. P., DeWitt, D. P., Bergman, T. L., and Lavine, A. S. (1996). *Fundamentals of heat and mass transfer*, 6. New York: Wiley, 116.
- Irandoost Shahrestani, M., Houshfar, E., Ashjaee, M., and Allahviridizadeh, P. (2021). Convective heat transfer and pumping power analysis of MWCNT+ Fe_3O_4 /water hybrid nanofluid in a helical coiled heat exchanger with orthogonal rib turbulators. *Front. Energy Res.* 9, 630805. doi:10.3389/fenrg.2021.630805
- Khan, M. I., Qayyum, S., Hayat, T., Khan, M. I., and Alsaedi, A. (2019). Entropy optimization in flow of Williamson nanofluid in the presence of chemical reaction and Joule heating. *Int. J. Heat Mass Transf.* 133, 959–967. doi:10.1016/j.ijheatmasstransfer.2018.12.168
- Khan, M. J., Duraisamy, B., Zuhra, S., Nawaz, R., Nisar, K. S., Jamshed, W., et al. (2021). Numerical solution of Cattaneo-Christov heat flux model over stretching/shrinking hybrid nanofluid by new iterative method. *Case Stud. Therm. Eng.* 28, 101673. doi:10.1016/j.csite.2021.101673
- Khan, N. S., Gul, T., Kumam, P., Shah, Z., Islam, S., Khan, W., et al. (2019). Influence of inclined magnetic field on Carreau nanoliquid thin film flow and heat transfer with graphene nanoparticles. *Energies* 12 (8), 1459. doi:10.3390/en12081459
- Khan, N. S., Zuhra, S., Shah, Z., Bonyah, E., Khan, W., Islam, S., et al. (2018). Slip flow of Eyring-Powell nanoliquid film containing graphene nanoparticles. *AIP Adv.* 8 (11), 115302. doi:10.1063/1.5055690
- Khan, U., Ahmed, N., Mohyud-Din, S. T., Hamadneh, N. N., Khan, I., and Andualem, M. (2021). The dynamics of H_2O suspended by multiple Shaped Cu nanoadditives in rotating system. *J. Nanomater.* 2022, 1–11. doi:10.1155/2021/7299143
- Khan, U., Ahmed, N., and Mohyud-Din, S. T. (2020). Surface thermal investigation in water functionalized Al_2O_3 and γAl_2O_3 nanomaterials-based nanofluid over a sensor surface. *Appl. Nanosci.* 1–11. doi:10.1007/s13204-020-01527-3
- Kumar, M. A., Reddy, Y. D., Rao, V. S., and Goud, B. S. (2021). Thermal radiation impact on MHD heat transfer natural convective nano fluid flow over an impulsively started vertical plate. *Case Stud. Therm. Eng.* 24, 100826. doi:10.1016/j.csite.2020.100826

- Mahdi, J. M., Lohrasbi, S., and Nsofor, E. C. (2019). Hybrid heat transfer enhancement for latent-heat thermal energy storage systems: A review. *Int. J. Heat Mass Transf.* 137, 630–649. doi:10.1016/j.jheatmasstransfer.2019.03.111
- Maxwell, J. C. (1881). "A treatise on electricity and magnetism: Pt. III," in *Magnetism. Pt. IV. Electromagnetism* (England: Clarendon Press), 2.
- Meseguer, J., Pérez-Grande, I., and Sanz-Andrés, A. (2012). *Spacecraft thermal control*. Sawston, Cambridge: Elsevier.
- Okonkwo, E. C., Abid, M., and Ratlamwala, T. A. (2018). Numerical analysis of heat transfer enhancement in a parabolic trough collector based on geometry modifications and working fluid usage. *J. Sol. Energy Eng.* 140 (5). doi:10.1115/1.4040076
- Okonkwo, E. C., Wole-Osho, I., Almanassra, I. W., Abdullatif, Y. M., and Al-Ansari, T. (2021). An updated review of nanofluids in various heat transfer devices. *J. Therm. Anal. Calorim.* 145 (6), 2817–2872. doi:10.1007/s10973-020-09760-2
- Pandya, N. S., Shah, H., Molana, M., and Tiwari, A. K. (2020). Heat transfer enhancement with nanofluids in plate heat exchangers: A comprehensive review. *Eur. J. Mech. - B/Fluids* 81, 173–190. doi:10.1016/j.euromechflu.2020.02.004
- Pare, A., and Ghosh, S. K. (2021). A unique thermal conductivity model (ANN) for nanofluid based on experimental study. *Powder Technol.* 377, 429–438. doi:10.1016/j.powtec.2020.09.011
- Raja, M. A. Z., Khan, Z., Zuhra, S., Chaudhary, N. I., Khan, W. U., He, Y., et al. (2021). Cattaneo-christov heat flux model of 3D hall current involving biconvection nanofluidic flow with Darcy-Forchheimer law effect: Backpropagation neural networks approach. *Case Stud. Therm. Eng.* 26, 101168. doi:10.1016/j.csite.2021.101168
- Raja, M. A. Z., Shoaib, M., Khan, Z., Zuhra, S., Saleel, C. A., Nisar, K. S., et al. (2022). Supervised neural networks learning algorithm for three dimensional hybrid nanofluid flow with radiative heat and mass fluxes. *Ain Shams Eng. J.* 13 (2), 101573. doi:10.1016/j.asej.2021.08.015
- Rasool, G., Zhang, T., Chamkha, A. J., Shafiq, A., Tlili, I., Shahzadi, G., et al. (2019). Entropy generation and consequences of binary chemical reaction on MHD Darcy-Forchheimer Williamson nanofluid flow over non-linearly stretching surface. *Entropy* 22 (1), 18. doi:10.3390/e22010018
- Sabir, Z., Raja, M. A. Z., Nguyen, T. G., Fathurrochman, I., Sadat, R., Ali, M. R., et al. (2022). Gudermannian neural networks using the optimization procedures of genetic algorithm and active set approach for the three-species food chain nonlinear model. *J. Ambient. Intell. Humaniz. Comput.*, 1–10. doi:10.1007/s12652-021-03638-3
- Sadeghi, G., Nazari, S., Ameri, M., and Shama, F. (2020). Energy and exergy evaluation of the evacuated tube solar collector using Cu2O/water nanofluid utilizing ANN methods. *Sustain. Energy Technol. Assessments* 37, 100578. doi:10.1016/j.seta.2019.100578
- Sajid, M. U., and Ali, H. M. (2019). Recent advances in application of nanofluids in heat transfer devices: A critical review. *Renew. Sustain. Energy Rev.* 103, 556–592. doi:10.1016/j.rser.2018.12.057
- Sakiadis, B. C. (1961). Boundary-layer behavior on continuous solid surfaces: I. Boundary-Layer equations for two-dimensional and axisymmetric flow. *AIChE J.* 7 (1), 26–28. doi:10.1002/aic.690070108
- Shah, S. L., Ayub, A., Dehraj, S., Wahab, H. A., Sagayam, K. M., Ali, M. R., et al. (2022). Magnetic dipole aspect of binary chemical reactive Cross nanofluid and heat transport over composite cylindrical panels. *Waves Random Complex Media*, 1–24. doi:10.1080/17455030.2021.2020373
- Shah, S. Z. H., Ayub, A., Sabir, Z., Adel, W., Shah, N. A., Yook, S. J., et al. (2021). Insight into the dynamics of time-dependent cross nanofluid on a melting surface subject to cubic autocatalysis. *Case Stud. Therm. Eng.* 27, 101227. doi:10.1016/j.csite.2021.101227
- Shah, Z., Raja, M. A. Z., Chu, Y. M., Khan, W. A., Abbas, S. Z., Shoaib, M., et al. (2021). Computational intelligence of Levenberg-Marquardt backpropagation neural networks to study the dynamics of expanding/contracting cylinder for cross magneto-nanofluid flow model. *Phys. Scr.* 96 (5), 055219. doi:10.1088/1402-4896/abe068
- Shah, Z., Tassaddiq, A., Islam, S., Alklaibi, A. M., and Khan, I. (2019). Cattaneo-Christov heat flux model for three-dimensional rotating flow of SWCNT and MWCNT Nanofluid with Darcy-Forchheimer porous medium induced by a linearly stretchable surface. *Symmetry* 11 (3), 331. doi:10.3390/sym11030331
- She, L., and Fan, G. (2018). Numerical simulation of flow and heat transfer characteristics of CuO-water nanofluids in a flat tube. *Front. Energy Res.* 6, 57. doi:10.3389/fenrg.2018.00057
- Sheikholeslami, M., Gerdroodbary, M. B., Moradi, R., Shafee, A., and Li, Z. (2019). Application of Neural Network for estimation of heat transfer treatment of Al2O3-H2O nanofluid through a channel. *Comput. Methods Appl. Mech. Eng.* 344, 1–12. doi:10.1016/j.cma.2018.09.025
- Sheikholeslami, M., Haq, R. U., Shafee, A., Li, Z., Elaraki, Y. G., Tlili, I., et al. (2019). Heat transfer simulation of heat storage unit with nanoparticles and fins through a heat exchanger. *Int. J. Heat Mass Transf.* 135, 470–478. doi:10.1016/j.jheatmasstransfer.2019.02.003
- Sheikholeslami, M., Jafaryar, M., Shafee, A., Li, Z., and Haq, R. U. (2019). Heat transfer of nanoparticles employing innovative turbulator considering entropy generation. *Int. J. Heat Mass Transf.* 136, 1233–1240. doi:10.1016/j.jheatmasstransfer.2019.03.091
- Shoaib, M., Raja, M. A. Z., Zubair, G., Farhat, I., Nisar, K. S., Sabir, Z., et al. (2021). Intelligent computing with levenberg-marquardt backpropagation neural networks for third-grade nanofluid over a stretched sheet with convective conditions. *Arab. J. Sci. Eng.*, 1–19. doi:10.1007/s13369-021-06202-5
- Subbarayudu, K., Suneetha, S., and Reddy, P. B. A. (2020). The assessment of time dependent flow of Williamson fluid with radiative blood flow against a wedge. *Propuls. Power Res.* 9 (1), 87–99. doi:10.1016/j.jprr.2019.07.001
- Toghraie, D. S., Sina, N., Mozafarifar, M., Alizadeh, A. A., Soltani, F., Fazilati, M. A., et al. (2020). Prediction of dynamic viscosity of a new non-Newtonian hybrid nanofluid using experimental and artificial neural network (ANN) methods. *Heat. Transf. Res.* 51 (15), 1351–1362. doi:10.1615/heattransres.2020034645
- Umar, M., Sabir, Z., Imran, A., Wahab, A. H., Shoaib, M., Raja, M. A. Z., et al. (2020). The 3-D flow of Casson nanofluid over a stretched sheet with chemical reactions, velocity slip, thermal radiation and Brownian motion. *Therm. Sci.* 24, 2929–2939. doi:10.2298/tsci190625339u
- Umar, M., Sabir, Z., Zahoor Raja, M. A., Gupta, M., Le, D. N., Aly, A. A., et al. (2021). Computational intelligent paradigms to solve the nonlinear SIR system for spreading infection and treatment using Levenberg-Marquardt backpropagation. *Symmetry* 13 (4), 618. doi:10.3390/sym13040618
- Vakili, M., Karami, M., Delfani, S., and Khosrojerdi, S. (2016). Experimental investigation and modeling of thermal radiative properties of f-CNTs nanofluid by artificial neural network with Levenberg-Marquardt algorithm. *Int. Commun. Heat Mass Transf.* 78, 224–230. doi:10.1016/j.icheatmasstransfer.2016.09.011
- Williamson, R. V. (1929). The flow of pseudoplastic materials. *Ind. Eng. Chem.* 21 (11), 1108–1111. doi:10.1021/ie50239a035
- Yang, X. H., and Liu, J. (2018). Liquid metal enabled combinatorial heat transfer science: Toward unconventional extreme cooling. *Front. Energy* 12 (2), 259–275. doi:10.1007/s11708-017-0521-3
- Zaman, S., and Gul, M. (2019). Magnetohydrodynamic bioconvective flow of Williamson nanofluid containing gyrotactic microorganisms subjected to thermal radiation and Newtonian conditions. *J. Theor. Biol.* 479, 22–28. doi:10.1016/j.jtbi.2019.02.015
- Zhao, N., Li, S., and Yang, J. (2016). A review on nanofluids: Data-driven modeling of thermalphysical properties and the application in automotive radiator. *Renew. Sustain. Energy Rev.* 66, 596–616. doi:10.1016/j.rser.2016.08.029
- Zuhra, S., Raja, M. A. Z., Shoaib, M., Khan, Z., Nisar, K. S., Islam, S., et al. (2022). Numerical analysis of Cattaneo-Christov heat flux model over magnetic couple stress Casson nanofluid flow by Lavenberg-Marquard backpropagated neural networks. *Waves Random Complex Media*, 1–28. doi:10.1080/17455030.2022.2062484



OPEN ACCESS

EDITED BY

Umar Khan,
Hazara University, Pakistan

REVIEWED BY

Muhammad Sohail,
Institute of Space Technology, Pakistan
Zubair Ahmad,
University of Campania "Luigi Vanvitelli,"
Italy
Waseem Sikander,
The University of Haripur, Pakistan

*CORRESPONDENCE

Aatif Ali,
atifkh98@gmail.com

SPECIALTY SECTION

This article was submitted to Process
and Energy Systems Engineering,
a section of the journal
Frontiers in Energy Research

RECEIVED 12 June 2022

ACCEPTED 15 July 2022

PUBLISHED 22 August 2022

CITATION

Alshahrani S, Ahammad NA, Bilal M,
Ghoneim ME, Ali A, Yassen MF and
Tag-Eldin E (2022), Numerical
simulation of ternary nanofluid flow with
multiple slip and thermal
jump conditions.
Front. Energy Res. 10:967307.
doi: 10.3389/fenrg.2022.967307

COPYRIGHT

© 2022 Alshahrani, Ahammad, Bilal,
Ghoneim, Ali, Yassen and Tag-Eldin.
This is an open-access article
distributed under the terms of the
Creative Commons Attribution License
(CC BY). The use, distribution or
reproduction in other forums is
permitted, provided the original
author(s) and the copyright owner(s) are
credited and that the original
publication in this journal is cited, in
accordance with accepted academic
practice. No use, distribution or
reproduction is permitted which does
not comply with these terms.

Numerical simulation of ternary nanofluid flow with multiple slip and thermal jump conditions

Saad Alshahrani¹, N. Ameer Ahammad², Muhammad Bilal³,
Mohamed E. Ghoneim^{4,5}, Aatif Ali^{6*}, Mansour F. Yassen^{7,8} and
Elsayed Tag-Eldin⁹

¹Department of Mechanical Engineering, College of Engineering, King Khalid University, Abha, Saudi Arabia, ²Department of Mathematics, Faculty of Science, University of Tabuk, Tabuk, Saudi Arabia, ³Department of Mathematics, City University of Science and Information Technology, Peshawar, Pakistan, ⁴Department of Mathematical Sciences, Faculty of Applied Science, Umm Al-Qura University, Makkah, Saudi Arabia, ⁵Faculty of Computers and Artificial Intelligence, Damietta University, Damietta, Egypt, ⁶Department of Mathematics, Abdul Wali Khan University Mardan, Mardan, Khyber Pakhtunkhwa, Pakistan, ⁷Department of Mathematics, College of Science and Humanities in Al-Aflaj, Prince Sattam Bin Abdulaziz University, Al-Aflaj, Saudi Arabia, ⁸Department of Mathematics, Faculty of Science, Damietta University, New Damietta, Damietta, Egypt, ⁹Faculty of Engineering and Technology, Future University in Egypt, New Cairo, Egypt

This study addresses the consequences of thermal radiation with slip boundary conditions and a uniform magnetic field on a steady 2D flow of trihybrid nanofluids over a spinning disc. The trihybrid nanocomposites are synthesized by the dispersion of aluminum oxide (Al_2O_3), zirconium dioxide (ZrO_2), and carbon nanotubes (CNTs) in water. The phenomena are characterized as a nonlinear system of PDEs. Using resemblance replacement, the modeled equations are simplified to a nondimensional set of ODEs. The parametric continuation method has been used to simulate the resulting sets of nonlinear differential equations. Figures and tables depict the effects of physical constraints on energy and velocity profiles. According to this study, the slip coefficient enormously decreases the velocity field. For larger approximations of thermal radiation characteristics and heat source term boosts the thermal profile. This proposed model will assist in the field of meteorology, atmospheric studies, biological technology, power generation, automotive manufacturing, renewable power conversions, and detecting microchips. In regard to such kinds of practical applications, the proposed study is being conducted. This study is unique due to slip conditions and ternary fluid, and it could be used by other scholars to acquire further information about nanofluid thermal exchanger performance and stability.

KEYWORDS

slip conditions, thermal radiation, heat generating source, computational approach, ternary nanofluid, rotating disc

Introduction

Rotating disks are used in a wide range of engineering and industrial applications such as gas flywheels, spinning disk electrodes, turbine engines, brakes, and gears (Li et al., 2021; Zhou et al., 2021; Chu et al., 2022a). The modeling and simulation of ferrofluid flow with heat transfer induced by an irregular rotatable disc oscillating upward were investigated by Zhang et al. (2021). The wavy rotating material increases energy conversion by up to 15% as compared to a level surface. Waini et al. (2022) used the bvp4c MATLAB programming to investigate the chaotic flow over a gyrating disc in nanofluids with deceleration and suction features. Alrabaiah et al. (2022) investigated the flow of magnesium oxide, silver, and gyrotactic microbe-based hybrid nano composites within the cylindrical space connecting the disc and cone in the context of thermal energy stabilization. It was discovered that by combining a rotating disc with an immobile cone, the cone–disk system may be cooled to its desired temperature, whereas the outer edge system is in equilibrium. The flow of nanofluids across a preheated revolving disc has been computationally evaluated as a result of random motion, heat conduction, and thermal radiation by Chu et al. (2021a). They described many features of momentum and heat transformation using Arrhenius kinetic energy. The radiation and Prandtl number effect are thought to promote heat exchange while enhancing the magnetic component which lowers velocity distribution. Naveen Kumar et al. (2022) evaluated the nanofluid flow over a spinning, stretchy disc with an unsteady heat source. The heat transmission of both fluids accelerates as the ratios of temperature- and space-related heat supplier factors increase. Alhowsaity et al. (2022) developed the energy transmission over a moving sheet. It was hypothesized that adding carbon nanotubes and nanoclusters to water improves its thermophysical and energy transport capabilities drastically. Sharma et al. (2022) proposed a spinning disc with temperature-dependent geothermal viscosity and thermal conductivity, causing the hydrodynamic flow of magnetized ferrofluid. Kumar and Mondal (2022) analyzed quantitatively the electrically radiating unsteady viscous fluid flow due to a stretchy spinning disc with an externally supplied magnetic field, looking at both descriptive and analytical aspects of heat transmission. Recently, many investigators have documented substantial involvement to the fluid flow across a rotating disc (Bilal et al., 2022a; Alsallami et al., 2022; Murtaza et al., 2022; Ramzan et al., 2022).

Hybrid and trihybrid nanofluids combine the metallic, non-metallic, or polymeric nano-size powder with a conventional fluid to maximize the thermal efficiency for a wide range of purposes such as, solar energy, refrigeration and heating, ventilation, heat transition, heat tubes, coolant in machines, and engineering. Many experiments have noted that hybrid nanofluids have a superior energy conduction rate than pure

fluids, both experimentally and statistically (Khan et al., 2020; Alhowsaity et al., 2022; Elattar et al., 2022). The working fluid in this study contained Al_2O_3 , ZrO_2 , and CNT. Sahu et al. (2021) analyzed the free convection steady-state and loop's transient features utilizing a variety of water-based trihybrid ($\text{Al}_2\text{O}_3 + \text{Cu} + \text{CNT}/\text{water}$) nanofluids. Ramadhan et al. (2019) examined the instability of trihybrid nanofluids. The tri-hybrid nanocomposite was successfully synthesized and displayed excellent compatibility. Muzaidi et al. (2021) addressed the physical parameters (crystallite size, surface shape, and density) of $\text{SiO}_2/\text{CuO}/\text{TiO}_2$ trihybrid nanofluids. The trihybrid solution exhibited the best thermal characteristics, based on thermal production, at roughly 55°C . Al-Mubaddel et al. (2022) documented the model for generalized energy and mass transfer comprising magnetized cobalt ferrite. The influence of permeability factor, inertial element, and buoyant ratio on the fluid velocity has been reported, while the temperature conversion curve improves dramatically with the increasing values of Eckert number, Hartmann number, and heat absorption/generation. Ullah et al. (2021); Ullah et al. (2022) used an elongated substrate to describe the convective flow of Prandtl–Eyring nanofluids, taking into account the important factors including activation energy, chemical reaction, and Joule heating. Safiei et al. (2021) used a newly created metal fabrication fluid called $\text{ZrO}_2\text{-SiO}_2\text{-Al}_2\text{O}_3$ trihybrid ferrofluid in the cutting zone to produce a good surface quality on manufactured items while also reducing the cutting forces. Gul and Saeed (2022) worked on improving thermal flow for trihybrid nanofluid flow across a nonlinear extending plate. It was discovered that as the volumetric fractions of NPs enhance the nonlinearity index of the sheet and velocity profile decreases. Lv et al. (2021) examined the Hall current and the heat radiation effect on hybrid nanofluid flow over a whirling disc. Their endeavor was motivated by the desire to improve the thermal energy transmission for mechanical and manufacturing uses. The heat transfer rate decreases with Hall current and increases with the radiative component, according to the findings. Palanisamy et al. (2021) investigated the characterization and thermophysical characteristics of trihybrid oxide nanostructures, including SiO_2 , TiO_2 , and Al_2O_3 , produced at 0.1 per concentration in three distinct ratios. Furthermore, many scholars have reported on the uses and applications of ternary nanofluid (Sohail et al., 2019; Ahmed et al., 2020a; Sohail et al., 2020a; Ahmed et al., 2020b; Chu et al., 2021b).

When viscosity effects at the wall are insignificant and mesh size is substantially larger than the boundary layer thickness, the slip wall condition is used. Hussain (2022) statistically and numerically assessed to capture the flow characteristics of hybrid nanofluid flow across an enormously extensible sheet with thermal and velocity slip conditions. The results show that a little increase in the thermal slip factor generates a significant change in the thermal transfer rate when compared to the radiation impact. Swain et al. (2022) addressed the uniform

chemical reaction and magnetic field effect on the water-based hybrid nanofluid passing over a dwindling permeable sheet with slip boundary conditions. The suction and injection component enhances the skin friction ratio; however, the velocity slip factor has the opposite trend. Ullah (2022) demonstrated the flow of a hydromagnetic hybrid nanofluid in a 3D nonlinear convection layer in the existence of microorganisms and different slip circumstances across a slandering substrate. Many scholars have recently hugely reported on thermal and velocity slip conditions (Khan et al., 2017; Sohail et al., 2020b; Ahmed et al., 2020c; Saeed et al., 2021; Algehyne et al., 2022).

The purpose of this research is to elaborate the consequences of slip boundary conditions on ternary hybrid nanofluid flow in the presence of heat source and thermal radiation over a rotating disc. The thermophysical properties of ternary nanoparticles (Al_2O_3 , ZrO_2 , and CNT) and base fluid (H_2O) are investigated in this study. To numerically resolve the dimensionless system of ODEs, the parametric continuation method has been applied using MATLAB's software. The current study's unique findings are useful and valuable in academic studies and other fields.

Mathematical formulation

A steady two-dimensional trihybrid nanofluid flow with nano composites (Al_2O_3 , ZrO_2 , and CNT) over a disc in the presence of thermal radiation and slip boundary conditions is studied. The (r, ϕ, z) cylindrical coordinate system is considered as elaborated in Figure 1. The disc rotates with fixed angular velocity Ω . The magnetic field B_0 is applied in the axial direction of fixed intensity. Moreover, we can ignore the induced magnetic field by considering low magnetic Reynolds number. T_w and T_∞ are the wall and ambient temperature of fluid, respectively. Based on abovementioned postulation, the elementary phenomena are modeled as (Iqbal et al., 2021):

$$\frac{\partial u}{\partial r} + \frac{u}{r} + \frac{\partial w}{\partial z} = 0, \quad (1)$$

$$\rho_{tnf} \left(u \frac{\partial u}{\partial r} + w \frac{\partial u}{\partial z} + \frac{v^2}{r} \right) = -\frac{\partial P}{\partial r} + \mu_{tnf} \left(\frac{\partial^2 u}{\partial r^2} - \frac{u}{r^2} + \frac{1}{r} \frac{\partial u}{\partial r} + \frac{\partial^2 u}{\partial z^2} \right) - \sigma_{tnf} B_0^2 u, \quad (2)$$

$$\rho_{tnf} \left(u \frac{\partial v}{\partial r} + w \frac{\partial v}{\partial z} + \frac{uv}{r} \right) = \mu_{tnf} \left(\frac{\partial^2 v}{\partial r^2} - \frac{v}{r^2} + \frac{1}{r} \frac{\partial v}{\partial r} + \frac{\partial^2 v}{\partial z^2} \right) - \sigma_{tnf} B_0^2 v, \quad (3)$$

$$\rho_{tnf} \left(u \frac{\partial w}{\partial r} + w \frac{\partial w}{\partial z} \right) = -\frac{\partial P}{\partial z} + \mu_{tnf} \left(\frac{\partial^2 w}{\partial r^2} + \frac{1}{r} \frac{\partial w}{\partial r} + \frac{\partial^2 w}{\partial z^2} \right), \quad (4)$$

$$(\rho C_p)_{tnf} \left(u \frac{\partial T}{\partial r} + w \frac{\partial T}{\partial z} \right) = k_{tnf} \left(\frac{\partial^2 T}{\partial r^2} + \frac{\partial^2 T}{\partial z^2} + \frac{1}{r} \frac{\partial T}{\partial r} \right) - q_r + Q_0 (T - T_\infty), \quad (5)$$

where

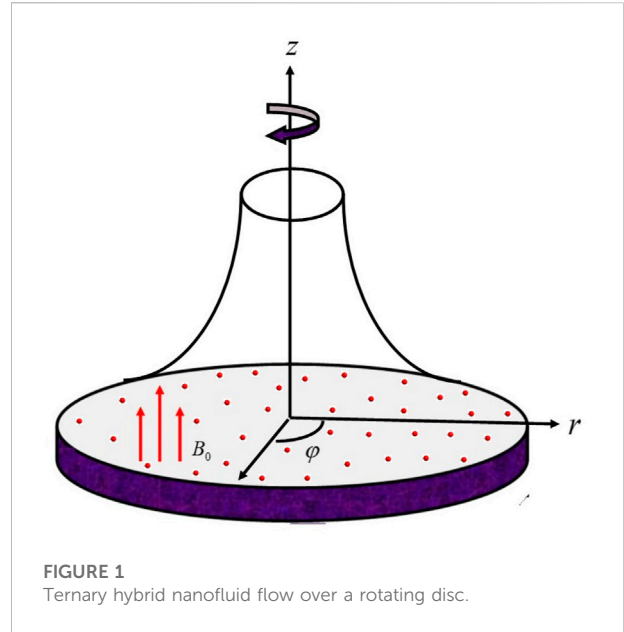


FIGURE 1
Ternary hybrid nanofluid flow over a rotating disc.

$$q_r = \frac{-4\sigma^*}{3k^*} \frac{\partial T^4}{\partial z} = \frac{-16\sigma^*}{3k^*} T^3 \frac{\partial T}{\partial z}.$$

The boundary conditions are

$$u = L_1 \frac{\partial u}{\partial z}, w = 0, v = L_1 \frac{\partial v}{\partial z} + \Omega r, T = L_2 \frac{\partial T}{\partial z} + T_w \text{ at } z = 0. \quad (6)$$

$$u \rightarrow 0, T \rightarrow T_\infty, v \rightarrow 0, p \rightarrow p_\infty \text{ as } z \rightarrow \infty.$$

Here, L_1 and L_2 are the wall slip and thermal jump constant, respectively; Q_0 is the generation and absorption; $U_0 = \Omega r$ is the free stream velocity; P is the pressure; σ_{tnf} is the electrical conductivity of ternary hybrid nanofluid; μ_{tnf} is the dynamic viscosity; ρ_{tnf} is the density; and (u, v, w) are the components of velocity.

The following variables are used to simplify Eqs 1–5 to the dimensionless system of ODEs:

$$\left. \begin{aligned} \zeta = z \sqrt{\frac{U_0}{r\nu_f}}, \quad u = r\Omega f'(\zeta), \quad w = -2\sqrt{\Omega\nu_f} g(\zeta), \quad v = r\Omega g(\zeta), \\ p = p_\infty - \Omega\mu_f P(\zeta), \quad T = T_\infty + (T_w - T_\infty)\theta(\zeta). \end{aligned} \right\} \quad (7)$$

We get,

$$2 \frac{\nu_{tnf}}{\nu_{mf}} f'''' - f'^2 + g^2 + 4f f'' - \frac{\rho_{hmf}}{\rho_{tnf}} M^2 f' = 0. \quad (8)$$

$$2 \frac{\nu_{tnf}}{\nu_{mf}} g'' + 2f g' - 2f' g - \frac{\rho_{hmf}}{\rho_{tnf}} M^2 g = 0. \quad (9)$$

$$\frac{\nu_{tnf}}{\nu_{mf}} f'' + f f'' - \frac{\rho_{hmf}}{\rho_{tnf}} \frac{\partial P}{\partial \zeta} = 0. \quad (10)$$

$$\left(\frac{\rho C_p}{\rho C_p} \right)_{hmf} \left(\frac{k_{tnf}}{k_{hmf}} + Rd \right) \theta'' + Pr f \theta' + Hs \theta = 0. \quad (11)$$

TABLE 1 Investigational values of Al_2O_3 , ZrO_2 , CNT, and water [Arif et al. \(2022\)](#).

| | k (W/m.K) | ρ (kg/m ³) | C_p (J/kg.K) | β (1/K) |
|-------------------------|-------------|-----------------------------|----------------|---------------|
| Water | 0.613 | 997.1 | 4,179 | 0.00021 |
| Al_2O_3 | 40 | 3,970 | 765 | 0.00000508 |
| ZrO_2 | 1.7 | 5,680 | 502 | — |
| CNT | 3,007.4 | 2,100 | 790 | −0.000008 |

$$f(0) = 0, g(0) = 1 + g'(0)\alpha, f'(0) = f''(0)\alpha, \theta(0) = 1 + \theta'(0)\beta. \\ f' \rightarrow 0, P \rightarrow 0, g \rightarrow 0, \theta \rightarrow 0 \text{ when } \zeta \rightarrow \infty. \quad (12)$$

Here, Pr is the Prandtl number, M is the magnetic constant, α is the slip velocity factor, β is the thermal slip constraint, and Rd is the thermal radiation term.

$$Pr = \frac{\mu_f(C_p)_f}{k_f}, M^2 = \frac{\sigma_{inf} B_0^2}{\Omega \rho_f}, \alpha = L_1 \sqrt{\frac{\Omega}{\nu_f}}, \beta = L_2 \sqrt{\frac{\Omega}{\nu_f}}, Rd = \frac{4\sigma T_\infty^3}{k^* k_f}. \quad (13)$$

The engineering interest quantities are

$$C_f = \frac{\sqrt{\tau_r^2 + \tau_\theta^2}}{\rho_{inf} (r\Omega)^2}, Nu_r = \frac{k_{inf}}{k_f} \frac{rq_w}{T_w - T_\infty}. \quad (14)$$

The dimensionless form of [Eq. 14](#) is

$$\tau_w = \mu_{inf} \left(\frac{\partial u}{\partial z} + \frac{\partial w}{\partial r} \right) \Big|_{z=0}, \tau_\theta = \mu_{inf} \left(\frac{\partial v}{\partial z} + \frac{\partial w}{\partial r} \right) \Big|_{z=0}, \\ q_w = -k_{inf} \frac{\partial T}{\partial z} \Big|_{z=0}. \quad (15)$$

$$Re_r^{\frac{1}{2}} C_f = \frac{\mu_{inf}}{\mu_{mf}} \left(f''(0)^2 + g'(0)^2 \right)^{\frac{1}{2}}. \quad (16)$$

$$Re_r^{\frac{1}{2}} Nu_r = \frac{-k_{mf}}{k_{inf}} Rd \theta'(0). \quad (17)$$

Here, $Re_r = \frac{2\Omega r^2}{\nu_f}$ is the local Reynolds number. [Table 1](#) illustrates the experimental values of ternary nanoparticles and base fluid. [Table 2](#) presented the mathematical model for trihybrid nanofluid.

Numerical solution

Many researchers have used different types of numerical and computational techniques to deal highly nonlinear PDEs ([Zhao et al., 2018](#); [Zhao et al., 2021a](#); [Zhao et al., 2021b](#); [Chu et al., 2022b](#); [Jin et al., 2022](#); [Nazeer et al., 2022](#); [Rashid et al., 2022](#); [Wang et al., 2022](#)). The main steps, while dealing with the PCM method, are as follows ([Shuaib et al., 2020a](#); [Shuaib et al., 2020b](#); [Bilal et al., 2022c](#)):

Step 1: Simplify [Eqs 8–11](#) to 1st order

$$\left. \begin{aligned} \lambda_1 &= f(\eta), \lambda_2 = f'(\eta), \lambda_3 = f''(\eta), \lambda_4 = g(\eta), \\ \lambda_5 &= g'(\eta), \lambda_6 = \theta(\eta), \lambda_7 = \theta'(\eta), \lambda_8 = p(\eta). \end{aligned} \right\} \quad (18)$$

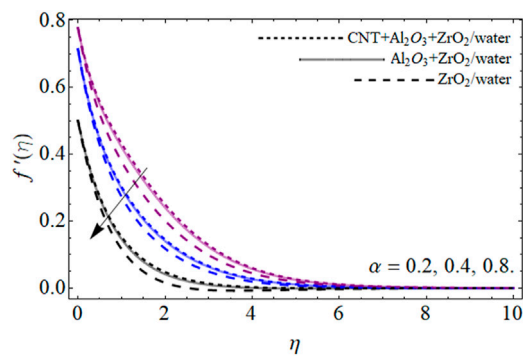
By substituting [Eq. 18](#) in [Eqs 8–12](#), we get

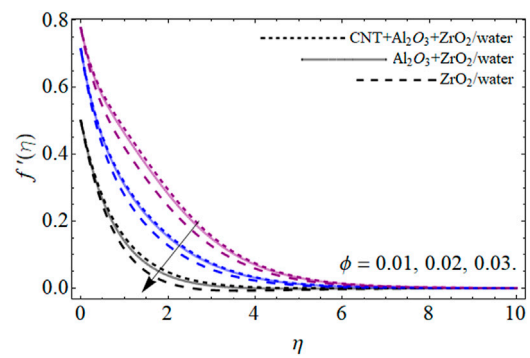
$$2 \frac{\nu_{mf}}{\nu_{mf}} \lambda_3' - \lambda_2^2 + \lambda_4^2 + 4\lambda_2 \lambda_3 - \frac{\rho_{mf}}{\rho_{inf}} M^2 \lambda_2 = 0. \quad (19)$$

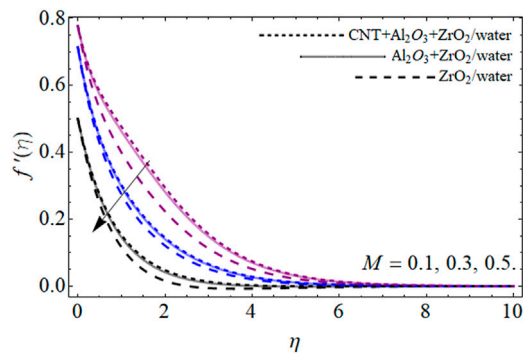
$$2 \frac{\nu_{mf}}{\nu_{mf}} \lambda_5' + 2\lambda_1 \lambda_5 - 2\lambda_2 \lambda_4 - \frac{\rho_{mf}}{\rho_{inf}} M^2 \lambda_4 = 0. \quad (20)$$

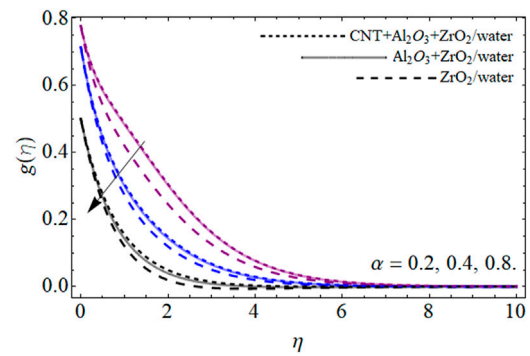
TABLE 2 Thermochemical properties of ternary hybrid nanofluids [Alharbi et al. \(2022\)](#), [Bilal et al. \(2022b\)](#).

| | |
|-------------------------|---|
| Viscosity | $\frac{\mu_{mf}}{\mu_f} = \frac{1}{(1-\phi_{\text{ZrO}_2})^{2.5} (1-\phi_{\text{Al}_2\text{O}_3})^{2.5} (1-\phi_{\text{CNT}})^{2.5}}$ |
| Density | $\frac{\rho_{mf}}{\rho_f} = (1 - \phi_{\text{Al}_2\text{O}_3}) [(1 - \phi_{\text{Al}_2\text{O}_3}) \{ (1 - \phi_{\text{CNT}}) + \phi_{\text{CNT}} \frac{\rho_{\text{CNT}}}{\rho_f} \} + \phi_{\text{Al}_2\text{O}_3} \frac{\rho_{\text{Al}_2\text{O}_3}}{\rho_f} + \phi_{\text{ZrO}_2} \frac{\rho_{\text{ZrO}_2}}{\rho_f}]$ |
| Specific heat | $\frac{(\rho C_p)_{mf}}{(\rho C_p)_f} = \phi_{\text{ZrO}_2} \frac{(\rho C_p)_{\text{ZrO}_2}}{(\rho C_p)_f} + (1 - \phi_{\text{ZrO}_2}) [(1 - \phi_{\text{Al}_2\text{O}_3}) \{ (1 - \phi_{\text{CNT}}) + \phi_{\text{CNT}} \frac{(\rho C_p)_{\text{CNT}}}{(\rho C_p)_f} \} + \phi_{\text{Al}_2\text{O}_3} \frac{(\rho C_p)_{\text{Al}_2\text{O}_3}}{(\rho C_p)_f}]$ |
| Thermal conduction | $\left. \begin{aligned} \frac{k_{inf}}{k_{mf}} &= \left(\frac{k_{\text{CNT}} + 2k_{mf} - 2\phi_{\text{CNT}}(k_{mf} - k_{\text{CNT}})}{k_{\text{CNT}} + 2k_{mf} + \phi_{\text{CNT}}(k_{mf} - k_{\text{CNT}})} \right) \frac{k_{mf}}{k_{nf}} = \left(\frac{k_{\text{Al}_2\text{O}_3} + 2k_{nf} - 2\phi_{\text{Al}_2\text{O}_3}(k_{nf} - k_{\text{Al}_2\text{O}_3})}{k_{\text{Al}_2\text{O}_3} + 2k_{nf} + \phi_{\text{Al}_2\text{O}_3}(k_{nf} - k_{\text{Al}_2\text{O}_3})} \right), \\ \frac{k_{nf}}{k_f} &= \left(\frac{k_{\text{ZrO}_2} + 2k_f - 2\phi_{\text{ZrO}_2}(k_f - k_{\text{ZrO}_2})}{k_{\text{ZrO}_2} + 2k_f + \phi_{\text{ZrO}_2}(k_f - k_{\text{ZrO}_2})} \right), \end{aligned} \right\}$ |
| Electrical conductivity | $\frac{\sigma_{inf}}{\sigma_{mf}} = \left(1 + \frac{3(\frac{\sigma_{\text{CNT}}}{\sigma_{mf}} - 1)\phi_{\text{CNT}}}{(\frac{\sigma_{\text{CNT}}}{\sigma_{mf}} + 2) - (\frac{\sigma_{\text{CNT}}}{\sigma_{mf}} - 1)\phi_{\text{CNT}}} \right), \frac{\sigma_{mf}}{\sigma_{nf}} = \left(1 + \frac{3(\frac{\sigma_{\text{Al}_2\text{O}_3}}{\sigma_{nf}} - 1)\phi_{\text{Al}_2\text{O}_3}}{(\frac{\sigma_{\text{Al}_2\text{O}_3}}{\sigma_{nf}} + 2) - (\frac{\sigma_{\text{Al}_2\text{O}_3}}{\sigma_{nf}} - 1)\phi_{\text{Al}_2\text{O}_3}} \right), \\ \frac{\sigma_{nf}}{\sigma_f} = \left(1 + \frac{3(\frac{\sigma_{\text{ZrO}_2}}{\sigma_f} - 1)\phi_{\text{ZrO}_2}}{(\frac{\sigma_{\text{ZrO}_2}}{\sigma_f} + 2) - (\frac{\sigma_{\text{ZrO}_2}}{\sigma_f} - 1)\phi_{\text{ZrO}_2}} \right).$ |


FIGURE 2

Velocity outlines $f'(\eta)$ versus velocity slip factor α .

FIGURE 4

Velocity outlines $f'(\eta)$ versus ternary nanoparticles ϕ .

FIGURE 3

Velocity outlines $f'(\eta)$ versus magnetic term M .

FIGURE 5

Velocity outlines $g(\eta)$ versus velocity slip factor α .

$$\frac{v_{tnf}}{v_{hmf}} \lambda_3 + \lambda_1 \lambda_3 - \frac{\rho_{hmf}}{\rho_{tnf}} \lambda_8' = 0. \quad (21)$$

$$\left(\frac{\rho C_p}{\rho C_p} \right)_{hmf} \left(\frac{k_{tnf}}{k_{hmf}} + Rd \right) \lambda_7' + Pr \lambda_1 \lambda_7 + Hs \lambda_6 = 0. \quad (22)$$

$$\lambda_1(0) = 0, \lambda_2(0) = \alpha \lambda_3(0), \lambda_4(0) = 1 + \alpha \lambda_5(0), \lambda_6(0) = 1 + \beta, \lambda_7(0), \lambda_2 \rightarrow 0, g \rightarrow 0, \lambda_8 \rightarrow 0, \lambda_6 \rightarrow 0 \text{ when } \zeta \rightarrow \infty. \quad (23)$$

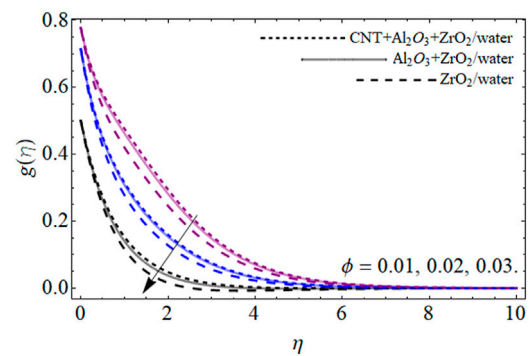
Step 2: Familiarizing parameter p in Eqs 19–22:

$$2 \frac{v_{tnf}}{v_{hmf}} \lambda_3' - \lambda_2^2 + \lambda_4^2 + 4 \lambda_2 (\lambda_3 - 1) p - \frac{\rho_{hmf}}{\rho_{tnf}} M^2 \lambda_2 = 0. \quad (24)$$

$$2 \frac{v_{tnf}}{v_{hmf}} \lambda_5' + 2 \lambda_1 (\lambda_5 - 1) p - 2 \lambda_2 \lambda_4 - \frac{\rho_{hmf}}{\rho_{tnf}} M^2 \lambda_4 = 0. \quad (25)$$

$$\frac{v_{tnf}}{v_{hmf}} \lambda_3 + \lambda_1 (\lambda_3 - 1) p - \frac{\rho_{hmf}}{\rho_{tnf}} \lambda_8' = 0. \quad (26)$$

$$\left(\frac{\rho C_p}{\rho C_p} \right)_{hmf} \left(\frac{k_{tnf}}{k_{hmf}} + Rd \right) \lambda_7' + Pr \lambda_1 (\lambda_7 - 1) p + Hs \lambda_6 = 0. \quad (27)$$


FIGURE 6

Velocity outlines $g(\eta)$ versus ternary nanoparticles ϕ .

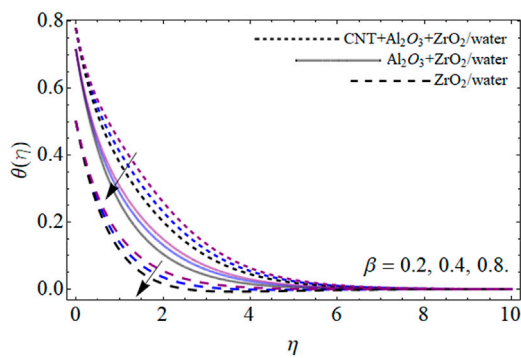


FIGURE 7
Energy outlines $\theta(\eta)$ versus thermal slip factor β .

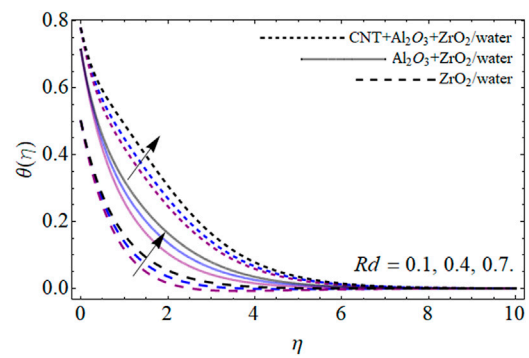


FIGURE 10
Energy outlines $\theta(\eta)$ versus thermal radiation Rd .

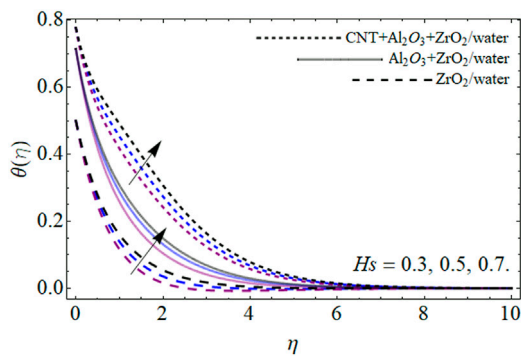


FIGURE 8
Energy outlines $\theta(\eta)$ versus heat source Hs .

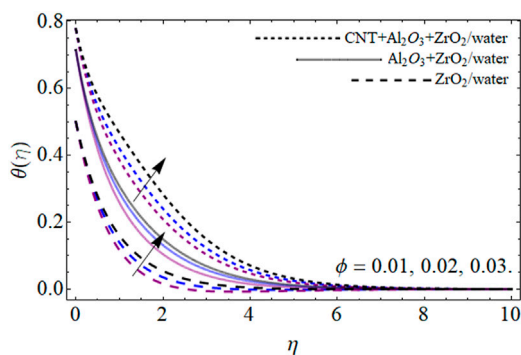


FIGURE 9
Energy outlines $\theta(\eta)$ versus ternary nanoparticles ϕ .

Results and discussion

This section elaborates the physics and trend behind each figure. The following statements are concluded from Figures 2–11.

Figures 2–4 revealed the axial velocity $f'(\eta)$ outlines versus velocity slip factor α , magnetic term M , and ternary nanoparticles ϕ , while Figures 5 and 6 display the radial velocity $g(\eta)$ outlines versus slip factor α and ternary nanoparticles ϕ , respectively. Figures 2 and 3 reported that the velocity contour diminishes with the influence of slip factor and magnetic term. The slip factor and magnetic force both resist the fluid field because the magnetic impact causes Lorentz strength, which opposes the fluid flow; hence, fluid velocity contour declines due to the increasing tendency of magnetic field and slip factor. Figure 4 shows that the dispersion of more quantity of ternary nanoparticles ($\phi = \phi_1 = \phi_2 = \phi_3$) to water decelerates the fluid velocity. Physically, the inclusion of trihybrid nano composites to the base fluid enhances its average viscosity, which results in such retardation. Figures 5 and 6 present that the radial velocity also declines with the velocity slip factor and ternary nanoparticles. The upshot of trihybrid nanoparticles enhances the fluid viscosity, which resists the fluid velocity $g(\eta)$.

Figures 7–10 show the energy outlines versus the thermal slip factor β , heat source Hs , ternary nanoparticles ϕ , and thermal radiation Rd . Figure 7 expresses that the thermal slip factor reduces to the energy contour because slip effect minimizes the rate of frictional force, which results in reduction of energy field. Physically, the frictional force generates heat, so its reduction also decreases the temperature of fluid. Figure 8 illustrated that the heat generation and absorption term boost the energy profile. An additional energy is provided due to the rising effect of heat source, which elevates the energy profile. Figure 9 expresses that the addition of ternary nanoparticles enhances the temperature profile. The specific heat capacity of water ($4,179 C_p$ (J/kg.K)) is much higher than that of Al_2O_3 ($765 C_p$ (J/kg.K)), ZrO_2 ($502 C_p$ (J/kg.K)), and CNT ($790 C_p$ (J/kg.K)) nanoparticles. Therefore, the dispersion of these NPs to water lessens its average heat capacity, which fallouts in the elevation of energy outlines.

Step 3: Apply Cauchy principal and discretized Eqs 24–27.

After discretization, the obtained set of equations is computed through the MATLAB code of PCM.

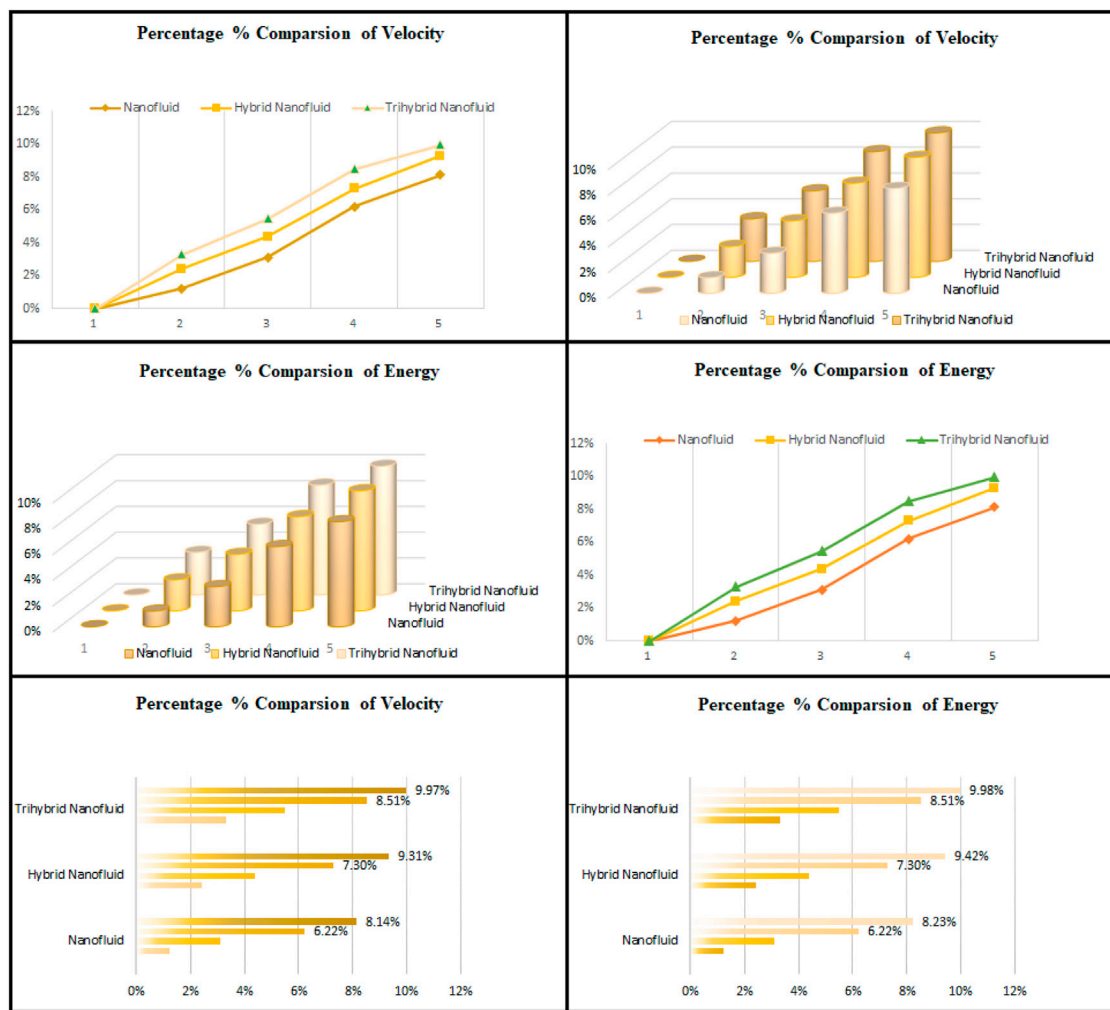


FIGURE 11
Percentage- and column-wise comparison of nanofluids.

Figure 10 displays that the upshot of radiation R_d term enhances the temperature contour. The impact of radiation term augments the energy of fluid, which causes in the inclination temperature contour.

Figure 11 demonstrates the comparative evaluation of nanofluid, hybrid, and ternary nanofluid. From all the subfigures of Figure 11, it can be noted that the ternary nanofluids have greater tendency to boost the energy transmission rate than hybrid and solo nanofluids.

Conclusion

We have examined the consequences of thermal radiation with slip boundary conditions and the uniform magnetic field on a steady 2D flow of trihybrid nanofluid over a rotating disc. The trihybrid nano composites are synthesized by the dispersion of Al_2O_3 , ZrO_2 , and CNT in water. A nonlinear system of PDEs is used to describe the phenomenon. The modeled equations are

reduced to a nondimensional collection of ODEs using similarity substitution. The PCM methodology is used to estimate the nonlinear differential equations that resulted. The key findings are

- The axial velocity $f'(\eta)$ outlines are reducing with the influence of slip factor and magnetic term.
- The dispersion of ternary nanoparticles ($\phi = \phi_1 = \phi_2 = \phi_3$) to water decelerates the fluid velocity.
- The radial velocity also declines with the velocity slip factor and ternary nanoparticles.
- The energy field declines with the increasing effects of thermal slip constraint.
- The influence of heat generation and absorption term boosts the energy profile.
- The addition of ternary nanoparticles magnifies the temperature profile.

- The fluid temperature augments with the effect of thermal radiation.
- The ternary nanofluid has higher thermal characteristics than simple and hybrid nanofluid.

Data availability statement

The original contributions presented in the study are included in the article/Supplementary Material; further inquiries can be directed to the corresponding author.

Author contributions

All authors listed have made a substantial, direct, and intellectual contribution to the work and approved it for publication.

Acknowledgments

The authors extend their appreciation to the Deanship of Scientific Research at King Khalid University, Saudi

Arabia for funding this work through large groups under Grant No. RGP 2/32/43. The authors would like to thank the Deanship of Scientific Research at Umm Al-Qura University for supporting this work by Grant Code: 22UQU4331317DSR001.

Conflict of interest

The authors declare that the research was conducted in the absence of any commercial or financial relationships that could be construed as a potential conflict of interest.

Publisher's note

All claims expressed in this article are solely those of the authors and do not necessarily represent those of their affiliated organizations, or those of the publisher, the editors, and the reviewers. Any product that may be evaluated in this article, or claim that may be made by its manufacturer, is not guaranteed or endorsed by the publisher.

References

- Ahmed, N., Khan, U., Mohyud-Din, S. T., Chu, Y. M., Khan, I., and Nisar, K. S. (2020). Radiative colloidal investigation for thermal transport by incorporating the impacts of nanomaterial and molecular diameters (dnanoparticles, dfluid): Applications in multiple engineering systems. *Molecules* 25 (8), 1896. doi:10.3390/molecules25081896
- Ahmed, N., Khan, U., and Mohyud-Din, S. T. (2020). Hidden phenomena of MHD on 3D squeezed flow of radiative-H₂O suspended by aluminum alloys nanoparticles. *Eur. Phys. J. Plus* 135 (11), 875. doi:10.1140/epjp/s13360-020-00870-2
- Ahmed, N., Khan, U., Mohyud-Din, S. T., Khan, I., Murtaza, R., Hussain, I., et al. (2020). A novel investigation and hidden effects of MHD and thermal radiations in viscous dissipative nanofluid flow models. *Front. Phys.* 8, 75. doi:10.3389/fphy.2020.00075
- Al-Mubaddel, F. S., Allehiany, F. M., Nofal, T. A., Alam, M. M., Ali, A., Asamoah, J. K. K., et al. (2022). Rheological model for generalized energy and mass transfer through hybrid nanofluid flow comprised of magnetized Cobalt ferrite nanoparticles. *J. Nanomater.* 2022, 1–11. doi:10.1155/2022/7120982
- Algehyne, E. A., Alhusayni, Y. Y., Tassaddiq, A., Saeed, A., and Bilal, M. (2022). The study of nanofluid flow with motile microorganism and thermal slip condition across a vertical permeable surface. *Waves Random Complex Media*, 1–18. doi:10.1080/17455030.2022.2071501
- Alharbi, K. A. M., Ahmed, A. E. S., Ould Sidi, M., Ahammad, N. A., Mohamed, A., El-Shorbagy, M. A., et al. (2022). Computational valuation of Darcy ternary-hybrid nanofluid flow across an extending cylinder with induction effects. *Micromachines* 13 (4), 588. doi:10.3390/mi13040588
- Alhawaity, A., Bilal, M., Hamam, H., Alqarni, M. M., Mukdasai, K., Ali, A., et al. (2022). Non-Fourier energy transmission in power-law hybrid nanofluid flow over a moving sheet. *Sci. Rep.* 12 (1), 10406. doi:10.1038/s41598-022-14720-x
- Alhawaity, A., Hamam, H., Bilal, M., and Ali, A. Numerical study of Williamson hybrid nanofluid flow with thermal characteristics past over an extending surface. *Heat. Trans.* doi:10.1002/hjt.22616
- Alrabaiah, H., Bilal, M., Khan, M. A., Muhammad, T., and Legas, E. Y. (2022). Parametric estimation of gyrotactic microorganism hybrid nanofluid flow between the conical gap of spinning disk-cone apparatus. *Sci. Rep.* 12 (1), 59. doi:10.1038/s41598-021-03077-2
- Alsallami, S. A., Zahir, H., Muhammad, T., Hayat, A. U., Khan, M. R., Ali, A., et al. (2022). Numerical simulation of Marangoni Maxwell nanofluid flow with Arrhenius activation energy and entropy anatomization over a rotating disk. *Waves Random Complex Media*, 1–19. doi:10.1080/17455030.2022.2045385
- Arif, M., Kumam, P., Kumam, W., and Mostafa, Z. (2022). Heat transfer analysis of radiator using different shaped nanoparticles water-based ternary hybrid nanofluid with applications: A fractional model. *Case Stud. Therm. Eng.* 31, 101837. doi:10.1016/j.csite.2022.101837
- Bilal, M., Ahmed, A. E. S., El-Nabulsi, R. A., Ahammad, N. A., Alharbi, K. A. M., Elkotb, M. A., et al. (2022). Numerical analysis of an unsteady, electroviscous, ternary hybrid nanofluid flow with chemical reaction and activation energy across parallel plates. *Micromachines* 13 (6), 874. doi:10.3390/mi13060874
- Bilal, M., Gul, T., Mouldi, A., Mukhtar, S., Alghamdi, W., Bouzgarrou, S. M., et al. (2022). Melting heat transition in a spinning flow of silver-magnesium oxide/engine oil hybrid nanofluid using parametric estimation. *J. Nanomater.* 2022, 1–13. doi:10.1155/2022/2891315
- Bilal, M., Saeed, A., Gul, T., Kumam, W., Mukhtar, S., Kumam, P., et al. (2022). Parametric simulation of micropolar fluid with thermal radiation across a porous stretching surface. *Sci. Rep.* 12 (1), 2542. doi:10.1038/s41598-022-06458-3
- Chu, Y. M., Bashir, S., Ramzan, M., and Malik, M. Y. (2022). Model-based comparative study of magnetohydrodynamics unsteady hybrid nanofluid flow between two infinite parallel plates with particle shape effects. *Math. Methods Appl. Sci.* doi:10.1002/mma.8234
- Chu, Y. M., Nazir, U., Sohail, M., Selim, M. M., and Lee, J. R. (2021). Enhancement in thermal energy and solute particles using hybrid nanoparticles by engaging activation energy and chemical reaction over a parabolic surface via finite element approach. *Fractal Fract.* 5 (3), 119. doi:10.3390/fractalfract5030119
- Chu, Y. M., Nazir, U., Sohail, M., Selim, M. M., and Lee, J. R. (2021). Enhancement in thermal energy and solute particles using hybrid nanoparticles by engaging activation energy and chemical reaction over a parabolic surface via finite element approach. *Fractal Fract.* 5 (3), 119. doi:10.3390/fractalfract5030119
- Chu, Y. M., Shankaralingappa, B. M., Gireesha, B. J., Alzahrani, F., Khan, M. I., Khan, S. U., et al. (2022). Combined impact of Cattaneo-Christov double diffusion and radiative heat flux on bio-convective flow of Maxwell liquid configured by a stretched nano-material surface. *Appl. Math. Comput.* 419, 126883. doi:10.1016/j.amc.2021.126883

- Elattar, S., Helmi, M. M., Elkotb, M. A., El-Shorbagy, M. A., Abdelrahman, A., Bilal, M., et al. (2022). Computational assessment of hybrid nanofluid flow with the influence of hall current and chemical reaction over a slender stretching surface. *Alexandria Eng. J.* 61 (12), 10319–10331. doi:10.1016/j.aej.2022.03.054
- Gul, T., and Saeed, A. (2022). Nonlinear mixed convection couple stress tri-hybrid nanofluids flow in a Darcy–Forchheimer porous medium over a nonlinear stretching surface. *Waves Random Complex Media*, 1–18. doi:10.1080/17455030.2022.2077471
- Hussain, S. M. (2022). Dynamics of ethylene glycol-based graphene and molybdenum disulfide hybrid nanofluid over a stretchable surface with slip conditions. *Sci. Rep.* 12 (1), 1751. doi:10.1038/s41598-022-05703-z
- Iqbal, Z., Azhar, E., and Maraj, E. N. (2021). Performance of nanopowders SiO₂ and SiC in the flow of engine oil over a rotating disk influenced by thermal jump conditions. *Phys. A Stat. Mech. its Appl.* 565, 125570. doi:10.1016/j.physa.2020.125570
- Jin, F., Qian, Z. S., Chu, Y. M., and ur Rahman, M. (2022). On nonlinear evolution model for drinking behavior under Caputo–Fabrizio derivative. *jaac.* 12 (2), 790–806. doi:10.11948/20210357
- Khan, U., Abbasi, A., Ahmed, N., and Mohyud-Din, S. T. (2017). 39. Engineering Computations, 00. doi:10.1108/EC-04-2017-0149 Particle shape, thermal radiations, viscous dissipation and joule heating effects on flow of magneto-nanofluid in a rotating system
- Khan, U., Ahmed, N., and Mohyud-Din, S. T. (2020). Surface thermal investigation in water functionalized Al₂O₃ and γAl₂O₃ nanomaterials-based nanofluid over a sensor surface. *Appl. Nanosci.*, 1–11. doi:10.1007/s13204-020-01527-3
- Kumar, M., and Mondal, P. K. (2022). Irreversibility analysis of hybrid nanofluid flow over a rotating disk: Effect of thermal radiation and magnetic field. *Colloids Surfaces A Physicochem. Eng. Aspects* 635, 128077. doi:10.1016/j.colsurfa.2021.128077
- Li, Y. X., Muhammad, T., Bilal, M., Khan, M. A., Ahmadian, A., Pansera, B. A., et al. (2021). Fractional simulation for Darcy–Forchheimer hybrid nanofluid flow with partial slip over a spinning disk. *Alexandria Eng. J.* 60 (5), 4787–4796. doi:10.1016/j.aej.2021.03.062
- Lv, Y. P., Algehyne, E. A., Alshehri, M. G., Alzahrani, E., Bilal, M., Khan, M. A., et al. (2021). Numerical approach towards gyrotactic microorganisms hybrid nanofluid flow with the hall current and magnetic field over a spinning disk. *Sci. Rep.* 11 (1), 8948. doi:10.1038/s41598-021-88269-6
- Murtaza, S., Kumam, P., Ahmad, Z., Sitthithakerngkiet, K., and Ali, I. E. (2022). Finite difference simulation of fractal-fractional model of electro-osmotic flow of casson fluid in a micro channel. *IEEE Access* 10, 26681–26692. doi:10.1109/access.2022.3148970
- Muzaidi, N. A. S., Fikri, M. A., Wong, K. N. S. W. S., Sofi, A. Z. M., Mamat, R., Adenam, N. M., et al. (2021). Heat absorption properties of CuO/TiO₂/SiO₂ trihybrid nanofluids and its potential future direction towards solar thermal applications. *Arabian J. Chem.* 14 (4), 103059. doi:10.1016/j.arabj.2021.103059
- Naveen Kumar, R., Mallikarjuna, H. B., Tigalappa, N., Punith Gowda, R. J., and Umrao Sarwe, D. (2022). Carbon nanotubes suspended dusty nanofluid flow over stretching porous rotating disk with non-uniform heat source/sink. *Int. J. Comput. Methods Eng. Sci. Mech.* 23 (2), 119–128. doi:10.1080/15502287.2021.1920645
- Nazeer, M., Hussain, F., Khan, M. I., El-Zahar, E. R., Chu, Y. M., and Malik, M. Y. (2022). Theoretical study of MHD electro-osmotically flow of third-grade fluid in micro channel. *Appl. Math. Comput.* 420, 126868. doi:10.1016/j.amc.2021.126868
- Palanisamy, R., Parthipan, G., and Palani, S. (2021). Study of synthesis, characterization and thermo physical properties of Al₂O₃-SiO₂-TiO₂/H₂O based tri-hybrid nanofluid. *Dig. J. Nanomater. Biostructures (DJNB)* 16 (3), 939.
- Ramadhan, A. I., Azmi, W. H., Mamat, R., Hamid, K. A., and Norsakinah, S. (2019). Investigation on stability of tri-hybrid nanofluids in water-ethylene glycol mixture IOP Conference Series: Materials Science and Engineering. *IOP Conf. Ser. Mat. Sci. Eng.* 469 (1), 012068. doi:10.1088/1757-899x/469/1/012068
- Ramzan, M., Saeed, A., Kumam, P., Ahmad, Z., Junaid, M. S., Khan, D., et al. (2022). Influences of Soret and Dufour numbers on mixed convective and chemically reactive Casson fluids flow towards an inclined flat plate. *Heat. Trans.* 51, 4393–4433. doi:10.1002/htj.22505
- Rashid, S., Sultana, S., Karaca, Y., Khalid, A., and Chu, Y. M. (2022). Some further extensions considering discrete proportional fractional operators. *Fractals* 30 (01), 2240026. doi:10.1142/s0218348x22400266
- Saeed, A., Bilal, M., Gul, T., Kumam, P., Khan, A., Sohail, M., et al. (2021). Fractional order stagnation point flow of the hybrid nanofluid towards a stretching sheet. *Sci. Rep.* 11 (1), 20429. doi:10.1038/s41598-021-00004-3
- Safiei, W., Rahman, M. M., Yusoff, A. R., Arifin, M. N., and Tasnim, W. (2021). Effects of SiO₂-Al₂O₃-ZrO₂ tri-hybrid nanofluids on surface roughness and cutting temperature in end milling process of aluminum alloy 6061-T6 using uncoated and coated cutting inserts with minimal quantity lubricant method. *Arab. J. Sci.* 46 (8), 7699–7718. doi:10.1007/s13369-021-05533-7
- Sahu, M., Sarkar, J., and Chandra, L. (2021). Steady-state and transient hydrothermal analyses of single-phase natural circulation loop using water-based tri-hybrid nanofluids. *AIChE J.* 67 (6), e17179. doi:10.1002/aic.17179
- Sharma, K., Vijay, N., Mabood, F., and Badruddin, I. A. (2022). Numerical simulation of heat and mass transfer in magnetic nanofluid flow by a rotating disk with variable fluid properties. *Int. Commun. Heat Mass Transf.* 133, 105977. doi:10.1016/j.icheatmasstransfer.2022.105977
- Shuaib, M., Shah, R. A., and Bilal, M. (2020). Variable thickness flow over a rotating disk under the influence of variable magnetic field: An application to parametric continuation method. *Adv. Mech. Eng.* 12 (6), 168781402093638. doi:10.1177/1687814020936385
- Shuaib, M., Shah, R. A., Durrani, I., and Bilal, M. (2020). Electrokinetic viscous rotating disk flow of Poisson–Nernst–Planck equation for ion transport. *J. Mol. Liq.* 313, 113412. doi:10.1016/j.molliq.2020.113412
- Sohail, M., Naz, R., and Abdelsalam, S. I. (2020). On the onset of entropy generation for a nanofluid with thermal radiation and gyrotactic microorganisms through 3D flows. *Phys. Scr.* 95 (4), 045206. doi:10.1088/1402-4896/ab3c3f
- Sohail, M., Naz, R., Shah, Z., Kumam, P., and Thounthong, P. (2019). Exploration of temperature dependent thermophysical characteristics of yield exhibiting non-Newtonian fluid flow under gyrotactic microorganisms. *AIP Adv.* 9 (12), 125016. doi:10.1063/1.5118929
- Sohail, M., Shah, Z., Tassaddiq, A., Kumam, P., and Roy, P. (2020). Entropy generation in MHD Casson fluid flow with variable heat conductance and thermal conductivity over non-linear bi-directional stretching surface. *Sci. Rep.* 10 (1), 12530. doi:10.1038/s41598-020-69411-2
- Swain, K., Mebarek-Oudina, F., and Abo-Dahab, S. M. (2022). Influence of MWCNT/Fe₃O₄ hybrid nanoparticles on an exponentially porous shrinking sheet with chemical reaction and slip boundary conditions. *J. Therm. Anal. Calorim.* 147 (2), 1561–1570. doi:10.1007/s10973-020-10432-4
- Ullah, I., Ali, R., Nawab, H., Uddin, I., Muhammad, T., Khan, I., et al. (2022). Theoretical analysis of activation energy effect on Prandtl–Eyring nanofluid flow subject to melting condition. *J. Non-Equilibrium Thermodyn.* 47 (1), 1–12. doi:10.1515/jnet-2020-0092
- Ullah, I. (2022). Heat transfer enhancement in Marangoni convection and nonlinear radiative flow of gasoline oil conveying Boehmite alumina and aluminum alloy nanoparticles. *Int. Commun. Heat Mass Transf.* 132, 105920. doi:10.1016/j.icheatmasstransfer.2022.105920
- Ullah, I., Ullah, R., Alqarni, M. S., Xia, W. F., and Muhammad, T. (2021). Combined heat source and zero mass flux features on magnetized nanofluid flow by radial disk with the applications of Coriolis force and activation energy. *Int. Commun. Heat Mass Transf.* 126, 105416. doi:10.1016/j.icheatmasstransfer.2021.105416
- Waini, I., Ishak, A., and Pop, I. (2022). Multiple solutions of the unsteady hybrid nanofluid flow over a rotating disk with stability analysis. *Eur. J. Mech. - B/Fluids* 94, 121–127. doi:10.1016/j.euromechflu.2022.02.011
- Wang, F., Khan, M. N., Ahmad, I., Ahmad, H., Abu-Zinadah, H., Chu, Y. M., et al. (2022). Numerical solution of traveling waves in chemical kinetics: Time-fractional Fishers equations. *Fractals* 30 (2), 2240051–2240134. doi:10.1142/s0218348x22400515
- Zhang, X. H., Algehyne, A., Ebrahem, A., Alshehri, G., Bilal, M., et al. (2021). The parametric study of hybrid nanofluid flow with heat transition characteristics over a fluctuating spinning disk. *Plos one* 16 (8), e0254457. doi:10.1371/journal.pone.0254457
- Zhao, T. H., Khan, M. I., and Chu, Y. M. (2021). Artificial neural networking (ANN) analysis for heat and entropy generation in flow of non-Newtonian fluid between two rotating disks. *Math. Methods Appl. Sci.* doi:10.1002/mma.7310
- Zhao, T. H., Wang, M. K., and Chu, Y. M. (2021). Concavity and bounds involving generalized elliptic integral of the first kind. *J. Math. Inequalities* 15 (2), 701–724. doi:10.7153/jmi-2021-15-50
- Zhao, T. H., Wang, M. K., Zhang, W., and Chu, Y. M. (2018). Quadratic transformation inequalities for Gaussian hypergeometric function. *J. Inequal. Appl.* 2018 (1), 251. doi:10.1186/s13660-018-1848-y
- Zhou, S. S., Bilal, M., Khan, M. A., and Muhammad, T. (2021). Numerical analysis of thermal radiative maxwell nanofluid flow over-stretching porous rotating disk. *Micromachines* 12 (5), 540. doi:10.3390/mi12050540



OPEN ACCESS

EDITED BY

Adnan,
Mohi-ud-Din Islamic University, Pakistan

REVIEWED BY

Syed Zulfiqar Ali Zaidi,
COMSATS IT Center, COMSATS University
Islamabad, Abbottabad Campus
Abbottabad, Pakistan
Zubair Ahmad,
University of Campania "Luigi Vanvitelli",
Italy

*CORRESPONDENCE

Mustafa Inc,
mustafainc1071@gmail.com

SPECIALTY SECTION

This article was submitted to Process and
Energy Systems Engineering,
a section of the journal Frontiers in Energy
Research

RECEIVED 07 June 2022

ACCEPTED 08 July 2022

PUBLISHED 25 August 2022

CITATION

Yao SW, Ahmad M, Inc M, Ahmad I, Asjad MI
and Nazar M (2022), Suction effect on MHD
flow of Brinkman-type fluid with heat
absorption and first-order chemical
reaction.

Front. Energy Res. 10:963583.

doi: 10.3389/fenrg.2022.963583

COPYRIGHT

© 2022 Yao, Ahmad, Inc, Ahmad, Asjad and
Nazar. This is an open-access article
distributed under the terms of the [Creative
Commons Attribution License \(CC BY\)](#). The
use, distribution or reproduction in other
forums is permitted, provided the original
author(s) and the copyright owner(s) are
credited and that the original publication in
this journal is cited, in accordance with
accepted academic practice. No use,
distribution or reproduction is permitted
which does not comply with these terms.

Suction effect on MHD flow of Brinkman-type fluid with heat absorption and first-order chemical reaction

Shao-Wen Yao¹, Mushtaq Ahmad², Mustafa Inc^{3,4*},
Ikhtlaq Ahmad², Muhammad Imran Asjad⁵ and
Mudassar Nazar^{2,6}

¹School of Mathematics and Information Science, Henan Polytechnic University, Jiaozuo, China,

²Centre for Advanced Studies in Pure and Applied Mathematics, Bahauddin Zakariya University,

Multan, Pakistan, ³Department of Computer Engineering, Biruni University, Istanbul, Turkey,

⁴Department of Medical Research, China Medical University Taichung, Taichung, Taiwan,

⁵Department of Mathematics, University of Management and Technology Lahore, Lahore, Pakistan,

⁶School of Mathematical Sciences, University of Science and Technology of China, Hefei, China

Suction/injection is a mechanical effect and used to control the energy losses in the boundary layer region by reducing the drag on the surface. In this study, unsteady MHD flow of Brinkman-type fluid with suction/injection, heat absorption, and chemical reaction is investigated and an analytical solution is established. The corresponding results for temperature, concentration, and velocity fields are obtained with the help of the Laplace transformation method analytically. The physical effects of thermal and mass Grashoff number, Prandtl number, Schmidt number, heat absorption parameter, first-order chemical reaction parameter, suction/injection, Brinkman parameter, and magnetic parameter have been discussed graphically. Finally, it is observed that in the presence of suction effect, fluid's velocity decreases gradually by increasing the value of suction parameter while show an increasing trend for the increasing value of the injection parameter.

KEYWORDS

suction/injection, MHD, Brinkman-type fluid, free convection, analytical solution

Introduction

In nature, the convective flow of fluids is not only induced by the temperature gradient but it is also generated due to the non-homogeneous concentration field. In several industrial and biological processes, the heat and mass transfer take place in chorus as a result of pooled buoyancy forces. In the presence of magnetic fields, such natural flows induced unevenness of thermal and species balances which are of great importance and have several applications in polymer industries and biological sciences. [Matin et al. \(2012\)](#) discussed the mixed convective flow of nanofluid past an extended surface under the influence of the fluctuating magnetic field. [Khan et al. \(2018\)](#) analyzed the MHD flow of viscous fluid enclosed in an open channel. Unsteady free convective

viscous fluid under a uniform magnetic field through porous media has been examined by Patel et al. (2015). Paul (2017) discussed the MHD free convection flow and presented the physical significance of magnetic force on fluid motion. Umavathi et al. (2018) also took into account the subjectivity of Lorentz forces on the electrically conducting fluid flow through a couple of parallel porous plates. Ali et al. (2013) investigated analytically the double convective flow with heat and mass transport in the presence of Lorentz forces. Ahmed et al. (2017) extended his work for an L-shaped porous medium and discussed the flow of fluid induced by temperature and concentration gradients. Babu et al. (2017) considered natural convected viscous fluid flow over an extended permeable flat surface in the presence of magnetic field of constant magnitude. Some studies regarding heat and mass transfer are found in Ahmad et al. (2019); Ahmed et al. (2019); Adnan et al. (2020); Ahmad et al. (2020); Khan et al. (2020); Yu-Ming Chu et al. (2020).

The suction/injection effect is significant in the boundary flow and is applied to minimize the energy losses due to the surface drag. This effect is also applied to construct the biological and mechanical suction devices. Bose et al. (2016) analyzed the suction/injection for MHD convective flow of fluid over a swinging role of the permeable plate. Modather et al. (2009) discussed MHD flow over an oscillatory surface of micropolar fluid. Jha et al. (2017) compared the numerical and analytical solutions by considering the effect of suction/injection. Ravindran (2013) examined slot suction/injection for convective flow and established numerical results for the conic domain. Aman (2017) established the results for the flow past an extended porous flat plate by imposing suction/injection on the boundary. Jha et al. (2015), Jha et al. (2018) presented the analytical solutions of natural convected flow with and without thermal radiation effects in vertical microchannel accompanied with a magnetic force by applying the suction/injection effect in the boundary layer region. Zeeshan et al. (2018) discussed the fluid motion generated by unbalanced temperature and mass distribution and blustered the effective role of uniform suction on fluid flow in the region of the boundary layer. Also, several other results regarding suction/injection boundary flows for transport phenomenon are found in Das (2010); Rajesh et al. (2010); Baoku et al. (2013); Ghosh et al. (2014); Akinshilo et al. (2017); Faladea et al. (2017).

The research work cited earlier regarding suction/injection is performed by numerical techniques. There is no exact result for velocity subjected to suction/injection and our main aim of the present research was to fill this gap. In this study, an unsteady free convective flow of chemically reacting Brinkman-type fluid by imposing suction/injection on the boundary is shown. The Laplace transformation technique is applied to obtain the analytical expressions for temperature, concentration, and velocity. The role of suction/injection in the flow domain is also explained with other physical parameters graphically.

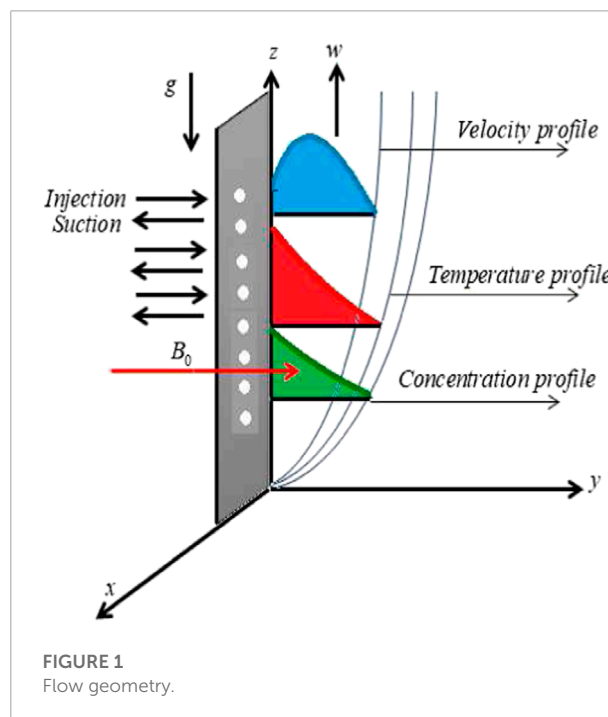
Formulation of problem

Suppose Brinkman fluid is lying at rest over an infinite plate placed in the xz -plane in such a way that the y -axis is taken along the outward normal to the plane of plate. In the beginning, time fluid with plate is in static equilibrium and physical state is described by temperature T_∞ and concentration C_∞ as shown in Figure 1. After the time $t > 0$, plate is supposed to move with velocity $U_0 f(t)$. Where $f(t)$ satisfied $f(0) = 0$. A constant temperature T_w is maintained with the concentration level near the plate. The flow is directed in the z -direction and the velocity gradient exists in the direction of the y -axis so velocity is as $\vec{V} = \vec{V}(0, 0, w) = w(y, t)\hat{k}$, where the unit vector \hat{k} is pointed in the direction of velocity. A suctional velocity orthogonal to the plane of plate may be written as $v = -v_0$. The momentum, energy, and mass balance equations which govern the flow may be taken in the following form (Modather et al., 2009; Bose et al., 2016):

$$\frac{\partial w(y, t)}{\partial t} - v_0 \frac{\partial w(y, t)}{\partial y} + \beta w(y, t) = \nu \frac{\partial^2 w(y, t)}{\partial y^2} + g\beta_T (T(y, t) - T_\infty) + g\beta_C (C(y, t) - C_\infty) - \frac{\sigma B_0^2 w(y, t)}{\rho}, \quad (1)$$

$$\frac{\partial T(y, t)}{\partial t} - v_0 \frac{\partial T(y, t)}{\partial y} = \frac{k}{\rho C_p} \frac{\partial^2 T(y, t)}{\partial y^2} - \frac{Q}{\rho c_p} (T(y, t) - T_\infty), \quad (2)$$

$$\frac{\partial C(y, t)}{\partial t} - v_0 \frac{\partial C(y, t)}{\partial y} = D \frac{\partial^2 C(y, t)}{\partial y^2} - K_r (C(y, t) - C_\infty), \quad (3)$$



where ρ is the density, v_0 is the constant suction velocity, β is the Brinkman parameter, w is the velocity of fluid, t is time, T is the fluid temperature, T_w is thermal state at wall, T_∞ is temperature at infinity, k denotes thermal conduction, β_T and β_C denote the constant of volumetric expansion, C_p is specific heat at perseverance, force (pressure), $Q \geq 0$ is heat absorption, K_r is the chemical reaction parameter, B_0 is the constant magnetic field, and D is mass diffusion.

The adequate conditions at boundary for field variables are:

$$\begin{aligned} w(y, 0) &= 0, \quad T(y, 0) = T_\infty, \quad C(y, 0) = C_\infty, \\ w(0, t) &= U_0 f(t), \quad T(0, t) = T_w, \quad C(0, t) = C_w, \\ w(\infty, t) &= 0, \quad T(\infty, t) = T_\infty, \quad C(\infty, t) = C_\infty. \end{aligned} \quad (4)$$

By inserting the following relations in Eqs 1–4:

$$\begin{aligned} y^* &= \frac{(U_0)y}{v}, \quad t^* = \frac{U_0^2 t}{v}, \quad w^* = \frac{w}{U_0}, \quad T^* = \frac{T - T_\infty}{T_w - T_\infty}, \\ C^* &= \frac{C - C_\infty}{C_w - C_\infty}, \quad Gr = \frac{g\beta_T(T_w - T_\infty)v}{U_0^3}, \\ Gm &= \frac{g\beta_C(C_w - C_\infty)v}{U_0^3}, \quad Pr = \frac{\mu C_p}{k}, \quad Sc = \frac{v}{D}, \\ M &= \frac{\sigma B_0 v}{U_0^2}, \quad Q_0 = \frac{Qv}{\rho C_p U_0^2}, \quad \lambda = \frac{K_r v}{U_0^2}, \quad s = \frac{v_0}{U_0}, \\ \beta_0 &= \frac{v\beta}{U_0^0}, \end{aligned} \quad (5)$$

we obtained the following equations:

$$\begin{aligned} \frac{\partial w(y, t)}{\partial t} - s \frac{\partial w(y, t)}{\partial y} + \frac{v\beta w(y, t)}{w_0^2} &= \frac{\partial^2 w(y, t)}{\partial y^2} + GrT(y, t) \\ &+ GmC(y, t) - Mw(y, t), \end{aligned} \quad (6)$$

$$\frac{\partial T(y, t)}{\partial t} - s \frac{\partial T(y, t)}{\partial y} = \frac{1}{Pr} \frac{\partial^2 T}{\partial y^2} - Q_0 T(y, t), \quad (7)$$

$$\frac{\partial C(y, t)}{\partial t} - s \frac{\partial C(y, t)}{\partial y} = \frac{1}{Sc} \frac{\partial^2 C}{\partial y^2} - \lambda C(y, t), \quad (8)$$

$$\begin{aligned} w(y, 0) &= 0, \quad T(y, 0) = 0, \quad C(y, 0) = 0, \\ w(0, t) &= h(t), \quad T(0, t) = 1, \quad C(0, t) = 1, \\ w(\infty, t) &= 0, \quad T(\infty, t) = 0, \quad C(\infty, t) = 0. \end{aligned} \quad (9)$$

Solution of problem

Calculation of temperature

Eq. 7 with Laplace transform and condition (9)₁, is transformed to ordinary differential equations in \bar{T}

$$\frac{\partial^2 \bar{T}(y, q)}{\partial y^2} + Prs \frac{\partial \bar{T}}{\partial y} - Pr(q + Q_0) \bar{T}(y, q) = 0. \quad (10)$$

Eq. 10 satisfies

$$\bar{T}(0, q) = \frac{1}{q}, \text{ and } \bar{T}(\infty, q) = 0. \quad (11)$$

The solution of Eq. 10 subjected to condition (11) is as follows:

$$\bar{T}(y, q) = \frac{1}{q} \exp \left(-y \left(\frac{Prs}{2} + \sqrt{\left(\frac{Prs}{2} \right)^2 + Pr(q + Q_0)} \right) \right). \quad (12)$$

In a suitable form:

$$\bar{T}(y, q) = e^{-yc_1} \frac{1}{q} \exp \left(-y\sqrt{Pr}\sqrt{q + d_1} \right). \quad (13)$$

where $c_1 = \left(\frac{Prs}{2} \right)$ and $d_1 = \frac{Prs^2}{4} + Q_0$.

Eq. 13 is re-transformed in the t -domain by inversion of Laplace transform with composite formula as:

$$\begin{aligned} T(y, t) &= \frac{e^{-yc_1}}{2} \left[\exp \left(-y\sqrt{Pr}\sqrt{d_1} \right) \times \operatorname{erfc} \left(\frac{y\sqrt{Pr}}{2\sqrt{t}} - \sqrt{d_1 t} \right) + \right. \\ &\quad \left. \exp \left(-y\sqrt{Pr}\sqrt{d_1} \right) \operatorname{erfc} \left(\frac{y\sqrt{Pr}}{2\sqrt{t}} + \sqrt{d_1 t} \right) \right]. \end{aligned} \quad (14)$$

Calculation of concentration

In a similar manner as adopted in the case of the temperature field, Eq. 8 with respective boundary conditions from Eq. 9 can be solved for the concentration field as follows:

$$\bar{C}(y, q) = \frac{1}{q} \exp \left(-y \left(\frac{Scs}{2} + \sqrt{\left(\frac{Scs}{2} \right)^2 + Sc(q + \lambda)} \right) \right). \quad (15)$$

In a suitable form:

$$\bar{C}(y, q) = e^{-yc_2} \frac{1}{q} \exp \left(-y\sqrt{Sc}\sqrt{q + d_2} \right), \quad (16)$$

where $c_2 = \left(\frac{Scs}{2} \right)$, $d_2 = \frac{Scs^2}{4} + \lambda$.

Eq. 16 is re-transformed as:

$$\begin{aligned} C(y, t) &= \frac{e^{-yc_2}}{2} \left[\exp \left(-y\sqrt{Sc}\sqrt{d_2} \right) \operatorname{erfc} \left(\frac{y\sqrt{Sc}}{2\sqrt{t}} - \sqrt{d_2 t} \right) \right. \\ &\quad \left. + \exp \left(-y\sqrt{Sc}\sqrt{d_2} \right) \operatorname{erfc} \left(\frac{y\sqrt{Sc}}{2\sqrt{t}} + \sqrt{d_2 t} \right) \right]. \end{aligned} \quad (17)$$

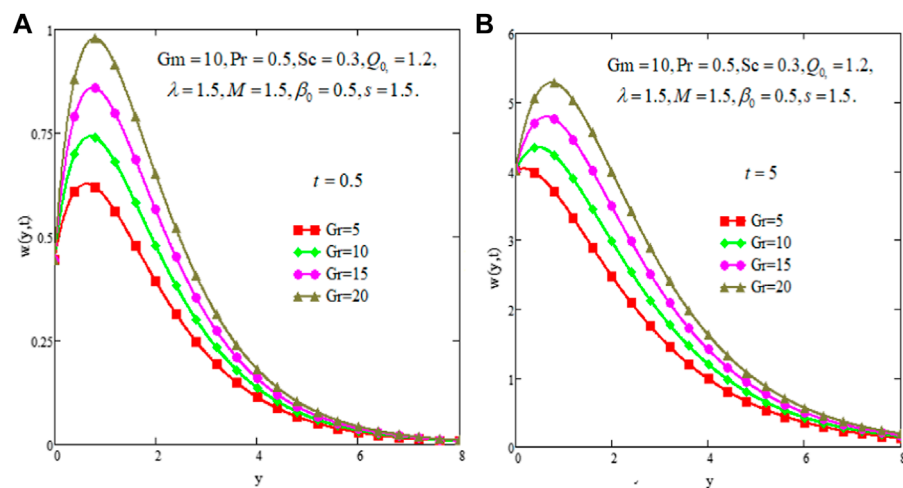


FIGURE 2
Velocity due to Gr for small time (A) and for large time (B).

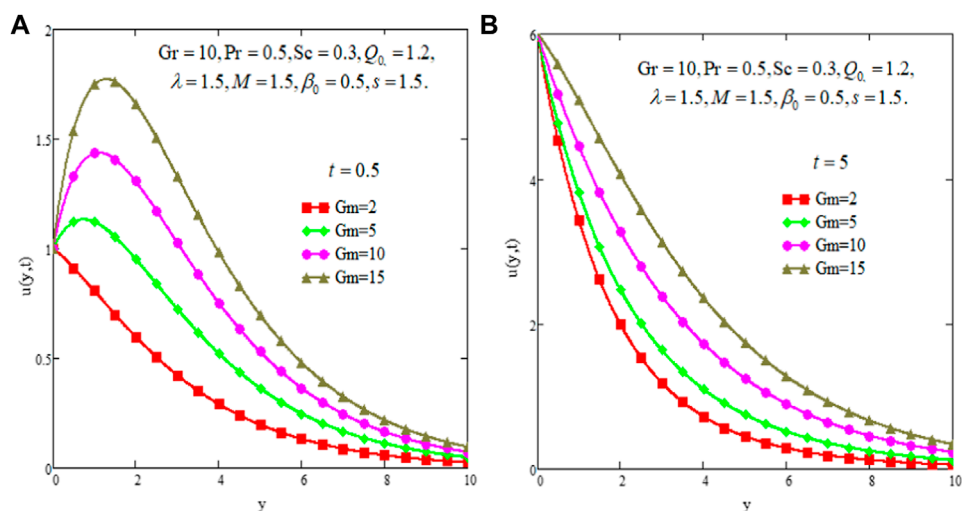


FIGURE 3
Velocity due to Gm for Small time (A) and for large time (B).

Velocity

Imposing Laplace transform to Eq. 6, we obtain the following transformed ordinary differential equation:

$$\frac{\partial^2 \bar{w}(y, q)}{\partial y^2} + s \frac{\partial \bar{w}(y, q)}{\partial y} - (q + M + \beta_0) \bar{w}(y, q) = -Gr \bar{T}(y, q) - Gm \bar{C}(y, q). \quad (18)$$

Eq. 18 is in hold for following specification:

$$\bar{w}(0, q) = \bar{f}(q) \quad \bar{w}(\infty, q) = 0. \quad (19)$$

Eq. 18 with condition (19) can be solved and after performing lengthy calculation, its solution takes the following

form:

$$\begin{aligned} \bar{w}(y, q) = & \bar{f}(q) \exp\left(-y\left(a + \sqrt{q+b}\right)\right) \\ & + \frac{Gr \left[\exp\left(-y\left(a + \sqrt{q+b}\right)\right) - \exp\left(-y\left(c_1 + \sqrt{Pr}\sqrt{q+d_1}\right)\right) \right]}{\left[\left(c_1 + \sqrt{Pr}\sqrt{q+d_1}\right)^2 - s\left(c_1 + \sqrt{Pr}\sqrt{q+d_1}\right) - (q + M + \beta_0) \right] q} \\ & + \frac{Gm \left[\exp\left(-y\left(a + \sqrt{q+b}\right)\right) - \exp\left(-y\left(c_2 + \sqrt{Sc}\sqrt{q+d_2}\right)\right) \right]}{\left[\left(c_2 + \sqrt{Sc}\sqrt{q+d_2}\right)^2 - s\left(c_2 + \sqrt{Sc}\sqrt{q+d_2}\right) - (q + M + \beta_0) \right] q}, \quad (20) \end{aligned}$$

where $a = \frac{s}{2}$ and $b = a^2 + M + \beta_0$.

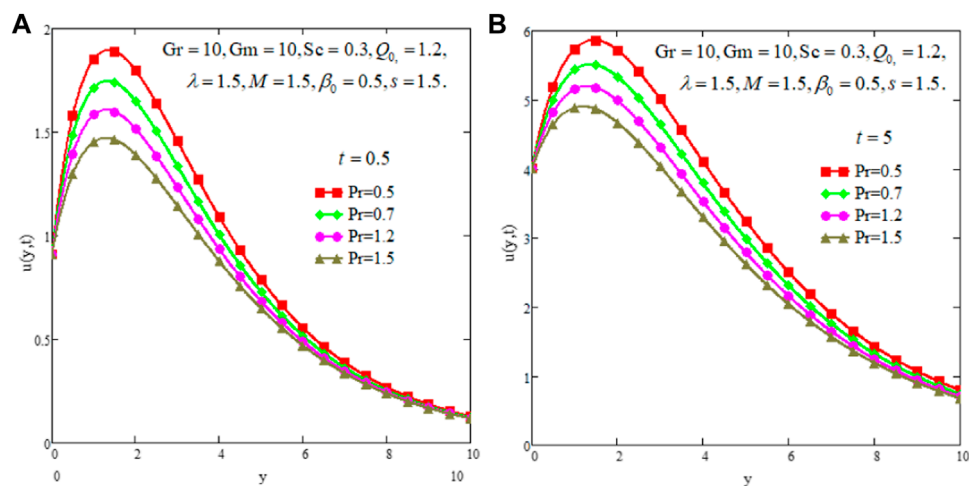


FIGURE 4
Velocity due to Pr for small time (A) and for large time (B).

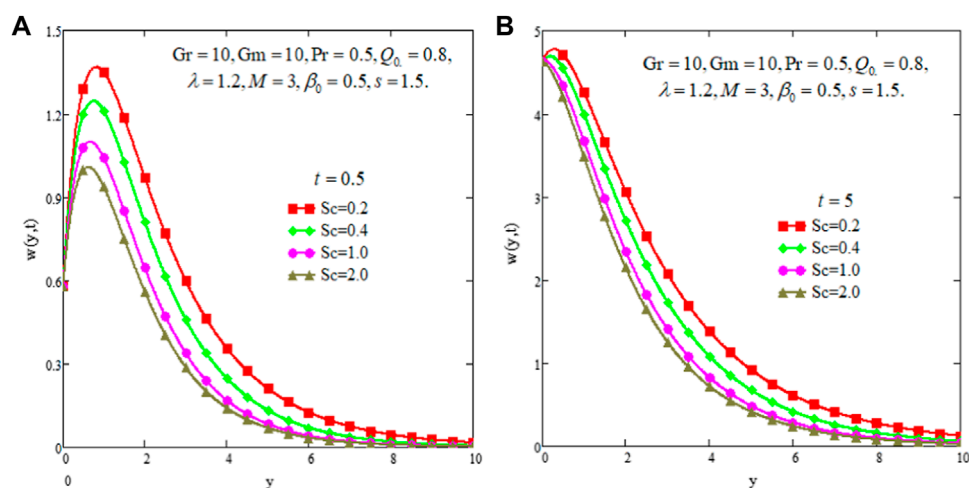


FIGURE 5
Velocity due to Sc for small time (A) and for large time (B).

In a suitable form:

$$\begin{aligned} \bar{w}(y, q) = & e^{-\gamma a} \bar{f}(q) \exp(-\gamma \sqrt{q+b}) \\ & + \frac{Gr}{\left[(c_1 + \sqrt{Pr} \sqrt{q+d_1})^2 - s(c_1 + \sqrt{Pr} \sqrt{q+d_1}) - (q+M+\beta_0) \right]} \\ & \times \left[e^{-\gamma a} \frac{1}{q} \exp(-\gamma \sqrt{q+b}) - e^{-\gamma c_1} \frac{1}{q} \exp(-\gamma \sqrt{Pr} \sqrt{q+d_1}) \right] \\ & + \frac{Gm}{\left[(c_2 + \sqrt{Sc} \sqrt{q+d_2})^2 - s(c_2 + \sqrt{Sc} \sqrt{q+d_2}) - (q+M+\beta_0) \right]} \\ & \times \left[e^{-\gamma a} \frac{1}{q} \exp(-\gamma \sqrt{q+b}) - e^{-\gamma c_2} \frac{1}{q} \exp(-\gamma \sqrt{Sc} \sqrt{q+d_2}) \right]. \quad (21) \end{aligned}$$

Consider the following equations:

$$F_1(y, q) = \exp(-\gamma \sqrt{q+b}), \quad (22)$$

$$F_2(y, q) = \frac{1}{q} \exp(-\gamma \sqrt{q+b}), \quad (23)$$

$$F_3(y, q) = \frac{1}{q} \exp(-\gamma \sqrt{Pr} \sqrt{q+d_1}), \quad (24)$$

$$F_4(y, q) = \frac{1}{q} \exp(-\gamma \sqrt{Sc} \sqrt{q+d_2}), \quad (25)$$

and

$$A_1(q) = \frac{1}{\left[\left(c_1 + \sqrt{\text{Pr}} \sqrt{q+d_1} \right)^2 - s \left(c_1 + \sqrt{\text{Pr}} \sqrt{q+d_1} \right) - (q+M+\beta_0) \right]}, \quad (26)$$

$$A_2(q) = \frac{1}{\left[\left(c_2 + \sqrt{\text{Sc}} \sqrt{q+d_2} \right)^2 - s \left(c_2 + \sqrt{\text{Sc}} \sqrt{q+d_2} \right) - (q+M+\beta_0) \right]}, \quad (27)$$

Eqs 26, 27 can be written in a suitable form as follows:

$$A_1(q) = \frac{1}{(m_1 - m_2)(\text{Pr} - 1)} \left[\frac{(r_1 + m_1)}{(q - m_1)} - \frac{(r_1 + m_2)}{(q - m_2)} - \frac{r_2(d_1 + m_1)}{\sqrt{q+d_1}(q - m_1)} + \frac{r_2(d_1 + m_2)}{\sqrt{q+d_1}(q - m_2)} \right], \quad (28)$$

$$A_2(q) = \frac{1}{(m_3 - m_4)(\text{Sc} - 1)} \left[\frac{(r_3 + m_3)}{(q - m_3)} - \frac{(r_3 + m_4)}{(q - m_4)} - \frac{r_4(d_2 + m_3)}{\sqrt{q+d_2}(q - m_3)} + \frac{r_4(d_2 + m_4)}{\sqrt{q+d_2}(q - m_4)} \right], \quad (29)$$

where

$$r_1 = \frac{c_1^2 + \text{Pr}d_1 + sc_1 - M - \beta_0}{\text{Pr} - 1}, \quad r_2 = \frac{\sqrt{\text{Pr}}(2c_1 + s)}{\text{Pr} - 1}, \quad r_3 = \frac{c_2^2 + \text{Sc}d_2 + sc_2 - M - \beta_0}{\text{Sc} - 1}, \quad r_4 = \frac{\sqrt{\text{Sc}}(2c_2 + s)}{\text{Sc} - 1},$$

$$(m_1, m_2) = \frac{-(2r_1 - r_2^2) \pm \sqrt{(2r_1 - r_2^2)^2 - 4(r_1^2 - r_2^2d_1)}}{2},$$

and

$$(m_3, m_4) = \frac{-(2r_3 - r_4^2) \pm \sqrt{(2r_3 - r_4^2)^2 - 4(r_3^2 - r_4^2d_2)}}{2}.$$

Inverting the Laplace transform in Eqs 22–25 and Eqs 28, 29.

$$F_1(y, t) = \frac{1}{2} \left[\exp(-y\sqrt{b}) \text{erfc} \left(\frac{y - 2\sqrt{bt}}{2\sqrt{t}} \right) + \exp(y\sqrt{b}) \text{erfc} \left(\frac{y + 2\sqrt{bt}}{2\sqrt{t}} \right) \right], \quad (30)$$

$$F_2(y, t) = \frac{1}{2} \left[\exp(-y\sqrt{b}) \text{erfc} \left(\frac{y}{2\sqrt{t}} - \sqrt{bt} \right) + \exp(-y\sqrt{b}) \text{erfc} \left(\frac{y}{2\sqrt{t}} - \sqrt{bt} \right) \right], \quad (31)$$

$$F_3(y, t) = \frac{1}{2} \left[\exp(-y\sqrt{\text{Pr}d_1}) \text{erfc} \left(\frac{y\sqrt{\text{Pr}}}{2\sqrt{t}} - \sqrt{d_1t} \right) + \exp(-y\sqrt{\text{Pr}d_1}) \text{erfc} \left(\frac{y\sqrt{\text{Pr}}}{2\sqrt{t}} + \sqrt{d_1t} \right) \right], \quad (32)$$

$$F_4(y, t) = \frac{1}{2} \left[\exp(-y\sqrt{\text{Sc}d_2}) \text{erfc} \left(\frac{y\sqrt{\text{Sc}}}{2\sqrt{t}} - \sqrt{d_2t} \right) + \exp(-y\sqrt{\text{Sc}d_2}) \text{erfc} \left(\frac{y\sqrt{\text{Sc}}}{2\sqrt{t}} + \sqrt{d_2t} \right) \right], \quad (33)$$

and

$$A_1(t) = \frac{1}{(\text{Pr} - 1)(m_1 - m_2)} \left[(r_1 + m_1) e^{m_1 t} - (r_1 + m_2) e^{m_2 t} - r_2(d_1 + m_1) r_2(d_1 + m_2) \frac{e^{m_1 t}}{\sqrt{d_1 + m_1}} \text{erf} \left(\sqrt{(d_1 + m_1)t} \right) \right], \quad (34)$$

$$A_2(t) = \frac{1}{(\text{Sc} - 1)(m_3 - m_4)} \left[(r_3 + m_3) e^{m_3 t} - (r_3 + m_4) e^{m_4 t} - r_4(d_2 + m_3) r_4(d_2 + m_4) \frac{e^{m_3 t}}{\sqrt{d_2 + m_3}} \text{erf} \left(\sqrt{(d_2 + m_3)t} \right) \right]. \quad (35)$$

After inverting Laplace transform in Eq. 21 and using Eqs 30–35, finally we obtained the velocity in the t-domain.

$$w(y, t) = \exp(-ya) \int_0^t f(t - \tau) F_1(\tau) d\tau + \text{Gr} \int_0^t A_1(t - \tau) [\exp(-ya) F_2(\tau) - \exp(-yc_1) F_3(\tau)] d\tau + \text{Gm} \int_0^t A_2(t - \tau) [\exp(-ya) F_2(\tau) - \exp(-yc_2) F_4(\tau)] d\tau. \quad (36)$$

Some specifications on arbitrary function $f(t)$

The velocity $w(y, t)$, given by Eq. 36, mainly contains two terms: the first term is the mechanical contribution due to the motion of plate with an arbitrary velocity while the other part of the solution is the result of heat and mass transfer. Therefore, the mechanical part is given as follows:

$$w_m(y, t) = \exp(-ya) \int_0^t f(t - \tau) F_1(\tau) d\tau. \quad (37)$$

Case-I [$f(t) = t^\alpha$].

By introducing the $f(t) = t^\alpha$ in Eq. 37 when plate is moving with a variable velocity.

$$w_m(y, t) = \exp(-ya) \int_0^t (t - \tau)^\alpha F_1(\tau) d\tau. \quad (38)$$

Case-II [$f(t) = \sin(\omega t)$].

$$w_m(y, t) = \exp(-ya) \int_0^t \sin(\omega(t - \tau)) F_1(\tau) d\tau. \quad (39)$$

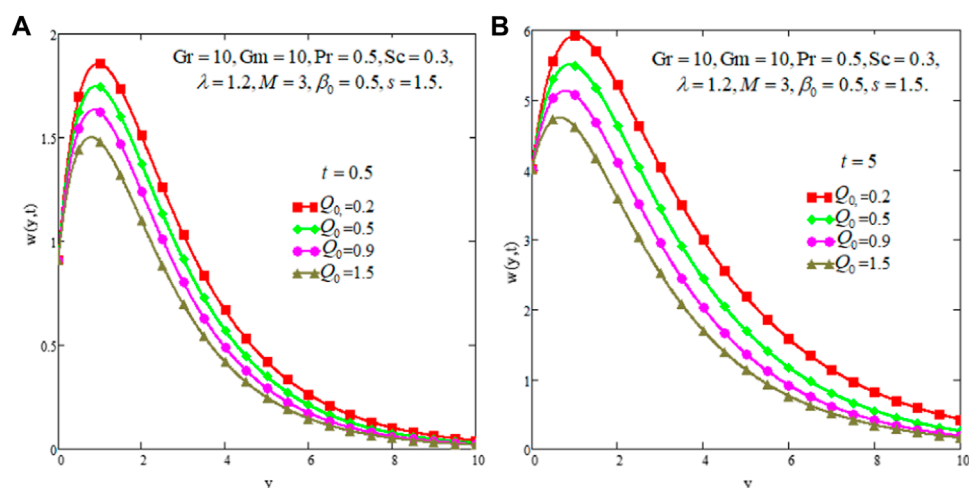


FIGURE 6
Velocity due to Q_0 for small time (A) and for large time (B).

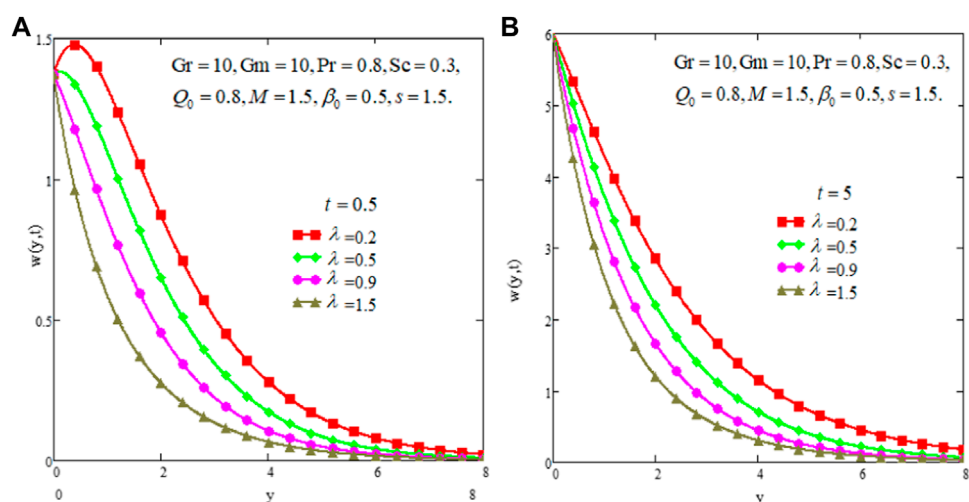


FIGURE 7
Velocity due to λ for small time (A) and for large time (B).

Numerical discussion and results

In this section, the impact of suction/injection and the other physical parameters in the flow domain are explained graphically. The effect of Gr for small and large times is elaborated in Figures 2A,B. Increasing values of Gr refer to stronger buoyancy forces which generate more convective effects, therefore; velocity profiles exhibit an increasing trend due to an increasing Gr in both figures drawn for small and large times and fluid velocity is higher for large time than that for the small time.

Figures 3A,B depicts the influence of mass Grashoff number Gm on velocity profiles. Figures outlined revealed that fluid velocity speeds up under the successive increment in the values of Gm . The greater values of Gm mean that there are large buoyancy forces due to the concentration gradient which generate more fluid motion.

The effect of Pr is discussed in Figures 4A,B. From the figures it is shown that there is a decreasing trend in velocity profiles for Pr . For larger values of Pr , the viscous forces dominate the inertial forces and create more internal friction in the fluid

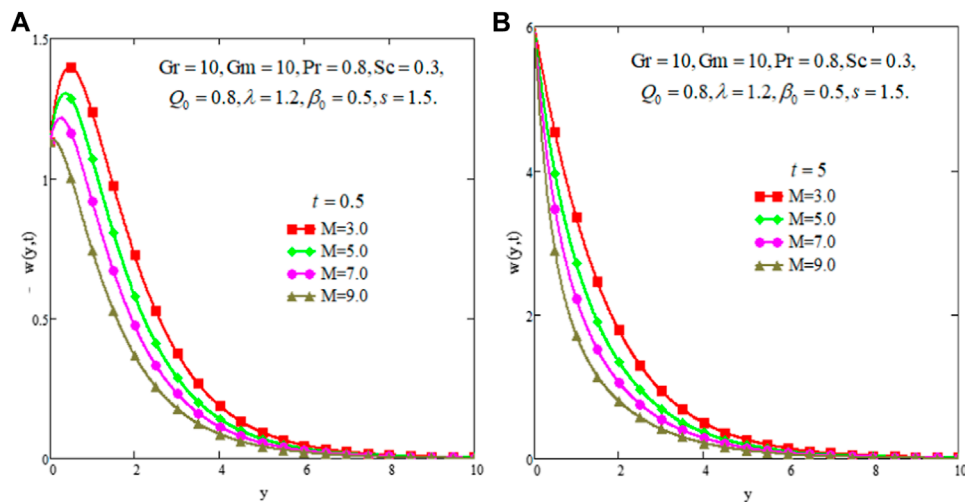


FIGURE 8
Velocity due to M for small time (A) and for large time (B).

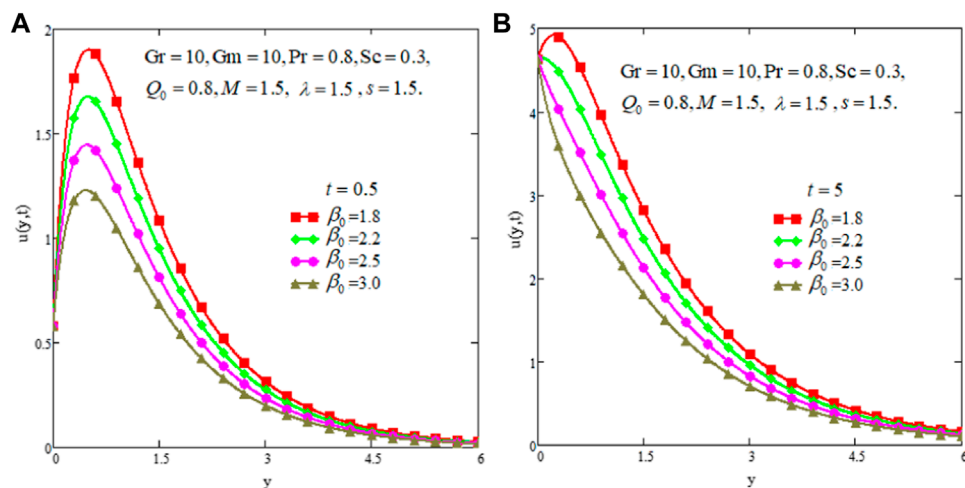


FIGURE 9
Velocity profile due to β_0 variation for small time (A) and for large time (B).

flow and consequently fluid slows down. Figures 5A,B present the effect of Sc on fluid velocity. As shown in both figures, velocity slows down for enhancing values of Sc but fluid velocity is higher for large time than that for the small time. In Figures 6A,B, the effect of heat absorption parameter Q_0 on fluid velocity is depicted. The figure graphic shows that the increase in Q_0 slows down the fluid motion. Whenever large numeric values are given to Q_0 , the fluid temperature is lowered down and consequently the fluid velocity decreases. However, for the large time; the fluid velocity remains higher than that for the small time. The effects

of chemical reaction parameter λ are shown in Figures 7A,B. The fluid velocity behaves against λ in similar a manner as due to Q_0 .

The subjectivity of fluid velocity under magnetic force is outlined in Figures 8A,B and fluid is retarded with the magnetic parameter. The physical significance of this effect is that the stronger magnetic field opposes the force to fluid velocity, therefore; the fluid motion slows down. The influence of the Brinkman parameter is shown in Figures 9A,B. It is clear that velocity profiles lower down with an enhancing β_0 for small and large times. β_0 is the material constant and its higher value refers

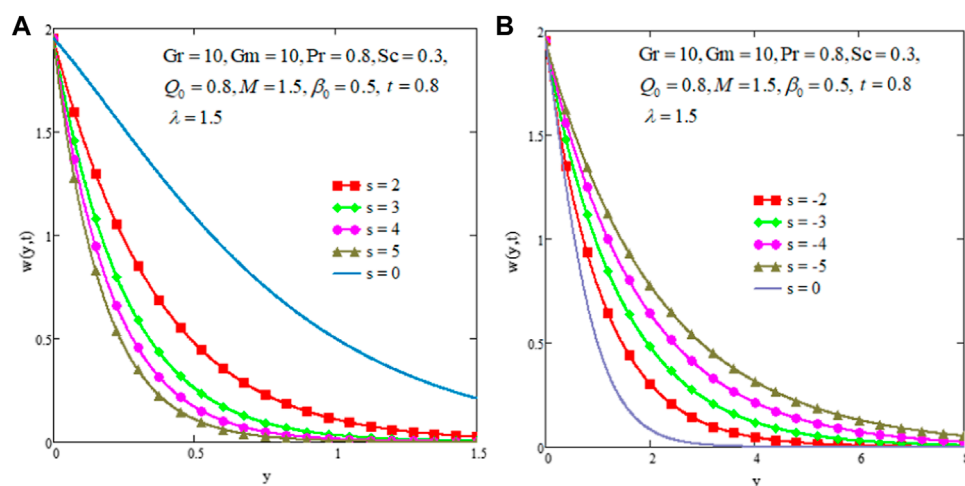


FIGURE 10
Velocity profile due to suction ($s > 0$) (A) and injection ($s < 0$) (B).

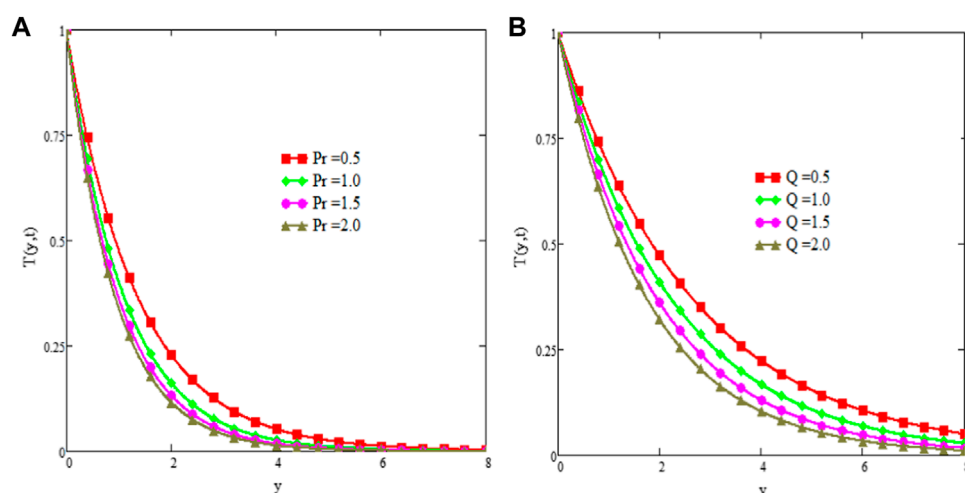


FIGURE 11
Temperature profiles for Pr (A) and Q (B) variations.

to more thick fluid. Therefore, the higher value of β_0 means that there is more dragging force to fluid flow, so consequently fluid velocity slows down.

The suction/injection effects on fluid velocity are presented in **Figures 10A,B**. The $s > 0$ refers to suction while $s < 0$ indicates the injection and $s = 0$ means no suction/injection in the flow domain. **Figure 10A** shows the effect of parameter s and it is observed that the fluid velocity decreases with the increasing values of suction parameter ($s > 0$). **Figure 10B** shows the variation in velocity of fluid with respect to injection and from this figure, it is clear that the fluid speeds up with injection ($s < 0$). In **Figures 11A,B**, the temperature profile is plotted for

the variation of Pr and Q , respectively. From the figures it is observed that temperature profiles lower down for the increasing value of Pr and Q .

Conclusion

The mathematical model of unsteady natural flow of MHD Brinkman-type fluid with suction/injection, heat absorption, and chemical reaction of first-order is considered. The corresponding solutions of temperature, concentration, and velocity fields are established. The physical effects of parameters are seen

graphically. Moreover, it is clear that in the presence of suction at the boundary the flow slows down while for the injection effect flow speeds up. The key outcomes of the study are listed as follows:

- The $s > 0$ refers to the suction and hence an increasing value of s slowdowns the fluid flow.
- The $s < 0$ refers to the injection and by increasing the numeric value of $(-s)$, it speeds up the fluid flow.
- The fluid velocity increases for Gr , Gm , time, t , and injection parameter $(-s)$.
- The fluid velocity decreases for M , β_0 , t , Q_0 , λ , and suction parameter (s) .

Data availability statement

Publicly available datasets were analyzed in this study. These data can be found here. No link.

Author contributions

All authors listed have made a substantial, direct, and intellectual contribution to the work and approved it for publication.

References

- Adnan, Ali Zaidi, S. Z., Khan, U., Abdeljawad, T., Ahmed, N., Mohyud-Din, S. T., et al. (2020). Investigation of thermal transport in multi-shaped Cu nanomaterial-based nanofluids. *Materials* 13, 2737. doi:10.3390/ma13122737
- Ahmad, M., Imran, M. A., and Nazar, M. (2020). Mathematical modeling of (Cu–Al₂O₃) water based Maxwell hybrid nanofluids with Caputo-Fabrizio fractional derivative. *Adv. Mech. Eng.* 12 (9), 168781402095884–11. doi:10.1177/1687814020958841
- Ahmad, M., Imran, M. A., Aleem, M., and Khan, I. (2019). A comparative study and analysis of natural convection flow of MHD non-Newtonian fluid in the presence of heat source and first-order chemical reaction. *J. Therm. Anal. Calorim.* 137 (5), 1783–1796. doi:10.1007/s10973-019-08065-3
- Ahmed, N., Adnan, Khan, U., Zaidi, S. Z. A., Faisal, I., and Mohyud-Din, S. T. (2019). Heat transfer intensification in hydromagnetic and radiative 3D unsteady flow regimes: A comparative theoretical investigation for aluminum and γ -aluminum oxides nanoparticles. *J. Cent. South Univ.* 26, 1233–1249. doi:10.1007/s11771-019-4083-x
- Ahmed, S., Azeem, N. J., and Yunus Khan, T. M. (2017). Heat and mass transfer in an L shaped porous medium. *IOP Conf. Ser. Mat. Sci. Eng.* 225, 012011–17. doi:10.1088/1757-899x/225/1/012011
- Akinshilo, A. T., Olofinlaja, J. O., and Olaye, O. (2017). Flow and heat transfer analysis of the sodium alginate conveying copper nanoparticles between two parallel plates. *J. Appl. Comput. Mech.* 3 (4), 258–266.
- Ali, F., Khan, I., Shafie, S., and Musthapa, N. (2013). Heat and mass transfer with free convection mhd flow past a vertical plate embedded in a porous medium. *Math. Problems Eng.* 2013, 1–13. doi:10.1155/2013/346281
- Aman, S., Salleh, M. Z., Ismail, Z., and Khan, I. (2017). Exact solution for heat transfer free convection flow of Maxwell nanofluids with graphene nanoparticles. *J. Phys.* 2017, 1–14.
- Babu, D. D., Venkateswarlu, S., and Reddy, E. K. (2017). Heat and mass transfer on mhd free convective flow of second grade fluid through porous medium over an infinite vertical plate. *IOP Conf. Ser. Mat. Sci. Eng.* 225, 012267–555. doi:10.1088/1757-899x/225/1/012267
- Baoku, I. G., Olajuwon, B. I., and Mustapha, A. O. (2013). Heat and mass transfer on a MHD third grade fluid with partial slip flow past an infinite vertical insulated porous plate in a porous medium. *Int. J. Heat Fluid Flow* 40, 81–88. doi:10.1016/j.ijheatfluidflow.2013.01.016
- Bose, D., and Basu, U. (2016). MHD convective flow of non-Newtonian fluid through porous medium over an oscillating porous plate with suction. *Int. J. Comput. Appl.* 134 (10), 15–19. doi:10.5120/ijca2016908066
- Das, K. (2010). Exact solution of MHD free convection flow and mass transfer near a moving vertical plate in presence of thermal radiation. *Afr. J. Math. Phys.* 8, 29–41.
- Faladea, J. A., Ukaegbu, C., EgerebSamue, A. C., and Adesanya, O. (2017). MHD oscillatory flow through a porous channel saturated with porous medium. *Alexandria Eng. J.* 56 (1), 147–152. doi:10.1016/j.aej.2016.09.016
- Ghosh, A. K., Datta, S. K., and Sen, P. (2014). A note on hydromagnetic flow of an Oldroyd-B fluid near an infinite plate induced by half rectified sine pulses. *Open J. Fluid Dyn.* 4, 226–240. doi:10.4236/ojfd.2014.42017
- Jha, B. K., Aina, B., and Ajiya, A. T. (2015). Role of suction/injection on mhd natural convection flow in a vertical microchannel. *Int. J. Energy Technol.* 7 (2), 30–39.

Funding

The study was supported by the National Natural Science Foundation of China (No. 71601072), the Fundamental Research Funds for the Universities of Henan Province (No. NSFRF210314), and the Innovative Research Team of Henan Polytechnic University (No. T2022-7).

Conflict of interest

The authors declare that the research was conducted in the absence of any commercial or financial relationships that could be construed as a potential conflict of interest.

Publisher's note

All claims expressed in this article are solely those of the authors and do not necessarily represent those of their affiliated organizations, or those of the publisher, the editors, and the reviewers. Any product that may be evaluated in this article, or claim that may be made by its manufacturer, is not guaranteed or endorsed by the publisher.

- Jha, B. K., Iro, C., and Joseph, S. B. (2017). Effects of suction-injection-combination (SIC) on transient free-convective-radiative flow in a vertical porous channel. *Proc. Institution Mech. Eng. Part E J. Process Mech. Eng.* 231 (2), 73–82. doi:10.1177/0954408915576300
- Jha, B. K., Isah, B. Y., and Uwanta, I. J. (2018). Combined effect of suction/injection on mhd free-convection flow in a vertical channel with thermal radiation. *Ain Shams Eng. J.* 9, 1069–1088. doi:10.1016/j.asej.2016.06.001
- Khan, U., Adnan, Ahmed, N., Mohyud-Din, S. T., Chu, Y.-M., Khan, I., et al. (2020). γ -Nanofluid thermal transport between parallel plates suspended by micro-cantilever sensor by incorporating the effective Prandtl model: Applications to biological and medical sciences. *Molecules* 25, 1777. doi:10.3390/molecules25081777
- Khan, Z. A., Haq, S., Khan, T. S., Khan, I., and Tlili, I. (2018). Unsteady MHD flow of a Brinkman type fluid between two side walls perpendicular to an infinite plate. *Results Phys.* 9, 1602–1608. doi:10.1016/j.rinp.2018.04.034
- Matin, M. H., Nobar, M. R., and Jahangiri, P. (2012). Entropy analysis in mixed convection MHD flow of nanofluid over a non-linear stretching sheet. *J. Therm. Sci. Technol.* 7 (1), 104–119. doi:10.1299/jtst.7.104
- Modather, M., Rashad, A. M., and Chamkha, A. J. (2009). An analytical study of MHD heat and mass transfer oscillatory flow of a micropolar fluid over a vertical permeable plate in a porous medium. *Turkish J. Eng. Environ. Sci.* 33, 245–257.
- Patel, H. K., Singh, R. K., and Singh, T. R. (2015). Transient free convective mhd flow through porous medium in slip flow regime. *IOSR J. Math.* 11 (5), 52–58.
- Paul, A., and Dek, R. K. (2017). Unsteady natural convection flow past an infinite cylinder with thermal and mass stratification. *Int. J. Eng. Math.* 2017, 1–13. doi:10.1155/2017/8410691
- Rajesh, V., and Varma, S. V. K. (2010). Heat source effects on mhd flow past an exponentially accelerated vertical plate with variable temperature through a porous medium. *Int. J. Appl. Math. Mech.* 6 (12), 68–78.
- Ravindran, R., and Ganspathirao, M. (2013). Non-uniform slot suction/injection into mixed convection boundary layer flow over vertical cone. *Appl. Math. Mech.* 34, 1327–38. doi:10.1007/s10483-013-1748-7
- Umavathi, J. C., Chamkh, A. J., and Shekar, M. (2018). Free convection flow of an electrically-conducting micropolar fluid between parallel porous vertical plates using differential transform. *J. Appl. Comput. Mech.* 4 (4), 286–298.
- Yu-Ming Chu, A., Khan, U., Ahmed, N., Din, S. T. M., and Khan, I. (2020). Heat and mass transport investigation in radiative and chemically reacting fluid over a differentially heated surface and internal heating. *Open Phys.* 18 (1), 842–852. doi:10.1515/phys-2020-0182
- Zeeshan, K., Ilyas, K., Murad, U., and Tlili, I. (2018). Effect of thermal radiation and chemical reaction on non-Newtonian fluid through vertical stretching porous plate with uniform suction. *Results Phys.* 9, 1086–1095.



OPEN ACCESS

EDITED BY

Adnan,
Mohi-ud-Din Islamic University,
Pakistan

REVIEWED BY

Muhammad Mubashir Bhatti,
Shandong University of Science and
Technology, China
Wasim Jamshed,
Capital University of Science &
Technology, Pakistan

*CORRESPONDENCE

Waseem Sikander,
waseemsp@gmail.com

SPECIALTY SECTION

This article was submitted to Process
and Energy Systems Engineering,
a section of the journal
Frontiers in Energy Research

RECEIVED 12 June 2022

ACCEPTED 21 July 2022

PUBLISHED 29 August 2022

CITATION

Zuhra S, Sikander W, Elkotb MA,
Tag-Eldin EM, Khattak SG and
Yassen MF (2022), Numerical analysis of
thermal transportation in nanodiamond
and silver-based nanofluid using the
Cattaneo–Christov heat flux model.
Front. Energy Res. 10:967444.
doi: 10.3389/fenrg.2022.967444

COPYRIGHT

© 2022 Zuhra, Sikander, Elkotb, Tag-
Eldin, Khattak and Yassen. This is an
open-access article distributed under
the terms of the [Creative Commons
Attribution License \(CC BY\)](#). The use,
distribution or reproduction in other
forums is permitted, provided the
original author(s) and the copyright
owner(s) are credited and that the
original publication in this journal is
cited, in accordance with accepted
academic practice. No use, distribution
or reproduction is permitted which does
not comply with these terms.

Numerical analysis of thermal transportation in nanodiamond and silver-based nanofluid using the Cattaneo–Christov heat flux model

Samina Zuhra¹, Waseem Sikander^{2*},
Mohamed Abdelghany Elkotb^{3,4}, E. M. Tag-Eldin⁵,
Sana Gul Khattak⁶ and Mansour F. Yassen^{7,8}

¹Department of Computing and Technology, Abasyn University, Peshawar, Khyber Pakhtunkhwa, Pakistan, ²Department of Mathematics and Statistics, University of Haripur, Haripur, Khyber Pakhtunkhwa, Pakistan, ³Mechanical Engineering Department, College of Engineering, King Khalid University, Abha, Saudi Arabia, ⁴Mechanical Engineering Department, College of Engineering, Kafrelsheikh University, Kafr El Sheikh, Egypt, ⁵Faculty of Engineering and Technology, Future University in Egypt, New Cairo, Egypt, ⁶Department of Physics, University of Peshawar, Peshawar, Khyber Pakhtunkhwa, Pakistan, ⁷Department of Mathematics, College of Science and Humanities, Prince Sattam Bin Abdulaziz University, Al-Kharj, Al-Aflaj, Saudi Arabia, ⁸Department of Mathematics, Faculty of Science, Damietta University, Damietta, Egypt

Background and Purpose: Studying the effects of suction and injection on heat transportation in nanofluids for time-dependent boundary layer flow is a key topic in fluid dynamics. Aerodynamics and the sciences of space both make extensive use of these types of flow. In this research, nanodiamond and silver nanoparticles in water-type base-fluid nanofluids flow are analyzed under the effects of thermal radiation and non-Fourier theory.

Methodology: A mathematical system having certain physical variations of the flow model is converted to a non-dimensional ordinary differential equation system via suitable similarity transformation variables. Then the flow model is numerically solved by RK4 and a shooting technique to describe the dynamics of the nanofluids under varied flow conditions. RK4 with the shooting approach gives a rapid result with high convergence accuracy. The relevant characteristics of physical quantities evaluated by an inclusive numerical scheme are observed for flow pattern, temperature distribution, and nanofluids concentration variations in the presence of suction and injection fluxes.

Finding: According to the findings, both ND-H₂O and Ag-H₂O have outstanding thermal performance characteristics. The Ag-based nanofluid, however, has a better heat transfer capability. To validate the analysis, a graphical and tabular comparison is presented under specified assumptions. The key finding is that, with the injection effect, the heat flow rate is larger than with the suction effect. The unsteadiness parameter causes a drop in the velocity profile, whereas energy distribution rises with this parameter.

KEYWORDS

hybrid nanofluid, micropolar, viscous dissipation, suction/injection, shooting technique, joule heating, thermal radiation

Introduction

The thermal performance of fluids is critical in the industrial and technical sectors. Many industrial and technical operations need a large quantity of heat transmission. Traditional liquids do not provide the required quantity of heat to complete the operation, which explains why there has been a need to understand how to enhance the heat transmission of ordinary liquids. Ultimately, in order to increase heat transfer in conventional liquids, researchers and scientists have devised the idea of utilizing metallic and non-metallic substances, in the form of nanoparticles, in the host liquid. These fluids' exceptional heat transfer capabilities have improved industrialists' and engineers' impact on the contemporary world. Nanofluids have been employed in aerodynamics, computer chips, medical sciences, the cosmetics industry, aviation parts manufacturing, and many other industries. As a result of the aforementioned uses, heat transport research is unavoidable. In many engineering areas, the modeling of unsteady flow phenomena is becoming more relevant. In turbomachinery, for instance, this encompasses the contact between stationary and rotating components, pistons engine, fluid-structure interactions, helicopter aerodynamics, applications in the automotive industry, the DNS or LES of turbulent flows, nuclear explosions, and so on. The heat transportation rate has been investigated for time-dependent nanofluid flow incorporating magnetic field and thermal conduction effects (Lahmar et al., 2020), for unsteady bioconvection hybrid nanofluid flow over a movable rotating disk in upward and downward directions (Jayadevumurthy et al., 2020), for time-dependent Carreau nanofluid flow under the effect of variable conductivity (Irfan et al., 2020), for unsteady nanofluid flow through a movable upper plate alongside suction and magnetic effects (Shuaib et al., 2020), and so on (Sreedevi et al., 2020; Khan et al., 2021; Alsallami et al., 2022; Raja et al., 2022; Rehman et al., 2022).

Nanodiamond particle dispersion in the host fluid water has been investigated theoretically and experimentally by many researchers aiming to enhance the thermal performance. Sundar et al. (2021) experimentally investigated the entropy and exergy of heat in nanodiamond/water nanofluid flow. With increasing nanofluid particle loadings, research has found a significant rise in the heat transfer coefficient and Nusselt number. Nanodiamond/water and cobalt oxide/water nanofluids have been placed in a square cavity containing heaters and treated to investigate the heat transfer rate (Kalidasan and Kanna, 2017). Numerical analysis has been made for entropy generation in laminar convective nanodiamond/water nanofluid through a rectangular channel (Uysal et al., 2019). Entropy

generation has been estimated for tangent hyperbolized hybrid nanofluid that enhances the thermal transportation capacity of regular fluid (Hussain and Jamshed, 2021). Similarly, tangent hyperbolized hybrid nanofluid in a solar wing parabolic trough solar collector, used in solar plants, has been studied by Jamshed et al. (2021a). The nanopolishing behavior of suspended nanodiamond in elasto-hydrodynamic lubrication has been studied by Shirvani et al. (2016). Similarly the silver/water nanofluid flow over a vertical Riga plate has been studied by Rawat et al. (2019). Analysis of the turbulent convective force of Ag/HEG type nanofluid flow that flows through a circular channel, silver/water nanofluid flow in mini channels, Ag/HEG water nanofluid in pipes, and Ag/water nanofluid inside a semi-circular lid-driven cavity has been conducted by Ny et al. (2016), Sinz et al. (2016), Raja Bose et al. (2017), and Hadavand et al. (2019), respectively. Bhatti et al. (2022a) studied nanofluids composed of nanoparticles such that nanodiamond and silica in the host fluid water flow through the elastic surface located exponentially, and Bhatti et al. (2022b) studied hybrid nanofluids comprising cobalt-oxide/graphene oxide nanoparticles in the base fluid water that flows across a circular elastic surface in a porous medium. This research is significant for improving the optical thermal performance in solar energy conversion systems. Dogonchi et al. (2017) analyzed the magnetohydrodynamic graphene oxide/water type nanofluid through a permeable channel under the effect of thermal radiation and found that when the Reynolds number and extension ratio increase, so does the skin friction coefficient. Alizadeh et al. (2018) studied the micropolar nanofluid flow that passes through penetrable sheets. According to their findings, the Nusselt number is a rising function of volume fraction and thermal radiation. Dib et al. (2015) studied the thermal transportation phenomena in nanofluid through a squeezing medium and found that nanofluids with different types have positive effects on heat transfer. Sheikhholeslami et al. (2012) examined the heat transfer rate in copper/water nanofluid flow between two rotating stretched surfaces. Their findings showed that the surface heat transfer rate increases the volume fraction of nanomaterials. Entropy generation has been measured by Jamshed (2021) in the MHD flow of Maxwell nanofluid that passes infinite horizontal sheets in terms of the imposed viscous dissipation and thermal radiation effects. Many researchers have been paying close attention to the study of nanofluid flow through porous surfaces, and Henry Darcy's 1856 Darcy model is the most used model in this kind of study (Darcy, 1965). Khanafer and Vafai (2019) discussed in detail the usages of nanofluid in a porous medium. Shahsavari et al. (2020) investigated the effects of a permeable medium using a silver/water nanofluid with a heat sink filled with metal foam, utilizing

the first and second laws of thermodynamics. Bioconvection phenomena have been used by [Bhatti et al. \(2022c\)](#) in magnetohydrodynamic Williamson nanofluid flow that passes a circular permeable medium when a nanofluid flows through a cylinder entirely saturated with a porous medium. Other useful literature about nanofluids in a porous medium can be found in [Ahmed et al. \(2019\)](#), [Menni et al. \(2019\)](#), [Zuhra et al. \(2020\)](#), and [Wang et al. \(2022\)](#).

Considerable focus has been placed on the flow and heat transmission of viscous fluids via surfaces that are constantly stretching in a fluid medium. Innovative and pioneering studies about stretching the surface for the fluid flow include those of [Sakiadis \(1961\)](#) and [Crane \(1970\)](#). Many researchers have since built on Crane's and Sakiadis's groundbreaking work to investigate various elements of flow and heat transmission in an infinite domain of fluid through a stretched sheet ([Laha et al., 1989](#); [Afzal, 1993](#); [Wang, 2006](#); [Ahmed et al., 2022a](#); [Ashraf et al., 2022](#); [Elattar et al., 2022](#)). These investigations are based on continuous flow. A quick stretching of the flat sheet or a steep shift in the sheet's temperature might cause the flow field and heat transmission to be unstable in some instances. [Hossain et al. \(1999\)](#) investigated the effect of radiation on free convection from a porous vertical plate. [Prasannakumara et al. \(2017\)](#) reported on the convective thermal performance of an unstable nanofluid passing through a stretchy sheet. They presented their findings for dusty nanofluid, concluding that a higher radiative surface is preferable for dusty nanofluid thermal increase. [Bhattacharyya and Layek \(2014\)](#) studied the heat transport of nanofluids in the presence of applied Lorentz forces. The time-dependent non-Newtonian Casson nanofluid flow through a slippery surface was assessed by [Jamshed et al. \(2021b\)](#) for entropy generation and thermal transportation measurement. [Dutta et al. \(1985\)](#) investigated the temperature behavior of a normal liquid across a stretchy sheet in the presence of a continuous heat flow condition. Many researchers have studied exponentially extending sheets ([Magyari and Keller, 1999](#); [Rehman et al., 2017](#); [Mushtaq et al., 2019](#)), which have the most important technological and industrial applications.

The heat conduction law developed by Fourier ([Fourier and Darboux, 1822](#)) has been used to forecast heat transfer behavior in a variety of practical circumstances. Since this model generates a parabolic energy equation, any initial perturbation would have a significant impact on the system under study. Fourier's law has been adjusted multiple times to solve this contradiction ([Dong et al., 2011](#); [Zhang et al., 2013](#); [Reddy and Sreedevi, 2021](#)). Fourier's law was updated by [Cattaneo \(1948\)](#) by including the relaxation time for heat flux, which is defined as the time it takes for heat conduction to stabilize once a temperature gradient has been introduced. [Christov \(2009\)](#) proposed a materially invariant version of Cattaneo's model based on Oldroyd's upper-convected derivative. To date, significant research has been undertaken on nanofluidic flow models adding non-Fourier heat conduction theory ([Alhowaity et al.,](#)

[2022](#); [Imtiaz et al., 2022](#); [Salmi et al., 2022](#)). In the present paper, non-Fourier heat flux theory and thermal radiation effects are imposed to investigate the heat transfer rate in two different types of nanofluids composed of nanodiamond-water and silver-water over an unsteady stretching sheet. Suction and injection fluxes are also considered in the model. The thermal properties of both nanoparticles are different; hence, this study shows the best heat transfer performance rate. The non-dimensional system of equations is achieved via the adjustment of suitable similarity variables in the traditional form of the flow model with many assumptions, which are further solved through the shooting technique. The resulting data are compared to the physical characteristics, and the findings are shown graphically in the form of graphs. Using Mathematica 11.0, a graphical comparison study is used to verify the colloidal analyses. The hydrothermal efficiency of heat transfer systems improved with smaller silver/water nanoparticle size and concentrations. Silver nanoparticles, when used in small enough concentrations and with a small enough size, may reduce the pressure drop and erosion problems that arise during the suspension of nanoparticles in the host fluid. Thus, such a type of nanoparticle is more stable in nanofluid over a long time. Additionally, thermal fluids based on nanodiamond may improve thermal conductivity by as much as 70%. Therefore, both of the nanofluids possess good thermal conductivity. Nanodiamond nanofluid is mostly used in electron microscopy, Raman spectroscopy, and X-ray diffraction analyses.

The flow model and its formulation

The model considers the unsteady, incompressible nanofluids flow that passes over a stretchable surface located horizontally. The nanofluids are composed of two types of nanoparticles, namely nanodiamond and silver nanoparticles, suspended in base fluid water. The flow is assumed under the effects of suction injection and non-Fourier theory for the stability of heat transfer at the boundary layer flow. In Cartesian coordinates, the flow scenario is configured as two-dimensional and unidirectional. Let \hat{u} and \hat{v} be the nanofluidic velocities in the horizontal x_* and vertical y_* directions, respectively. T is the temperature variation with ambient temperature T_∞ . [Figure 1](#) displays the flow pattern of ND-H₂O and Ag-H₂O nanofluids flow across an unstable stretching sheet.

Governing equation: In light of the aforementioned restrictions, the following is the form of mass, momentum, and energy conservations ([Ahmed et al., 2022b](#)):

$$\frac{\partial \hat{u}}{\partial \hat{x}} + \frac{\partial \hat{v}}{\partial \hat{y}} = 0 \quad (1)$$

$$\frac{\partial \hat{u}}{\partial \hat{t}} + \hat{u} \frac{\partial \hat{u}}{\partial \hat{x}} + \hat{v} \frac{\partial \hat{u}}{\partial \hat{y}} = \frac{\mu_{nf}}{\rho_{nf}} \left(\frac{\partial^2 \hat{u}}{\partial \hat{y}^2} \right) \quad (2)$$

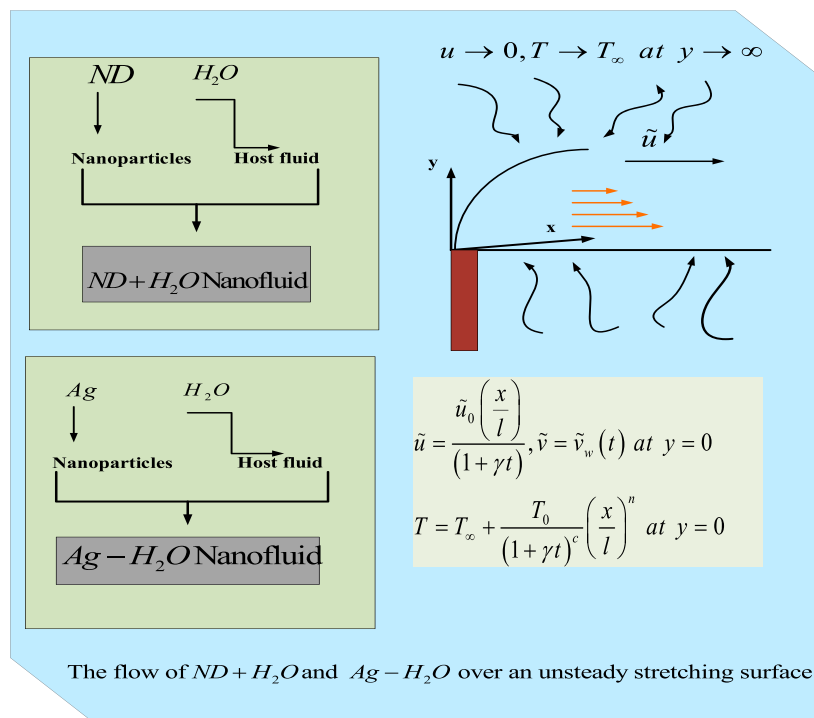


FIGURE 1

Flow geometry of nanodiamond-water and silver-water nanofluids.

TABLE 1 Thermophysical values of nanodiamond and silver nanoparticles.

| Characteristics | Density ($\frac{\rho g}{m^3}$) | Heat-capacity ($\frac{J}{KgK}$) | Thermal conductivity | Electrical-conductivity |
|------------------|----------------------------------|-----------------------------------|----------------------|-------------------------|
| Silver | 10,500 | 234 | 425 | 6.210×10^6 |
| Nanodiamond | 3,100 | 516 | 1,000 | 34.840×10^6 |
| H ₂ O | 997.1 | 4,179 | 0.613 | 0.005 |

$$\frac{\partial \hat{T}}{\partial t} + \hat{u} \frac{\partial \hat{T}}{\partial \hat{x}} + \hat{v} \frac{\partial \hat{T}}{\partial \hat{y}} = \frac{k_{nf}}{(\rho C_p)_{nf}} \left(\frac{\partial^2 \hat{T}}{\partial \hat{y}^2} \right) + \lambda \left(\left(\hat{u} \frac{\partial \hat{u}}{\partial \hat{x}} + \hat{v} \frac{\partial \hat{u}}{\partial \hat{y}} \right) \frac{\partial \hat{T}}{\partial \hat{x}} + \left(\hat{u} \frac{\partial \hat{v}}{\partial \hat{x}} + \hat{v} \frac{\partial \hat{v}}{\partial \hat{y}} \right) \frac{\partial \hat{T}}{\partial \hat{y}} + \hat{u}^2 \frac{\partial^2 \hat{T}}{\partial \hat{x}^2} + \hat{v}^2 \frac{\partial^2 \hat{T}}{\partial \hat{y}^2} + 2\hat{u}\hat{v} \frac{\partial^2 \hat{T}}{\partial \hat{x} \partial \hat{y}} \right) \quad (3)$$

where μ_{nf} is dynamic viscosity, ρ_{nf} is density, k_{nf} is thermal conductivity, and $(\rho C_p)_{nf}$ is heat capacity defined as:

$$\begin{aligned} \rho_{nf} &= ((1 - \phi) + \phi \rho_s (\rho_f)^{-1}) \rho_f \\ (\rho C_p)_{nf} &= ((1 - \phi) + \phi (\rho C_p)_s (\rho C_p)_f^{-1}) (\rho C_p)_f \\ \mu_{nf} &= \mu_f (1 - \phi)^{2.5} \\ k_{nf} &= k_s ((k_s + 2k_f) - 2\phi(k_f - k_s)) ((k_s + 2k_f) + \phi(k_f - k_s))^{-1} \end{aligned}$$

According to the above assumption, the acceptable flow conditions at the surface and far from it are defined as:

$$\begin{aligned} \hat{u} &= \hat{u}_0 \frac{(\hat{x} \hat{l}^{-1})}{(1 + a \hat{t})}, \quad \hat{v} = \hat{v}_w(\hat{t}), \\ \hat{T} &= \hat{T}_\infty + \frac{\hat{T}_0 (\hat{x}^n \hat{l}^{-n})}{(1 + a \hat{t})^c} \text{ at the surface} \end{aligned} \quad (4)$$

$$\hat{u} \rightarrow 0, \text{ and } \hat{T} \rightarrow T_\infty \text{ far from the surface} \quad (5)$$

where $y, \hat{T}_\infty, \hat{u}_0, \hat{T}_0$ are positive constants with reference length l , n , and c . Moreover, if $Re = \frac{l \hat{u}_0}{\hat{\nu}_f}$ and $Pr = \frac{\hat{\nu}_f}{k_f}$, then the stream function $\varphi(\hat{x}, \hat{y})$ can be defined as:

$$\varphi(\hat{x}, \hat{y}) = \frac{\hat{x}}{\hat{l}} \left(\sqrt{Re} \sqrt{(1 + \gamma \hat{t})} \right) f(\eta) \quad (6)$$

TABLE 2 Assessment of present study with literature.

| A | 0.8 | 1.2 | 2.1 |
|------------------------------|---------|---------|---------|
| Ahmed et al. (2022b) | 1.32342 | 1.42353 | 1.61214 |
| Elbashbeshy and Bazid (2004) | 1.3321 | 1.4691 | 1.7087 |
| Present study | 1.3332 | 1.4783 | 1.73424 |

From the stream function, velocity components may be expressed as:

$$\hat{u} = \frac{\partial \varphi(\hat{x}, \hat{y})}{\partial \hat{y}}, \hat{v} = -\frac{\partial \varphi(\hat{x}, \hat{y})}{\partial \hat{x}}$$

Suitable similarity variables for the above model are defined as:

$$\eta = \frac{1}{l} \left(\frac{Re}{(1+at)} \right)^{1/2} \hat{y}, \text{ and } \hat{T} = \hat{T}_\infty + \hat{T}_0 \frac{(\hat{x}^n l^{-n})}{(1+at)^c} \theta(\eta) \quad (7)$$

As a result, the velocities components in horizontal and vertical directions are defined as:

$$\hat{u} = \frac{\hat{u}_0 \hat{x}}{(l(1+at))} f'(\eta) \quad (8)$$

$$\hat{v} = -\frac{\hat{u}_0}{\left(\sqrt{Re} \sqrt{(1+at)} \right)} f(\eta) \quad (9)$$

The required partial derivatives can be formulated as follows:

$$\begin{aligned} \frac{\partial \hat{u}}{\partial \hat{x}} &= \frac{\hat{u}_0}{l(1+at)} f'(\eta), \quad \frac{\partial \hat{u}}{\partial \hat{y}} = \frac{\hat{u}_0 \hat{x} \sqrt{Re}}{l^2 (1+at)^{3/2}} f''(\eta), \quad \frac{\partial^2 \hat{u}}{\partial \hat{y}^2} = \frac{\hat{u}_0 \hat{x} Re}{l^3 (1+at)^{5/2}} f'''(\eta), \quad \frac{\partial \hat{v}}{\partial \hat{x}} = 0, \\ \frac{\partial \hat{u}}{\partial t} &= -\hat{u}_0 \frac{\hat{x} a}{l(1+at)^2} f'(\eta) - \frac{\hat{u}_0 \hat{x} a \sqrt{Re}}{2l^2 (1+at)^{3/2}} f''(\eta), \quad \frac{\partial \hat{T}}{\partial \hat{x}} = \frac{\hat{T}_0 \left(\frac{\hat{x}}{l} \right)^{n-1}}{l(1+at)^c} \theta(\eta), \quad \frac{\partial^2 \hat{T}}{\partial \hat{y}^2} = \frac{\hat{T}_0 \left(\frac{\hat{x}}{l} \right)^c \sqrt{Re}}{l^2 (1+at)^{c+1}} \theta''(\eta) \\ \frac{\partial \hat{T}}{\partial t} &= -\hat{T}_0 \left(\frac{\hat{x}}{l} \right)^c \frac{a}{(1+at)^{c+1}} \theta(\eta) - \frac{\hat{T}_0 \left(\frac{\hat{x}}{l} \right)^c a \sqrt{Re}}{2l(1+at)^{c+1/2}} \theta'(\eta), \quad \frac{\partial \hat{T}}{\partial \hat{y}} = \frac{\hat{T}_0 \left(\frac{\hat{x}}{l} \right)^c \sqrt{Re}}{l(1+at)^{c+1/2}} \theta'(\eta) \end{aligned} \quad (10)$$

Substituting Eqs 8–10 into Eqs 1–5 yields the following non-dimensional system of momentum and energy equation:

$$f'''(\eta) + d_1 (f(\eta) f''(\eta) - f'^2(\eta) + A(f'(\eta) + 0.5 \eta f''(\eta))) = 0, \quad (11)$$

$$\theta''(\eta) + d_2 \left(\text{Pr} A (\hat{c} \theta(\eta) + 0.5 \eta \theta'(\eta)) + \text{Pr} (\eta \theta(\eta) f'(\eta) + \theta'(\eta) f(\eta)) + \text{Pr} \gamma (f(\eta) f'(\eta) \theta'(\eta) - f'^2(\eta) \theta''(\eta)) \right) = 0, \quad (12)$$

where $A = \frac{\gamma l}{\hat{u}_0}$ is the unsteadiness parameter, and where $\text{Pr} = \frac{\hat{v}_f}{\hat{k}_f}$, $d_1 = (1-\phi)^{2.5} (1-\phi + \phi \frac{\rho_s}{\rho_f})$, and

$$d_2 = \frac{(1-\phi) + \phi \left(\frac{\rho_s \hat{C}_p}{\rho_f \hat{C}_p} \right)}{\left((\hat{k}_s + 2\hat{k}_f) - 2\phi(\hat{k}_f - \hat{k}_s) \right) \left((\hat{k}_s + 2\hat{k}_f) + \phi(\hat{k}_f - \hat{k}_s) \right)^{-1}}$$

The corresponding boundary conditions of Eq. 11 and Eq. 12 are:

$$f(\eta) = f_w, \quad f'(\eta) = 1, \quad \theta(\eta) = 1, \quad \text{at } \eta = 0, \quad (13)$$

$$f'(\eta) \rightarrow 0, \quad \theta(\eta) \rightarrow 0, \quad \text{at } \eta \rightarrow \infty, \quad (14)$$

Solution process of the nanofluidic system

Computational fluid dynamics (CFD) has been an increasingly significant technology in chemical and engineering since the 1990s. Transport processes including heat, momentum, and mass transfer may be studied using CFD (Thabet and Thabit, 2018). In CFD, the geometry of the process being modeled is first split into tiny volumes called computational meshes. It is then applied and solved for each mesh point using the governing equations (such as heat and mass transport, as well as boundary conditions). Graphical representations of mesh findings are the most typical way to analyze CFD results (Pandey et al., 2017). In order to solve

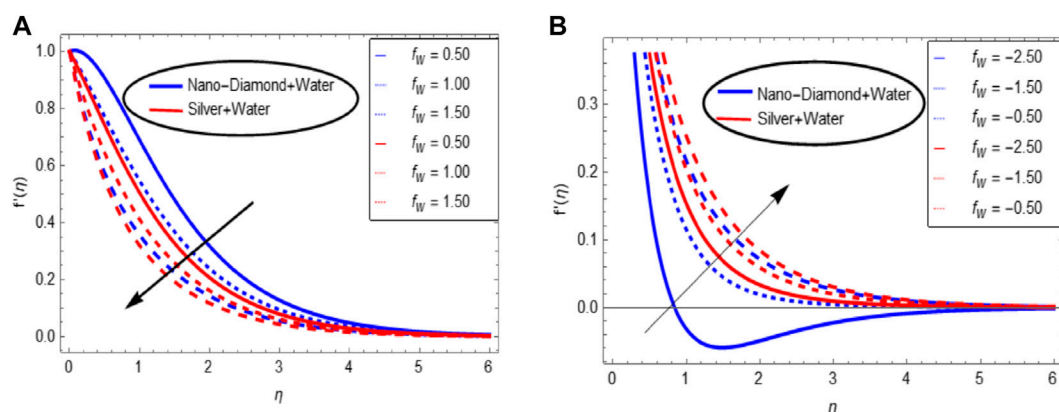


FIGURE 2 Influence of (A) suction and (B) injection on the velocity profile.

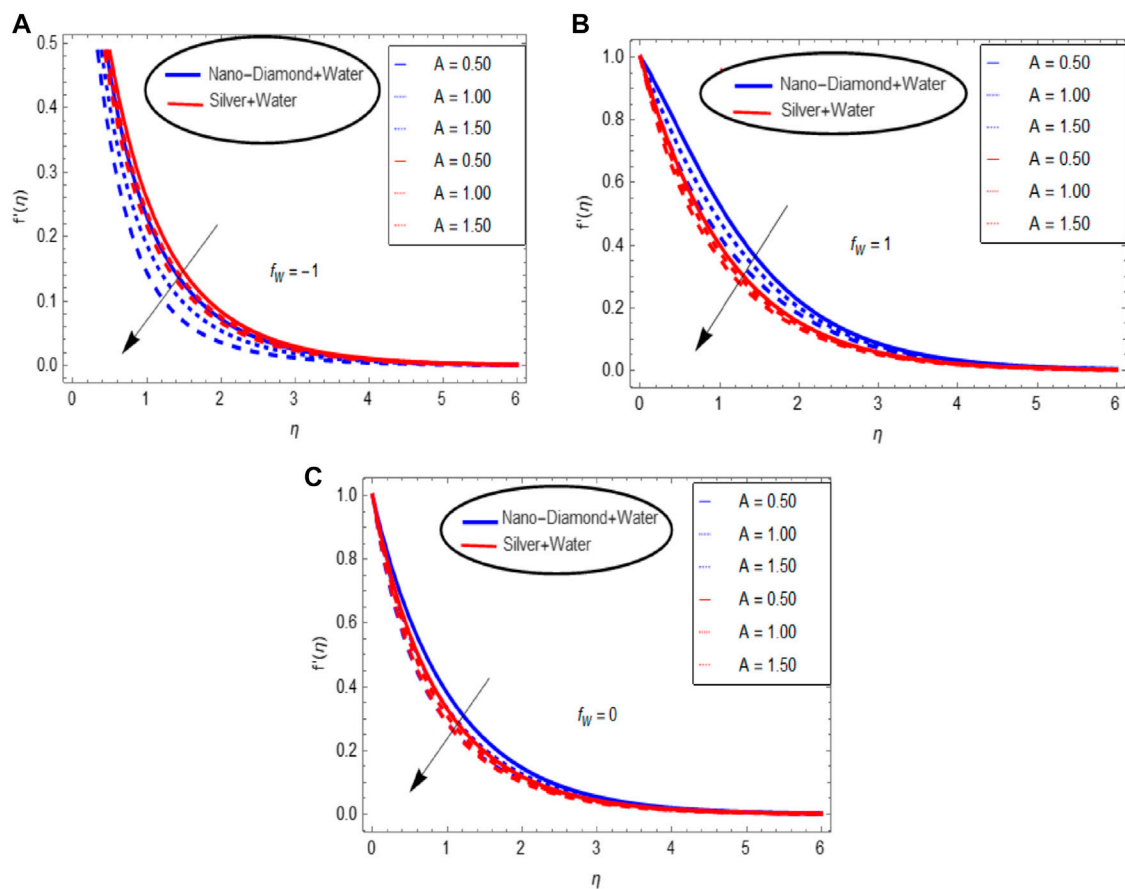


FIGURE 3

Influence of the unsteadiness parameter in the presence of (A) suction, (B) injection, and (C) without suction/injection on the velocity profile.

highly nonlinear differential equations involving energy, temperature, and air velocity, CFD uses numerical shooting and RK4 methods.

Basic principles of the shooting technique

The transport equations are quite nonlinear and can be affected by boundary circumstances. The RK4 scheme and shooting approach may be used to compute this numerically. This method has a small margin of error. Converting the resultant differential equations into first-order equations is the first step in solving the framed model of a nanofluid flow problem. The essential replacements for the aforementioned step are as follows:

$$(f, f', f'', \theta, \theta')^T = \left(\hat{x}_1, \hat{x}'_1 = \hat{x}_2, \hat{x}''_2 = \hat{x}_3, \hat{x}_4, \hat{x}'_4 = \hat{x}_5 \right)^T \quad (15)$$

Some assumptions are made to solve the fluidic model:

- a relevant value for η , representing the field distance, is taken as 10 for the far field;
- conditions in the far field w.r.t. $\eta \rightarrow \infty$ are $\hat{f}'(\eta) \rightarrow 1$, $\hat{\theta}(\eta) \rightarrow 0$, $\hat{G}(\eta) \rightarrow 0$;
- the scale of convergence is 10^{-5} ; and
- for calculations, the step size is recorded as $\eta = 0.025$.

Eqs 11–14 can thus be written as:

$$\begin{pmatrix} \hat{x}_2 \\ \hat{x}_3 \\ \hat{x}_4 \\ \hat{x}_5 \\ \theta'' \end{pmatrix} = \begin{pmatrix} \hat{x}_2 \\ \hat{x}_3 \\ -d_1 (\hat{x}_1 \hat{x}_3 - \hat{x}_2^2 + A(\hat{x}_2 + 0.5\eta \hat{x}_2)) \\ \hat{x}_5 \\ \frac{-d_2}{(1 - \text{Pr}\gamma \hat{x}_1^2)} (\text{Pr}A(\hat{c}\hat{x}_4 + 0.5\eta \hat{x}_5) + \text{Pr}(\eta \hat{x}_4 \hat{x}_2 + \hat{x}_5 \hat{x}_1) - \text{Pr}\gamma(\hat{x}_1 \hat{x}_2 \hat{x}_{57})) \end{pmatrix} \quad (16)$$

The corresponding conditions according to the variables are as follows:

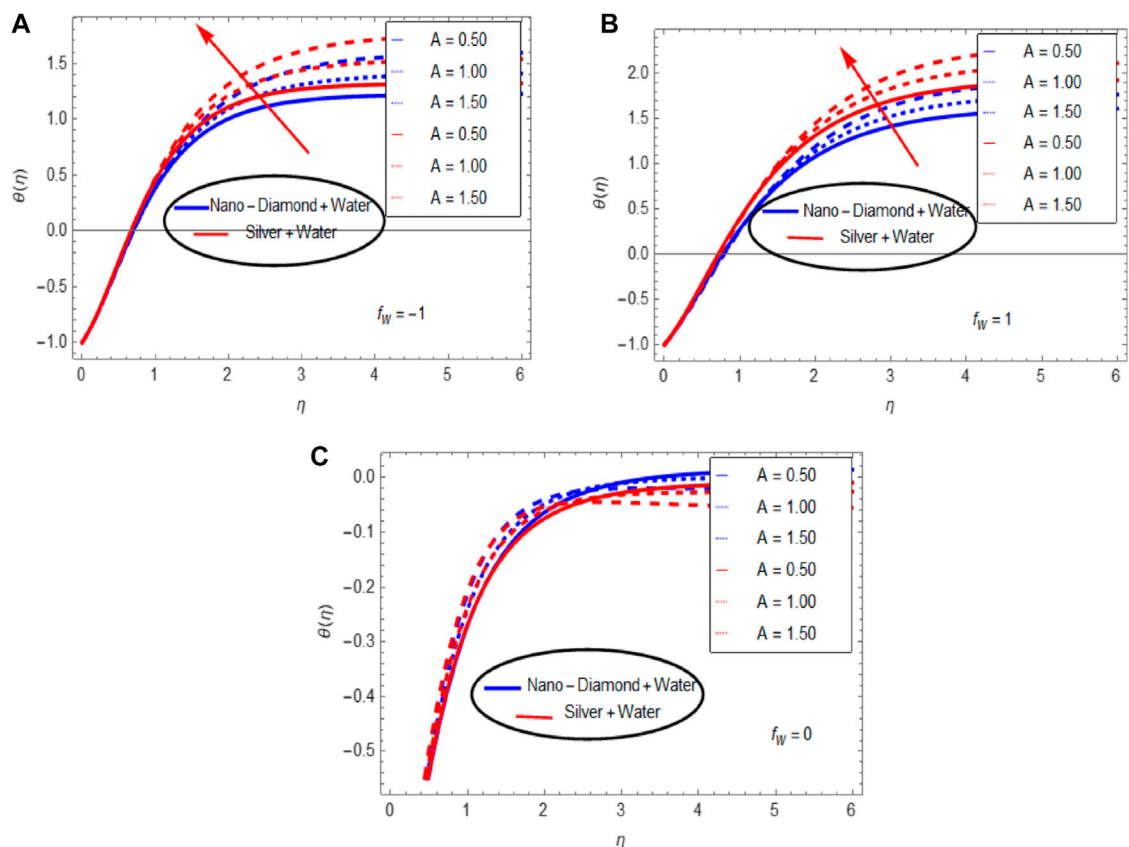


FIGURE 4

Influence of the unsteadiness parameter in the presence of (A) suction, (B) injection, and (C) without suction/injection on the temperature distribution.

$$\begin{cases} \hat{x}_1(0) = f_w, \hat{x}_2(0) = 1, \hat{x}_4(0) = 1, \\ \hat{x}_2(\infty) = 0, \hat{x}_4(\infty) = 0. \end{cases} \quad (17)$$

which can be determined via the shooting method and the first-order system in Eqs 11–14 is integrated via the RK4 scheme.

Results and discussion

The intended domain's flow properties are greatly modified by varying the amount of flow. As a result, this section investigates the behavior of the non-dimensional flow field $f'(\eta)$ and energy distribution $\theta(\eta)$ of ND-H₂O and Ag-H₂O nanofluids by adjusting the flow quantities. Using the shooting technique in Eqs 11–12 with the boundary conditions in Eqs 13–14 provides the significant results of the proposed model. Table 1 show the values of four main thermophysical properties of nanodiamond, Silver and water (Ahmed et al., 2022b). Table 2 shows the close agreement of the shooting-RK4 technique with the existing literature for the proposed flow model.

Flow distribution $f'(\eta)$

The velocity of a nanofluid in relation to f_w is given by $f'(\eta)$. Figures 2A,B

depict the flow of ND-H₂O and Ag-H₂O nanofluids as a function of suction and injection values. As shown in Figure 2A, the velocity $f'(\eta)$ for both nanofluids decreases because of higher suction impacts at the plates. As a result of the suction effects, more nanofluid particles adhere to the surface, lowering the velocity profile. The motion of Ag-H₂O quickly decreases as the nanofluid gets thicker for the higher density compared to the ND nanoparticles. Because of the low density of ND, the fluid velocity $f'(\eta)$ (ND-H₂O) decreases slowly. The effects of injecting fluid from the surface on ND-H₂O and Ag-H₂O velocity $f'(\eta)$ are shown in Figure 2B. As a result of the fluid particles being physically separated from the sheet surface because of injection, their momentum has increased, causing an upturn in the flow. ND-H₂O has a lower density; therefore, intermolecular interactions are lessened, allowing fluid particles to move freely across the required area. In comparison to Ag-H₂O nanofluid, the velocity of

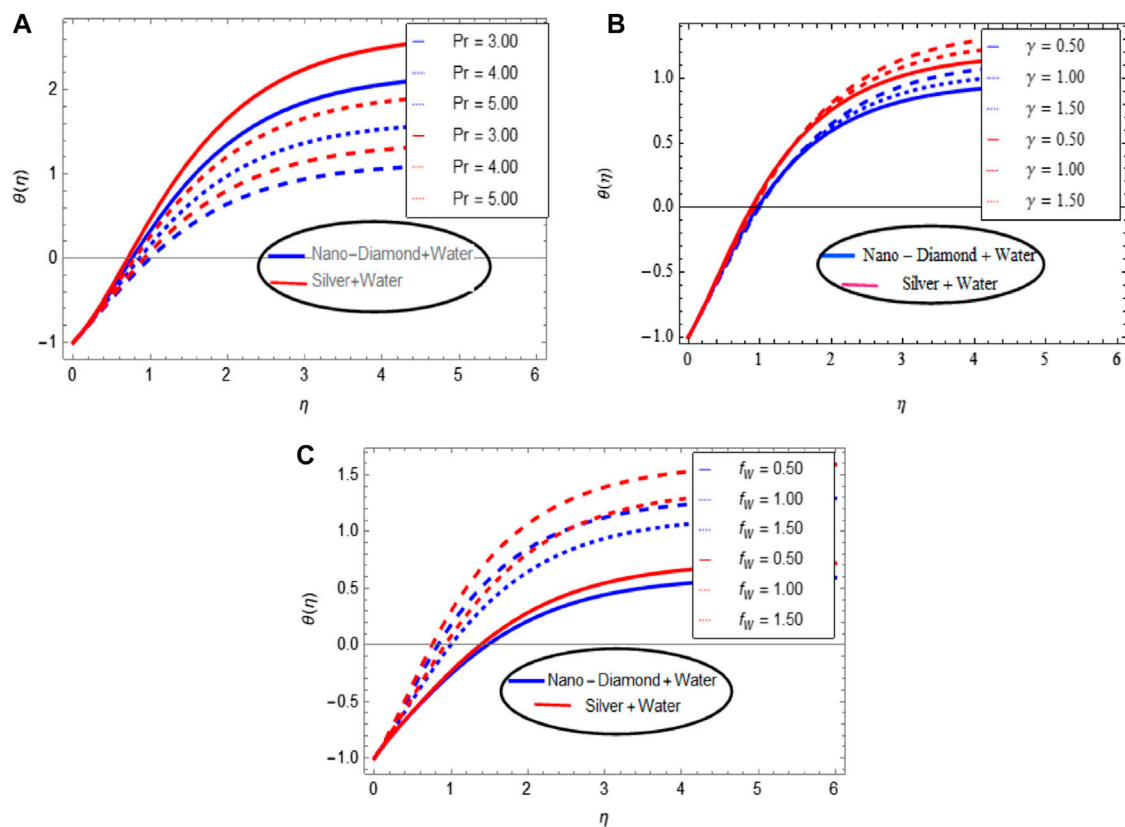


FIGURE 5

Influence of (A) Prandtl number, (B) thermal relaxation parameter, and (C) suction/injection on the temperature distribution.

ND-H₂O increases more suddenly as a response of this. The velocity $f'(\eta)$ of a nanofluid in relation to the unsteadiness parameter A are presented in Figures 3A,B,C showing the impacts of the time-dependent quantity on nanofluid velocities at fixed suction and injection, respectively. Both ND-H₂O and Ag-H₂O nanofluids yielded similar results. The velocity $f'(\eta)$ decreases rapidly as the unsteadiness parameter increases in the presence of suction/injection and when there is no suction or injection over the surface. The fluid motion decreases towards the surface and then begins to rise. The decrease in the fluid's velocity, $f'(\eta)$ slows down over time, eventually disappearing asymptotically beyond values greater than 5.

The temperature distribution $\theta(\eta)$

The significant thermal physical properties of nano-materials are critical in determining the heat transport procedure of nanofluids. These values have a substantial impact on the fluid's thermal properties. As a result, this section presents the temperature profile $\theta(\eta)$ of ND-H₂O and

Ag-H₂O as a function of several factors. These factors are estimated in the presence of suction or injection fluxes to control the boundary layer and reduce the losses of energy in the medium. Figures 4A,B,C show the time-dependent parameter in the presence of suction effect, injection, and no suction/injection impacts on energy distribution, respectively. Due to the unsteadiness parameter, the temperature of the nanofluids rises significantly. Suction causes the fluid velocity to rise quickly, resulting in an increase in the kinetic energy of the fluid particles. The collision of particles increases as the kinetic energy of the particles increases. As a result, the temperature quickly rises. Due to increased injection effects near the surface, the temperature quickly rises. In these cases, the silver/water nanofluid temperature increases more rapidly compared to the ND/water nanofluid. Figures 5A,B,C display the influence of the Prandtl number, thermal relaxation parameter, and suction/injection for temperature distributions. The boundary layer thickness of energy distribution has an inverse relationship with thermal diffusivity, which slows down the temperature profile for both nanofluids. At the initial boundary layer, the thickness rapidly decreases, but

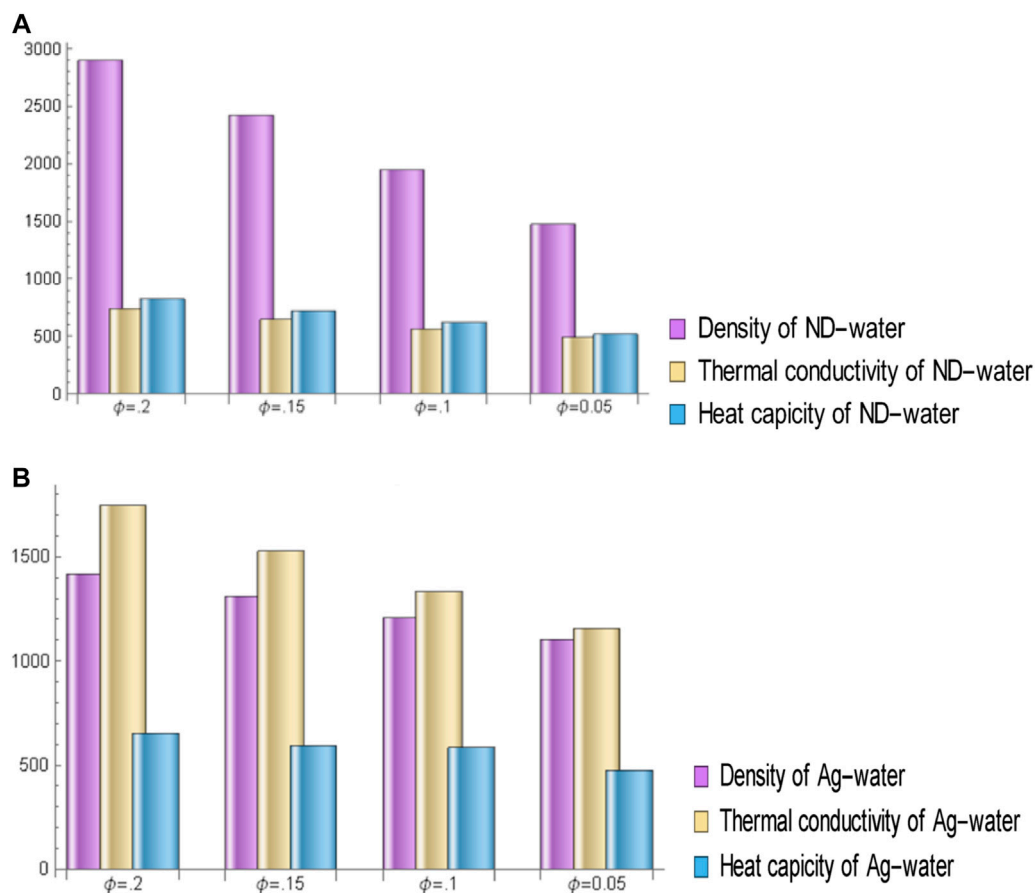


FIGURE 6

(A) Influence of volume fraction on the thermos-physical values for nanodiamond/water. (B) Influence of volume fraction on the thermos-physical values for silver/water.

further away, the energy distribution shows a constant decrease when the values of the Prandtl parameter increase simultaneously. Thermal relaxation time occurs when time is required for thermal conductivity in the region far from the directly heated surface. Here, thermal relaxation does not affect the energy distribution at the boundary layer surface but decreases this temperature distribution far from the boundary layer. The presence of suction and injection fluxes boosts the heat distribution source, as shown in Figure 5C. Moreover, the silver/water nanofluid temperature increases more rapidly compared to the ND/water nanofluid.

The volume fraction (ϕ)

Nanomaterials effectively change the thermophysical parameters in nanofluids, which plays an important role in the heat transfer process. Figures 6A,B show the values for the

effective density, thermal conductivity, and dynamic viscosity for the nanofluids under study, respectively. The thermal conductivity of Ag-H₂O is greater than that of ND-H₂O, as can be seen upon close examination. As a result, Ag-H₂O nanofluid is a better conductor and has excellent heat transmission properties. Similarly, increasing the volumetric proportion of nanomaterials improves their effective density and heat capacity.

Major findings

The current investigation focuses on the thermal transfer enhancement over the unsteady surface of nanofluids composed of nanodiamond-water and silver-water. The flow model is taken under the effect of heat source sink, thermal radiation, and non-Fourier heat theory. Such flows may occur on the bonnet of a vehicle, on the surface of a solar thermal aircraft, and on the surface of a bullet. An unstable

surface has been used to study the effects of embedded factors on heat transport in ND-H₂O and Ag-H₂O nanofluids. According to the results of this study, nanofluids are better heat conductors than normal liquids and might be employed for industrial and technical applications.

The main findings are as follows:

- When suction increases, the flow speed drops rapidly but the flow is boosted under the effect of the injection parameter.
- The velocity profile decreases for the unsteadiness parameter in the presence of suction/injection parameters.
- The energy distribution rises rapidly with the unsteadiness parameter and is high on the far boundary.
- The effect of the Prandtl number drops the temperature of the flow but, due to the thermal relaxation parameter, energy distribution rises and is stable on the boundary.
- Numerical shooting along with RK4 gives the best assessment results in comparison with the existing literature.
- The thermal conductivity of Ag-H₂O is found to be higher than that of ND-H₂O. Since it is a better conductor and has a higher heat capacity, Ag-H₂O nanofluid is a superior choice.

Data availability statement

The original contributions presented in the study are included in the article/Supplementary Material, and further inquiries can be directed to the corresponding author.

References

- Afzal, N. (1993). Heat transfer from a stretching surface. *Int. J. Heat Mass Transf.* 36 (4), 1128–1131. doi:10.1016/s0017-9310(05)80296-0
- Ahmed, N., Mohyud-Din, S. T., Alharbi, S. O., and Khan, I. (2022). Thermal improvement in magnetized nanofluid for multiple shapes nanoparticles over radiative rotating disk. *Alexandria Eng. J.* 61 (3), 2318–2329. doi:10.1016/j.aej.2021.07.021
- Ahmed, N., Mohyud-Din, S. T., Alsulami, M. D., and Khan, I. (2022). A novel analysis of heat transfer in the nanofluid composed by nanodiamond and silver nanomaterials: Numerical investigation. *Sci. Rep.* 12 (1), 1284–1295. doi:10.1038/s41598-021-04658-x
- Ahmed, N., Tassaddiq, A., Alabdan, R., Noor, S., Mohyud-Din, S. T., Khan, I., et al. (2019). Applications of nanofluids for the thermal enhancement in radiative and dissipative flow over a wedge. *Appl. Sci.* 9 (10), 1976. doi:10.3390/app9101976
- Alhowaity, A., Bilal, M., Hamam, H., Alqarni, M. M., Mukdasai, K., and Ali, A. (2022). Non-Fourier energy transmission in power-law hybrid nanofluid flow over a moving sheet. *Sci. Rep.* 12 (1), 10406–10412. doi:10.1038/s41598-022-14720-x
- Alizadeh, M., Dogonchi, A. S., and Ganji, D. D. (2018). Micropolar nanofluid flow and heat transfer between penetrable walls in the presence of thermal radiation and magnetic field. *Case Stud. Therm. Eng.* 12, 319–332. doi:10.1016/j.csite.2018.05.002
- Alsallami, S. A., Zahir, H., Muhammad, T., Hayat, A. U., Khan, M. R., and Ali, A. (2022). Numerical simulation of Marangoni Maxwell nanofluid flow with Arrhenius activation energy and entropy atomization over a rotating disk. *Waves in random and complex media*, 1–19.
- Ashraf, W., Al-Johani, A. S., Ahmed, N., Mohyud-Din, S. T., Khan, I., and Anduallem, M. (2022). Impact of freezing temperature (T_{fr}) of Al₂O₃ and molecular diameter (H₂O) d on thermal enhancement in magnetized and radiative nanofluid with mixed convection. *Sci. Rep.* 12 (1), 1–13.
- Bhattacharyya, K., and Layek, G. C. (2014). Magnetohydrodynamic boundary layer flow of nanofluid over an exponentially stretching permeable sheet. *Phys. Res. Int.*, 1–12. doi:10.1155/2014/592536
- Bhatti, M. M., Arain, M. B., Zeeshan, A., Ellahi, R., and Doranehgard, M. H. (2022). Swimming of Gyrotactic Microorganism in MHD Williamson nanofluid flow between rotating circular plates embedded in porous medium: Application of thermal energy storage. *J. Energy Storage* 45, 103511. doi:10.1016/j.est.2021.103511
- Bhatti, M. M., Ellahi, R., and Doranehgard, M. H. (2022). Numerical study on the hybrid nanofluid (Co₃O₄-Go/H₂O) flow over a circular elastic surface with non-Darcy medium: Application in solar energy. *J. Mol. Liq.* 361, 119655. doi:10.1016/j.molliq.2022.119655
- Bhatti, M. M., Öztop, H. F., Ellahi, R., Sarris, I. E., and Doranehgard, M. H. (2022). Insight into the investigation of diamond (C) and Silica (SiO₂) nanoparticles suspended in water-based hybrid nanofluid with application in solar collector. *J. Mol. Liq.* 357, 119134. doi:10.1016/j.molliq.2022.119134
- Cattaneo, C. (1948). Sulla conduzione del calore. *Atti Sem. Mat. Fis. Univ. Modena* 3, 83–101.
- Christov, C. I. (2009). On frame indifferent formulation of the Maxwell–Cattaneo model of finite-speed heat conduction. *Mech. Res. Commun.* 36 (4), 481–486. doi:10.1016/j.mechrescom.2008.11.003

Author contributions

All authors listed have made a substantial, direct, and intellectual contribution to the work and approved it for publication.

Acknowledgments

The authors extend their appreciation to the Deanship of Scientific Research at King Khalid University, Abha, Saudi Arabia, for funding this work through the Research Group Program under Grant No. RGP. 2/19/43.

Conflict of interest

The authors declare that the research was conducted in the absence of any commercial or financial relationships that could be construed as a potential conflict of interest.

Publisher's note

All claims expressed in this article are solely those of the authors and do not necessarily represent those of their affiliated organizations, or those of the publisher, the editors and the reviewers. Any product that may be evaluated in this article, or claim that may be made by its manufacturer, is not guaranteed or endorsed by the publisher.

- Crane, L. J. (1970). Flow past a stretching plate. *J. Appl. Math. Phys.* 21 (4), 645–647. doi:10.1007/bf01587695
- Darcy, H. (1965). Des Principes a Suivre et des Formules a Employer dans les Questions de Distribution D'eau Ouvrage Termine Par un Appendice Relatif aux Fournitures D'eau de Plusieurs Villes AU Filtrage des Eaux et a la Fabrication des Tuyaux de Fonte, de Plomb, de Tole et de Bitume. *JAWRA J. Am. Water Resour. Assoc.* 1 (2), 4–11. doi:10.1111/jawr.1965.1.2.4
- Dib, A., Haiahem, A., and Bou-Said, B. (2015). Approximate analytical solution of squeezing unsteady nanofluid flow. *Powder Technol.* 269, 193–199. doi:10.1016/j.powtec.2014.08.074
- Dogonchi, A. S., Alizadeh, M., and Ganji, D. D. (2017). Investigation of MHD Go-water nanofluid flow and heat transfer in a porous channel in the presence of thermal radiation effect. *Adv. Powder Technol.* 28 (7), 1815–1825. doi:10.1016/j.appt.2017.04.022
- Dong, Y., Cao, B. Y., and Guo, Z. Y. (2011). Generalized heat conduction laws based on thermomass theory and phonon hydrodynamics. *J. Appl. Phys.* 110 (6), 063504.
- Dutta, B. K., Roy, P., and Gupta, A. S. (1985). Temperature field in flow over a stretching sheet with uniform heat flux. *Int. Commun. Heat Mass Transf.* 12 (1), 89–94. doi:10.1016/0735-1933(85)90010-7
- Elattar, S., Helmi, M. M., Elkotb, M. A., El-Shorbagy, M. A., Abdelrahman, A., Bilal, M., et al. (2022). Computational assessment of hybrid nanofluid flow with the influence of hall current and chemical reaction over a slender stretching surface. *Alexandria Eng. J.* 61 (12), 10319–10331. doi:10.1016/j.aej.2022.03.054
- Elbashbeshy, E. M. A., and Bazid, M. A. A. (2004). Heat transfer over an unsteady stretching surface. *Heat. Mass Transf.* 41 (1), 1–4. doi:10.1007/s00231-004-0520-x
- Fourier, J. B. J., and Darboux, G. (1822). *Théorie analytique de la chaleur*, 504. Paris: Didot.
- Hadavand, M., Yousefzadeh, S., Akbari, O. A., Pourfattah, F., Nguyen, H. M., and Asadi, A. (2019). A numerical investigation on the effects of mixed convection of Ag-water nanofluid inside a sim-circular lid-driven cavity on the temperature of an electronic silicon chip. *Appl. Therm. Eng.* 162, 114298. doi:10.1016/j.applthermaleng.2019.114298
- Hossain, M. A., Alim, M. A., and Rees, D. A. S. (1999). The effect of radiation on free convection from a porous vertical plate. *Int. J. Heat Mass Transf.* 42 (1), 181–191. doi:10.1016/s0017-9310(98)00097-0
- Hussain, S. M., and Jamshed, W. (2021). A comparative entropy based analysis of tangent hyperbolic hybrid nanofluid flow: Implementing finite difference method. *Int. Commun. Heat Mass Transf.* 129, 105671. doi:10.1016/j.icheatmasstransfer.2021.105671
- Imtiaz, M., Mabood, F., Hayat, T., and Alsaedi, A. (2022). Impact of non-Fourier heat flux in bidirectional flow of carbon nanotubes over a stretching sheet with variable thickness. *Chin. J. Phys.* 77, 1587–1597. doi:10.1016/j.cjph.2021.10.024
- Irfan, M., Rafiq, K., Khan, W. A., and Khan, M. (2020). Numerical analysis of unsteady Carreau nanofluid flow with variable conductivity. *Appl. Nanosci.* 10 (8), 3075–3084. doi:10.1007/s13204-020-01331-z
- Jamshed, W., Goodarzi, M., Prakash, M., Nisar, K. S., Zakarya, M., Abdel-Aty, A. H., et al. (2021). Evaluating the unsteady Casson nanofluid over a stretching sheet with solar thermal radiation: An optimal case study. *Case Stud. Therm. Eng.* 26, 101160. doi:10.1016/j.csite.2021.101160
- Jamshed, W., Nisar, K. S., Ibrahim, R. W., Shahzad, F., and Eid, M. R. (2021). Thermal expansion optimization in solar aircraft using tangent hyperbolic hybrid nanofluid: A solar thermal application. *J. Mater. Res. Technol.* 14, 985–1006. doi:10.1016/j.jmrt.2021.06.031
- Jamshed, W. (2021). Numerical investigation of MHD impact on Maxwell nanofluid. *Int. Commun. Heat Mass Transf.* 120, 104973. doi:10.1016/j.icheatmasstransfer.2020.104973
- Jayadevamurthy, P. G. R., Rangaswamy, N. K., Prasannakumara, B. C., and Nisar, K. S. (2020). Emphasis on unsteady dynamics of bioconvective hybrid nanofluid flow over an upward-downward moving rotating disk. In *Numerical methods for partial differential equations*.
- Kalidasan, K., and Kanna, P. R. (2017). Natural convection on an open square cavity containing diagonally placed heaters and adiabatic square block and filled with hybrid nanofluid of nanodiamond-cobalt oxide/water. *Int. Commun. Heat Mass Transf.* 81, 64–71. doi:10.1016/j.icheatmasstransfer.2016.12.005
- Khan, M. J., Duraisamy, B., Zuhra, S., Nawaz, R., Nisar, K. S., Jamshed, W., et al. (2021). Numerical solution of Cattaneo-Christov heat flux model over stretching/shrinking hybrid nanofluid by new iterative method. *Case Stud. Therm. Eng.* 28, 101673. doi:10.1016/j.csite.2021.101673
- Khanafer, K., and Vafai, K. (2019). Applications of nanofluids in porous medium. *J. Therm. Anal. Calorim.* 135 (2), 1479–1492. doi:10.1007/s10973-018-7565-4
- Laha, M. K., Gupta, P. S., and Gupta, A. S. (1989). Heat transfer characteristics of the flow of an incompressible viscous fluid over a stretching sheet. *Wärme-Stoffübertragung* 24 (3), 151–153. doi:10.1007/bf01590013
- Lahmar, S., Kezzar, M., Eid, M. R., and Sari, M. R. (2020). Heat transfer of squeezing unsteady nanofluid flow under the effects of an inclined magnetic field and variable thermal conductivity. *Phys. A Stat. Mech. Its Appl.* 540, 123138. doi:10.1016/j.physa.2019.123138
- Magyari, E., and Keller, B. (1999). Heat and mass transfer in the boundary layers on an exponentially stretching continuous surface. *J. Phys. D. Appl. Phys.* 32 (5), 577–585. doi:10.1088/0022-3727/32/5/012
- Menni, Y., Chamkha, A. J., and Azzi, A. (2019). Nanofluid transport in porous media: A review. *Spec. Top. Rev. Porous Media*. 10 (1), 49–64. doi:10.1615/specialtopicsrevporousmedia.2018027168
- Mushtaq, A., Farooq, M. A., Sharif, R., and Razzaq, M. (2019). The impact of variable fluid properties on hydromagnetic boundary layer and heat transfer flows over an exponentially stretching sheet. *J. Phys. Commun.* 3 (9), 095005. doi:10.1088/2399-6528/ab31e2
- Ny, G., Barom, N., Noraziman, S., and Yeow, S. (2016). Numerical study on turbulent forced convective heat transfer of Ag/Heg water nanofluid in pipe. *J. Adv. Res. Mat. Sci.* 22 (1), 11–27.
- Pandey, P., Bharadwaj, R., and Chen, X. (2017). “Modeling of drug product manufacturing processes in the pharmaceutical industry,” in *Predictive modeling of pharmaceutical unit operations*, 1–13. Woodhead Publishing.
- Prasannakumara, B. C., Gireesha, B. J., Krishnamurthy, M. R., and Gorla, R. S. R. (2017). Unsteady boundary layer flow and convective heat transfer of a fluid particle suspension with nanoparticles over a stretching surface. *J. Model. Mech. Mater.* 1 (2). doi:10.1515/jmmm-2017-0002
- Raja Bose, J., Godson Asirvatham, L., N Kumar, T. M., and Wongwises, S. (2017). Numerical study on convective heat transfer characteristics of silver/water nanofluid in minichannel. *Curr. Nanosci.* 13 (4), 426–434. doi:10.2174/1573413713666161110154001
- Raja, M. A. Z., Shoaib, M., Khan, Z., Zuhra, S., Saleel, C. A., Nisar, K. S., et al. (2022). Supervised neural networks learning algorithm for three dimensional hybrid nanofluid flow with radiative heat and mass fluxes. *Ain Shams Eng. J.* 13 (2), 101573. doi:10.1016/j.asej.2021.08.015
- Rawat, S. K., Mishra, A., and Kumar, M. (2019). Numerical study of thermal radiation and suction effects on copper and silver water nanofluids past a vertical Riga plate. In *Multidiscipline modeling in materials and structures*.
- Reddy, P. S., and Sreedevi, P. (2021). Flow and heat transfer analysis of carbon nanotubes based nanofluid flow inside a cavity with modified Fourier heat flux. *Phys. Screen.* 96 (5), 055215. doi:10.1088/1402-4896/abe90f
- Rehman, F. U., Nadeem, S., and Haq, R. U. (2017). Heat transfer analysis for three-dimensional stagnation-point flow over an exponentially stretching surface. *Chin. J. Phys.* 55 (4), 1552–1560. doi:10.1016/j.cjph.2017.05.006
- Rehman, R., Wahab, H. A., and Khan, U. (2022). Heat transfer analysis and entropy generation in the nanofluids composed by Aluminum and γ -Aluminum oxides nanoparticles. *Case Stud. Therm. Eng.* 31, 101812. doi:10.1016/j.csite.2022.101812
- Sakiadis, B. C. (1961). Boundary-layer behavior on continuous solid surfaces: I. Boundary-layer equations for two-dimensional and axisymmetric flow. *AIChE J.* 7 (1), 26–28. doi:10.1002/aic.690070108
- Salmi, A., Madkhali, H. A., Nawaz, M., Alharbi, S. O., and Alqahtani, A. S. (2022). Numerical study on non-Fourier heat and mass transfer in partially ionized MHD Williamson hybrid nanofluid. *Int. Commun. Heat Mass Transf.* 133, 105967. doi:10.1016/j.icheatmasstransfer.2022.105967
- Shahsavari, A., Entezari, S., Toghray, D., and Barnoon, P. (2020). Effects of the porous medium and water-silver biological nanofluid on the performance of a newly designed heat sink by using first and second laws of thermodynamics. *Chin. J. Chem. Eng.* 28 (11), 2928–2937. doi:10.1016/j.cjche.2020.07.025
- Sheikholeslami, M., Ashorynejad, H. R., Domairry, G., and Hashim, I. (2012). Flow and heat transfer of Cu-water nanofluid between a stretching sheet and a porous surface in a rotating system. *J. Appl. Math.*, 1–18. doi:10.1155/2012/421320
- Shirvani, K. A., Mosleh, M., and Smith, S. T. (2016). Nanopolishing by colloidal nanodiamond in elastohydrodynamic lubrication. *J. Nanopart. Res.* 18 (8), 248–257. doi:10.1007/s11051-016-3526-7
- Shuaib, M., Ali, A., Khan, M. A., and Ali, A. (2020). Numerical investigation of an unsteady nanofluid flow with magnetic and suction effects to the moving upper plate. *Adv. Mech. Eng.* 12 (2), 168781402090358. doi:10.1177/1687814020903588
- Sinz, C. K., Woei, H. E., Khalis, M. N., and Abbas, S. A. (2016). Numerical study on turbulent force convective heat transfer of hybrid nanofluid, Ag/HEG in a circular channel with constant heat flux. *J. Adv. Res. Fluid Mech. Therm. Sci.* 24 (1), 1–11.

- Sreedevi, P., Sudarsana Reddy, P., and Chamkha, A. (2020). Heat and mass transfer analysis of unsteady hybrid nanofluid flow over a stretching sheet with thermal radiation. *SN Appl. Sci.* 2 (7), 1222–1236. doi:10.1007/s42452-020-3011-x
- Sundar, L. S., Punnaiah, V., Sharma, K. V., Chamkha, A. J., and Sousa, A. C. (2021). Thermal entropy and exergy efficiency analyses of nanodiamond/water nanofluid flow in a plate heat exchanger. *Diam. Relat. Mater.* 120, 108648. doi:10.1016/j.diamond.2021.108648
- Thabet, S., and Thabit, T. H. (2018). Computational fluid dynamics: Science of the future. *Int. J. Res. Eng.* 5 (6), 430–433. doi:10.21276/ijre.2018.5.6.2
- Uysal, C., Ü. N. E. Y. T., Gedik, E., and Chamkha, A. J. (2019). A numerical analysis of laminar forced convection and entropy generation of a diamond-Fe₃O₄/water hybrid nanofluid in a rectangular minichannel. *J. Appl. Fluid Mech.* 12 (2), 391–402. doi:10.29252/jafm.12.02.28923
- Wang, C. (2006). Analytic solutions for a liquid film on an unsteady stretching surface. *Heat. Mass Transf.* 42 (8), 759–766. doi:10.1007/s00231-005-0027-0
- Wang, J., Xu, Y. P., Qahiti, R., Jafaryar, M., Alazwari, M. A., Abu-Hamdeh, N. H., et al. (2022). Simulation of hybrid nanofluid flow within a microchannel heat sink considering porous media analyzing CPU stability. *J. Petroleum Sci. Eng.* 208, 109734. doi:10.1016/j.petrol.2021.109734
- Zhang, M. K., Cao, B. Y., and Guo, Y. C. (2013). Numerical studies on dispersion of thermal waves. *Int. J. Heat Mass Transf.* 67, 1072–1082. doi:10.1016/j.ijheatmasstransfer.2013.08.102
- Zuhra, S., Khan, N. S., Alam, M., Islam, S., and Khan, A. (2020). Buoyancy effects on nanoliquids film flow through a porous medium with gyrotactic microorganisms and cubic autocatalysis chemical reaction. *Adv. Mech. Eng.* 12 (1), 168781401989751. doi:10.1177/1687814019897510

Nomenclature

\hat{u} and \hat{v} Velocity components in \hat{x} and \hat{y} directions

\hat{t} Time component

$\hat{T}_\infty, \hat{u}_0, \hat{T}_0$ Positive constant with reference length l , n , and c

$A = \frac{\gamma l}{u_0}$ Unsteadiness parameter

a Constant parameter $[\frac{1}{s}]$

C Nanoparticle concentration

C_∞ Concentration of nanoparticles in the free stream

C_w Concentration of nanoparticles at the wall of the sheet

$Pr = \frac{\nu_f}{k_f}$ Prandtl number

$f(\eta)$ Dimensionless stream function

f_w Suction injection quantity

$Re_x^{1/2}$ Reynolds number

T Temperature [K]

T_w Temperature in free stream [K]

α_m Thermal diffusivity $[m^2s^{-1}]$

η Similarity variable

$(\rho C_p)_{nf}$ Specific heat capacity of the nanofluid [J/K],

λ Constant with dimension reciprocal of time $[1/s]$

μ_{nf} Dynamic viscosity of nanofluid

ρ_{nf} Density of nanofluid $[kg.m^{-3}]$,

ν Coefficient of kinematic viscosity $[(m^2s)^{-1}]$

k_{nf} Thermal conductivity of nanofluid

σ^* Boltzmann constant $[W(m^2K^4)^{-1}]$

σ Specific heat capacity of nanoparticles/specific heat capacity of fluid

τ_w Wall shear stress $[kg(m^2s)^{-1}]$,

$\theta(\eta)$ Dimensionless temperature

τ Specific heat capacity of nanoparticles/specific heat capacity of fluid

ϕ Dimensionless nanoparticle concentration

γ Time relaxation parameter

Greek Symbols

$\varphi(\hat{x}, \hat{y})$ Stream functions $[m^2s^{-1}]$



OPEN ACCESS

EDITED BY

Adnan,
Mohi-ud-Din Islamic University,
Pakistan

REVIEWED BY

Ali Akgül,
Siirt University, Turkey
Siti Suzilliana Putri Mohamed Isa,
Putra Malaysia University, Malaysia

*CORRESPONDENCE

Sohail Ahmad,
sohailkhan1058@gmail.com

SPECIALTY SECTION

This article was submitted to Process
and Energy Systems Engineering,
a section of the journal
Frontiers in Energy Research

RECEIVED 26 June 2022

ACCEPTED 21 July 2022

PUBLISHED 29 August 2022

CITATION

Ahmad S, Ali K, Haider T, Jamshed W,
Tag El Din ESM and Hussain SM (2022),
Thermal characteristics of kerosene oil-
based hybrid nanofluids (Ag-
MnZnFe₂O₄): A comprehensive study.
Front. Energy Res. 10:978819.
doi: 10.3389/fenrg.2022.978819

COPYRIGHT

© 2022 Ahmad, Ali, Haider, Jamshed,
Tag El Din and Hussain. This is an open-
access article distributed under the
terms of the [Creative Commons
Attribution License \(CC BY\)](#). The use,
distribution or reproduction in other
forums is permitted, provided the
original author(s) and the copyright
owner(s) are credited and that the
original publication in this journal is
cited, in accordance with accepted
academic practice. No use, distribution
or reproduction is permitted which does
not comply with these terms.

Thermal characteristics of kerosene oil-based hybrid nanofluids (Ag-MnZnFe₂O₄): A comprehensive study

Sohail Ahmad^{1*}, Kashif Ali², Tahir Haider³, Wasim Jamshed⁴,
El Sayed M. Tag El Din⁵ and Syed M. Hussain⁶

¹Centre for Advanced Studies in Pure and Applied Mathematics (CASPAM), Bahauddin Zakariya University, Multan, Pakistan, ²Department of Basic Sciences and Humanities, Muhammad Nawaz Sharif University of Engineering and Technology, Multan, Pakistan, ³Punjab Danish School and Centre of Excellence (Boys), Dera Ghazi Khan, Pakistan, ⁴Department of Mathematics, Capital University of Science and Technology, Islamabad, Pakistan, ⁵Electrical Engineering, Faculty of Engineering and Technology, Future University in Egypt, New Cairo, Egypt, ⁶Department of Mathematics, Faculty of Science, Islamic University of Madinah, Medina, Saudi Arabia

Hybrid nanofluids are new and most fascinating types of fluids that involve superior thermal characteristics. These fluids exhibit better heat-transfer performance as equated to conventional fluids. Our concern, in this paper, is to numerically interpret the kerosene oil-based hybrid nanofluids comprising dissimilar nanoparticles like silver (Ag) and manganese zinc ferrite (MnZnFe₂O₄). A numerical algorithm, which is mainly based on finite difference discretization, is developed to find the numerical solution of the problem. A numerical comparison appraises the efficiency of this algorithm. The effects of physical parameters are examined via the graphical representations in either case of nanofluids (pure or hybrid). The results designate that the porosity of the medium causes a resistance in the fluid flow. The enlarging values of nanoparticle volume fraction of silver sufficiently increase the temperature as well as velocity. It is examined here that mixture of hybrid nanoparticles (Ag-MnZnFe₂O₄) together with kerosene oil can provide assistance in heating up the thermal systems.

KEYWORDS

manganese zinc ferrite, silver, kerosene oil, Darcy Forchheimer medium, activation energy

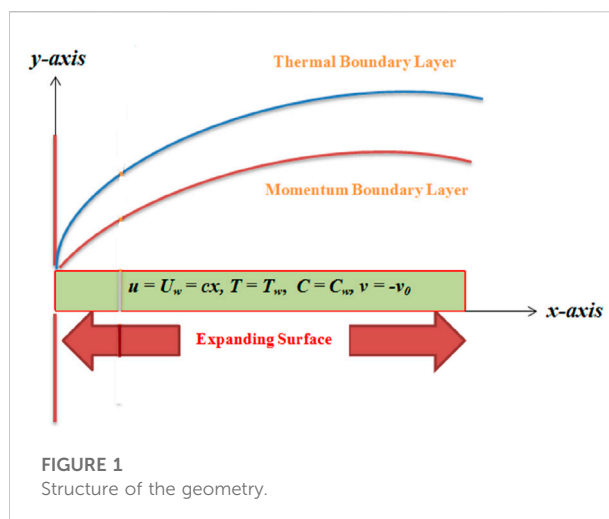
Introduction

Kerosene oil-based hybrid nanofluids can embellish the thermal characteristics; that is why these fluids have several uses in modern engineering and technology (Upreti et al., 2021; Yahya et al., 2022). The host or base fluid such as kerosene oil also plays an important role in augmentation of the heat-transfer performance rather than the nanoparticles. A combustible hydrocarbon-type liquid often obtained from petroleum can be referred to as kerosene oil, which is also known as paraffin or lamp oil. It is used as jet fuel in jet engines, as lighting and cooking fuel, as aviation fuel, as an oil-based paint,

and in corrosion experiments. Due to these characteristics, we have chosen kerosene oil as the host fluid in the current analysis. To prepare the hybrid composition (Ahmad et al., 2021a), nanoparticles of manganese zinc ferrite and silver are mixed in kerosene oil. Silver is a metal or chemical element having the highest thermal and electrical conductivity as compared to other metals. It is usually found in Earth's crust as a free element. Many substances are made of silver, such as ornaments, jewellery, utensils, solar panels, high-value tableware, and lead, and it is used in stained glass, catalysis of chemical reactions, window coatings, specialized mirrors, zinc refining, gold, and so forth. Manganese zinc ferrites belong to ferrite materials and exhibit high magnetic permeability (Ahmad et al., 2022a). These are widely used in noise filters, choke coils, transformers, and memory devices. Some recent investigations on nanofluids and hybrid nanofluids are discussed in reference articles (Abdal et al., 2021; Ahmad et al., 2021b; Zahid et al., 2021; Ayub et al., 2022; Nisar et al., 2022; Safdar et al., 2022).

Recently, many researchers have evaluated the thermal performance of usual and hybrid nanofluids numerically, theoretically, and experimentally. Dawar et al. (2022) investigated the kerosene oil and water-based hybrid nanofluid flow of copper and copper oxide nanoparticles. The magnetohydrodynamic effect was also taken into account, and the flow was taken over a bi-directional expanding surface. Comparative results of both hybrid nanofluids were established. The hybrid mixture of copper and aluminum oxide particles was prepared to form water-based hybrid nanofluid flow of Cu- Al_2O_3 /water (Zainal et al., 2022). The outcomes of this study revealed that the Nusselt number got reduced when the values of slip parameter increased. Akhter et al. (2022) and Ali et al. (2022) numerically simulated the nanofluid and hybrid nanofluid flows using the quasilinearization technique, respectively. Ezhil et al. (2021) presented the analysis of ferrous oxide Fe_3O_4 and copper (Cu) taking ethylene glycol as the base fluid. Flow was assumed to be fully developed occurring over a stretching sheet. The same work was carried out by Unyong et al. (2022) taking the effects of an inclined magnetic field and partial slip.

Heat transmission and fluid flow in permeable media have gained utmost attention of researchers due to their practical employments. Flow of Williamson nanofluids over a horizontal sheet embedded in a porous medium taking the combined impact of Brownian motion and thermal radiation was studied by Mishra and Mathur (2020). A boundary layer flow involving gyrotactic microorganisms and nanofluids was examined by Elbashbeshy and Asker (2022). The nonlinear velocity caused the stretching of sheets, and the controlling parameters were discussed quantitatively. The characteristics of flow dynamics in porous media and in the presence of nanoparticles have substantial effects on heat-transfer effects (Dastvareh and Azaiez, 2017). In this paper, it was determined that nanoparticles decreased the viscosity



distribution monotonically. Flow and heat transfer of ferro-nanofluids through Darcian porous media between channel walls were numerically simulated by Das et al. (2019). The heat-transfer rate at the upper channel wall was noticed to be increasing as compared to the lower wall. Flow of nanoparticles in the presence of peristaltic waves and porous media has been investigated by Kareem and Abdulhadi (2020). They achieved numerical results using the Mathematica 11 program. More recent numerical investigations on nanofluids can be found in Ahmed et al., 2017a; Ahmed et al., 2017b; Ahmed et al., 2018; Ahmed et al., 2020; Adnan et al., 2022a; Adnan et al., 2022e; Adnan et al., 2022f; Adnan et al., 2022b; Adnan et al., 2022d; and Adnan et al., 2022c.

In spite of so much efforts to explore and discover the new energy sources, still, struggle is continued. New types of hybrid nanocompositions are being introduced. The available literature evidently discloses that kerosene oil-based nanofluids and hybrid nanofluids consisting of silver (Ag) and manganese zinc ferrite ($\text{MnZnFe}_2\text{O}_4$) nanoparticles have not been numerically investigated yet. However, our analysis is a first effort to examine the nanocomposition of Ag- $\text{MnZnFe}_2\text{O}_4$ -KO. The role of chemical reaction, suction, and porous media is also discussed in both pure and hybrid cases of nanofluids. Numerical solutions are found with the help of finite difference discretization via MATLAB. Thermal systems can manage and maintain their temperature and heat-transfer rate with the help of proposed hybrid compositions, for example, Ag- $\text{MnZnFe}_2\text{O}_4$ -KO.

Problem formulation

The nanoparticles of silver (Ag) and manganese zinc ferrite ($\text{MnZnFe}_2\text{O}_4$) are mixed in kerosene oil to form the hybrid nanocomposite of Ag- $\text{MnZnFe}_2\text{O}_4$ /kerosene oil. The x - and

TABLE 1 Thermal properties of silver, kerosene oil, and manganese zinc ferrite.

| Properties | Ag (s_2) | Kerosene oil (f) | MnZnFe ₂ O ₄ (s_1) |
|-----------------------------|--------------|------------------|--|
| k (W/mK) | 429.0 | 0.145 | 3.9 |
| C_p (J/kgK) | 235.00 | 2090.0 | 1050 |
| ρ (kg/m ³) | 10500.0 | 783.0 | 4700 |

y -axes are taken in such a way that the fluid flowing along the x -axis and y -axis is vertical to the surface. Figure 1 demonstrates the structure of the extending surface. It is assumed that the fluid is flowing through a porous medium with the effect of chemical reaction.

The model governing equations have the following form (Ahmad et al., 2021c):

$$\frac{\partial u}{\partial x} + \frac{\partial v}{\partial y} = 0 \quad (1)$$

$$u \frac{\partial u}{\partial x} + v \frac{\partial u}{\partial y} = v_{mf} \frac{\partial^2 u}{\partial y^2} - \frac{\mu_{mf}}{\rho_{mf} k^*} u \quad (2)$$

$$u \frac{\partial T}{\partial x} + v \frac{\partial T}{\partial y} = \frac{K_{mf}}{(\rho C_p)_{mf}} \frac{\partial^2 T}{\partial y^2} \quad (3)$$

$$u \frac{\partial C}{\partial x} + v \frac{\partial C}{\partial y} = D_B \frac{\partial^2 C}{\partial y^2} - K_r (C - C_\infty). \quad (4)$$

The analogous boundary conditions (BCs) are

$$\left. \begin{aligned} y = 0: u(x, 0) = U_w(x) = cx, T(x, 0) = T_w, v(x, 0) = -v_0, C(x, 0) = C_w \\ y \rightarrow \infty: u(x, \infty) = 0, T(x, \infty) = T_\infty, C(x, \infty) = C_\infty \end{aligned} \right\} \quad (5)$$

The suction velocity is denoted by $v_0 > 0$. The notations T_w and T_∞ represent the temperatures at the surface boundary and away from the boundary. Likewise, the concentrations away from the boundary and at the boundary are respectively represented by C_∞ and C_w . The surface is stretching with the velocity $U_w(x) = u(x, 0) = cx$. The hybrid nanofluid is expressed by the notation hmf .

Formation of pure (Ag/KO) and hybrid nanofluids (MnZnFe₂O₄-Ag/KO)

The hybrid nanocomposite MnZnFe₂O₄-Ag/KO can be achieved by mixing the nanoparticles of manganese zinc ferrite (MnZnFe₂O₄) and silver (Ag) in the kerosene oil (KO). Initially, the volume fraction of MnZnFe₂O₄ (ϕ_1) is considered as 0.2 when resolved in the kerosene oil to form the pure nanofluid MnZnFe₂O₄/KO. Afterward, the particles of Ag (ϕ_2) are inserted in this solution, which give rise to the hybrid nanofluids (MnZnFe₂O₄-Ag/KO). Thermal properties of manganese zinc ferrite, silver, and kerosene oil are specified in Table 1. Further characteristics like specific heat, thermal conductivity, and

density (in both cases of nanofluids) are assumed to be the same as those taken by Ahmad et al. (2021d). The notation s_2 expresses the silver volume fraction, and s_1 is used for the volume fraction of manganese zinc ferrite. The host fluid kerosene oil is represented by f .

Dimensionless variables

The following dimensionless variables are introduced in order to convert partial differential equations (PDEs) into a dimensionless system of ordinary differential equations (ODEs):

$$\xi = \sqrt{\frac{c}{v_f}} y, \psi = \sqrt{c v_f} x f(\xi), \theta(\xi) = \frac{T - T_\infty}{T_w - T_\infty}, \phi(\xi) = \frac{C - C_\infty}{C_w - C_\infty} \quad (6)$$

The continuity equation (Eq. 1) is identically satisfied by relation (6), and this relation renovates the system of Eqs. 2–4 in the form

$$f''' = \Delta_1 (f'^2 - f f'') + \varepsilon f' \quad (7)$$

$$\frac{1}{Pr} \Delta_2 \theta'' + \Delta_3 f \theta' = 0 \quad (8)$$

$$\frac{1}{Sc} \phi'' + f \phi' - C_R \phi = 0 \quad (9)$$

where

$$\Delta_1 = (1 - \phi_1)^{2.5} (1 - \phi_2)^{2.5} \left[(1 - \phi_2) \left\{ (1 - \phi_1) + \phi_1 \frac{\rho_{s1}}{\rho_f} \right\} + \phi_2 \frac{\rho_{s2}}{\rho_f} \right] \quad (10)$$

$$\Delta_2 = \frac{K_{hmf}}{K_f} \quad (11)$$

$$\Delta_3 = \left[(1 - \phi_2) \left\{ (1 - \phi_1) + \phi_1 \frac{(\rho C_p)_{s1}}{(\rho C_p)_f} \right\} + \phi_2 \frac{(\rho C_p)_{s2}}{(\rho C_p)_f} \right] \quad (12)$$

The BCs (5) take the following form now:

$$\left. \begin{aligned} \xi = 0: f = \lambda_s, f' = 1, \theta = 1, \phi = 1, \\ \xi \rightarrow \infty: f' \rightarrow 0, \theta \rightarrow 0, \phi \rightarrow 0. \end{aligned} \right\} \quad (13)$$

Problem parameters

The problem parameters of dimensionless Eqs. 7–9 are identified as follows:

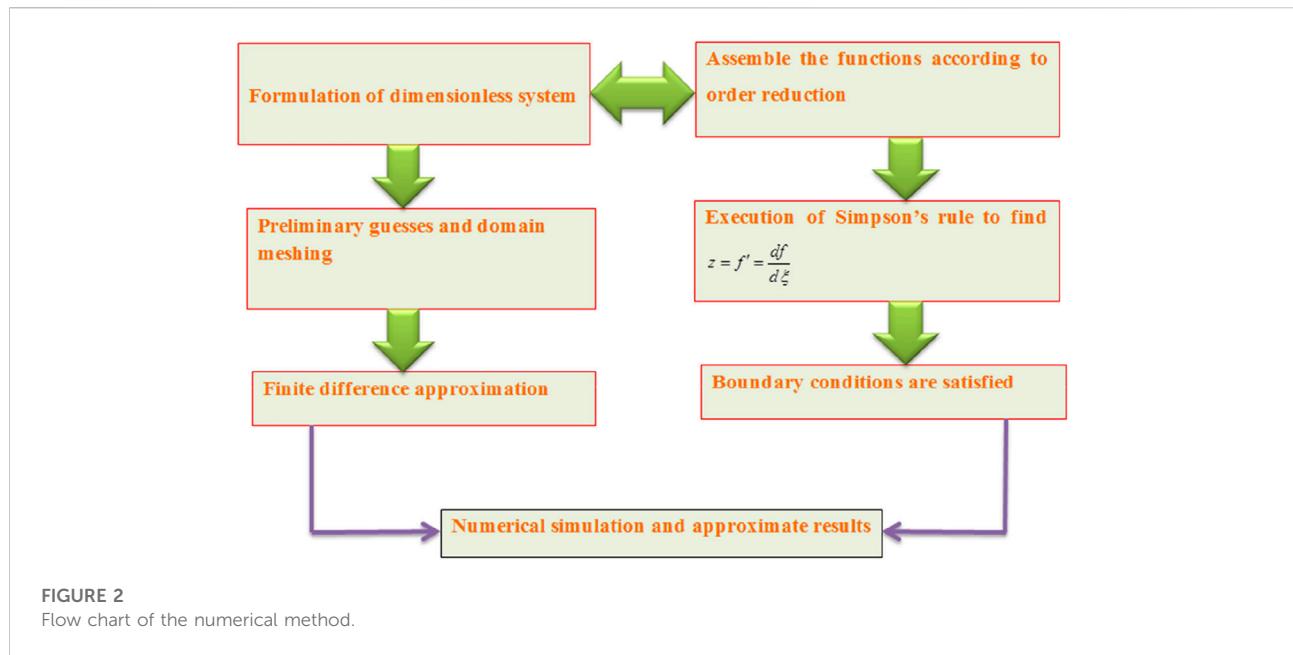
$S_c = \frac{v_f}{D_B}$ is the Schmidt number

$\lambda_s = \frac{v_0}{\sqrt{c v_f}}$ is the suction parameter

$Pr = \frac{\mu_f (c_p)_f}{k_f}$ is the Prandtl number

$\varepsilon = \frac{v_f}{c k^*}$ is the porosity parameter

$C_R = \frac{K_r}{c}$ is the chemical reaction parameter



The relations for shear stress as well as Sherwood and Nusselt number are given by

$$\text{Re}_x^{\frac{1}{2}} C_{fx} = \frac{f''(0)}{(1-\phi_1)^{2.5}(1-\phi_2)^{2.5}}, \quad Sh_x \text{Re}_x^{\frac{1}{2}} = -\phi'(0),$$

$$Nu_x \text{Re}_x^{\frac{1}{2}} = -\frac{k_{mf}}{k_f} \theta'(0). \quad (14)$$

whereas the local Reynolds number is given as $\text{Re}_x = \frac{U_w x}{\nu_f}$.

Numerical scheme based on finite difference discretization

Finding the analytical solution of the coupled Eqs. 7–9 may be so much time-consuming as these equations are not only higher-order but also highly nonlinear. However, we require some persuasive numerical technique which could be employed to determine the solution of the problem. Therefore, we adopt a finite difference methodology in order to find the numerical solution of the problem under consideration. The different numerical methods (to solve such types of dynamical problems) that we adopted in our earlier work can be seen in reference articles (Ahmad et al., 2021e; Ahmad et al., 2021f; Jamshed, et al., 2021; Ahmad et al., 2022b). We describe the structure of this methodology in the following flow chart diagram (Figure 2).

Results and discussion

This section depicts the analysis of mono (Ag/kerosene oil) and hybrid (Ag-MnZnFe₂O₄/kerosene oil) cases of

TABLE 2 Change in heat-transfer rate for different Prandtl numbers when $\phi_1 = \phi_2 = 0$.

| Pr | Literature results (Khan and Pop, 2010) | Present results |
|----|---|-----------------|
| 2 | 0.9113 | 0.91045 |
| 7 | 1.8954 | 1.89083 |
| 20 | 3.3539 | 3.35271 |
| 70 | 6.4621 | 6.47814 |

TABLE 3 Impact of porosity parameter on $\text{Re}_x^{\frac{1}{2}} C_f$ and $\text{Re}_x^{-\frac{1}{2}} Nu_x$.

| ϵ | $\text{Re}_x^{\frac{1}{2}} C_f$ | | $\text{Re}_x^{-\frac{1}{2}} Nu_x$ | |
|------------|---------------------------------|---|-----------------------------------|---|
| | Ag/KO | Ag-MnZnFe ₂ O ₄ /KO | Ag/KO | Ag-MnZnFe ₂ O ₄ /KO |
| 1.2 | -4.1328499 | -6.8013631 | 9.8973507 | 13.7221408 |
| 2.2 | -4.3509353 | -7.1978370 | 9.8899404 | 13.7081393 |
| 3.3 | -4.5731705 | -7.5998153 | 9.8825911 | 13.6943887 |
| 4.2 | -4.7438059 | -7.9072949 | 9.8770823 | 13.6841633 |

nanofluids. The nanocomposites of silver (Ag) into the kerosene oil give rise to the mono nanofluid, whereas the amalgamation of manganese zinc ferrite and silver produces the hybrid mixture. The effects of physical parameters are deliberated via the graphs and tables. Table 2 portrays a comparison which is found to be in a good correlation with the existing outcomes under limiting cases.

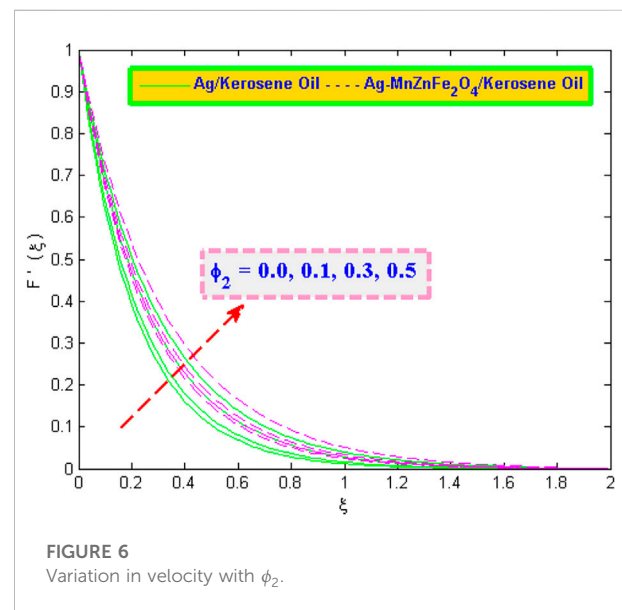
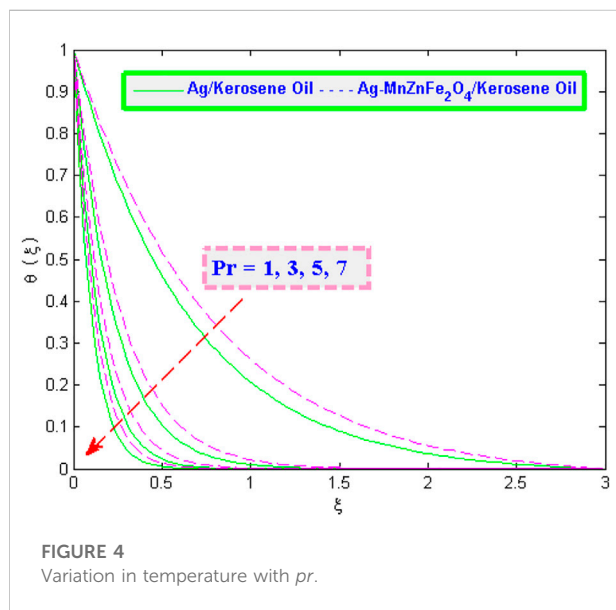
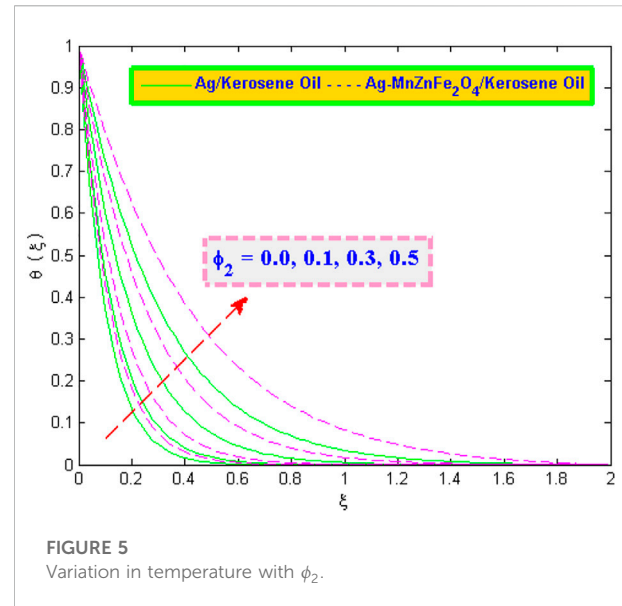
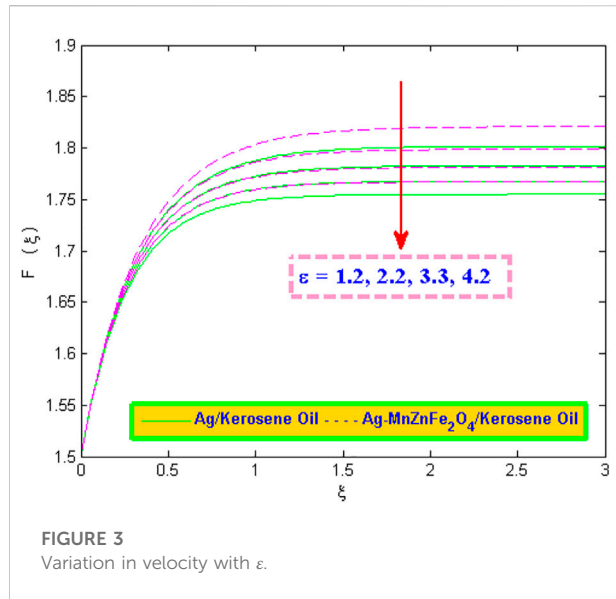
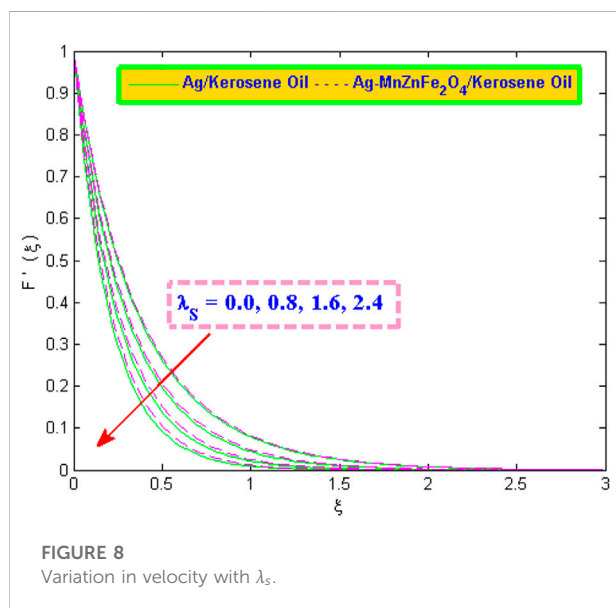
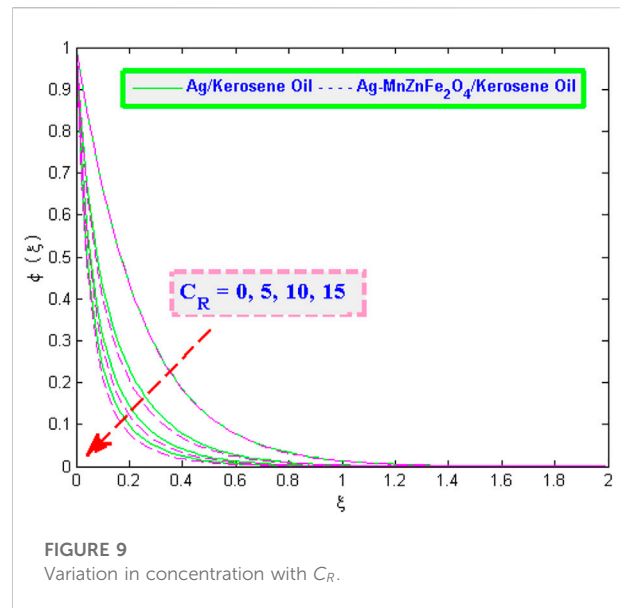
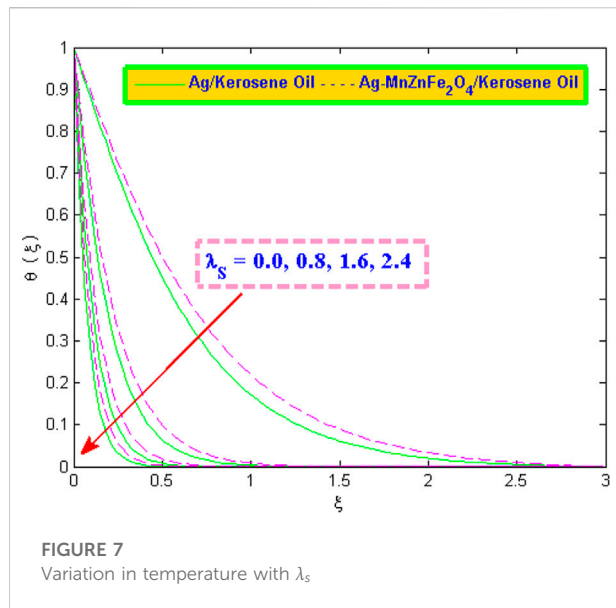


TABLE 4 Impact of nanoparticle volume fraction and Prandtl number on $Re_x^{-1/2} Nu_x$.

| ϕ_2 | $Re_x^{-1/2} Nu_x$ | | Pr | $Re_x^{-1/2} Nu_x$ | |
|----------|--------------------|---|------|--------------------|---|
| | Ag/KO | Ag-MnZnFe ₂ O ₄ /KO | | Ag/KO | Ag-MnZnFe ₂ O ₄ /KO |
| 0.0 | 9.6014532 | 13.5632834 | 1 | 1.8078974 | 2.5876586 |
| 0.1 | 10.1558546 | 13.8085327 | 3 | 4.9757331 | 6.8999489 |
| 0.3 | 11.3109163 | 14.3420655 | 5 | 8.1204811 | 11.2517676 |
| 0.5 | 12.6458643 | 15.1546670 | 7 | 11.2068343 | 15.5277464 |



We assign fixed values to the parameters such as $Pr = 6.135$. The other specified values which have been used in finding the numerical solution are

$$\varepsilon = 4, \phi_1 = 0.2, Sc = 2.5, \phi_2 = 0.05, \lambda_s = 1.5, C_R = 4.$$

The change in surface drag $Re_x^{-1/2} C_f$ and Nusselt number $Re_x^{-1/2} Nu_x$ against porosity parameter ε can be observed from Table 3. An increase in the values of porosity parameter tends to enhance the skin friction, but its effect is to deteriorate the rate of heat transfer. The fluid flow is resisted by the porosity of the medium due to which the velocity of the fluid reduces (see Figure 3). The Prandtl number tends to deteriorate the temperature as shown in Figure 4.

Thermal characteristics in either case of nanofluids are affected by the volume fraction ϕ_2 of silver nanoparticles. The required outcomes can be attained by suitably taking the volume fractions of nanoparticles. It is comparatively noticed from Figure 5 that the temperature increases rapidly in the case of

TABLE 5 Impact of activation energy and chemical reaction on $Re_x^{-1/2} Sh_x$.

| λ_s | $Re_x^{-1/2} Nu_x$ | | C_R | $Re_x^{-1/2} Sh_x$ | |
|-------------|--------------------|---|-------|--------------------|---|
| | Ag/KO | Ag-MnZnFe ₂ O ₄ /KO | | Ag/KO | Ag-MnZnFe ₂ O ₄ /KO |
| 0.0 | 1.4868709 | 2.1831767 | 0 | 4.0539553 | 4.0604246 |
| 0.8 | 5.7505953 | 8.0283592 | 5 | 10.5963505 | 4.0604246 |
| 1.6 | 10.4093347 | 14.4429463 | 10 | 14.8876215 | 15.5156646 |
| 2.4 | 15.0452404 | 20.8890408 | 15 | 18.1589037 | 18.8270273 |

the hybrid composition Ag-MnZnFe₂O₄/KO rather than the composition of Ag/KO when we increase the volume concentration ϕ_2 . In the same way, the velocity of the fluid accelerates quickly in the hybrid case of the nanofluid as pictured in Figure 6. The impact of both volume fraction ϕ_2 and the Prandtl number Pr is to escalate the Nusselt number $Re_x^{-1/2} Nu_x$ for both pure and hybrid nanofluids (see Table 4).

The variation in temperature and velocity for diverse values of the suction parameter can be examined from Figures 7, 8. Both the temperature $\theta(\xi)$ and velocity $F'(\xi)$ turn toward reduction (in both cases of nanofluids) with the effect of suction. Figure 9 illustrates the influence of the chemical reaction parameter on concentration in either case of the nanofluid. A decreasing trend is noticed in the concentration profile, which shows that the chemical reaction parameter C_R causes a substantial decrease in the concentration.

The mass-transfer rate increases with an increase in the values of C_R as observed in Table 6. It has also been deduced from Table 5 that the suction parameter λ_s marginally enhances the heat-transfer rate in the case of the hybrid nanofluid Ag-MnZnFe₂O₄/KO rather than the usual case of the nanofluid Ag/KO.

Conclusion

Specific rate of heat transfer plays an important role in many engineering systems as it can affect the quality of the product. A certain or specific heat-transfer rate is essentially required in many energy systems, for example, metal expulsion, nuclear system cooling, refrigeration, thermal storage, cooling generator, and so on. The amalgamation of manganese zinc ferrites (MnZnFe₂O₄) and silver (Ag) in kerosene oil can provide assistance in increasing the heat-transfer rate. The main results of this study are listed as follows:

- The nanoparticle volume fraction of silver (ϕ_2) tends to elevate the velocity and temperature of Ag/KO as well as Ag-MnZnFe₂O₄/KO, which are mono and hybrid cases of nanofluids, respectively.
- The fluid motion and temperature are reduced due to the suction phenomenon. On the other hand, the surface drag got increased with suction for both cases of nanofluids.
- The heat-transfer rate is an increasing function of Prandtl number, whereas the temperature is decelerated with the effect of Prandtl number.
- The concentration profile seems to be falling down with an increase in the chemical reaction parameter.
- The porosity of the medium resists the flow in either case of nanofluids, for example, the pure or hybrid case.

Data availability statement

The raw data supporting the conclusions of this article will be made available by the authors, without undue reservation.

Author contributions

All authors listed have made a substantial, direct, and intellectual contribution to the work and approved it for publication.

Funding

The authors are grateful to the Deanship of Scientific Research, Islamic University of Madinah, Ministry of Education, KSA, for supporting this research work through a research project grant under Research Group Program/1/804.

Conflict of interest

The authors declare that the research was conducted in the absence of any commercial or financial relationships that could be construed as a potential conflict of interest.

Publisher's note

All claims expressed in this article are solely those of the authors and do not necessarily represent those of their affiliated organizations or those of the publisher, the editors, and the reviewers. Any product that may be evaluated in this article or claim that may be made by its manufacturer is not guaranteed or endorsed by the publisher.

References

- Abdal, S., Habib, U., Siddique, I., Akgül, A., and Ali, B. (2021). Attribution of multi-slips and bioconvection for micropolar nanofluids transpiration through porous medium over an extending sheet with PST and PHF conditions. *Int. J. Appl. Comput. Math.* 7 (6), 235. doi:10.1007/s40819-021-01137-9
- Adnan, Ashraf, W., Khan, I., and Andualem, M. (2022a). Thermal transport investigation and shear drag at solid-liquid interface of modified permeable radiative-SRID subject to Darcy-Forchheimer fluid flow composed by γ -nanomaterial. *Sci. Rep.* 12, 3564. doi:10.1038/s41598-022-07045-2
- Adnan, Ashraf, W., Khan, I., Shemseldin, M. A., and Mousa, A. A. A. (2022c). Numerical energy storage efficiency of MWCNTs-Propylene Glycol by inducing thermal radiations and combined convection effects in the constitutive model. *Front. Chem.* 10, 879276. doi:10.3389/fchem.2022.879276

- Adnan, Ashraf, W., Khan, U., Al-Johani, A. S., Ahmed, N., Mohyud-Din, S. T., et al. (2022b). Impact of freezing temperature (T_{fr}) of Al₂O₃ and molecular diameter (H₂O)_d on thermal enhancement in magnetized and radiative nanofluid with mixed convection. *Sci. Rep.* 12, 703. doi:10.1038/s41598-021-04587-9
- Adnan, Khan, U., Ahmed, N., Mohyud-Din, S. T., Alharbi, S. O., and Khan, I. (2022d). Thermal improvement in magnetized nanofluid for multiple shapes nanoparticles over radiative rotating disk. *Alexandria Eng. J.* 61 (3), 2318–2329. doi:10.1016/j.aej.2021.07.021
- Adnan, Khan, U., Ahmed, N., Mohyud-Din, S. T., Alsulami, M. D., and Khan, I. (2022e). A novel analysis of heat transfer in the nanofluid composed by nanodiamond and silver nanomaterials: Numerical investigation. *Sci. Rep.* 12, 1284. doi:10.1038/s41598-021-04658-x
- Adnan, Murtaza, R., Hussain, I., Rehman, Z., Khan, I., and Andualem, M. (2022f). Thermal enhancement in Falkner-Skan flow of the nanofluid by considering molecular diameter and freezing temperature. *Sci. Rep.* 12, 9415. doi:10.1038/s41598-022-13423-7
- Ahmad, S., Akhter, S., and Shahid, M. I. (2022). Novel thermal aspects of hybrid nanofluid flow comprising of Manganese zinc ferrite MnZnFe₂O₄, Nickel zinc ferrite NiZnFe₂O₄ and motile microorganisms. *Ain Shams Eng. J.* 13 (5), 101668. doi:10.1016/j.asej.2021.101668
- Ahmad, S., Ali, K., Ahmad, S., and Cai, J. (2021). Numerical study of Lorentz force interaction with micro structure in channel flow. *Energies* 14 (14), 4286. doi:10.3390/en14144286
- Ahmad, S., Ali, K., and Ashraf, M. (2021). MHD flow of Cu-Al₂O₃/water hybrid nanofluid through a porous media. *J. Por. Media* 24 (7), 61–73. doi:10.1615/JPorMedia.2021036704
- Ahmad, S., Ali, K., Faridi, A. A., and Ashraf, M. (2021). Novel thermal aspects of hybrid nanoparticles Cu-TiO₂ in the flow of Ethylene Glycol. *Int. Commun. Heat. Mass Transf.* 129, 105708. doi:10.1016/j.icheatmasstransfer.2021.105708
- Ahmad, S., Ali, K., Nisar, K. S., Faridi, A. A., Khan, N., Jamshed, W., et al. (2021). Features of Cu and TiO₂ in the flow of engine oil subject to thermal jump conditions. *Sci. Rep.* 11, 19592. doi:10.1038/s41598-021-99045-x
- Ahmad, S., Ali, K., Rizwan, M., and Ashraf, M. (2021). Heat and mass transfer attributes of copper-aluminum oxide hybrid nanoparticles flow through a porous medium. *Case Stud. Therm. Eng.* 25, 100932. doi:10.1016/j.csite.2021.100932
- Ahmad, S., Ashraf, M., and Ali, K. (2021). Simulation of thermal radiation in a micropolar fluid flow through a porous medium between channel walls. *J. Therm. Anal. Calorim.* 144 (3), 941–953. doi:10.1007/s10973-020-09542-w
- Ahmad, S., Younis, J., Ali, K., Rizwan, M., Ashraf, M., and Abd El Salam, M. A. (2022). Impact of swimming gyrotactic microorganisms and viscous dissipation on nanoparticles flow through a permeable medium: A numerical assessment. *J. Nanomater.* 2022, 1–11. doi:10.1155/2022/4888128
- Ahmed, N., Abbasi, A., Khan, U., and Mohyud-Din, S. T. (2018). Thermal radiation effects on flow of Jeffery fluid in converging and diverging stretchable channels. *Neural Comput. Applic.* 30, 2371–2379. doi:10.1007/s00521-016-2831-5
- Ahmed, N., Adnan, Khan, U., Mohyud-Din, S. T., and Manzoor, R. (2017). Influence of viscous dissipation on a copper oxide nanofluid in an oblique channel: Implementation of the KKL model. *Eur. Phys. J. Plus* 132, 237. doi:10.1140/epjp/i2017-11504-y
- Ahmed, N., Adnan, Khan, U., and Mohyud-Din, S. T. (2020). Modified heat transfer flow model for SWCNTs-H₂O and MWCNTs-H₂O over a curved stretchable semi infinite region with thermal jump and velocity slip: A numerical simulation. *Phys. A Stat. Mech. its Appl.* 545, 123431. doi:10.1016/j.physa.2019.123431
- Ahmed, N., Adnan, Khan, U., Mohyud-Din, S. T., and Saat Erturk, V. S. (2017). Influence of thermal and concentration gradients on unsteady flow over a stretchable surface. *Results Phys.* 7, 3153–3162. doi:10.1016/j.rinp.2017.08.034
- Akhter, S., Ahmad, S., and Ashraf, M. (2022). Cumulative impact of viscous dissipation and heat generation on MHD Darcy-Forchheimer flow between two stretchable disks: Quasi linearization technique. *J. Sci. Arts* 22 (1), 219–232. doi:10.46939/J.Sci.Arts.22.1-c01
- Ali, K., Faridi, A. A., Ahmad, S., Jamshed, W., Khan, N., and Alam, M. M. (2022). Quasi-linearization analysis for heat and mass transfer of magnetically driven 3rd-grade (Cu-TiO₂/engine oil) nanofluid via a convectively heated surface. *Int. Commun. Heat Mass Transf.* 135, 106060. doi:10.1016/j.icheatmasstransfer.2022.106060
- Ayub, R., Ahmad, S., Ahmad, S., Akhtar, Y., Alam, M. M., and Mahmoud, O. (2022). Numerical assessment of dipole interaction with the single-phase nanofluid flow in an enclosure: A pseudo-transient approach. *Materials* 15, 2761. doi:10.3390/ma15082761
- Das, S., Tarafdar, B., Jana, R. N., and Makinde, O. D. (2019). Magnetic ferro-nanofluid flow in a rotating channel containing darcian porous medium considering induced magnetic field and Hall currents. *Spec. Top. Rev. Porous Media* 10 (4), 357–383. doi:10.1615/SpecialTopicsRevPorousMedia.2019028377
- Dastvareh, B., and Azaiez, J. (2017). Instabilities of nanofluid flow displacements in porous media. *Phys. Fluids* 29, 044101. doi:10.1063/1.4978890
- Dawar, A., Islam, S., and Shah, Z. (2022). A comparative analysis of the performance of magnetised copper-copper oxide/water and copper-copper oxide/kerosene oil hybrid nanofluids flowing through an extending surface with velocity slips and thermal convective conditions. *Int. J. Ambient Energy*, 1–19. doi:10.1080/01430750.2022.2063387
- Elbashbesy, E. M. A., and Asker, H. G. (2022). Fluid flow over a vertical stretching surface within a porous medium filled by a nanofluid containing gyrotactic microorganisms. *Eur. Phys. J. Plus* 137, 541. doi:10.1140/epjp/s13360-022-02682-y
- Ezhil, K., Thavada, S. K., and Ramakrishna, S. B. (2021). MHD slip flow and heat transfer of Cu-Fe₃O₄/Ethylene glycol-based hybrid nanofluid over a stretching surface. *Biointerface Res. Appl. Chem.* 11 (4), 11956–11968. doi:10.33263/BRIAC114.1195611968
- Jamshed, W., Baleanu, D., Nasir, N. A. A. M., Shahzad, F., Nisar, K. S., Shoaib, M., et al. (2021). The improved thermal efficiency of Prandtl-eyring hybrid nanofluid via classical keller box technique. *Sci. Rep.* 11, 23535. doi:10.1038/s41598-021-02756-4
- Kareem, R. S., and Abdulhadi, A. M. (2020). Effect of MHD and porous media on nanofluid flow with heat transfer: Numerical treatment. *J. Adv. Res. Fluid Mech. Therm. Sci.* 63 (2), 317–328.
- Khan, W. A., and Pop, I. (2010). Boundary-layer flow of a nanofluid past a stretching sheet. *Int. J. Heat Mass Transf.* 53, 2477–2483. doi:10.1016/j.ijheatmasstransfer.2010.01.032
- Mishra, S. R., and Mathur, P. (2020). Williamson nanofluid flow through porous medium in the presence of melting heat transfer boundary condition: Semi-analytical approach. *Mmms* 17 (1), 19–33. doi:10.1108/MMMS-12-2019-0225
- Nisar, K. S., Faridi, A. A., Ahmad, S., Khan, N., Ali, K., Jamshed, W., et al. (2022). Cumulative impact of micropolar fluid and porosity on mhd channel flow: A numerical study. *Coatings* 12, 93. doi:10.3390/coatings12010093
- Safdar, R., Jawad, M., Hussain, S., Imran, M., Akgül, A., and Jamshed, W. (2022). Thermal radiative mixed convection flow of MHD Maxwell nanofluid: Implementation of buongiorno's model. *Chin. J. Phys.* 77, 1465–1478. doi:10.1016/j.cjph.2021.11.022
- Unyong, B., Vadivel, R., Govindaraju, M., Anbuviya, R., and Gunasekaran, N. (2022). Entropy analysis for ethylene glycol hybrid nanofluid flow with elastic deformation, radiation, non-uniform heat generation/absorption, and inclined Lorentz force effects. *Case Stud. Therm. Eng.* 30, 101639. doi:10.1016/j.csite.2021.101639
- Upreti, H., Pandey, A. K., and Kumar, M. (2021). Assessment of entropy generation and heat transfer in three-dimensional hybrid nanofluids flow due to convective surface and base fluids. *J. Porous Media* 24 (3), 35–50. doi:10.1615/JPorMedia.2021036038
- Yahya, A. U., Siddique, I., Jarad, F., Salamat, N., Abdal, S., Hamed, Y. S., et al. (2022). On the enhancement of thermal transport of Kerosene oil mixed TiO₂ and SiO₂ across Riga wedge. *Case Stud. Therm. Eng.* 34, 102025. doi:10.1016/j.csite.2022.102025
- Zahid, M., Asjad, M. I., Hussain, S., and Akgül, A. (2021). Nonlinear magnetohydrodynamic flow of nanofluids across a porous matrix over an extending sheet with mass transpiration and bioconvection. *Heat. Transf.* 50 (8), 7588–7603. doi:10.1002/htj.22244
- Zainal, N. A., Nazar, R., Naganthran, K., and Pop, I. (2022). Slip effects on unsteady mixed convection of hybrid nanofluid flow near the stagnation point. *Appl. Math. Mech.-Engl. Ed.* 43, 547–556. doi:10.1007/s10483-022-2823-6

Nomenclature

| | | | |
|----------------|---|-------------|---|
| ρ_{hnf} | Density of the hybrid nanofluid | c | Stretching/shrinking constant |
| v | Component of velocity along the y -axis | ν_{hnf} | Kinematic viscosity of the hybrid nanofluid |
| σ_{hnf} | Electrical conductivity of the hybrid nanofluid | T | Temperature of the fluid |
| k^* | Darcy permeability | μ_{hnf} | Hybrid nanofluid viscosity |
| ν_0 | Suction velocity (where $\nu_0 > 0$) | T_∞ | Temperature far away from the sheet |
| $C_{p_{hnf}}$ | Specific heat of the hybrid nanofluid | C | Concentration of the fluid |
| u | Component of velocity along the x -axis | T_w | Fixed temperature at the surface |
| K_r | Rate constant of chemical reaction | D_B | Diffusion coefficient |
| k_{hnf} | Thermal conductivity of the hybrid nanofluid | C_∞ | Concentration far away from the sheet |



OPEN ACCESS

EDITED BY

Umar Khan,
Hazara University, Pakistan

REVIEWED BY

Naveed Ahmed,
HITEC University, Pakistan
M. Ijaz Khan,
Peking University, China

*CORRESPONDENCE

Mustafa Inc,
mustafainc1071@gmail.com

SPECIALTY SECTION

This article was submitted to Process and Energy Systems Engineering, a section of the journal Frontiers in Energy Research

RECEIVED 05 June 2022

ACCEPTED 13 July 2022

PUBLISHED 02 September 2022

CITATION

Aleem M, Inc M, Sarwar S, Asjad MI and Alsubaie ASA (2022), Analysis of fractional MHD convective flow with CTNs' nanoparticles and radiative heat flux in human blood.
Front. Energy Res. 10:962086.
doi: 10.3389/fenrg.2022.962086

COPYRIGHT

© 2022 Aleem, Inc, Sarwar, Asjad and Alsubaie. This is an open-access article distributed under the terms of the [Creative Commons Attribution License \(CC BY\)](#). The use, distribution or reproduction in other forums is permitted, provided the original author(s) and the copyright owner(s) are credited and that the original publication in this journal is cited, in accordance with accepted academic practice. No use, distribution or reproduction is permitted which does not comply with these terms.

Analysis of fractional MHD convective flow with CTNs' nanoparticles and radiative heat flux in human blood

Maryam Aleem¹, Mustafa Inc^{2,3*}, Shahzad Sarwar⁴,
Muhammad Imran Asjad¹ and A. S. A. Alsubaie⁵

¹Department of Mathematics, University of Management and Technology, Lahore, Pakistan,

²Department of Computer Engineering, Biruni University, Zeytinburnu, Istanbul, Turkey,

³Department of Medical Research, China Medical University, Taichung, Taiwan, ⁴King Fahd University of Petroleum and Minerals, Department of Mathematics and Statistics, Dhahran, Saudi Arabia, ⁵Department of Physics, College of Khurma University College, Taif University, Taif, Saudi Arabia

The aim of the article is two-fold. We first analyze and investigate free convective, unsteady, MHD blood flow with single- and multiwalled carbon nanotubes (*SWCNTs*) as nanoparticles. The blood flow has been taken across an upright vertical plate, oscillating in its own plane, and engrafted in a porous medium with slip, radiation, and porosity effects. Nanofluids consist of human blood as the base fluid and *SWCNTs* and *MWCNTs* as nanoparticles. The second aim is to discuss the three different definitions of fractional derivatives, namely, Caputo (*C*), Caputo–Fabrizio (*CF*), and Atangana–Baleanu (*ABC*), to obtain the solutions of such proposed models by the Adomian decomposition method. The impact of fractional and physical parameters on the concentration, velocity, and temperature of human blood in the presence of the slip effect is studied and projected diagrammatically. The article ends by providing numerical results such as the reliableness, efficiency, and significant features that are simple in computation with eminent accuracy of the process for non-Newtonian Casson nanofluid fractional order models. It is observed that the velocity of the fluid decreases with *SWCNTs*' and *MWCNTs*' volume fraction, and an increase in the *CNTs*' volume fraction increases blood temperature, which ultimately enhances heat transfer rates. The results acquired are in excellent correspondence with the reported results.

KEYWORDS

heat and mass transfer, radiative heat transfer, Atangana–Baleanu derivative, Caputo–Fabrizio derivative, slip condition

Introduction

Recently, the contemplation of fractional calculus has been broadened with eminent implication because of its diverse applications in physical sciences, hydraulics, mathematical physics, electric electronic network, wave theory, nuclear

and chemical industries, etc. (Podlubny, 1999; Tarasov, 2010; Uchaikin, 2013; Herrmann, 2014; Li and Zeng, 2015; Povstenko, 2015; Li and Cai, 2019). It is notable that the classical derivative (integer-order operator) is local while the noninteger operators specified as Riemann–Liouville, Caputo, Caputo–Fabrizio, and Atangana–Baleanu are nonlocal operators. The nonlocality enables us to foresee the advanced stage of the system and reckons the present and its continuing phases. It is always a challenging task for researchers to accomplish analytical or exact solutions of nonlinear models by fractional operators due to their complexity. In the past couple of years, several investigators have worked to inquire about the fractional differential operators in varied aspects. Caputo and Fabrizio (Caputo, 1967) modified the existing Caputo operator in a new conformation, and Atangana and Baleanu evoked a new fractional manipulator labeled Atangana–Baleanu derivative by combining Riemann–Liouville and Caputo differential operators.

In this article, we have concentrated on convective heat conveyance, which plays a critical role in the working of non-Newtonian fluid streams. The mechanics of non-Newtonian flux exhibits an exceptional challenge for mathematicians, physicists, and engineers. This is due to the fact that non-Newtonian fluids (NNFs) because of their complex behavior cannot be described mathematically using a single constitutive equation catering to all parameters. For this, a dedicated constitutive model is needed to describe such flows, for instance, in the case of Brinkman fluid (Ali et al., 2020; Ali et al., 2021), viscoplastic fluids (Hassan et al., 2013), second-grade fluid (Ali et al., 2016; Imran et al., 2017b), Walter's-B fluid (Ali et al., 2014; Imran et al., 2018), Bingham plastic (Kleppe and Marner, 1970), and Maxwell fluids (Tahir et al., 2017). Among the non-Newtonian fluid models, the Casson model is highly recommended by numerous researchers. Let us consider that such nonlinearity is expressed in numerous domains such as food processing, oil suspensions of pigments to predict flow behavior, mud drilling processors, blood flow in the circulatory system, and other fields of bioengineering.

It should be pointed out that Casson initiated these models for the nonlinear flow of pigment–oil suspensions. The Casson fluid is a pseudoplastic, also termed shear thinning. It possesses infinite viscosity and acts like solids at zero shear rate, termed as yield stress, below which no flow occurs. If yield stress is more than shear stress, i.e., viscosity ($\eta = 0$), the fluid behaves as a solid. In other situations, when shear stress is higher than yield stress, the fluid starts to accelerate.

Many researchers have considered the Casson fluid model and investigated its behavior in different situations; Bhattacharyya investigated the boundary layer stagnation point flow of a Casson-type fluid with heat transfer along a stretching or shrinking sheet of infinite length (Bhattacharyya, 2013). In another research article, he figured out the exact results for boundary layer flux of a Casson liquid flowing across a porous

stretching/shrinking sheet (Bhattacharyya et al., 2014). Hayat et al. (Hayat et al., 2012) studied the boundary layer flux of MHD Casson liquid across an elongated sheet. Nadeem et al. (Nadeem et al., 2012) investigated the influence of electricity on the boundary layer flux of a Casson liquid flowing across an exponentially contracting canvas.

Raju et al. (Raju et al., 2016) reckoned the Casson liquid to analyze the significance of magnetic flux by an elongated canvas and comprehended the fact that an induced magnetized field possesses the tendency to increase the heat transfer rate. Kumar et al. investigated the combined effect of magnetic flux and heat source and worked out the numerical results for a Casson liquid flowing through two parallel plates (Kumar et al., 2018a). In another study, Kumar et al. investigated the conjugate impact of mass and heat transfer rate of MHD Casson fluid under Brownian motion, and thermophoresis demonstrated that the fluid's temperature is manipulated by the Casson parameter (Kumar et al., 2018b).

Kataria and Patel established the effluence, thermic, and mass transmit characteristics of Casson MHD liquid and ascertained that modified magnetic flux decays its speed and boundary layer heaviness (Kataria and Patel, 2018). Casson fluid's stagnancy point has been illustrated by Shaw et al. (Shaw et al., 2019) to determine encroachment of radiation, thermic dissemination, and diffusion thermal effectuates due to chemical reactions. Hussanan et al. (Hussanan et al., 2016) demonstrated unsteady invariant warmth transfer flux of Casson-type fluid bearing the checks of Newtonian heating and thermal radiation across an oscillating upright erect plate of infinite dimensions. They concluded that the velocity of Casson fluid decreases due to the Casson parameter and it shows an oscillating turnover for dissimilar phase angles. More research in this area has been conducted by various researchers (Kameswaran et al., 2014; Animasaun et al., 2015; Ramesh and Devakar, 2015; Ahmed et al., 2016; Imran et al., 2016; Ahmad et al., 2019; Rehman et al., 2019; Sheikh et al., 2020; Aleem et al., 2021).

In this article, our major objective is to demonstrate free convective, MHD unsteady blood flow with single (SWCNTs) and multiwalled carbon nanotubes (MWCNTs) as nanospecks. The blood flow is considered over an oscillating vertically upright plate engrafted in a porous medium with slip, radiation, and porosity effects. Nanofluids consist of human blood as the base fluid and SWCNTs and MWCNTs as nanoparticles. Three fractional approaches Caputo (C), Caputo–Fabrizio (CF), and Atangana–Baleanu (ABC) are used to develop the fractional blood flow model, which is solved using the Adomian decomposition method (ADM). Equations of dimensionless temperature, velocity, and concentration fields have been solved analytically, and the results are compared. The graphical analysis is performed to envision the effect of fractional and tangible flow parameters on velocity u , concentration C , and temperature

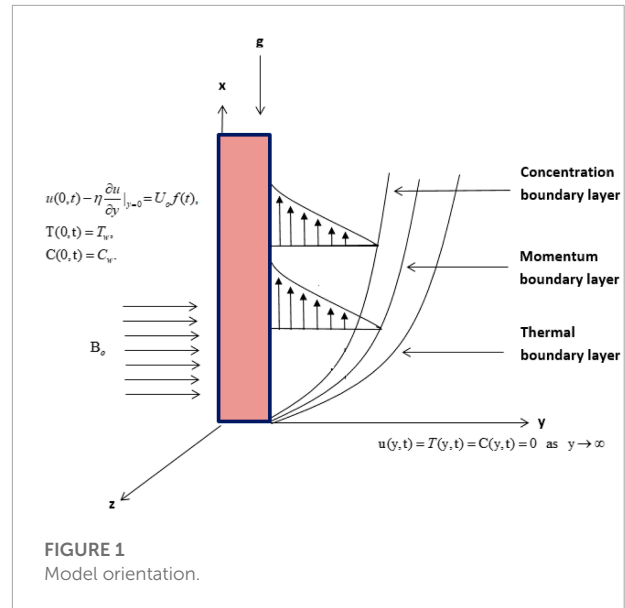
θ using MathCad and Mathematica software packages. This article is structured as follows. In section 1, latest research related to Casson fluid and its application in the industry are presented, and in Section 2, problem formulation and assumptions are illustrated. In section 3, we have developed a fractional model for Casson nanofluid and its solution with the Adomian decomposition method with Caputo, Caputo Fabrizio, and Atangana–Baleanu fractional operators that are given in Sections 4 and 5. The obtained results are analyzed and discussed in Section 6. Solutions obtained via ADM are compared with existing literature results and are presented in Section 6.

Problem formulation

We investigate an unsteady viscoelastic incompressible Casson nanofluid containing human blood as the base liquid and CNTs as nanoparticles. It flows across an infinite vertical upright plate located in the xy -plane implanted in a porous medium and is fixed in the x -direction, whereas y – axis is normal to the plate. Consequently, the rate of flow is enclosed only in the half plane where $y > 0$. At $t = 0$, the nanofluid and plate are at rest with the set temperature T_∞ and concentration C_∞ . The base fluid, which is human blood, and nanoparticles (SWCNTs and MWCNTs) are considered to be in thermal equilibrium. As time increases $t = 0^+$, the plate starts its sinusoidal oscillation with slip effect at the boundary, and its velocity at the boundary wall is $V = u(0, t) - \eta \frac{\partial u(y, t)}{\partial y} \big|_{y=0} = U_o f(t)$, where η is the slip parameter, which is always positive since negative values of η have no physical sense, U_o is the characteristic velocity, and $f(t)$ is a piecewise continuous general function satisfying $f(0) = 0$. When the plate moves in the x -direction, its concentration and temperature change to C_w and T_w , respectively. The physical model of our problem is shown in Figure 1. Furthermore, assumptions are as follows:

- 1) The plate is assumed to be electrically conducting and bearing uniform magnetic flux B_o , which is applied in the direction perpendicular to the plate.
- 2) The slip boundary condition at the wall is considered, and the relative velocity between the wall and fluid is directly proportional to the shear rate or the rate of deformation at the wall.
- 3) Since the flow is unidirectional, all tangible variables are functions of time t and space coordinate y .
- 4) The impression of enforced magnetic flux is negligible, referring to a really small magnetized Reynolds' number Re .
- 5) The Casson nanofluid consists of SWCNTs and MWCNTs of invariant kinematic viscosity ν_{nf} occupying a semifinite space $y > 0$.

Under these assumptions and using Boussinesq's approximation, the governing equations for energy, diffusion,



and momentum are (Imran et al., 2017a; Khalid et al., 2018).

$$\rho_{nf} \partial_t u(y, t) - \mu_{nf} \left(1 + \frac{1}{\gamma} \right) \partial_{yy} u(y, t) + \left(\sigma_{nf} B_o^2 + \frac{\varphi \mu_{nf}}{\kappa_1} \right) u(y, t) = g(\rho \beta_T)_{nf} (T - T_\infty) + g(\rho \beta_C)_{nf} (C - C_\infty), \quad (1)$$

$$(\rho C_p)_{nf} \partial_t T(y, t) = \kappa_{nf} \partial_{yy} T(y, t) - \partial_y q_r, \quad (2)$$

$$\partial_t C(y, t) = D \partial_{yy} C(y, t). \quad (3)$$

Under Rossenold approximation for radiative heat flux, by assuming that the temperature difference between fluid T and ambient T_∞ is very small, Eq. 2 becomes (Imran et al., 2017a)

$$\partial_t T(y, t) = \frac{\kappa_{nf}}{(\rho C_p)_{nf}} \left(1 + \frac{16\sigma^* T_\infty^3}{3\kappa_{nf} \kappa^*} \right) \partial_{yy} T(y, t), \quad (4)$$

where u , C , T , q_r , σ^* , κ^* , g , γ , D , μ_{nf} , κ_{nf} , $C_{p,nf}$, $\beta_{C,nf}$, $\beta_{T,nf}$ are velocity, concentration, temperature, radiative heat flux, Stefan–Boltzman constant, mean absorption coefficient, gravity, Casson parameter, molecular diffusion constant, dynamic viscosity of Casson nanofluid, thermal conductivity, heat capacitance, and diffusion and thermal expansion coefficients of nanoparticles, respectively.

The appropriate initial and boundary conditions are as follows:

$$u(y, 0) = 0, \quad T(y, 0) = T_\infty, \quad C(y, 0) = C_\infty, \quad \forall y \geq 0, \quad (5)$$

$$\begin{aligned}
 u(y, t) - \eta \frac{\partial u(y, t)}{\partial y} \Big|_{y=0} &= U_o f(t), \\
 T(y, t) &= T_w, \\
 C(y, t) &= C_w \quad \forall \quad y = 0, t \geq 0,
 \end{aligned} \quad (6)$$

$$u(y, t) \rightarrow 0, \quad T(y, t) \rightarrow T_\infty, \quad C(y, t) \rightarrow C_\infty, \quad \text{as } y \rightarrow \infty, t > 0. \quad (7)$$

A theoretical model for nanofluids was introduced by Xue (Xue, 2005) based on Maxwell theory for elliptic-shaped rotational CNTs with a large axial ratio, and compensating space distribution impact is used and given as follows:

$$\frac{\kappa_{nf}}{\kappa_f} - \frac{(1-\phi) + 2\phi \left(\frac{\kappa_{CNT}}{\kappa_{CNT} - \kappa_f} \right) \ln \left(\frac{\kappa_{CNT} - \kappa_f}{2\kappa_f} \right)}{(1-\phi) + 2\phi \left(\frac{\kappa_{CNT}}{\kappa_{CNT} - \kappa_f} \right) \ln \left(\frac{\kappa_{CNT} + \kappa_f}{2\kappa_f} \right)} = 0,$$

where κ_{nf} , κ_f and κ_{CNT} are the thermal conduction coefficients of the nanofluid, base liquid, and carbon nanotubes (S&MWCNTs), respectively. The theoretical density values are described by Yu et al. (Yu et al., 2008) as follows:

$$\rho_{nf} = (1-\phi)\rho_f + \phi\rho_{CNT},$$

where ρ_f is blood density, ϕ is the volume fraction of nanoparticles, and ρ_{CNT} is the density of carbon nanotubes (S&MWCNTs). The effective dynamic viscosity μ_{nf} for cylindrical nanotubes can be defined in two ways as proposed by Loganathan et al. (Loganathan et al., 2015) and Rajesh et al. (Rajesh et al., 2016).

$$\mu_{nf} = \frac{\mu_f}{(1-\phi)^{2.5}},$$

where μ_f and μ_{nf} are densities of blood as the base fluid and the nanofluid with CNTs. Heat capacitance for nanofluid is as follows:

$$(\rho C_p)_{nf} = (1-\phi)(\rho C_p)_f + \phi(\rho C_p)_{CNT}.$$

The thermal and diffusion expansion are defined by Bourantas and Loukopoulos (Bourantas and Loukopoulos, 2014) as follows:

$$(\rho\beta_T)_{nf} = (1-\phi)(\rho\beta_T)_f + \phi(\rho\beta_T)_{CNT},$$

$$(\rho\beta_C)_{nf} = (1-\phi)(\rho\beta_C)_f + \phi(\rho\beta_C)_{CNT},$$

where ρ is the density; ϕ is the nanoparticle volume fraction; and $(\beta_T)_f$, $(\beta_C)_f$, $(\beta_T)_{CNT}$, and $(\beta_C)_{CNT}$ are thermal and mass expansion coefficients of the base fluid and carbon nanotubes. $\sigma_{nf} = \sigma_f \left(1 + \frac{3(\frac{\sigma_{CNT}}{\sigma_f} - 1)\phi}{(\frac{\sigma_{CNT}}{\sigma_f} + 2) - 3(\frac{\sigma_{CNT}}{\sigma_f} - 1)\phi} \right)$ and $\sigma = \frac{\sigma_s}{\sigma_f}$, where the subscripts f and CNT represent the base fluid and carbon nanotube

nanoparticles. Thermophysical properties of carbon nanotubes and the carried Casson fluid (human blood) are given in Table 1.

Introducing dimensionless variables

$$\begin{aligned}
 u^* &= \frac{u}{U_o}, \quad y^* = \frac{U_o}{v_f} y, \quad t^* = \frac{U_o^2}{v_f} t, \quad \theta = \frac{T - T_\infty}{T_w - T_\infty}, \\
 \Phi &= \frac{C - C_\infty}{C_w - C_\infty}, \quad \eta^* = \frac{U_o \eta}{v_f}.
 \end{aligned} \quad (8)$$

Using dimensionless parameters from Eq. 8 in Eqs. (1) and (3)–(7), we get

$$\begin{aligned}
 \partial_t u(y, t) - \frac{b_1}{b_3} \left(1 + \frac{1}{y} \right) \partial_{yy} u(y, t) + \left(\frac{b_2}{b_3} M + \frac{1}{K} \frac{b_1}{b_3} \right) u(y, t) \\
 - b_4 \text{Gr} \theta(y, t) - b_5 \text{Gm} \Phi(y, t) = 0,
 \end{aligned} \quad (9)$$

$$\partial_t \theta(y, t) - \frac{\lambda}{b_6} \frac{1}{\text{Pr}_{eff}} \partial_{yy} \theta(y, t) = 0, \quad (10)$$

$$\partial_t \Phi(y, t) - \frac{1}{\text{Sc}} \partial_{yy} \Phi(y, t) = 0, \quad (11)$$

and dimensionless initial and boundary conditions are as follows:

$$u(y, 0) = 0, \quad \theta(y, 0) = 0, \quad \Phi(y, 0) = 0, \quad \forall \quad y \geq 0, t = 0, \quad (12)$$

$$\begin{aligned}
 u(y, t) - \eta \frac{\partial u(y, t)}{\partial y} \Big|_{y=0} &= f(t), \\
 \theta(y, t) &= 1, \\
 \Phi(y, t) &= 1, \quad \forall \quad t > 0, \quad y = 0,
 \end{aligned} \quad (13)$$

$$u(\infty, t) \rightarrow 0, \quad \theta(\infty, t) \rightarrow 0, \quad \Phi(\infty, t) \rightarrow 0, \quad \text{as } t > 0, \quad (14)$$

where $\text{Sc} = \frac{v_f}{D}$, k_1 is the permeability of porous medium, $\text{Gr} = \frac{g\beta_f(T_w - T_\infty)v_f}{U_o^3}$, $\text{Gm} = \frac{g\beta_f(C_w - C_\infty)v_f}{U_o^3}$, $\text{Pr}_{eff} = \frac{\text{Pr}}{1 + \text{Nr}^*}$, $\text{Nr}^* = \frac{\text{Nr}}{\lambda}$, $\lambda = \frac{\kappa_{nf}}{\kappa_f}$, $\text{Nr} = \frac{16\sigma^* T_\infty^3}{3\kappa_f \kappa^*}$, $M = \frac{\sigma_f v_f B_o^2}{\rho_f U_o^2}$, $K = \frac{\kappa_1 U_o^2}{\mu_f^2 \phi}$, $b_1 = \frac{1}{(1-\phi)^{2.5}}$, $b_2 = \left[1 + \frac{3(\frac{\sigma_{CNT}}{\sigma_f} - 1)\phi}{(\frac{\sigma_{CNT}}{\sigma_f} + 2) - 3(\frac{\sigma_{CNT}}{\sigma_f} - 1)\phi} \right]$, $b_3 = \left[(1-\phi) + \phi \frac{\rho_{CNT}}{\rho_f} \right]$, $b_4 = \left[(1-\phi) + \phi \frac{(\rho\beta_T)_{CNT}}{(\rho\beta_T)_f} \right]$, $b_5 = \left[(1-\phi) + \phi \frac{(\rho\beta_C)_{CNT}}{(\rho\beta_C)_f} \right]$, $b_6 = \left[(1-\phi) + \phi \frac{(\rho C_p)_{CNT}}{(\rho C_p)_f} \right]$, and $f^*(t) = f\left(\frac{v_f t^*}{U_o^2}\right)$.

where Sc is the dimensionless Schmidt number, Gr and Gm are thermal and mass Grashof numbers, respectively, Pr_{eff} is the effective Prandtl number depend on radiation-conduction parametric quantity Nr and Prandtl number Pr , M is the magnetic field parameter, η is slip, and K is the porosity parameter. Solving Eqs. (9)–(11) under conditions (12)–(14) is generalized by adapting Caputo (Caputo, 1967), Caputo–Fabrizio (Caputo and Fabrizio, 2015), and Atangana–Baleanu (Atangana and Baleanu, 2016) fractional operators. The obtained fractional model is solved using ADM (Stehfest, 1970; Tzou, 1997; Sarwar, 2020).

TABLE 1 Thermophysical traits of SWCNTs, MWCNTs, and human blood (Casson, 1959; Pramanik, 2014; Imran et al., 2017a).

| | $\rho(Kgm^{-3})$ | $C_p(JKg^{-1}K^{-1})$ | $\kappa(Wm^{-1}K^{-1})$ | $\sigma(Sm^{-1})$ | $\beta \times 10^5(K^{-1})$ |
|-------------|------------------|-----------------------|-------------------------|----------------------|-----------------------------|
| SWCNTs | 2,600 | 425 | 6,600 | 10^6-10^7 | 27 |
| MWCNTs | 1,600 | 796 | 3,000 | 1.9×10^{-4} | 44 |
| Human blood | 1,053 | 3,594 | 0.492 | 0.8 | 0.18 |

TABLE 2 Effect of fractional parameter on skin friction C_f for $K = 3$, $M = 0.5$, $\eta = 0.1$, $Gr = 0.3$, $Gm = 0.01$, $\gamma = 0.2$, $Pr = 25$, $Nr = 18$, and $Sc = 0.22$.

| α | $t = 0.5$ | | | $t = 1.0$ | | |
|----------|-------------|------------|---------|-------------|------------|---------|
| | ADM_{ABC} | ADM_{CF} | ADM_C | ADM_{ABC} | ADM_{CF} | ADM_C |
| 0.1 | 4.2029 | 3.8283 | 4.0174 | 4.2585 | 4.2002 | 4.5741 |
| 0.2 | 4.1305 | 3.4472 | 3.6539 | 4.3519 | 4.1450 | 4.7342 |
| 0.3 | 3.9699 | 3.075 | 3.2047 | 4.4531 | 4.0530 | 4.7187 |
| 0.4 | 3.7039 | 2.7125 | 2.7294 | 4.5138 | 3.9242 | 4.5582 |
| 0.5 | 3.3323 | 2.3589 | 2.2698 | 4.4894 | 3.7586 | 4.2878 |
| 0.6 | 2.8705 | 2.0147 | 1.8516 | 4.3452 | 3.5562 | 3.9428 |
| 0.7 | 2.3454 | 1.6795 | 1.4875 | 4.0604 | 3.3170 | 3.5554 |
| 0.8 | 1.7903 | 1.3536 | 1.1813 | 3.6294 | 3.0410 | 3.1524 |
| 0.9 | 1.2405 | 1.0369 | 0.9305 | 3.0615 | 2.7283 | 2.7551 |
| 1 | 0.7293 | 0.7293 | 0.7293 | 2.3787 | 2.3787 | 2.3787 |

TABLE 3 Effect of fractional parameter on Nusselt number Nu for $Pr_{eff} = 0.71$.

| α | $t = 0.5$ | | | $t = 1.0$ | | |
|----------|-------------|------------|---------|-------------|------------|---------|
| | ADM_{ABC} | ADM_{CF} | ADM_C | ADM_{ABC} | ADM_{CF} | ADM_C |
| 0.1 | 4.9335 | 4.1308 | 4.2673 | 4.9782 | 4.3876 | 4.6468 |
| 0.2 | 5.3846 | 3.8689 | 4.0346 | 5.5883 | 4.3578 | 4.7758 |
| 0.3 | 5.6183 | 3.6124 | 3.7437 | 6.1079 | 4.3081 | 4.7955 |
| 0.4 | 5.5370 | 3.3603 | 3.4299 | 6.4005 | 4.2386 | 4.7231 |
| 0.5 | 5.1355 | 3.1134 | 3.1188 | 6.3766 | 4.1491 | 4.5786 |
| 0.6 | 4.5050 | 2.8714 | 2.8263 | 6.0387 | 4.0398 | 4.3819 |
| 0.7 | 3.7793 | 2.6345 | 2.5615 | 5.4697 | 3.9106 | 4.1518 |
| 0.8 | 3.0742 | 2.4025 | 2.3281 | 4.7822 | 3.7615 | 3.9041 |
| 0.9 | 2.4576 | 2.1755 | 2.1261 | 4.0731 | 3.5926 | 3.6515 |
| 1 | 1.9534 | 1.9534 | 1.9534 | 3.4037 | 3.4037 | 3.4037 |

TABLE 4 Effect of fractional parameter on Sherwood number Sh for $Sc = 0.22$.

| α | $t = 0.5$ | | | $t = 1.0$ | | |
|----------|-------------|------------|---------|-------------|------------|---------|
| | ADM_{ABC} | ADM_{CF} | ADM_C | ADM_{ABC} | ADM_{CF} | ADM_C |
| 0.1 | 110.256 | 84.1198 | 88.274 | 111.73 | 92.3223 | 100.566 |
| 0.2 | 125.199 | 75.7107 | 80.2105 | 132.01 | 91.0826 | 104.047 |
| 0.3 | 132.893 | 67.5083 | 70.2508 | 149.366 | 89.0165 | 103.623 |
| 0.4 | 129.869 | 59.5124 | 59.7288 | 158.844 | 86.124 | 99.9792 |
| 0.5 | 116.018 | 51.7231 | 49.5758 | 157.155 | 82.405 | 93.9026 |
| 0.6 | 94.727 | 44.1405 | 40.3619 | 144.402 | 77.8595 | 86.1829 |
| 0.7 | 70.8693 | 36.7645 | 32.3699 | 123.672 | 72.4876 | 77.5375 |
| 0.8 | 48.5335 | 29.595 | 25.6758 | 99.1383 | 66.2893 | 68.5693 |
| 0.9 | 29.9881 | 22.6322 | 20.222 | 74.3272 | 59.2645 | 59.7485 |
| 1.0 | 15.876 | 15.876 | 15.876 | 51.4132 | 51.4132 | 51.4132 |

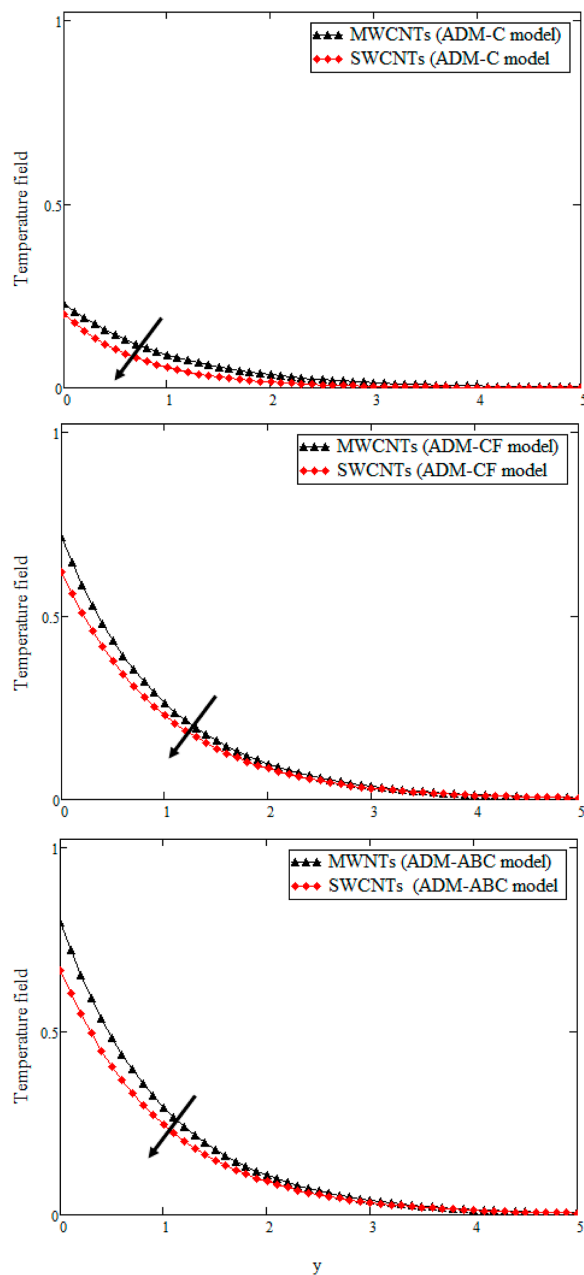


FIGURE 2
Temperature comparison of SWCNTs and MWCNTs when $t = 0.28$, $Pr = 21$, $Nr = 18$, and $\beta = 0.8$.

Proposed fractional-order nanofluid model

Equations 10 and 11 are homogenous and Eq. 9 is a nonhomogeneous second-order PDE. We construct the fractional-order Casson nanofluid models by changing time derivative with Caputo (C), Caputo–Fabrizio (CF), and

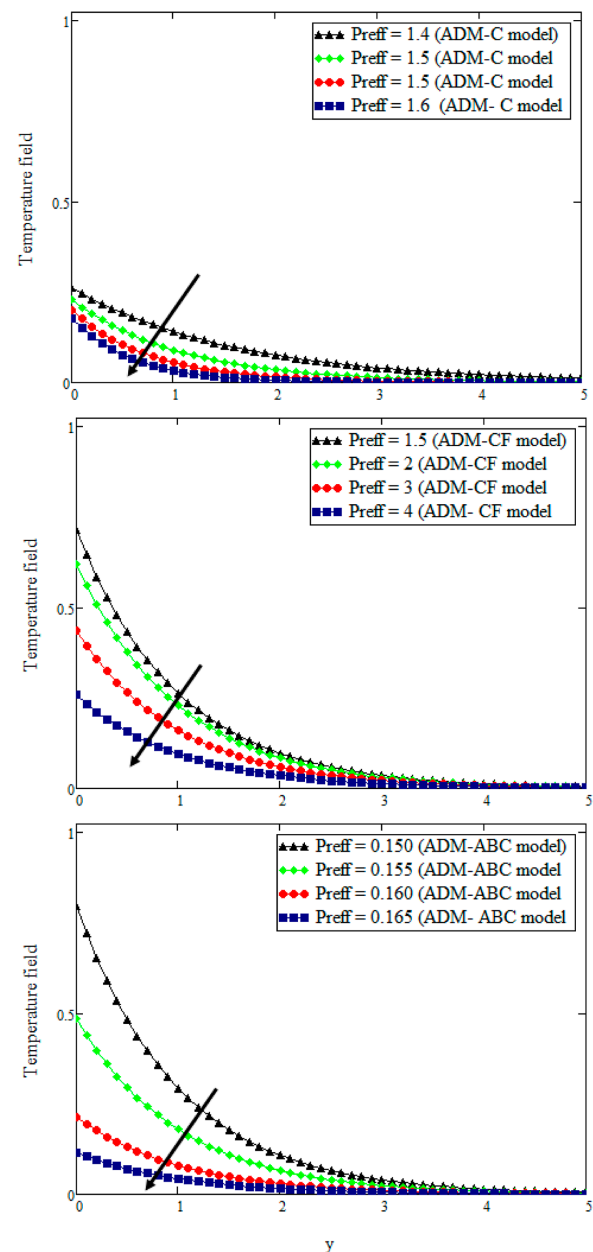
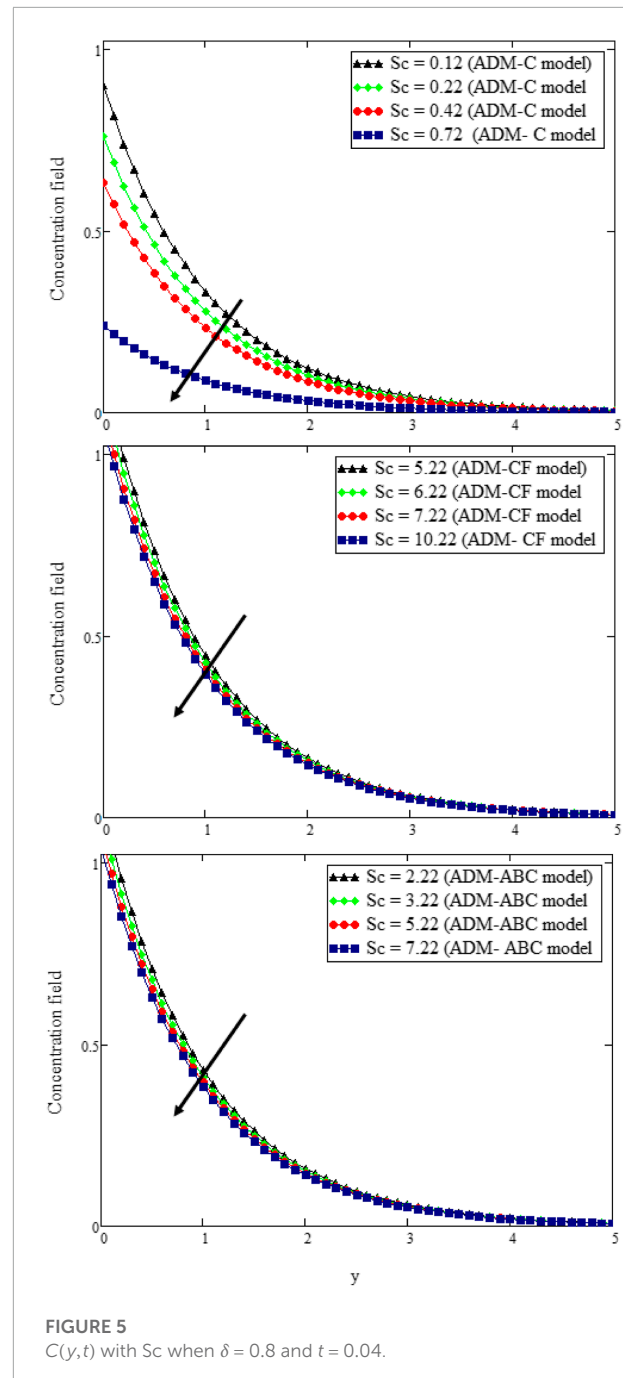
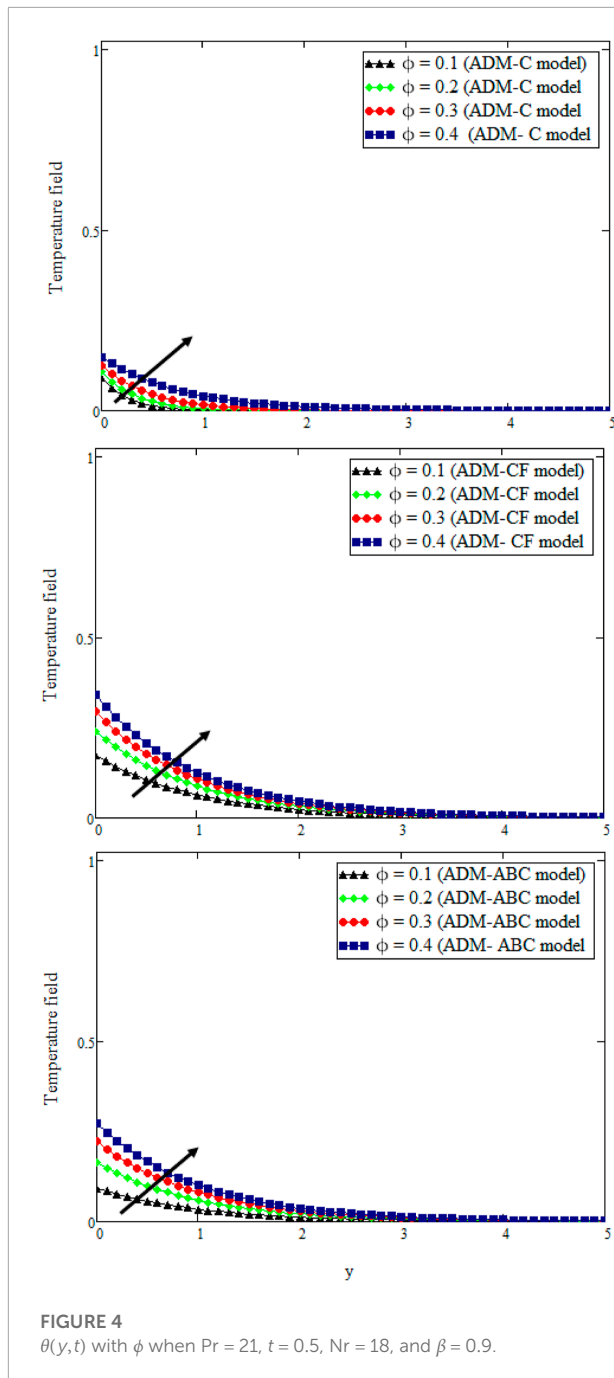


FIGURE 3
 $\theta(y, t)$ with Pr_{eff} when $\phi = 0.002$, $t = 0.28$, and $\beta = 0.8$.

Atangana–Baleanu (ABC) fractional derivatives. We get

$$D_t^\alpha u(y, t) - \frac{b_1}{b_3} \left(1 + \frac{1}{\gamma} \right) \partial_{yy} u(y, t) + \left(\frac{b_2}{b_3} M + \frac{1}{K} \frac{b_1}{b_3} \right) u(y, t) - b_4 Gr \theta(y, t) - b_5 Gm \Phi(y, t) = 0, \quad (15)$$

$$D_t^\beta \theta(y, t) - \frac{\lambda}{b_6} \frac{1}{Pr_{eff}} \partial_{yy} \theta(y, t) = 0, \quad (16)$$



$$D_t^\delta \Phi(y,t) - \frac{1}{Sc} \partial_{yy} \Phi(y,t) = 0, \quad (17)$$

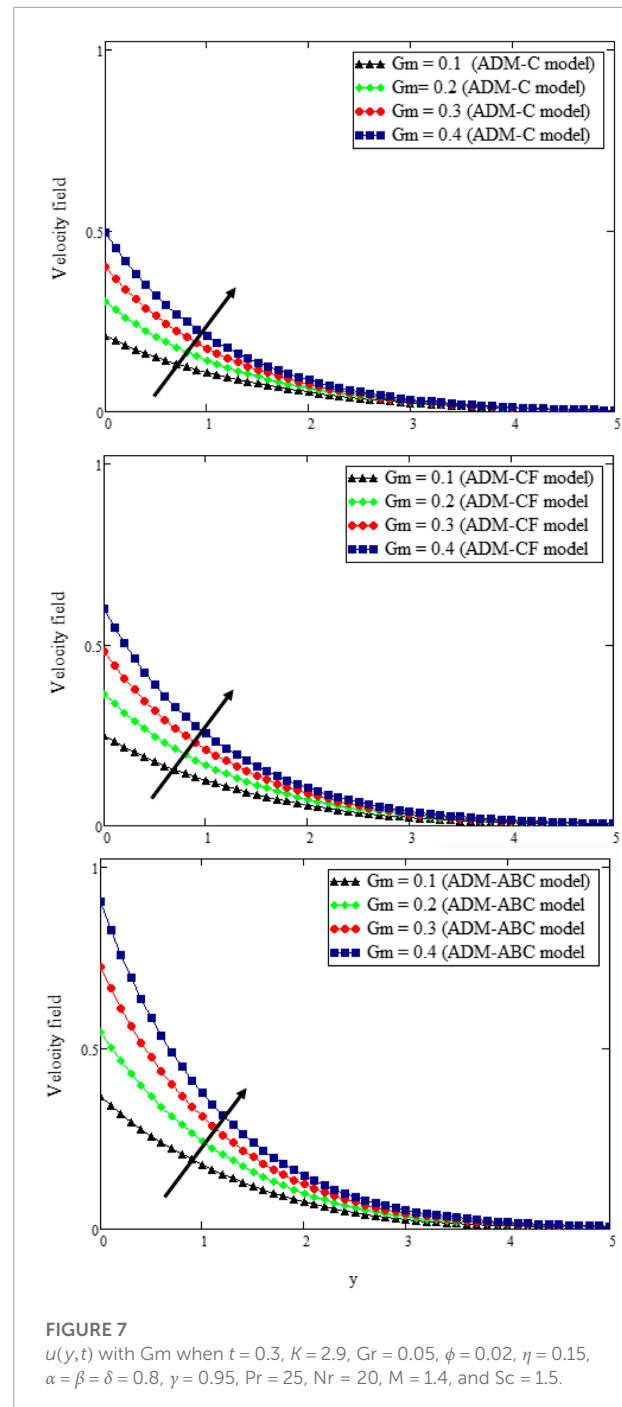
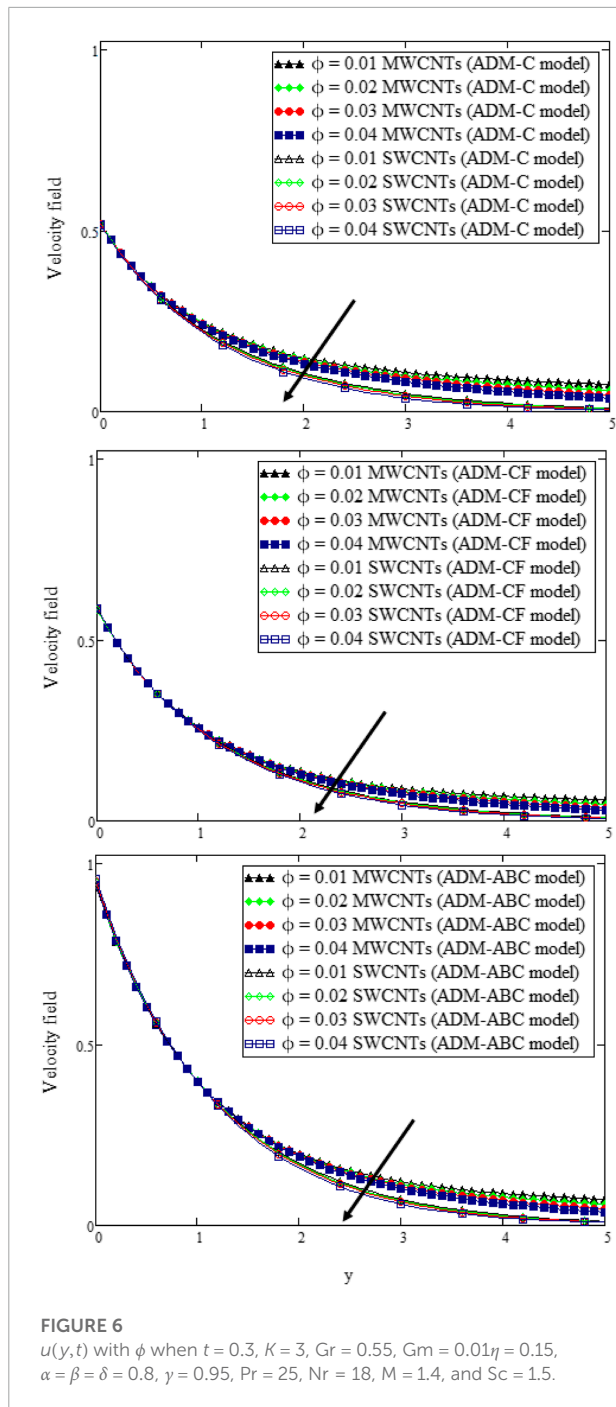
where $0 < \alpha, \beta, \delta \leq 1$, $q \in \{\alpha, \beta, \delta\}$, and $D_t^q(\cdot)$ denotes the fractional Caputo, Caputo–Fabrizio, or Atangana–Baleanu operators which are defined as follows:

- the fractional Caputo differential operator of order $q \in (0, 1)$ and a function $f(t) \in H^1[a, b]$ is defined (Caputo, 1967) as follows:

$${}^C D_{a,t}^q f(t) = \frac{1}{\Gamma(1-q)} \int_a^t (t-\tau)^{-q} f'(\tau) d\tau, \quad t > a, \quad (18)$$

- the Caputo–Fabrizio fractional derivative of order $q \in (0, 1)$ and a function $f(t) \in H^1[a, b]$ is defined (Caputo and Fabrizio, 2015) as follows:

$${}^{CF} D_{a,t}^q f(t) = \frac{1}{1-q} \int_a^t \exp\left(-\frac{q(t-\tau)}{1-q}\right) f'(\tau) d\tau, \quad t > a, \quad (19)$$



- the new fractional derivative Atangana–Baleanu operator of order $q \in (0, 1)$ (Atangana and Baleanu, 2016) is as follows:

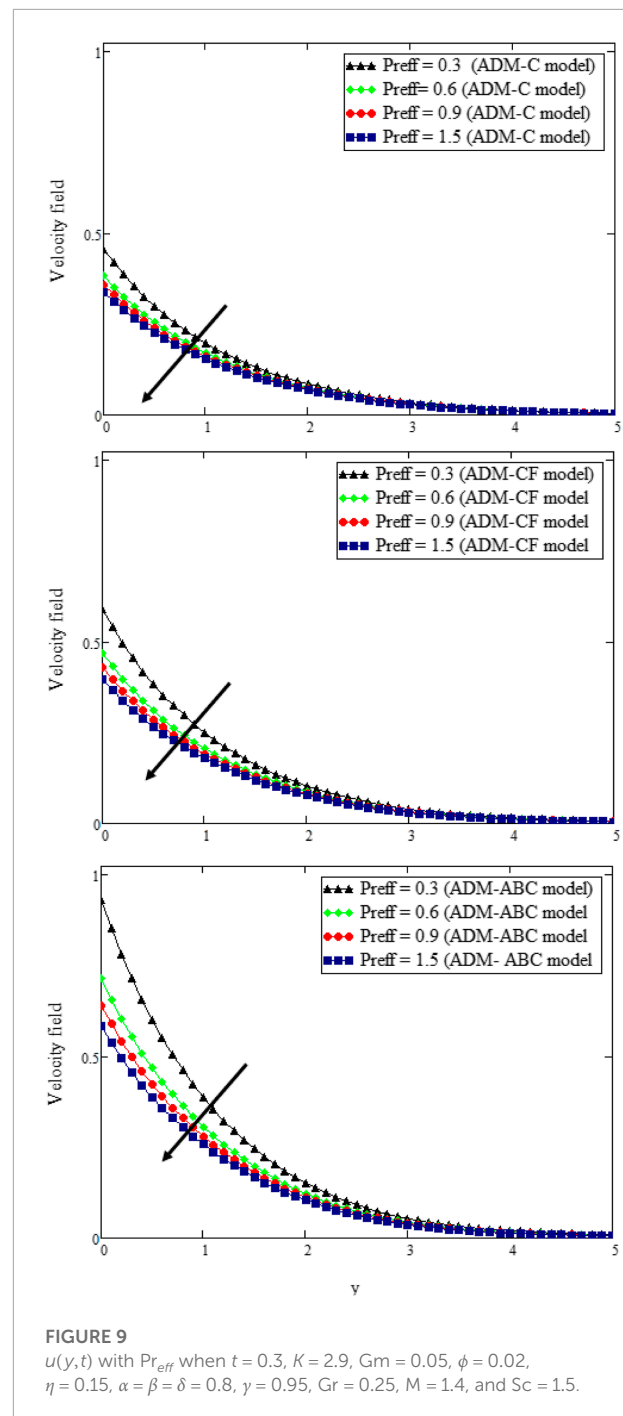
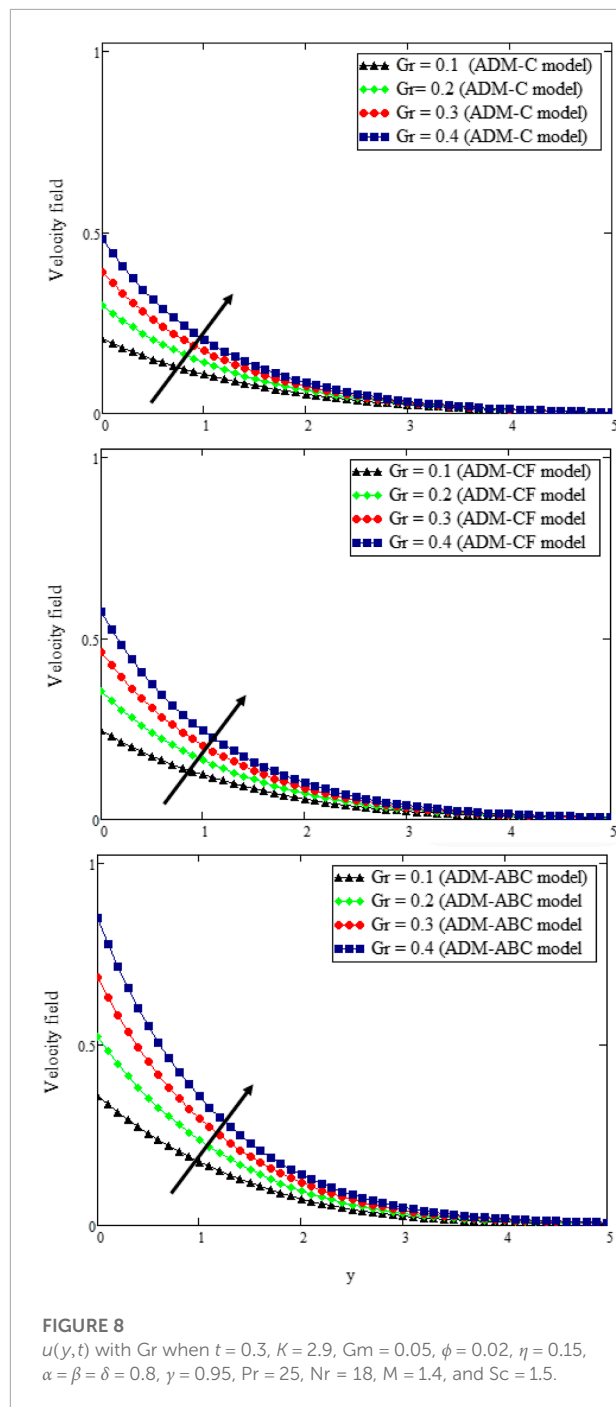
$${}^{ABC}D_{a,t}^q f(t) = \frac{M(q)}{1-q} \int_a^t E_q \left[\frac{-q(t-\tau)^q}{1-q} \right] f'(\tau) d\tau, \quad t > a, \quad (20)$$

where $E_q(x) = \sum_{k=1}^{\infty} \frac{x^k}{\Gamma(qk+1)}$ is the Mittag–Leffler function and $M(q)$ is the normalization function satisfying the conditions $M(0) = M(1) = 0$.

Formulation of Adomian decomposition method

As mentioned, ADM is used for approximation. The algorithm of fractional ADM is as follows:

- 1) Consider the fractional PDE as follows:



$$D_{a,t}^q \Psi(t,s) + L(\Psi(t,s)) + N(\Psi(t,s)) = F(t,s) \quad n-1 < q \leq n, \quad (21)$$

where $D_{a,t}^q(\cdot)$ is the fractional derivative in C, CF, or AB sense; L and N are linear and nonlinear differential operators, respectively; F is an analytical function; and s is the spatial dimension. For the sake of simplicity, we use $\Psi = \Psi(t,s)$ in the following steps.

We write Eq. 21 in the form

$$D_{a,t}^q \Psi = F - L(\Psi) - N(\Psi). \quad (22)$$

2) Using the fractional integral I^q on both sides of Eq. 22, we get

$$\Psi = I^q(F - \mathcal{L}(\Psi) - \mathcal{N}(\Psi)). \quad (23)$$

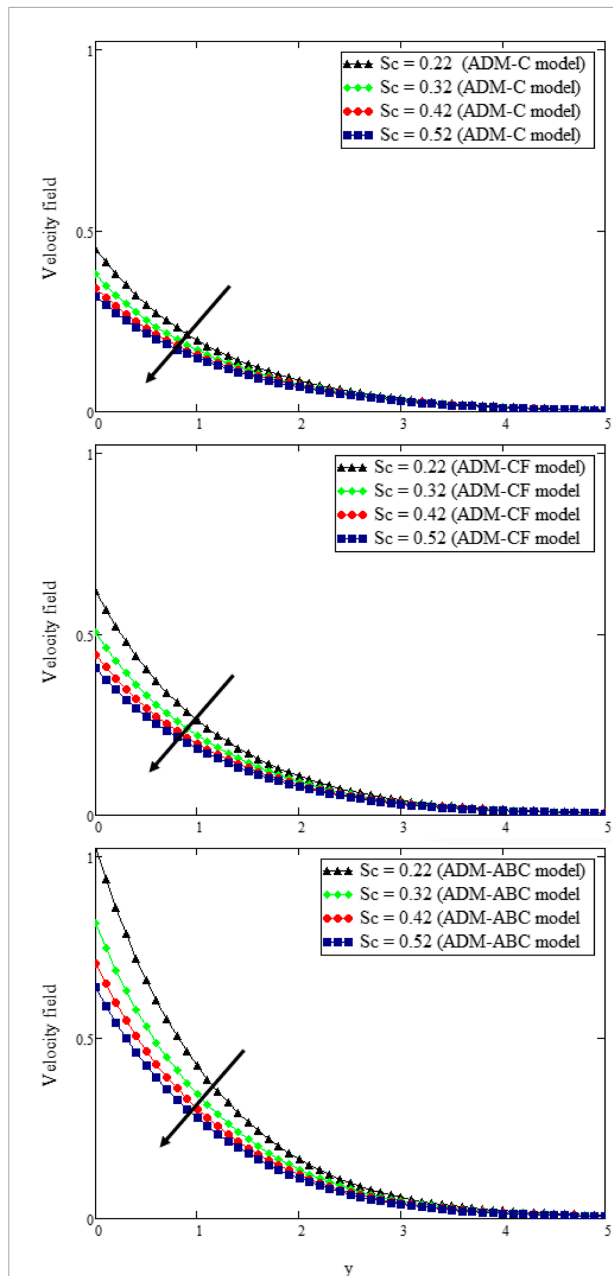


FIGURE 10

$u(y,t)$ with Sc when $t = 0.3$, $K = 2.9$, $Gm = 0.15$, $\eta = 0.15$, $\phi = 0.02$, $\alpha = \beta = \delta = 0.8$, $\gamma = 0.95$, $Pr = 25$, $Nr = 22$, $M = 1.4$, and $Gr = 0.05$.

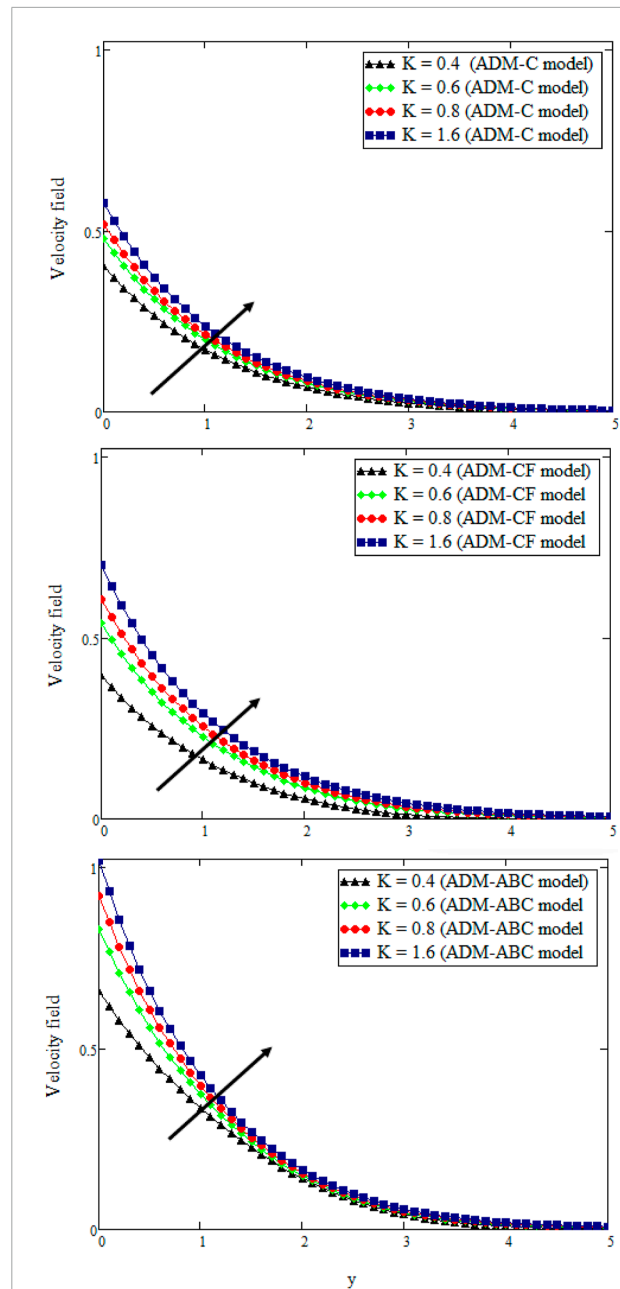


FIGURE 11

$u(y,t)$ with K when $t = 0.3$, $Gm = 0.5$, $\eta = 0.15$, $Sc = 1.2$, $\phi = 0.02$, $\alpha = \beta = \delta = 0.8$, $\gamma = 0.95$, $Pr = 25$, $Nr = 18$, $M = 1.5$, and $Gr = 0.05$.

This methods gives the solution Ψ in convergent series form as

$$\Psi = \sum_{n=1}^{\infty} \Psi_{n-1}, \quad (24)$$

and the decomposition of $N(\Psi)$ in Eq. 23 is

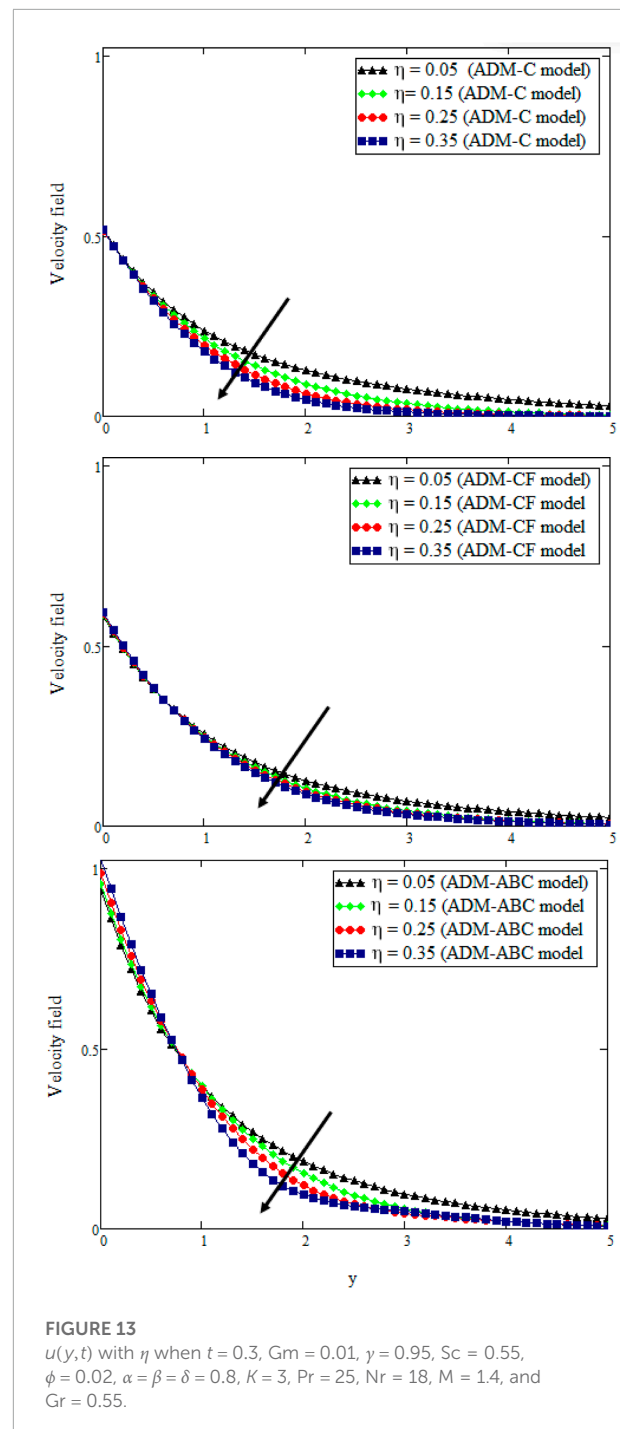
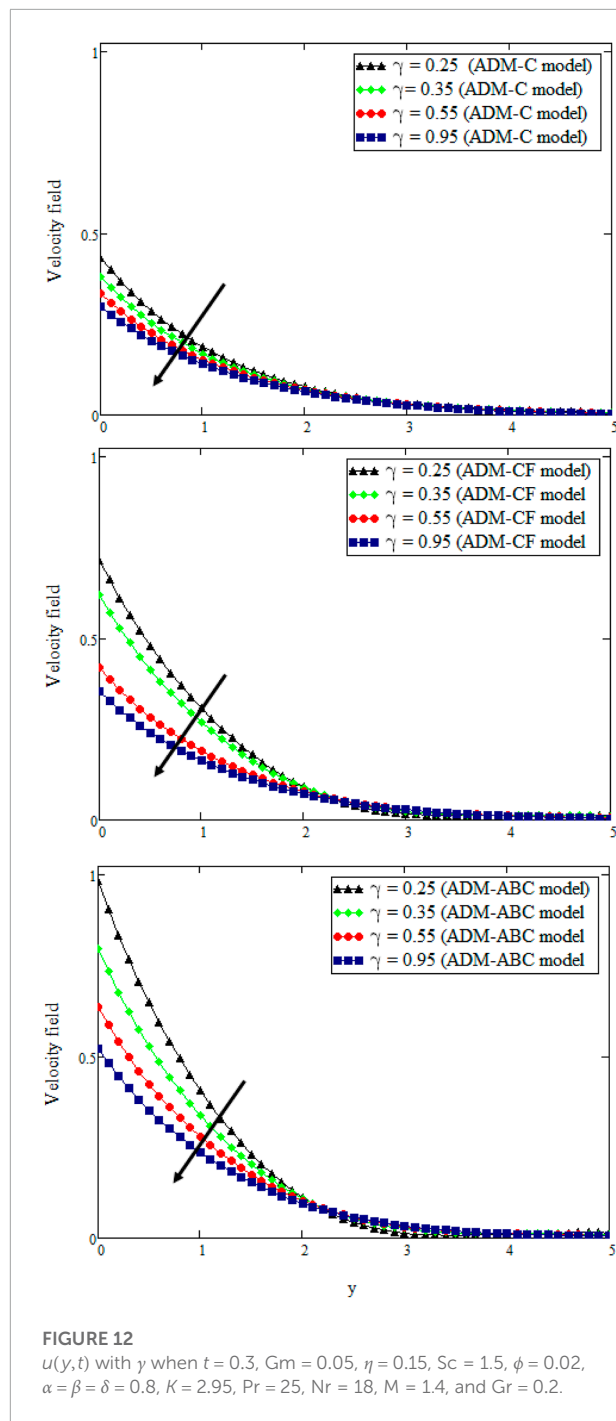
$$N(\Psi) = \sum_{n=1}^{\infty} A_{n-1}. \quad (25)$$

In the work by Adomian (Adomian, 1988; Adomian, 1994), he provided the algorithm to find any kind of nonlinearity. To

calculate the Adomian polynomials A_{n-1} in Eq. 25, we consider the following general formula:

$$A_{n-1} = \frac{1}{(n-1)!} \left[\frac{d^{n-1}}{d\lambda^{n-1}} \left(N \left(\sum_{n=1}^{\infty} \lambda^{n-1} \Psi_{n-1} \right) \right) \right]_{\lambda=0}, \quad n \geq 1. \quad (26)$$

3) Substitute Eq. 24 and Eq. 25 into both sides of Eq. 23, we get

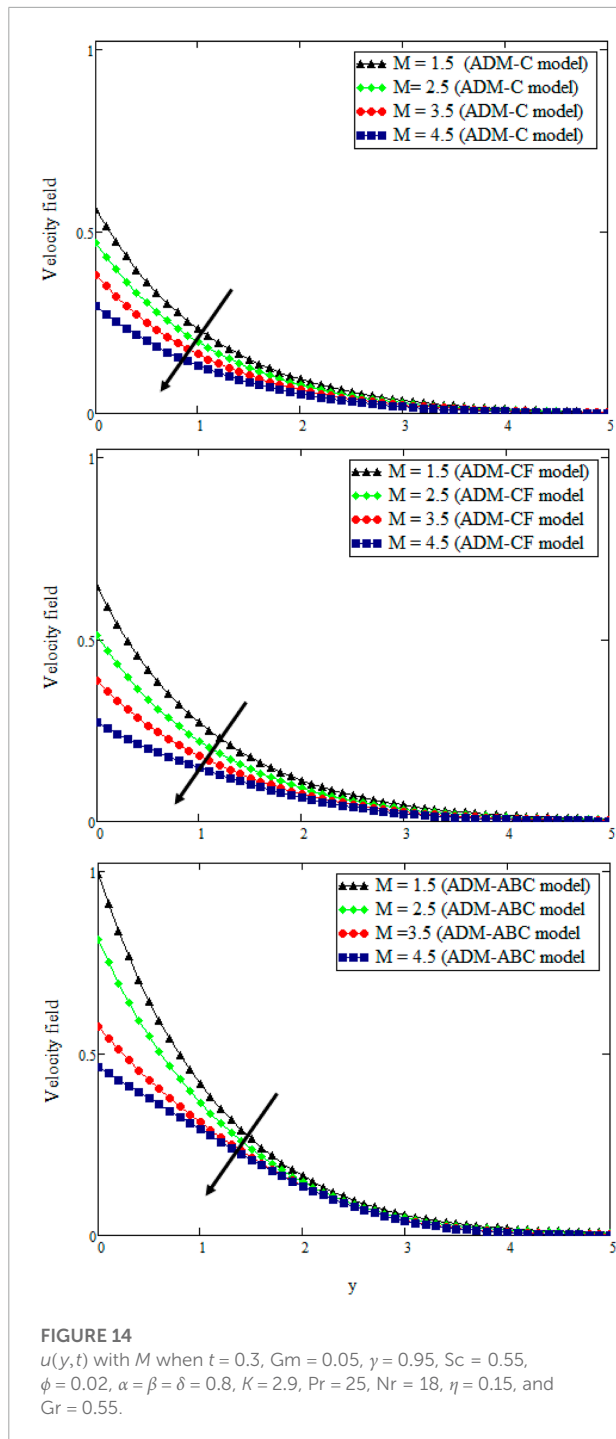


$$\sum_{n=1}^{\infty} \Psi_{n-1} = I^q \left(F - L \left(\sum_{n=1}^{\infty} \Psi_{n-1} \right) - \sum_{n=1}^{\infty} A_{n-1} \right). \quad (27)$$

- 4) Using Ψ_0 as an initial condition with Eq. 27, we can obtain Ψ_1, Ψ_2, \dots .
- 5) Substituting these $\Psi_0, \Psi_1, \Psi_2, \dots$ in Eq. 24, $\Psi(t,s)$ is obtained in a convergent series solution.

Numerical study

In order to solve the model (15)–(17) with Eqs 12–14, the given initial estimates are recommended to begin the simulations $u_0 = t^2 e^{-\gamma}$, $\theta_0 = e^{-\gamma}$, and $C_0 = e^{-\gamma}$. We assume that $\alpha = \beta = \delta$.



Application of ADM with the caputo derivative

In problems (15)–(17), we consider $D_t^\alpha(\cdot)$ in the Caputo sense. Following the formulation of Adomian decomposition method, the following results are obtained. Result of the

fractional concentration field:

$$C(y, t) = e^{-y} \left(1 + \frac{2t^\alpha \left(\frac{Sc}{\Gamma(1+\alpha)} + \frac{2t^\alpha}{\Gamma(1+2\alpha)} \right)}{Sc^2} \right). \quad (28)$$

Result of the fractional temperature field:

$$\theta(y, t) = e^{-y} \left(1 + \frac{t^\alpha \lambda \left(\frac{t^\alpha \lambda}{\Gamma(1+2\alpha)} + \frac{Pr b_6}{\Gamma(1+\alpha)} \right)}{Pr^2 b_6^2} \right). \quad (29)$$

Result of the fractional velocity field:

$$u(y, t) = e^{-y^2 \eta} t^2 + \frac{1}{\Gamma(1+\alpha)} \left(e^{-y(1+\gamma \eta)} t^\alpha \left(e^{y^2 \eta} (1.642 Gm + 1.741 Gr) + \frac{1}{K(1+\alpha)(2+\alpha) \gamma} \right. \right. \\ \times (1.998 e^{y^2 \eta} (-1.006 K M \gamma + 1.005 (-\gamma - 2K(1+\gamma) \times \eta + 4K \gamma^2 (1+\gamma) \eta^2))) + (3.541374^{-\alpha} e^{-y(1+\gamma \eta)} \\ \times t^{2\alpha} (1+\alpha)(2+\alpha) (1.002 e^{y^2 \eta} K^2 (3.28072 Gm Pr + 1.741 Gr Sc) \times (1+\alpha)(1+2\alpha) \gamma^2 + 0.999999 e^{y^2 \eta} \\ \times (1.642 Gm + 1.741 Gr) K Pr Sc (1+\alpha)(1+2\alpha) \gamma \\ \times (-1.006 K M \gamma + 1.005 (K + (-1+K) \gamma)) + 0.999 e^{y^2 \eta} \\ \times Pr Sc t^2 (1.01204 K^2 M^2 \gamma^2 + 2.02206 K M \gamma \\ \times (\gamma + 2K(1+\gamma) \eta - 4K \gamma^2 (1+\gamma) \eta^2) + 1.01003 \\ \times (\gamma^2 + 4K \gamma (1+\gamma) \eta + 4K(1+\gamma) (-2\gamma^2 \gamma + 3K \\ \times (1+\gamma)) \eta^2 - 48K^2 \gamma^2 (1+\gamma)^2 \eta^3 \\ + 16K^2 \gamma^4 (1+\gamma)^2 \eta^4)) \times \Gamma(1 \\ + 2\alpha)) / \left(K^2 Pr Sc \gamma^2 \Gamma\left(\frac{1}{2} + \alpha\right) \Gamma(3+\alpha) \Gamma(3+2\alpha) \right) \right). \quad (30)$$

Application of ADM with the Caputo–Fabrizio derivative

In problems (15)–(17), we consider $D_t^\alpha(\cdot)$ in the Caputo–Fabrizio sense. Following the formulation of the Adomian decomposition method, the following results are obtained. Fractional concentration field's result is as follows:

$$C(y, t) = \frac{e^{-y} (4 + 2Sc + Sc^2 + 2(4 + Sc)(-1+t)\alpha + 2(2 + (-4+t)t)\alpha^2)}{Sc^2}. \quad (31)$$

Fractional temperature field's result is as follows:

$$\theta(y, t) = \frac{e^{-y} ((2 + 4(-1+t)\alpha + (2 + (-4+t)t)\alpha^2) \lambda^2 + 2Pr b_6 ((1 + (-1+t)\alpha) \lambda + Pr b_6))}{2Pr^2 b_6^2}. \quad (32)$$

Fractional velocity field's result is as follows:

$$\begin{aligned}
 u(y, t) &= e^{-\gamma^2 t^2} + \frac{1}{K\gamma} \left(0.333e^{-\gamma(1+\gamma)\eta} \left(3.003e^{\gamma^2 \eta} (1.642\text{Gm} \right. \right. \\
 &\quad + 1.741\text{Gr}) K(1 + (-1+t)\alpha) \gamma + e^{\gamma} t^2 (3 + (-3+t)\alpha) \\
 &\quad \times (-1.006KM\gamma + 1.005(-\gamma - 2K(1+\gamma)\eta \\
 &\quad + 4Ky^2(1+\gamma)\eta^2)) \left. \right) + \frac{0.0832502e^{-\gamma(2+\gamma)\eta}}{K^2\text{PrSc}\gamma^2} \\
 &\quad \times \left(6.01201e^{\gamma(1+\gamma)\eta} K^2 (3.28072\text{GmPr} + 1.741\text{GrSc}) \right. \\
 &\quad \times (2 + 4(-1+t)\alpha + (2 + (-4+t)t)\alpha^2) \gamma^2 \\
 &\quad + 5.99999e^{\gamma(1+\gamma)\eta} (1.642\text{Gm} + 1.741\text{Gr}) K \\
 &\quad \times \text{PrSc} (2 + 4(-1+t)\alpha + (2 + (-4+t)t)\alpha^2) \\
 &\quad \times \gamma (-1.006KM\gamma + 1.005(K + (-1+K)\gamma)) \\
 &\quad + 0.999e^{2\gamma} \text{PrSc} t^2 (6 + (-6+t)\alpha) (2 + (-2+t)\alpha) \\
 &\quad \times (1.01204K^2 M^2 \gamma^2 + 2.02206KM\gamma (\gamma + 2K(1+\gamma)\eta \\
 &\quad - 4Ky^2(1+\gamma)\eta^2) + 1.01003(\gamma^2 + 4Ky(1+\gamma)\eta \\
 &\quad + 4K(1+\gamma)(-2\gamma^2\gamma + 3K(1+\gamma))\eta^2 - 48K^2\gamma^2(1+\gamma)^2\eta^3 \\
 &\quad + 16K^2\gamma^4(1+\gamma)^2\eta^4)) \left. \right). \quad (33)
 \end{aligned}$$

Application of ADM with the Atangana–Baleanu derivative

In problems (15)–(17), we consider $D_t^\alpha(\cdot)$ in the Atangana–Baleanu sense. Following the formulation of the Adomian decomposition method, the following results are obtained. Fractional concentration field's result is as follows:

$$\begin{aligned}
 C(y, t) &= e^{-\gamma} \left(1 + \frac{2(t^\alpha + \Gamma(\alpha) - \alpha\Gamma(\alpha))}{\text{Sc}(\alpha + \Gamma(\alpha) - \alpha\Gamma(\alpha))} + \frac{4\Gamma(\alpha)}{\text{Sc}^2(\alpha + \Gamma(\alpha) - \alpha\Gamma(\alpha))^2 \Gamma\left(\frac{1}{2} + \alpha\right)} \right. \\
 &\quad \times \left(4^{-\alpha} \sqrt{\pi} t^{2\alpha} \alpha + (-1+\alpha)(-2t^\alpha + (-1+\alpha)\Gamma(\alpha))\Gamma\left(\frac{1}{2} + \alpha\right) \right) \left. \right). \quad (34)
 \end{aligned}$$

Fractional temperature field's result is as follows:

$$\begin{aligned}
 \theta(y, t) &= e^{-\gamma} \left(1 + \frac{4^{-\alpha} \lambda^2 \Gamma(\alpha) \left(\sqrt{\pi} t^{2\alpha} \alpha + 4^\alpha (-1+\alpha)(-2t^\alpha + (-1+\alpha)\Gamma(\alpha))\Gamma(1/2 + \alpha) \right)}{\text{Pr}^2(\alpha + \Gamma(\alpha) - \alpha\Gamma(\alpha))^2 \Gamma(1/2 + \alpha) b_6^2} \right. \\
 &\quad \left. + \frac{\lambda(t^\alpha + \Gamma(\alpha) - \alpha\Gamma(\alpha))}{\text{Pr}(\alpha + \Gamma(\alpha) - \alpha\Gamma(\alpha)) b_6} \right). \quad (35)
 \end{aligned}$$

Fractional velocity field's result is as follows:

$$\begin{aligned}
 u(y, t) &= e^{-\gamma^2 t^2} + \frac{e^{-\gamma(1+\gamma)\eta}}{BK\gamma b_3} \left(t^{-1+\alpha} \alpha \left(\frac{1}{\Gamma(3+\alpha)} (2t^3 (2K\eta \right. \right. \\
 &\quad \times (-1\eta) + 2\gamma^2 + \gamma(-1 + 2K\eta(-1 + 2\gamma^2\eta))) \\
 &\quad \times (\cosh(y) \sinh(y)) b_1) \\
 &\quad - \frac{2KMt^3 \gamma (\cosh(y) + \sinh(y)) b_2}{\Gamma(3+\alpha)} \\
 &\quad + \frac{Kt\gamma (\cosh(y^2\eta) + \sinh(y^2\eta)) b_3 (\text{Gr}b_4 + \text{Gmb}_5)}{\Gamma(1+\alpha)} \\
 &\quad - (-1+\alpha)(e^{\gamma} t^2 (2K\eta(-1 + 2\gamma^2\eta) \\
 &\quad + \gamma(-1 + 2K\eta(-1 + 2\gamma^2\eta))) b_1 \\
 &\quad + Ky(-e^{\gamma} M t^2 b_2 + e^{\gamma^2 \eta} b_3 (\text{Gr}b_4 + \text{Gmb}_5))) \\
 &\quad + (e^{-\gamma(2+\gamma)\eta} (t^\alpha \alpha (\text{Gr}K^2 \text{Sc}\gamma^2 \lambda \Gamma(\alpha) \Gamma(3+\alpha) \\
 &\quad \times (\cosh(y(1+\gamma\eta)) + \sinh(y(1+\gamma\eta))) b_3^2 b_4 \\
 &\quad - \text{Gr}K^2 \text{Sc}\gamma^2 \lambda \Gamma(\alpha) \Gamma(3+\alpha) \\
 &\quad \times (\cosh(y(1+\gamma\eta)) + \sinh(y(1+\gamma\eta))) b_3^2 b_4 \\
 &\quad + \frac{\text{Gr}K^2 \text{Sc} t^\alpha \gamma^2 \lambda \Gamma(1+\alpha)^2 \Gamma(3+\alpha) (\cosh(y(1+\gamma\eta)) + \sinh(y(1+\gamma\eta))) b_3^2 b_4}{\Gamma(1+2\alpha)} \\
 &\quad - 2\text{PrSc} t^2 (-1+\alpha) \Gamma(\alpha) \Gamma(1+\alpha) \\
 &\quad \times (\cosh(2\gamma) + \sinh(2\gamma)) ((\gamma^2 + 4Ky(1+\gamma)\eta \\
 &\quad + 4K(1+\gamma)(-2\gamma^2\gamma + 3K(1+\gamma))\eta^2 \\
 &\quad - 48K^2\gamma^2(1+\gamma)^2\eta^3 + 16K^2\gamma^4(1+\gamma)^2\eta^4) b_1^2 \\
 &\quad + 2KM\gamma(2K\eta(1 - 2\gamma^2\eta) + \gamma(1 + 2K\eta(1 - 2\gamma^2\eta))) \\
 &\quad \times b_1 b_2 + K^2 M^2 \gamma^2 b_2^2) b_6 + 1/\Gamma(3+2\alpha)^2 \text{PrSc} t^{2+\alpha} \\
 &\quad \times \alpha \Gamma(\alpha) \Gamma(1+\alpha) \Gamma(3+\alpha) (\cosh(2\gamma) + \sinh(2\gamma)) \\
 &\quad \times ((\gamma^2 + 4Ky(1+\gamma)\eta + 4K(1+\gamma) \\
 &\quad \times (-2\gamma^2\gamma + 3K(1+\gamma))\eta^2 - 48K^2\gamma^2(1+\gamma)^2\eta^3 \\
 &\quad + 16K^2\gamma^4(1+\gamma)^2\eta^4) b_1^2 + 2KM\gamma(2K\eta(1 - 2\gamma^2\eta) \\
 &\quad + \gamma(1 + 2K\eta(1 - 2\gamma^2\eta))) b_1 b_2 + K^2 M^2 \gamma^2 b_2^2) b_6 \\
 &\quad + 2\text{Gm}K^2 \text{Pr}\gamma^2 \Gamma(\alpha) \Gamma(3+\alpha) (\cosh(y(1+\gamma\eta)) \\
 &\quad + \sinh(y(1+\gamma\eta))) b_3^2 b_5 b_6 - 2\text{Gm}K^2 \text{Pr}\alpha \gamma^2 \Gamma(\alpha) \Gamma \\
 &\quad \times (3+\alpha) (\cosh(y(1+\gamma\eta)) + \sinh(y(1+\gamma\eta))) b_3^2 b_5 b_6 \\
 &\quad + 2\text{Gm}K^2 \text{Pr} t^\alpha \gamma^2 \Gamma(1+\alpha)^2 \Gamma(3+\alpha) (\cosh(y(1+\gamma\eta)) + \sinh(y(1+\gamma\eta))) b_3^2 b_5 b_6 \\
 &\quad + \frac{1}{\Gamma\left(\frac{1}{2} + \alpha\right)} \left(4^{-\alpha} K \sqrt{\pi} \text{PrSc} t^\alpha \alpha \gamma \Gamma(\alpha) \Gamma(3+\alpha) \right. \\
 &\quad \times (\cosh(y(1+\gamma\eta)) + \sinh(y(1+\gamma\eta))) \\
 &\quad \times ((K - \gamma + Ky) b_1 - KMyb_2) b_3 (\text{Gr}b_4 + \text{Gmb}_5) b_6 \\
 &\quad + \frac{1}{\Gamma(1+\alpha)} \times (K\text{PrSc}\alpha \Gamma(\alpha)^2 \Gamma(3+\alpha) \\
 &\quad \times (\cosh(y(1+\gamma\eta)) + \sinh(y(1+\gamma\eta))) \\
 &\quad \times ((K - \gamma + Ky) b_1 - KMyb_2) b_3 (\text{Gr}b_4 + \text{Gmb}_5) b_6 \\
 &\quad - \frac{1}{\Gamma(1+\alpha)} (K\text{PrSc}\alpha^2 \gamma \Gamma(\alpha)^2 \Gamma(3+\alpha) \\
 &\quad \times (\cosh(y(1+\gamma\eta)) + \sinh(y(1+\gamma\eta))) \\
 &\quad \times ((K - \gamma + Ky) b_1 - KMyb_2) b_3 (\text{Gr}b_4 + \text{Gmb}_5) b_6 \\
 &\quad + (1-\alpha)(e^{2\gamma} \text{PrSc} t^2 \Gamma(\alpha) \Gamma(1+\alpha) (2t^\alpha \alpha - (-1+\alpha) \\
 &\quad \times \Gamma(3+\alpha)) ((\gamma^2 + 4Ky(1+\gamma)\eta + 4K(1+\gamma) \\
 &\quad \times (-2\gamma^2\gamma + 3K(1+\gamma))\eta^2 - 48K^2\gamma^2(1+\gamma)^2\eta^3 \\
 &\quad + 16K^2\gamma^4(1+\gamma)^2\eta^4) b_1^2 + 2KM\gamma(\gamma + 2K(1+\gamma)\eta \\
 &\quad - 4Ky^2(1+\gamma)\eta^2) b_1 b_2 + K^2 M^2 \gamma^2 b_2^2) b_6 + e^{\gamma(1+\gamma)\eta} \\
 &\quad \times K\text{PrSc}\alpha \gamma \Gamma(\alpha) (t^\alpha + \Gamma(\alpha) - \alpha\Gamma(\alpha)) \Gamma(3+\alpha) \\
 &\quad \times ((K + (-1+K)\gamma) b_1 - KMyb_2) b_3 (\text{Gr}b_4 \\
 &\quad + \text{Gmb}_5) b_6 + e^{\gamma(1+\gamma)\eta} K^2 \gamma^2 (t^\alpha + \Gamma(\alpha) - \alpha\Gamma(\alpha)) \\
 &\quad \times \Gamma(1+\alpha) \Gamma(3+\alpha) b_3^2 (\text{GrSc}\lambda b_4 + 2\text{GmPr}b_5 b_6))) \\
 &\quad \left. \right) / (B^2 K^2 \text{PrSc}\gamma^2 \Gamma(\alpha) \Gamma(1+\alpha) \Gamma(3+\alpha) b_3^2 b_6). \quad (36)
 \end{aligned}$$

Nusselt number, Sherwood number, and skin friction

Heat and mass transfer rates and skin friction for ADM_C , ADM_{CF} and ADM_{AB} are obtained using results from [Section 5.1](#), [Section 5.2](#), and [Section 5.3](#).

$$Nu = -\partial_y \theta(y, t) |_{y=0},$$

$$Sh = -\partial_y C(y, t) |_{y=0},$$

$$(C_f) = -\partial_y u(y, t) |_{y=0}.$$

The numerical analyses for Nusselt number, Sherwood number, and skin friction under the influence of fractional parameters are given in [Tables 2–4](#) for all three models.

Results and discussions

In the present study, a fractional model is articulated utilizing three different differential approaches, i.e., Caputo (C), Caputo–Fabrizio (CF), and Atangana–Baleanu (ABC). ADM is used to obtain semianalytical solutions for compactness, velocity, and temperature domains. The received upshots are projected graphically to present the influence of fractional and flow parameters.

General approximative numerical solutions for unfirm incompressible, viscoelastic Casson nanofluid carrying human blood as the base fluid and CNTs (SWCNTs/ MWCNTs) as nanoparticles were obtained by ADM. It was reckoned that the upright plate was translating in its plane having velocity $U_0 f(t)$, where U_0 is the characteristic velocity and $f(t)$ is a piecewise continuous function specified on $[0, \infty)$ satisfying the condition $f(0) = 0$. In the present study, $f(t) = t^2$ was presumed, which makes us speculate that the plate is rendered with unvarying apparent motion and hence also the fluid. The physical characteristics of blood and CNTs (SWCNTs/ MWCNTs) are acquired from [Table 1](#) for numeric calculation.

The temperature for SWCNT and MWCNT human blood-based nanofluid is compared in [Figure 2](#). It is evident that the MWCNT Casson fluid depicts more heat conduction as compared to SWCNT nanoparticles. This is due to the differences between the thermal conductivities of both types of nanoparticles. the thermal conductivity for MWCNTs is $3000 \text{ Wm}^{-1} \text{ K}^{-1}$ while for SWCNTs it is $6600 \text{ Wm}^{-1} \text{ K}^{-1}$, which clearly shows that the temperature of MWCNTs has higher values as compared to SWCNTs. A similar behavior can be seen for all three models, which was described by [Imran et al. \(2020\)](#).

[Figure 3](#) Plots revealing the impact of Pr_{eff} on temperature fields obtained by the three fractional approaches. It can be clearly seen from the graph that temperature and boundary layer

thickness are reduced by maximizing Pr_{eff} . The value of Pr_{eff} depends on the radiation–conduction parametric quantity Nr and Prandtl number Pr . Graphically, as the Pr_{eff} value intensifies, the fluid temperature is minimized. When the Pr_{eff} value is increased, it reduces thermal conductivity and enhances liquid viscosity leading to an abbreviation of the thickness of the thermic boundary layer. Nonetheless, the ADM_{AB} model delineates this deportment better due to the presence of Mittag–Leffler kernel when equated with ADM_{CF} and ADM_C models. All models demonstrate a similar pattern.

[Figure 4](#) shows the effect of nanoparticle volume fraction ϕ on the temperature domain. Temperature enhances upon increasing the value of nanoparticle volume fraction ϕ ; physically, it occurs because of the addition of MWCNT nanoparticles into the Casson fluid, leading to elevated thermic conduction and, therefore, increasing temperature. The plots in [Figure 5](#) help us understand the upshot of Sc on concentration by taking other parameters to be fixed. It is determined, that with an increase of Sc the thickness of the liquid decreases, which is due to a reduction of molecular diffusivity.

The plots in [Figure 6](#) help us envision the impact of SWCNTs and MWCNTs in Casson fluid, which in our case is human blood, on velocity domains obtained by the three fractional approaches. Graphically, it can be envisioned that MWCNTs' nanoliquid moves faster than SWCNTs' nanofluid. Physically, this occurs due to the density of carbon nanotube nanoparticles. The density of MWCNTs is $(1600 \text{ Wm}^{-1} \text{ K}^{-1})$ whereas the density of SWCNTs is $(2600 \text{ Wm}^{-1} \text{ K}^{-1})$, which makes SWCNT-based nanofluid thick, resulting in slower motion of the fluid. Similar behavior can be seen in the work by [Imran et al. \(2020\)](#). Dispersing MWCNT nanoparticles into the Casson liquid decreases its velocity due to increased thickness. Similar patterns can be seen for all three fractional models.

Figures (7–14) show numerical traits of MWCNTs' nanospecks and human blood presented in [Table 1](#). [Figures 7, 8](#) determine the outcome of mass and thermal Grashof numbers, i.e., Gm and Gr , respectively. The fluid speed in both cases is enhanced with Gr and Gm . The fluid flow is simply imputable to buoyant pressures. When this force is zero, the fluid will not be no displaced. For $Gr > 0$, the natural convection is imputable, and heat is channelized to the fluid through the plate; afterward, the plate is tranquilized. When the Grashof number is increased, the buoyant force originates and becomes less glutinous, which institutes liquid flow faster as seen in these graphs for both frameworks. Moreover, [Figure 9](#) is plotted for Pr_{eff} versus y by keeping other parameters fixed. It is pertinent to mention that by invoking Pr_{eff} , the fluid speed decreases and the boundary layer thickness is reduced. The reason for this is the increased value of Pr_{eff} leads to acquiring fluid viscosity, and the reduced caloric boundary layer leads to slower apparent motion. This can be further elaborated from the graphical analysis; the ADM_{ABC} model describes the behavior of the function in the best possible

way because it holds Mittag–Leffler kernel, which stores the memory factor, and is therefore better in describing the fluid's flow fields when compared with ADM_{CF} and ADM_C . When the fractional parameter approaches 1, ADM_{ABC} gives velocity values closer to the classical results.

The plots in **Figure 10** probe the invasion of Schmidt number Sc on liquid velocity by confining the parametric quantities constantly. It is observed that an increase in Sc leads to a decrease in the speed. **Figure 11** is diagrammed to ascertain the impression of porosity parameter K on velocity. For large values of K , speed and boundary layer thickness are increased. The reason behind this phenomenon is that by increasing the permeability of the porous medium its resistance is decreased, which contributes to increasing the momentum of the flux regime. **Figure 12** is diagrammed to project the impression of the Casson parameter γ , which unveils tangible traits of plasticity. When γ decreases, blood plasticity increases, which ultimately deaccelerates the motion of the fluid.

Figure 13 is diagrammed to ascertain the effect of the slip parameter on Casson MWCNTs' nanofluid. By increasing the value of η , velocity is deaccelerated as displayed in **Figure 13** for increasing three fractional models. **Figure 14** shows the plots for magnetic field parameter M , which produces a magnetic field during the fluid's flow. An increase in the magnetic flux parametric quantity decreases the velocity. An increase in the magnetic field parameter engenders the drag force to the stream, termed as Lorentz force. These retarding forces understate the velocity profiles and reduce the thickness of MBL.

Table 2 presents fractional parameters' impact on skin friction for small and large durations by keeping other parametric quantities fixed. By increasing the fractional parametric value, skin friction decreases for all models for small and large durations. However, for small duration, results are $ADM_{CF} < ADM_C < ADM_{ABC}$, and for large durations, ADM_C and ADM_{ABC} show reverse behavior. The effect of the fractional variable on Nu , the Nusselt number, and Sherwood number Sh is given in **Tables 3** and **4**. For large and small durations, Nu and Sh for ADM_{ABC} first increase by increasing α and then show a decreasing behavior. For ADM_C and ADM_{CF} , Nusselt number and Sherwood number decrease by increasing α . All three models show a similar result for $\alpha = 1$.

Conclusion

This study was performed to investigate free convective, unsteady, MHD blood flow with single (SWCNTs) and multiwalled carbon nanotubes (MWCNTs) as nanoparticles. The blood flow is considered over an oscillating vertically upright plate engrafted in a porous medium with slip, radiation, and porosity effects. Three fractional approaches Caputo (C), Caputo–Fabrizio (CF), and Atangana–Baleanu (ABC) are used

to develop a fractional blood flow model, which is solved by the Adomian decomposition method (ADM). Some key findings are as follows:

- 1) Fractional parameter controls the rates of heat and mass transfer and maximum rates can be achieved for smaller values of the fractional parameter for small and large durations.
- 2) Fractional parameters can be used to control the thermal, diffusion, and momentum boundary layers, respectively, and are applicable in some experimental work where needed.
- 3) Fluid properties can be enhanced by increasing the concentration of nanoparticles and decreasing the velocity.
- 4) SWCNTs' nanoparticles are more reliable and efficient in the heating process such as in electronics devices due to the higher value of thermal conductivity.
- 5) ADM_{ABC} model described the behavior of the function in a better way because it holds Mittag–Leffler kernel, which stores memory factors, and therefore is better in describing the fluid's flow fields when compared with ADM_{CF} and ADM_C . When the fractional parameter approaches 1, ADM_{ABC} gives velocity values closer to the classical results.
- 6) Nusselt number and skin frictions are decreasing functions of α . However, for small durations, results are $ADM_{CF} < ADM_C < ADM_{ABC}$, and for large durations, ADM_C and ADM_{ABC} show reverse behavior.

Data availability statement

The original contributions presented in the study are included in the article/Supplementary Material, and further inquiries can be directed to the corresponding author.

Author contributions

All authors listed have made a substantial, direct, and intellectual contribution to the work and have approved it for publication.

Acknowledgments

The authors acknowledge the financial support of Taif University Researchers Supporting Project number (TURSP-2020/189), Taif University, Taif, Saudi Arabia.

Conflict of interest

The authors declare that the research was conducted in the absence of any commercial or financial relationships that could be construed as a potential conflict of interest.

Publisher's note

All claims expressed in this article are solely those of the authors and do not necessarily represent those of

their affiliated organizations or those of the publisher, the editors, and the reviewers. Any product that may be evaluated in this article, or claim that may be made by its manufacturer, is not guaranteed or endorsed by the publisher.

References

- Adomian, G. (1988). A review of the decomposition method in applied mathematics. *J. Math. Analysis Appl.* 135, 501–544. doi:10.1016/0022-247x(88)90170-9
- Adomian, G. (1994). *Solving frontier problems of physics: The decomposition method*. Boston: Kluwer Academic Publishers.
- Ahmad, M., Imran, M. A., Aleem, M., and Khan, I. (2019). A comparative study and analysis of natural convection flow of MHD non-Newtonian fluid in the presence of heat source and first-order chemical reaction. *J. Therm. Anal. Calorim.* 137, 1783–1796. doi:10.1007/s10973-019-08065-3
- Ahmed, N., Mohyud-Din, S. T., and Saleh Hassan, M. (2016). Flow and heat transfer of nanofluid in an asymmetric channel with expanding and contracting walls suspended by carbon nanotubes: A numerical investigation. *Aerosp. Sci. Technol.* 48, 53–60. doi:10.1016/j.ast.2015.10.022
- Aleem, M., Imran, M. A., and Akgul, A. (2021). Heat transfer analysis of magnetohydrodynamic Casson fluid through a porous medium with constant proportional Caputo derivative. *Heat. Transf.* 50, 6444–6464. doi:10.1002/htj.22179
- Ali, F., Ali, F., Sheikh, N. A., Khan, I., and Nisar, K. S. (2020). Caputo–Fabrizio fractional derivatives modeling of transient MHD Brinkman nanoliquid: Applications in food technology. *Chaos Solit. Fractals* 131. doi:10.1016/j.chaos.2019.109489
- Ali, F., Khan, I., and Shafie, S. (2014). Closed form solutions for unsteady free convection flow of a second grade fluid over an oscillating vertical plate. *PLoS One* 9 (2), e85099. doi:10.1371/journal.pone.0085099
- Ali, F., Saqib, M., Khan, I., and Sheikh, N. A. (2016). Application of Caputo–Fabrizio derivatives to MHD free convection flow of generalized Walters'–B fluid model. *Eur. Phys. J. Plus* 131 (10), 377. doi:10.1140/epjp/i2016-16377-x
- Animasaun, I. L., Adebile, E. A., and Fagbade, A. I. (2015). Casson fluid flow with variable thermo physical property along exponentially stretching sheet with suction and exponentially decaying internal heat generation using the homotopy analysis method. *J. Niger. Math. Soc.* 2 (1), 1–17. doi:10.1016/j.jnnms.2015.02.001
- Atangana, A., and Baleanu, D. (2016). New fractional derivatives with non-local and non-singular kernel: Theory and application to heat transfer model. *J. Therm. Sci.* 20, 763–769. doi:10.2298/sci160110118a
- Bhattacharyya, K. (2013). Boundary layer stagnation-point flow of casson fluid and heat transfer towards a shrinking/stretching sheet. *Front. Heat Mass Transf.* 4 (2). doi:10.5098/hmt.v4.2.3003
- Bhattacharyya, K., Hayat, T., and Alsaedi, A. (2014). Exact solution for boundary layer flow of Casson fluid over a permeable stretching/ shrinking sheet. *Z. Angew. Math. Mech.* 94 (6), 522–528. doi:10.1002/zamm.201200031
- Bourantas, G. C., and Loukopoulos, V. C. (2014). Modeling the natural convective flow of micropolar nanofluids. *Int. J. Heat Mass Transf.* 68, 35–41. doi:10.1016/j.jheatmasstransfer.2013.09.006
- Caputo, M., and Fabrizio, M. (2015). A new definition of fractional derivative without singular kernel. *Prog. Fract. Differ. Appl. Int. J.* 1 (2), 1–13.
- Caputo, M. (1967). Linear models of dissipation whose Q is almost frequency independent. *Geophys. J. Int.* 13 (5), 529–539. doi:10.1111/j.1365-246x.1967.tb02303.x
- Casson, N. (1959). *A flow equation for the pigment oil suspensions of the printing ink type, Rheology of Disperse Systems*. New York, USA: Pergamon, 84–104.
- Hassan, M. A., Pathak, M., and Khan, M. K. (2013). Natural convection of viscoplastic fluids in a square enclosure. *J. Heat Transf.* 135, 122501–122512. doi:10.1115/1.4024896
- Hayat, T., Shehzad, S. A., and Alsaedi, A. (2012). Soret and Dufour effects on magnetohydrodynamic (MHD) flow of Casson fluid. *Appl. Math. Mech.* 33 (10), 1301–1312. doi:10.1007/s10483-012-1623-6
- Herrmann, R. (2014). *Fractional calculus: An introduction for physicists*. 2nd ed. Singapore: World Scientific.
- Hussanan, A., Salleh, M. Z., Khan, I., and Tahar, R. M. (2016). Unsteady heat transfer flow of a Casson fluid with Newtonian heating and thermal radiation. *J. Teknol.* 78, 1–7. doi:10.11113/jt.v78.8264
- Imran, M. A., Aleem, M., Ahmadian, A., Salahshour, S., and Ferrara, M. (2020). New trends of fractional modeling and heat and mass transfer investigation of (SWCNTs and MWCNTs)-CMC based nanofluids flow over inclined plate with generalized boundary conditions. *Chin. J. Phys.* 66, 497–516. doi:10.1016/j.cjph.2020.05.026
- Imran, M. A., Aleem, M., and Riaz, M. B. (2018). Exact analysis of MHD Walters'–B fluid flow with non-singular fractional derivatives of Caputo–Fabrizio in the presence of radiation and chemical reaction. *J. Polym. Sci. Eng.* 1 (2). doi:10.24294/jpse.v1i2.599
- Imran, M. A., Sarwar, S., and Imran, M. (2016). Effects of slip on free convection flow of Casson fluid over an oscillating vertical plate. *Bound. Value Probl.* 30. doi:10.1186/s13661-016-0538-2
- Imran, M. A., Shah, N. A., Aleem, M., and Khan, I. (2017). Heat transfer analysis of fractional second-grade fluid subject to Newtonian heating with Caputo and caputo-fabrizio fractional derivatives: A comparison. *Eur. Phys. J. Plus* 32, 340. doi:10.1140/epjp/i2017-11606-6
- Imran, M. A., Shah, N. A., Rafique, K., Sohail, A., and Ejaz, E. (2017). General solutions of convective flows of MHD casson fluid with slip and radiative heat transfer at the boundary. *Comput. Therm. Sci.* 9 (1), 1–11. doi:10.1615/computthermalsci.2016016971
- Kameswaran, P. K., Shaw, S., and Sibanda, P. (2014). Dual solutions of Casson fluid flow over a stretching or shrinking sheet. *Sadhana* 39 (6), 1573–1583. doi:10.1007/s12046-014-0289-7
- Kataria, H. R., and Patel, H. R. (2018). Heat and mass transfer in magnetohydrodynamic (MHD) Casson fluid flow past over an oscillating vertical plate embedded in porous medium with ramped wall temperature. *Propuls. Power Res.* 7 (3), 257–267. doi:10.1016/j.jprr.2018.07.003
- Khalid, A., Khan, I., Khan, A., Shafie, S., and Tlili, I. (2018). Case study of MHD blood flow in a porous medium with CNTs and thermal analysis. *Case Stud. Therm. Eng.* 12, 374–380. doi:10.1016/j.csce.2018.04.004
- Kleppe, J., and Marner, W. J. (1970). Transient free convection in a Bingham plastic on a vertical flat plate. *J. Heat Transf.* 94, 371–376. doi:10.1115/1.3449954
- Kumar, M. S., Sandeep, N., Kumar, B. P., and Saleem, S. (2018). A comparative study of chemically reacting 2D flow of Casson and Maxwell fluids. *Alexandria Eng. J.* 57 (3), 2027–2034. doi:10.1016/j.aej.2017.05.010
- Kumar, M. S., Sandeep, N., Kumar, B. R., and Saleem, S. (2018). Effect of aligned magnetic field on MHD squeezing flow of Casson fluid between parallel plates. *Defect Diffusion Forum* 384, 1–11. doi:10.4028/www.scientific.net/ddf.384.1
- Li, C. P., and Cai, M. (2019). *Theory and numerical approximations of fractional integrals and derivatives*. Philadelphia: SIAM.
- Li, C. P., and Zeng, F. H. (2015). *Numerical methods for fractional differential calculus*. Boca Raton, USA: Chapman and Hall/CRC.
- Loganathan, P., Nirmal, C., and Ganesan, P. (2015). Transient natural convective flow of a nanofluid past a vertical plate in the presence of heat generation. *J. Appl. Mech. Tech. Phys.* 56 (3), 433–442. doi:10.1134/s002189441503013x
- Nadeem, S., Haq, R. U., and Lee, C. (2012). MHD flow of a Casson fluid over an exponentially shrinking sheet. *Sci. Iran.* 19 (6), 1550–1553. doi:10.1016/j.scient.2012.10.021
- Podlubny, I. (1999). *Fractional differential equations*. San Diego: Academic Press.
- Povstenko, Y. (2015). *Linear Fractional diffusion-wave equation for scientists and engineers*. New York: Birkhäuser.
- Pramanik, S. (2014). Casson fluid flow and heat transfer past an exponentially porous stretching surface in presence of thermal radiation. *Ain Shams Eng. J.* 5 (1), 205–212. doi:10.1016/j.asej.2013.05.003

- Rajesh, V., Chamkha, A. J., and Mallesh, M. P. (2016). GITAM University Hyderabad Campus, unspecified, GITAM University Hyd. Transient MHD free convection flow and heat transfer of nanofluid past an impulsively started semi-infinite vertical plate, *J. Appl. Fluid Mech.*, 9(5), 2016, 2457–2467. doi:10.18869/acadpub.jafm.68.236.23443
- Raju, C. K., Sandeep, N., and Saleem, S. (2016). Effects of induced magnetic field and homogeneous-heterogeneous reactions on stagnation flow of a Casson fluid. *Eng. Sci. Technol. Int. J.* 19 (2), 875–887. doi:10.1016/j.jestch.2015.12.004
- Ramesh, K., and Devakar, M. (2015). Some analytical solutions for flows of Casson fluid with slip boundary conditions. *Ain Shams Eng. J.* 6 (3), 967–975. doi:10.1016/j.asej.2015.02.007
- Rehman, H., Ullah, N., and Imran, M. A. (2019). Highly dispersive optical solitons using Kudryashov's method. *Optik* 199, 163349. doi:10.1016/j.ijleo.2019.163349
- Sarwar, S. (2020). New rational solutions of fractional-order sharma-tasso-olver equation with atangana-baleanu derivative arising in physical sciences. *Results Phys.* 19, 103621. doi:10.1016/j.rinp.2020.103621
- Shaw, S., Mahanta, G., and Das, M. (2019). Thermal and solutal Marangoni stagnation point Casson fluid flow over a stretching sheet in the presence of radiation, Soret and Dofour effect with chemical reaction. *Heat. Trans. Res.* 48, 323–342. doi:10.1002/htj.21386
- Sheikh, N. A., Ching, D. L. C., Khan, I., Kumar, D., and Nisar, K. S. (2020). A new model of fractional Casson fluid based on generalized Fick's and Fourier's laws together with heat and mass transfer. *Alexandria Eng. J.* 59 (5), 2865–2876. doi:10.1016/j.aej.2019.12.023
- Stehfest, H. (1970). Algorithm 368: Numerical inversion of laplace transforms [D5]. *Commun. ACM* 13, 47–49. doi:10.1145/361953.361969
- Tahir, M., Imran, M. A., Raza, N., Abdullah, M., and Aleem, M. (2017). Wall slip and non-integer order derivative effects on the heat transfer flow of Maxwell fluid over an oscillating vertical plate with new definition of fractional Caputo-Fabrizio derivatives. *Results Phys.* 7, 1887–1898. doi:10.1016/j.rinp.2017.06.001
- Tarasov, V. E. (2010). *Fractional dynamics: Applications of fractional calculus to dynamics of particles, fields and media*. Berlin: Springer.
- Tzou, D. Y. (1997). *Macro to microscale heat transfer: The lagging behavior*. Washington: Taylor & Francis.
- Uchaikin, V. V. (2013). *Fractional derivatives for physicists and engineers*. Berlin: Springer.
- Xue, Q. (2005). Model for thermal conductivity of carbon nanotube based composites. *Phys. B Condens. Matter* 368 (1), 302–307. doi:10.1016/j.physb.2005.07.024
- Yu, W., France, D. M., Routbort, J. L., and Choi, S. U. S. (2008). Review and comparison of nanofluid thermal conductivity and heat transfer enhancements. *Heat. Transf. Eng.* 29 (5), 432–460. doi:10.1080/01457630701850851



OPEN ACCESS

EDITED BY

Adnan,
Mohi-ud-Din Islamic University,
Pakistan

REVIEWED BY

Iskander Tlili,
National School of Engineers of
Monastir, Tunisia
N. Ameer Ahammad,
University of Tabuk, Saudi Arabia

*CORRESPONDENCE

Muhammad Amjad,
muhammadamjad@cuivehari.edu.pk

SPECIALTY SECTION

This article was submitted to Process
and Energy Systems Engineering,
a section of the journal
Frontiers in Energy Research

RECEIVED 25 July 2022

ACCEPTED 22 August 2022

PUBLISHED 29 September 2022

CITATION

Ali A, Bukhari Z, Amjad M, Ahmad S,
Tag El. Din ESM and Hussain SM (2022),
Newtonian heating effect in pulsating
magnetohydrodynamic nanofluid flow
through a constricted channel: A
numerical study.
Front. Energy Res. 10:1002672.
doi: 10.3389/fenrg.2022.1002672

COPYRIGHT

© 2022 Ali, Bukhari, Amjad, Ahmad, Tag
El. Din and Hussain. This is an open-
access article distributed under the
terms of the [Creative Commons
Attribution License \(CC BY\)](https://creativecommons.org/licenses/by/4.0/). The use,
distribution or reproduction in other
forums is permitted, provided the
original author(s) and the copyright
owner(s) are credited and that the
original publication in this journal is
cited, in accordance with accepted
academic practice. No use, distribution
or reproduction is permitted which does
not comply with these terms.

Newtonian heating effect in pulsating magnetohydrodynamic nanofluid flow through a constricted channel: A numerical study

Amjad Ali¹, Zainab Bukhari¹, Muhammad Amjad^{2*},
Sohail Ahmad¹, El. Sayed M. Tag El. Din³ and Syed M. Hussain⁴

¹Centre for Advanced Studies in Pure and Applied Mathematics, Bahauddin Zakariya University, Multan, Pakistan, ²Department of Mathematics, COMSATS University Islamabad, Vehari Campus, Vehari, Pakistan, ³Electrical Engineering, Faculty of Engineering and Technology, Future University in Egypt, New Cairo, Egypt, ⁴Department of Mathematics, Faculty of Science, Islamic University of Madinah, Medina, Saudi Arabia

This article investigates the pulsatile flow of viscous incompressible MHD nanofluid in a rectangular channel. At the upper and lower walls, the channel has symmetrical constrictions. The goal is to analyze the heat transfer features of the nanofluid flow under the effect of the magnetic field and thermal radiation. Five different nanofluids, formed with nanoparticles of copper (*Cu*), magnetite (*Fe₃O₄*), silver (*Ag*), titanium oxide (*TiO₂*), and single wall carbon nanotube (*SWCNT*) in the base fluid of water, are considered in the study. The unsteady governing equations are transformed using the vorticity-stream function approach. The solution is obtained using the finite difference technique (FDM). The effect of various flow controlling parameters on velocity, temperature, Nusselt, and skin-friction profiles is inspected by using graphs. Across the channel, graphs of vorticity, streamlines, and temperature distribution are also displayed. The thickness of the thermal boundary layer upsurges with escalating values of the magnetic field, radiation parameters, and solid volume fraction, whereas it declines with escalating values of the Strouhal and Prandtl numbers. The profiles are usually found to have a more regular pattern upstream of the constriction than that downstream of the constriction. At the throat of the constriction, the carbon nanotube-based nanofluid attains higher temperatures than the other nanofluids downstream of the constriction. However, in the lee of the constriction, silver-based nanofluid attains higher temperatures than the other nanofluids downstream of the constriction. The behavior, in most cases, is opposite upstream of the constriction. The findings of the study can be utilized to cure stenosis in blood vessels, design biomechanical devices, and employ flow pulsation to control industrial operations.

KEYWORDS

pulsatile flow, constricted channel, heat transfer analysis, nanofluid, carbon nanotube

1 Introduction

Conventional heat transfer liquid sources are incapable of satisfying current cooling requirements largely due to their poor convective heat transfer coefficients. Researchers have demonstrated that nanoparticles (NPs) usually made of metals or oxides enhance the coefficients of heat convection and conduction in fluids, allowing for higher heat transfer rates for the coolants. Thus, the heat transfer and thermal system effectiveness can be improved significantly by mixing NPs in pure fluid, forming nanofluid (NF). NFs have promising applications in many areas of industry and biomedicine due to their enhanced thermal conductivity. The characteristic of improved thermal conductivity might serve as a major factor for performance improvement. As NFs can enhance heat transfer, heat exchangers can be designed to be both energy efficient and small.

Wang and Mujumdar (2008) investigated the convective heat transfer of NF flow (NFF). Saidur et al. (2011a), Saidur et al. (2011b), Mahian et al. (2013), and Kasaeian et al. (2015) worked to enhance the thermophysical properties as well as heat transfer capacity of the fluids using NPs. The study of these flows through stretching surfaces got motivation from the perspective of its application, particularly in plastic film drawing. Hence, several researchers paid a lot of attention to this issue and studied the movement of boundary layers over different forms of stretching surfaces. Akbar et al. (2014) used a homogeneous model to study NFF at stagnation point above a stretching plate with slip boundary conditions. Analysis of pulsatile flow in a constricted channel under the impact of magnetic field was presented by Bandyopadhyay and Layek (2011) and Bandyopadhyay and Layek (2012). Nasir et al. (2019) explained the Darcy–Forchheimer 2D thin-film fluid of NF. Mustafa et al. (2011) considered the NFF at the stagnation point above a stretching sheet. Wong and Leon (2010) reported that the thermophysical properties of fluids are improved significantly, even at moderate NP concentrations. Haq et al. (2016) investigated the fully developed flow of water-functionalized magnetite NPs among two parallel disks by taking water as the base fluid. The peristaltic flow of incompressible viscous fluid having metallic NPs was examined by Akbar (2014) via an irregular duct. Aly (2020) explained a non-homogeneous two-phase model for Al_2O_3 –water NF-filled annulus used for the simulation of an incompressible smoothed particle hydrodynamic system (ISPH) between a wavelength rectangle and the square cavity. Two-dimensional Fe_3O_4 –water NF under the combined impact of Lorentz and Kelvin forces was inspected by Sheikholeslami et al. (2017a). Said et al. (2015) analyzed the influence of short suspended SWCNT thermophysical properties in water and enhanced the thermal productivity of a flat plate solar collector. Sheikholeslami and Ganji (2013) explained the $Cu-H_2O$ NFF between parallel plates. Yang et al. (2020)

explained air purification with total heat recovery using NFs for the first time, demonstrating the synergistic application of NFs for heat, mass transfer, photocatalysis, and sterilization.

In the magnetohydrodynamic (MHD) flow, the magnetic area induces an electric current in a moving conductive fluid. The induced current causes force on conductive fluid ions. Natural convection under the impact of the magnetic field remained a topic of great interest because of its comprehensive applications in the design of liquid-metal cooling systems, accelerators, and pumps, as well as MHD generators and flow meters (Cha et al., 2002). In a single constricted channel, Ali et al. (2020) investigated the steady and pulsatile modes of non-Newtonian MHD Casson fluid. Sheikholeslami (2017a) researched the hydrothermal study of MHD nanofluid in an open porous cavity by using the Lattice–Boltzmann method with the Brownian motion impact on NF properties. Shah et al. (2019) addressed the idea of the electrical MHD rotational flow of SWCNTs and MWCNTs for engine oils. Sheikholeslami et al. (2017b) researched the forced convection of MHD NFF. They considered the power of Brownian motion for modeling NF. Haq et al. (2017) supposed the heat transfer efficiency of engine oil between two dispersed cylinders with MHD effects in the presence of both SWCNTs and MWCNTs, to monitor the spontaneous motion of the NPs. There are several studies, as well, regarding MHD NF flow problems past a plate/sheet under various physical conditions and objectives (Narayana and Venkateswarlu, 2016; Babu et al., 2018; Tarakaramu et al., 2019; Devaki et al., 2020; Tarakaramu et al., 2020; Venkateswarlu and Narayana, 2021; Alzahrani et al., 2022; Mahmood et al., 2022; Puneeth et al., 2022; Qi et al., 2022; Ramadan et al., 2022; Tlili and Alharbi, 2022; Tlili et al., 2022).

Kakarantzas et al. (2009) investigated the natural convection of MHD at the sinusoidal upper wall temperature in a vertical cylindrical cavity. Rashidi et al. (2016) examined the convective heat transfer of MHD NFF in a vertical channel with sinusoidal walls. Sheikholeslami (2017b) tested the Buongiorno model to investigate the melting heat transfer of NFF due to the magnetic field. The impacts of heat and mass transfer of NFF flow over a vertical infinite flat plate were investigated by Turkyilmazoglu and Pop (2013). They derived the exact analytical solutions for various water-based NFs containing Cu , Ag , CuO , Al_2O_3 , and TiO_2 . Pakdaman et al. (2012) explored the thermophysical properties and overall efficiency of MWCNT NFs flowing within vertical helically coiled tubes. In the occurrence of a non-uniform magnetic field, Sheikholeslami et al. (2015) explored the transport of forced convection heat within a lid-driven semi-annulus enclosure filled with Fe_3O_4 –water NF. Using a continuously stretching porous layer, Gopal et al. (2021) investigated the thermo-physical properties characteristics of complex order chemical processing and viscous dissipation on NF. Two space coordinates are used to model the porous medium, laminar, time-invariant, and MHD incompressible Newtonian NF. The role of heat source and Soret

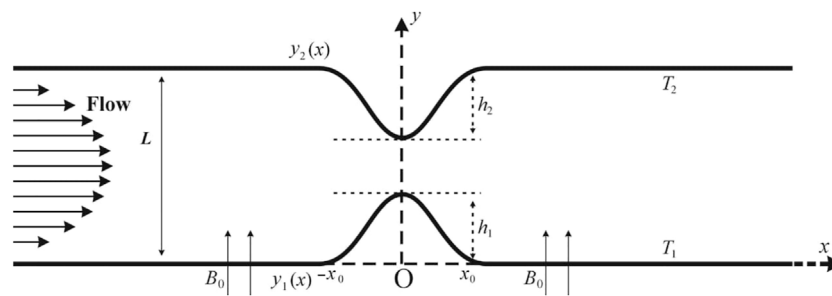


FIGURE 1
The channel geometry with a constriction on each wall. The walls are defined by.

TABLE 1 Thermophysical properties of different NPs and the base fluid.

| Physical properties | Base Fluid H_2O | Cu | Ag | Fe_3O_4 | TiO_2 | $SWCNT$ |
|-----------------------------|----------------------|------|--------|-----------|---------|---------|
| c_p (J/kg K) | 4076.4 | 385 | 235 | 670 | 686.2 | 600 |
| ρ (Kg/m ³) | 997.8 | 8933 | 10,500 | 5180 | 4250 | 2100 |
| K (W/m K) | 0.60475 | 401 | 429 | 9.7 | 8.9538 | 3500 |

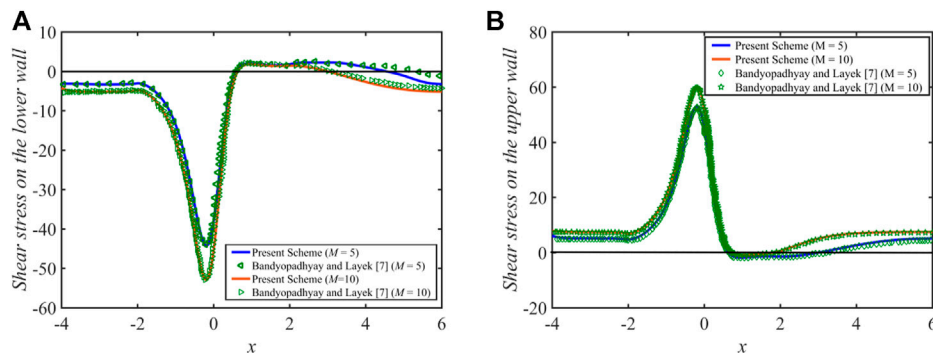


FIGURE 2
WSS distribution for the pulsatile flow, for $M = 5, 10$, at $Re = 700$, $h_1 = h_2 = 0.35$, $St = 0.02$, and $t = 0.25$.

impacts on MHD convective Ferro-NF (Fe_3O_4 -water) flow across an inclined channel with a porous media were examined by Sabu et al. (2021). The heat transfer of NFF from an inclined channel in the occurrence of a magnetic field, heat flux, and mass diffusion was explored using the FDM by Kumar et al. (2021).

Krishna et al. (2021a) and Krishna et al., (2021b) investigated the radiative MHD flow of an incompressible viscous electrically conducting non-Newtonian Casson hybrid NF over vertical moving porous surface under the influence of slip velocity in a rotating frame. Kavya et al. (2022) explore the varying fluid

momentum and thermal energy characteristics of the laminar, steady, incompressible, 2D, non-Newtonian pseudo-plastic Williamson hybrid NF over a stretching cylinder with MHD effects.

Shah et al. (2022) determined the heat transfer properties of a MHD Prandtl hybrid NF over a stretched surface in the presence of bioconvection and chemical reaction effects. Zhang et al. (2022) presented the solar source, although it can reduce energy consumption (EC) for buildings on cold days; in the summer, its presence on the envelopes intensifies EC. Gao et al. (2022) examined the hydrodynamic and thermal performances

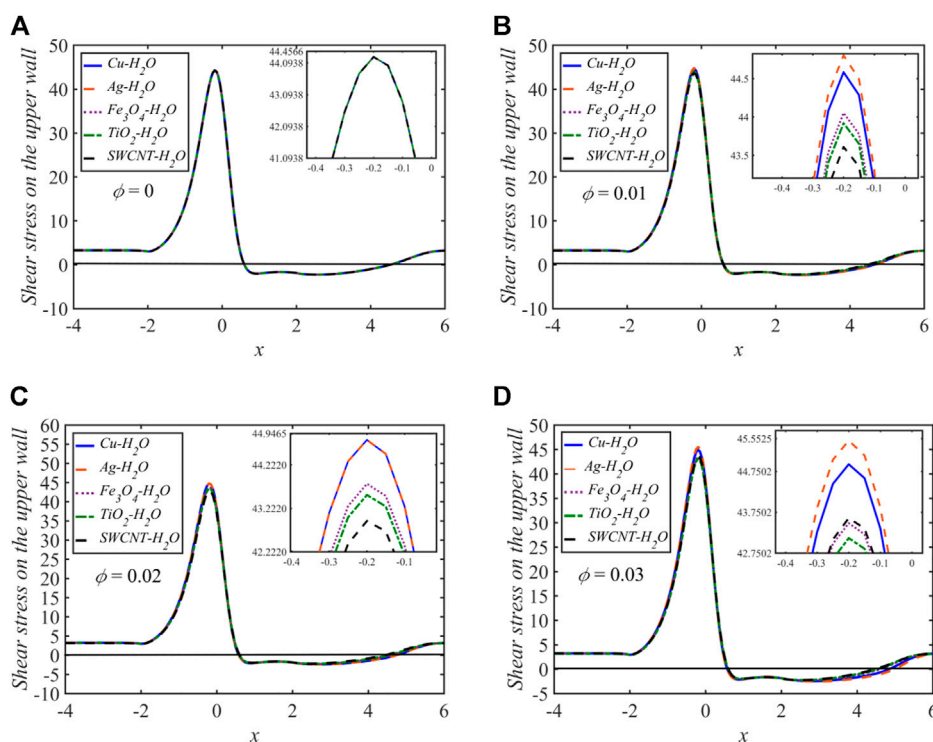


FIGURE 3
The WSS distribution for distinct values of ϕ for the five NFs at $t = 0.25$.

of liquid water in the attendance of two carbon structures by molecular dynamics simulation (MDS). Nayak et al. (2022) conducted a numerical treatment on flow and heat transfer of radiative hybrid NF past an isothermal stretched cylinder set in a porous medium.

The goal of the present work is to numerically investigate the heat transfer characteristics of pulsatile viscous MHD NFF in a constricted channel. The study is conducted for five different nano-impurities (Cu, Fe₃O₄, Ag, TiO₂, and SWCNT), which have been chosen for the preparation of NFs. The mathematical analysis is done using the transformation of the vorticity-stream function, and numerical computations are made using FDM. The impact of the flow controlling parameters (M , St , Pr , Rd) on the flow profiles of the five NFs, as well as on the skin-friction and Nusselt number profiles, are also observed. The objective is to examine the cumulative impact of the applied magnetic field and thermal radiation on the wall shear stress (WSS), velocity, and temperature profiles in 2D. The Newtonian pulsatile NF flows help in understanding the influence of various metallic NPs homogeneously suspended in the blood, which is driven by drug trafficking (pharmacology) applications.

The following is how the article's next section is organized. Section 2 defines the mathematical model and transformation. The outcomes and relevant discussions are presented in Section 3. The final remarks are eventually presented in Section 4.

2 Mathematical model

We are working at an incompressible electrically conducting NF flowing via a rectangular channel that should be laminar at Reynolds number 700. The channel walls have a pair of symmetrical constrictions. The resulting electric field \mathbf{J} is normal, and the direction of \mathbf{B} is perpendicular to the plane of flow. We take a Cartesian coordinate system (x, y) in which the flow direction and the direction of \mathbf{B} are, respectively, along the \tilde{x} -axis and \tilde{y} -axis. Because the magnetic Reynolds number (Re_m) for the flow is so small, the induced electric can be deemed insignificant. In the transformed coordinate system (to be discussed later on), as illustrated in Figure 1, the constrictions span from $x = -x_0$ to $x = x_0$, with the center at $x = 0$

$$y_1(x) = \begin{cases} \frac{h_1}{2} \left[1 + \cos\left(\frac{\pi x}{x_0}\right) \right], & |x| \leq x_0 \\ 0, & |x| > x_0 \end{cases}$$

$$y_2(x) = \begin{cases} 1 - \frac{h_2}{2} \left[1 + \cos\left(\frac{\pi x}{x_0}\right) \right], & |x| \leq x_0 \\ 1, & |x| > x_0 \end{cases} \quad (1)$$

where $y = y_1(x)$ and $y = y_2(x)$ symbolize the lower and upper walls, respectively, and h_1 and h_2 are the heights of the

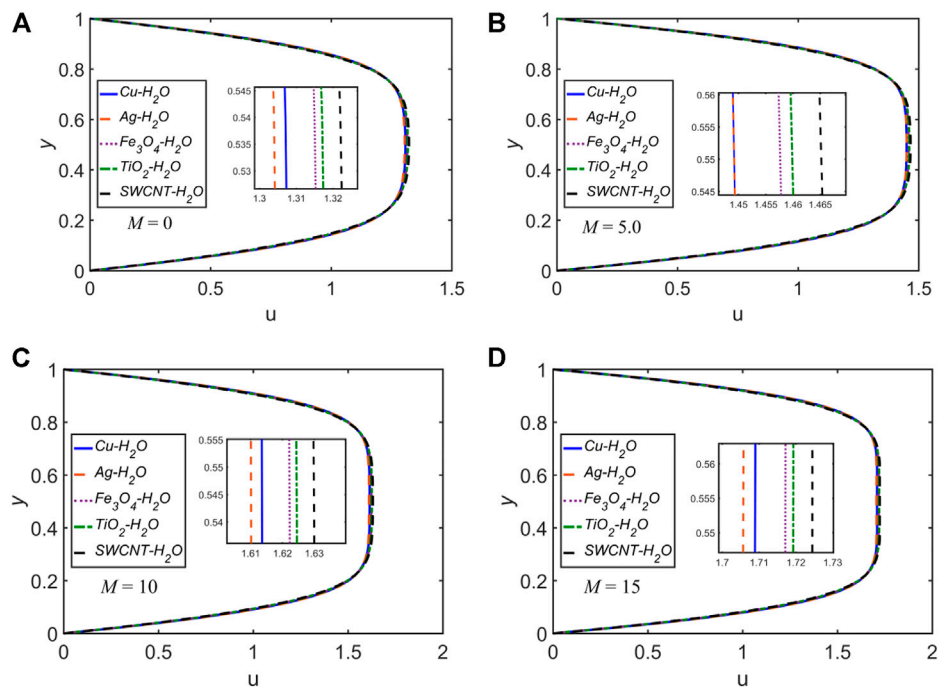


FIGURE 4

The velocity profile u versus y at $x = 0$ and $t = 0.25$ for the five NFs for distinct values of M .

constrictions at the lower and upper walls, respectively (Bandyopadhyay and Layek, 2012; Ali et al., 2020).

The flow phenomenon is represented by the unsteady incompressible viscous flow equations as follows.

The continuity equation:

$$\frac{\partial \tilde{u}}{\partial \tilde{x}} + \frac{\partial \tilde{v}}{\partial \tilde{y}} = 0. \quad (2)$$

The momentum equation:

$$\frac{\partial \tilde{u}}{\partial \tilde{t}} + \tilde{u} \frac{\partial \tilde{u}}{\partial \tilde{x}} + \tilde{v} \frac{\partial \tilde{u}}{\partial \tilde{y}} = -\frac{1}{\rho_{nf}} \frac{\partial \tilde{p}}{\partial \tilde{x}} + \frac{\mu_{nf}}{\rho_{nf}} \nabla^2 \tilde{u} + \frac{1}{\rho_{nf}} (\mathbf{J} \times \mathbf{B})_x, \quad (3)$$

$$\frac{\partial \tilde{v}}{\partial \tilde{t}} + \tilde{u} \frac{\partial \tilde{v}}{\partial \tilde{x}} + \tilde{v} \frac{\partial \tilde{v}}{\partial \tilde{y}} = -\frac{1}{\rho_{nf}} \frac{\partial \tilde{p}}{\partial \tilde{y}} + \frac{\mu_{nf}}{\rho_{nf}} \nabla^2 \tilde{v}. \quad (4)$$

The energy equation:

$$\frac{\partial \tilde{T}}{\partial \tilde{t}} + \tilde{u} \frac{\partial \tilde{T}}{\partial \tilde{x}} + \tilde{v} \frac{\partial \tilde{T}}{\partial \tilde{y}} = \frac{k_{nf}}{(\rho C_p)_{nf}} \nabla^2 \tilde{T} - \frac{1}{(\rho C_p)_{nf}} \frac{\partial q}{\partial \tilde{y}}, \quad (5)$$

where $q = -\left(\frac{4\sigma}{3k^*} 4T_\infty^3 \frac{\partial \tilde{T}}{\partial \tilde{y}}\right)$ is the radiative heat flux. We get by expanding \tilde{T}^4 about T_∞ and omitting higher-order terms

$$\tilde{T}^4 \cong 4T_\infty^3 \tilde{T} - 3T_\infty^4$$

$$\text{Then, } q = -\left(\frac{4\sigma}{3k^*} 4T_\infty^3 \frac{\partial \tilde{T}}{\partial \tilde{y}}\right) \text{ and } \frac{\partial q}{\partial \tilde{y}} = -\left(\frac{16\sigma}{3k^*} T_\infty^3 \frac{\partial^2 \tilde{T}}{\partial \tilde{y}^2}\right).$$

Eq. 5 becomes

$$\frac{\partial \tilde{T}}{\partial \tilde{t}} + \tilde{u} \frac{\partial \tilde{T}}{\partial \tilde{x}} + \tilde{v} \frac{\partial \tilde{T}}{\partial \tilde{y}} = \frac{k_{nf}}{(\rho C_p)_{nf}} \left(\frac{\partial^2 \tilde{T}}{\partial \tilde{x}^2} + \frac{\partial^2 \tilde{T}}{\partial \tilde{y}^2} \right) + \frac{16\sigma T_\infty^3}{3k^* (\rho C_p)_{nf}} \frac{\partial^2 \tilde{T}}{\partial \tilde{y}^2}, \quad (6)$$

where \tilde{u} (along \tilde{x} -axis) and \tilde{v} (along \tilde{y} -axis) show the velocity components and the subscript “nf” represents the nanofluid, \tilde{p} symbolizes the pressure, ρ symbolizes the density, U symbolizes the characteristic flow velocity, ν symbolizes the kinematic viscosity, and \tilde{T} symbolizes the temperature. k symbolizes the thermal conductivity, C_p symbolizes the specific heat, $\mathbf{J} \equiv (J_x, J_y, J_z)$ symbolizes current density, $\mathbf{B} \equiv (0, B_0, 0)$ symbolizes the magnetic field, B_0 symbolizes the strength of the uniform magnetic field, σ symbolizes electric conductivity, and μ_m symbolizes the magnetic permeability of the medium. As the electric current direction is normal to the channel plane, therefore $\mathbf{E} \equiv (0, 0, E_z)$. Ohm’s law gives

$$J_x = 0, J_y = 0, J_z = \sigma_f (E_z + \tilde{u} B_0). \quad (7)$$

Maxwell’s equation $\nabla \times \mathbf{E} = 0 \Rightarrow E_z = C$ (constant) for the steady flow. For the present study, E_z is assumed to be zero. Then, Eq. 7 gives $J_z = \sigma_f \tilde{u} B_0$. Therefore, $\mathbf{J} \times \mathbf{B} = -\sigma_f \tilde{u} B_0^2$. Hence, Eq. 3 becomes

$$\frac{\partial \tilde{u}}{\partial \tilde{t}} + \tilde{u} \frac{\partial \tilde{u}}{\partial \tilde{x}} + \tilde{v} \frac{\partial \tilde{u}}{\partial \tilde{y}} = -\frac{1}{\rho_{nf}} \frac{\partial \tilde{p}}{\partial \tilde{x}} + \frac{\mu_{nf}}{\rho_{nf}} \nabla^2 \tilde{u} - \frac{1}{\rho_{nf}} \sigma_f \tilde{u} B_0^2. \quad (8)$$

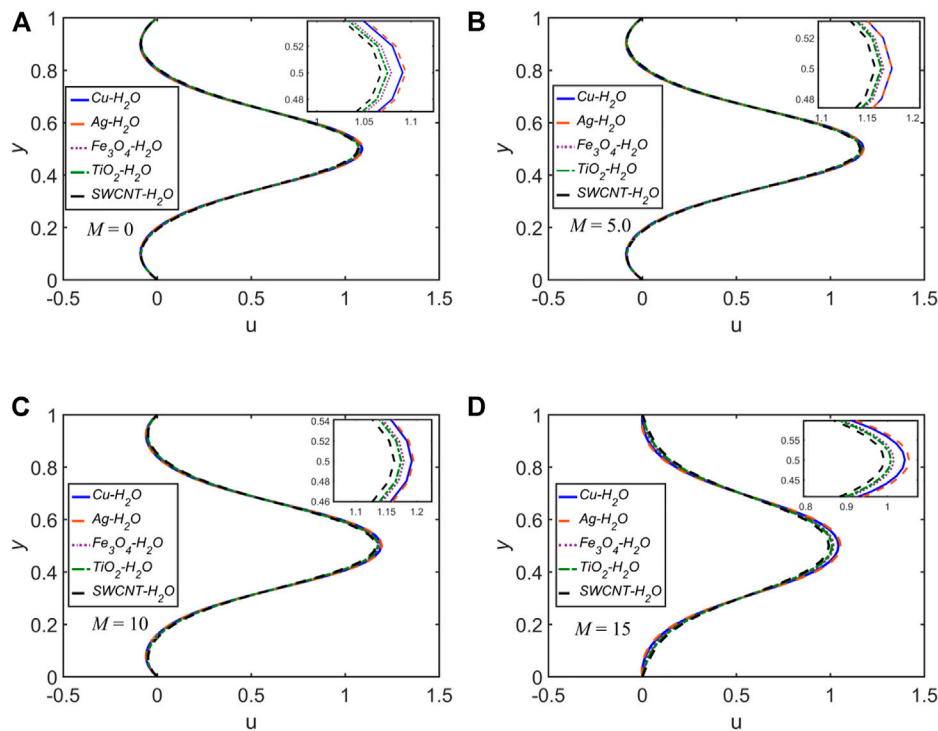


FIGURE 5

The velocity profile u versus y at $x = 2$ and $t = 0.25$ for the five NFs for distinct values of M .

The dimensionless version of the governing model is created by considering the following quantities:

$$x = \frac{\tilde{x}}{L}, \quad y = \frac{\tilde{y}}{L}, \quad u = \frac{\tilde{u}}{U}, \quad v = \frac{\tilde{v}}{U}, \quad t = \frac{\tilde{t}}{T},$$

$$\theta = \frac{\tilde{T} - T_2}{T_1 - T_2}, \quad P = \frac{\tilde{p}}{\rho_f U^2}, \quad Re = \frac{\rho_f U L}{\mu_f}, \quad St = \frac{L}{UT}, \quad M = B_0 L \sqrt{\frac{\sigma_f}{\rho_f \nu_f}}, \quad Pr = \frac{\mu_f C_{p,f}}{k_f}, \quad Rd = \frac{16\sigma T_\infty^3}{3k^* k_f} \quad (9)$$

Here, L symbolizes the maximum width of the channel, U symbolizes the characteristic flow velocity, T symbolizes the period of the pulse, Re symbolizes the Reynolds number, St symbolizes the Strouhal number, M symbolizes the Hartmann number, Pr symbolizes the Prandtl number, and Rd symbolizes the radiation parameter.

The effective dynamic viscosity μ_{nf} , effective density ρ_{nf} , heat capacitance $(\rho C_p)_{nf}$, and effective thermal conductivity k_{nf} of a NF are given as:

$$\mu_{nf} = \frac{\mu_f}{(1-\phi)^{2.5}}$$

$$\rho_{nf} = (1-\phi)\rho_f + \phi\rho_s$$

$$(\rho C_p)_{nf} = (1-\phi)(\rho C_p)_f + \phi(\rho C_p)_s$$

$$\frac{k_{nf}}{k_f} = \frac{k_s + 2k_f - 2\phi(k_f - k_s)}{k_s + 2k_f + 2\phi(k_f - k_s)} \quad (10)$$

where ϕ symbolizes the volume fraction of NF, and the subscripts nf correspond to NF, f corresponds to the pure fluid, and s corresponds to the solid state. For the present work, the following five different NFs are considered: $Cu-H_2O$, $Fe_3O_4-H_2O$, $Ag-H_2O$, TiO_2-H_2O , and $SWCNT-H_2O$. The thermophysical properties of the five different NPs and water are shown in Table 1 (Sheikholeslami and Ganji, 2013; Sheikholeslami et al., 2017a). Using the quantities from Eqs 9, 10 in Eqs 2–4, 6 gives

$$\frac{\partial u}{\partial x} + \frac{\partial u}{\partial y} = 0 \quad (11)$$

$$St \frac{\partial u}{\partial t} + u \frac{\partial u}{\partial x} + v \frac{\partial u}{\partial y} = -\frac{1}{\varnothing_1} \frac{\partial p}{\partial x} + \frac{1}{Re \varnothing_3} \nabla^2 u - \frac{1}{\varnothing_1} \frac{M^2}{Re} u \quad (12)$$

$$St \frac{\partial v}{\partial t} + u \frac{\partial v}{\partial x} + v \frac{\partial v}{\partial y} = -\frac{1}{\varnothing_1} \frac{\partial p}{\partial y} + \frac{1}{Re \varnothing_3} \nabla^2 v \quad (13)$$

$$St \frac{\partial \theta}{\partial t} + u \frac{\partial \theta}{\partial x} + v \frac{\partial \theta}{\partial y} = \frac{1}{Pr Re} \frac{\varnothing_5}{\varnothing_4} \left(\frac{\partial^2 \theta}{\partial x^2} + \left(1 + \frac{Rd}{\varnothing_5} \right) \frac{\partial^2 \theta}{\partial y^2} \right) \quad (14)$$

where $\varnothing_1 = 1 - \phi + \frac{\rho_s}{\rho_f} \phi$, $\varnothing_2 = \frac{1}{(1-\phi)^{2.5}}$, $\varnothing_3 = (1-\phi)^{2.5} (1 - \phi + \frac{\rho_s}{\rho_f} \phi)$, $\varnothing_4 = 1 - \phi + \frac{(\rho C_p)_s}{(\rho C_p)_f} \phi$, $\varnothing_5 = \frac{k_{nf}}{k_f}$.

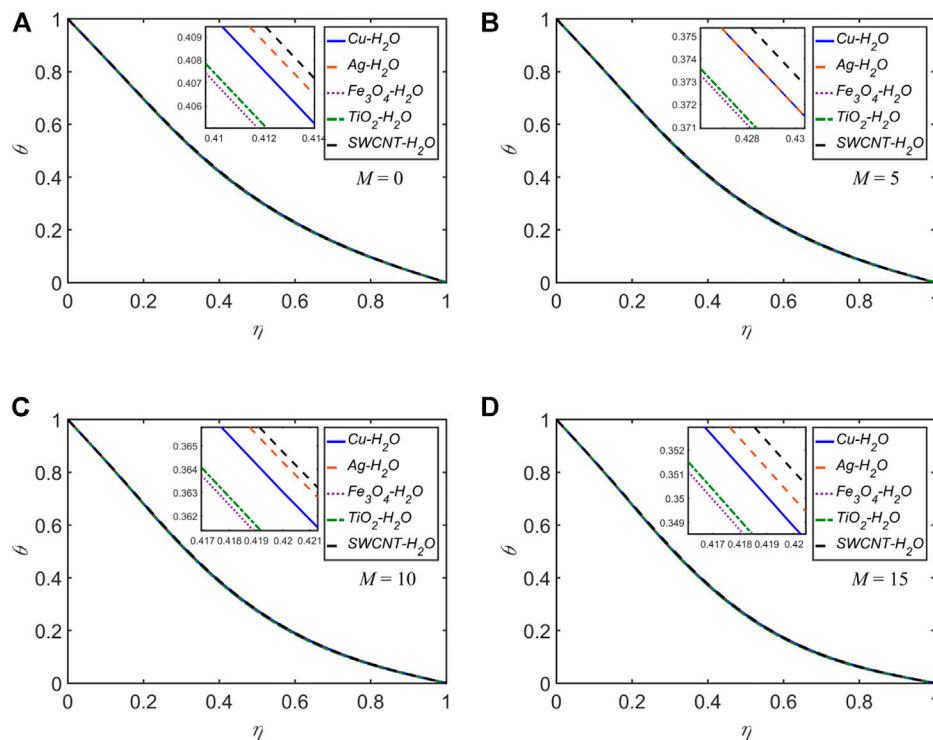


FIGURE 6

The temperature profile θ versus η at $x = 0$ and $t = 0.25$ for the five NFs for distinct values of M .

2.1 Boundary conditions

For the steady case of the flow problem under consideration, the boundary conditions, obtained by solving the dimensionless form of Eq. 8 and performing some manipulations using Eq. 10, are given as follows:

$$u(y) = \left[\frac{\cosh\left(\frac{M}{2}\right) \left[\cosh\left(\frac{M}{2\sqrt{\phi_2}}\right) - \cosh\left(\frac{M}{\sqrt{\phi_2}}\left(y - \frac{1}{2}\right)\right) \right]}{8\sinh^2\left(\frac{M}{4}\right)\cosh\left(\frac{M}{2\sqrt{\phi_2}}\right)} \right] \quad (15)$$

$v = 0, M \neq 0.$

When $M = 0$, the u -velocity at the inlet takes the form:

$$u(y) = y - y^2, v = 0. \quad (16)$$

The flow is classified as sinusoidal for the pulsatile flow:

$$u(y, t) = u(y)[1 + \sin(2\pi t)], v = 0. \quad (17)$$

Furthermore, $u = 0$ and $v = 0$ (i.e., no-slip conditions) are assumed on the walls. For the outlet boundary, the fully developed flow conditions are incorporated. In the dimensionless form, the temperature condition at the lower wall, $\theta = 1$, and at the upper wall, $\theta = 0$.

2.2 Vorticity-stream function formulation

$$u = \frac{\partial \psi}{\partial y}, v = -\frac{\partial \psi}{\partial x}, \omega = \frac{\partial v}{\partial x} - \frac{\partial u}{\partial y} \quad (18)$$

We differentiate Eqs 12, 13 with respect to y and x , respectively. Then, from their subtraction and using Eq. 18, we get transformed equations from the variables (u, v) to vorticity-stream functions (ψ, ω) as follows:

$$\begin{aligned} St \frac{\partial}{\partial t} \left(\frac{\partial v}{\partial x} - \frac{\partial u}{\partial y} \right) + u \frac{\partial}{\partial x} \left(\frac{\partial v}{\partial x} - \frac{\partial u}{\partial y} \right) + v \frac{\partial}{\partial y} \left(\frac{\partial v}{\partial x} - \frac{\partial u}{\partial y} \right) \\ = \frac{1}{Re\phi_3} \left[\frac{\partial^2}{\partial x^2} \left(\frac{\partial v}{\partial x} - \frac{\partial u}{\partial y} \right) + \frac{\partial^2}{\partial y^2} \left(\frac{\partial v}{\partial x} - \frac{\partial u}{\partial y} \right) \right] + \frac{1}{\phi_1} \frac{M^2}{Re} \frac{\partial u}{\partial y}, \\ St \frac{\partial \omega}{\partial t} + \frac{\partial \psi}{\partial y} \frac{\partial \omega}{\partial x} - \frac{\partial \psi}{\partial x} \frac{\partial \omega}{\partial y} = \frac{1}{\phi_3} \frac{1}{Re} \left[\frac{\partial^2 \omega}{\partial x^2} + \frac{\partial^2 \omega}{\partial y^2} \right] + \frac{1}{\phi_1} \frac{M^2}{Re} \frac{\partial^2 \psi}{\partial y^2} \end{aligned} \quad (19)$$

And the stream function ψ equation (Poisson equation) is given as

$$\frac{\partial^2 \psi}{\partial x^2} + \frac{\partial^2 \psi}{\partial y^2} = -\omega. \quad (20)$$

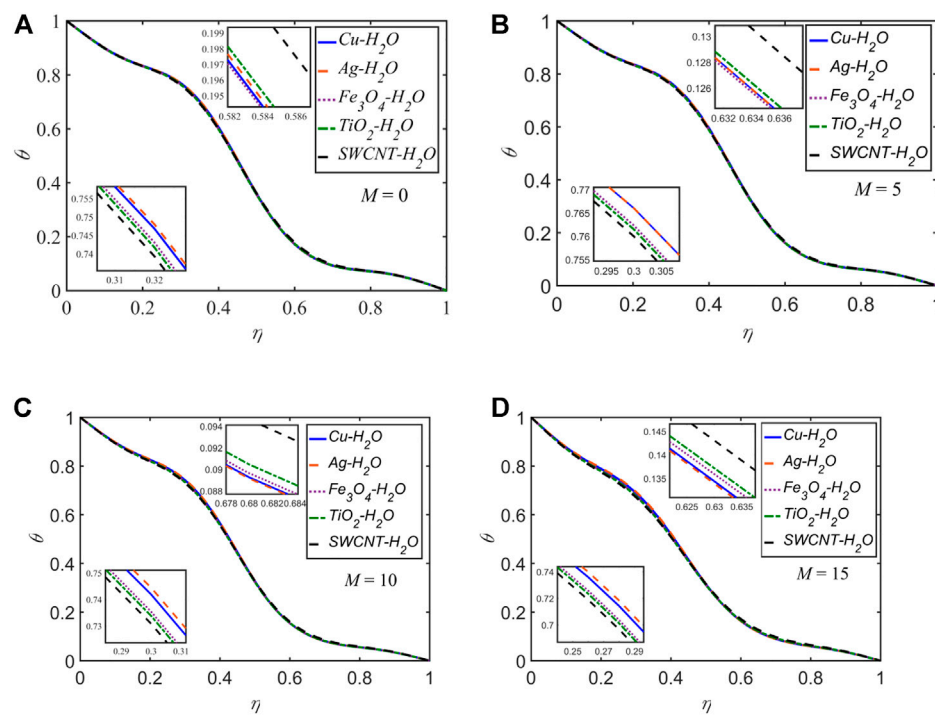


FIGURE 7

The temperature profile θ versus η at $x = 2$ and $t = 0.25$ for the five NFs for distinct values of M .

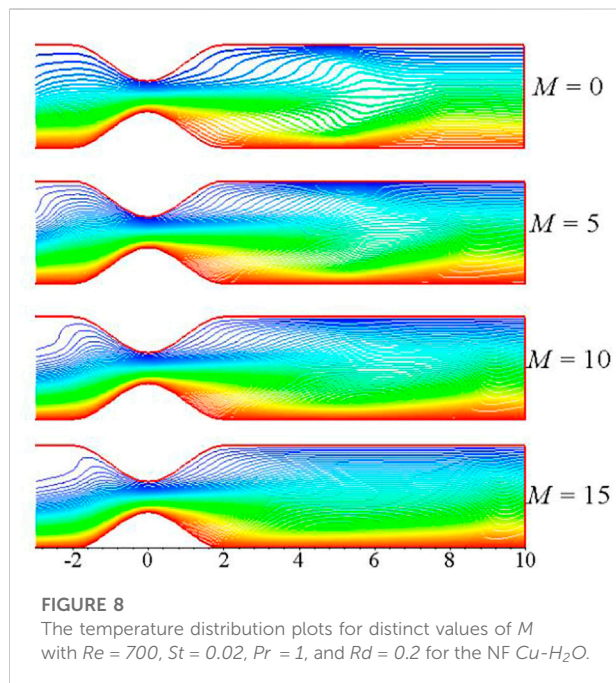


FIGURE 8

The temperature distribution plots for distinct values of M with $Re = 700$, $St = 0.02$, $Pr = 1$, and $Rd = 0.2$ for the NF $Cu-H_2O$.

2.3 Transformation of coordinates

For treating the channel walls as the straighten ones, the coordinates are transformed as

$$\xi = x, \eta = \frac{y - y_1(x)}{y_2(x) - y_1(x)} \quad (21)$$

Thus, the lower wall symbolizes by $\eta = 0$ and the upper wall symbolizes by $\eta = 1$. In the updated coordinate system (ξ, η) , Eqs 14, 19, 20 are

$$St \frac{\partial \omega}{\partial t} + u \left(\frac{\partial \omega}{\partial \xi} - Q \frac{\partial \omega}{\partial \eta} \right) + \nu D \frac{\partial \omega}{\partial \eta} = \frac{1}{\varnothing_3} \frac{1}{Re} \left[\frac{\partial^2 \omega}{\partial \xi^2} - (P - 2QR) \frac{\partial \omega}{\partial \eta} - 2Q \frac{\partial^2 \omega}{\partial \xi \partial \eta} + (Q^2 + D^2) \frac{\partial^2 \omega}{\partial \eta^2} \right] + \frac{1}{\varnothing_1} \frac{M^2}{Re} D^2 \frac{\partial^2 \psi}{\partial \eta^2}, \quad (22)$$

$$\frac{\partial^2 \psi}{\partial \xi^2} - (P - 2QR) \frac{\partial \psi}{\partial \eta} - 2Q \frac{\partial^2 \psi}{\partial \xi \partial \eta} + (Q^2 + D^2) \frac{\partial^2 \psi}{\partial \eta^2} = -\omega, \quad (23)$$

$$St \frac{\partial \theta}{\partial t} + u \left(\frac{\partial \theta}{\partial \xi} - Q \frac{\partial \theta}{\partial \eta} \right) + \nu D \frac{\partial \theta}{\partial \eta}$$

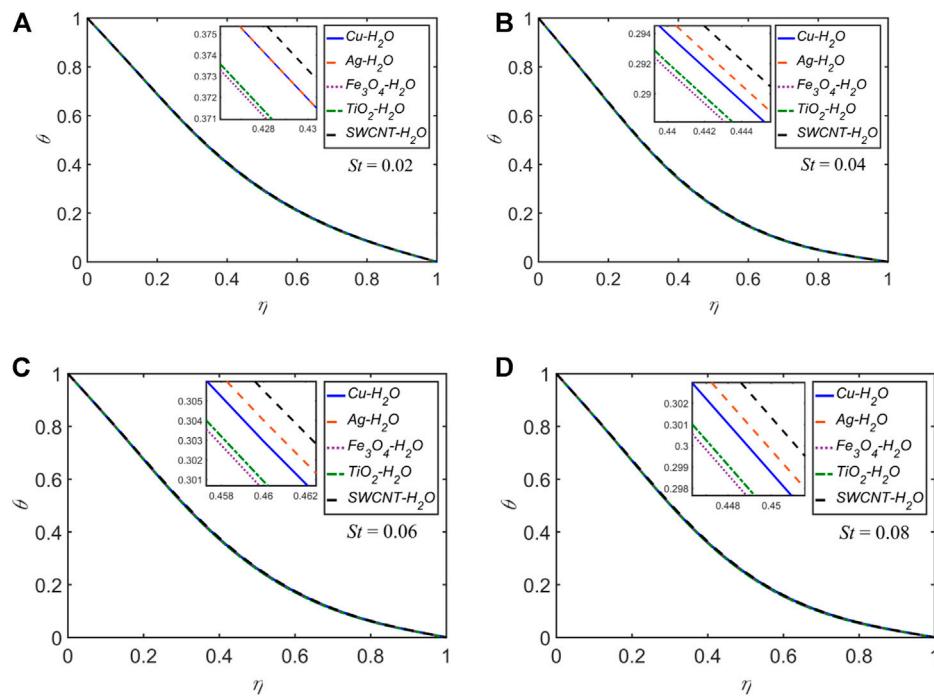


FIGURE 9

The temperature profile θ versus η at $x=0$ and $t=0.25$ for the five NFs for distinct values of St .

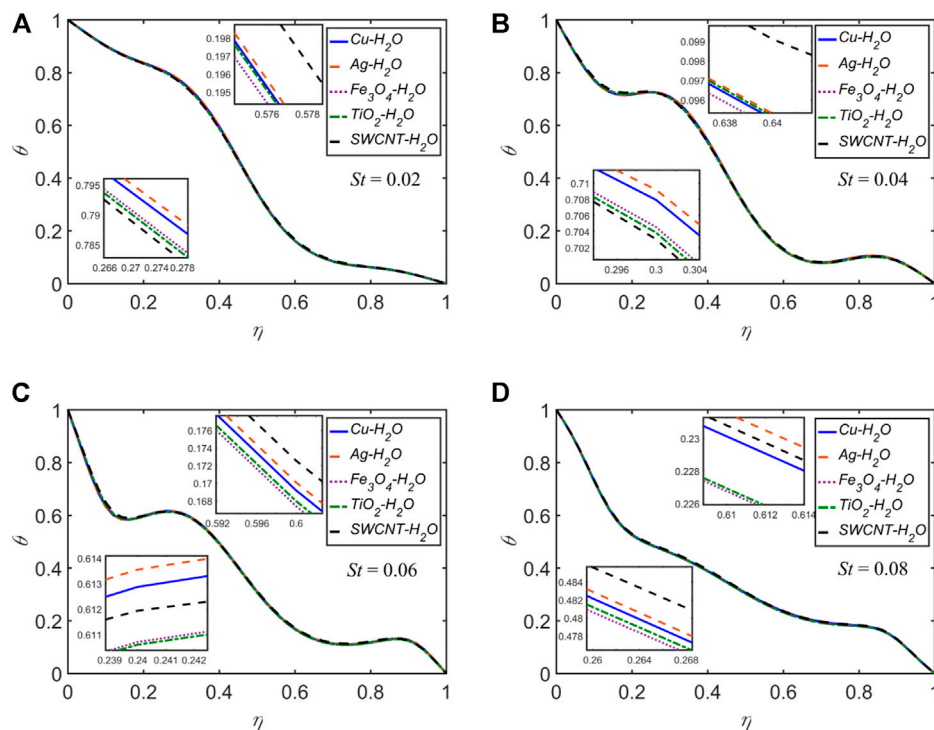


FIGURE 10

The temperature profile θ versus η at $x=2$ and $t=0.25$ for the five NFs for distinct values of St .

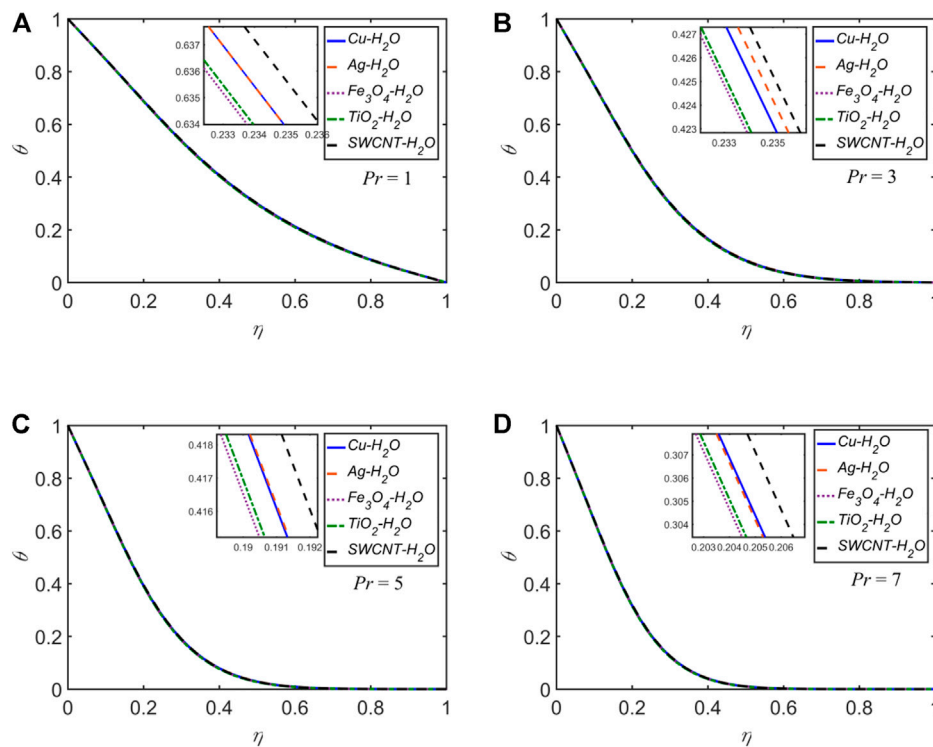


FIGURE 11

The temperature profile θ versus η at $x = 0$ and $t = 0.25$ for the five NFs for distinct values of Pr .

$$= \frac{1}{RePr} \frac{\partial^2 \theta}{\partial \xi^2} - (P - 2QR) \frac{\partial \theta}{\partial \eta} - 2Q \frac{\partial^2 \theta}{\partial \xi \partial \eta} + \left(Q^2 + \left(1 + \frac{Rd}{\partial_5} \right) D^2 \right) \frac{\partial^2 \theta}{\partial \eta^2}, \quad (24)$$

where

$$P = P(\xi, \eta) = \frac{\eta y_2''(\xi) + (1 - \eta) y_1''(\xi)}{y_2(\xi) - y_1(\xi)},$$

$$Q = Q(\xi, \eta) = \frac{\eta y_2'(\xi) + (1 - \eta) y_1'(\xi)}{y_2(\xi) - y_1(\xi)}, R = R(\xi) = \frac{y_2'(\xi) - y_1'(\xi)}{y_2(\xi) - y_1(\xi)}, D = D(\xi) = \frac{1}{y_2(\xi) - y_1(\xi)}. \quad (25)$$

The velocity components u and v in terms of (ξ, η) take the forms

$$u = D(\xi) \frac{\partial \psi}{\partial \eta}, v = Q(\xi, \eta) \frac{\partial \psi}{\partial \eta} - \frac{\partial \psi}{\partial \xi} \quad (26)$$

Furthermore, the wall boundary conditions in (ξ, η) system for ψ and ω are given by

$$\psi(\eta, t) = \left[\frac{\sqrt{\partial_2} \cosh\left(\frac{M}{2}\right) \tanh\left(\frac{M}{2\sqrt{\partial_2}}\right)}{8M \sinh^2\left(\frac{M}{4}\right)} \right] [1 + \epsilon \sin(2\pi t)], \text{ at } \eta = 0,$$

$$\psi(\eta, t) = \frac{M \cosh\left(\frac{M}{2}\right)}{8\sqrt{\partial_2} \sinh^2\left(\frac{M}{4}\right)} \left[1 - \frac{\sqrt{\partial_2}}{M} \tanh\left(\frac{M}{2\sqrt{\partial_2}}\right) \right] [1 + \epsilon \sin(2\pi t)], \text{ at } \eta = 1,$$

where ϵ symbolizes the pulsating amplitude. If $\epsilon = 0$, we get steady flow

$$\omega = - \left[(Q^2 + D^2) \frac{\partial^2 \psi}{\partial \eta^2} \right]_{\eta=0,1}. \quad (27)$$

The temperature's converted boundary conditions are $\theta = 1$, at $\eta = 0$; $\theta = 0$, at $\eta = 1$.

The other concerning non-dimensional physical quantities comprise the skin-friction coefficient and Nusselt number, defined by

$$C_f = \frac{\tau_w}{\rho u_w^2}, Nu = - \left(\frac{L}{k_f (T_1 - T_2)} \right) \left(k_{nf} + \frac{16\sigma T_\infty^3}{3k^*} \right) \frac{\partial \tilde{T}}{\partial \tilde{y}} \Big|_{\tilde{y}=0}$$

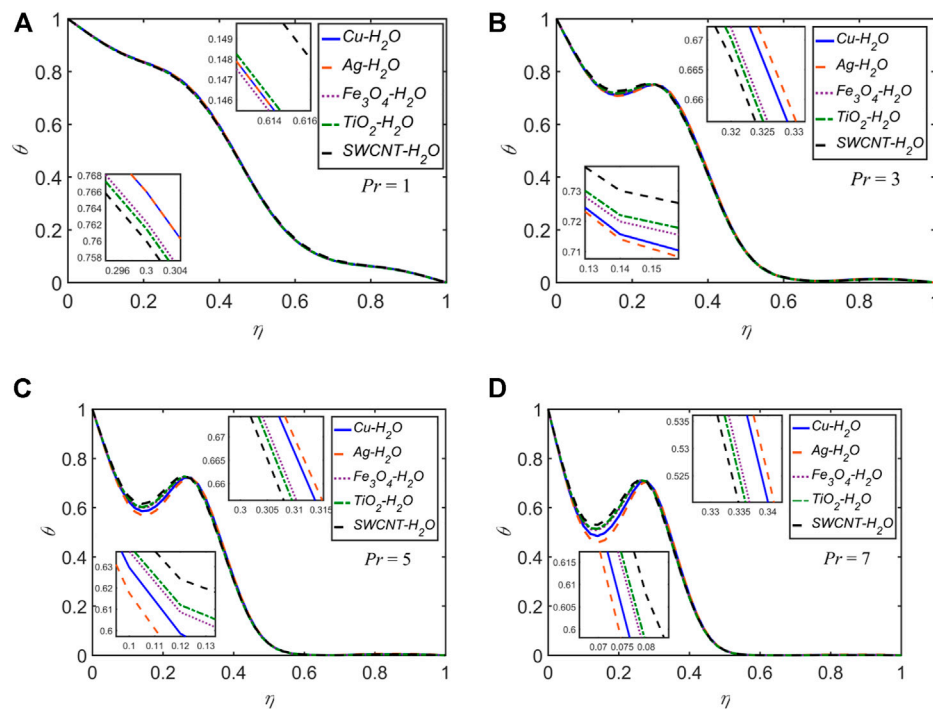


FIGURE 12

The temperature profile θ versus η at $x = 2$ and $t = 0.25$ for the five NFs for distinct values of M .

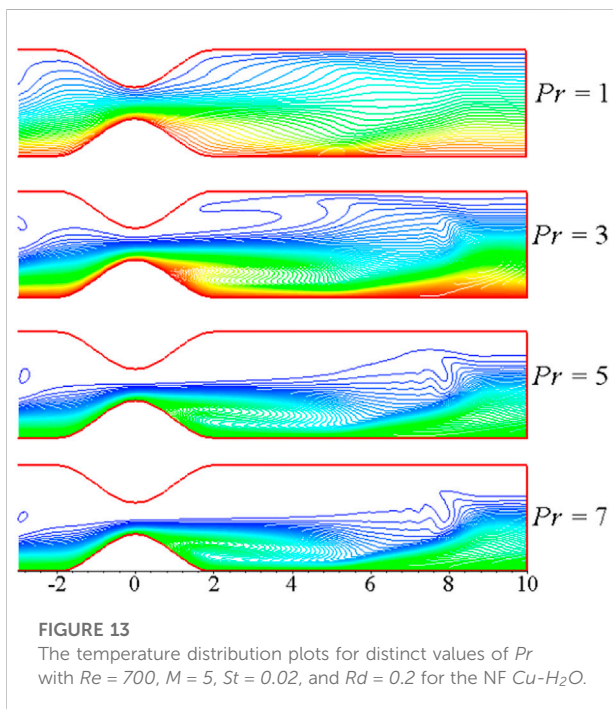


FIGURE 13

The temperature distribution plots for distinct values of Pr with $Re = 700$, $M = 5$, $St = 0.02$, and $Rd = 0.2$ for the NF $Cu-H_2O$.

where τ_w and q_w are defined as

$$\tau_w = \left[\mu_{nf} \frac{\partial \tilde{u}}{\partial \tilde{y}} \right]_{\tilde{y}=0}, \quad q_w = \left[\frac{\partial \tilde{T}}{\partial \tilde{y}} \right]_{\tilde{y}=0}$$

By using dimensionless variables from Eq. 9 and the coordinate transformation from Eq. 21, we get

$$C_f = \frac{1}{u_w^2} \left[-\frac{1}{Re\varnothing_5} D \frac{\partial u}{\partial \eta} \right]_{\eta=0}, \quad Nu = \left[-\varnothing_5 (1 + Rd) D \frac{\partial \theta}{\partial \eta} \right]_{\eta=0} \quad (28)$$

where $Rd = \frac{16\sigma T_\infty^3}{3k^*k_{nf}}$ and $\varnothing_5 = \frac{k_{nf}}{k_f}$.

3 Results and discussion

The problem Eqs 22–24 is computed using a numerical scheme based on FDM, subject to the relevant boundary conditions in Sections 2.1, 2.3. The numerical scheme adopts a standard approach, as used by Bandyopadhyay and Layek (2011), Bandyopadhyay and Layek (2012), and Ali et al. (2020). The computational domain is assumed as

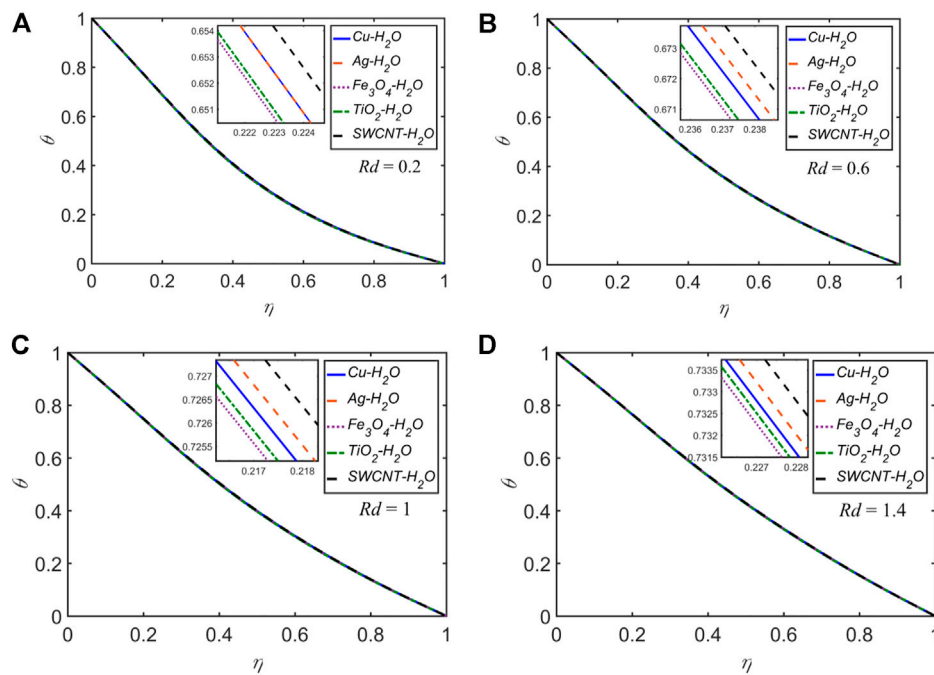


FIGURE 14

The temperature profile θ versus η at $x = 0$ and $t = 0.25$ for the five NFs for distinct values of Rd .

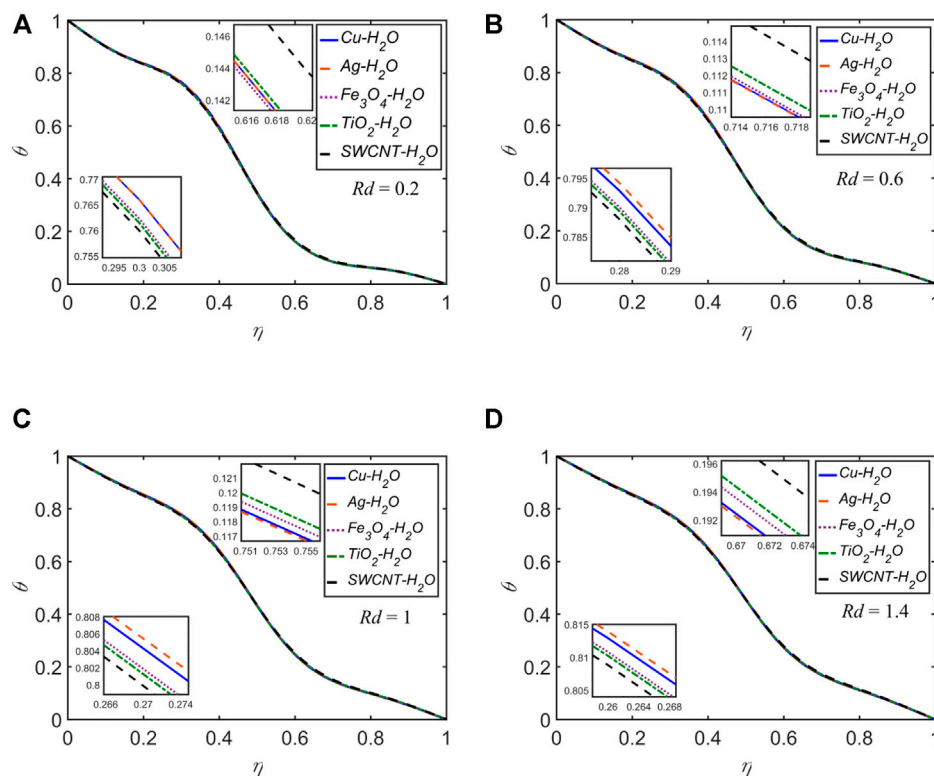
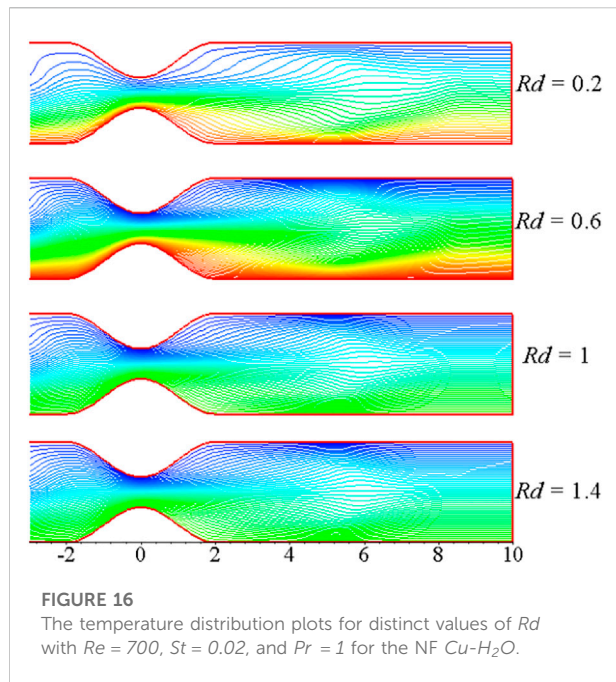


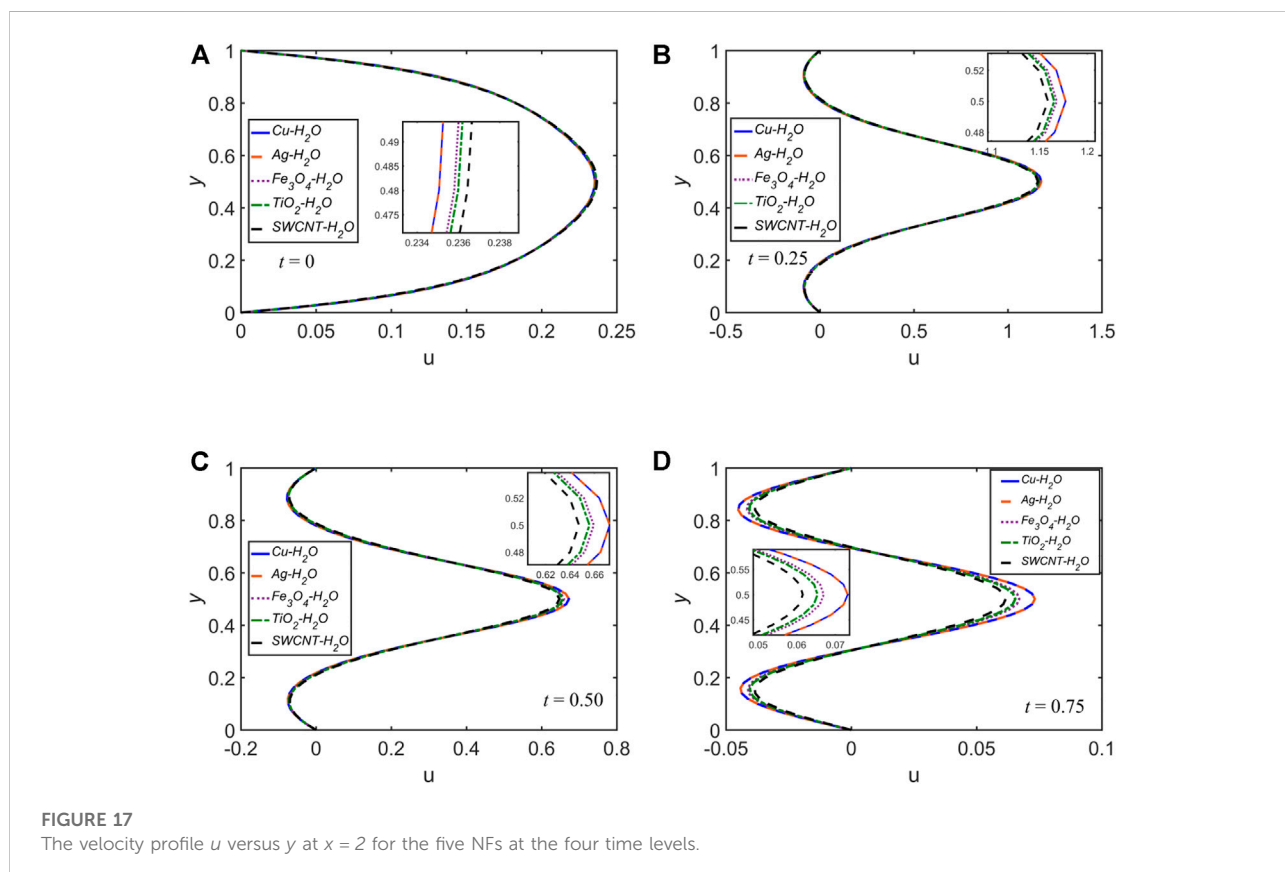
FIGURE 15

The temperature profile θ versus η at $x = 2$ and $t = 0.25$ for the five NFs for distinct values of Rd .



$\{(\xi, \eta) | \xi \in [-x_1, x_1] \text{ and } \eta \in [0, 1]\}$. The resulting linear systems are solved using TDMA during each of the ADI process's two half-steps. A Cartesian grid (ξ_i, η_j) of 400×50 elements is formed for $-10 \leq \xi \leq 10$ and $0 \leq \eta \leq 1$, with $\Delta\xi = 0.05$ and $\Delta\eta = 0.02$. For time integration, a step size of $\Delta t = 0.00005$ is considered. The constriction length is assumed as $2x_0 = 4$. The constrictions on the lower and upper walls are assumed to have heights $h_1 = h_2 = 0.35$; hence, at the constricted part of the channel, the minimum width is still 30% of the maximum channel width L . The computations for the current study are performed in a sequential fashion. The results can be found by parallel computing for time-efficient solutions (Ali and Syed, 2013).

The pulsatile motion is modeled by adding in the inflow boundary condition the sinusoidal time-dependent function $\sin(2\pi t)$. For comparison of the five NFs, the effects of the physical parameters such as M , St , Pr , and Rd on the existence of the dimensionless streamwise velocity (u) and temperature (θ) are analyzed. We perform simulations for a long enough time but display the results graphically only for $t = 0.25$, the point at which the flow rate is at its maximum and taking the location $x = 0$ (throat of the constriction) as well as $x = 2$ (in



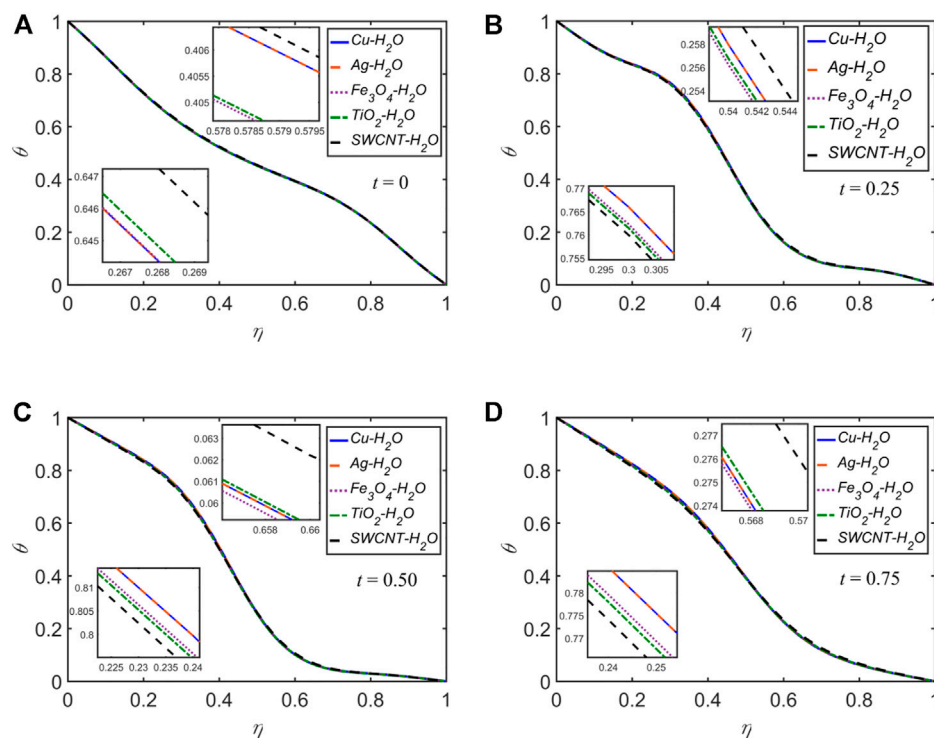


FIGURE 18

The temperature profile θ versus η at $x = 2$ for the five NFs at the four time levels.

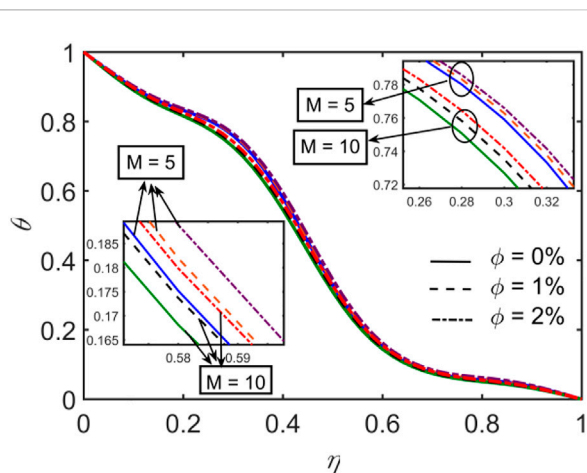


FIGURE 19

The temperature profile θ versus η for distinct values of ϕ for $\text{Cu-H}_2\text{O}$.

the lee of the constriction) where the fluid has entered in the low-pressure zone from the high-pressure zone. For a pulse cycle, $0 < t < 0.25$ is the acceleration phase, and $0.25 < t < 0.75$ is the deceleration phase.

For validation, the present results for the pulsatile flow condition are compared with those obtained by Bandyopadhyay and Layek (2012) without the heat effect. Figure 2 shows a good agreement of the present results, specifically for the wall shear stress (WSS), with (Bandyopadhyay and Layek, 2012) for $M = 5$, and 10 at $t = 0.25$.

The effects of varying the volume fraction on the wall shear stresses (WSS) at the upper wall are computed for $\phi = 0, 0.01, 0.02, 0.03$ with $M = 5$, $St = 0.02$, $Pr = 1$, and $Rd = 0.2$ of the five NFs. The results are shown in Figure 3 at $x = 0$ and $t = 0.25$. The WSS is maximum at $t = 0.25$ as the flow rate is maximum. The WSS decreases for $\text{SWCNT-H}_2\text{O}$, $\text{TiO}_2\text{-H}_2\text{O}$, and $\text{Fe}_3\text{O}_4\text{-H}_2\text{O}$ on increasing ϕ , whereas the WSS slightly increases for $\text{Cu-H}_2\text{O}$ and $\text{Ag-H}_2\text{O}$ on increasing ϕ .

The velocity and temperature profiles for each of the five NFs for $M = 0, 5, 10, 15$ are shown in Figures 4, 5 and Figures 6, 7, respectively, by setting the other parameters as $St = 0.02$, $Pr = 1$, $Rd = 0.2$, and $\phi = 0.02$. The slope/gradient of the velocity profile rises with rising values of M , i.e., the viscous boundary layer declines with rising values of M . In Figure 4, u profiles at $x = 0$ and $t = 0.25$ are shown. It has been noted that the peak value of u rises with M and exhibits a parabolic profile at $t = 0.25$. The velocity reaches its maximum at the middle of the constriction. SWCNT -based NF attains the peak value of the velocity higher than that of the other NFs. In Figure 5, u profiles at $x = 2$ and $t = 0.25$ are shown. The profiles are not parabolic as some

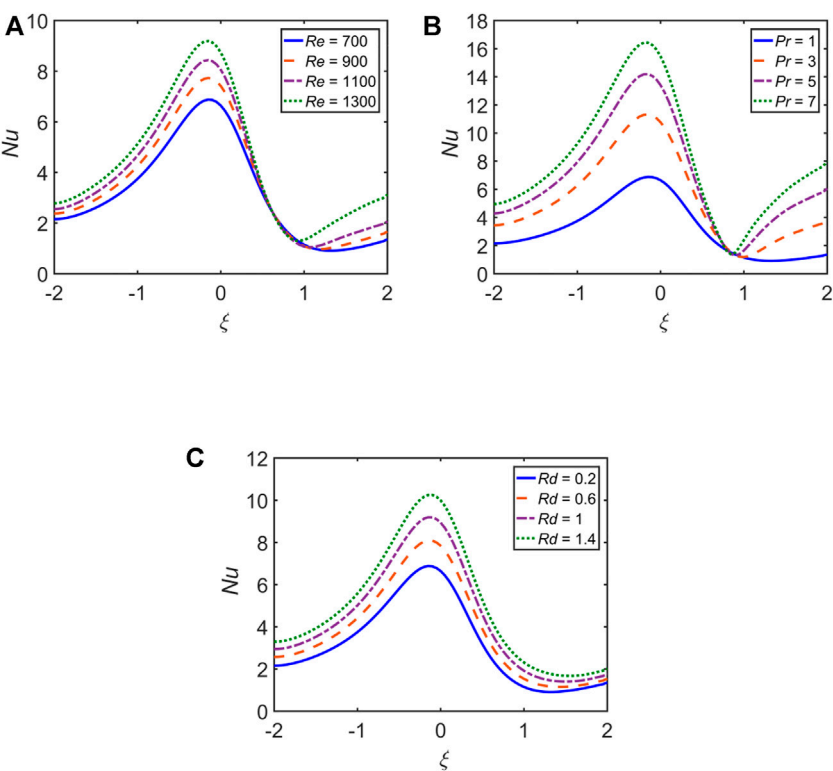


FIGURE 20
Impact of (A) Re , (B) Pr , and (C) Rd on Nu .

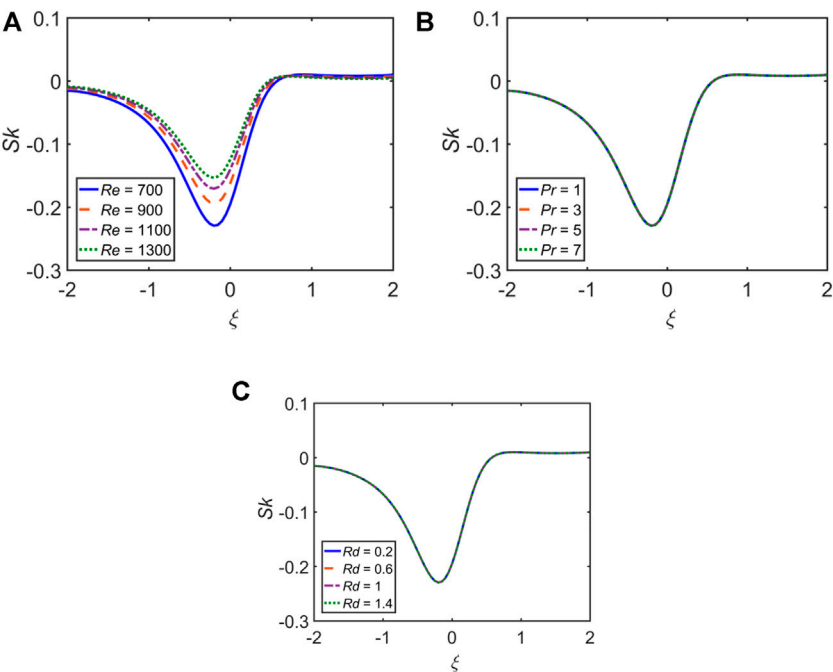


FIGURE 21
Impact of (A) Re , (B) Pr , and (C) Rd on Sk .

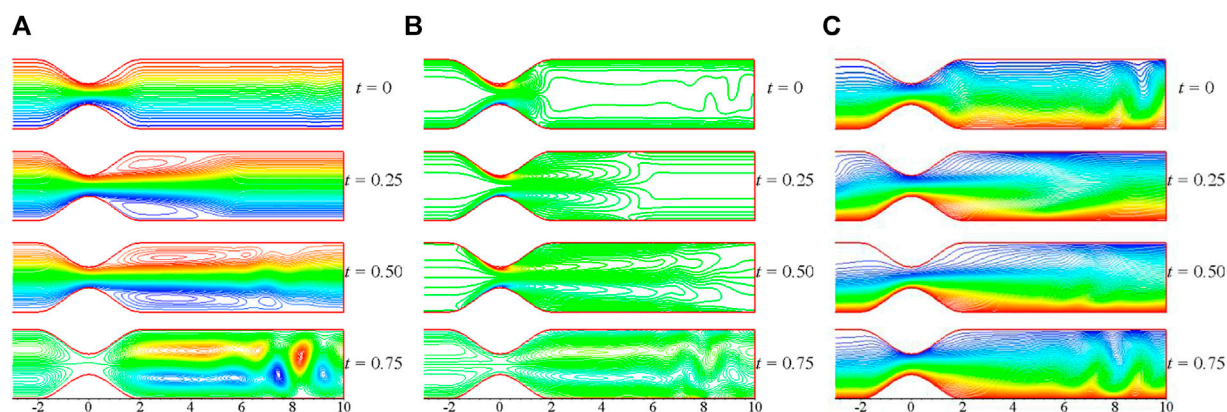


FIGURE 22

(A) Streamlines, (B) vorticity, and (C) temperature distribution plots at the four instants of a pulse cycle with $Re = 700$, $M = 5$, $St = 0.02$, $Pr = 1$, and $Rd = 0.2$ for $Cu-H_2O$.

backflow in the vicinity of the walls is observed. The backflow reduces with an increase in M . Ag -based NF attains the peak value of velocity higher than that of the other NFs. In Figures 6, 7, the temperature profiles θ for $t = 0.25$ are shown at $x = 0$ and $x = 2$, respectively. It is seen that the thickness of the thermal boundary layer increases, resulting in the rise of the temperature as M is increased. The temperature distribution across the channel at $t = 0.25$ for distinct values of M is shown in Figure 8.

The temperature profiles for each of the five NFs for $St = 0.02, 0.04, 0.06, 0.08$ are computed by setting the other parameters as $M = 5$, $Pr = 1$, $Rd = 0.2$, and $\phi = 0.02$. In Figures 9, 10, the temperature profiles θ for $t = 0.25$ are shown at $x = 0$ and $x = 2$, respectively. It is seen that the thickness of the thermal boundary layer declines, resulting in a decline of the temperature profile as the St rises.

The temperature profiles for each of the five NFs for $Pr = 1, 3, 5, 7$ are computed by setting the other parameters as $M = 5$, $St = 0.02$, $Rd = 0.2$, and $\phi = 0.02$. In Figures 11, 12, the temperature profiles θ for $t = 0.25$ are shown at $x = 0$ and $x = 2$, respectively. It is seen that the thickness of the thermal boundary layer declines, resulting in a decline of the temperature profile as the Pr increases. The temperature distribution across the channel at $t = 0.25$ for distinct values of Pr is shown in Figure 13.

The temperature profiles for each of the five NFs for $Rd = 0.2, 0.6, 1, 1.4$ are computed by setting the other parameters as $M = 5$, $St = 0.02$, $Pr = 1$, and $\phi = 0.02$. In Figures 14, 15, the temperature profiles θ for $t = 0.25$ are shown at $x = 0$ and $x = 2$, respectively. It is seen that the thickness of the thermal boundary layer rises, resulting in the rise of the temperature as Rd rises. The temperature distribution across the channel at $t = 0.25$ for distinct values of Rd is shown in Figure 16.

Nearly for all of the cases discussed above, for the variation of any of M , St , Pr , and Rd , a common behavior can be noticed. At

the throat of the constriction, $SWCNT$ -based NF attains higher temperatures than the other NFs downstream of the constriction. In the lee of the constriction, Ag -based NF attains higher temperatures than the other NFs downstream of the constriction. The behavior, in most cases, is opposite upstream of the constriction.

The velocity and temperature profiles for each of the five NFs for the four selected time levels: $t = 0, 0.25, 0.5, 0.75$, are shown in Figures 17, 18, respectively, by setting the parameters as $M = 5$, $St = 0.02$, $Pr = 1$, $Rd = 0.2$, and $\phi = 0.02$. The selected time levels are related to the start of pulsatile motion, the maximum flow rate, the minimum flow rate, and the instant zero net flow, respectively. In Figure 17, it is observed that the streamwise velocity achieves its peak value when the flow rate is maximum during the pulse cycle. The profiles are parabolic at $t = 0$. It is found that the u profile is symmetric for all t . Ag -based NF attains the peak value of the velocity higher than that of the other NFs. In Figure 18, it is detected that during the acceleration ($0 \leq t \leq 0.25$) and deceleration ($0.25 \leq t \leq 0.75$) phases of the pulsation cycle, Ag - and Cu -based NFs attain higher temperature values than that of the other NFs downstream of the constriction. Whereas, for the same phases, $SWCNT$ -based NF attains higher temperature values than that of the other NFs upstream of the constriction.

The effects of the variation of the solid volume fraction for $\phi = 0, 0.01, 0.02$ and $M = 5, 10$ on the temperature profiles are presented in Figure 19 for Cu -based NF. It is evident that the heat transfer rate is higher for the NF with a higher concentration of NPs. Moreover, the temperature gradients are higher near the lower wall of the channel.

The effects of Re , Pr , and Rd on the Nusselt number, as well as skin-friction profiles, are shown in Figures 20, 21, respectively. It is observed that the Nusselt number rises for higher values of Re , Pr , and Rd . The Nusselt number grows as the flow becomes more turbulent due to the rising number of collisions among the

fluid particles. Also, the skin friction coefficient as the values of Re upsurges. However, it remains unchanged for Pr and Rd .

The streamlines, vorticity, and temperature distribution plots at distinct instants of a pulse cycle with $Re = 700$, $M = 5$, $St = 0.02$, $Pr = 1$, and $Rd = 0.2$ are shown in Figure 22 for Cu -based NF. In Figure 22, the formation of vertical eddies in the vicinity of the walls can be observed. Over time, the eddies grow for a specific value of M and slowly occupy a greater part of the channel downstream. At $t = 0.75$, the presence of the backflow is observed, and even before the constriction bump, the vertical eddies are formed. The formation of these vertical eddies and flow separation is essential. However, these can be handled by increasing the strength of the magnetic field.

4 Concluding remarks

In this research, the numerical analysis of the pulsatile flow of five different NFs in a channel impacted by the magnetic field and thermal radiation through a rectangular channel having constricted walls is presented. The NPs include Cu , Fe_3O_4 , Ag , TiO_2 , and $SWCNT$ that are mixed in the base fluid, water (H_2O), to form the five NFs. The impacts of each of M , St , Pr , and Rd on the flow profiles are studied. In this analysis, the following major outcomes were observed:

- The streamwise velocity escalates as the values of M upsurge. The slope/gradient of the velocity profile is higher for higher values of M , i.e., the viscous boundary layer declines with rising values of M . At the throat of the constriction, $SWCNT-H_2O$ attains the velocity's peak value higher than that of the other NFs. However, in the lee of the constriction, $Ag-H_2O$ attains the velocity's peak value higher than that of the other NFs.
- The thickness of the thermal boundary layer rises as any of M , Rd , and ϕ is increased. This results in the rise of temperature.
- The thickness of the thermal boundary layer declines as any of St , and Pr is increased. This results in a decline in the temperature profile.
- At the throat of the constriction, $SWCNT-H_2O$ attains higher temperatures than the other NFs downstream of the constriction.
- In the lee of the constriction, $Ag-H_2O$ attains higher temperatures than the other NFs downstream of the constriction. The behavior, in most cases, is opposite upstream of the constriction.
- The streamwise velocity attains its maximum at the middle of the constriction at $t = 0.25$ during the pulse cycle. $Ag-H_2O$ attains the velocity's peak value higher than that of the other NFs.
- During the acceleration and deceleration phases of the pulsation cycle, Ag - and Cu -based NFs attain higher temperature values than that of the other NFs downstream

of the constriction. Whereas, for the same phases, $SWCNT$ -based NF attains higher temperature values than that of the other NFs upstream of the constriction.

- The heat transfer rate is higher for the NF with a higher concentration of the NPs.
- The skin-friction coefficient escalates with escalating values of Re . However, no difference is found in the case of variation in Pr and Rd .

Data availability statement

The original contributions presented in the study are included in the article/supplementary material; further inquiries can be directed to the corresponding author.

Author contributions

AA: conceptualization; ZB: methodology; MA: validation; S.A.: Coding; ESM Tag El Din: Analysis; SM Hussain: Data Curation.

Funding

The authors are grateful to the Deanship of Scientific Research, Islamic University of Madinah, Ministry of Education, KSA, for supporting this research work through research project grant under Research Group Program/1/804.

Acknowledgments

The authors are thankful to the reviewer for the comments and suggestions. The authors highly appreciate the reviewer for the high standard review.

Conflict of interest

The authors declare that the research was conducted in the absence of any commercial or financial relationships that could be construed as a potential conflict of interest.

Publisher's note

All claims expressed in this article are solely those of the authors and do not necessarily represent those of their affiliated organizations, or those of the publisher, the editors, and the reviewers. Any product that may be evaluated in this article, or claim that may be made by its manufacturer, is not guaranteed or endorsed by the publisher.

References

- Akbar, N. S., Khan, Z. H., and Nadeem, S. (2014). The combined effects of slip and convective boundary conditions on stagnation-point flow of CNT suspended nanofluid over a stretching sheet. *J. Mol. Liq.* 196, 21–25. doi:10.1016/j.molliq.2014.03.006
- Akbar, N. S. (2014). Metallic nanoparticles analysis for the peristaltic flow in an asymmetric channel with MHD. *IEEE Trans. Nanotechnol.* 13 (2), 357–361. doi:10.1109/tnano.2014.2304362
- Ali, A., Farooq, H., Abbas, Z., Bukhari, Z., and Fatima, A. (2020). Impact of Lorentz force on the pulsatile flow of a non-Newtonian Casson fluid in a Constricted channel using Darcy's law: A numerical study. *Sci. Rep.* 10, 10629. doi:10.1038/s41598-020-67685-0
- Ali, A., and Syed, K. S. (2013). *Adv. Comp.* 91, 87–118.
- Aly, A. M. (2020). *ZAMM J. App. Math. Mech.* 100 (9).
- Alzahrani, J., Vaidya, H., Prasad, K. V., Rajashekhar, C., Mahendra, D. L., and Tlili, I. (2022). Micro-polar fluid flow over a unique form of vertical stretching sheet: Special emphasis to temperature-dependent properties. *Case Stud. Therm. Eng.* 34, 102037. doi:10.1016/j.csite.2022.102037
- Babu, H., Ajmath, K. A., Venkateswarlu, B., and Narayana, P. V. S. (2018). Thermal radiation and heat source effects on MHD non-Newtonian nanofluid flow over a stretching sheet. *J. nanofluids* 8, 1085–1092. doi:10.1166/jon.2019.1666
- Bandyopadhyay, S., and Layek, G. C. (2011). Numerical computation of pulsatile flow through a locally constricted channel. *Commun. Nonlinear Sci. Numer. Simul.* 16, 252–265. doi:10.1016/j.cnsns.2010.03.017
- Bandyopadhyay, S., and Layek, G. C. (2012). Study of magnetohydrodynamic pulsatile flow in a constricted channel. *Commun. Nonlinear Sci. Numer. Simul.* 17, 2434–2446. doi:10.1016/j.cnsns.2011.09.040
- Cha, J. E., Ahn, Y. C., and Kim, M. H. (2002). Flow measurement with an electromagnetic flowmeter in two-phase bubbly and slug flow regimes. *Flow. Meas. Instrum.* 12 (5–6), 329–339. doi:10.1016/s0955-5986(02)00007-9
- Devaki, P., Venkateswarlu, B., Srinivas, S., and Sreenadh, S. (2020). *Nonlin. Eng.* 9, 51–59.
- Gao, J., Liu, J., Yue, H., Zhao, Y., Tlili, I., and Karimipour, A. (2022). Effects of various temperature and pressure initial conditions to predict the thermal conductivity and phase alteration duration of water based carbon hybrid nanofluids via MD approach. *J. Mol. Liq.* 351, 118654. doi:10.1016/j.molliq.2022.118654
- Gopal, D., Saleem, S., Jagadha, S., Ahmad, F., Almatroud, A. O., and Kishan, N. (2021). Numerical analysis of higher order chemical reaction on electrically MHD nanofluid under influence of viscous dissipation. *Alexandria Eng. J.* 60, 1861–1871. doi:10.1016/j.aej.2020.11.034
- Haq, R. U., Noor, N. F. M., and Khan, Z. H. (2016). *Adv. Powder Technol.* 27 (4), 1568–1575.
- Haq, R. U., Shahzad, F., and Almdallal, Q. (2017). MHD pulsatile flow of engine oil based carbon nanotubes between two concentric cylinders. *Results Phys.* 7, 57–68. doi:10.1016/j.rinp.2016.11.057
- Kakarantzas, S. C., Sarris, I. E., Grecos, A. P., and Vlachos, N. S. (2009). Magnetohydrodynamic natural convection in a vertical cylindrical cavity with sinusoidal upper wall temperature. *Int. J. Heat. Mass Transf.* 52, 250–259. doi:10.1016/j.ijheatmasstransfer.2008.06.035
- Kasaean, A., Eshghi, A. T., and Sameti, M. (2015). A review on the applications of nanofluids in solar energy systems. *Renew. Sustain. Energy Rev.* 43, 584–598. doi:10.1016/j.rser.2014.11.020
- Kavya, S., Nagendramma, V., Ahammad, N. A., Ahmad, S., Raju, C. S. K., and Shah, N. A. (2022). Magnetic-hybrid nanoparticles with stretching/shrinking cylinder in a suspension of MoS₄ and copper nanoparticles. *Int. Commun. Heat Mass Transf.* 136, 106150. doi:10.1016/j.icheatmasstransfer.2022.106150
- Krishna, M. V., Ahammad, N. A., and Chamkha, A. J. (2021). *Ain. Sh. Eng. J.* 12 (3), 3043–3056.
- Krishna, M. V., Ahammad, N. A., and Chamkha, A. J. (2021). Radiative MHD flow of Casson hybrid nanofluid over an infinite exponentially accelerated vertical porous surface. *Case Stud. Therm. Eng.* 27, 101229. doi:10.1016/j.csite.2021.101229
- Kumar, M. A., Reddy, Y. D., Rao, V. S., and Goud, B. S. (2021). Thermal radiation impact on MHD heat transfer natural convective nano fluid flow over an impulsively started vertical plate. *Case Stud. Therm. Eng.* 24, 100826. doi:10.1016/j.csite.2020.100826
- Mahian, O., Kianifar, A., Kalogirou, S. A., Pop, I., and Wongwises, S. (2013). A review of the applications of nanofluids in solar energy. *Int. J. Heat. Mass Transf.* 57, 582–594. doi:10.1016/j.ijheatmasstransfer.2012.10.037
- Mahmood, R. T., Asad, M. J., Hadri, S. H., El-Shorbagy, M. A., Mousa, A. A. A., et al. (2022). *Hum. Ecol. risk assess.*
- Mustafa, M., Hayat, T., Pop, I., Asghar, S., and Obaidat, S. (2011). Stagnation-point flow of a nanofluid towards a stretching sheet. *Int. J. Heat. Mass Transf.* 54, 5588–5594. doi:10.1016/j.ijheatmasstransfer.2011.07.021
- Narayana, P. V. S., and Venkateswarlu, B. (2016). *Front. Heat. Mass Trans.* 7.
- Nasir, S., Shah, Z., Islam, S., Bonyah, E., and Gul, T. (2019). Darcy Forchheimer nanofluid thin film flow of SWCNTs and heat transfer analysis over an unsteady stretching sheet. *AIP Adv.* 9, 015223–15310. doi:10.1063/1.5083972
- Nayak, M. K., Mabood, F., Dogonchi, A. S., Ramadan, K. M., Tlili, I., and Khan, W. A. (2022). *Wave random complex.*
- Pakdaman, M. F., Akhavan-Behabadi, M. A., and Razi, P. (2012). *Exp. Therm. Fluid Sci.* 40, 103–111.
- Puneeth, V., Ali, F., Khan, M. R., Anwar, M. S., and Ahammad, N. A. (2022). *Bio. Conv. Ref.* 21.
- Qi, X., Sidi, M. O., Tlili, I., Ibrahim, T. K., Elkotb, M. A., El-Shorbagy, M. A., et al. (2022). Optimization and sensitivity analysis of extended surfaces during melting and freezing of phase changing materials in cylindrical Lithium-ion battery cooling. *J. Energy Storage* 51, 104545. doi:10.1016/j.est.2022.104545
- Ramadan, K. M., Qisieh, O., and Tlili, I. (2022). Thermal creep effects on fluid flow and heat transfer in a microchannel gas cooling. *Proc. Institution Mech. Eng. Part C J. Mech. Eng. Sci.* 236, 5033–5047. doi:10.1177/09544062211057039
- Rashidi, M. M., Nasiri, M., Khezerloo, M., and Laraqi, N. (2016). Numerical investigation of magnetic field effect on mixed convection heat transfer of nanofluid in a channel with sinusoidal walls. *J. Magn. Magn. Mat.* 401, 159–168. doi:10.1016/j.jmmm.2015.10.034
- Sabu, A. S., Mathew, A., Neethu, T. S., and George, K. A. (2021). Statistical analysis of MHD convective ferro-nanofluid flow through an inclined channel with hall current, heat source and solet effect. *Therm. Sci. Eng. Prog.* 22, 100816. doi:10.1016/j.tsep.2020.100816
- Said, Z., Saidur, R., Sabiha, M. A., Rahim, N. A., and Anisur, M. R. (2015). Thermophysical properties of Single Wall Carbon Nanotubes and its effect on exergy efficiency of a flat plate solar collector. *Sol. Energy* 115, 757–769. doi:10.1016/j.solener.2015.02.037
- Saidur, R., Kazi, S. N., Husain, M. S., Rahman, M. M., and Mohammed, H. A. (2011). *Renew. Sust. Energy Rev.* 15, 310–323.
- Saidur, R., Leong, K. Y., and Mohammed, H. A. (2011). A review on applications and challenges of nanofluids. *Renew. Sustain. Energy Rev.* 15 (3), 1646–1668. doi:10.1016/j.rser.2010.11.035
- Shah, S. A. A., Ahammad, N. A., Din, E. M. T. E., Gamaoun, F., Awan, A. U., and Ali, B., *Nanomater.* 12, 2174, (2022).
- Shah, Z., Bonyah, E., Islam, S., and Gul, T. (2019). Impact of thermal radiation on electrical MHD rotating flow of Carbon nanotubes over a stretching sheet. *AIP Adv.* 9 (1), 015115–15213. doi:10.1063/1.5048078
- Sheikholeslami, M., and Ganji, D. D. (2013). Heat transfer of Cu-water nanofluid flow between parallel plates. *Powder Technol.* 235, 873–879. doi:10.1016/j.powtec.2012.11.030
- Sheikholeslami, M., Ganji, D. D., and Moradi, R. (2017). Forced convection in existence of Lorentz forces in a porous cavity with hot circular obstacle using nanofluid via Lattice Boltzmann method. *J. Mol. Liq.* 246, 103–111. doi:10.1016/j.molliq.2017.09.053
- Sheikholeslami, M., Hayat, T., and Alsaedi, A. (2017). Numerical study for external magnetic source influence on water based nanofluid convective heat transfer. *Int. J. Heat. Mass Transf.* 106, 745–755. doi:10.1016/j.ijheatmasstransfer.2016.09.077
- Sheikholeslami, M. (2017). Influence of magnetic field on nanofluid free convection in an open porous cavity by means of Lattice Boltzmann method. *J. Mol. Liq.* 234, 364–374. doi:10.1016/j.molliq.2017.03.104
- Sheikholeslami, M. (2017). Numerical simulation of magnetic nanofluid natural convection in porous media. *Phys. Lett. A* 381, 494–503. doi:10.1016/j.physleta.2016.11.042
- Sheikholeslami, M., Rashidi, M. M., and Ganji, D. D. (2015). Effect of non-uniform magnetic field on forced convection heat transfer of Fe₃O₄-water nanofluid. *Comput. Methods Appl. Mech. Eng.* 294, 299–312. doi:10.1016/j.cma.2015.06.010
- Tarakaramu, N., Narayana, P. V. S., and Venkateswarlu, B. (2019). *App. Math. Sci. Comp.* 87–97.

Tarakaramu, N., Narayana, P. V. S., and Venkateswarlu, B. (2020). Numerical simulation of variable thermal conductivity on 3D flow of nanofluid over a stretching sheet. *Nonlinear Eng.* 9, 233–243. doi:10.1515/nleng-2020-0011

Tlili, I., and Alharbi, T. (2022). Investigation into the effect of changing the size of the air quality and stream to the trombe wall for two different arrangements of rectangular blocks of phase change material in this wall. *J. Build. Eng.* 52, 104328. doi:10.1016/j.jobe.2022.104328

Tlili, I., Sajadi, S. M., Baleanu, D., and Ghaemi, F. (2022). *Sustain. Energy Technol. Assess.* 52, 102100.

Turkyilmazoglu, M., and Pop, I. (2013). Heat and mass transfer of unsteady natural convection flow of some nanofluids past a vertical infinite flat plate with radiation effect. *Int. J. Heat. Mass Transf.* 59, 167–171. doi:10.1016/j.ijheatmasstransfer.2012.12.009

Venkateswarlu, B., and Narayana, P. V. S. (2021). *Heat. Trans.* 50, 432–449.

Wang, X. Q., and Mujumdar, A. (2008). A review on nanofluids - part II: Experiments and applications. *Braz. J. Chem. Eng.* 25 (4), 631–648. doi:10.1590/s0104-66322008000400002

Wong, K. V., and Leon, O. D. (2010). *Adv. Mech. Eng.* 2, 1–11.

Yang, L., Huang, J. N., Ji, W., and Mao, M. (2020). Investigations of a new combined application of nanofluids in heat recovery and air purification. *Powder Technol.* 360, 956–966. doi:10.1016/j.powtec.2019.10.053

Zhang, J., Sajadi, S. M., Tlili, I., and YangChen, I. Tlili and M. A. Fagiry (2022). Effects of Al₂O₃ and TiO₂ nanoparticles in order to reduce the energy demand in the conventional buildings by integrating the solar collectors and phase change materials. *Sustain. Energy Technol. Assessments* 52, 102114. doi:10.1016/j.seta.2022.102114



OPEN ACCESS

EDITED BY

Adnan,
Mohi-ud-Din Islamic University,
Pakistan

REVIEWED BY

Fateh Ali,
Xi'an Jiaotong University, China
Muhammad Azam,
Beijing Institute of Technology, China
Mohsan Hassan,
COMSATS University Islamabad, Lahore
Campus, Pakistan

*CORRESPONDENCE

Muhammad Bilal,
bilalchd345@gmail.com

SPECIALTY SECTION

This article was submitted to Process
and Energy Systems Engineering,
a section of the journal
Frontiers in Energy Research

RECEIVED 04 July 2022

ACCEPTED 09 August 2022

PUBLISHED 04 October 2022

CITATION

Alqarni MM, Bilal M, Allogmany R,
Tag-Eldin E, Ghoneim ME and
Yassen MF (2022), Mathematical analysis
of casson fluid flow with energy and
mass transfer under the influence of
activation energy from a non-coaxially
spinning disc.
Front. Energy Res. 10:986284.
doi: 10.3389/fenrg.2022.986284

COPYRIGHT

© 2022 Alqarni, Bilal, Allogmany, Tag-
Eldin, Ghoneim and Yassen. This is an
open-access article distributed under
the terms of the [Creative Commons
Attribution License \(CC BY\)](#). The use,
distribution or reproduction in other
forums is permitted, provided the
original author(s) and the copyright
owner(s) are credited and that the
original publication in this journal is
cited, in accordance with accepted
academic practice. No use, distribution
or reproduction is permitted which does
not comply with these terms.

Mathematical analysis of casson fluid flow with energy and mass transfer under the influence of activation energy from a non-coaxially spinning disc

M. M. Alqarni¹, Muhammad Bilal^{2*}, Reem Allogmany³,
Elsayed Tag-Eldin⁴, Mohamed E. Ghoneim⁵ and
Mansour F. Yassen^{6,7}

¹Department of Mathematics, College of Sciences, King Khalid University, Abha, Saudi Arabia,

²Department of Mathematics, City University of Science and Information Technology, Peshawar,

Pakistan, ³Department of Mathematics, Faculty of Science, Taibah University, Al-Madinah Al-

Munawarah, Saudi Arabia, ⁴Faculty of Engineering and Technology, Future University in Egypt, New

Cairo, Egypt, ⁵Department of Mathematical Sciences, Faculty of Applied Science, Umm Al-Qura

University, Makkah, Saudi Arabia, ⁶Department of Mathematics, College of Science and Humanities in

Al-Aflaj, Prince Sattam Bin Abdulaziz University, Al-Kharj, Saudi Arabia, ⁷Department of Mathematics,

Faculty of Science, Damietta University, Damietta, Egypt

A Casson fluid is the most suitable rheological model for blood and other non-Newtonian fluids. Casson fluids hold yield-stress and have great significance in biomechanics and polymer industries. In this analysis, a numerical simulation of non-coaxial rotation of a Casson fluid over a circular disc was estimated. The influence of thermal radiation, second-order chemical reactions, buoyancy, and heat source on a Casson fluid above a rotating frame was studied. The time evolution of secondary and primary velocities, solute particles, and energy contours were also examined. A magnetic flux of varying intensity was applied to the fluid flow. A nonlinear sequence of partial differential equations was used to describe the phenomenon. The modeled equations were reduced to a non-dimensional set of ordinary differential equations (ODEs) using similarity replacement. The obtained sets of ODEs were further simulated using the parametric continuation method (PCM). The impact of physical constraints on energy, concentration, and velocity profiles are presented through figures and tables. It should be noted that the effect of the Casson fluid coefficient, the Grashof number, and the magnetic field reduces the fluid's primary velocity contour. The mass transfer field decreases with the action of constructive chemical reactions, but is augmented by the effects of destructive chemical reactions. The accelerating trend in Schmidt number lowers the mass profile, while it is enhanced by increasing values of activation energy and Soret number.

KEYWORDS

non-coaxial rotation, activation energy, pcm, heat source, chemical reaction, thermal radiation

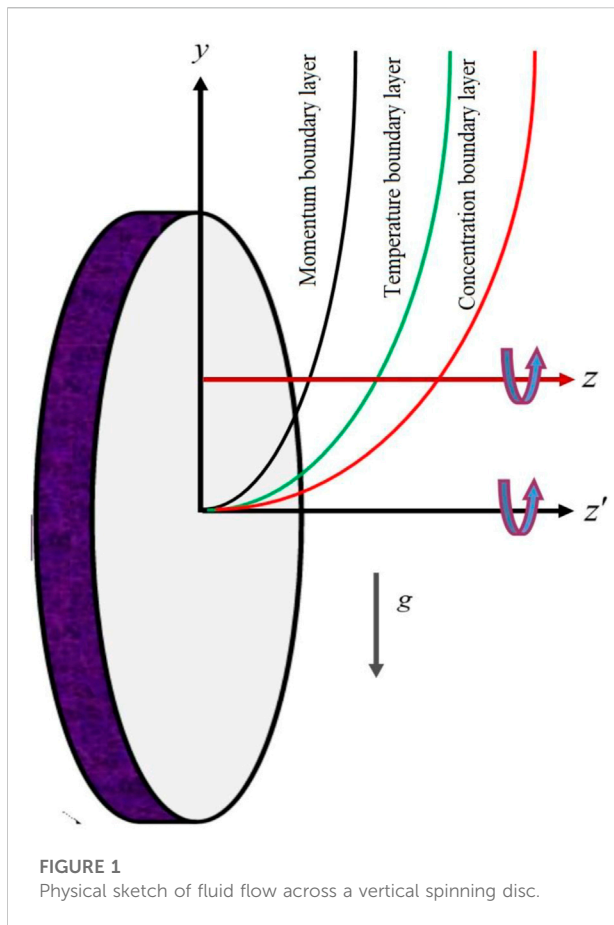
Introduction

Many natural and commercial processes use non-coaxial fluid motion. Non-coaxial and coaxial rotation of fluid and solids such as by discs, cylinders, and spheres are used in multiple industrial operations (Erdogan, 1977; Erdoğan, 1997; Asghar et al., 2007). As a result of variations in temperature and chemical transmission, several types of non-coaxial and coaxial spinning of fluids in industrial systems arise. Swirling flows and spinning tubes while engaged in oil exploration and transit, and food manufacturing layouts are well-known instances of rotating mechanisms. In order to understand the underlying engineering mechanism, scientists and engineers have modeled the non-coaxial motion of fluids and calculated the results using a variety of approaches (Hayat et al., 2001; Hayat et al., 2004; Alharbi et al., 2022). Non-coaxial spinning of a disc has a wide range of uses, including food manufacturing and industrial production, jet turbines, squeeze bottles, hydrological flows, and chilling rotor blades, among others (Ullah et al., 2022a; Benhacine et al., 2022). Noranuar et al. (2021) used a computational approach to investigate the fluid flow and energy transport of MHD Casson ferrofluid affected by the coaxial rotation of a movable disc traveling through a permeable medium. Jabbar et al. (Jabbar et al., 2021) analyzed the influence of non-coaxial movement on the distribution of mass in a first-order biochemical reaction. It was discovered that the effect of buoyant force on secondary velocity was the polar opposite of its effect on primary velocity. Sharma et al. (Sharma et al., 2022) measured the thermal control of the flow of a hybrid nanoliquid over a stretchable rotating disc and discovered that a revolving disc with a static cone could attain the optimum condensation of disk-cone components while the exterior heat remained fixed. Das et al. (Das et al., 2018) determined the Hall impacts on MHD flow of an electrically charged particle induced by non-coaxial repetitions of a highly permeable disc and a fluid. The irregular flow of an oscillating disc in a Newtonian fluid about its own plane was reported by Ersoy (2017); when fluctuation occurred across the elliptical direction, the x - and y -terms exerted by the fluid on the disc varied in nearly opposite directions. The Darcy–Forchheimer hybrid nano-composite fluid flow across a permeable rotating disc was studied by Yaseen et al. (2022). Hassan et al. (2018) investigated the effects of a strong oscillating magnetic flux and a large concentration of nanoparticles on physical characteristics as well as energy and mass transport. Many researchers have recently reported on the study of non-coaxial motion of discs and fluids (Ali et al., 2020; Ali et al., 2022; Fei et al., 2022).

Thermal radiation is an electromagnetic wave-based heat transfer phenomenon. It is caused by a large temperature difference between two mediums. Many technological activities take place at extremely high temperatures. With regard to nuclear reactors, space technology, engineering and physics, glass production, power plants, furnace design, and

other related areas, the contribution of thermal radiation to flow and thermal expansion may be observed. Satellites and other spacecraft, missiles, aircraft propulsion systems, atomic power plants, solar power plants, and combustion engines such as IC engines and furnaces are all dependent on radiation effects. Hassan et al. (2022) studied non-Newtonian fluid flows and determined their thermo-physical characteristics. In the presence of activation energy and a magnetic field, Rizwan and Hassan (2022), Raja et al. (2022), and Lin et al. (2014) documented the nanofluid flow of copper and cobalt nanocomposites under the influence of thermal radiation in different configurations. Hang et al. (2021) tested the ability of new smart materials to dynamically regulate thermal radiation and found that these materials could be employed in a variety of situations, resulting in better options and a significant increase in economic potential. Al and CuO nanoparticles were examined by Wakif et al. (2021) in the context of thermal radiation, and they concluded that the presence of convection cells was stabilized more by improving the strength of Lorentz forces, heat radiation, and surface roughness. The Jeffery hybrid nanofluid flow with thermal characteristics and magnetic effect was studied by Ishtiaq et al. (2022), and their data showed that a $Cu-H_2O$ nanoliquid was more stable than one of TiO_2-H_2O . Mabood et al. (2021) experimentally determined how hybrid nanoparticles influenced a variety of physical properties of hybrid nanoliquids across an overextended surface. The findings of their research were crucial in determining the influence of several key design elements on heat transmission and in improving industrial processes. The characteristics of fluid flow under the influence of thermal radiation and energy transmission over different geometries was reported by (Ahmed et al., 2018; Hassan et al., 2021a; Azam, 2022a; Azam, 2022b; Dadheech et al., 2022).

The minimum energy required to initiate an operation (such as a chemical reaction) is known as the activation energy, and the rate of a chemical reaction is directly proportional to its activation energy (Alsallami et al., 2022; Rehman et al., 2022). Punith et al. (2021) examined the effects of activation energy on the reactive species in a non-Newtonian nanofluid with energy and mass-exchange properties. The results showed that as the Marangoni number increased, the relative velocity improved, and the energy transmission decreased. Chemical processes, activation energy, and heat source/sink effects were used by Ramesh et al. (2022) to model the momentum and energy transport of a hybrid nanoliquid across two surfaces. The mass outlines were minimized by greater chemical reactions, whereas activation energy exhibited the reverse pattern. Hassan et al. (2021b) addressed the boundary layer behavior of the well-known non-Newtonian dilatant and pseudoplastic fluids over a moving belt. Ullah (Ullah et al., 2022b; Ullah et al., 2022c; Ullah, 2022) investigated the effects of activation energy and molten heat flux on an unstable Prandtl–Eyring model caused by a strained cylinder with varying thermal conductivity. It was



discovered that increasing the reaction rate improved fluid temperature, while decreasing it had the opposite effect when activation energy and unsteadiness characteristics were considered. Many scholars have recently made significant contributions in this area (Azam and Abbas, 2021; Azam et al., 2021; Al-Mubaddel et al., 2022; Azam et al., 2022).

In reviewing the existing literature, we found that no analysis of combined transit of energy and mass in the flow caused by non-coaxial motion of a disc and surrounding fluid with respect to second-order chemical reactions, activation energy and buoyancy force had been performed. Therefore, we numerically simulated the non-coaxial rotation of a Casson fluid and disc under the influence of thermal radiation, second-order chemical reactions, buoyancy, and heat source in a rotating frame. A nonlinear sequence of partial differential equations was used to describe the phenomenon. The modeled equations were reduced to a non-dimensional set of ODEs using similarity replacement. The obtained sets of ODEs were further simulated using PCM methodology. The effect of physical constraints on energy, concentration and velocity profiles are presented in figures and tables. In the next section, the model is formulated, and in succeeding sections, we present the results and discussion.

Mathematical formulation

We considered the solute particles and thermal energy transmission in Casson fluid flow above a non-coaxial rotating disc with uniform angular velocity as displayed in Figure 1. The disc and ambient fluid both rotated on different axes under a fixed magnetic field, B_0 . The disc temperature was higher than the heat energy. Initially, the temperature and concentration of the disc and the ambient fluid were assumed to be the same. After a period of time, the temperature of the disc was changed. We observed that the motion of the fluid was created by the surface motion of the disc. The disc wall stretched and shrank with the positive and negative values of Ω . The gravitational and pressure effects are signified by g and p . In the proposed model, the opposing motions of the walls produced changes in vertical and horizontal velocities. The above-specified conditions produced results similar to (Erdogan, 1977; Benhacine et al., 2022)

$$\left. \begin{aligned} u &= -(y-1)\Omega, & T &= T_\infty, & v &= \Omega x, & C &= C_\infty & \text{at } t &= 0 \\ t > 0, & u &= -\Omega y, & T_w &= T, & v &= \Omega x, & C_w &= C, & z &= 0, \\ z \rightarrow \infty, & C &= C_\infty, & u &= -\Omega y + 1, & v &= \Omega x, & T_\infty &= T \end{aligned} \right\} \quad (1)$$

Based on the above conditions, the following field was considered:

$$V = f - \Omega y, \quad g + \Omega x + 0, \quad C = C(z, t), \quad T = T(z, t). \quad (2)$$

The basic equations were designed according to (Erdogan, 1977; Benhacine et al., 2022)

$$\begin{aligned} \frac{1}{\rho} \frac{\partial p}{\partial x} &= 2\Omega^2 x + v \left(\frac{1}{\beta} + 1 \right) \frac{\partial^2 f}{\partial z^2} - \frac{\partial f}{\partial t} + \Omega g - \frac{\sigma B_0^2}{\rho} (f - \Omega l) \\ &\quad - \frac{\mu}{\rho k} f + \frac{\mu \Omega}{\rho k} y, \end{aligned} \quad (3)$$

$$\begin{aligned} \frac{1}{\rho} \frac{\partial p}{\partial y} &= 2\Omega^2 y + v \left(\frac{1}{\beta} + 1 \right) \frac{\partial^2 g}{\partial z^2} - \frac{\partial g}{\partial t} - \Omega f - \frac{\sigma B_0^2}{\rho} g \\ &\quad + \beta_T (-T_\infty + T) \bar{g} - \frac{\mu}{\rho k} g + \frac{\mu \Omega}{\rho k} x, \end{aligned} \quad (4)$$

$$\frac{\partial T}{\partial t} = \frac{K}{\rho C_p} \frac{\partial^2 T}{\partial z^2} - \frac{1}{\rho C_p} \frac{16\sigma_1 T_\infty^3}{3K^*} \frac{\partial^2 T}{\partial z^2} + \frac{Q_0}{\rho C_p} (T - T_\infty), \quad (5)$$

$$\frac{\partial C}{\partial t} = D \frac{\partial^2 C}{\partial z^2} + \frac{DK_T}{T_m} \frac{\partial^2 T}{\partial z^2} - k_r^2 (C - C_0) \left(\frac{T}{T_\infty} \right)^n \exp \left(-\frac{E_a}{\kappa T} \right), \quad (6)$$

Eliminating the pressure terms and employing the ambient conditions gives

$$v \left(\frac{1}{\beta} + 1 \right) \frac{\partial^2 f}{\partial z^2} - \frac{\partial f}{\partial t} + \Omega g - \frac{\sigma B_0^2}{\rho} (f - \Omega l) - \frac{\mu}{\rho k} f (\Omega l - f) = 0, \quad (7)$$

$$\begin{aligned} v \left(\frac{1}{\beta} + 1 \right) \frac{\partial^2 g}{\partial z^2} - \frac{\partial g}{\partial t} - \Omega f - \frac{\sigma B_0^2}{\rho} g + \Omega^2 l + \beta_T (-T_\infty + T) \bar{g} \\ - \frac{\mu}{\rho k} g = 0, \end{aligned} \quad (8)$$

$$\frac{\partial T}{\partial t} = \frac{K}{\rho C_p} \frac{\partial^2 T}{\partial Z^2} + \frac{1}{\rho C_p} \frac{16\sigma_1 T_\infty^3}{3K^*} \frac{\partial^2 T}{\partial Z^2} + \frac{Q_0}{\rho C_p} (T - T_\infty), \quad (9)$$

$$\frac{\partial C}{\partial t} = D \frac{\partial^2 C}{\partial z^2} + \frac{DK_T}{T_\infty} \frac{\partial^2 T}{\partial Z^2} - k_r^2 (C - C_0) \left(\frac{T}{T_\infty} \right)^n \exp\left(-\frac{E_a}{\kappa T}\right), \quad (10)$$

Resulting in

$$\left. \begin{aligned} T &= T, & f &= \Omega l, & g &= 0, & C &= C_\infty & t &= 0, \\ t > 0, & T &= T_\infty, & C_w &= C, & g &= 0, & f &= 0, & z &= 0, \\ C &= 0, & f &= \Omega l, & T &= 0, & g &= 0 & z &\rightarrow \infty. \end{aligned} \right\} \quad (11)$$

The similarity variables are as (Benhacine et al., 2022)

$$\begin{aligned} \tau &= \Omega t, \quad \eta = \sqrt{\frac{\Omega}{\nu}} z, \quad \theta(T_w - T_\infty) = T - T_\infty, \\ \varphi(C_w - C_\infty) &= C - C_\infty, \quad \Gamma = \frac{k\Omega}{\nu}. \end{aligned} \quad (12)$$

In Eqs 7–10, we get

$$\left(1 + \frac{1}{\beta}\right) \frac{\partial^2 \bar{F}}{\partial \eta^2} - \left(i\bar{F} + \frac{1}{\Gamma}\bar{F} + p\bar{F}\right) = -iGr\bar{\theta}, \quad -\frac{1}{p} = \bar{F}(0, p), \quad (13)$$

$$0 = \bar{F}(\infty, p),$$

$$\frac{\partial^2 \theta}{\partial \eta^2} - \frac{Pr}{\lambda} \frac{\partial \theta}{\partial \tau} + Q\theta = 0, \quad \theta(0, \tau) = 1, \quad \theta(\infty, \tau) = 0, \quad \theta(\eta, 0) = 0, \quad (14)$$

$$\begin{aligned} \frac{\partial^2 \phi}{\partial \eta^2} - Sc \frac{\partial \phi}{\partial \tau} + ScSr \frac{\partial^2 \theta}{\partial \eta^2} - Sc\gamma(1 + \delta\theta)^n \varphi \exp\left(-\frac{E}{1 + \delta\theta}\right) &= 0, \\ \phi(0, \tau) &= 1, \quad \phi(\infty, \tau) = 0, \quad \phi(\eta, 0) = 0. \end{aligned} \quad (15)$$

The dimensionless parameters are

$$\left. \begin{aligned} F(\eta, \tau) &= \frac{(f + ig)}{\Omega l - 1}, \quad \lambda = 1 + \frac{4}{3N_R}, \quad N_R = \frac{KK^*}{4\sigma_1 T_\infty^3}, \\ Gr &= \frac{\beta_T \bar{g}(T_w - T_\infty)}{\Omega^2 l}, \quad Pr = \frac{\nu_p C_p}{k}, \\ M^2 &= \frac{\sigma B_0^2}{\rho \Omega}, \quad Sc = \frac{\nu}{D}, \quad Sr = \frac{DK_T(T_w - T_\infty)}{\nu T_m(C_w - C_\infty)}, \\ \gamma &= \frac{K_1}{\Omega}, \quad \Gamma = \frac{k\Omega}{\nu}. \end{aligned} \right\} \quad (16)$$

Numerical solution

Different researchers have used various numerical and computational techniques to solve nonlinear PDEs (Tie-Hong et al., 2019; Chu et al., 2021; Zhao et al., 2021; Chu et al., 2022a; Chu et al., 2022b; Iqbal et al., 2022; Jin et al., 2022; Nazeer et al., 2022; Rashid et al., 2022; Wang et al., 2022). The main steps in employing the PCM method were taken from (Shuaib et al., 2020a; Shuaib et al., 2020b; Elattar et al., 2022):

Step 1: Simplifying Eqs 13–15 to first order:

$$\left. \begin{aligned} \lambda_1(\eta) &= f(\eta), \quad \lambda_2(\eta) = f'(\eta), \quad \lambda_3(\eta) = \theta(\eta), \\ \lambda_4(\eta) &= \theta'(\eta), \quad \lambda_5(\eta) = \phi(\eta), \quad \lambda_6(\eta) = \phi'(\eta). \end{aligned} \right\} \quad (17)$$

By putting Eq. 17 in Eqs 13–15, we get

$$\left(1 + \frac{1}{\beta}\right) \lambda_2' - \left(i\lambda_1 + \frac{1}{\Gamma}\lambda_1 + p\lambda_1\right) = -iGr\lambda_3, \quad -\frac{1}{p} = \lambda_1(0, p), \quad (18)$$

$$0 = \lambda_1(\infty, p),$$

$$\lambda_4' - \frac{Pr}{\lambda^*} \lambda_3 + Q\lambda_3 = 0, \quad \lambda_3(0, \tau) = 1, \quad \lambda_3(\infty, \tau) = 0, \quad \lambda_3(\eta, 0) = 0, \quad (19)$$

$$\lambda_6' - Sc\lambda_5 + ScSr\lambda_4' - Sc\sigma(1 + \delta\lambda_3)^n \varphi \exp\left(-\frac{E}{1 + \delta\lambda_3}\right) = 0, \quad (20)$$

$$\lambda_5(0, \tau) = 1, \quad \lambda_5(\infty, \tau) = 0, \quad \lambda_5(\eta, 0) = 0.$$

Step 2: Familiarizing the embedding term p in Eqs 18–20:

$$\begin{aligned} \left(1 + \frac{1}{\beta}\right) \lambda_2' - \left(i\lambda_1 + \frac{1}{\Gamma}\lambda_1 + p\lambda_1\right) + \lambda_2 - (\lambda_2 - 1)p &= -iGr\lambda_3, \quad -\frac{1}{p} \\ &= \lambda_1(0, p), \quad 0 = \lambda_1(\infty, p), \end{aligned} \quad (21)$$

$$\lambda_4' - \frac{Pr}{\lambda^*} \lambda_3 + \lambda_4 - (\lambda_4 - 1)p + Q\lambda_3 = 0,$$

$$\lambda_3(0, \tau) = 1, \quad \lambda_3(\infty, \tau) = 0, \quad \lambda_3(\eta, 0) = 0, \quad (22)$$

$$\begin{aligned} \lambda_6' - Sc\lambda_5 + ScSr\lambda_4' + \lambda_6 - (\lambda_6 - 1)p - Sc\sigma(1 + \delta\lambda_3)^n \varphi \\ \exp\left(-\frac{E}{1 + \delta\lambda_3}\right) &= 0, \end{aligned} \quad (23)$$

$$\lambda_5(0, \tau) = 1, \quad \lambda_5(\infty, \tau) = 0, \quad \lambda_5(\eta, 0) = 0.$$

Step 3: Apply the Cauchy principal and discretized Eqs 21–23.

After discretization, the obtained set of equations was computed through Matlab, using the code PCM.

Results and discussion

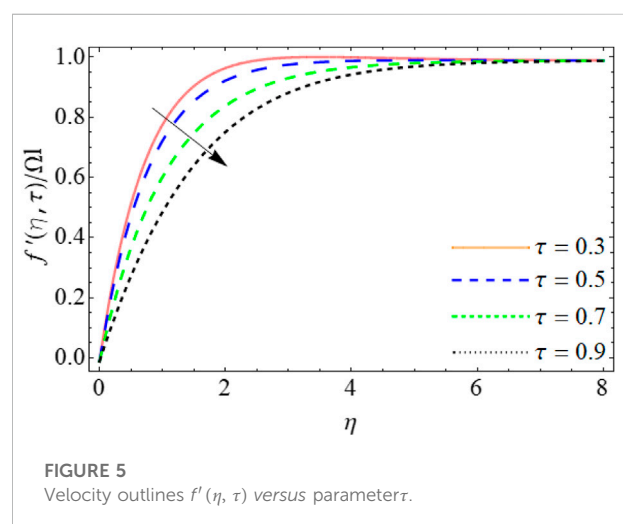
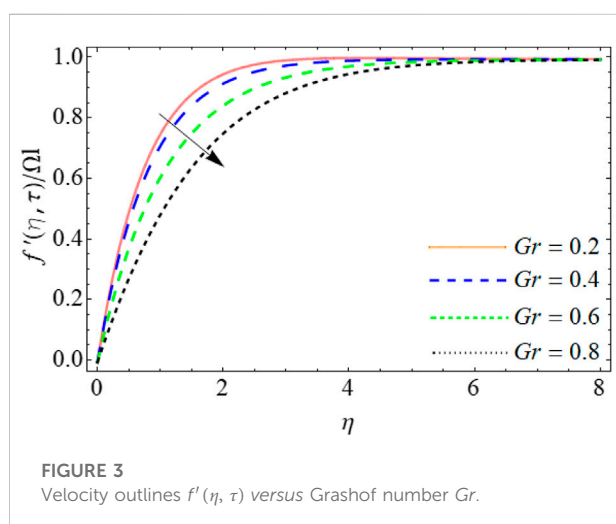
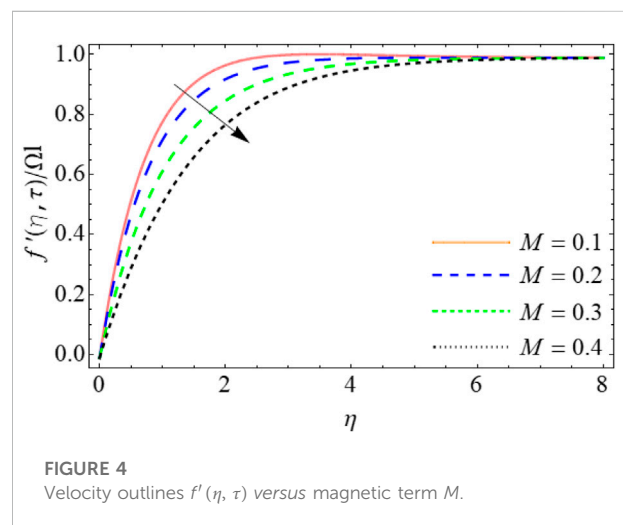
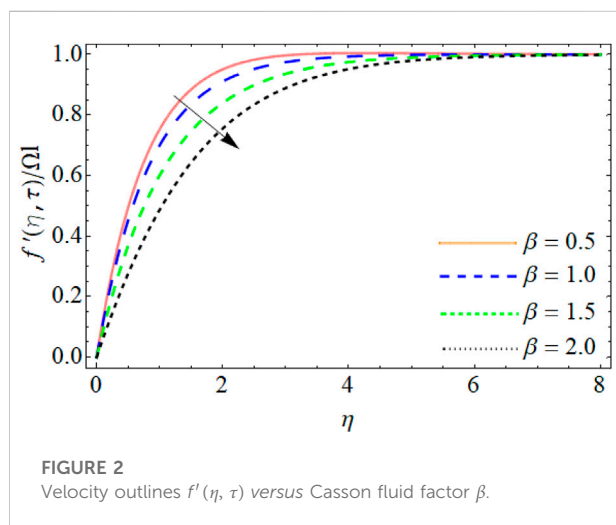
In this section, we present the trends and physical mechanism behind each figure. Table 1 compares our calculations to those in the published literature. It can be concluded that the proposed technique and results are reliable. The following explanations have been noticed from velocity, energy and concentration profiles:

Velocity Profile ($f'(\eta, \tau)$, $g(\eta, \tau)$):

Figures 2–5 display the trend of velocity outlines $f'(\eta, \tau)$ versus the Casson fluid factor, β , Grashof number, Gr , magnetic term, M , and parameter, τ , respectively. The primary velocity of the fluid significantly declines with the impact of Casson fluid factor, Grashof number, magnetic term and parameter τ . It can be seen that the effect of Casson fluid factor lessens the fluid velocity $f'(\eta, \tau)$ as presented in Figure 2. The gravitational

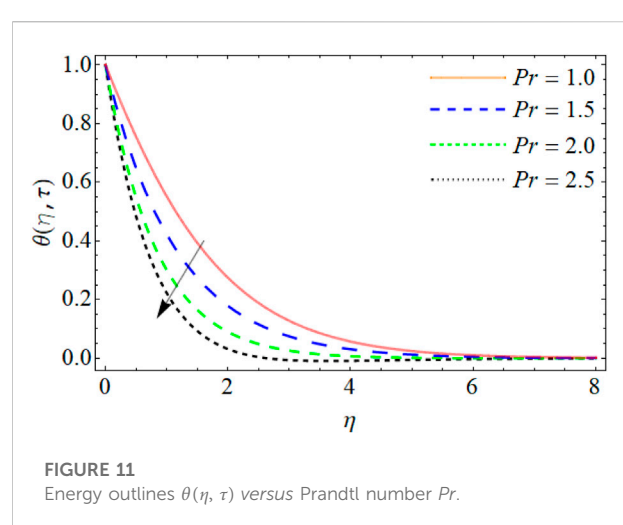
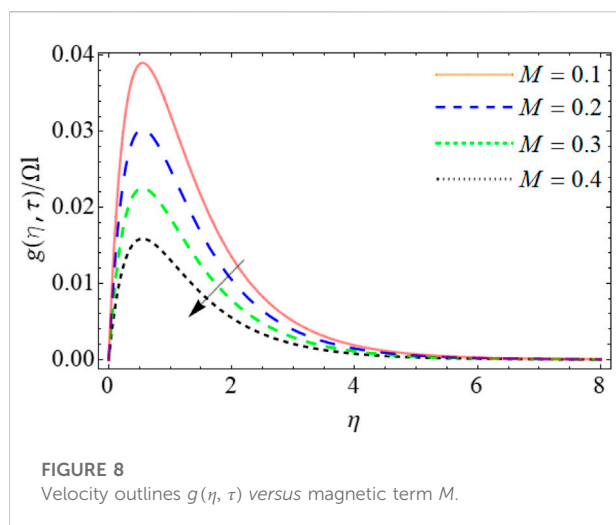
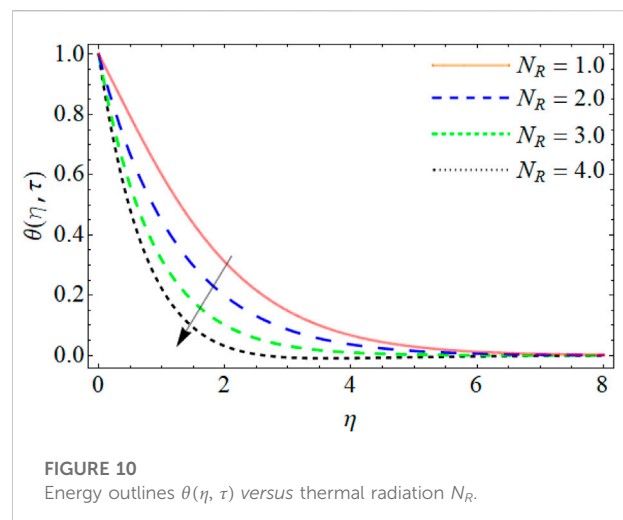
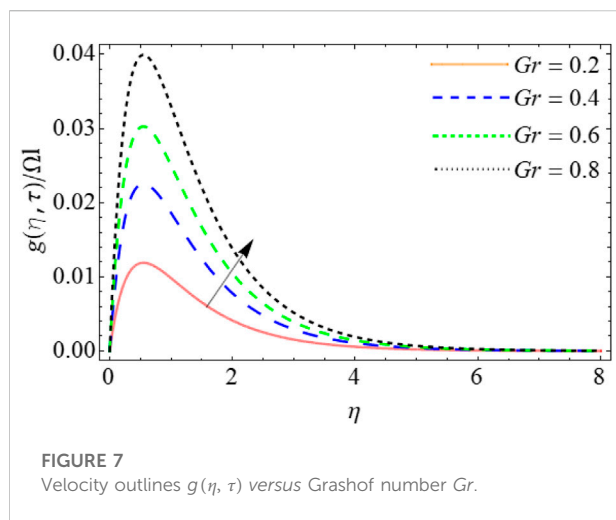
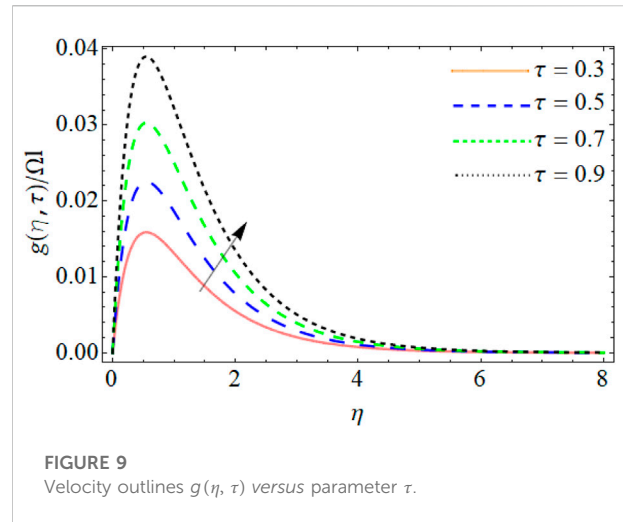
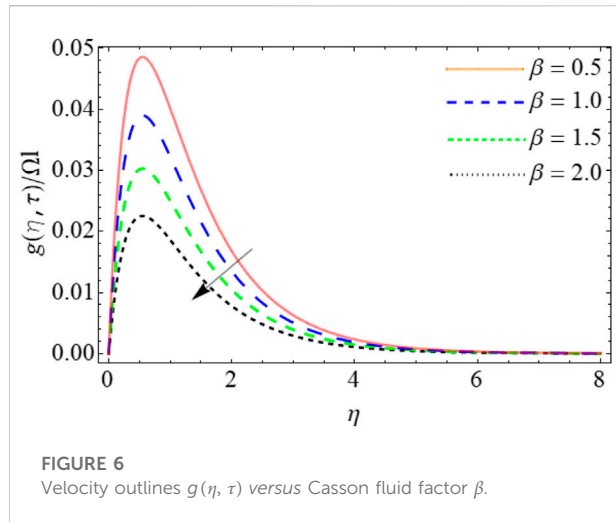
TABLE 1 Comparison of the present outcomes with published work for skin friction, Nusselt and Sherwood numbers, where $\beta = Gr = 0$.

| Parameters | | | $f''(0)$ | $f''(0)$ | $\theta'(0)$ | $\theta'(0)$ | $\phi'(0)$ | $\phi'(0)$ |
|------------|-----|------|---------------------|--------------|---------------------|--------------|---------------------|--------------|
| N_R | M | Sc | Hayat et al. (2004) | Present work | Hayat et al. (2004) | Present work | Hayat et al. (2004) | Present work |
| 1.0 | 0.1 | 0.2 | 0.273064 | 0.273171 | 0.185187 | 0.185284 | 0.170700 | 0.170801 |
| 2.0 | | | 0.312694 | 0.312782 | 0.277738 | 0.277837 | 0.254406 | 0.254423 |
| 3.0 | 0.1 | | 0.348706 | 0.348727 | 0.277698 | 0.277787 | 0.295049 | 0.295055 |
| | 0.2 | | 0.363114 | 0.363126 | 0.282798 | 0.282896 | 0.295116 | 0.295137 |
| | 0.3 | 0.2 | 0.364484 | 0.364495 | 0.284353 | 0.284454 | 0.296016 | 0.296024 |
| | | 0.4 | 0.378266 | 0.378277 | 0.291206 | 0.291227 | 0.296911 | 0.296940 |
| | | 0.6 | 0.391649 | 0.391667 | 0.297673 | 0.297684 | 0.297412 | 0.297443 |



force enhances, while the angular rotation of the spinning disc decreases the effect of Grashof number, which is why the increasing effect of Gr reduces the velocity field $f'(\eta, \tau)$ as

shown in Figure 3. The improving tendency of the magnetic field causes the generation of Lorentz forces, which resist the flow field and decrease its velocity (Figure 4). Figure 5



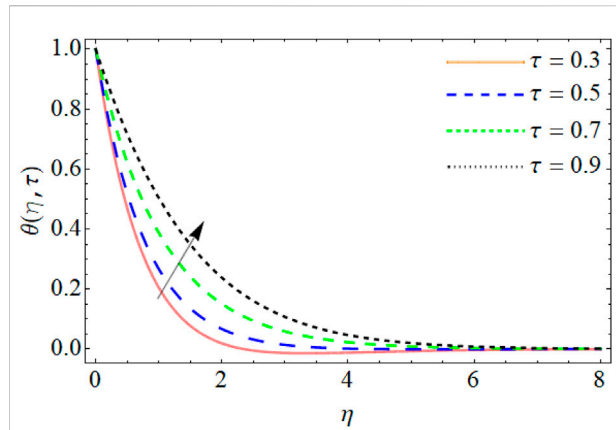


FIGURE 12

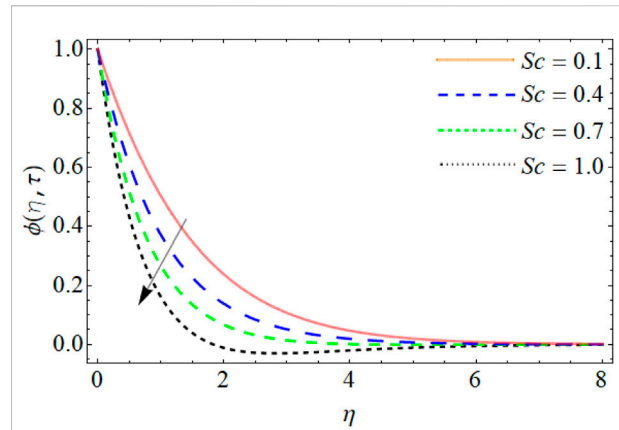
Energy outlines $\theta(\eta, \tau)$ versus parameter τ .

FIGURE 15

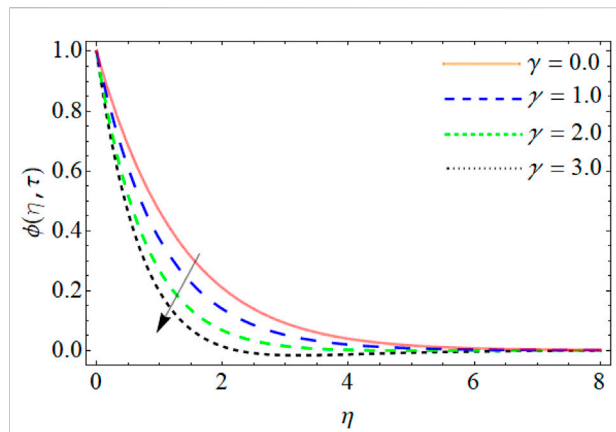
Mass outlines $\phi(\eta, \tau)$ versus Schmidt number Sc .

FIGURE 13

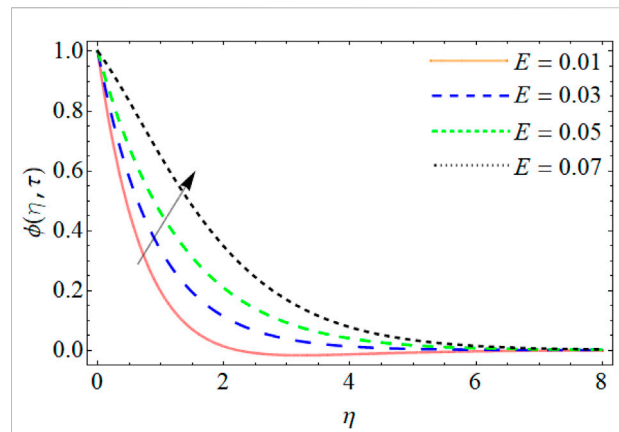
Mass outlines $\phi(\eta, \tau)$ versus constructive chemical reaction γ .

FIGURE 16

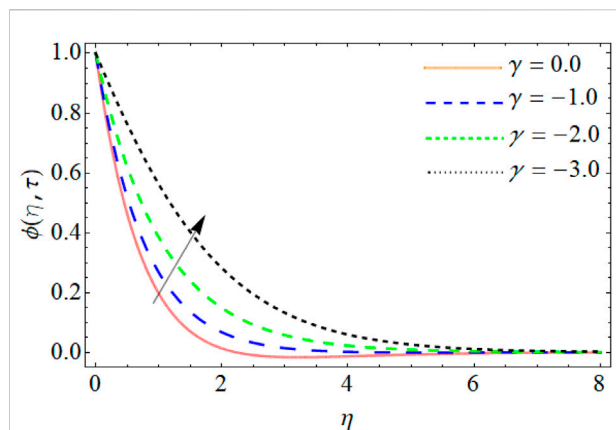
Mass outlines $\phi(\eta, \tau)$ versus activation energy E .

FIGURE 14

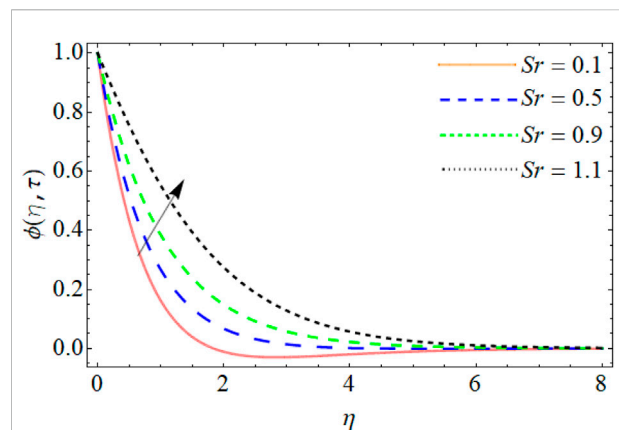
Mass outlines $\phi(\eta, \tau)$ versus destructive chemical reaction γ .

FIGURE 17

Mass outlines $\phi(\eta, \tau)$ versus Soret number Sr .

illustrated that the influence of parameter τ declines the primary velocity contour.

Figures 6–8 illustrate the velocity outlines $g(\eta, \tau)$ versus Casson fluid factor β , Grashof number Gr , magnetic term M and parameter τ , respectively. It can be seen in Figure 6, that the Casson fluid factor lessens the fluid velocity $g(\eta, \tau)$. The gravitational effect augments, while the angular revolution of revolving disc moderates, the value of the Grashof number, because the increasing effect of Gr boosts the secondary velocity field $g(\eta, \tau)$ as shown in Figure 7. Figures 8 and 9 illustrate that the secondary velocity frameworks decrease with the influence of magnetic field, while they increase with the increase in τ . Physically, the repellant force of the magnetic flux resists the fluid motion, decreasing the velocity field, $g(\eta, \tau)$.

Energy Profile ($\theta(\eta, \tau)$):

Figures 10–12 illustrate the mechanism behind the energy outlines $\theta(\eta, \tau)$ versus the thermal radiation, N_R , the Prandtl number, Pr , and the parameter, τ , respectively. Figures 10, 11 revealed that the energy contours decline with the rising values of thermal radiation and Prandtl number. Physically, radiation from the surface of the fluid transfers thermal energy to the surrounding system, which lowers the fluid temperature and results in the lessening of the energy outline $\theta(\eta, \tau)$ as shown in Figure 10. Fluids with higher Prandtl numbers always have lower thermal diffusivity; therefore, an increase in Prandtl number decreases the energy field. Figure 12 shows that the action of parameter τ diminishes the thermal distribution, $\theta(\eta, \tau)$.

Concentration Profile ($\phi(\eta, \tau)$):

Figures 13–17 reveal the mass profile outlines $\phi(\eta, \tau)$ versus the constructive chemical reaction, $+\gamma$, the destructive chemical reaction, $-\gamma$, the Schmidt number, Sc , the activation energy, E , and the Soret number, Sr , respectively. Figures 13, 14 depict that the mass transfer field is reduced by the action of positive chemical reaction, $+\gamma$, but augmented by negative chemical reaction, $-\gamma$. The chemical reaction is inversely related to the angular rotation of the circular disk. The increase in chemical reaction regulates the angular motion of disc, as shown in Figures 13, 14. The kinetic viscosity of the fluid is increased, while the molecular diffusion of particles is reduced by the intensifying influence of Sc , which is why an increase in Sc reduces the mass field as presented in Figure 15. Figures 16, 17 show that the concentration contour increases with increasing activation energy and Soret number. The increased activation energy boosts the kinetic energy of fluid particles, which results in acceleration of mass transfer as depicted in Figure 16. Molecular diffusion is enhanced, while the kinetic viscosity increases at high Soret numbers, and, as a consequence, mass transition is enhanced (Figure 17).

Conclusion

We have examined the numerical simulation of non-coaxial rotation of a Casson fluid and disc. The influence of thermal radiation, second-order chemical reaction, buoyancy, and heat source in a Casson fluid over a rotating frame is also studied. A nonlinear sequence of partial differential equations was used to describe the phenomenon. The modeled equations were reduced to a non-dimensional set of ODEs using similarity replacement. The obtained sets of ODEs were simulated using PCM. The key findings are:

- The Casson fluid coefficient, Grashof number, and magnetic field reduce the fluid's primary velocity contour $f'(\eta, \tau)$.
- The secondary velocity $g(\eta, \tau)$ outline decreases with the increasing value of magnetic field and Casson fluid parameter, but is increased from the effects of parameter τ and the Grashof number.
- The energy field $\theta(\eta, \tau)$ decays with the rising values of thermal radiation, parameter τ , and Prandtl number.
- The mass transfer field is decreased by the action of the positive chemical reaction, $+\gamma$, but increases from the effects of negative chemical reactions.
- An increase in the Schmidt number results in a decrease in the mass profile, while the mass profile is enhanced by increasing values of activation energy and Soret number.
- Our mathematical model may be modified for other types of non-Newtonian fluid models and may be solved through fractional and analytical techniques.

Data availability statement

The original contributions presented in the study are included in the article/Supplementary Material, and further inquiries can be directed to the corresponding author.

Author contributions

All authors listed have made a substantial, direct, and intellectual contribution to the work and approved it for publication.

Acknowledgments

The authors extend their appreciation to the Deanship of Scientific Research at King Khalid University for funding this work through Large Groups [Project under grant number (RGP.2/116/43)]. The authors would like to thank the Deanship of Scientific Research at Umm Al-Qura University

for supporting this work by Grant Code: 22UQU4350057DSR004.

Conflict of interest

The authors declare that the research was conducted in the absence of any commercial or financial relationships that could be construed as a potential conflict of interest.

References

- Ahmed, N., Khan, U., and Mohyud-Din, S. T. (2018). A theoretical investigation of unsteady thermally stratified flow of $\text{Al}_2\text{O}_3\text{--H}_2\text{O}$ and $\text{Al}_2\text{O}_3\text{--C}_2\text{H}_6\text{O}_2$ nanofluids through a thin slit. *J. Phys. Chem. Solids* 119, 296–308. doi:10.1016/j.jpcs.2018.01.046
- Al-Mubaddel, F. S., Allehian, F. M., Nofal, T. A., Alam, M. M., Ali, A., and Asamoah, J. K. K. (2022). Rheological model for generalized energy and mass transfer through hybrid nanofluid flow comprised of magnetized cobalt ferrite nanoparticles. *J. Nanomater.* 2022, 1–11. doi:10.1155/2022/7120982
- Alharbi, K. A. M., Ahmed, A. E. S., Ould Sidi, M., Ahammad, N. A., Mohamed, A., El-Shorbagy, M. A., et al. (2022). Computational valuation of Darcy ternary-hybrid nanofluid flow across an extending cylinder with induction effects. *Micromachines* 13 (4), 588. doi:10.3390/mi13040588
- Ali, F., Hou, Y., Zahid, M., and Rana, M. A. (2020). Theoretical study of the reverse roll coating of non-isothermal magnetohydrodynamics viscoplastic fluid. *Coatings* 10 (10), 940. doi:10.3390/coatings10100940
- Ali, F., Zahid, M., Hou, Y., Manafian, J., Rana, M. A., and Hajar, A. (2022). A theoretical study of reverse roll coating for a non-isothermal third-grade fluid under lubrication approximation theory. *Math. Problems Eng.* 2022, 1–18. doi:10.1155/2022/5029132
- Alsallami, S. A., Zahir, H., Muhammad, T., Hayat, A. U., Khan, M. R., and Ali, A. (2022). Numerical simulation of Marangoni Maxwell nanofluid flow with Arrhenius activation energy and entropy anatomization over a rotating disk. *Waves Random Complex Media*, 1–19. doi:10.1080/17455030.2022.2045385
- Asghar, S., Hanif, K., and Hayat, T. (2007). The effect of the slip condition on unsteady flow due to non-coaxial rotations of disk and a fluid at infinity. *Meccanica* 42 (2), 141–148. doi:10.1007/s11012-006-9027-5
- Azam, M., and Abbas, Z. (2021). Recent progress in Arrhenius activation energy for radiative heat transport of cross nanofluid over a melting wedge. *Propuls. Power Res.* 10, 383–395. doi:10.1016/j.jppr.2021.11.004
- Azam, M. (2022). Bioconvection and nonlinear thermal extrusion in development of chemically reactive Sutterby nano-material due to gyrotactic microorganisms. *Int. Commun. Heat Mass Transf.* 130, 105820. doi:10.1016/j.icheatmasstransfer.2021.105820
- Azam, M. (2022). Effects of Cattaneo-Christov heat flux and nonlinear thermal radiation on MHD Maxwell nanofluid with Arrhenius activation energy. *Case Stud. Therm. Eng.* 34, 102048. doi:10.1016/j.csite.2022.102048
- Azam, M., Mabood, F., and Khan, M. (2022). Bioconvection and activation energy dynamics on radiative sutterby melting nanomaterial with gyrotactic microorganism. *Case Stud. Therm. Eng.* 30, 101749. doi:10.1016/j.csite.2021.101749
- Azam, M., Xu, T., Mabood, F., and Khan, M. (2021). Non-linear radiative bioconvection flow of cross nano-material with gyrotactic microorganisms and activation energy. *Int. Commun. Heat Mass Transf.* 127, 105530. doi:10.1016/j.icheatmasstransfer.2021.105530
- Benhacine, H., Mahfoud, B., and Salmi, M. (2022). Stability of conducting fluid flow between coaxial cylinders under thermal gradient and axial magnetic field. *Int. J. Thermofluid Sci. Technol.* 9 (2). doi:10.36963/ijst.2022090202
- Chu, Y. M., Bashir, S., Ramzan, M., and Malik, M. Y. (2022). Model-based comparative study of magnetohydrodynamics unsteady hybrid nanofluid flow between two infinite parallel plates with particle shape effects. *Math. Methods Appl. Sci.* doi:10.1002/mma.8234
- Chu, Y. M., Nazir, U., Sohail, M., Selim, M. M., and Lee, J. R. (2021). Enhancement in thermal energy and solute particles using hybrid nanoparticles by engaging activation energy and chemical reaction over a parabolic surface via finite element approach. *Fractal Fract.* 5 (3), 119. doi:10.3390/fractalfract5030119
- Chu, Y. M., Shankaralingappa, B. M., Gireesha, B. J., Alzahrani, F., Khan, M. I., and Khan, S. U. (2022). Combined impact of Cattaneo-Christov double diffusion and radiative heat flux on bio-convective flow of Maxwell liquid configured by a stretched nano-material surface. *Appl. Math. Comput.* 419, 126883. doi:10.1016/j.amc.2021.126883
- Dadheech, P. K., Agrawal, P., Sharma, A., Nisar, K. S., and Purohit, S. D. (2022). Marangoni convection flow of $\gamma\text{-Al}_2\text{O}_3$ nanofluids past a porous stretching surface with thermal radiation effect in the presence of an inclined magnetic field. *Heat. Trans.* 51 (1), 534–550. doi:10.1002/htj.22318
- Das, S., Tarafdar, B., and Jana, R. N. (2018). Hall effects on magnetohydrodynamics flow of nanofluids due to non-coaxial rotation of a porous disk and a fluid at infinity. *J. nanofluids* 7 (6), 1172–1186. doi:10.1166/jon.2018.1527
- Elattar, S., Helmi, M. M., Elkotb, M. A., El-Shorbagy, M. A., Abdelrahman, A., Bilal, M., et al. (2022). Computational assessment of hybrid nanofluid flow with the influence of hall current and chemical reaction over a slender stretching surface. *Alexandria Eng. J.* 61 (12), 10319–10331. doi:10.1016/j.aej.2022.03.054
- Erdogan, M. E. (1977). Flow due to noncoaxial rotations of a porous disk and a fluid at infinity. *Rev. Roum. Sci. Tech. Ser. Mec. Appl.* 22, 171–178.
- Erdogan, M. E. (1997). Unsteady flow of a viscous fluid due to non-coaxial rotations of a disk and a fluid at infinity. *Int. J. non-linear Mech.* 32 (2), 285–290. doi:10.1016/s0020-7462(96)00065-0
- Ersoy, H. V. (2017). Unsteady flow due to a disk executing non-torsional oscillation and a Newtonian fluid at infinity rotating about non-coaxial axes. *Sādhanā* 42 (3), 307–315. doi:10.1007/s12046-017-0600-5
- Fei, J., Lin, B., Huang, T., and Xiao, J. (2022). Thin floor milling using moving support. *Int. J. Adv. Manuf. Technol.* 120 (1), 1385–1397. doi:10.1007/s00170-022-08814-z
- Hassan, M., Ali, S., Aich, W., Khliisa, F., Ayadi, B., and Kolsi, L. (2022). Transport pattern of Non-Newtonian mass and thermal energy under two diverse flow conditions by using modified models for thermodynamics properties. *Case Stud. Therm. Eng.* 29, 101714. doi:10.1016/j.csite.2021.101714
- Hassan, M., Al-Khaled, K., Khan, S. U., Tlili, I., and Chammam, W. (2021). Assessment of boundary layer for flow of non-Newtonian material induced by a moving belt with power law viscosity and thermal conductivity models. *Numer. Methods Partial Differ. Equ. num.* 22743. doi:10.1002/num.22743
- Hassan, M., El-Zahar, E. R., Khan, S. U., Rahimi-Gorji, M., and Ahmad, A. (2021). Boundary layer flow pattern of heat and mass for homogenous shear thinning hybrid-nanofluid: An experimental data base modeling. *Numer. Methods Partial Differ. Equ.* 37 (2), 1234–1249. doi:10.1002/num.22575
- Hassan, M. (2018). Impact of iron oxide particles concentration under a highly oscillating magnetic field on ferrofluid flow. *Eur. Phys. J. Plus* 133 (6), 1–14. doi:10.1140/epjp/i2018-12045-7
- Hayat, T., Asghar, S., Siddiqui, A. M., and Haroon, T. (2001). Unsteady MHD flow due to non-coaxial rotations of a porous disk and a fluid at infinity. *Acta Mech.* 151 (1), 127–134. doi:10.1007/bf01272530
- Hayat, T., Ellahi, R., Asghar, S., and Siddiqui, A. M. (2004). Flow induced by non-coaxial rotation of a porous disk executing non-torsional oscillations and a second-grade fluid rotating at infinity. *Appl. Math. Model.* 28 (6), 591–605. doi:10.1016/j.apm.2003.10.011
- Iqbal, S. A., Hafez, M. G., Chu, Y. M., and Park, C. (2022). Dynamical Analysis of nonautonomous RLC circuit with the absence and presence of Atangana-Baleanu fractional derivative. *jaac.* 12 (2), 770–789. doi:10.11948/20210324
- Ishtiaq, F., Ellahi, R., Bhatti, M. M., and Alamri, S. Z. (2022). Insight in thermally radiative cilia-driven flow of electrically conducting non-Newtonian Jeffrey fluid

Publisher's note

All claims expressed in this article are solely those of the authors and do not necessarily represent those of their affiliated organizations, or those of the publisher, the editors and the reviewers. Any product that may be evaluated in this article, or claim that may be made by its manufacturer, is not guaranteed or endorsed by the publisher.

under the influence of induced magnetic field. *Mathematics* 10 (12), 2007. doi:10.3390/math10122007

Jabbar, N., Hafeez, M. B., Askar, S., and Nazir, U. (2021). Non-coaxially rotating motion in Casson martial along with temperature and concentration gradients via first-order chemical reaction. *Energies* 14 (22), 7784. doi:10.3390/en14227784

Jin, F., Qian, Z. S., Chu, Y. M., and ur Rahman, M. (2022). On nonlinear evolution model for drinking behavior under Caputo-Fabrizio derivative. *jaac*. 12 (2), 790–806. doi:10.11948/20210357

Lin, Y., Zheng, L., and Zhang, X. (2014). Radiation effects on Marangoni convection flow and heat transfer in pseudo-plastic non-Newtonian nanofluids with variable thermal conductivity. *Int. J. Heat Mass Transf.* 77, 708–716. doi:10.1016/j.jheatmasstransfer.2014.06.028

Mabood, F., Yusuf, T. A., and Khan, W. A. (2021). Cu–Al₂O₃–H₂O hybrid nanofluid flow with melting heat transfer, irreversibility analysis and nonlinear thermal radiation. *J. Therm. Anal. Calorim.* 143 (2), 973–984. doi:10.1007/s10973-020-09720-w

Nazeer, M., Hussain, F., Khan, M. I., El-Zahar, E. R., Chu, Y. M., Malik, M. Y., et al. (2022). Theoretical study of MHD electro-osmotically flow of third-grade fluid in micro channel. *Appl. Math. Comput.* 420, 126868. doi:10.1016/j.amc.2021.126868

Noranur, W. N. I. N., Mohamad, A. Q., Shafie, S., Khan, I., Jiann, L. Y., and Ilias, M. R. (2021). Non-coaxial rotation flow of MHD Casson nanofluid carbon nanotubes past a moving disk with porosity effect. *Ain Shams Eng. J.* 12 (4), 4099–4110. doi:10.1016/j.asej.2021.03.011

Punith Gowda, R. J., Naveen Kumar, R., Jyothi, A. M., Prasannakumara, B. C., and Saris, I. E. (2021). Impact of binary chemical reaction and activation energy on heat and mass transfer of marangoni driven boundary layer flow of a non-Newtonian nanofluid. *Processes* 9 (4), 702. doi:10.3390/pr9040702

Raja, M. A. Z., Shoaib, M., Hussain, S., Nisar, K. S., and Islam, S. (2022). Computational intelligence of Levenberg-Marquardt backpropagation neural networks to study thermal radiation and Hall effects on boundary layer flow past a stretching sheet. *Int. Commun. Heat Mass Transf.* 130, 105799. doi:10.1016/j.icheatmasstransfer.2021.105799

Ramesh, G. K., Madhukesh, J. K., Prasannakumara, B. C., and Roopa, G. S. (2022). Significance of aluminium alloys particle flow through a parallel plates with activation energy and chemical reaction. *J. Therm. Anal. Calorim.* 147 (12), 6971–6981. doi:10.1007/s10973-021-10981-2

Rashid, S., Sultana, S., Karaca, Y., Khalid, A., and Chu, Y. M. (2022). Some further extensions considering discrete proportional fractional operators. *Fractals* 30 (01), 2240026. doi:10.1142/s0218348x22400266

Rehman, S., Gul, T., Khan, W., Khan, A., and Zee, S. (2022). Effects of chemical reaction, viscosity, thermal conductivity, heat source, radiation/absorption, on MHD mixed convection nano-fluids flow over an unsteady stretching sheet by HAM and numerical method. *Adv. Mech. Eng.* 14 (1), 168781402210743. doi:10.1177/16878140221074301

Rizwan, M., and Hassan, M. (2022). Feature of metallic oxide nanoparticles in the thermal efficiency and flow structure of non-Newtonian homogeneous nanofluid: Experimental data-based mathematical approach. *Waves Random Complex Media*, 1–20.

Sharma, K., Kumar, S., Narwal, A., Mebarek-Oudina, F., and Animasaun, I. L. (2022). Convective MHD fluid flow over stretchable rotating disks with dufour and Soret effects. *Int. J. Appl. Comput. Math.* 8 (4), 159–212. doi:10.1007/s40819-022-01357-7

Shuaib, M., Shah, R. A., and Bilal, M. (2020). Variable thickness flow over a rotating disk under the influence of variable magnetic field: An application to parametric continuation method. *Adv. Mech. Eng.* 12 (6), 168781402093638. doi:10.1177/1687814020936385

Shuaib, M., Shah, R. A., Durrani, I., and Bilal, M. (2020). Electrokinetic viscous rotating disk flow of Poisson-Nernst-Planck equation for ion transport. *J. Mol. Liq.* 313, 113412. doi:10.1016/j.molliq.2020.113412

Tie-Hong, Z., Zhou, B. C., Miao-Kun, W., and Yu-Ming, C. (2019). On approximating the quasi-arithmetic mean. *J. Inequalities Appl.* 2019 (1), 1–12.

Ullah, I. (2022). Activation energy with exothermic/endothermic reaction and Coriolis force effects on magnetized nanomaterials flow through Darcy–Forchheimer porous space with variable features. *Waves in random and complex media*, 1–14.

Ullah, I., Ali, R., Nawab, H., Uddin, I., Muhammad, T., Khan, I., et al. (2022). Theoretical analysis of activation energy effect on Prandtl–Eyring nanoliquid flow subject to melting condition. *J. Non-Equilibrium Thermodyn.* 47 (1), 1–12. doi:10.1515/jnet-2020-0092

Ullah, I., Hayat, T., Aziz, A., and Alsaedi, A. (2022). Significance of entropy generation and the coriolis force on the three-dimensional non-Darcy flow of ethylene-glycol conveying carbon nanotubes (SWCNTs and MWCNTs). *J. Non-Equilibrium Thermodyn.* 47 (1), 61–75. doi:10.1515/jnet-2021-0012

Ullah, Z., Ullah, I., Zaman, G., and Sun, T. C. (2022). A numerical approach to interpret melting and activation energy phenomenon on the magnetized transient flow of Prandtl–Eyring fluid with the application of Cattaneo–Christov theory. *Waves in Random and Complex Media*, 1–21.

Wakif, A., Chamkha, A., Thumma, T., Animasaun, I. L., and Sehaqui, R. (2021). Thermal radiation and surface roughness effects on the thermo-magneto-hydrodynamic stability of alumina–copper oxide hybrid nanofluids utilizing the generalized Buongiorno's nanofluid model. *J. Therm. Anal. Calorim.* 143 (2), 1201–1220. doi:10.1007/s10973-020-09488-z

Wang, F., Khan, M. N., Ahmad, I., Ahmad, H., Abu-Zinadah, H., and Chu, Y. M. (2022). Numerical solution of traveling waves in chemical kinetics: Time-fractional Fishers equations. *Fractals* 30 (2), 2240051–2240134. doi:10.1142/s0218348x22400515

Wei, H., Gu, J., Ren, F., Zhang, L., Xu, G., Wang, B., et al. (2021). Smart materials for dynamic thermal radiation regulation. *Small* 17 (35), 2100446. doi:10.1002/smll.202100446

Yaseen, M., Rawat, S. K., and Kumar, M. (2022). Cattaneo–Christov heat flux model in Darcy–Forchheimer radiative flow of MoS₂–SiO₂/kerosene oil between two parallel rotating disks. *J. Therm. Anal. Calorim.* 147, 10865–10887. doi:10.1007/s10973-022-11248-0

Zhao, T. H., Khan, M. I., and Chu, Y. M. (2021). Artificial neural networking (ANN) analysis for heat and entropy generation in flow of non-Newtonian fluid between two rotating disks. *Math. Methods Appl. Sci.* doi:10.1002/mma.7310



OPEN ACCESS

EDITED BY

Umar Khan,
Hazara University, Pakistan

REVIEWED BY

Basharat Ullah,
Mohi-Ud-Din Islamic University,
Pakistan
Muhammad Farooq,
University of Engineering and
Technology, Lahore, Pakistan
Zulqurnain Sabir,
United Arab Emirates University, United
Arab Emirates

*CORRESPONDENCE

Elsayed Tag Eldin,
Elsayed.tageldin@fue.edu.eg

SPECIALTY SECTION

This article was submitted to Process
and Energy Systems Engineering,
a section of the journal
Frontiers in Energy Research

RECEIVED 15 June 2022

ACCEPTED 01 August 2022

PUBLISHED 04 October 2022

CITATION

Gul T, Mukhtar S, Alghamdi W,
Tag Eldin E, Yassen MF and Guedri K
(2022), The radiative flow of the thin-
film Maxwell hybrid nanofluids on an
inclined plane in a porous space.
Front. Energy Res. 10:970293.
doi: 10.3389/fenrg.2022.970293

COPYRIGHT

© 2022 Gul, Mukhtar, Alghamdi, Tag
Eldin, Yassen and Guedri. This is an
open-access article distributed under
the terms of the [Creative Commons
Attribution License \(CC BY\)](https://creativecommons.org/licenses/by/4.0/). The use,
distribution or reproduction in other
forums is permitted, provided the
original author(s) and the copyright
owner(s) are credited and that the
original publication in this journal is
cited, in accordance with accepted
academic practice. No use, distribution
or reproduction is permitted which does
not comply with these terms.

The radiative flow of the thin-film Maxwell hybrid nanofluids on an inclined plane in a porous space

Taza Gul¹, Safyan Mukhtar², Wajdi Alghamdi³,
Elsayed Tag Eldin^{4*}, Mansour F. Yassen^{5,6} and Kamel Guedri⁷

¹Department of Mathematics, City University of Science and Information Technology, Peshawar, Pakistan, ²Department of Basic Sciences, Deanship of Preparatory Year, King Faisal University, Hafuf, Al Ahsa, Saudi Arabia, ³Department of Information Technology, Faculty of Computing and Information Technology, King Abdulaziz University, Jeddah, Saudi Arabia, ⁴Faculty of Engineering and Technology, Future University in Egypt New Cairo, Cairo, Egypt, ⁵Department of Mathematics, College of Science and Humanities in Al-Aflaj, Prince Sattam Bin Abdulaziz University, Al-Aflaj, Saudi Arabia, ⁶Department of Mathematics, Faculty of Science, Damietta University, Damietta, New Damietta, Egypt, ⁷Mechanical Engineering Department, College of Engineering and Islamic Architecture, Umm Al-Qura University, Makkah, Saudi Arabia

Due to their accelerated rate of heat transfer, nanofluids are of immense interest. This work analyzes an innovative concept of hybrid nanoemulsion with an optimized design under the chemical radiative flow and its thermophysical properties. We are able to achieve great aspects of the flow with the assistance of the sheet's permeable texture and inclined surface. Furthermore, the effects of thermal conductivity mix convection, chemical reaction, and thermal radiations on velocity, temperature, and concentration fields are also investigated. After converting the fundamental equations to ordinary differential equations with the use of similarity transportation, the problem is then solved analytically with the HAM technique. To investigate key attributes and parameters, a hybrid nanofluid with Ag and Al₂O₃ nanoparticles as well as Al₂O₃ for conventional nanofluids with the base solvent water is taken. To illustrate the effects of chemical radiative and mix convection on the thin-film flow, numerous graphs, charts, and tables are shown. Calculations and reviews are performed for reduced friction coefficient, heat, and mass transportation. According to this study, hybrid nanofluids have a higher heat-transfer rate than nanofluids when exposed to thermal radiation and at the appropriate surface angle of inclination. Due to $\phi_{Al_2O_3}$, ϕ_{Ag} , S , Rd , the temperature increases, but velocity has the opposite effect. This investigation's innovative findings will promote the study of condensed nanostructures and nanomaterials.

KEYWORDS

Maxwell hybrid nanofluid, thin film, heat and mass transfer, inclined stretching sheet, MgO and TiO₂

Introduction

Table 1 shows the thermophysical properties of the materials. It is common practice to utilize the power-law model when modeling the flow of fluids that have a viscosity that varies with shear. On the other hand, it is not possible to forecast the results of elasticity. Fluids of the second or third grade have the potential to produce the desired outcomes in terms of elasticity. However, in these models, the viscosity is not shear-dependent. Furthermore, they are impotent to assess the effects of reducing stress. A subcategory of fluids known as the Maxwell model, which has become more popular, can identify stress relaxation. A perfectly viscous obstruction and a strictly elastic spring can be represented, much like in the Maxwell model. Maxwell nanofluid flow simulations have drawn the attention of numerous researchers. Abro et al. (2020), Sharama et al. (2020), and Ramesh et al. (2020) have used various mathematical models for the Maxwell fluid flow. The influence of radiative heat flux on the flow of Maxwell nanofluids across a chemically reacting spiraling disc was analyzed by Ahmed et al. (2020). Hussain et al. (2020) took into consideration the mathematical analysis of a Maxwell nanofluid with hydromagnetic dissipative and radiation. Jawad et al. (2021) have analyzed the entropy impact on the flow of Maxwell fluids using stretched surfaces.

The most appealing and affordable method of thermal transportation was proposed by the revolutionary advancement in science using the concept of nanoparticles. Researchers are constantly examining the thermal characteristics of nanoparticles related to engineering and manufacturing usages because they have the highest proficiency of thermal transportation and stable forceful features. The formation of nanofluids is caused by the dispersion of nanoparticles in the base solvent. Plications for nanofluids are anticipated in a variety of fields, including nuclear engineering, mechanical and cooling devices, extrusion systems, and many others. In recent years, the role of nanofluids in energy production has moved into more essential applications. When nanoparticles are adequately dissolved in the base fluid, it is expected that mass and heat transmission will improve. Nanofluids are widely used in biotechnology, medicine delivery, renewable energy, and several technical fields. Choi (1995) coordinated the basic analysis and experimental investigation of the nanofluid characteristics. The thermal measurements of a nanofluid containing micropolar material were described by Khan et al. (2020) using modified diffusion concepts. Khan et al. (2019) have depicted the Oldroyd-B nanofluid flow using the optimal Prandtl number technique. Turkyilmazoglu (2020) used the single-phase model to declare the stability of nanofluids. The impact of porous space over moving surfaces susceptible to the Jeffrey nanofluid was determined by Khan and Shehzad (2020). The dual solution prediction for

the nanofluid flow subject to asymmetrical slip was observed by Nadeem et al. (2020). Some other researchers have proposed different forms of nanofluids to study the many uses of nanofluids in various aspects (Sabir et al., 2019; Umar et al., 2020; Ayub et al., 2021a; Ayub et al., 2021b; Sabir et al., 2021).

As an alternative to conventional fluids, nanofluids are renowned for their exceptional capacity to transport energy. In order to make it significantly better, the hybrid nanoliquid is being produced. When two or more types of metals are combined in such a way as to produce different chemical bonds, the resulting substances are referred to be hybrid metals. A “hybrid nanofluid” can also be created by the uniform dispersion of two very small particles into the liquid that is acting as the mother liquid. Comparing this highly developed type of solution to unitary nanofluids or any other common functional fluids, it shows promising heat transmission. The innovative uses for hybrid nanosolutions include the fabrication of aviation devices, power systems, welding, lubricants, spacecraft, and electronic cooling devices. The influence of the magnetic field in the transverse direction to the flow field is discussed by Devi and Devi (2016). Babar and Ali (2019) discussed the specific thermophysical environment, applications, setup, and inherent issues of hybrid composites. Recently, more studies about hybrid nanofluid flow through various configurations can be decoded in Acharya et al. (2020), Yaseen et al. (2022), and Joshi et al. (2022).

The transportation of liquids in thin layers is frequently seen in daily life; one illustration of this is the way raindrops move across rooftops, road surfaces, and window glass. Understanding the process of thin films is crucial since they frequently occur in nature and have numerous useful applications. Whether there are inertial forces present or absent, thin films of liquids are driven by surface or body forces. Depending on the flow pattern under consideration, the strength of these forces acting on the fluid may be increased or decreased. In situations like dropping films or spray coating, inertia is crucial, but it is sometimes disregarded when the flow Reynolds number is low, as in the flow motion over an inclined plane in a sluggish motion. Thin-film flows have drawn a great deal of interest in recent years. Photovoltaic panels, lamination, biofluid flows, hydrophilicity, and other commercial and technical applications all involve film flowing over stirring flat, vertical, and inclined planes (Liu et al., 2017). The first person to look at the case of the dropping liquid films was Nusselt (1916). Jeffrey (1925) also explored the film flow in the scenario of an inclined plane. There are a lot of research studies on film flow on diverse models, which may be found in the Refs. Wang, 1990; Qasim et al., 2016; Zhang et al., 2021; Shah et al., 2022.

The radiation impact plays an important role in almost all the design approaches. Thermal radiation plays a significant role in a variety of mechanical processes, such as missiles, nuclear power plants, spacecraft and other communications satellites, steam

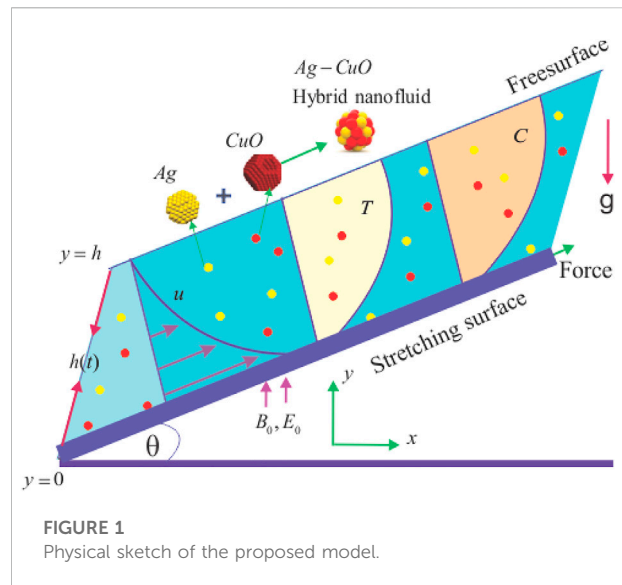
turbines, and the many driving mechanisms for aviation. In addition to radiation, Ghadikolaei et al. (2018) and Ali et al. (2020) focused on the thermal radioactive effects in addition to the transfer of nanofluids when studying peristaltic pressing. CuO-Ag/water micropolar hybrid nanofluid flow across a vertically positioned plate was studied by Gumber et al. (2022) with the help of heat radiation and the suction/injection mechanism.

The possibilities for higher thermal transport illustrate the knowledge of the existing literature. Recent investigations of unsteady thin-film flow impacted by advanced ablation/accretion (Wang, 1990; Qasim et al., 2016; Zhang et al., 2021; Shah et al., 2022) address conventional heat transmission modes. We focused on expanding such work to include the chemical radiative effect and the mix convectional characteristics of Maxwell hybrid nanofluid flow. The cited works mentioned aforesaid highlight that less attention is paid to the study of nanofluid flow impressions over an inclined stretched plane keeping insight of Maxwell fluid flow. Nevertheless, the flow of the hybrid nanofluid in the same context is rare. We in this exploration discussed the hybrid nanofluid flow comprising silver with aluminum oxide, nanocomposites, and thin-film flow over an inclined plane. The thermal effects of the nanocomposites are also taken into account in the presence of radiation. The composite factor of the particles plays a significant role in thermal conduction. The film width along with the applied magnetic field has been studied additionally in the graphical form by using the HAM method. The impression of varied parameters versus involved profiles is studied logically.

The following are some of the innovative aspects of this work:

- Due to the intensive use of both laboratory and computational studies, the novel heat-transfer fluid is focused on the appropriate Maxwell fluid-based Al_2O_3 -Ag-hybrid nanofluid.
- To explore the heat-transfer phenomenon, a thin film of Maxwell hybrid nanofluid flow on an inclined extended surface using thermal conductivity models has been used.
- To find an analytical solution for heat-transfer effects in hybrid nanofluid flow with thermal radiation, chemical reaction, porosity, and mix convection present.
- The governing equations for heat, mass transport, and fluid motion are transformed into self-similar differential equations using the standard factors, and the HAM method is then used to evaluate them analytically.
- The results are represented in diagrams that correspond to various numeric values of the relevant parameters.

Chemical radiative and convectional heat exchange between the surface and the surrounding fluid is essential in many real-world applications involving the cooling or heating of surfaces.



The problem is more realistic and produces better results because of its cumulative proportion.

Problem development and the governing model

Let us examine the improvement of energy and mass transformation in time-dependent thin-film flow of Maxwell fluids with hybrid and mononanoparticles. Over an extended inclined plane making an angle θ with the surface, a thin film flows. The following considerations are made while modeling the transportation of mass and heat:

- 1 The surface over which the thin film exists is moving with velocity $U = bx(1 - \alpha t)^{-0.5}$; here, the operative elasticity of the velocity is $b(1 - \alpha t)^{-\frac{1}{2}}$ toward the x -axis, where " α " signifies the increment of time ($0 \leq \alpha < 1$) and " b " represents the elasticity.
- 2 The surface temperature of the extending sheet is signified as " T_s ", and the temperatures of the slit are defined as T_0 and T_r . The range of these constraints is referred to as $0 \leq T_r \leq T_0$.
- 3 $\frac{3xU_w}{\nu} = \frac{bx^2(1 - \alpha t)^{-1}}{\nu}$ is the local Reynolds number dependent on U_w .
- 4 $h(t)$ represents the thickness of the film.
- 5 We consider pressure to be constant.
- 6 The nanoparticles Al_2O_3 and Ag are used.
- 7 The magnetic field in a perpendicular direction is defined as $B_0(x, t) = (1 - \alpha t)^{-\frac{1}{2}} B_0$.
- 8.8 The flow configuration for the problem is shown in Figure 1.

The fundamental equations for boundary layers that govern flow, heat, and mass transfer have the following forms (Jawad et al., 2021; Acharya et al., 2020; Zhang et al., 2021; Shah et al., 2022; Gumber et al., 2022):

$$\frac{\partial u}{\partial x} + \frac{\partial v}{\partial y} = 0 \quad (1)$$

$$\left(\frac{\partial u}{\partial t} + u \frac{\partial u}{\partial x} + v \frac{\partial u}{\partial y} \right) = \nu_{hmf} \frac{\partial^2 u}{\partial y^2} - \lambda_1 \left(2uv \frac{\partial^2 u}{\partial x \partial y} + u^2 \frac{\partial^2 u}{\partial x^2} + v^2 \frac{\partial^2 u}{\partial y^2} \right) - \left[\frac{\nu_{hmf}}{k^*} \left(\lambda_1 v \frac{\partial u}{\partial y} + u \right) + \frac{\sigma_{hmf}}{\rho_{hmf}} \left(B^2(x, t) \left(\lambda_1 v \frac{\partial u}{\partial y} + u \right) - E_0 B(x, t) \right) \right] + g \left\{ \pm (T - T_h) (\beta_T)_{hmf} + (C - C_h) (\beta_C)_{hmf} \right\} \sin \theta, \quad (2)$$

$$\frac{\partial T}{\partial t} + u \frac{\partial T}{\partial x} + v \frac{\partial T}{\partial y} = \alpha_{hmf} \left[\frac{\partial^2 T}{\partial y^2} \right] + \frac{16\sigma^* T_h^3}{3k^* (\rho C p)_{hmf}} \frac{\partial^2 T}{\partial y^2} \quad (3)$$

$$\frac{\partial C}{\partial t} + u \frac{\partial C}{\partial x} + v \frac{\partial C}{\partial y} = D_{Bhmf} \frac{\partial^2 C}{\partial y^2} - Kr(C - C_h) \quad (4)$$

The components of velocity are represented by u, v and act along x, y directions, respectively; λ_1 is the Maxwell relaxation time parameter (note that for $\lambda_1 = 0$, the problems reduce to the case of classical heat and mass transport of Newtonian fluids); k^* is the permeability of the porous medium; β_T, β_C are the coefficients of linear thermal and concentration expansion, respectively; σ^* is the Stefan-Boltzmann constant; k^* is the coefficient of mean absorption; D_{Bhmf} is the diffusion coefficient of the hybrid nanofluid; and Kr is the chemical reaction. Also, the σ_{hmf} (electrical conductivity), μ_{hmf} (dynamic viscosity), ρ_{hmf} (density), $(\rho C p)_{hmf}$ (capacity of specific heat), and k_{hmf} (thermal conductivity) are some of the hybrid nanofluid quantities that can be described in this way (Acharya et al., 2020 and Joshi et al., 2022).

$$\frac{\mu_{hmf}}{\mu_f} = \frac{(1 - \phi_{Ag})^{-2.5}}{(1 - \phi_{Al_2O_3})^{2.5}}, \quad \frac{\mu_{nf}}{\mu_f} = (1 - \phi_{Al_2O_3})^{-2.5} \quad (5)$$

$$\left. \begin{aligned} \frac{\rho_{hmf}}{\rho_f} &= (1 - \phi_{Al_2O_3})(1 - \phi_{Ag}) + \phi_{Al_2O_3}(1 - \phi_{Ag}) \frac{\rho_{Ag}}{\rho_f} + \phi_{Ag} \frac{\rho_{Al_2O_3}}{\rho_f} \\ \frac{\rho_{nf}}{\rho_f} &= (1 - \phi_{Al_2O_3}) + \phi_{Al_2O_3} \frac{\rho_{Al_2O_3}}{\rho_f} \end{aligned} \right\} \quad (6)$$

$$\left. \begin{aligned} \frac{(\rho C p)_{hmf}}{(\rho C p)_f} &= (1 - \phi_{Ag})(1 - \phi_{Al_2O_3}) + (1 - \phi_{Ag}) \phi_{Al_2O_3} (\rho C p)_{Ag} + \phi_{Ag} (\rho C p)_{Al_2O_3} \\ \frac{(\rho C p)_{nf}}{(\rho C p)_f} &= (1 - \phi_{Al_2O_3}) + \frac{(\rho C p)_{Al_2O_3}}{(\rho C p)_f} \phi_{Al_2O_3} \end{aligned} \right\} \quad (7)$$

$$\left. \begin{aligned} \frac{k_{hmf}}{k_{nf}} &= (1 - \phi_{Ag}) + 2 \left(\frac{k_{Al_2O_3}}{k_{Al_2O_3} - k_{nf}} \right) k_{Ag} \log_e \left(\frac{k_{Al_2O_3} + k_{nf}}{k_{nf}} \right) \\ \frac{k_{nf}}{k_f} &= (1 - \phi_{Al_2O_3}) + 2 \left(\frac{k_{Ag}}{k_{Ag} - k_{nf}} \right) k_{Al_2O_3} \log_e \left(\frac{k_{Ag} + k_{nf}}{k_{nf}} \right) \end{aligned} \right\} \quad (8)$$

$$\frac{\sigma_{hmf}}{\sigma_f} = 1 + \frac{3 \phi_{Al_2O_3} \sigma_{Al_2O_3} + 3 \phi_{Ag} \sigma_{Ag} - 3 \phi \sigma_f}{\sigma_f (2 + \phi) + (1 - \phi_{Al_2O_3}) \sigma_{Al_2O_3} + (1 - \phi_{Ag}) \sigma_{Ag}} \quad (9)$$

Therefore, we assumed the composition of Ag into Al_2O_3/H_2O ; in the proposed investigation, a hybrid nanofluid was developed. Al_2O_3 nanoparticles ($\phi_{Al_2O_3}$) are first dispersed in H_2O to make a Al_2O_3/H_2O ordinary nanofluid, and then Ag nanomaterials of diverse ratios (ϕ_{Ag}) are mixed to make a consistent hybrid nanofluid of Al_2O_3 -Ag/ H_2O . We assume that $\phi = \phi_{Al_2O_3} + \phi_{Ag}$ throughout the study.

The physical conditions for the thin-film flow are defined as

$$\left\{ \begin{aligned} u|_{y=0} &= U_w, \quad v|_{y=0} = 0, \quad \mu_{hmf} \frac{\partial u}{\partial y} \Big|_{y=h(t)}, \quad v = \frac{\partial h}{\partial t} \Big|_{y=h(t)}, \\ T|_{y=0} &= T_w, \quad C|_{y=0} = C_w, \quad \frac{\partial T}{\partial y} \Big|_{y=h(t)} = \frac{\partial C}{\partial y} \Big|_{y=h(t)} = 0. \end{aligned} \right\} \quad (10)$$

The non-dimensional variables and coordinates that we present are as follows (Zhang et al., 2021; Shah et al., 2022):

$$\left\{ \begin{aligned} \psi &= \left(\frac{bv}{1 - \alpha t} \right)^{\frac{1}{2}} x f(\eta), \quad \eta = \left(\frac{b}{v(1 - \alpha t)} \right)^{\frac{1}{2}} y, \\ T &= T_0 - T_r \left(\frac{bx^2}{2v} \right) \frac{\Theta(\eta)}{(1 - \alpha t)^{\frac{1}{2}}}, \quad C = C_0 - C_r \left(\frac{bx^2}{2v} \right) \frac{\Phi(\eta)}{(1 - \alpha t)^{\frac{1}{2}}}, \end{aligned} \right\} \quad (11)$$

where

$$u = \frac{\partial \psi}{\partial y}, \quad v = -\frac{\partial \psi}{\partial x} \quad (12)$$

Eq. 1 is satisfied, while Eqs 2–4 are transformed as

$$\beta = \left(\frac{b}{v(1 - \alpha t)} \right)^{\frac{1}{2}} h(t) \quad (13)$$

$$\frac{dh}{dt} = \frac{\alpha \beta}{2} \left(\frac{v}{b(1 - \alpha t)} \right)^{\frac{1}{2}} \quad (14)$$

$$\begin{aligned} \frac{\mu_{hmf}}{\mu_f} \frac{\rho_f}{\rho_{hmf}} f''' - S \left(f' + \frac{\eta}{2} f'' \right) - (f')^2 + f f'' + \lambda (2 f f' f'' - f^2 f''') - \lambda r (f' - \lambda f f'') \\ + \frac{\mu_f}{\mu_{hmf}} M [E - (f' - \lambda f f'')] \pm \frac{\beta_{Thmf}}{\beta_f} (Gr \Theta) + \frac{\beta_{Chmf}}{\beta_f} (Gc \Phi) = 0, \end{aligned} \quad (15)$$

$$\begin{aligned} \frac{1}{Pr} \frac{(\rho C p)_f}{(\rho C p)_{hmf}} \left(\frac{k_{hmf}}{k_f} + \frac{4}{3} Rd \right) \Theta'' - \frac{S}{2} (3 \Theta + \eta \Theta') - 2 f' \Theta + f \Theta' \\ = 0 \end{aligned} \quad (16)$$

$$\Phi'' + Sc \left(\frac{S}{2} (3 \Phi + \eta \Phi') - 2 f' \Phi + f \Phi' \right) - \gamma Sc \Phi = 0 \quad (17)$$

$$\left\{ \begin{aligned} S &= \frac{\alpha}{a} \lambda = \frac{\lambda_1}{(1 - \alpha t)}, \quad \lambda_p = \frac{v}{k^* a}, \quad Pr = \frac{\mu C p}{k}, \quad Rd = \frac{4 \sigma^* T_h^3}{3 k^* k_f (\rho C p)_{hmf}}, \quad \gamma = \frac{Kr}{a}, \\ Gr &= \frac{g \beta_T [T_w - T_h] x^3}{v_f^2}, \quad Gc = \frac{g \beta_C [C_w - C_h] x^3}{v_f^2}. \end{aligned} \right\} \quad (18)$$

TABLE 1 Thermophysical features of the nanoparticles.

| Parameter | APS (average particle size), nm | ρ Kg m^{-3} | k W $m^{-1}K^{-1}$ | C_p J $kg^{-1}K^{-1}$ |
|-------------------------------|---------------------------------|--------------------|----------------------|-------------------------|
| Al_2O_3 | 25–45 | 3,970 | 40 | 765 |
| Ag | 18–23 | 10,500 | 429 | 250 |
| 80 wt% Al_2O_3 –20 wt% Ag | 10–45 | 2.87 | 4.768 | 0.842 |

where $S, \lambda_p, Pr, \lambda, \gamma, Gr, Rd, Gc$ are the unsteadiness parameter, porosity term, Prandtl number, Maxwell parameter, chemical reaction, thermal Grashof number, radiation parameter, and mass Grashof number, respectively.

The transform forms of the physical conditions are taken as

$$\left\{ \begin{array}{l} f(0) = 0, f'(0) = 1, \Theta(0) = 1, \Phi(0) = 1, \\ f''(\beta) = 0, f(\beta) = \frac{S\beta}{2}, \Theta'(\beta) = 0, \Phi'(\beta) = 0 \end{array} \right\} \quad (19)$$

The skin friction and the local Nusselt and Sherwood numbers are defined as

$$C_f = \frac{2\tau_w}{\rho U_w^2}, N_u = \frac{q_w x}{k(T_w - T_0)}, S_n = \frac{q_m x}{D_B(C_w - C_0)} \quad (20)$$

where

$$\tau_w = \mu \left(\frac{\partial u}{\partial y} \right) \Big|_{y=0}, q_w = -k \left(\frac{\partial T}{\partial y} \right) \Big|_{y=0}, q_m = -D_B \left(\frac{\partial C}{\partial y} \right) \Big|_{y=0} \quad (21)$$

The transformed terms are stated as

$$\left\{ \begin{array}{l} Re^{\frac{1}{2}} C_f = -\frac{\mu_f}{\mu_{mf}} f''(0), \quad Re^{\frac{1}{2}} N_u = -\left(\frac{k_{mf}}{k_f} + Rd \right) \Theta'(0), \\ Re^{\frac{1}{2}} S_n = -\Phi'(0), \quad Re = \frac{x U_w}{\nu} \end{array} \right\} \quad (22)$$

Results and discussion

In this section, we display and discuss the results that were computed using the aforementioned technique, HAM. Additionally, as illustrated in Figures 2–17 and Tables 2, Tables 3, the performance of hybrid nanofluid and nanofluid flow $f'(\eta)$, energy $\Theta(\eta)$, and concentration distribution $\Phi(\eta)$ under the impact of fluid parameters is explored. For these purposes, numerical simulations are carried out, with $S = 0.4, \lambda_p = 1, Pr = 7.5, \lambda = 0.3, \gamma_c = 0.5, Gr = 2, Rd = 0.6, Gc = 1.5$. When the current findings are compared with the previous study of Wang, 1990; Qasim et al., 2016 under limiting circumstances, the validity of the current results is demonstrated. The two sets

of results are shown in Tables 2 and 3, and there is considerable agreement between them. According to Table 2, the progressive variation of S is added to the surface and wall temperature gradients.

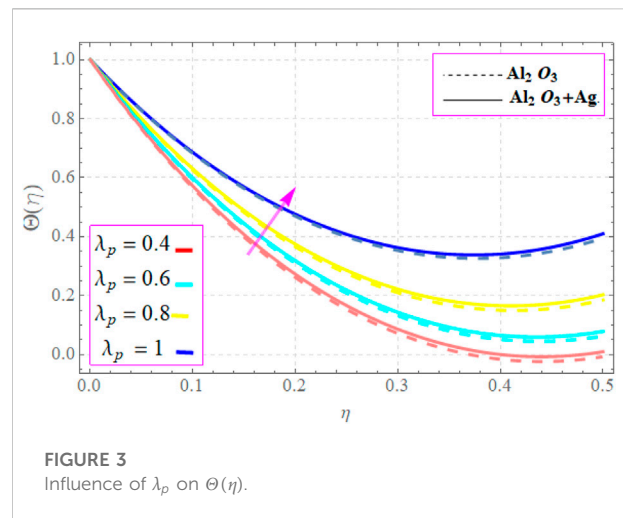
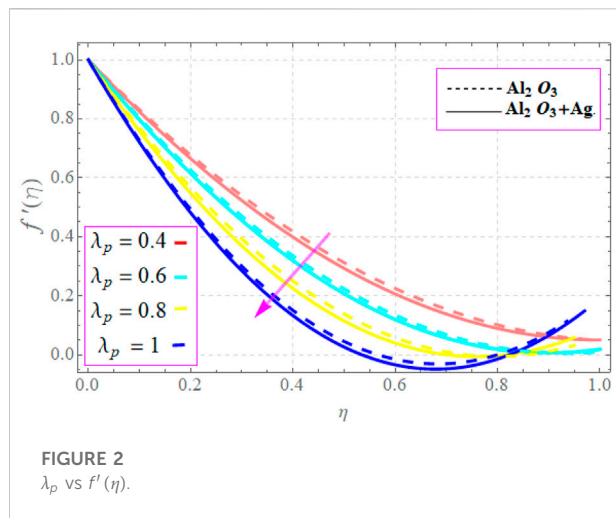
The characteristics of $f'(\eta)$ (velocity field) and $\Theta(\eta)$ (thermal distributions) in the presence of λ_p (permeability variable) are delineated by Figures 2,3 for nanofluids and hybrid nanofluids. Figure 2 shows that a depletion of $f'(\eta)$ distribution results from increasing λ_p values. This is realistic because a porous medium presents a resistance in the way to fluid flow. Therefore, as demonstrated in Figure 2, high values of the λ_p parameter diminish the fluid velocity. The suspensions of hybrid nanofluids are declined more quickly as compared to monofluids. Additionally, as seen in Figure 3, there is an increase in temperature distributions when the values of the λ_p parameter are improved. Figures 4,5 demonstrate the variations in $f'(\eta)$ (velocity field) and $\Theta(\eta)$ (thermal distributions) with respect to the $\phi_{Al_2O_3}, \phi_{Ag}$ (volume fractions of nanoparticles). Figure 4 shows that the velocity profile appears to decrease when the values of $\phi_{Al_2O_3}, \phi_{Ag}$ nanoparticles grow statistically. In terms of physics, the rise in the values of $\phi_{Al_2O_3}, \phi_{Ag}$ denotes an increase in the number of nanoparticles scattered in the base fluid. The results imply that the minor volume percentage helps the hybrid nanofluid. When compared to ordinary nanofluids, the hybrid suspension achieves a prominent position. According to Figure 5, the $\Theta(\eta)$ distribution improved due to an increase in $\phi_{Al_2O_3}, \phi_{Ag}$. Physically, the emergence of a greater number of small components into the host liquid makes it easier for the nanoliquids to release a greater quantity of their stored energy in the form of heat. As a result, there was an increase in the effective distribution of heat. Therefore, the hybrid nanofluid achieves a higher level than the typical one. The incorporation of nanocomposites results in an intensification of the process of heat transfer. It is perfectly reasonable because the incorporation of a greater number of nanoparticles into the nanosolution makes it easier to obtain a high rate of heat transmission. Figure 6 illustrates the impact of M (magnetic parameter) on the $f'(\eta)$ field for all cases of nanofluids and hybrid nanofluids. As M is estimated to be a larger value, the velocity of nanofluids decreases. Because an increase in M signifies an improvement in resistive force (the Lorentz force), this results in a reduction in the velocity of the nanofluid and hybrid nanoliquid. According to Figure 7, a higher E value results in an improved $f'(\eta)$ field. This is due to the fact that an increase in E contributes to the

TABLE 2 Comparison between the published work and present work for the surface and wall temperature gradients considering common factors using the regular fluid having $Pr = 7.56$. Note that they used small and variable values of the Prandtl number.

| | Wang (1990) | Wang (1990) | Qasim et al. (2016) | Qasim et al. (2016) | Present | Present |
|-----|-------------|---------------|---------------------|---------------------|-----------------|--------------------|
| S | $\Theta(1)$ | $-\Theta'(0)$ | $\Theta(\beta)$ | $-\beta\Theta'(0)$ | $\Theta(\beta)$ | $-\beta\Theta'(0)$ |
| 0.3 | 0.45312 | 0.6413 | 0.45921 | 0.64374 | 0.4594251 | 0.64365 |
| 0.5 | 0.47683 | 0.7658 | 0.47941 | 0.76832 | 0.4794732 | 0.768320 |
| 0.7 | 0.49587 | 0.8513 | 0.49926 | 0.85383 | 0.4992763 | 0.853241 |
| 0.9 | 0.51325 | 0.9924 | 0.51732 | 0.51823 | 0.517276 | 0.5172751 |

TABLE 3 Comparison between the published work and present work for the Sherwood number considering the common factor using the regular fluid having $Pr = 7.56, S = 0.8$.

| | Qasim et al. (2016) | Qasim et al. (2016) | Present | Present |
|----|---------------------|---------------------|---------------|-------------|
| Sc | $\Phi(\beta)$ | $-\Phi'(0)$ | $\Phi(\beta)$ | $-\Phi'(0)$ |
| 9 | 0.13743 | 0.4587 | 0.137563 | 0.458872 |
| 11 | 0.129341 | 0.44575 | 0.129432 | 0.445834 |
| 13 | 0.11832 | 0.42782 | 0.11843 | 0.427942 |



generation of a stronger electric field, which in turn speeds up the flow of nanofluids and hybrid nanofluids. The characteristics of the flow field $f'(\eta)$ for different values of Gr and Gc (thermal and mass buoyancy parameters) are shown in Figures 8, 9. Figure 8 illustrates the unique effects of Gr on the resulting velocity. The $f'(\eta)$ of the thin-film fluid increases as Gr rises. Actually, Gr is the ratio of thermal buoyant forces to viscous forces. As a consequence, the strengths of thermal forces rise as the magnitude of Gr increases. Huge quantities of the Grashof number are used to provide the buoyancy forces. Thus, as Gr rises, the resulting momentum boundary layer's thickness also rises. The special impact of Gc

on the fluid velocity $f'(\eta)$ is shown in Figure 9. As the Gc increases, the $f'(\eta)$ of the hybrid thin-film fluid also increases. The Gc is the proportionality of concentration buoyant forces to viscous forces. The intensities of solutal force increase as the magnitude of the Gc increases. Also, when compared to ordinary nanofluids, the hybrid suspension achieves a prominent position.

The changes in the $\Theta(\eta)$ profile relative to the Rd (radiation parameter) are shown in Figure 10 for nanofluids and hybrid nanofluids. It is considered that an elevation in Rd factor leads the temperature to rise. Physically, the Rd factor compares the input of heat exchange through conduction to transfer using thermal

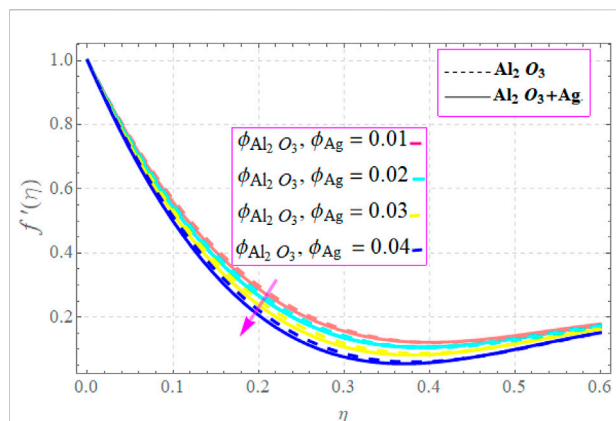


FIGURE 4
Influence of $\phi_{\text{Al}_2\text{O}_3}, \phi_{\text{Ag}}$ on $f'(\eta)$.

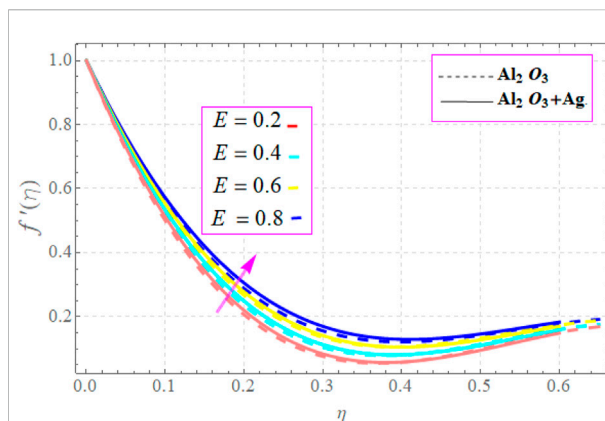


FIGURE 7
Influence of E on $f'(\eta)$.

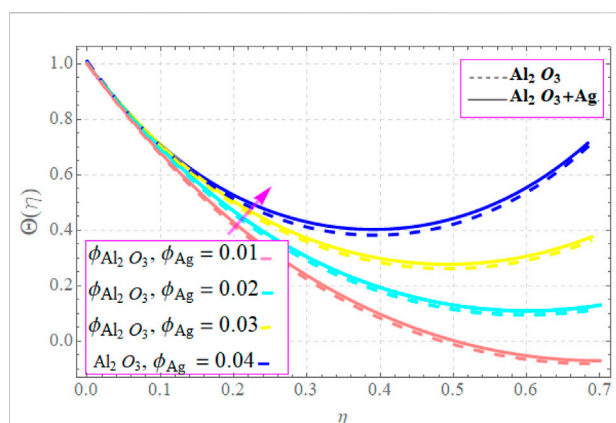


FIGURE 5
Influence of $\phi_{\text{Al}_2\text{O}_3}, \phi_{\text{Ag}}$ on $\Theta(\eta)$.

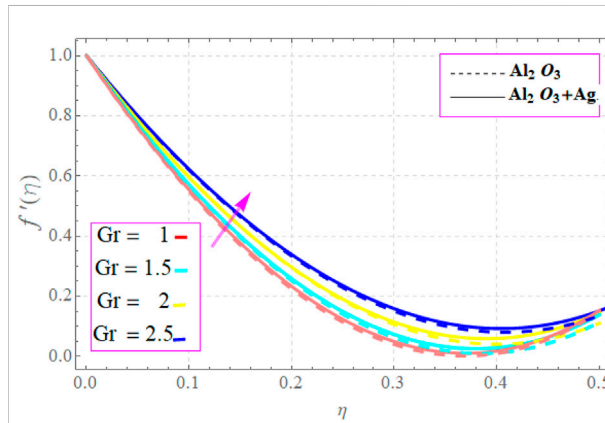


FIGURE 8
Influence of Gr on $f'(\eta)$.

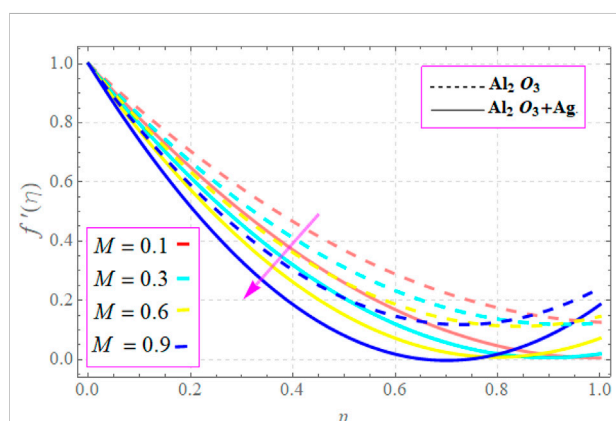


FIGURE 6
Influence of M on $f'(\eta)$.

radiation. It is obvious that an increase in the radiation parameter causes the temperature to rise. Additionally, there is a positive association between the Rd and the temperature gradient close to the surface of the plate. Hence, the hybrid nanofluid shows the leading nature as compared to the nanofluid. The effect of S (unsteadiness factor) on the $f'(\eta)$ profile is shown in Figure 11 for nanofluids and hybrid nanofluids. The plot reveals that a gradual increase in the magnitude of S causes the $f'(\eta)$ profile to gradually decline, improving the momentum boundary film viscosity. The hybrid suspension also holds a prominent position when compared to regular nanofluids. Figure 12 predicts the significance of the $\Theta(\eta)$ distribution on the S (unsteadiness factor) for both the types of nanofluids and hybrid nanofluids. It is important to note that S has an increasing impact on the temperature of the liquid film. A slight temperature improvement is shown to increase the values of S in the boundary layer.

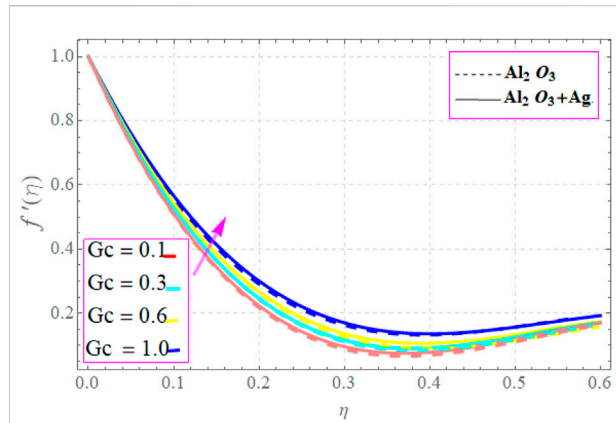


FIGURE 9
Influence of Gc on $f'(\eta)$.

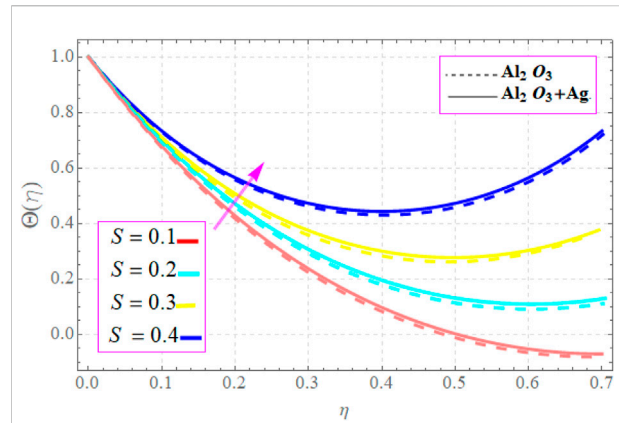


FIGURE 12
Influence of S on $\theta(\eta)$.

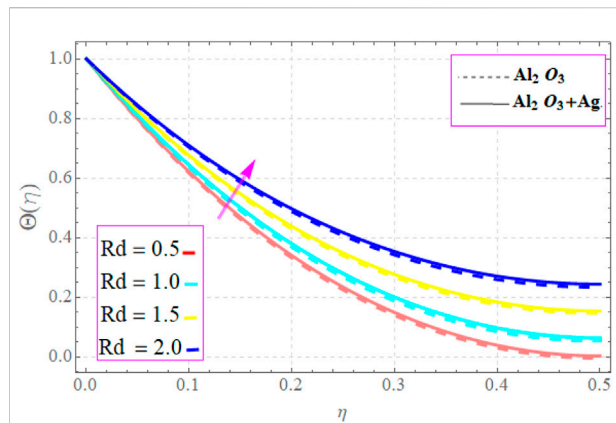


FIGURE 10
Influence of Rd on $\theta(\eta)$.

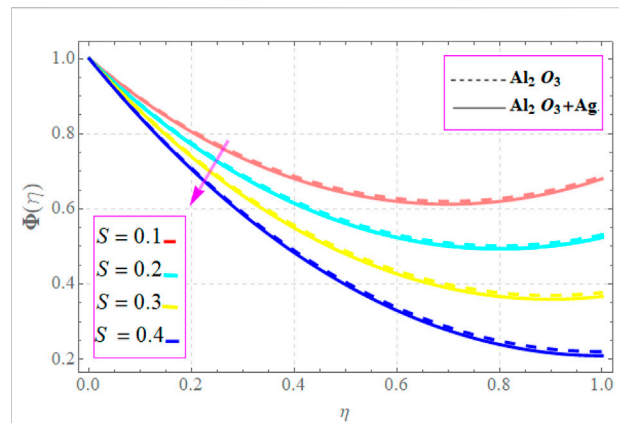


FIGURE 13
Influence of S on $\Phi(\eta)$.

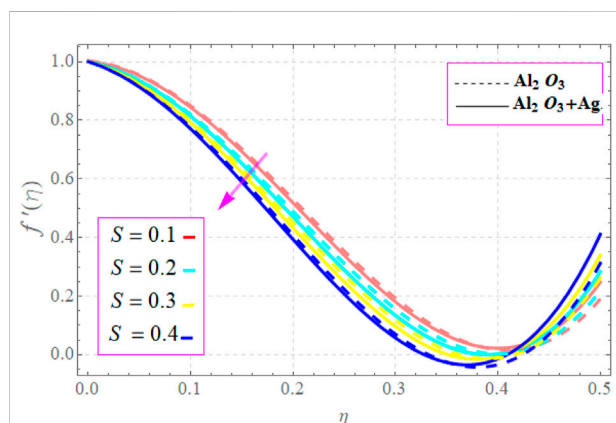


FIGURE 11
Influence of S on $f'(\eta)$.

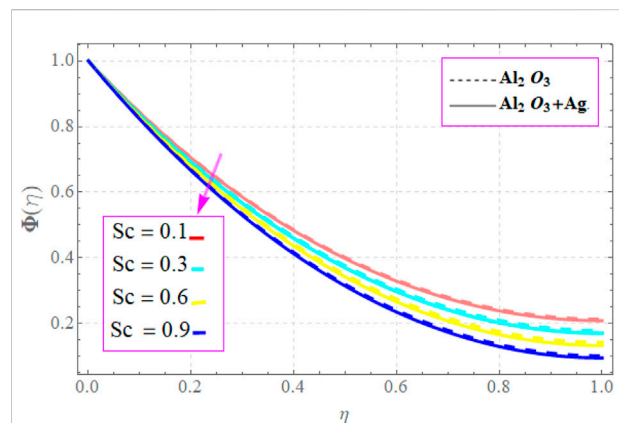


FIGURE 14
Influence of Sc on $\Phi(\eta)$.

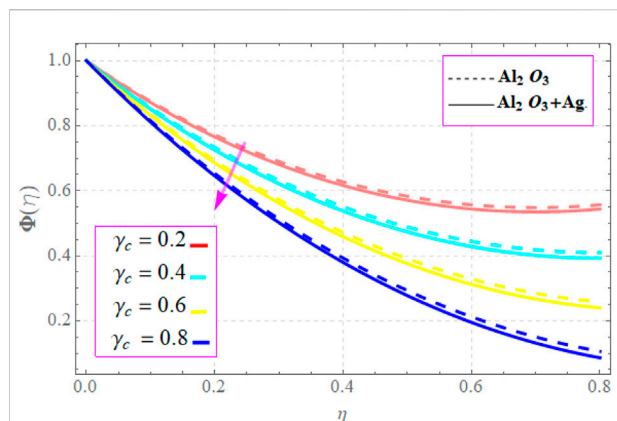


FIGURE 15
Influence of γ_c on $\Phi(\eta)$.

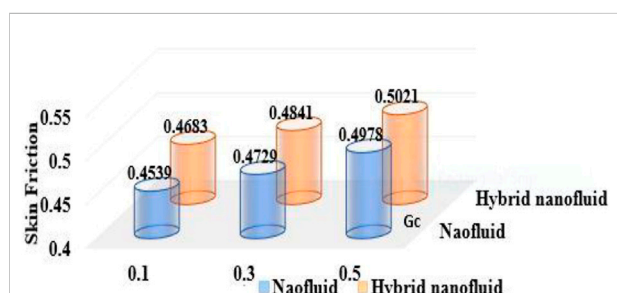


FIGURE 16
 G_c vs skin friction.

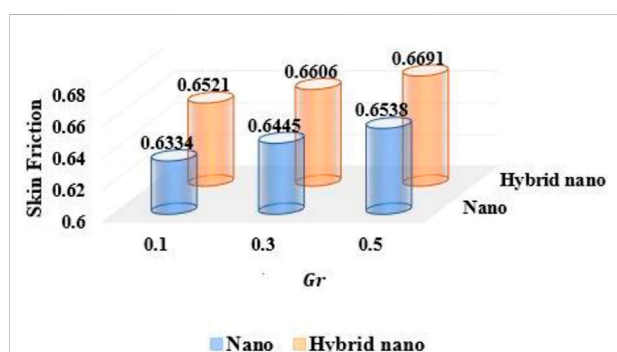


FIGURE 17
 Gr vs skin friction.

Figure 13 illustrates how the presence of S changed the $\Phi(\eta)$ concentration profile for both types of nanofluids. The tendency occurs for the liquid to be pushed into empty spaces as a result of the enhancement of S . As a result, the $\Phi(\eta)$ increases, as depicted in Figure 13, for both the Al_2O_3 and Al_2O_3 -Ag nanosolutions. Plot

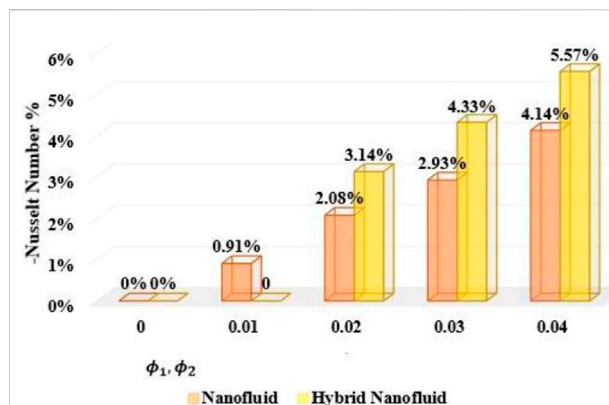


FIGURE 18
 ϕ_1, ϕ_2 vs Nusselt number enhancement in %.

Figure 14 illustrates the significance of Sc (Schmidt number) in regard to the $\Phi(\eta)$ profile for nanofluids and hybrid nanofluids. As Sc increases, a noticeable lowering of the $\Phi(\eta)$ distribution can be seen. According to its definition, Sc is the ratio of the momentum diffusivity to the mass diffusivity. Therefore, more species (higher Sc) depreciate the solutal fields. The behavior of the dimensionless $\Phi(\eta)$ distribution for various values in γ_c (chemical reactions) is depicted in Figure 15 for the cases of nanofluids and hybrid nanofluids. In this study, $\gamma_c > 0$, and the effects of destructive chemical reactions are investigated. The plot shows a decrease in the $\Phi(\eta)$ field as γ_c rises. Physically, high values of the γ_c parameter indicate that there are many solute molecules taking part in the reaction, which causes the $\Phi(\eta)$ field to drop. As a result, a destructive chemical reaction dramatically reduces the thickness of the solutal border layer. Also, when compared to the Al_2O_3 nanofluid, the Al_2O_3 -Ag suspension achieves a prominent position. Figures 16, 17 show the variation of the skin friction coefficient for different values of G_c and Gr for nanofluids and hybrid nanofluids. Also, the consequences of ϕ_1, ϕ_2 against Nusselt number enhancement in % are presented in Figures 18.

Conclusion

We focused on describing the chemical radiative and convective effects on the hydrothermal characteristics of two different types of Maxwell nanoliquids, the Ag hybrid nanofluid and Al_2O_3 regular nanofluid, during the entire study. Over a permeable stretched inclined surface, the desired thin-film flow has been passed. Through tables and figures, exhaustive properties of porosity, volume fraction, unsteadiness, radiation, chemical reaction, and thermal and mass buoyancy components are explained. Through a comprehensive examination, some guiding points help focus our attention on the following findings:

- Maxwell hybrid nanofluids' thin-film flow is slowed down by increased λ_p (porosity).
- $\phi_{Al_2O_3}$, ϕ_{Ag} (nanoparticle volume fraction), S (unsteadiness), Gr , and Gc (Thermal and mass buoyancy parameters) parameters highly influence the thin-film flow of Maxwell hybrid nanofluids compared to nanofluids.
- For the thermal profile, $\phi_{Al_2O_3}$, ϕ_{Ag} (nanoparticle volume fraction), S (unsteadiness), and λ_p (porosity) have similar effects. These factors have a greater impact on hybrid nanofluids than on nanofluids.
- For the concentration profile, the thin film of the hybrid fluid is more influenced than the nanofluid by S as compared to the other various parameters like Sc and γ_c .
- The skin friction coefficient, Nusselt number, and Sherwood number reduce when uplifting the parameter S , while it increases for $\phi_{Al_2O_3}$, ϕ_{Ag} , and λ_p .

Future direction

These results of thin-film flows can also be used for other models like discs and cylinders, different flow factors, and trihybrid nanofluids with the execution of numerical and analytical techniques.

Data availability statement

The raw data supporting the conclusions of this article will be made available by the authors, without undue reservation.

References

- Abro, K. A., Soomro, M., Atangana, A., and Gómez-Aguilar, J. F. (2020). Thermophysical properties of Maxwell nanofluids via fractional derivatives with regular kernel. *J. Therm. Analysis Calorim.* 147, 1–11. doi:10.1007/s10973-020-10287-9
- Acharya, N., Maity, S., and Kundu, P. K. (2020). Influence of inclined magnetic field on the flow of condensed nanomaterial over a slippery surface: The hybrid visualization. *Appl. Nanosci.* 10 (2), 633–647. doi:10.1007/s13204-019-01123-0
- Ahmed, J., Khan, M., and Ahmad, L. (2020). Radiative heat flux effect in flow of Maxwell nanofluid over a spiraling disk with chemically reaction. *Phys. A Stat. Mech. its Appl.* 551, 123948. doi:10.1016/j.physa.2019.123948
- Ali, L., Liu, X., and Ali, B. (2020). Finite element analysis of variable viscosity impact on MHD flow and heat transfer of nanofluid using the cattaneo-christov model. *Coatings* 10 (4), 395. doi:10.3390/coatings10040395
- Ayub, A., Sabir, Z., Altamirano, G. C., Sadat, R., and Ali, M. R. (2021). Characteristics of melting heat transport of blood with time-dependent cross-nanofluid model using Keller–Box and BVP4C method. *Eng. Comput.* 1, 1–15.
- Ayub, A., Wahab, H. A., Shah, S. Z., Shah, S. L., Darvesh, A., Haider, A., et al. (2021). Interpretation of infinite shear rate viscosity and a nonuniform heat sink/source on a 3D radiative cross nanofluid with buoyancy assisting/opposing flow. *Heat. Transf.* 50 (5), 4192–4232. doi:10.1002/htj.22071
- Babar, H., and Ali, H. M. (2019). Towards hybrid nanofluids: Preparation, thermophysical properties, applications, and challenges. *J. Mol. Liq.* 281, 598–633. doi:10.1016/j.molliq.2019.02.102
- Choi, S. U. S. (1995). Enhancing thermal conductivity of fluids with nanoparticles. *ASME-Publications-Fed* 231, 99–106.
- Devi, S. A., and Devi, S. S. U. (2016). Numerical investigation of hydromagnetic hybrid Cu - Al₂O₃/water nanofluid flow over a permeable stretching sheet with suction. *Int. J. Nonlinear Sci. Numer. Simul.* 17 (5), 249–257. doi:10.1515/ijnsns-2016-0037
- Ghadikolaei, S. S., Hosseinzadeh, K., Ganji, D. D., and Jafari, B. (2018). Nonlinear thermal radiation effect on magneto Casson nanofluid flow with Joule heating effect over an inclined porous stretching sheet. *Case Stud. Therm. Eng.* 12, 176–187. doi:10.1016/j.csite.2018.04.009
- Gumber, P., Yaseen, M., Rawat, S. K., and Kumar, M. (2022). Heat transfer in micropolar hybrid nanofluid flow past a vertical plate in the presence of thermal radiation and suction/injection effects. *Partial Differ. Equations Appl. Math.* 5, 100240. doi:10.1016/j.padiff.2021.100240
- Hussain, S. M., Sharma, R., Mishra, M. R., and Alrashidy, S. S. (2020). Hydromagnetic dissipative and radiative graphene Maxwell nanofluid flow past a stretched sheet-numerical and statistical analysis. *Mathematics* 8 (11), 1929. doi:10.3390/math8111929
- Jawad, M., Saeed, A., and Gul, T. (2021). Entropy generation for MHD Maxwell nanofluid flow past a porous and stretching surface with Dufour and Soret effects. *Braz J. Phys.* 51 (3), 469–480. doi:10.1007/s13538-020-00835-x
- Jeffreys, H. (1925). LIV. The flow of water in an inclined channel of rectangular section. *Lond. Edinb. Dublin Philosophical Mag. J. Sci.* 49 (293), 793–807. doi:10.1080/14786442508634662
- Joshi, N., Upreti, H., and Pandey, A. K. (2022). MHD Darcy-Forchheimer Cu-Ag/H₂O-C₂H₆O₂ hybrid nanofluid flow via a porous stretching sheet with suction/blowing and viscous dissipation. *Int. J. Comput. Methods Eng. Sci. Mech.* 1, 1–9.

Author contributions

TG, modeling and solution; SM, writing draft WA, editing. ETE, Validated, MFY and KG, participated in revision and provide funding source.

Funding

The authors would like to thank the Deanship of Scientific Research at Umm Al-Qura University for supporting this work by Grant Code: (22UQU4331317DSR78).

Conflict of interest

The authors declare that the research was conducted in the absence of any commercial or financial relationships that could be construed as a potential conflict of interest.

Publisher's note

All claims expressed in this article are solely those of the authors and do not necessarily represent those of their affiliated organizations or those of the publisher, the editors, and the reviewers. Any product that may be evaluated in this article or claim that may be made by its manufacturer is not guaranteed or endorsed by the publisher.

- Khan, S. U., Rauf, A., Shehzad, S. A., Abbas, Z., and Javed, T. (2019). Study of bioconvection flow in Oldroyd-B nanofluid with motile organisms and effective Prandtl approach. *Phys. A Stat. Mech. its Appl.* 527, 121179. doi:10.1016/j.physa.2019.121179
- Khan, S. U., and Shehzad, S. A. (2020). Flow of Jeffrey nanofluids over convectively heated oscillatory moving sheet with magnetic field and porosity effects. *J. Por Media* 23 (9), 907–922. doi:10.1615/jpormedia.2020025508
- Khan, S. U., Shehzad, S. A., Rauf, A., and Abbas, Z. (2020). Thermally developed unsteady viscoelastic micropolar nanofluid with modified heat/mass fluxes: A generalized model. *Phys. A Stat. Mech. its Appl.* 550, 123986. doi:10.1016/j.physa.2019.123986
- Liu, Y., Itoh, M., and Kyotoh, H. (2017). Flow of a falling liquid curtain onto a moving substrate. *Fluid Dyn. Res.* 49 (5), 055501. doi:10.1088/1873-7005/aa7ee8
- Nadeem, S., Israr-ur-Rehman, M., Saleem, S., and Bonyah, E. (2020). Dual solutions in MHD stagnation point flow of nanofluid induced by porous stretching/shrinking sheet with anisotropic slip. *AIP Adv.* 10 (6), 065207. doi:10.1063/5.0008756
- Nusselt, W. (1916). Die oberflächenkondensation des wasserdampfes. *VDI-Zs* 60, 541.
- Qasim, M., Khan, Z. H., Lopez, R. J., and Khan, W. A. (2016). Heat and mass transfer in nanofluid thin film over an unsteady stretching sheet using Buongiorno's model. *Eur. Phys. J. Plus* 131 (1), 1–11. doi:10.1140/epjp/i2016-16016-8
- Ramesh, K., Khan, S. U., Jameel, M., Khan, M. I., Chu, Y. M., and Kadry, S. (2020). Bioconvection assessment in Maxwell nanofluid configured by a Riga surface with nonlinear thermal radiation and activation energy. *Surfaces Interfaces* 21, 100749. doi:10.1016/j.surfin.2020.100749
- Sabir, Z., Akhtar, R., Zhiyu, Z., Umar, M., Imran, A., Wahab, H. A., et al. (2019). A computational analysis of two-phase casson nanofluid passing a stretching sheet using chemical reactions and gyrotactic microorganisms. *Math. Problems Eng.* 2019, 1–12. doi:10.1155/2019/1490571
- Sabir, Z., Imran, A., Umar, M., Zeb, M., Shoaib, M., and Raja, M. A. Z. (2021). A numerical approach for 2-D Sutterby fluid-flow bounded at a stagnation point with an inclined magnetic field and thermal radiation impacts. *Therm. Sci.* 25 (3), 1975–1987.
- Shah, S. A., Mouldi, A., and Sene, N. (2022). Nonlinear convective SiO₂ and TiO₂ hybrid nanofluid flow over an inclined stretched surface. *J. Nanomater.* 2022, 1–15.
- Sharma, R., Hussain, S. M., Raju, C. S. K., Seth, G. S., and Chamkha, A. J. (2020). Study of graphene Maxwell nanofluid flow past a linearly stretched sheet: A numerical and statistical approach. *Chin. J. Phys.* 68, 671–683. doi:10.1016/j.cjph.2020.10.013
- Turkyilmazoglu, M. (2020). Single phase nanofluids in fluid mechanics and their hydrodynamic linear stability analysis. *Comput. Methods Programs Biomed.* 187, 105171. doi:10.1016/j.cmpb.2019.105171
- Umar, M., Sabir, Z., Imran, A., Wahab, H. A., Shoaib, M., and Raja, M. A. Z. (2020). The 3-D flow of Casson nanofluid over a stretched sheet with chemical reactions, velocity slip, thermal radiation and Brownian motion. *Therm. Sci.* 24 (5), 2929–2939. doi:10.2298/tsci190625339u
- Wang, C. Y. (1990). Liquid film on an unsteady stretching surface. *Quart. Appl. Math.* 48 (4), 601–610. doi:10.1090/qam/1079908
- Yaseen, M., Rawat, S. K., and Kumar, M. (2022). Hybrid nanofluid (MoS₂-SiO₂/water) flow with viscous dissipation and Ohmic heating on an irregular variably thick convex/concave-shaped sheet in a porous medium. *Heat. Trans.* 51 (1), 789–817. doi:10.1002/htj.22330
- Zhang, Y., Shahmir, N., Ramzan, M., Ghazwani, H. A. S., and Malik, M. Y. (2021). Comparative analysis of Maxwell and Xue models for a hybrid nanofluid film flow on an inclined moving substrate. *Case Stud. Therm. Eng.* 28, 101598. doi:10.1016/j.csite.2021.101598

Nomenclature

λ_1 relaxation time

τ tensor for extra stress

κ thermal conductivity

C_p heat capacitance

η similarity variable

T_0, T_{ref} temperature terms

S unstable parameter

T temperature

ν_{hnf} , kinematic viscosity

u, v velocity components

ρ density

μ_{hnf} dynamic viscosity of the hybrid nanofluid

Sc Schmitt number

k^\oplus permeability coefficient

λ time relaxation

Pr Prandtl number

Θ dimensionless temperature

$h(t)$ film thickness



OPEN ACCESS

EDITED BY
Umar Khan,
Hazara University, Pakistan

REVIEWED BY
Basharat Ullah,
Mohi-Ud-Din Islamic University,
Pakistan
Zulqurnain Sabir,
United Arab Emirates University, United
Arab Emirates

*CORRESPONDENCE
Arshad Khan,
arshad8084@gmail.com

SPECIALTY SECTION
This article was submitted to Process
and Energy Systems Engineering,
a section of the journal
Frontiers in Energy Research

RECEIVED 13 July 2022
ACCEPTED 02 September 2022
PUBLISHED 06 October 2022

CITATION
Khan A, Alyami MA, Alghamdi W,
Alqarni MM, Yassen MF and Tag Eldin E
(2022), Thermal examination for the
micropolar gold–blood nanofluid flow
through a permeable channel subject to
gyrotactic microorganisms.
Front. Energy Res. 10:993247.
doi: 10.3389/fenrg.2022.993247

COPYRIGHT
© 2022 Khan, Alyami, Alghamdi, Alqarni,
Yassen and Tag Eldin. This is an open-
access article distributed under the
terms of the [Creative Commons
Attribution License \(CC BY\)](https://creativecommons.org/licenses/by/4.0/). The use,
distribution or reproduction in other
forums is permitted, provided the
original author(s) and the copyright
owner(s) are credited and that the
original publication in this journal is
cited, in accordance with accepted
academic practice. No use, distribution
or reproduction is permitted which does
not comply with these terms.

Thermal examination for the micropolar gold–blood nanofluid flow through a permeable channel subject to gyrotactic microorganisms

Arshad Khan^{1*}, Maryam Ahmed Alyami², Wajdi Alghamdi³,
M. M. Alqarni⁴, Mansour F. Yassen^{5,6} and Elsayed Tag Eldin⁷

¹College of Aeronautical Engineering, National University of Sciences and Technology (NUST), Islamabad, Pakistan, ²Department of Mathematics, Faculty of Sciences, University of Jeddah, Jeddah, Saudi Arabia, ³Department of Information Technology, Faculty of Computing and Information Technology, King Abdulaziz University, Jeddah, Saudi Arabia, ⁴Department of Mathematics, College of Sciences, King Khalid University, Abha, Saudi Arabia, ⁵Department of Mathematics, College of Science and Humanities in Al-Aflaj, Prince Sattam Bin Abdulaziz University, Al-Aflaj, Saudi Arabia, ⁶Department of Mathematics, Faculty of Science, Damietta University, Damietta, Egypt, ⁷Faculty of Engineering and Technology, Future University in Egypt New Cairo, New Cairo, Egypt

Presently, scientists across the world are carrying out theoretical and experimental examinations for describing the importance of nanofluids in the heat transfer phenomena. Such fluids can be obtained by suspending nanoparticles in the base fluid. Experimentally, it has proved that the thermal characteristics of nanofluids are much better and more appealing than those of traditional fluids. The current study investigates the heat transfer for the flow of blood that comprises micropolar gold nanoparticles. The influence of chemically reactive activation energy, thermophoresis, thermal radiations, and Brownian motion exists between the walls of the channel. A microorganism creation also affects the concentration of nanoparticles inside the channel. Suitable transformation has been used to change the mathematical model to its dimensionless form and then solve by using the homotopy analysis method. In this investigation, it has been revealed that the linear velocity behavior is two-folded over the range $0 \leq \eta \leq 1$. The flow is declining in the range $0 \leq \eta \leq 0.5$, whereas it is augmenting upon the range $0.5 \leq \eta \leq 1$. Thermal characteristics are supported by augmentation in volumetric fraction, thermophoresis, radiation, and Brownian motion parameters while opposed by the Prandtl number. The concentration of the fluid increases with augmentation in activation energy parameters and decays with an increase in

Abbreviations: \hat{u} , \hat{v} , dimensional velocity components (m/s); \hat{p} , dimensional pressure (Pa); P , dimension-free pressure; H , channel height (m); N , microrotational velocity (m/sec); u_t , u_b , velocities of the top and bottom walls (m/sec); v_t , v_b , normal velocities of the top and bottom walls (m/sec); T , dimensional temperature (K); C_p , specific heat ($\text{J kg}^{-1} \text{K}^{-1}$); Nu , Nusselt number; C_f , skin friction coefficient; Sh , Sherwood number; N_b , Brownian parameter; η , similarity variable; Re , Reynolds number; Da , Darcy number; Pr , Prandtl number; K , material parameter; R_d , radiation parameter; Ω , temperature parameter; E , activation energy parameter; Sc , Schmidt number; T , chemical reaction parameter; L_b , bioconvection Lewis number; Pe , Peclet number; δ , microorganism concentration number; N_t , thermophoresis parameter.

thermophoresis, Brownian motion, chemical reaction parameters, and the Schmidt number. The density of microorganisms weakens by growth in Peclet and bioconvection Lewis numbers.

KEYWORDS

heat transfer, micropolar nanoparticles, gyrotactic microorganisms, porous channel, chemical reaction, thermal radiation, HAM

1 Introduction

The limitations on improving the transfer of heat in engineering systems, for instance, cooling of electronic and solar systems, are essentially due to the slower thermal conductivity in traditional fluids like oil, ethylene glycol, and water. Solids normally have better characteristics for heat transmission than liquids, like copper which has 700 times better thermal conductivity in comparison with water and 3,000 times better than engine oil. Choi and Eastman (1995) were the first to introduce the concept of nanofluids by mixing the nano-sized particles in a pure fluid. Afterward, various researchers have conducted plenty of investigations for fluids flowing through channels with the main focus on the augmentation of heat transfer characteristics by suspending different kinds of nanoparticles in different base fluids. Sheikholeslami and Ganji (2013) have discussed the thermal flow characteristics for the $Cu - H_2O$ nanofluid flow amid two parallel plates. In this study, the Maxwell–Garnets and Brinkman models have been employed by the authors to determine the viscosity and thermal flow behavior of nanofluids. It has also been established in this inspection that the rate of thermal flow has amplified with greater values of the volumetric fraction and Eckert number. Ayub et al. (2022a) have inspected the thermal flow characteristics for cross-nanofluids by using various flow conditions and revealed that augmentation in the cross-fluid index has supported velocity profiles. Shah et al. (2022a) have inspected the MHD nanofluid flow with multiple features past wedge geometry. Shah et al. (2020) have extended the study of Srinivas et al. (2017) by introducing the micropolar gold–blood nanofluid to the flow system in a channel. They have used the homotopy analysis method to model equations and have revealed that the thermal flow has improved for higher values of the volumetric fraction and radiation parameter which, on the other hand, has declined the flow profiles in all directions. Further investigation about heat transmission regarding nanofluids can be studied in Ayub et al. (2021a), Ayub et al. (2021b), Ayub et al. (2021c), Shah et al. (2021), Ayub et al. (2022b), Shah et al. (2022b), and Ayub et al. (2022c).

The fundamental requirement to model the fluid that comprises microrotational components has introduced the theory of micropolar fluids. These fluids actually couple the rotational motion of fluid particles with the field of macroscopic velocity. By structure, these fluids consist of hard particles suspended in the viscous medium, for instance, bubbly

liquid, paint, ferrofluids, and blood flows. Such fluids have abundant applications in engineering and industries, like lubricant fluids, biological structures, and polymer solutions. The idea of micropolar fluids was introduced first by Eringen (1966). Afterward, this term became an area of dynamic exploration in the field of research. This class of fluid could describe the fluid's characteristics at a micro-scale. In these fluids, the spinning motion is described by microrotational vectors. Singkibud et al. (2022) have investigated the influence of cubical catalyst-based activation energy and thermophoresis diffusions for a time-free micropolar nanofluid flow on a semi-infinite stretching surface. Fakour et al. (2015) inspected the thermal flow of micropolar fluids flowing through a channel. It has been concluded in this investigation that the rate of thermal flow has augmented with growth in the strength of the Reynolds number and has declined with augmentation in the Peclet number. Abbas et al. (2020) have revealed thermal characteristics for the micropolar nanofluid flow between two plates using slip conditions. Baharifard et al. (2020) studied the mass and heat transfers for the MHD micropolar fluid flow past a stirring surface with injection and suction behavior on the surface.

Recently, the exploration of the laminar flow and transmission of heat through porous channels has appealed to many researchers due to its industrial and biological applications. These applications include biological fluid transportation through contracting or expanding vessels, underground resources of water, and the synchronous pulsation of permeable diaphragms. Many investigations have been conducted for heat and mass transfer between porous plates using various flow conditions. In this study, magnetic effects have been practiced in the flow system both in parallel and perpendicular directions, and it has been highlighted that by removing the impact of the Hall current, the flow has remained unchanged even by changing the direction of the applied magnetic field. Hassan (2020) has analyzed the production of irreversibility for the MHD fluid flowing in a permeable channel. Islam et al. (2020) have examined the micropolar fluid flow amid two plates by considering different flow conditions in the flow system. The authors have used the nanoparticles of graphene oxide and copper in water as the base fluid and have established that the expansion in volumetric fractions has reduced the flow characteristics and has increased the thermal characteristics. Delhi Babu and Ganesh (2020) have

discussed mathematically the model for the steady MHD fluid flow amid two porous plates with revolving flow.

Nanoparticles are not self-driven and start motion only when it is affected by thermophoresis and Brownian motion. Even in the augmentation of mass and heat transformation, the high concentration of nanoparticles can affect the stability of this phenomenon. A combination of biotechnological mechanisms with nanofluids that are established by motile microorganisms can provide better results in such a physical phenomenon. Gyrotactic microorganisms are actually self-driven and can gather in the closed vicinity of the top layer of the fluid flow which causes the upper surface of the fluid to be denser. The dispersal of gyrotactic microorganisms in nanofluids normally enhances the heat transfer characteristics of the fluid. Platt (1961) was the first gentleman who floated the idea of the configurations in the thicker culture of free spinning organisms. Afterward, many studies have been carried out by different scientists with the main focus on the impact of gyrotactic microorganisms on the fluid flow systems. Bin-Mohsin et al. (2017) have examined the squeezing liquid flow using gyrotactic microorganisms amid two opposite and parallel plates. It has been highlighted in this investigation that the augmentation in thermophoresis effects and random motion has enhanced the thermal flow and has declined the mass transmission. Zhang et al. (2020) studied the influence of the magnetized Reynolds number upon motile microorganisms between circular plates filled with nanoparticles. The authors have noticed that the distribution of nanoparticle concentration, thermal profiles, and microorganisms have been highly suppressed by augmenting values of the squeezed Reynolds number. Ahmad et al., (2020) inspected the nanofluid flow influenced by microorganisms through a porous plate. It has been noticed in this investigation that the heat and mass transfer rates have been augmented by considering the impact of gyrotactic microorganisms. More comprehensive investigations have been conducted by Khan et al. (2021a) and Khan et al. (2021b). The authors have highlighted the effect of different parameters on flow systems. In these inspections, it has been noticed that the flow and concentration profiles have been reduced with augmentation in thermophoretic and Brownian motion parameters, while the thermal profiles have been augmented on the other hand. Moreover, in these investigations, the density number of motile microorganisms has declined with the augmenting values of the Peclet number.

From the mentioned literature and similar related studies, the authors have noticed that a large number of research studies have been published to describe the flow of nanoparticles by using different geometrical shapes. However, comparatively less attention has been paid to micropolar fluids with gold–blood nanoparticles flowing through the channel. Moreover, to the best of the author's knowledge, no investigation so far has been

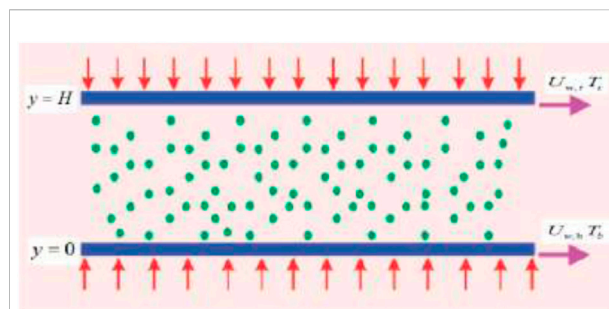


FIGURE 1
Graphical view of the flow problem.

performed for micropolar gold–blood nanoparticles flowing through a porous channel with the effects of gyrotactic microorganisms. The collective influence of chemically reactive activation energy in the current study further expands the newness of the study. For augmenting the heat transfer characteristics in the current investigation, the thermophoretic effects along with Brownian motion and thermal radiations have also been applied to the flow system. HAM (Liao, 1999; Liao, 2010) has been used to find the solution to modeled equations.

The first section of the study introduces the related literature. The second section comprises physical and mathematical description of the problem along with quantities of interest. The third section defines the solution method along with steps for the solution. The fourth section defines the results and discussion along with an explanation of tables. Conclusions of the current study are given in the last section.

2 Physical and mathematical descriptions

Next, the problem will be described physically by considering some assumptions and by taking the physical view of the flow problem. Afterward, these assumptions will be employed to describe the problem in the mathematical form. This mathematical description will then be transformed into the dimensionless form with the help of similarity variables. In this process, some physical parameters will be recovered that will be discussed briefly along with mathematical expressions at the end of the section.

2.1 Physical description

A steady two-dimensional incompressible laminar flow of micropolar nanofluids amid two permeable plates is taken. The base fluid is taken as blood with gold nanoparticles

suspended in it. The influence of thermal radiation, thermophoresis, and Brownian motion exists in the channel with static or moving walls. Moreover, the fluid flow is also influenced by the collective impact of chemically reactive activation energy in the presence of gyrotactic microorganisms. The geometrical view with conditions at the boundaries is presented in Figure 1. The fluid is flowing in the \hat{x} -direction, while the \hat{y} -axis is normal to the channel's walls. The walls of the channel are apart by a distance, L is the axial length, while W is the width of the channel walls. The suction and injection of flow at the walls of the channel are fixed and unvarying. Moreover, the body forces such as gravity, Coriolis, centrifugal force, and magnetic effects are ignored. At the walls, the axial velocities are assumed to be linear with the mathematical description as

$$u_{w,t} = u_t(\hat{x}/H), u_{w,b} = u_b(\hat{x}/H).$$

2.2 Mathematical description of the problem

By the suppositions in Subsection 2.1, the problem can be described mathematically as follows (Misra and Ghosh, 1997; Papadopoulos and Tzirtzilakis, 2004; Tzirtzilakis, 2005; Hatami et al., 2014; Srinivas et al., 2017):

$$\frac{\partial \hat{u}}{\partial \hat{x}} + \frac{\partial \hat{v}}{\partial \hat{y}} = 0, \quad (1)$$

$$\frac{\rho_{nf}}{\varepsilon} \left(\hat{u} \frac{\partial \hat{u}}{\partial \hat{x}} + \hat{v} \frac{\partial \hat{u}}{\partial \hat{y}} \right) = -\frac{\partial \hat{p}}{\partial \hat{x}} + \left(\mu_{nf} + \hat{k} \right) \left(\frac{\partial^2 \hat{u}}{\partial \hat{x}^2} + \frac{\partial^2 \hat{u}}{\partial \hat{y}^2} \right) + \hat{k} \frac{\partial N}{\partial \hat{y}} - \frac{\mu_{nf}}{k_1} \hat{u}, \quad (2)$$

$$\frac{\rho_{nf}}{\varepsilon} \left(\hat{u} \frac{\partial \hat{v}}{\partial \hat{x}} + \hat{v} \frac{\partial \hat{v}}{\partial \hat{y}} \right) = -\frac{\partial \hat{p}}{\partial \hat{y}} + \left(\mu_{nf} + \hat{k} \right) \left(\frac{\partial^2 \hat{v}}{\partial \hat{x}^2} + \frac{\partial^2 \hat{v}}{\partial \hat{y}^2} \right) - \hat{k} \frac{\partial N}{\partial \hat{x}} - \frac{\mu_{nf}}{k_1} \hat{v}, \quad (3)$$

$$\rho_{nf} j \left(\hat{u} \frac{\partial N}{\partial \hat{x}} + \hat{v} \frac{\partial N}{\partial \hat{y}} \right) = -k \left(2N + \frac{\partial \hat{u}}{\partial \hat{y}} - \frac{\partial \hat{v}}{\partial \hat{x}} \right) + \gamma_{nf} \left(\frac{\partial^2 N}{\partial \hat{x}^2} + \frac{\partial^2 N}{\partial \hat{y}^2} \right), \quad (4)$$

$$\hat{u} \frac{\partial T}{\partial \hat{x}} + \hat{v} \frac{\partial T}{\partial \hat{y}} = \frac{k_{nf}}{(\rho C_p)_{nf}} \left(\frac{\partial^2 T}{\partial \hat{x}^2} + \frac{\partial^2 T}{\partial \hat{y}^2} \right) - \frac{1}{(\rho C_p)_{nf}} \frac{\partial q_r}{\partial \hat{y}} + \tau \left[D_B \left(\frac{\partial C}{\partial \hat{x}} \frac{\partial T}{\partial \hat{x}} + \frac{\partial C}{\partial \hat{y}} \frac{\partial T}{\partial \hat{y}} \right) + \frac{D_T}{T_t} \left(\left(\frac{\partial T}{\partial \hat{x}} \right)^2 + \left(\frac{\partial T}{\partial \hat{y}} \right)^2 \right) \right], \quad (5)$$

$$\hat{u} \frac{\partial C}{\partial \hat{x}} + \hat{v} \frac{\partial C}{\partial \hat{y}} = D_B \left(\frac{\partial^2 C}{\partial \hat{x}^2} + \frac{\partial^2 C}{\partial \hat{y}^2} \right) + \frac{D_T}{T_t} \left(\frac{\partial^2 T}{\partial \hat{x}^2} + \frac{\partial^2 T}{\partial \hat{y}^2} \right) - k_r^2 (C - C_t) \left(\frac{T}{T_t} \right)^n \exp \left(-\frac{E_a}{k_B T} \right), \quad (6)$$

$$\hat{u} \frac{\partial n}{\partial \hat{x}} + \hat{v} \frac{\partial n}{\partial \hat{y}} + \left(\frac{bW_c}{C_b - C_t} \right) \frac{\partial}{\partial \hat{y}} \left(n \frac{\partial C}{\partial \hat{y}} \right) = D_m \frac{\partial^2 n}{\partial \hat{y}^2}. \quad (7)$$

In the aforementioned system of equations, the flow along \hat{x} , \hat{y} axes is, respectively, denoted by the components \hat{u} , \hat{v} ; \hat{p} is pressure; μ_{nf} , ρ_{nf} are dynamic viscosity and the density of the nanofluid, respectively; k_1 is permeability; ε is the porosity of walls; q_r is the heat flux due to radiation; $(\rho C_p)_{nf}$ is the effective heat capacity; k_{nf} is the thermal conductivity; D_T , D_B , D_m are diffusion coefficients for thermophoresis, Brownian motion, and microorganism, respectively; C_b , T_b , n_b are the concentration, temperature, and microorganism at the bottom plate of the channel, respectively, while C_t , T_t , n_t are the corresponding quantities at the top plate of the channel; γ_{nf} is the spine gradient viscosity which is mathematically expressed as $\gamma_{nf} = (\mu_{nf} + \hat{k}/2)j$ with j as the density of micro-inertia. Moreover, $(T/T_t)^n e^{(-E_a/k_B T)}$ is the modified Arrhenius function, E_a is the activation energy, k_r is the rate of the reaction, and W_c is the speed of microorganism cells.

The related conditions at boundaries are:

$$u(\hat{x}, \hat{y}) = u_b \frac{\hat{x}}{H}, v(\hat{x}, \hat{y}) = v_b, \quad T = T_b, \quad C = C_b,$$

$$n = n_b, \quad N = -k \frac{\partial \hat{u}}{\partial \hat{y}} \quad \text{at } \hat{y} = 0, \quad u(\hat{x}, \hat{y}) = u_t \frac{\hat{x}}{H},$$

$$v(\hat{x}, \hat{y}) = v_t, \quad T = T_t, \quad C = C_t, \quad n = n_t, \quad N = -k \frac{\partial \hat{u}}{\partial \hat{y}} \quad \text{at } \hat{y} = H. \quad (8)$$

In Eq. 8, the subscript notations b , t are used to represent the bottom and top plates of the channel, respectively. The velocities at the bottom and top walls are, respectively, denoted by v_t , v_b . It is to be noticed that these are different velocities so due to the difference in their directions, various combinations can arise. For instance, the combination $v_b > 0$, $v_t < 0$ leads to injection at the bottom and top walls. Similarly the combination $v_b < 0$, $v_t > 0$ confirms the suction at these walls (Seyf and Rassoulinejad-Mousavi, 2011). The thermophysical characteristics of gold nanoparticles are described as follows (Bachok et al., 2012; Srinivas et al., 2014; Srinivas et al., 2017):

$$\rho_{nf} = (1 - \varphi) \rho_f + \varphi \rho_s, \quad \mu_{nf} = \frac{\mu_f}{(1 - \varphi)^{2.5}}, \quad (\rho C_p)_{nf} = (1 - \varphi)(\rho C_p)_f + \varphi(\rho C_p)_s, \quad \frac{k_{nf}}{k_f} = \frac{k_s + 2k_f - 2\varphi(k_f - k_s)}{k_s + 2k_f + \varphi(k_f - k_s)}. \quad (9)$$

In Eq. 9, ρ_f , k_f , $(\rho C_p)_f$ are the notations for density, thermal conductivity, and heat capacity for the base fluid, while ρ_s , k_s , $(\rho C_p)_s$ are the corresponding notations for the nanofluid. Moreover, μ_f is the viscosity of the pure fluid, while the volumetric fraction of gold nanoparticles is φ . The thermophysical characteristics of the base and nanofluids are

described numerically in Table 1 (Hatami et al., 2014; Srinivas et al., 2017):

For simplification of q_r using the Rosseland approximation as given in the following (Hatami et al., 2014; Zhang et al., 2015)

$$q_r = -\frac{4}{3} \left(\frac{\sigma^* \partial T^4}{\kappa^* \partial y} \right), \quad (10)$$

In Eq. 10, σ^* , κ^* are termed as the Stefan Boltzmann constant and the coefficient of Rosseland mean absorption such that $\sigma^* = 5.6697 \times 10^{-8} \text{ W m}^{-2} \text{ K}^{-4}$. If the thermal gradient is sufficiently small within the flow of the fluid, then T^4 can be simplified by using Taylor's expansion as (Zhang et al., 2015)

$$T^4 \cong 4TT_t^3 - T_t^4, \quad (11)$$

In light of Eqs. 10, 11, we have from Eq. 5 as

$$\begin{aligned} u \frac{\partial T}{\partial x} + v \frac{\partial T}{\partial y} &= \frac{k_{nf}}{(\rho C_p)_{nf}} \left(\frac{\partial^2 T}{\partial x^2} + \frac{\partial^2 T}{\partial y^2} \right) + \frac{1}{(\rho C_p)_{nf}} \left(\frac{16\sigma^* T_t^3}{3\kappa^*} \frac{\partial^2 T}{\partial y^2} \right) \\ &+ \tau \left[D_B \left(\frac{\partial C}{\partial x} \frac{\partial T}{\partial x} + \frac{\partial C}{\partial y} \frac{\partial T}{\partial y} \right) + \frac{D_T}{T_t} \left(\left(\frac{\partial T}{\partial x} \right)^2 + \left(\frac{\partial T}{\partial y} \right)^2 \right) \right]. \end{aligned} \quad (12)$$

The following set of variables (Srinivas et al., 2017; Shah et al., 2020; Khan et al., 2021a) will convert the leading equations into the dimensionless form:

$$\begin{aligned} x &= \frac{\hat{x}}{H}; \quad P = \frac{\hat{p}}{\rho_f v_b^2}; \quad u = \frac{\hat{u}}{v_b}; \quad v = \frac{\hat{v}}{v_b}; \quad \theta(\eta) = \frac{T - T_t}{T_b - T_t}; \\ \phi(\eta) &= \frac{C - C_t}{C_b - C_t}; \quad \chi(\eta) = \frac{n - n_t}{n_b - n_t}; \quad N = -\frac{x v_b G(\eta)}{H} \quad \text{with } \eta = \frac{y}{H}. \end{aligned} \quad (13)$$

The dimensionless velocity components are assumed as

$$u(x, \eta) = x f'(\eta); \quad v(x, \eta) = -f(\eta). \quad (14)$$

By incorporating Eqs. 13, 14 into Eqs. 1–4, 6, 7, 12, we have

$$\begin{aligned} &(1 + (1 - \varphi)^{2.5} K) f^{(iv)} - (1 - \varphi)^{2.5} K G'' - \\ &\left(1 - \varphi + \varphi \frac{\rho_s}{\rho_f} \right) (1 - \varphi)^{2.5} \text{Re} (f' f'' - f f''') - \frac{1}{Da} f'' = 0, \end{aligned} \quad (15)$$

$$\begin{aligned} &\left(1 + (1 - \varphi)^{2.5} \frac{K}{2} \right) G'' + K (1 - \varphi)^{2.5} (f'' - 2G) \\ &+ \text{Re} \left(1 - \varphi + \frac{\rho_s}{\rho_f} \varphi \right) (1 - \varphi)^{2.5} (f G' - f' G) = 0, \end{aligned} \quad (16)$$

$$\left(\frac{k_{nf}}{k_f} + \frac{4}{3} R_d \right) \theta'' + \left(1 - \varphi + \frac{(\rho C_p)_s}{(\rho C_p)_f} \right) \text{Pr} (\text{Re} \theta' f + N_b \theta' \phi')$$

$$+ N_t (\theta')^2 = 0, \quad (17)$$

$$\phi'' + \text{ScRe} f \phi' + \frac{N_t}{N_b} \theta'' - \text{Sc} \Gamma \phi (1 + \Omega \theta)^n \exp \left(\frac{-E}{1 + \Omega \theta} \right) = 0, \quad (18)$$

$$\chi'' - \text{Re} L_b f \chi' + \text{Pe} [\chi' \phi' + (\delta + \chi) \phi''] = 0. \quad (19)$$

In the aforementioned system of equations, $\text{Re} = v_b H / \nu_f$ is Reynolds number, $Da = k / H^2$ is the Darcy number, $\text{Pr} = (\rho C_p)_f \nu_f / k_f$ is the Prandtl number, $K = k / \mu_f$ is the material parameter, $R_d = 4\sigma^* T_t^3 / 3\kappa^* k_f$ is the radiation parameter, $N_b = \tau D_B (C_b - C_t) / \nu_f$ is the Brownian parameter, $N_t = \tau D_T (T_b - T_t) / T_t \nu_f$ is the thermophoresis parameter, $\Omega = T_b - T_t / T_t$ is the temperature parameter, $E = E_a / k_B T_t$ is the activation energy parameter, $\text{Sc} = \nu_f / D_B$ is the Schmidt number, $\Gamma = k_r^* H^2 / \nu_f$ is the chemical reaction parameter, $L_b = \nu_f / D_m$ is the bioconvection Lewis number, $\text{Pe} = b W_c / D_m$ is the Peclet number, and $\delta = n_t / n_b - n_t$ is the microorganism concentration difference parameter.

Related conditions at boundaries are

$$\begin{aligned} f'(0) &= \lambda, \quad f(0) = -\alpha, \quad f'(1) = \gamma, \quad f(1) = -\beta, \\ \theta(0) &= 1, \quad \theta(1) = 0, \quad \phi(0) = 1, \quad \phi(1) = 0, \quad \chi(0) = 1, \\ \chi(1) &= 0, \quad G(0) = k f''(0), \quad G(1) = k f''(1). \end{aligned} \quad (20)$$

$$\text{where } \beta = \frac{v_t}{v_b}; \quad \lambda = \frac{u_t}{v_b}; \quad \gamma = \frac{u_t}{v_b}; \quad \alpha = \begin{cases} 1, & \text{for injection} \\ -1, & \text{for suction.} \end{cases} \quad (21)$$

2.3 Engineering quantities of interest

Different quantities of engineering interest for the flow system under consideration can be expressed mathematically as follows:

$$\begin{aligned} C_f &= \frac{2}{\rho_f \bar{u}^2} \left(\mu_{nf} + \bar{k} \right) \frac{\partial \bar{u}}{\partial y} \bigg|_{y=0}, \quad Nu = \frac{x}{k_f (T_b - T_t)} \left(k_{nf} + \frac{16\sigma^* T_t^3}{3\kappa^*} \right) \frac{\partial T}{\partial y} \bigg|_{y=0}, \\ Sh &= \frac{x}{D_B (C_b - C_t)} \left\{ -D_B \frac{\partial C}{\partial y} \bigg|_{y=0} \right\}, \quad Nn = \frac{x}{D_m (n_b - n_t)} \left\{ -D_m \frac{\partial n}{\partial y} \bigg|_{y=0} \right\}. \end{aligned} \quad (22)$$

Substituting Eq. 9 in Eq. 19 we have the following dimensionless quantities:

$$\begin{aligned} C_f &= \left((1 - \varphi)^{2.5} + K \right) f''(0), \quad Nu = \frac{k_{nf}}{k_f} \left(1 + \frac{4}{3} R_d \right) \theta'(0), \quad Sh \\ &= -\phi'(0), \quad Nn = -\chi'(0). \end{aligned} \quad (23)$$

3 Method for the solution

In the universe physical phenomenon, when a model give rise normally to a nonlinear mathematical model, it is very difficult and

sometimes impossible to determine the analytical solution for such a higher nonlinear mathematical model. To determine solutions to such problems, researchers have introduced different techniques. The homotopy analysis method (Liao, 1999; Liao, 2010) is one such technique that is used to solve nonlinear problems. This technique requires some initial guesses which are defined as follows:

$$\begin{aligned}\hat{f}_0(\eta) &= (\gamma + \lambda - 2\alpha + 2\beta)\eta^3 + (3\alpha - 3\beta - 2\lambda - \gamma)\eta^2 + \lambda\eta - \alpha, \\ \hat{G}_0(\eta) &= K(18\beta + 10\lambda + 8\gamma - 18\alpha)\eta + K(6\alpha - 6\beta - 4\lambda - 2\gamma), \\ \hat{\Theta}_0(\eta) &= 1 - \eta, \quad \hat{\Phi}_0(\eta) = 1 - \eta, \quad \hat{\chi}_0(\eta) = 1 - \eta.\end{aligned}\quad (24)$$

With linear operators expressed as

$$\begin{aligned}L_f(f) &= f''' - f', \quad L_g(g) = g'' - g, \quad L_\Theta(\Theta) = \Theta'' - \Theta, \quad L_\Phi(\Phi) \\ &= \Phi'' - \Phi, \quad L_\chi(\chi) = \chi'' - \chi.\end{aligned}\quad (25)$$

In expanded form, relations in Eq. 25 can be expressed as

$$\begin{aligned}L_f(d_1 + d_2e^\eta + d_3e^{-\eta}) &= 0, \quad L_g(d_4e^\eta + d_5e^{-\eta}) = 0, \\ L_\Theta(d_6e^\eta + d_7e^{-\eta}) &= 0, \quad L_\Phi(d_8e^\eta + d_9e^{-\eta}) = 0, \\ L_\chi(d_{10}e^\eta + d_{11}e^{-\eta}) &= 0.\end{aligned}\quad (26)$$

Above d_i for $i = 1, 2, 3, \dots, 11$ are constants proceeding further as follows:

$$\begin{aligned}&N_{\hat{f}}[\hat{f}(\eta; \chi), \hat{G}(\eta; \chi)\hat{\theta}(\eta; \chi), \hat{\phi}(\eta; \chi), \hat{\chi}(\eta; \chi)] \\ &= (1 + (1 - \varphi)^{2.5}K)\hat{f}_{\eta\eta\eta} + (1 - \varphi)^{2.5}K\hat{G}_{\eta\eta} - \left(1 - \varphi\right. \\ &\quad \left.+ \varphi\frac{\rho_s}{\rho_f}\right)(1 - \varphi)^{2.5}\text{Re}(\hat{f}_\eta\hat{f}_{\eta\eta} - \hat{f}\hat{f}_{\eta\eta\eta}) - \frac{1}{Da}\hat{f}_{\eta\eta},\end{aligned}\quad (27)$$

$$\begin{aligned}&N_{\hat{G}}[\hat{f}(\eta; \chi), \hat{G}(\eta; \chi)\hat{\theta}(\eta; \chi), \hat{\phi}(\eta; \chi), \hat{\chi}(\eta; \chi)] \\ &= \left(1 + (1 - \varphi)^{2.5}\frac{K}{2}\right)\hat{G}_{\eta\eta} + K(1 - \varphi)^{2.5}(\hat{f}_{\eta\eta} - 2\hat{G}) \\ &\quad + \text{Re}\left(1 - \varphi + \frac{\rho_s}{\rho_f}\varphi\right)(1 - \varphi)^{2.5}(\hat{f}\hat{G}_\eta - \hat{f}_\eta\hat{G}),\end{aligned}\quad (28)$$

$$\begin{aligned}&N_{\hat{\theta}}[\hat{f}(\eta; \chi), \hat{G}(\eta; \chi)\hat{\theta}(\eta; \chi), \hat{\phi}(\eta; \chi), \hat{\chi}(\eta; \chi)] \\ &= \left(\frac{k_{nf}}{k_f} + \frac{4}{3}R_d\right)\hat{\theta}_{\eta\eta} + \left(1 - \hat{\phi} + \frac{(\rho C_p)_s}{(\rho C_p)_f}\right)\text{Pr}(\text{Re}\hat{\theta}_\eta\hat{f} + N_b\hat{\theta}_\eta\hat{\phi}_\eta \\ &\quad + N_t(\hat{\theta}_\eta)^2),\end{aligned}\quad (29)$$

$$\begin{aligned}&N_{\hat{\phi}}[\hat{f}(\eta; \chi), \hat{G}(\eta; \chi)\hat{\theta}(\eta; \chi), \hat{\phi}(\eta; \chi), \hat{\chi}(\eta; \chi)] \\ &= \hat{\phi}_{\eta\eta} + \text{ScRe}\hat{f}\hat{\phi}_\eta + \frac{N_t}{N_b}\theta'' - \text{Sc}\Gamma\hat{\phi}(1 + \Omega\hat{\theta})^n \exp\left(\frac{-E}{1 + \Omega\hat{\theta}}\right),\end{aligned}\quad (30)$$

$$\begin{aligned}&N_{\hat{\chi}}[\hat{f}(\eta; \chi), \hat{G}(\eta; \chi)\hat{\theta}(\eta; \chi), \hat{\phi}(\eta; \chi), \hat{\chi}(\eta; \chi)] \\ &= \hat{\chi}_{\eta\eta} - \text{Re}L_b\hat{f}\hat{\chi}_\eta + \text{Pe}[\hat{\chi}_\eta\hat{\phi}_\eta + (\delta + \hat{\chi})\hat{\phi}_{\eta\eta}].\end{aligned}\quad (31)$$

The zero-ord/er system in respect of Eqs. 8–11 can be described as follows:

$$\begin{aligned}(1 - \zeta)L_{\hat{f}}[\hat{f}(\eta; \zeta) - \hat{f}_0(\eta)] &= \zeta\hat{h}_{\hat{f}}N_{\hat{f}} \\ &[\hat{f}(\eta; \chi), \hat{G}(\eta; \chi)\hat{\theta}(\eta; \chi), \hat{\phi}(\eta; \chi), \hat{\chi}(\eta; \chi)],\end{aligned}\quad (32)$$

$$\begin{aligned}(1 - \zeta)L_{\hat{G}}[\hat{G}(\eta; \zeta) - \hat{G}_0(\eta)] &= \zeta\hat{h}_{\hat{G}}N_{\hat{G}} \\ &[\hat{f}(\eta; \chi), \hat{G}(\eta; \chi)\hat{\theta}(\eta; \chi), \hat{\phi}(\eta; \chi), \hat{\chi}(\eta; \chi)],\end{aligned}\quad (33)$$

$$\begin{aligned}(1 - \zeta)L_{\hat{\theta}}[\hat{\theta}(\eta; \zeta) - \hat{\theta}_0(\eta)] &= \zeta\hat{h}_{\hat{\theta}}N_{\hat{\theta}} \\ &[\hat{f}(\eta; \chi), \hat{G}(\eta; \chi)\hat{\theta}(\eta; \chi), \hat{\phi}(\eta; \chi), \hat{\chi}(\eta; \chi)],\end{aligned}\quad (34)$$

$$\begin{aligned}(1 - \zeta)L_{\hat{\phi}}[\hat{\phi}(\eta; \zeta) - \hat{\phi}_0(\eta)] &= \zeta\hat{h}_{\hat{\phi}}N_{\hat{\phi}} \\ &[\hat{f}(\eta; \chi), \hat{G}(\eta; \chi)\hat{\theta}(\eta; \chi), \hat{\phi}(\eta; \chi), \hat{\chi}(\eta; \chi)],\end{aligned}\quad (35)$$

$$\begin{aligned}(1 - \zeta)L_{\hat{\chi}}[\hat{\chi}(\eta; \zeta) - \hat{\chi}_0(\eta)] &= \zeta\hat{h}_{\hat{\chi}}N_{\hat{\chi}} \\ &[\hat{f}(\eta; \chi), \hat{G}(\eta; \chi)\hat{\theta}(\eta; \chi), \hat{\phi}(\eta; \chi), \hat{\chi}(\eta; \chi)].\end{aligned}\quad (36)$$

The BCs are

$$\begin{aligned}\frac{\partial \hat{f}(\eta; \zeta)}{\partial \eta}\bigg|_{\eta=0} &= \lambda, \quad \frac{\partial \hat{f}(\eta; \zeta)}{\partial \eta}\bigg|_{\eta=1} = \gamma, \quad \hat{f}(\eta; \zeta)\bigg|_{\eta=0} = -\alpha, \quad \hat{f}(\eta; \zeta)\bigg|_{\eta=1} \\ &= -\beta, \quad \hat{\theta}(\eta; \zeta)\bigg|_{\eta=0} = 1, \quad \hat{\theta}(\eta; \zeta)\bigg|_{\eta=1} = 0, \quad \hat{\phi}(\eta; \zeta)\bigg|_{\eta=0} = 1, \quad \hat{\phi}(\eta; \zeta)\bigg|_{\eta=1} \\ &= 0, \quad \hat{\chi}(\eta; \zeta)\bigg|_{\eta=0} = 1, \quad \hat{\chi}(\eta; \zeta)\bigg|_{\eta=1} = 0, \quad \hat{G}(\eta; \zeta)\bigg|_{\eta=0} \\ &= k\frac{\partial^2 \hat{f}(\eta; \zeta)}{\partial \eta^2}\bigg|_{\eta=0}, \quad \hat{G}(\eta; \zeta)\bigg|_{\eta=1} = k\frac{\partial^2 \hat{f}(\eta; \zeta)}{\partial \eta^2}\bigg|_{\eta=1}.\end{aligned}\quad (37)$$

It is to be noticed that $\zeta \in [0, 1]$, so for $\zeta = 0$ and $\zeta = 1$ we have

$$\begin{aligned}\hat{f}(\eta; 1) &= \hat{f}(\eta), \quad \hat{G}(\eta; 1) = \hat{G}(\eta), \quad \hat{\theta}(\eta; 1) = \hat{\theta}(\eta), \quad \hat{\phi}(\eta; 1) \\ &= \hat{\phi}(\eta), \quad \hat{\chi}(\eta; 1) = \hat{\chi}(\eta).\end{aligned}\quad (38)$$

The expansion of Taylor's series for $\hat{f}(\eta; \zeta)$, $\hat{G}(\eta; \zeta)$, $\hat{\theta}(\eta; \zeta)$, $\hat{\phi}(\eta; \zeta)$, and $\hat{\chi}(\eta; \zeta)$ around $\zeta = 0$

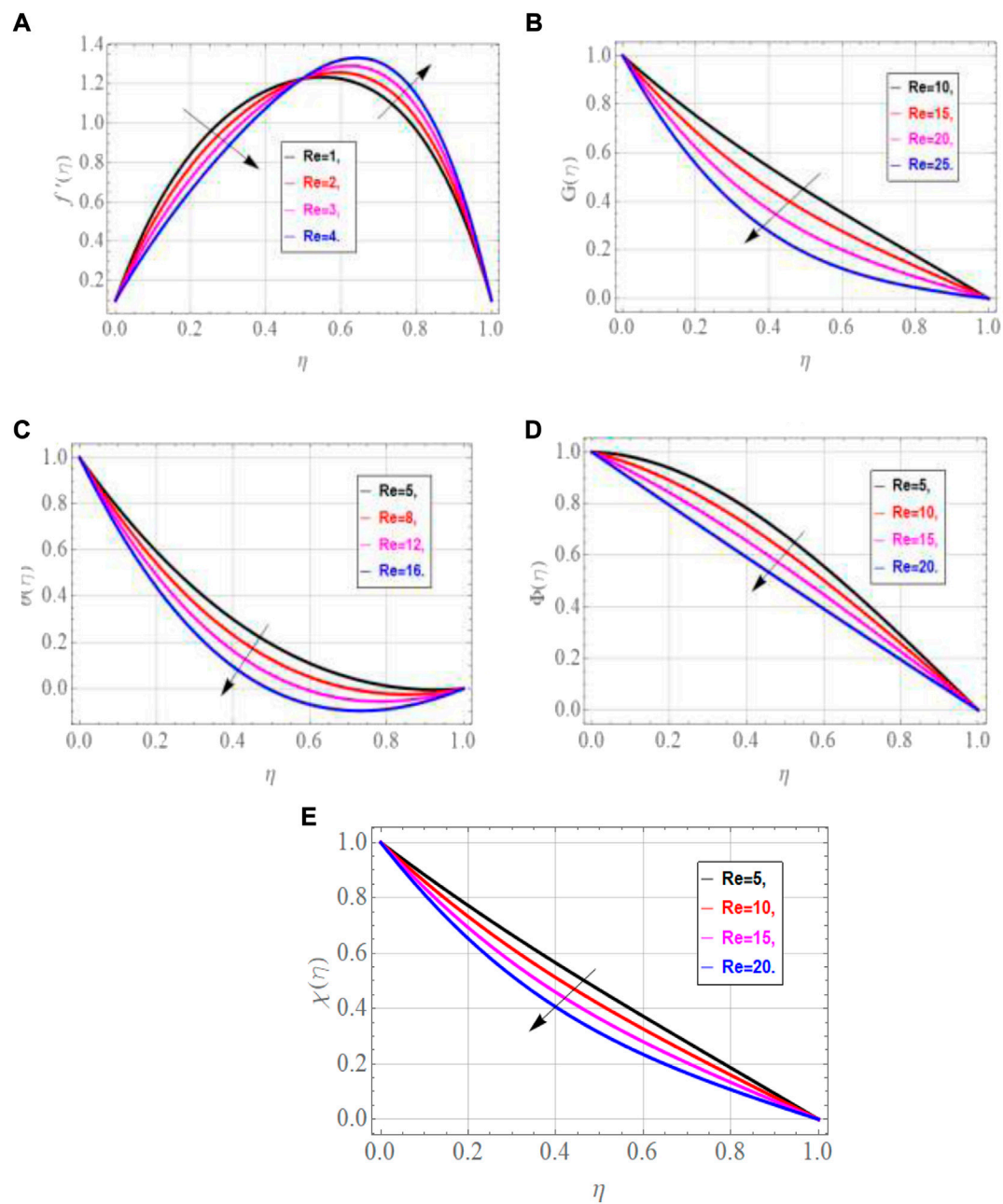


FIGURE 2
Impact of Re on $f'(\eta)$, $G(\eta)$, $\theta(\eta)$, $\Phi(\eta)$, $\chi(\eta)$.

$$\begin{aligned}
 \widehat{f}(\eta; \zeta) &= \widehat{f}_0(\eta) + \sum_{n=1}^{\infty} \widehat{f}_n(\eta) \zeta^n, \\
 \widehat{G}(\eta; \zeta) &= \widehat{G}_0(\eta) + \sum_{n=1}^{\infty} \widehat{G}_n(\eta) \zeta^n, \\
 \widehat{\theta}(\eta; \zeta) &= \widehat{\theta}_0(\eta) + \sum_{n=1}^{\infty} \widehat{\theta}_n(\eta) \zeta^n, \\
 \widehat{\phi}(\eta; \zeta) &= \widehat{\phi}_0(\eta) + \sum_{n=1}^{\infty} \widehat{\phi}_n(\eta) \zeta^n, \\
 \widehat{\chi}(\eta; \zeta) &= \widehat{\chi}_0(\eta) + \sum_{n=1}^{\infty} \widehat{\chi}_n(\eta) \zeta^n,
 \end{aligned}
 \quad (39)$$

$$\begin{aligned}
 \widehat{f}_n(\eta) &= \frac{1}{n!} \left. \frac{\partial \widehat{f}(\eta; \zeta)}{\partial \zeta} \right|_{\zeta=0}, \quad \widehat{G}_n(\eta) = \frac{1}{n!} \left. \frac{\partial \widehat{G}(\eta; \zeta)}{\partial \zeta} \right|_{\zeta=0}, \quad \widehat{\theta}_n(\eta) \\
 &= \frac{1}{n!} \left. \frac{\partial \widehat{\theta}(\eta; \zeta)}{\partial \zeta} \right|_{\zeta=0}, \quad \widehat{\phi}_n(\eta) = \frac{1}{n!} \left. \frac{\partial \widehat{\phi}(\eta; \zeta)}{\partial \zeta} \right|_{\zeta=0}, \quad \widehat{\chi}_n(\eta) = \frac{1}{n!} \left. \frac{\partial \widehat{\chi}(\eta; \zeta)}{\partial \zeta} \right|_{\zeta=0}.
 \end{aligned}
 \quad (40)$$

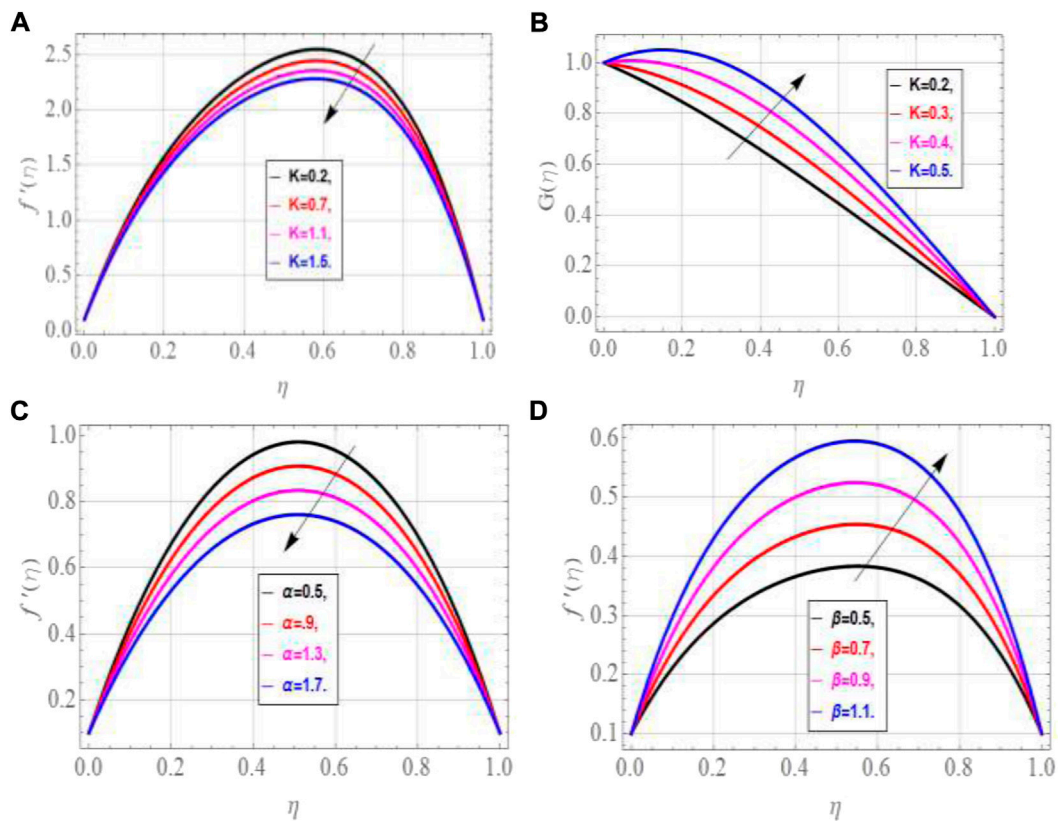


FIGURE 3
Impact of K, α, β on $f'(\eta)$, $G(\eta)$.

With boundary conditions as follows

$$\sim f'(0) = \lambda, \sim f'(1) = \gamma, \hat{f}(0) = -\alpha, \quad \hat{f}(1) = -\beta, \hat{G}(0)$$

$$= k\sim f''(0), \hat{G}(1)$$

$$= k\sim f''(1), \hat{\theta}(0) = 1, \hat{\theta}(1) = 0, \quad (41)$$

$$\hat{\phi}(0) = 1, \hat{\phi}(1) = 0, \hat{\chi}(0) = 1, \quad \hat{\chi}(1) = 0.$$

Next, we have

$$\Re_n \hat{f}(\eta) = (1 + (1 - \varphi)^{2.5} K) \hat{f}_{n-1} + (1 - \varphi)^{2.5} K \hat{G}_{n-1}'' - \left(1 - \varphi + \varphi \frac{\rho_s}{\rho_f}\right) (1 - \varphi)^{2.5} \text{Re} \left(\hat{f}_{n-1}' \hat{f}_{n-1}'' \sum_{j=0}^{w-1} \hat{f}_{w-1-j} \hat{f}_j''' \right) - \frac{1}{Da} \hat{f}_{n-1}'', \quad (42)$$

$$\Re_n \hat{G}(\eta) = \left(1 + (1 - \varphi)^{2.5} \frac{K}{2}\right) \hat{G}'' + K(1 - \varphi)^{2.5} \sum_{j=0}^{w-1} \left(\hat{f}_{n-1}' \hat{f}_{n-1}'' 2\hat{G}_{w-1-j} \right) + \text{Re} \left(1 - \varphi + \varphi \frac{\rho_s}{\rho_f} \right) (1 - \varphi)^{2.5} \sum_{j=0}^{w-1} \left(\hat{f}_{w-1-j} \hat{G}_{n-1}' \hat{f}_{n-1}' \hat{G}_{w-1-j} \right), \quad (43)$$

$$\Re_n \hat{\theta}(\eta) = \left(\frac{k_{nf}}{k_f} + \frac{4}{3} R_d \right) \hat{\theta}_{n-1}'' \left(1 - \hat{\phi} + \frac{(\rho C_p)_s}{(\rho C_p)_f} \right)$$

$$\Pr \left(\text{Re} \sum_{j=0}^{w-1} \hat{\theta}_{n-1}' \hat{f}_{w-1-j} + N_b \hat{\theta}_{n-1}' \hat{\phi}_{n-1}' + N_t (\hat{\theta}_{n-1}')^2 \right), \quad (44)$$

$$\Re_n \hat{\phi}(\eta) = \hat{\phi}_{n-1}'' + \text{Sc} \text{Re} \hat{f} \hat{\phi}_{n-1}' + \frac{N_t}{N_b} \hat{\theta}_{n-1}'' - \text{Sc} \Gamma (1 + \Omega \hat{\theta})^n \exp \left(\frac{-E}{1 + \Omega \hat{\theta}} \right) \sum_{j=0}^{w-1} \hat{\phi}_{w-1-j}, \quad (45)$$

$$\Re_n \hat{\chi}(\eta) = \hat{\chi}_{n-1}'' \text{Re} \sum_{j=0}^{w-1} L_b \hat{f}_j \hat{\chi}_{w-1-j} \hat{P}_e \left(\sum_{j=0}^{w-1} \hat{\chi}_{w-1-j}' \hat{\phi}_j + \sum_{j=0}^{w-1} (\delta + \hat{\chi}_{w-1-j}) \hat{\phi}_{n-1}'' \right). \quad (46)$$

Moreover, we have

$$\xi_n = \begin{cases} 0, & \text{if } \zeta \leq 1 \\ 1, & \text{if } \zeta > 1. \end{cases} \quad (47)$$

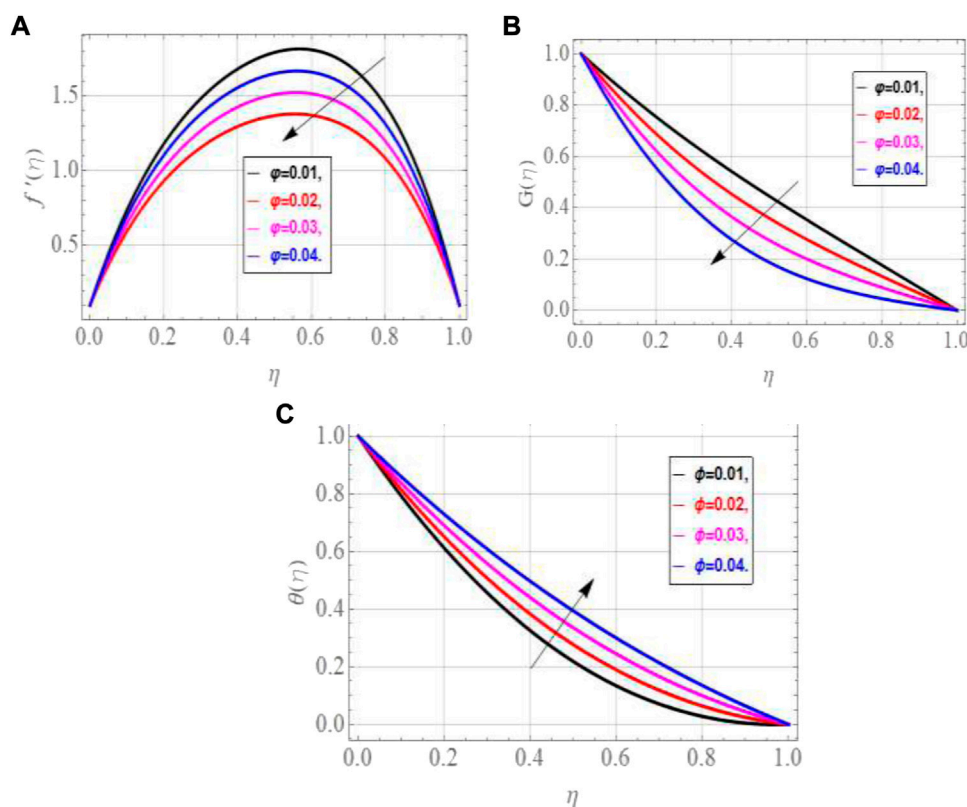


FIGURE 4
Impact of ϕ on $f'(\eta)$, $G(\eta)$, $\theta(\eta)$.

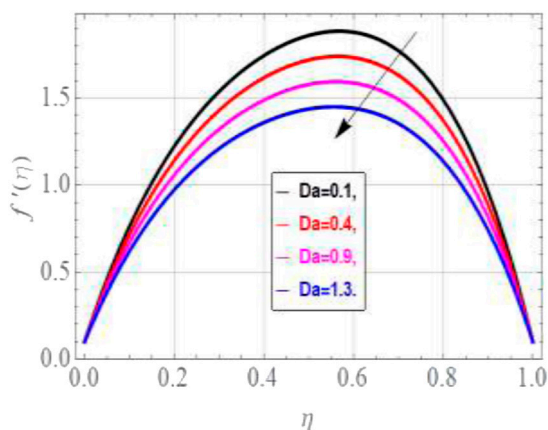


FIGURE 5
Impact of Da on $f'(\eta)$.

4 Discussion of results

The current study examines the flow and heat transfer for the flow of blood that comprises micropolar gold

nanoparticles. The influence of chemically reactive activation energy, thermophoresis, thermal radiations, and Brownian motion also exists between the walls of the channel. A microorganism creation also affects the concentration of nanoparticles inside the channel. Suitable transformation has been used to change the mathematical model to the dimensionless form and then has been solved by employing the homotopy analysis method. The impact upon different profiles of flow systems in response to variations in the physical parameter has been comprehended in the following.

Figure 2 depicts the influence of the Reynolds number Re on different profiles of the flow system. Since the Reynolds number signifies the comparison of inertial force to viscous force, so augmentation in Re causes domination of inertial to viscous force. This physical phenomenon declines the rotational flow, thermal characteristics, motility, and concentration of micropolar nanoparticles. In the case of linear velocity, the flow behavior is two-folded over the range $0 \leq \eta \leq 1$. The flow is declining in the range $0 \leq \eta \leq 0.5$, whereas it is augmenting on the range $0.5 \leq \eta \leq 1$.

Figure 3 describes the changing behavior of fluid's motion for variation in the values of the material parameter. From

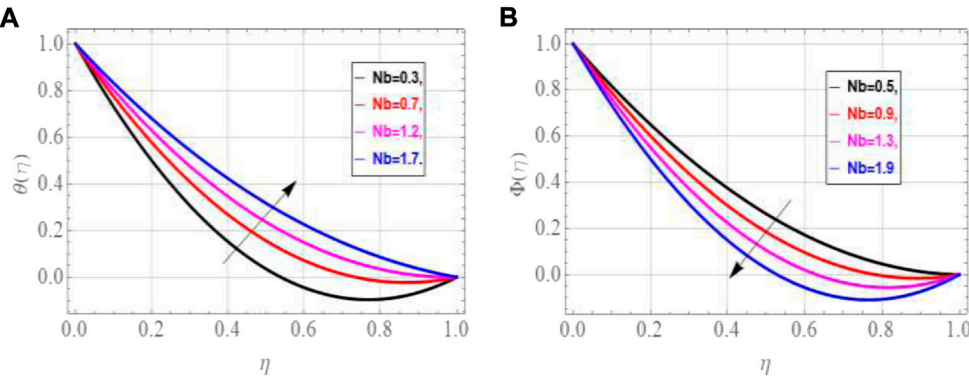


FIGURE 6
Impact of Nb on $\theta(\eta)$, $\Phi(\eta)$.

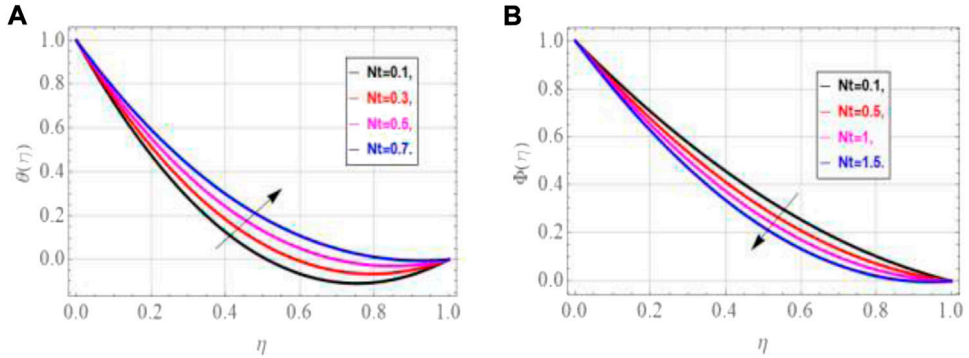


FIGURE 7
Impact of Nt on $\theta(\eta)$, $\Phi(\eta)$.

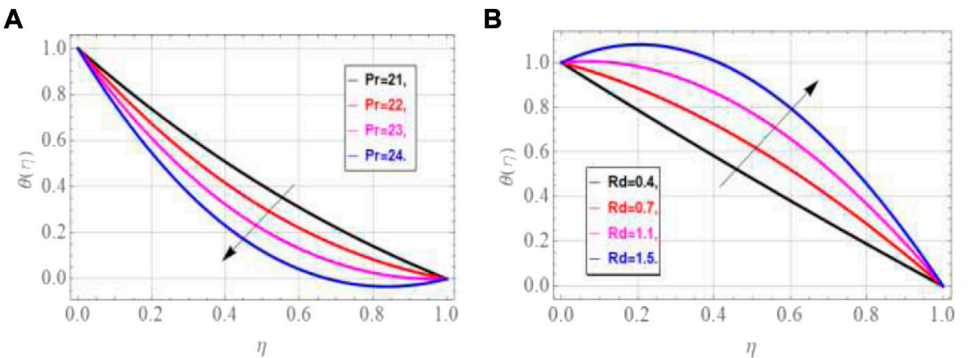


FIGURE 8
Impact of Pr and Rd on $\theta(\eta)$.

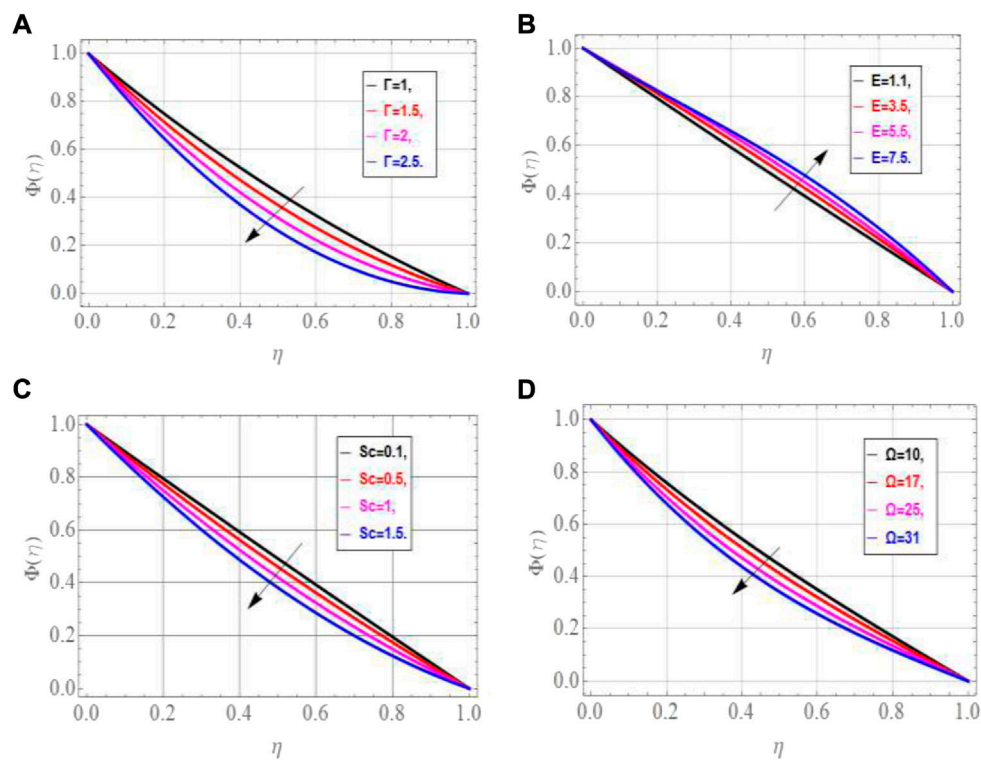


FIGURE 9
Impact of Γ , E , Sc and Ω on $\Phi(\eta)$.

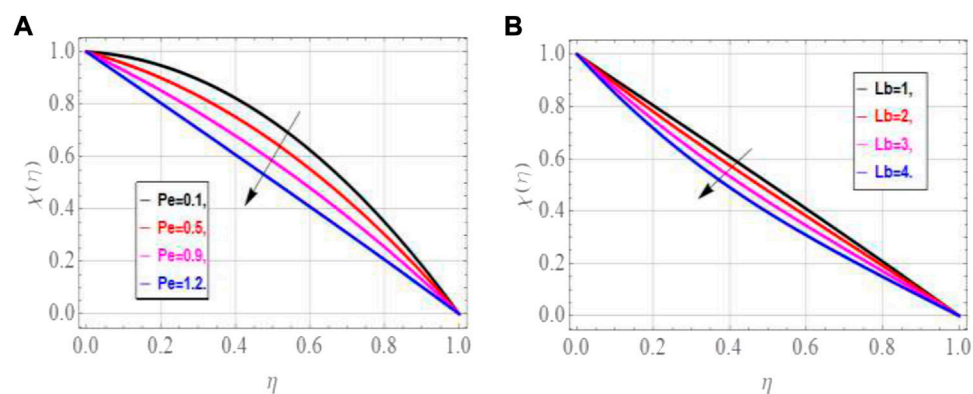


FIGURE 10
Impact of Pe , Lb on $\chi(\eta)$.

Figure 3A, it can be perceived that fluid's motion declines in the closed locality of the porous plate with augmentation in K due to domination of vertex viscosity to dynamic viscosity. In this physical process, the rotational effects are enhanced in the fluid particles that cause augmentation in the microrotation

flow of nanofluids, as depicted in Figure 3B. It has also been noticed that the flow profiles have declined with augmentation in the suction parameter, as depicted in Figure 3C. Moreover, augmenting values of the injection parameter have supported the velocity, as depicted in Figure 3D.

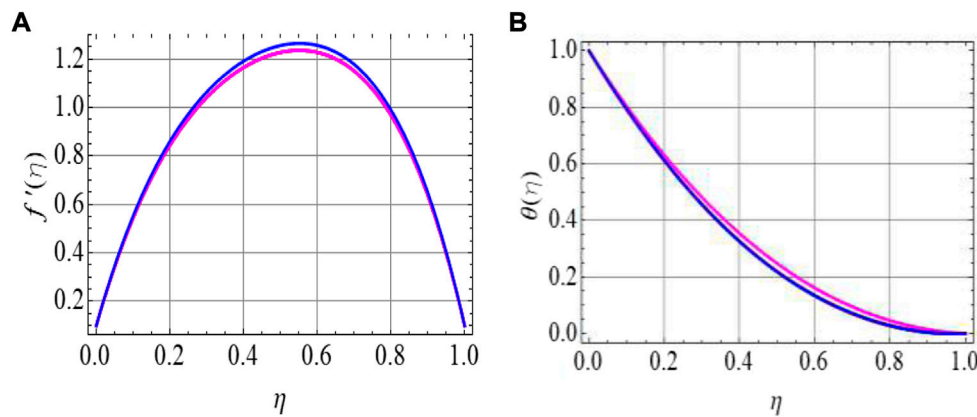


FIGURE 11
Validation of the current study with established results.

TABLE 1 Thermophysical properties of the base fluid and nanoparticles.

| Material | Density (kg/m^3) | Specific heat (J/kgK) | Thermal conductivity (W/mK) |
|----------|----------------------|---------------------------|---------------------------------|
| Blood | 1,050 | 3,617 | 0.52 |
| Gold | 19,300 | 129 | 318 |

TABLE 2 Skin friction C_f variations for different values of Re and Da .

| ϕ | K | Re | Da | $f'(1)$ | $f'(0)$ |
|--------|-----|------|------|---------|-----------|
| 0.02 | 0.3 | 1 | 0.5 | 6.1963 | -0.15248 |
| 0.04 | | | | 6.98229 | -0.21329 |
| 0.06 | | | | 7.87492 | -0.27577 |
| | 0.3 | | | 6.19630 | -0.15248 |
| | 0.4 | | | 5.94500 | -0.13451 |
| | 0.5 | | | 5.14270 | -0.08936 |
| | | 1 | | 6.19630 | -0.15248 |
| | | 3 | | 6.71085 | -0.210436 |
| | | 5 | | 7.30327 | -0.295691 |
| | | | 0.5 | 6.19630 | -0.152480 |
| | | | 1 | 6.49150 | -0.249460 |
| | | | 1.5 | 6.97020 | -0.305632 |

TABLE 3 Nusselt number Nu for variations Nb and Rd .

| Nt | Nb | Rd | $\theta'(1)$ | $\theta'(0)$ |
|------|------|------|--------------|--------------|
| 0.2 | 0.5 | 0.5 | 5.29822 | -0.73111 |
| 0.4 | | | 6.06530 | -0.80198 |
| 0.6 | | | 6.28720 | -0.84279 |
| | 0.5 | | 5.29822 | -0.73111 |
| | 0.8 | | 6.10851 | -0.74766 |
| | 1.1 | | 6.33041 | -0.78847 |
| | | 0.35 | 5.29822 | -0.73111 |
| | | 1 | 6.07098 | -0.70144 |
| | | 1.5 | 6.29288 | -0.74225 |

Figure 4 depicts the impact of volumetric fraction ϕ on the flow, microrotational flow, and thermal profiles of the micropolar nanofluid. Since the augmenting values of ϕ cause an enhancement in the viscous forces amongst the fluid nanoparticles, the fluid becomes more dense and viscous. During this process, higher resistance is experienced by micropolar nanoparticles that decline the fluid flow in all

directions, as shown in Figures 4A,B, while augmenting the thermal profiles of micropolar nanofluids, as depicted in Figure 4C.

Figure 5 portrays that augmenting values in the Darcy number Da decay the flow profiles. Actually, the void spaces in the porous plates are augmented with growing values of Da that offer more confrontation to the fluid's flow and decline the flow profile.

Figure 6 reveals that augmentation in Nb supports the thermal profile and opposes the mass flow of the micropolar

TABLE 4 Sherwood number Sh variation for different values of Nb and Rd .

| Nt | Nb | Re | Sc | $\phi'(1)$ | $\phi'(0)$ |
|------|------|------|------|------------|------------|
| 0.2 | 0.5 | 0.5 | | 0.314193 | -3.49654 |
| 0.4 | | | | 0.3702185 | -3.56741 |
| 0.6 | | | | 0.4208461 | -3.60822 |
| | 0.5 | | | 0.314193 | -3.49654 |
| | 0.8 | | | 0.2764301 | -3.07410 |
| | 1.1 | | | 0.2064107 | -2.49630 |
| | | 0.35 | | 0.314193 | -3.49654 |
| | | 1 | | 0.4864106 | -4.17539 |
| | | 1.5 | | 0.5475302 | -4.932865 |
| | | | 0.3 | 0.314193 | -3.49654 |
| | | | 0.5 | 0.2953106 | -3.18640 |
| | | | 0.7 | 0.2507270 | -2.70871 |

nanofluid. Physically an enhancement in Nb causes an increment in the collision amongst the nanoparticles due to their random motion between the porous plates. In this process, kinetic energy amongst the particles is transformed to thermal energy and causes less transfer of the mass of the fluid. Hence, the thermal profiles enhance and the concentration of fluid declines for augmenting values of Nb .

Figure 7 depicts the influence of the thermophoresis parameter Nt on (η) , $\Phi(\eta)$. Actually, augmentation in Nt corresponds to more thermal and less mass diffusivity of the micropolar nanofluid. Hence, the thermal characteristics increase, and the mass flow declines with augmenting values of Nt .

Figure 8 depicts the impact of the Prandtl number Pr and radiation parameter Rd upon thermal profiles. Figure 8A reveals a significant decline in thermal profiles. Actually, Pr is inversely proportional to heat diffusion due to which the thermal profiles decline for augmenting values of Pr . Figure 8B shows that for enhancing values of Rd , more heat transfer takes place that augments the thermal profiles.

Figure 9 portrays the variations in concentration in response to the chemical reaction parameter Γ , dimensionless activation energy parameter E , Schmidt number Sc , and temperature ratio parameter Ω . For augmentation in Γ , the molecules of the micropolar fluid diffuse slowly due to which less mass diffusion occurs and decays the concentration, as depicted in Figure 9A. For greater values of E , the bulk of molecules that requires less energy supports maximum transmission of mass. Hence, greater values of E cause growth in the concentration of micropolar nanoparticles, as depicted in Figure 9B. For augmenting values of Sc , less mass transfer takes place which weakens the strength of the concentration layer and decays the concentration profiles, as portrayed in Figure 9C. The difference in temperature enhances growth in Ω and causes maximum transmission of heat at the free

stream. In this physical process, less mass diffuses which causes a decline in the concentration, as shown in Figure 9D.

Figure 10 depicts the effects of Peclet and bioconvection Lewis numbers Pe , Lb on the density number of motile microorganisms. It has been noticed from this figure that the growth in Pe , Lb causes a decline in the spread of microorganisms that weakens the strength of its boundary layer. Hence, the growing values of Pe , Lb decline the density number of microorganisms.

Figures 11A,B present the validation of the current investigation. In this figure, the present results are validated with published studies given in Shah et al. (2019) by considering the common parameters. This figure shows a close agreement between the present results and published studies.

4.1 Table discussion

The influence upon various physical quantities in response to different emerging parameters has been presented numerically in Table 1. The numerical results of the velocity gradient C_f against different emerging parameters are given in Table 2. One can find that the velocity gradient upsurges for the particle concentration, Reynolds number Re , and Darcy number. Prominent performances of various engineering parameters on the Nusselt number Nu are examined in Table 3. As expected, the Nusselt number is augmented for expansion in the thermophoresis parameter, Brownian parameter Nb , and radiation parameter Rd . The characteristics of Nb and Re on the Sherwood number Sh are scrutinized in Table 4. One can clearly notice that the concentration gradient is augmented for a higher approximation of Re , while declines with Nb and Sc .

5 Conclusion

In this investigation, the flow and heat transfer for the flow of blood comprises micropolar gold nanoparticles. The influence of chemically reactive activation energy, thermophoresis, thermal radiations, and Brownian motion exists between the walls of the channel. A microorganism creation also affects the concentration of nanoparticles inside the channel. The impact on different profiles of flow systems in response to variations in the physical parameter has been discussed graphically. After a detailed inspection of the research, some main points have been noted and appended in the following:

- Reynolds number reduces all the profiles of the flow system.
- The augmentation in the material parameter and Darcy number declines the flow of the fluid and upsurges the microrotation velocity of nanoparticles.
- The augmenting values of the volumetric fraction cause an enhancement in viscous forces amongst the fluid

nanoparticles and cause a reduction in the flow of the fluid in all direction while supporting the thermal profiles.

- Thermal profiles are supported while concentration profiles are opposed by the growing values of thermophoresis and the Brownian motion parameter.
- Thermal profiles are also growing up with augmenting values of the radiation parameter and decline with enhancement in the Prandtl number.
- The concentration of fluid upsurgs by higher values of the activation energy parameter and reduces by growth in the chemical reaction parameter, Schmidt number, and temperature ratio parameter.
- An augmentation in the bioconvection Lewis number and Peclet number opposes the growth in motile microorganisms.

Data availability statement

The original contributions presented in the study are included in the article/supplementary material; further inquiries can be directed to the corresponding author.

Author contributions

AK has modeled the problem. Dr. Safyan Mukhtar has solved the modeled problem by HAM. AK and WA wrote the manuscript. Dr. Safyan Mukhtar and AK have also contributed to the numerical computations and plotting of the graphical results of the manuscript. MA, MMA,

MPFY, ET participated in revision of manuscript. All the authors have finalized the manuscript after its internal evaluation.

Acknowledgments

“The authors extend their appreciation to the Deanship of Scientific Research at King Khalid University for funding this work through Large Groups” [Project under grant number (RGP.2/116/43)].

Conflict of interest

The authors declare that the research was conducted in the absence of any commercial or financial relationships that could be construed as a potential conflict of interest.

Publisher's note

All claims expressed in this article are solely those of the authors and do not necessarily represent those of their affiliated organizations, or those of the publisher, the editors, and the reviewers. Any product that may be evaluated in this article, or claim that may be made by its manufacturer, is not guaranteed or endorsed by the publisher.

References

- Abbas, N., Nadeem, S., and Malik, M. Y. (2020). Theoretical study of micropolar hybrid nanofluid over Riga channel with slip conditions. *Phys. A Stat. Mech. Its Appl.* 551, 124083. doi:10.1016/j.physa.2019.124083
- Ahmad, S., Ashraf, M., and Ali, K. (2020). Nanofluid flow comprising gyrotactic microorganisms through a porous medium. *J. Appl. Fluid Mech.* 13 (5), 1539–1549. doi:10.36884/jafm.13.05.31030
- Ayub, A., Darvesh, A., Altamirano, G. C., and Sabir, Z. (2021). Nanoscale energy transport of inclined magnetized 3D hybrid nanofluid with Lobatto IIIA scheme. *Heat. Transf.* 50 (7), 6465–6490. doi:10.1002/htj.22188
- Ayub, A., Sabir, Z., Le, D. N., and Aly, A. A. (2021). Nanoscale heat and mass transport of magnetized 3-D chemically radiative hybrid nanofluid with orthogonal/inclined magnetic field along rotating sheet. *Case Stud. Therm. Eng.* 26, 101193. doi:10.1016/j.csite.2021.101193
- Ayub, A., Sabir, Z., Shah, S. Z. H., Mahmoud, S. R., Algarni, A., Sadat, R., et al. (2022b). Aspects of infinite shear rate viscosity and heat transport of magnetized Carreau nanofluid. *Eur. Phys. J. Plus* 137 (2), 1–25. doi:10.1140/epjp/s13360-022-02410-6
- Ayub, A., Sabir, Z., Shah, S. Z. H., Wahab, H. A., Sadat, R., and Ali, M. R. (2022c). Effects of homogeneous-heterogeneous and Lorentz forces on 3-D radiative magnetized cross nanofluid using two rotating disks. *Int. Commun. Heat Mass Transf.* 130, 105778. doi:10.1016/j.icheatmasstransfer.2021.105778
- Ayub, A., Shah, S. Z. H., Sabir, Z., Rao, N. S., Sadat, R., and Ali, M. R. (2022). Spectral relaxation approach and velocity slip stagnation point flow of inclined magnetized cross-nanofluid with a quadratic multiple regression model. *Waves Random Complex Media* 107, 1–25. doi:10.1080/17455030.2022.2049923
- Ayub, A., Wahab, H. A., Shah, S. Z., Shah, S. L., Darvesh, A., Haider, A., et al. (2021). Interpretation of infinite shear rate viscosity and a nonuniform heat sink/source on a 3D radiative cross nanofluid with buoyancy assisting/opposing flow. *Heat. Transf.* 50 (5), 4192–4232. doi:10.1002/htj.22071
- Bachok, N., Ishak, A., and Pop, I. (2012). The boundary layers of an unsteady stagnation-point flow in a nanofluid. *Int. J. Heat Mass Transf.* 55 (23–24), 6499–6505. doi:10.1016/j.ijheatmasstransfer.2012.06.050
- Baharifar, F., Parand, K., and Rashidi, M. M. (2020). Novel solution for heat and mass transfer of a MHD micropolar fluid flow on a moving plate with suction and injection. *Eng. Comput.* 38, 13–30. doi:10.1007/s00366-020-01026-7
- Bin-Mohsin, B., Ahmed, N., Khan, U., Mohyud-Din, S. T., and Tauseef Mohyud-Din, S. (2017). A bioconvection model for a squeezing flow of nanofluid between parallel plates in the presence of gyrotactic microorganisms. *Eur. Phys. J. Plus* 132 (4), 1–12. doi:10.1140/epjp/i2017-11454-4
- Choi, S. U., and Eastman, J. A. (1995). Enhancing thermal conductivity of fluids with nanoparticles. *ASME Fluids Eng. Div.* 231, 99–105.
- Delhi Babu, R., and Ganesh, S. (2020). The mathematical model for steady magnetohydrodynamic flow between parallel porous plates with an angular velocity. *Int. J. Ambient Energy* 41 (11), 1284–1292. doi:10.1080/01430750.2018.1507944
- Eringen, A. C. (1966). Theory of micropolar fluids. *Indiana Univ. Math. J.* 16, 1–18. doi:10.1512/iumj.1967.16.16001
- Fakour, M., Vahabzadeh, A., Ganji, D. D., and Hatami, M. (2015). Analytical study of micropolar fluid flow and heat transfer in a channel with permeable walls. *J. Mol. Liq.* 204, 198–204. doi:10.1016/j.molliq.2015.01.040

- Hassan, A. R. (2020). The entropy generation analysis of a reactive hydromagnetic couple stress fluid flow through a saturated porous channel. *Appl. Math. Comput.* 369, 124843. doi:10.1016/j.amc.2019.124843
- Hatami, M., Hatami, J., and Ganji, D. D. (2014). Computer simulation of MHD blood conveying gold nanoparticles as a third grade non-Newtonian nanofluid in a hollow porous vessel. *Comput. methods programs Biomed.* 113 (2), 632–641. doi:10.1016/j.cmpb.2013.11.001
- Islam, S., Khan, A., Deebani, W., Bonyah, E., Alreshidi, N. A., and Shah, Z. (2020). Influences of Hall current and radiation on MHD micropolar non-Newtonian hybrid nanofluid flow between two surfaces. *AIP Adv.* 10 (5), 055015. doi:10.1063/1.5145298
- Khan, A., Saeed, A., Tassaddiq, A., Gul, T., Kumam, P., Ali, I., et al. (2021). Bio-convective and chemically reactive hybrid nanofluid flow upon a thin stirring needle with viscous dissipation. *Sci. Rep.* 11 (1), 1–17. doi:10.1038/s41598-021-86968-8
- Khan, A., Saeed, A., Tassaddiq, A., Gul, T., Mukhtar, S., Kumam, P., et al. (2021). Bio-convective micropolar nanofluid flow over thin moving needle subject to Arrhenius activation energy, viscous dissipation and binary chemical reaction. *Case Stud. Therm. Eng.* 25, 100989. doi:10.1016/j.csite.2021.100989
- Liao, S. J. (1999). An explicit, totally analytic approximate solution for Blasius' viscous flow problems. *Int. J. Non. Linear. Mech.* 34, 759–778. doi:10.1016/s0020-7462(98)00056-0
- Liao, S. J. (2010). An optimal homotopyanalysis approach for strongly nonlinear differential equations. *Commun. Nonlinear Sci. Numer. Simul.* 15, 2003–2016. doi:10.1016/j.cnsns.2009.09.002
- Misra, J. C., and Ghosh, S. K. (1997). A mathematical model for the study of blood flow through a channel with permeable walls. *Acta Mech.* 122 (1), 137–153. doi:10.1007/bf01181995
- Papadopoulos, P. K., and Tzirtzilakis, E. E. (2004). Biomagnetic flow in a curved square duct under the influence of an applied magnetic field. *Phys. Fluids* 16 (8), 2952–2962. doi:10.1063/1.1764509
- Platt, J. R. (1961). Bioconvection patterns in cultures of free-swimming organisms. *Science* 133 (3466), 1766–1767. doi:10.1126/science.133.3466.1766
- Seyf, H. R., and Rassoulinejad-Mousavi, S. M. (2011). An analytical study for fluid flow in a porous media imbedded inside a channel with moving or stationary walls subjected to injection/suction. *J. Fluids Eng.* 133, 091203. doi:10.1115/1.4004822
- Shah, S. L., Ayub, A., Dehraj, S., Wahab, H. A., Sagayam, K. M., Ali, M. R., et al. (2022). Magnetic dipole aspect of binary chemical reactive Cross nanofluid and heat transport over composite cylindrical panels. *Waves Random Complex Media* 12, 1–24. doi:10.1080/17455030.2021.2020373
- Shah, S. Z. H., Ayub, A., Sabir, Z., Adel, W., Shah, N. A., and Yook, S. J. (2021). Insight into the dynamics of time-dependent cross nanofluid on a melting surface subject to cubic autocatalysis. *Case Stud. Therm. Eng.* 27, 101227. doi:10.1016/j.csite.2021.101227
- Shah, S. Z. H., Fathurrochman, I., Ayub, A., Altamirano, G. C., Rizwan, A., Núñez, R. A. S., et al. (2022). Inclined magnetized and energy transportation aspect of infinite shear rate viscosity model of Carreau nanofluid with multiple features over wedge geometry. *Heat. Trans.* 51 (2), 1622–1648. doi:10.1002/htj.22367
- Shah, Z., Islam, S., Ayaz, H., and Khan, S. (2019). Radiative heat and mass transfer analysis of micropolar nanofluid flow of Casson fluid between two rotating parallel plates with effects of Hall current. *J. Heat Transf.* 141 (2), 022401. doi:10.1115/1.4040415
- Shah, Z., Khan, A., Khan, W., Alam, M. K., Islam, S., Kumam, P., et al. (2020). Micropolar gold blood nanofluid flow and radiative heat transfer between permeable channels. *Comput. methods programs Biomed.* 186, 105197. doi:10.1016/j.cmpb.2019.105197
- Sheikholeslami, M., and Ganji, D. D. (2013). Heat transfer of Cu-water nanofluid flow between parallel plates. *Powder Technol.* 235, 873–879. doi:10.1016/j.powtec.2012.11.030
- Singkidub, P., Sabir, Z., Al Nuwairan, M., Sadat, R., and Ali, M. R. (2022). Cubic autocatalysis-based activation energy and thermophoretic diffusion effects of steady micro-polar nano-fluid. *Microfluid. Nanofluidics* 26 (7), 50–12. doi:10.1007/s10404-022-02554-y
- Srinivas, S., Vijayalakshmi, A., Ramamohan, T. R., and Reddy, A. S. (2014). Hydromagnetic flow of a nanofluid in a porous channel with expanding or contracting walls. *J. Porous Media* 17 (11), 953–967. doi:10.1615/jpormedia.v17.i11.20
- Srinivas, S., Vijayalakshmi, A., and Subramanyam Reddy, A. (2017). Flow and heat transfer of gold-blood nanofluid in a porous channel with moving/stationary walls. *J. Mech.* 33 (3), 395–404. doi:10.1017/jmech.2016.102
- Tzirtzilakis, E. E. (2005). A mathematical model for blood flow in magnetic field. *Phys. fluids* 17 (7), 077103. doi:10.1063/1.1978807
- Zhang, C., Zheng, L., Zhang, X., and Chen, G. (2015). MHD flow and radiation heat transfer of nanofluids in porous media with variable surface heat flux and chemical reaction. *Appl. Math. Model.* 39 (1), 165–181. doi:10.1016/j.apm.2014.05.023
- Zhang, L., Arain, M. B., Bhatti, M. M., Zeeshan, A., and Hal-Sulami, H. (2020). Effects of magnetic Reynolds number on swimming of gyrotactic microorganisms between rotating circular plates filled with nanofluids. *Appl. Math. Mech.* 41 (4), 637–654. doi:10.1007/s10483-020-2599-7



OPEN ACCESS

EDITED BY

Umar Khan,
Hazara University, Pakistan

REVIEWED BY

Sohail Ahmad,
Bahauddin Zakariya University, Pakistan
Fateh Ali,
Xi'an Jiaotong University, China

*CORRESPONDENCE

Kanayo Kenneth Asogwa,
kanasogwa@gmail.com

SPECIALTY SECTION

This article was submitted to Process and Energy Systems Engineering, a section of the journal Frontiers in Energy Research

RECEIVED 30 July 2022

ACCEPTED 15 August 2022

PUBLISHED 06 October 2022

CITATION

Reddy SC, Asogwa KK, Yassen MF, Adnan, Iqbal Z, M-Eldin S, Ali B and KM S (2022), Dynamics of MHD second-grade nanofluid flow with activation energy across a curved stretching surface.
Front. Energy Res. 10:1007159.
doi: 10.3389/fenrg.2022.1007159

COPYRIGHT

© 2022 Reddy, Asogwa, Yassen, Adnan, Iqbal, M-Eldin, Ali and KM. This is an open-access article distributed under the terms of the [Creative Commons Attribution License \(CC BY\)](#). The use, distribution or reproduction in other forums is permitted, provided the original author(s) and the copyright owner(s) are credited and that the original publication in this journal is cited, in accordance with accepted academic practice. No use, distribution or reproduction is permitted which does not comply with these terms.

Dynamics of MHD second-grade nanofluid flow with activation energy across a curved stretching surface

Srinivas C. Reddy¹, Kanayo Kenneth Asogwa^{2*},
Mansour F. Yassen^{3,4}, Adnan⁵, Zahoor Iqbal⁶, Sayed M-Eldin⁷,
Bagh Ali⁸ and Swarnalatha KM¹

¹Department of Mathematics, Govt. City College, Hyderabad, Telangana, India, ²Department of Mathematics, Nigeria Maritime University, Okerenkoko, Delta State, Nigeria, ³Department of Mathematics, College of Science and Humanities in Al-Aflaj, Prince Sattam Bin Abdulaziz University, Al-Aflaj, Saudi Arabia, ⁴Department of Mathematics, Faculty of Science, Damietta University, New Damietta, Damietta, Egypt, ⁵Department of Mathematics, Mohi-ud-Din Islamic University, Nerian Sharif, AJ&K, Pakistan, ⁶Department of Mathematics, Quaid-i-Azam University, Islamabad, Pakistan, ⁷Center of Research, Faculty of Engineering, Future University in Egypt, New Cairo, Egypt, ⁸Faculty of Computer Science and Information Technology, Superior University, Lahore, Pakistan

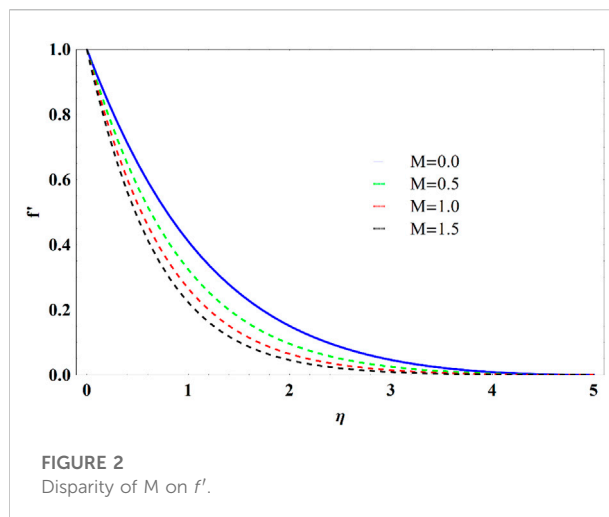
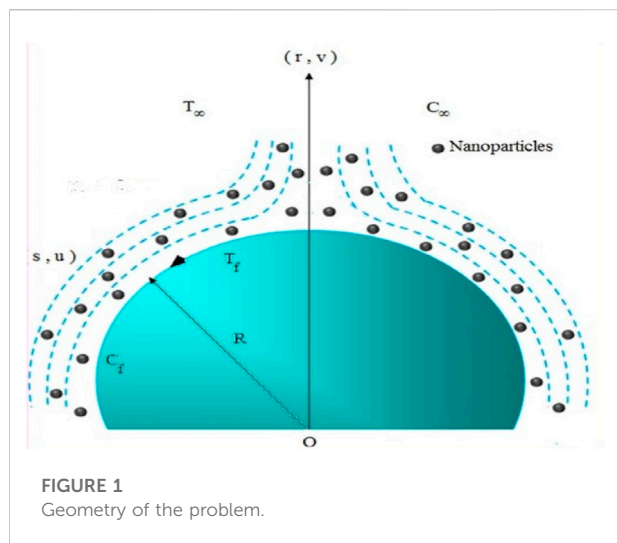
This analysis addresses the influence of activation energy on the MHD flow of second-grade nanofluid over a convectively heated curved stretched surface. The impact of heat generation/absorption, thermophoresis, and Brownian motion are also incorporated. This current study in addendum reveals the solution narrating the nanofluid flow behaviour of the stretched curve to better the performance of the system. Hence, the mathematical construction of governing partial differential equations (PDEs) is transmitted into nonlinear ODEs by employing appropriate transformations. The attained ODEs are conducted numerically via ND-Solve. It is consequential to report that fluid velocity and temperature fields significantly rise with concurrent enhancing values of the fluid parameter and curvature parameter. Moreover, the concentration field enhances considering the energy activation variable and suppresses with the reaction rate constant while thermophoresis escalates the temperature distribution as the Nusselt number lowers with a stronger internal heat source parameter Q .

KEYWORDS

activation energy, heat generation, nanofluid, second-grade, MHD

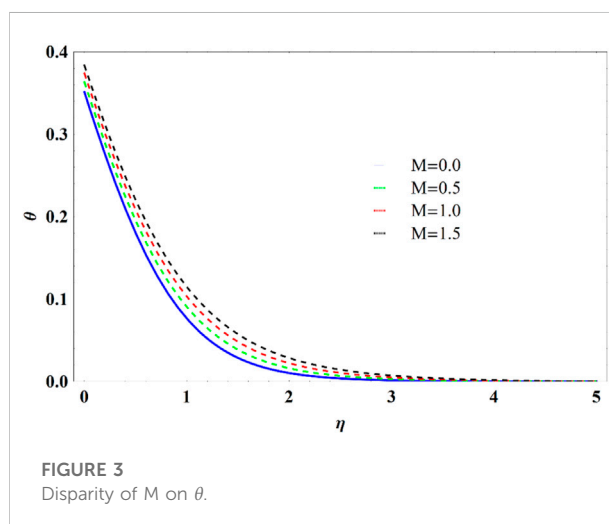
Introduction

In recent advancements, nanofluids have obtained immense attention due to their notable thermal transfer and fascinating applications in numerous fields such as computer processes, hybrid power, fuel cell, and other high-energy devices. The fluids are prepared by suspending nanoparticles in base fluids. The size of nanoparticles ≤ 100 nm. The prime idea of nanofluid was coined by Choi and Eastman (1995). Later, Buongiorno (2006) suggested the two main characteristics, namely, Brownian movement and thermophoretic

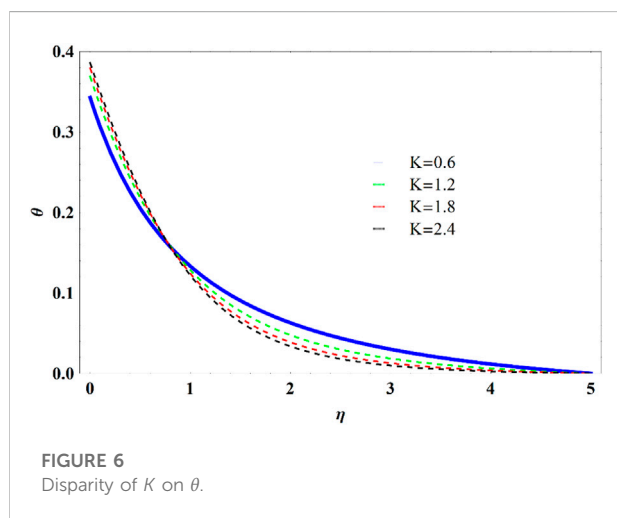
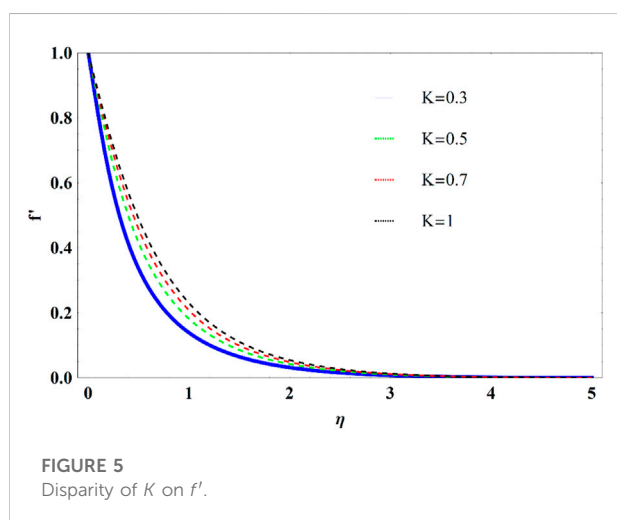
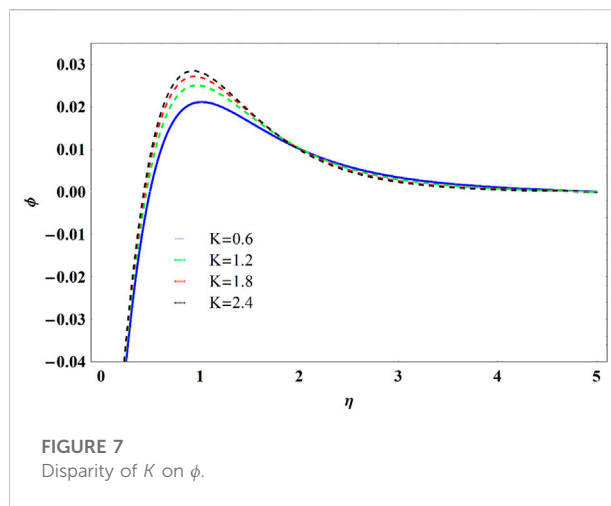
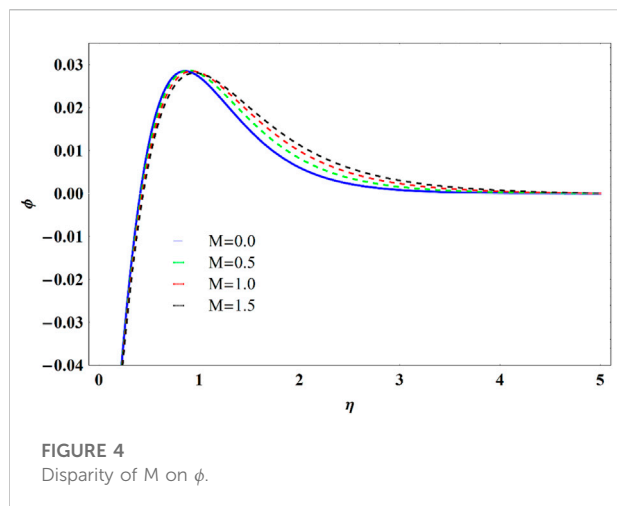


force, to enhance the ability of the ordinary fluid. He found that enhancing the Nusselt number leads to a rise in the nanoparticle volume fraction. Sheikhholeslami et al. (2014) discussed the impact of MHD copper nanofluid flow. The theoretical investigation of Al_2O_3 water nano liquid was examined by Malvandi et al. (2015). They discovered that the enforced heat irregularity alters the path of nanoparticle movement and modifies the patterns of the fields. Mahanthesh et al. (2016) reported the squeezing effect of nanofluids which escalates the thermal layer and leads to a depreciation of the rate of heat transport. Ibáñez et al. (2016) explored the MHD nanoliquid flow in a porous channel with a radiation effect. Eid et al. (2017) considered gold nanoparticles in the flow of Sisko nanofluid and revealed that radiation production boosts thermal transport. The Burgers flow of nanofluid with the effect of Cattaneo–Christov was examined by Hayat et al. (2017a). Also, Hayat et al. (2017b) swotted numerically the flow of nanoliquid over a revolving disk in the presence of the slip effect. Zuhra et al. (2018) considered MHD second-grade nanoliquid comprising gyrotactic microorganisms. They concluded that microorganism density leads to increases with momentum slip. The MHD Carreau nanoliquid over a permeable stretching sheet was considered by Khan and Shehzad (2020). Reddy et al. (2019) analyzed the MHD nanoliquid *via* a stretching sheet. Shah et al. (2021) considered numerical computation of entropy production of nanoliquid due to a porous surface. Khan et al. (2020) thrashed out the consequences of entropy minimization of Casson nanofluid over a rotating cylinder.

The exploration of non-Newtonian fluid has inspired scholars due to its several applications, such as the production of plastic, food processing, and exclusion of tumors. In this current investigation is a subcategory of non-Newtonian fluid termed second-grade fluid. This model takes into consideration the consequences of normal stress in flow conditions, as well as

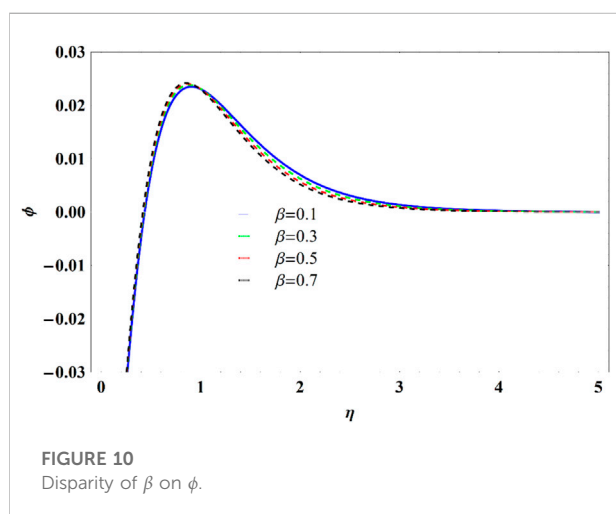
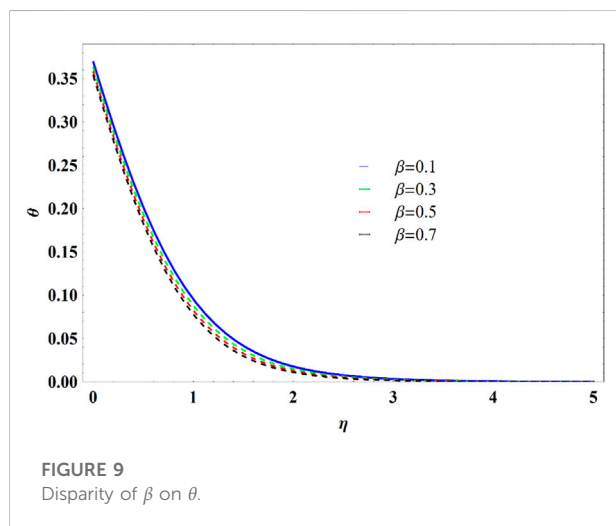
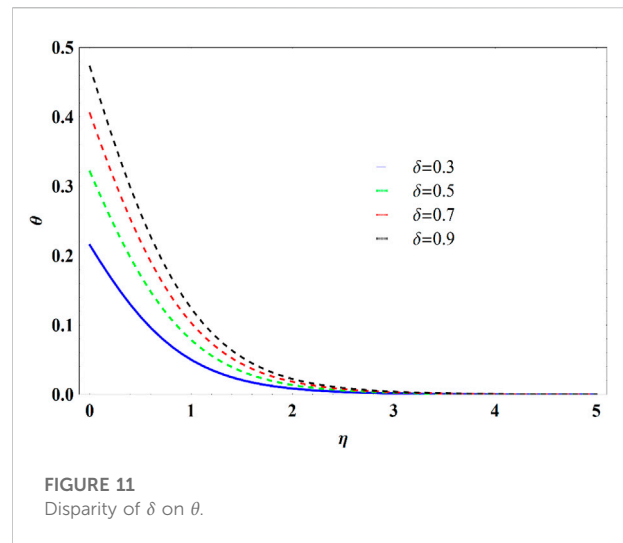
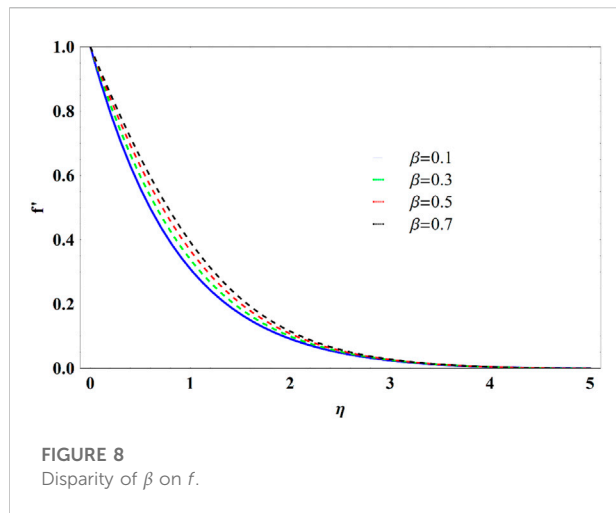


shear thinning and thickening. Tan and Masuoka (2005) described the flow of nanofluid with variable thermal conductivity for the second grade. Rashidi and Majid (2010) analyzed the time-dependent squeezing flow for second-grade fluid. The thermal and species transport analysis of second-grade fluid over a surface with heat flux was deliberated by Das et al. (2016). Jamil et al. (2011) reported the helical flow of second-grade fluid over coaxial cylinders. Turkyilmazoglu (2012) analytically examined the flow of second-grade non-Newtonian fluid with mass transfer over a shrinking sheet. Khan and Pop (2010), Makinde and Aziz (2011), and Hsiao (2010) evaluated the magnetohydrodynamic flow of liquid of second grade with electromagnetic dispersion and non-uniform heat source/sink. Akinbobola and Okoya (2015) swotted second-grade fluid with heat generation. The exact solution of a second-grade fluid *via* coaxial cylinders was reported by Erdogan and Imrak (2008). Nadeem et al. (2012) explored second-grade fluid over a horizontal cylinder.



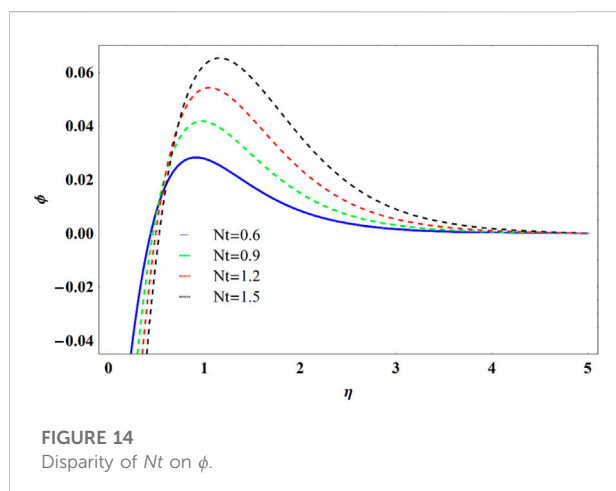
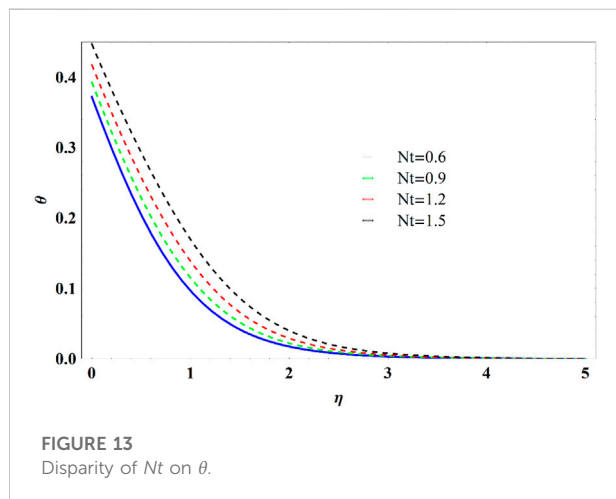
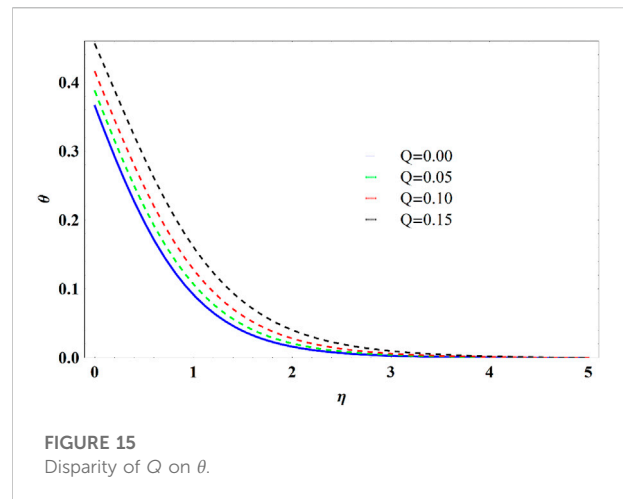
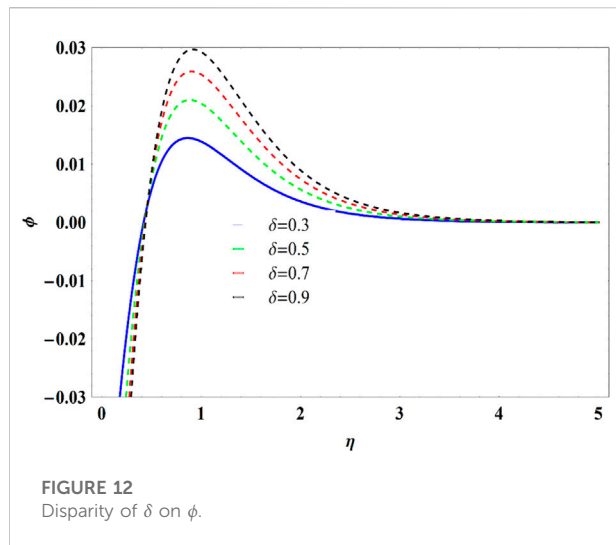
Magnetohydrodynamics (MHD) flow has gained the interest of scholars due to its remarkable applications in the industry and engineering. As contained in the structure of the MHD generator, the cooling system is filled with fluids metal, the deposit of energy, pumps, and flow meters. Theoretically, the magnetic fields can persuade a drag identified as Lorentz force in a moving liquid, which depreciates the fluid velocity. Thus, boosting the fluid temperature and concentration. Numerous researchers have analyzed the impact of magnetic parameters, specifically in the boundary layer problem. The impact of magnetic field flow on permeable surfaces with slip conditions was elaborated by Hayat et al. (2011). Makinde et al. (2013) delineated the influence of MHD on nanoliquid with buoyancy effect. The flow of nanoliquid through two-phase models was visualized by Sheikholeslami et al. (2015). Hayat et al. (2016) addressed the influence of second-grade nanofluid. MHD flows over radially shrinking/stretching disks were reported by Soid et al. (2018). Hayat et al. (2015) considered the 3D flow of MHD nanoliquid. Sharif et al. (2019) elucidated MHD nanoliquid via an exponential sheet. Shah et al. (2020) conducted water base nanoparticles consisting of SWCNT and MWCNT over a vertical cone. Shoaib et al. (2020) evaluated numerically MHD hybrid nanoliquid with thermal radiation. They found that thermal transport rate enhances with growing values of magnetic effect and biot number. Recently, Alamri et al. (2019) discussed the second-grade fluid in the presence of Fourier's heat flux theory.

Activation energy (AE) is the minimal amount of energy needed for a reaction to occur. The activation energy required to transfer energized particles or macromolecules to a location where they would undergo physical transit can be overestimated. The notion of activation energy is commonly useful in thermal engineering. The Bestman (Bestman, 1990) was initially coined with the activation



energy of a binary amalgam phenomenon in a porous space. The unsteady natural convective flow was reported by [Makinde et al. \(2011\)](#) with AE. The influences of activation energy on a magnetic nanofluid were investigated by [Hamid et al. \(2018\)](#). [Mustafa et al. \(2017\)](#) and [Dhlamini et al. \(2022\)](#) elaborated on the behaviour of magneto nanoliquid with activation energy. [Dawar et al. \(2020\)](#) conducted a magnetic field flow of nanoliquid with activation energy. [Hayat et al. \(2022\)](#) addressed the effect of AE on the MHD flow of third-grade nanofluid over convective condition. The 3D flow of Casson nanoliquid for the thermal radiative flow with AE was examined by [Khan et al. \(2019\)](#). [Hayat et al. \(2018\)](#) inspected the 3D flow of Darcy–Forchheimer rotating AE. The 3D time-dependent flow of Carreau nanofluid on chemical reaction and AE was explored by [Irfan et al. \(2019\)](#). Other materials that have added value to this work are in the studies by [Asogwa et al. \(2013\)](#); [Khan et al. \(2017\)](#); [Ali et al. \(2020\)](#); [Bilal et al. \(2021\)](#); [Jayaprakash et al. \(2021\)](#); [Ali et al. \(2022a\)](#); [Adnan et al. \(2022\)](#); [AdnanAshraf, \(2022\)](#); [AdnanAshraf et al. \(2022\)](#); [AdnanMurtaza et al. \(2022\)](#); [Asogwa et al. \(2022\)](#); [Ali et al. \(2022b\)](#); [Goud et al. \(2022\)](#); and [Weera et al. \(2022\)](#).

Considering the overview of the abovementioned work, the prime focus of the current analysis is to scrutinize the impact of Arrhenius activation energy on the MHD flow of second-grade nanofluid toward a curved stretched surface. By employing the transformation procedure, PDEs have been transmuted into ODEs, which are then established numerically by ND-Solve using Mathematica. Our obtained physical parameters are prescribed through tables and graphs.



Modeled equation

The second-grade fluid Cauchy stress tensor is given by [Mabood and Das \(2016\)](#).

$$\tau = -pI + \mu A_1 + \alpha_1 A_2 + \alpha_2 A_1^2$$

Where $\mu, I, A_1, A_2, \alpha_1$, and α_2 are the identity tensor, dynamic viscosity, first and second Rivlin Erickson tensor, and material constant.

$$A_1 = \nabla V + (\nabla V)^T$$

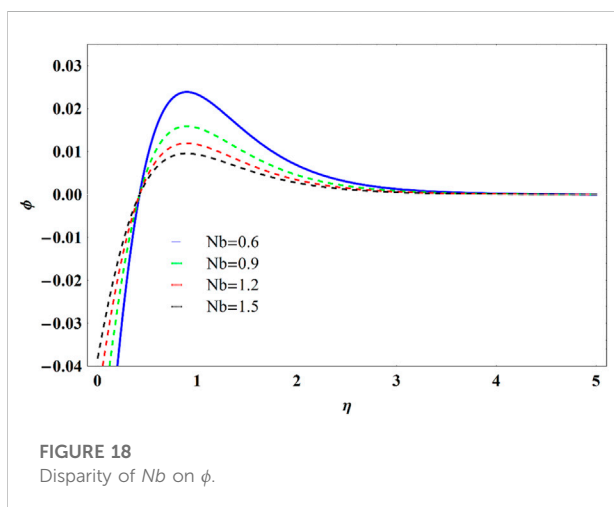
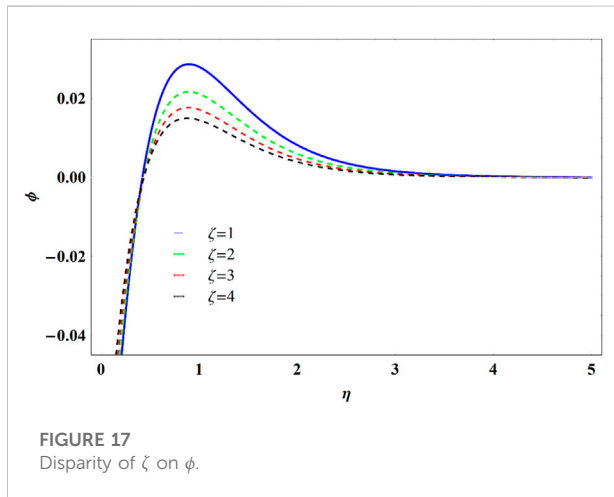
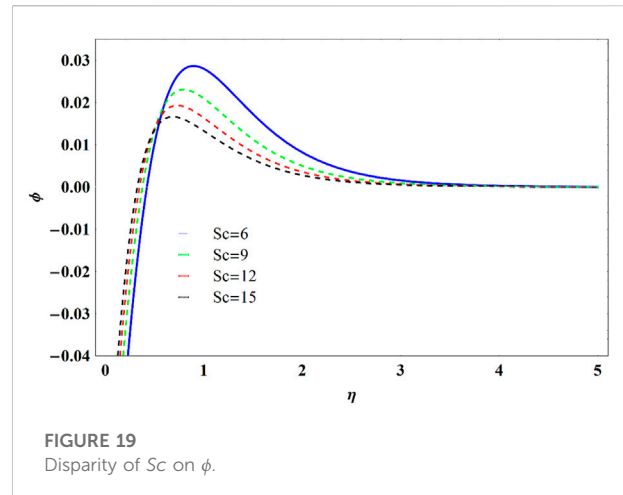
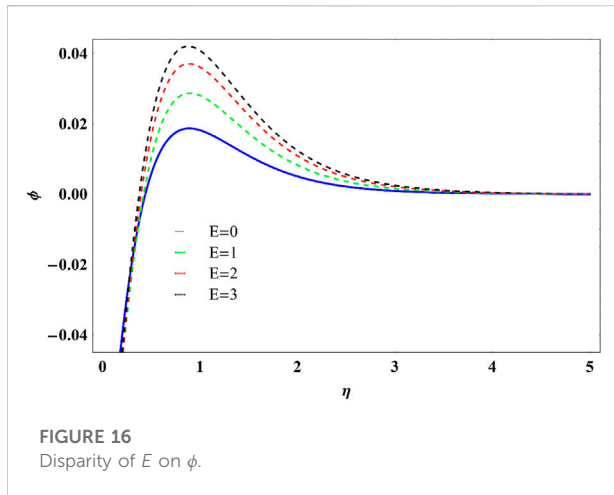
$$A_n = (\nabla V)^T A_1 + A_1 (\nabla V) + \frac{dA_{n-1}}{dt}$$

Mathematical formulation

We consider the 2D flow of MHD second-grade nanoliquid flow due to the curved stretched surface. Featuring AE, chemical reaction (binary), and heat generation. We consider (r, s) to be the curvilinear coordinates (see [Figure 1](#)). The stretched sheet in s path with $U_w = as$ and r is considered orthogonal to s . Then, B_0 is applied along the transverse path of flow from the magnetic field. Assuming that the moderate magnetic field in the form of Re_s generated is ignored, a nanostructured materials framework is utilized for erratic motion and thermophoresis. Under the aforementioned assumptions, equations ([Mabood and Das, 2016](#); [Imtiaz et al., 2019](#)) are written for the boundary layer as follows:

$$(r + R) \frac{\partial v}{\partial r} + v + R \frac{\partial v}{\partial s} = 0 \quad (1)$$

$$\frac{u^2}{r + R} = -\frac{1}{\rho} \frac{\partial p}{\partial r} \quad (2)$$



$$\begin{aligned}
 v \frac{\partial u}{\partial r} + \frac{Ru}{r+R} \frac{\partial u}{\partial s} + \frac{uv}{r+R} = & \\
 -\frac{1}{\rho} \frac{R}{r+R} \frac{\partial p}{\partial s} + v \left(\frac{\partial^2 u}{\partial r^2} + \frac{1}{r+R} \frac{\partial u}{\partial r} - \frac{u}{(r+R)^2} \right) & \\
 + \frac{\alpha_1}{\rho} \left\{ \frac{2R}{r+R} \frac{\partial^2 u}{\partial r^2} \frac{\partial u}{\partial s} - \frac{2R}{(r+R)^2} \frac{\partial u}{\partial r} \frac{\partial u}{\partial s} + \frac{2}{r+R} \frac{\partial v}{\partial r} \frac{\partial u}{\partial r} \right. & \\
 + \frac{2}{r+R} v \frac{\partial^2 u}{\partial r^2} - \frac{2}{(r+R)^2} v \frac{\partial u}{\partial r} - u \frac{4R}{(r+R)^2} \frac{\partial^2 u}{\partial s \partial r} & \\
 \left. - u \frac{4}{(r+R)^2} \frac{\partial v}{\partial r} + u \frac{2R}{(r+R)^3} u \frac{\partial u}{\partial s} \right\} - \frac{\sigma B_0^2 u}{\rho} & \quad (3)
 \end{aligned}$$

$$\begin{aligned}
 v \frac{\partial T}{\partial r} + \frac{Ru}{r+R} \frac{\partial T}{\partial s} = \alpha \left(\frac{\partial^2 T}{\partial r^2} + \frac{1}{r+R} \frac{\partial T}{\partial r} \right) + \tau \left[D_B \frac{\partial C}{\partial r} \frac{\partial T}{\partial r} \right. & \\
 \left. + \frac{D_T}{T_\infty} \left(\frac{\partial T}{\partial r} \right)^2 \right] + \frac{Q_0}{\rho c_p} (T - T_w) & \quad (4)
 \end{aligned}$$

$$\begin{aligned}
 v \frac{\partial C}{\partial r} + \frac{Ru}{r+R} \frac{\partial C}{\partial s} = D_B \left(\frac{\partial^2 C}{\partial r^2} + \frac{1}{r+R} \frac{\partial C}{\partial r} \right) + \frac{D_T}{T_\infty} \left[\frac{\partial^2 T}{\partial r^2} \right. & \\
 \left. + \frac{1}{r+R} \frac{\partial T}{\partial r} \right] - T_r^2 \left(\frac{T}{T_\infty} \right)^n e^{-\frac{E_a}{RT}} (C - C_\infty) & \quad (5)
 \end{aligned}$$

With associated BCs (Mabood and Das, 2016) – (Imtiaz et al., 2019)

$$\left. \begin{aligned} u = U_w = cs, \quad v = 0, \quad \frac{\partial T}{\partial r} = -hf(T_f - T_\infty), \quad D_B \frac{\partial C}{\partial y} + \frac{D_T}{T_\infty} \frac{\partial T}{\partial y} = 0 \text{ at } y = 0 \\ u \rightarrow 0, \quad \frac{\partial u}{\partial r} \rightarrow 0, \quad T \rightarrow T_\infty, \quad C \rightarrow C_\infty \text{ as } y \rightarrow \infty \end{aligned} \right\} \quad (6)$$

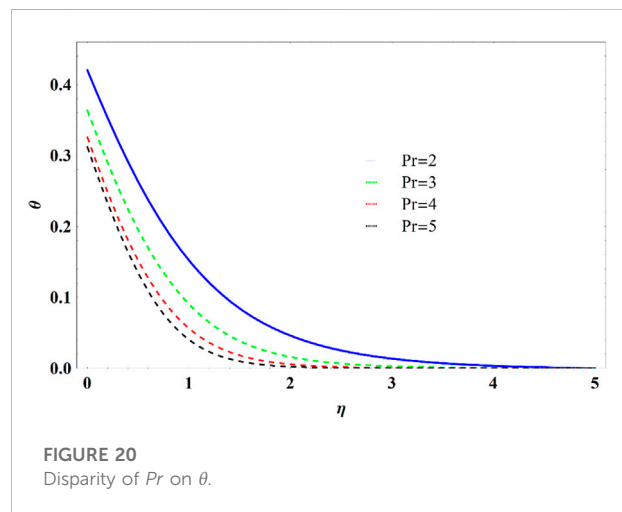
Transformation consideration

TABLE 1 Contrasting outputs of $-f''(0)$ for selected values of M when $K = \infty$ and $\beta = 0$.

| M | Reference (Mabood and Das, 2016) | Reference (Imtiaz et al., 2019) | Present results |
|-----|----------------------------------|---------------------------------|-----------------|
| 1 | 1.4142135 | 1.4142266 | 1.414328374 |
| 5 | 2.4494897 | 2.4495271 | 2.449788955 |
| 10 | 3.31666 | 3.3166679 | 3.316366745 |
| 50 | 7.1414284 | 7.1414769 | 7.143182469 |
| 100 | 10.049875 | 10.049924 | 10.048234644 |

TABLE 2 Friction co-efficient for various values M, K , and β .

| K | M | β | $\frac{1}{2}C_f Re_s^{1/2}$ |
|-----|-----|---------|-----------------------------|
| 1.0 | 1 | 0.2 | 1.81567 |
| 1.5 | | | 1.76525 |
| 2.0 | | | 1.75389 |
| 3 | 0.0 | | 1.28664 |
| | 0.4 | | 1.49317 |
| | 0.8 | | 1.67268 |
| | | 0 | 2.10848 |
| | | 0.1 | 1.91158 |
| | | 0.2 | 1.75485 |

FIGURE 20
Disparity of Pr on θ .

$$\eta = \sqrt{\frac{c}{v}}r, \quad u = csf'(\eta), \quad v = -\frac{R}{r+R}\sqrt{cv}f(\eta), \quad \tau = \frac{(\rho_c)_p}{(\rho_c)_f} \quad (7)$$

$$p = \rho c^2 s^2 P(\eta), \quad \phi(\eta) = \frac{C - C_\infty}{C_w - C_\infty}, \quad \theta(\eta) = \frac{T - T_\infty}{T_w - T_\infty}$$

Eq. 3 is satisfied, and with the help of the abovementioned transformation Eqs 1–5 are reduced

$$\frac{\partial P}{\partial \eta} = \frac{f'^2}{n+K} \quad (8)$$

$$\begin{aligned} \frac{2K}{\eta+K}P &= f''' + \frac{1}{\eta+K}f' - \frac{1}{(\eta+K)^2}f'' + \frac{K}{n+K}ff'' + \frac{K}{(\eta+K)^2}ff' \\ &- \frac{K}{(\eta+K)^3}f'^2 + \beta \left\{ \frac{2K}{\eta+K}ff'' - \frac{2K}{(\eta+K)^2}ff''' - \frac{8K}{(\eta+K)^2}ff'' \right. \\ &+ \frac{4K}{(\eta+K)^3}ff'' + \frac{6K}{(\eta+K)^3}f'^2 - \left. \frac{4K}{(\eta+K)^4}ff' \right\} - Mf' \\ &- \frac{K}{(\eta+K)}f'^2 + \beta \left\{ \frac{2K}{\eta+K}ff'' - \frac{2K}{(\eta+K)^2}ff''' - \frac{8K}{(\eta+K)^2}ff'' \right\} \quad (9) \end{aligned}$$

$$\theta'' + \frac{1}{\eta+K}\theta' + Pr \left(\frac{K}{\eta+K}f\theta' + Nb\theta'\phi' + Nt\theta'^2 \right) + Q\theta = 0 \quad (10)$$

$$\begin{aligned} \phi'' + \frac{1}{\eta+K}\phi' + \frac{K}{\eta+K}Scf\theta' + \frac{Nt}{Nb} \left(\theta'' + \frac{1}{\eta+K}\theta' \right) \\ - Sc\zeta(1 + \delta_1\theta)^m \exp\left(\frac{-E}{1 + \delta_1\theta}\right)\phi \\ = 0 \end{aligned} \quad (11)$$

with transformed BCs

$$\begin{aligned} f'(0) = 1, \quad \theta'(0) = -\delta(1 - \theta(0)), \quad Nb\phi'(0) + Nt\theta'(0) = 0 \quad \text{at } \eta = 0 \\ f' \rightarrow 0, \quad \theta \rightarrow 0, \quad \phi \rightarrow 0 \quad \text{as } \eta \rightarrow \infty. \end{aligned} \quad (12)$$

$$\begin{aligned} \text{We have, } \beta &= \frac{\alpha_1 c}{\eta + K}, \quad \delta = \frac{h_f}{k} \sqrt{\frac{v}{a}}, \quad Nb = \frac{\tau D_B (C_w - C_\infty)}{v}, \\ K &= R \sqrt{\frac{c}{v}}, \quad Nt = \frac{\tau D_T (T_w - T_\infty)}{T_\infty v}, \\ Sc &= \frac{v}{D_B}, \quad E = \frac{E_a}{kT_\infty}, \quad Q = \frac{Q_0}{\rho C_p}, \quad \zeta = \frac{k_c^2}{c}, \quad Pr = \frac{v}{\alpha}, \quad \delta_1 = \frac{T_w - T_\infty}{T_\infty}. \end{aligned}$$

Now, removing the P between Eqs 8 and 9, we get

$$\begin{aligned} f''' + \frac{2}{\eta+K}f'' - \frac{1}{(\eta+K)^2}f'' + \frac{1}{(\eta+K)^3}f' + \frac{K}{\eta+K}(ff''' + f'f'') + \frac{K}{(\eta+K)^2}(ff'' + f'^2) \\ - \frac{K}{(\eta+K)^3}ff' + \beta \left\{ \frac{2K}{\eta+K}ff'' - \frac{2K}{(\eta+K)^2}ff''' - \frac{8K}{(\eta+K)^2}ff'' \right. \\ + \frac{4K}{(\eta+K)^3}ff'' + \frac{6K}{(\eta+K)^3}f'^2 - \left. \frac{4K}{(\eta+K)^4}ff' \right\} - Mf'' - \frac{M}{(\eta+K)}f' \quad (13) \end{aligned}$$

TABLE 3 Local Nusselt number for various values K, δ, Nt, Nb, Sc, E , and Q .

| K | δ | Nt | Nb | Sc | Q | E | $NuRe_s^{-1/2}$ |
|-----|----------|------|------|------|-----|-----|-----------------|
| 1.0 | 0.5 | 0.2 | 0.2 | 5 | 0.1 | 1 | 0.30889 |
| 1.5 | | | | | | | 0.31461 |
| 2 | | | | | | | 0.31716 |
| 3 | 0.6 | | | | | | 0.35622 |
| | 0.7 | | | | | | 0.38809 |
| | 0.8 | | | | | | 0.41584 |
| | | 0.3 | | | | | 0.31559 |
| | | 0.4 | | | | | 0.31162 |
| | | 0.5 | | | | | 0.30729 |
| | | 0.2 | 0.3 | | | | 0.31926 |
| | | | 0.4 | | | | 0.31926 |
| | | | 0.5 | | | | 0.31926 |
| | | | 0.2 | 3 | | | 0.32053 |
| | | | | 6 | | | 0.31881 |
| | | | | 9 | | | 0.31780 |
| | | | | 6 | 0 | | 0.34414 |
| | | | | | 0.1 | | 0.31926 |
| | | | | | 0.2 | | 0.25176 |
| | | | | | | 0.5 | 0.31873 |
| | | | | | | 1.5 | 0.31963 |
| | | | | | | 2.5 | 0.31996 |

Expressions for the local C_{fs} and Nu_s gives

$$C_{fs} = \frac{\mu}{\frac{1}{2}\rho U_w^2} \tau_{rs}, \quad Nu_s = \frac{sq_w}{k(T_w - T_\infty)} \quad (14)$$

$$\tau_{rs} = \mu \left[\frac{\partial u}{\partial r} - \frac{u}{r+R} + \frac{2\alpha_1}{\mu} \left(\frac{R}{r+R} \frac{\partial u}{\partial r} \frac{\partial u}{\partial s} + \frac{\nu}{r+R} \frac{\partial u}{\partial r} - \frac{2Ru}{(r+R)^2} \frac{\partial u}{\partial s} - \frac{2uv}{(r+R)^2} \right) \right]_{r=0} \quad (15)$$

$$q_w = -k \left(\frac{\partial T}{\partial y} \right)_{r=0} \quad (16)$$

Non-dimensional Nusselt number and friction coefficient

$$Re_s^{-1/2} C_{fs} = \left[f''(0) - \frac{f'(0)}{K} + \beta \left(f'(0) f''(0) - \frac{2}{K} f'(0)^2 \right) \right]$$

$$Re_s^{-1/2} Nu_s = -\theta'(0)$$

where $Re_s = \frac{cs^2}{\nu}$

Results and discussion

The key emphasis of this article is highlighted *via* the numerical approach integrated by utilizing the NDSolve technique by using Mathematica. The main emphasis of pertained physical variables on $f'(\eta)$, $\theta(\eta)$, and $\phi(\eta)$ fields, as well as drag fraction and Nusselt number, are elaborated and delineated through Figures 2–20 and Tables 1–3. Table 1 is adorned to check the compatibility of the current analysis by constructing a contrasting $-f''(0)$. An excellent achievement has been found with a previously published result. 8. The reference values in the current study have been taken as $K = 5, \delta = 0.8, Nt = Nb = 0.4, Sc = 5, Q = 0.1, \beta = 0.3, M = 1, E = 1$, and $\zeta = 1$ kept constant throughout the computation, and the variations have been mentioned in the graphs and tables accordingly.

Table 2 is equipped to check the variance in $\frac{1}{2}C_{fs}Re_s^{1/2}$. For empowered fluid parameter β and curvature parameter K , friction factor decreases, whereas the reverse trend is observed with M . Table 3 is elaborated in variance in Nusselt number for selected values of K, δ, Nt, Nb, Sc, Q , and E . It is noticed that $NuRe_s^{-1/2}$ rises with uplifting values of K, δ and E . $NuRe_s^{-1/2}$ declines with rising values of Nt, Sc and Q and there are no significant changes with Nb .

The impact of M on $f'(\eta)$, $\theta(\eta)$, and $\phi(\eta)$ fields is illustrated in Figures 2–4. It is revealed that velocity diminishes with an escalation in M . This notifies that increase in magnetic field obtains the resistive force (Lorentz force) leading to a reduction in the fluid velocity. This also means a reduction in the thickness of the thermal boundary layer. The heat generated causes resistance of the fluid for a greater value of M , which escalates the fluid temperature, and similar behaviour is also seen for the concentration field. Figures 5–7 presents the disparity of curvature parameter K on $f'(\eta)$, $\theta(\eta)$, and $\phi(\eta)$ fields. Figure 5 displays the enhancing values of curvature parameter K on velocity field. Here, velocity escalates with a larger value of K . This is because enhancing values of K lessens the kinematic viscosity of the fluid, which causes a reduction in viscosity and, as a result, the velocity of the fluid gains momentum. Temperature and concentration profiles for various values of K are revealed in Figures 6 and 7. It is seen that temperature and concentration decline for augmenting the value of K .

Figures 8–10 analyze the fluid parameter β on $f'(\eta)$, $\theta(\eta)$, and $\phi(\eta)$ fields. It can be seen from Figure 8 that velocity profile enhances for a larger value of β . Physically, fluid parameter β has a reverse relation with viscosity. In contrast, temperature and concentration profiles (Figures 9 and 10) offer a reducing behaviour with a rising value of β . Figures 11 and 12 presented the effect of Biot number δ on $\theta(\eta)$ and $\phi(\eta)$ fields. Physical involvement of a larger heat transfer coefficient corresponds to enhancement on $\theta(\eta)$ and $\phi(\eta)$ fields. Therefore, $\theta(\eta)$ and $\phi(\eta)$ layer thickness is escalated by increasing Biot number δ .

Figure 13 affirms the increasing activity of temperature profile and thermal boundary layer with Nt . The Nt increase produces a much strong thermophoretic force, causing nanoparticles to move

away from the plate. This results in the growth of the $\theta(\eta)$ Figure 14 symbolizes an upsurge in concentration profile for different values of the thermophoresis variable Nt . Because microscopic particles move from the hot region towards the cold region during the process of thermophoresis. Figure 15 plotted the numerous values of heat source input Q against the temperature profile. Physically, the existence of Q in the boundary layer improves energy and causes a boost in temperature. Figure 16 explicates the enhancing trend of activation energy E on nanoparticle concentration. The activation energy reduces the modified Arrhenius function and causes boosting generative chemical reaction.

Figure 17 presents the dimensionless concentration on the chemical reaction variable ζ . The concentration of nanoparticle is depreciated on the rise of ζ . This behaviour characterizes the decreasing effect of buoyancy force due to concentration gradient, which causes the reduction of concentration profile.

Figure 18 exhibits the variation of the concentration field to diverse values of the Nb . The thickness of the boundary layer and concentration profile decline on increasing Nb input. The reason behind this is that this enriches the pace at which tiny particles drive with various velocities in separate unexpected directions. Figure 19 affirms the declining trend in the concentration field on the escalating values of Sc . This happens because of decaying mass diffusion. Fluctuation for differing values of Prandtl number on temperature is evident in Figure 20. $\theta(\eta)$ minifies with upshot values of Pr because larger Pr results in lesser thermal diffusivity, thereby bringing about a decrease in temperature.

Conclusion

In this analysis of MHD second-grade nanoliquid over a curved stretched sheet with activation energy is explored. The observations are concluded as follows:

- Increment exists in the momentum and thermal boundary layer thickness when the fluid parameter enhances.
- Velocity distributions show decreasing phenomenon with enhancement in M .
- Both velocity and temperature have increasing behaviour for higher K .

References

- Adnan, A., Khan, I., Shemseldin, A., and Mousa, A. (2022). Numerical energy storage efficiency of MWCNTs-propylene glycol by inducing thermal radiations and combined convection effects in the constitutive model. *Front. Chem.* 10, 879276. doi:10.3389/fchem.2022.879276
- Adnan and Ashraf, W. (2022). Thermal efficiency in hybrid (Al_2O_3 -CuO/ H_2O) and ternary hybrid nanofluids (Al_2O_3 -CuO-Cu/ H_2O) by considering the novel effects of imposed magnetic field and convective heat condition. *Waves in Random and Complex Media*, 1–16. doi:10.1080/17455030.2022.2092233
- Adnan Ashraf, W., Khan, I., and Andualem, M. (2022). Thermal transport investigation and shear drag at solid-liquid interface of modified permeable

- Convective heating condition enhances the thermal field significantly.
- Brownian movement Nb depreciate for concentration profile.
- Concentration is diminished for higher value of Sc .
- Increment in fluid parameter β decreases the friction factor.
- Thermophoresis reduces the volume fraction field and enhances the temperature field.
- The temperature profile increases due to temperature heat source Q . An opposite trend is noted in the heat transfer rate.

Data availability statement

The original contributions presented in the study are included in the article/Supplementary Material, further inquiries can be directed to the corresponding author.

Author contributions

All authors listed have made a substantial, direct, and intellectual contribution to the work and approved it for publication.

Conflict of interest

The authors declare that the research was conducted in the absence of any commercial or financial relationships that could be construed as a potential conflict of interest.

Publisher's note

All claims expressed in this article are solely those of the authors and do not necessarily represent those of their affiliated organizations, or those of the publisher, the editors, and the reviewers. Any product that may be evaluated in this article, or claim that may be made by its manufacturer, is not guaranteed or endorsed by the publisher.

radiative-SRID subject to Darcy-Forchheimer fluid flow composed by γ -nanomaterial. *Sci. Rep.* 12, 3564. doi:10.1038/s41598-022-07045-2

Adnan Murtaza, R., Hussain, I., Rehman, Z., Khan, I., and Andualem, M. (2022). Thermal enhancement in Falkner-Skan flow of the nanofluid by considering molecular diameter and freezing temperature. *Sci. Rep.* 12, 9415. doi:10.1038/s41598-022-13423-7

Akinbobola, T. E., and Okoya, S. S. (2015). The flow of second grade fluid over a stretching sheet with variable thermal conductivity and viscosity in the presence of heat source/sink. *J. Niger. Math. Soc.* 34, 331–342. doi:10.1016/j.jnms.2015.10.002

- Alamri, S. Z., Khan, A. A., Azeez, M., and Ellahi, R. (2019). Effects of mass transfer on MHD second grade fluid towards stretching cylinder: A novel perspective of cattaneo-christov heat flux model. *Phys. Lett. A* 383, 276–281. doi:10.1016/j.physleta.2018.10.035
- Ali, F., Hou, Y., Zahid, M., Rana, M., and Usman, M. (2022). Influence of magnetohydrodynamics and heat transfer on the reverse roll coating of a Jeffrey fluid: A theoretical study. *J. Plastic Film Sheeting* 38 (1), 72–104. doi:10.1177/87560879211029693
- Ali, F., Zahid, M., Hou, Y., Manafian, M. A., Rana, M. A., and Hajar, A. (2022). A theoretical study of reverse roll coating for a non-isothermal third-grade fluid under lubrication approximation theory. *Math. Problems Eng.* 2022, 1–18. Article ID 5029132. doi:10.1155/2022/5029132
- Ali, F., Hou, Y., Zahid, M., and Rana, M. A. (2020). Theoretical study of the reverse roll coating of non-isothermal magnetohydrodynamics viscoplastic fluid. *Coatings* 10 (10), 940. MDPI AG. Retrieved from. doi:10.3390/coatings10100940
- Asogwa, K. K., Alsulami, M. D., Prasannakumara, B. C., and Muhammad, T. (2022). Double diffusive convection and cross diffusion effects on Casson fluid over a Lorentz force driven Riga plate in a porous medium with heat sink: An analytical approach. *Int. Commun. Heat Mass Transf.* 131, 105761. doi:10.1016/j.icheatmasstransfer.2021.105761
- Asogwa, K. K., Uwanta, I. J., Momoh, A. A., Omokhuale, E., and Omokhuale, E. (2013). Heat and mass transfer over a vertical plate with periodic Suction and heat sink. *Rjaset* 5 (1), 07–15. doi:10.19026/rjaset.5.077
- Bestman (1990). Natural convection boundary layer with suction and mass transfer in a porous medium. *A. R. Int. J. Energy Res.* 14, 389–396. doi:10.1002/er.4440140403
- Bilal, S., Asogwa, K. K., Alotaibi, H., Malik, M. Y., and Khan, I. (2021). Analytical treatment of radiative Casson fluid over an isothermal inclined Riga surface with aspects of chemically reactive species. *Alexandria Eng. J.* 60 (5), 4243–4253. doi:10.1016/j.aej.2021.03.015
- Buongiorno, J. (2006). Convective transport in nanofluid. *J. Heat. Trans.* 128, 240–250.
- Choi, S. U., and Eastman, J. A. (1995). *ASME international mechanical engineering congress & exposition*. San Francisco: American Society of Mechanical Engineers (ASME). Enhancing thermal conductivity of fluids with nanoparticles
- Das, K., Sharma, R. P., and Sarkar, A. (2016). Heat and mass transfer of a second grade magnetohydrodynamic fluid over a convectively heated stretching sheet. *J. Comput. Des. Eng.* 3, 330–336. doi:10.1016/j.jcde.2016.06.001
- Dawar, A., Shah, Z., and Islam, S. (2020). Mathematical modeling and study of MHD flow of Williamson nanofluid over a nonlinear stretching plate with activation energy. *Heat. Trans.* 50, 2558–2570. doi:10.1002/hjt.21992
- Dhramini, M., Mondal, H., Sibanda, P., and Motsa, S. (2022). Activation energy and entropy generation in viscous nanofluid with higher order chemically reacting species. *Int. J. Ambient Energy* 43, 1495–1507. doi:10.1080/01430750.2019.1710564
- Eid, M. R., Alsaedi, A., Muhammad, T., and Hayat, T. (2017). Comprehensive analysis of heat transfer of gold-blood nanofluid (Sisko-model) with thermal radiation. *Results Phys.* 7, 4388–4393. doi:10.1016/j.rinp.2017.11.004
- Erdogan, M. E., and Imrak, C. E. (2008). Steady flow of a second-grade fluid two coaxial porous cylinders. *Mathe. Prob. Engg.* doi:10.1155/2007/4265
- Goud, B. S., Reddy, Y. D., and Asogwa, K. K. (2022). Inspection of chemical reaction and viscous dissipation on MHD convection flow over an infinite vertical plate entrenched in porous medium with Soret effect. *Biomass Conv. bioref.* doi:10.1007/s13399-022-02886-3
- Hamid, A., Hashim, K. M., and Khan, M. (2018). Impacts of binary chemical reaction with activation energy on unsteady flow of magneto-Williamson nanofluid. *J. Mol. Liq.* 262, 435–442. doi:10.1016/j.molliq.2018.04.095
- Hayat, T., Aziz, A., Muhammad, A., and Alsaedi, A. (2017). On model for flow of Burgers nanofluid with Cattaneo-Christov double diffusion. *Chin. J. Phys.* 55, 916–929. doi:10.1016/j.cjph.2017.02.017
- Hayat, T., Aziz, A., Muhammad, T., and Ahmad, B. (20150145332). Influence of magnetic field in three-dimensional flow of couple stress nanofluid over a nonlinearly stretching surface with convective condition. *Plos One* 10, e0145332. doi:10.1371/journal.pone.0145332
- Hayat, T., Aziz, A., Muhammad, T., and Ahmad, B. (2016). On magnetohydrodynamic flow of second grade nanofluid over a nonlinear stretching sheet. *J. Magnetism Magnetic Mater.* 408, 99–106. doi:10.1016/j.jmmm.2016.02.017
- Hayat, T., Aziz, A., Muhammad, T., and Alsaedi, A. (2018). Effects of binary chemical reaction and Arrhenius activation energy in Darcy-Forchheimer three-dimensional flow of nanofluid subject to rotating frame. *J. Therm. Anal. Calorim.* 136, 1769–1779. doi:10.1007/s10973-018-7822-6
- Hayat, T., Muhammad, T., Shehzad, S. A., and Alsaedi, A. (2017). On magnetohydrodynamic flow of nanofluid due to a rotating disk with slip effect: A numerical study. *Comput. Methods Appl. Mech. Eng.* 315, 467–477. doi:10.1016/j.cma.2016.11.002
- Hayat, T., Qasim, M., and Mesloub, S. (2011). MHD flow and heat transfer over permeable stretching sheet with slip conditions. *Int. J. Numer. Meth. Fluids* 66, 963–975. doi:10.1002/fld.2294
- Hayat, T., Riaz, R., Aziz, A., and Alsaedi, A. (2020). Influence of Arrhenius activation energy in MHD flow of third grade nanofluid over a nonlinear stretching surface with convective heat and mass conditions. *Phys. A Stat. Mech. its Appl.* 549, 124006. doi:10.1016/j.physa.2019.124006
- Hsiao, K. (2010). Viscoelastic fluid over a stretching sheet with electromagnetic effects and nonuniform heat source/sink. *Math. Problems Eng.* 2010, 1–14. Article ID 740943. doi:10.1155/2010/740943
- Ibáñez, G., López, A., Pantoja, J., and Moreira, J. (2016). Entropy generation analysis of a nanofluid flow in MHD porous microchannel with hydrodynamic slip and thermal radiation. *Int. J. Heat Mass Transf.* 100, 89–97. doi:10.1016/j.jheatmasstransfer.2016.04.089
- Imtiaz, M., Mabood, F., Hayat, T., and Alsaedi, A. (2019). Homogeneous-heterogeneous reactions in MHD radiative flow of second grade fluid due to a curved stretching surface. *Int. J. Heat Mass Transf.* 145, 118781. doi:10.1016/j.jheatmasstransfer.2019.118781
- Irfan, M., Khan, W. A., Khan, M., and Gulzar, M. M. (2019). Influence of Arrhenius activation energy in chemically reactive radiative flow of 3D Carreau nanofluid with nonlinear mixed convection. *J. Phys. Chem. Solids* 125, 141–152. doi:10.1016/j.jpcs.2018.10.016
- Jamil, M., Rauf, A., Fetecau, C., and Khan, N. A. (2011). Helical flows of second grade fluid due to constantly accelerated shear stresses. *Commun. Nonlinear Sci. Numer. Simul.* 16, 1959–1969. doi:10.1016/j.cnsns.2010.09.003
- Jayaprakash, M. C., Asogwa, K. K., Lalitha, K. R., Veeranna, Y., and Sreenivasa, G. T. (2021). Passive control of nanoparticles in stagnation point flow of Oldroyd-B Nanofluid with aspect of magnetic dipole. *Proc. Institution Mech. Eng. Part E J. Process Mech. Eng.* 095440892110655. doi:10.1177/09544089211065550
- Khan, A., Shah, Z., Alzahrani, E., and Islam, S. (2020). Entropy generation and thermal analysis for rotary motion of hydromagnetic Casson nanofluid past a rotating cylinder with Joule heating effect. *Int. Commun. Heat Mass Transf.* 119, 104979. doi:10.1016/j.icheatmasstransfer.2020.104979
- Khan, S. U., and Shehzad, S. A. (2020). Electrical MHD Carreau nanofluid over porous oscillatory stretching surface with variable thermal conductivity: Application of thermal extrusion system. *Phys. A Stat. Mech. Its Appl.* 550, 124–132.
- Khan, U., Abbasi, A., Ahmed, N., and Mohyud-Din, S. T. (2017). Particle shape, thermal radiations, viscous dissipation and joule heating effects on flow of magneto-nanofluid in a rotating system. *Ec* 34 (8), 2479–2498. doi:10.1108/EC-04-2017-0149
- Khan, W. A., and Pop, I. (2010). Boundary-layer flow of a nanofluid past a stretching sheet. *Int. J. Heat Mass Transf.* 53, 2477–2483. doi:10.1016/j.jheatmasstransfer.2010.01.032
- Khan, W. A., Sultan, F., Ali, M., Shahzad, M., KhanIrfan, M. M., and Irfan, M. (2019). Consequences of activation energy and binary chemical reaction for 3D flow of Cross-nanofluid with radiative heat transfer. *J. Braz. Soc. Mech. Sci. Eng.* 41, 4. doi:10.1007/s40430-018-1482-0
- Mabood, F., and Das, K. (2016). Melting heat transfer on hydromagnetic flow of a nanofluid over a stretching sheet with radiation and second-order slip. *Eur. Phys. J. Plus* 131, 3–42. doi:10.1140/epjp/i2016-16003-1
- Mahanthesh, B., Gireesha, B. J., and Gorla, R. S. R. (2016). Mixed convection squeezing three-dimensional flow in a rotating channel filled with nanofluid. *Int. J. Numer. Methods Heat. Fluid Flow.* 26, 1460–1485. doi:10.1108/hff-03-2015-0087
- Makinde, O. D., and Aziz, A. (2011). Boundary layer flow of a nanofluid past a stretching sheet with a convective boundary condition. *Int. J. Therm. Sci.* 50, 1326–1332. doi:10.1016/j.ijthermalsci.2011.02.019
- Makinde, O. D., Khan, W. A., and Khan, Z. H. (2013). Buoyancy effects on MHD stagnation point flow and heat transfer of a nanofluid past a convectively heated stretching/shrinking sheet. *Int. J. Heat Mass Transf.* 62, 526–533. doi:10.1016/j.jheatmasstransfer.2013.03.049
- Makinde, O. D., Olanrewaju, P. O., and Charles, W. M. (2011). Unsteady convection with chemical reaction and radiative heat transfer past a flat porous plate moving through a binary mixture. *Afr. Mat.* 22, 65–78. doi:10.1007/s13370-011-0008-z
- Malvandi, A., Safaei, M. R., Kaffash, M. H., and Ganji, D. D. (2015). MHD mixed convection in a vertical annulus filled with Al₂O₃-water nanofluid considering nanoparticle migration. *J. Magnetism Magnetic Mater.* 382, 296–306. doi:10.1016/j.jmmm.2015.01.060

- Mustafa, M., Hayat, T., Alsaedi, T., and Alsaedi, A. (2017). Buoyancy effects on the MHD nanofluid flow past a vertical surface with chemical reaction and activation energy. *Int. J. Heat Mass Transf.* 108, 1340–1346. doi:10.1016/j.ijheatmasstransfer.2017.01.029
- Nadeem, S., Rehman, A., Lee, C., and Lee, J. (2012). Boundary layer flow of second grade fluid in a cylinder with heat transfer. *Math. Problems Eng.* 2012, 1–13. Article ID 640289. doi:10.1155/2012/640289
- Rashidi, M. M., and Majid, S. A. (2010). Application of Homotopy Analysis method to the unsteady squeezing flow of second grade fluid between circular plate. *Math. Prob* 18, 706840.
- Reddy, N. V. B., Kishan, N., and Reddy, C. S. (2019). Melting heat transfer and MHD boundary layer flow of eyring-powell nanofluid over a nonlinear stretching sheet with slip. *Int. J. Appl. Mech. Eng.* 24, 161–178. doi:10.2478/ijame-2019-0011
- Shah, Z., Alzahrani, E., Jawad, M., and Khan, U. (2020). Microstructure and inertial characteristics of MHD suspended SWCNTs and MWCNTs based maxwell nanofluid flow with bio-convection and entropy generation past a permeable vertical cone. *Coatings* 10, 998. doi:10.3390/coatings10100998
- Shah, Z., Sheikholeslami, M., Ikramullah, K. P., and Kumam, P. (2021). Simulation of entropy optimization and thermal behavior of nanofluid through the porous media. *Int. Commun. Heat Mass Transf.* 120, 105039. doi:10.1016/j.icheatmasstransfer.2020.105039
- Sharif, R., Farooq, M. A., and Mushtaq, A. (2019). Magnetohydrodynamic study of variable fluid properties and their impact on nanofluid over an exponentially stretching sheet. *J. Nanofluids* 8, 1249–1259. doi:10.1166/jon.2019.1671
- Sheikholeslami, M., Domiri Ganji, D. D., Younus Javed, M. Y., and Ellahi, R. (2015). Effect of thermal radiation on magnetohydrodynamics nanofluid flow and heat transfer by means of two phase model. *J. Magnetism Magnetic Mater.* 374, 36–43. doi:10.1016/j.jmmm.2014.08.021
- Sheikholeslami, M., Gorji Bandpy, M. G., Ellahi, R., Hassan, M., and Soleimani, S. (2014). Effects of MHD on Cu-water nanofluid flow and heat transfer by means of CVFEM. *J. Magnetism Magnetic Mater.* 349, 188–200. doi:10.1016/j.jmmm.2013.08.040
- Shoaib, M., Raja, M. A. Z., Sabir, M. T., Islam, S., Shah, Z., Kumam, P., et al. (2020). Numerical investigation for rotating flow of MHD hybrid nanofluid with thermal radiation over a stretching sheet. *Sci. Rep.* 10, 18533. doi:10.1038/s41598-020-75254-8
- Soid, S. K., Ishak, A., and Pop, I. (2018). MHD flow and heat transfer over a radially stretching/shrinking disk. *Chin. J. Phys.* 56, 58–66. doi:10.1016/j.cjph.2017.11.022
- Tan, W., and Masuoka, T. (2005). Stokes' first problem for a second grade fluid in a porous half-space with heated boundary. *Int. J. Non-Linear Mech.* 40, 515–522. doi:10.1016/j.ijnonlinmec.2004.07.016
- Turkyilmazoglu, M. (2012). Dual and triple solutions for MHD slip flow of non-Newtonian fluid over a shrinking surface. *Comput. Fluids* 70, 53–58. doi:10.1016/j.compfluid.2012.01.009
- Weera, W., Maneengam, A., Saeed, A. M., Aissa, A., Guedri, K., Younis, O., et al. (2022). Effects of branched fins on alumina and N-octadecane melting performance inside energy storage system. *Front. Phys.* 10, 957025. doi:10.3389/fphy.2022.957025
- Zuhra, S., Khan, N. S., and Islam, S. (2018). Magnetohydrodynamic second-grade nanofluid flow containing nanoparticles and gyrotactic microorganisms. *Comp. Appl. Math.* 37, 6332–6358. doi:10.1007/s40314-018-0683-6

Glossary

α_1 fluid parameter

α thermal diffusivity

s & r

curvilinear co-ordinates

p pressure

Sc Schmidt number

σ electrical conductivity

ν kinematic viscosity

T fluid temperature

D_B Brownian diffusion coefficient

R radius

Q heat generation/absorption

T_∞ ambient temperature

C concentration of the fluid

B_0 magnetic field strength

D_T thermophoretic diffusion coefficient

u and v velocity components

T_w surface temperature

C_∞ ambient fluid concentration

k_r^2 reaction rate

ρ fluid density

k Boltzmann constant

E_a coefficient of activation energy

τ nanoparticle heat capacity against base fluid heat capacity

Pr Prandtl number

β fluid parameter

BCs boundary conditions

K curvature parameter

δ Biot number

Nb Brownian motion

C_w surface concentration

T fluid temperaturefluid temperature

Re_s local Reynolds number

Nt thermophoresis

E energy parameter

ζ reaction rate parameter

δ_1 temperature difference parameter

t_{rs} shear stress

q_w heat flux



OPEN ACCESS

EDITED BY

Adnan,
Mohi-ud-Din Islamic University,
Pakistan

REVIEWED BY

Saqib Murtaza,
King Mongkut's University of
Technology Thonburi, Thailand
Muhammad Bilal,
City University of Science and
Information Technology, Pakistan
Muhammad Mubashir Bhatti,
Shandong University of Science and
Technology, China

*CORRESPONDENCE

M. Riaz Khan,
mrkhan.math@gmail.com
Aatif Ali,
atifkh98@gmail.com

SPECIALTY SECTION

This article was submitted to Process
and Energy Systems Engineering,
a section of the journal
Frontiers in Energy Research

RECEIVED 28 June 2022

ACCEPTED 09 August 2022

PUBLISHED 06 October 2022

CITATION

Khan MR, Ahammad NA, Alhazmi SE,
Ali A, Abdelmohimen MAH,
Allogmany R, Tag-Eldin E and Yassen MF
(2022), Energy and mass transport
through hybrid nanofluid flow passing
over an extended cylinder with the
magnetic dipole using a
computational approach.
Front. Energy Res. 10:980042.
doi: 10.3389/fenrg.2022.980042

COPYRIGHT

© 2022 Khan, Ahammad, Alhazmi, Ali,
Abdelmohimen, Allogmany, Tag-Eldin
and Yassen. This is an open-access
article distributed under the terms of the
[Creative Commons Attribution License
\(CC BY\)](https://creativecommons.org/licenses/by/4.0/). The use, distribution or
reproduction in other forums is
permitted, provided the original
author(s) and the copyright owner(s) are
credited and that the original
publication in this journal is cited, in
accordance with accepted academic
practice. No use, distribution or
reproduction is permitted which does
not comply with these terms.

Energy and mass transport through hybrid nanofluid flow passing over an extended cylinder with the magnetic dipole using a computational approach

M. Riaz Khan^{1*}, N. Ameer Ahammad², Sharifah E. Alhazmi³,
Aatif Ali^{4*}, Mostafa A. H. Abdelmohimen^{5,6}, Reem Allogmany⁷,
Elsayed Tag-Eldin⁸ and Mansour F. Yassen^{9,10}

¹Department of Mathematics, Quaid-i-Azam University, Islamabad, Pakistan, ²Department of Mathematics, Faculty of Science, University of Tabuk, Tabuk, Saudi Arabia, ³Mathematics Department, Al-Qunfudah University College, Umm Al-Qura University, Mecca, Saudi Arabia, ⁴Department of Mathematics, Abdul Wali Khan University Mardan, Mardan, Pakistan, ⁵Mechanical Engineering Department, College of Engineering, King Khalid University, Abha, Saudi Arabia, ⁶Shoubra Faculty of Engineering, Benha University, Cairo, Egypt, ⁷Department of Mathematics, Faculty of Science, Taibah University, Al-Madinah Al-Munawarah, Saudi Arabia, ⁸Faculty of Engineering and Technology, Future University in Egypt, New Cairo, Egypt, ⁹Department of Mathematics, College of Science and Humanities in Al-Aflaj, Prince Sattam Bin Abdulaziz University, Al-Kharj, Saudi Arabia, ¹⁰Department of Mathematics, Faculty of Science, Damietta University, Damietta, Egypt

The objective of this research is to evaluate the heat and mass transfer in a water-based Darcy–Forchheimer hybrid nanofluid (HNF) flow across an expanding cylinder. The fluid flow has been studied under the influence of a magnetic field, viscous dissipation, heat source, thermal radiation, concentration stratification, and chemical reaction. Carbon nanotubes (CNTs) and iron ferrite (Fe₃O₄) nanoparticles (NPs) are added to the water, for the purpose of synthesizing the HNF. The fluid flow has been induced in the presence of gyrotactic microorganisms and the non-Fick's model. Microorganisms are used to stabilize scattered nanoparticles through the hybrid nanofluid. The phenomena have been modeled in the form of a nonlinear system of partial differential equations (PDEs). The modeled equations are reduced to a dimensionless system of ODEs by using similarity substitution. The numerical solution of the derived sets of nonlinear differential equations is obtained by using the parametric continuation method. The impact of physical constraints on temperature, velocity, concentration, and microorganism profiles is presented through figures and tables. It has been observed that the heat and mass transport rates increase with the rising effect of the curvature parameter, while declining with the effect of the thermal stratification parameter.

KEYWORDS

hybrid nanofluid, iron oxide, magnetic dipole, CNTs, PCM, gyrotactic microorganism, extended cylinder

Introduction

The study of boundary layer flow through a cylinder gained the attention of researchers due to its broad array of applications in numerous sectors, including manufacture and extraction of glass fiber, bridges and funnel stacks in civil engineering, paper production, melt-spinning rubber sheets, blood transportation in heart-lung machine, risers and channels, polymer production, carriage of noxious fluids at nuclear power plants, carriage of destructive fluids when fluid contact with machinery and equipment is restricted, and many others (Ma et al., 2020; Dou, 2022; Hussain et al., 2022). For about the last 2 decades, various investigators chose to conduct their research in the cylindrical channel because of the aforementioned applicability. The mathematical analysis of power-law nanofluid flow across a circular surface is documented by Ullah et al. (2021a) who concluded that the natural frequency has a momentous effect on the fluid's properties. Zhang et al. (2021) numerically assessed the HNF flow across a circular cylinder. It was observed that the rotating cylinders containing a splitting sheet, may be effective options for energy transfer. Numerical simulations and tests to lower the drag of a cylinder for both smooth and round cylinders with dimpled surfaces are investigated by Ullah et al. (2021b). The results show that within a particular range of Reynolds numbers, the dimpled structure can efficiently reduce cylinder drag, with a maximum drag reduction rate of up to 19%. Using the modified Fourier heat flux law, Varun Kumar et al. (2021) scrutinized the upshot of hybrid NPs on the dusty flow behavior through an enlarging cylinder. Their observations show that increasing particle mass concentration reduces the velocity and temperature gradient, whereas increasing the curvature factor increases the thermal gradient and velocity within the boundary. Poply (2021) evaluated the influence of MHD flux over an extending cylinder with a heat source. Their research aided in controlling the frequency of energy transmission and flow stream in a variety of industrial applications and manufacturing processes to achieve the desired end production efficiency. The influence of MHD Newtonian nanofluid flow across a stretchable cylinder was inspected by Waqas et al. (2021). The fallouts reveal that the velocity is increased by increasing the buoyancy constraint and declines by increasing the magnetic parameter. Chu et al. (2022b) analyzed the Maxwell MHD NF flow over a prolonged cylinder using nonlinear heat emission. An incompressible and 2D flow of viscoelastic NF over an extended cylinder was considered by Al-Mubaddel et al. (2022). Dey et al. (2021) investigated boundary layer viscous fluid flow via a stretchable cylinder with varying heat flux and molecular diffusion. They observed that due to the stretching of the cylinder, dual solutions are discovered, and an unusual increase in heat near the cylinder's surface. Energy consumption has grown exponentially over the world, demanding more efficient energy use because the demand

exceeds the supply. Within a thermal system, a significant quantity of temperature is generated, needing efficient and rapid heat transfer employing high-performance thermal management systems. Some new efforts have been documented by many academics on fluid flow across different configurations (Chu et al., 2021; Zhao et al., 2021; Benhacine et al., 2022; Kumar and Sahu, 2022; Lim et al., 2022).

Many modern technological applications that previously required ordinary fluids (water, engine oil, ethylene glycol, and propylene glycol) have been replaced with nanofluids, which are the composition of the base fluid with nano-sized particles (Alsallami et al., 2022; Bhatti et al., 2022a; Rafiei et al., 2022). Nanofluids have garnered a huge interest in research and development in the last decade, especially in the fields of heat assignment improvement techniques and renewable and sustainable energy systems. Solar collectors, hydrodynamics, hydropower rotors, thermodynamics, ocean power plants, wind turbines, and geothermal heat exchangers are just a few of the applications for nanofluids (Ma et al., 2021). A new mechanism of thermal expansion within nanofluids has recently been introduced. The process involves mixing two or more different nanoparticles in the primary fluid. These nanofluids are referred to as hybrid nanofluids, and they have a higher heat transfer efficiency due to their improved thermo-physical properties. Propagation of the HNF flow and heat and mass transport play essential roles in biotechnology, crude oils, nuclear sectors, paper manufacturing, suspended and colloidal solutions, polyethylene solution, geophysics, unusual lubricants, and chemical plants, which are only some of the uses in the industry (Kumar et al., 2022). The fluid flow of a blood-based HNF with variable viscosity and CNTs via a stretching sheet was discovered by Chu et al. (2022a). The inclusion of CNTs proved to be more successful, according to their findings. Shruthy and Mahanthesh (2019) discussed the thermal Bénard convection analytically in HNF and Casson fluid. It has been discovered in their finding that using a hybrid nanofluid to postpone convection can improve the rate of heat allocation. A two-dimensional time-dependent radiative Casson fluid flow across a porous stretched superficial is examined by Zhou et al. (2021). They discovered that as the Casson component and magnetic field rise, the friction drags increase, whereas the Nusselt number drops with increasing Eckert number. Syam Sundar et al. (2015) measured the heat exchange ratio and friction coefficient for CNT- Fe_3O_4 /water HNF flow through a cylinder under constant heat flux. Soran et al. Lung et al. (2021) evaluated the efficacy of carboxylic-synthesized CNTs modified with Fe and Mn metal to remove two pesticides from an aqueous medium. Their findings demonstrate that the CNT-COOH/ MnO_2 / Fe_3O_4 NPs are a viable adsorbent for the removal of pesticides from wastewater. The NPs' shape characterization and the heat transfer characteristics of an

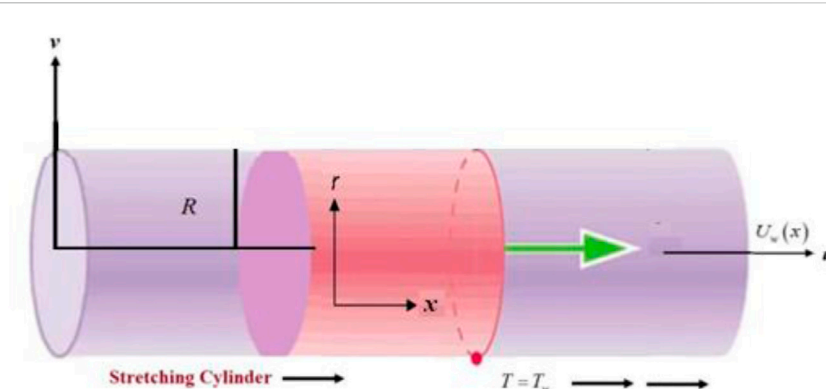


FIGURE 1

Fluid flow over a stretching cylinder.

Au-Fe₃O₄-blood HNF flowing across a stretching surface over a magnetohydrodynamic medium were presented by Ullah et al. (2019). The thermal conductivity of blade-shaped Au and Fe₃O₄ nanoparticles is found to be superior to platelet, needle, cylinder, brick, and sphere shapes. To create blood-based HNF, Mohamed et al. (2021) quantitatively studied CoFe₂O₄ and Fe₃O₄ ferroparticles embedded in Casson fluid, which resembles human blood. According to their findings, when magnetic effects were present, the CNT-based Casson NF flow offered 46% more heat than blood-based NF. Many scholars have recently studied hybrid nanofluid flow comprised of CNTs and iron oxide nanoparticles (Alharbi et al., 2022; Bhatti et al., 2022b; Elattar et al., 2022; Khashi'i'e et al., 2022; Nazeer et al., 2022; Ullah et al., 2022).

Bioconvection has a huge involvement in manufacturing and medicine (Areekara et al., 2021; Khan et al., 2021). Elayarani et al. (2021) described the adaptive neuro-fuzzy inferential simulations for the unsteady 2D bio-convective flow of Carreau NF containing gyrotactic microbes over an elongating sheet with magnetism and multiple slip conditions. Hosseinzadeh et al. (2020) explored cross-fluid flow on a horizontal and 3D cylinder with gyrotactic microbes and NPs while accounting for viscous dissipation and magnetic field. Muhammad et al. (2021) evaluated the flow of magnetized viscoelastic Carreau NF carrying microbes through a sliding wedge with slip effects and thermal radiation parameters. Waqas et al. Muhammad et al. (2022) considered the features of the Jeffrey nanofluid flow over a sheet and the effects of activation energy and motile microorganisms. It was observed that the bioconvection Rayleigh number and resistance ratio parameter play an essential role in the Jeffrey nanofluid's falling flow. Ahmad et al. (2022) investigated the novel properties of hybrid nanofluids such as NiZnFe₂O₄ and MnZnFe₂O₄. Recently, gyrotactic microorganism fluid flow

and the comprising nanoparticles have been reported by Alhowaity et al. (2022b), Ashraf et al. (2022), and Habib et al. (2022).

The current research focuses on the amazing evaluation of CNTs and iron oxide-based HNF flow with magnetic dipole and triple stratification over an extending cylinder. Viscous dissipation, heat radiation, generalized Fick's law, and partial slip are also taken into account. The proposed study is significant because it examines the chemically reactive CNTs + Fe₃O₄/water Casson hybrid nanofluid with magnetic dipole and stratification effects created by an elongating cylinder. To the best of our experience, no previous research has looked into these impacts. The MATLAB function PCM and bvp4c have been used to estimate the numerical simulation of the current analysis. Graphs depict the effects of various parameters, while tables show the statistical valuation of skin friction, Nusselt number, and microorganisms.

Mathematical formulation

Over an extending cylinder, we addressed a 2D laminar and radiative Casson HNF flow in the presence of slip and microbe effects. The CNTs and iron oxide are described as NPs in the Casson fluid. The magnetic effect B_0 is executed in the r -direction. The temperature, concentration, and microorganism are symbolized as T_w , C_w , and N_w , respectively. Under the aforementioned description, the leading equations are expressed as (Ahmad et al., 2021)

$$\frac{\partial(ru)}{\partial x} + \frac{\partial(rv)}{\partial r} = 0, \quad (1)$$

$$\begin{aligned} \nu \frac{\partial u}{\partial x} + \nu \frac{\partial u}{\partial r} = \frac{\mu_{hnf}}{\rho_{hnf}} \left(1 + \frac{1}{\beta} \right) \left(\frac{\partial^2 u}{\partial r^2} + \frac{1}{r} \frac{\partial u}{\partial r} \right) + \frac{\mu_0}{\rho_{hnf}} M \frac{\partial H}{\partial x} - \nu_{hnf} \frac{u}{k^*} \\ - \frac{C_b}{\sqrt{k^*}} u^2, \end{aligned} \quad (2)$$

$$u \frac{\partial T}{\partial x} + v \frac{\partial T}{\partial r} = \alpha_{hmf} \left(\frac{\partial^2 T}{\partial r^2} + \frac{1}{r} \frac{\partial T}{\partial r} \right) - \mu_0 T \frac{\partial M}{\partial T} \left(u \frac{\partial H}{\partial x} + v \frac{\partial H}{\partial r} \right) + \frac{1}{(\rho C_p)_{hmf}} \left\{ \mu_{hmf} \left(1 + \frac{1}{\beta} \right) \left(\frac{\partial u}{\partial y} \right)^2 + \frac{16\sigma^* T_\infty^3}{3k^*} \left(\frac{\partial^2 T}{\partial r^2} + \frac{1}{r} \frac{\partial T}{\partial r} \right) \right\}, \quad (3)$$

$$u \frac{\partial C}{\partial x} + v \frac{\partial C}{\partial r} = (D_B)_{hmf} \left(\frac{\partial^2 C}{\partial r^2} + \frac{1}{r} \frac{\partial C}{\partial r} \right) - k(C - C_\infty) - \lambda_c \left(v \frac{\partial v}{\partial r} \frac{\partial C}{\partial r} + v \frac{\partial u}{\partial r} \frac{\partial C}{\partial x} + u \frac{\partial v}{\partial r} \frac{\partial C}{\partial x} + u \frac{\partial u}{\partial r} \frac{\partial C}{\partial r} + 2uv \frac{\partial^2 C}{\partial x \partial r} + u^2 \frac{\partial^2 C}{\partial x^2} + v^2 \frac{\partial^2 C}{\partial r^2} \right), \quad (4)$$

$$u \frac{\partial N}{\partial x} + v \frac{\partial N}{\partial r} + \frac{bW_c}{C_w - C_0} \frac{\partial}{\partial r} \left(N \frac{\partial C}{\partial r} \right) = (D_m)_{hmf} \left(\frac{\partial^2 N}{\partial r^2} + \frac{1}{r} \frac{\partial N}{\partial r} \right). \quad (5)$$

Here, (u, v) determine the velocity factors in the x and r direction, respectively, while μ_{hmf} is the dynamic viscosity, α_{hmf} is the thermal diffusivity, $(D_B)_{hmf}$ is the mass diffusivity, ρ_{hmf} is the density, $(D_m)_{hmf}$ is the microorganism diffusivity, λ_c is the concentration relaxation time, and w_1 is the slip factor. Additionally, $\mu_0 T \partial M / \partial T$ denotes the ferromagnetic force.

The boundary conditions are expressed as (Ahmad et al., 2021)

$$u = U_w + \nu_{hmf} w_1 \left(1 + \frac{1}{\beta} \right) \frac{\partial u}{\partial r}, v = 0, C = C_0 + \frac{bx}{l},$$

$$\begin{aligned} T &= T_0 + \frac{bx}{l}, N_0 + \frac{bx}{l} = N \text{ at } r = R, u \rightarrow 0, C \rightarrow C_\infty \\ &= C_0 + \frac{ex}{l}, T \rightarrow T_\infty = T_0 + \frac{cx}{l}, N_0 + \frac{a_1 x}{l} \\ &= N \rightarrow N_\infty \text{ when } r \rightarrow \infty. \end{aligned} \quad (6)$$

In the aforementioned equation, l specifies the magnetic strength. ν_{hmf} shows the kinematic viscosity of the hybrid nanofluid, while a, b, c, d , and a_1 are the constant number.

The magnetic dipole is specified as

$$\Omega = \frac{x l}{2\pi(x^2 + (r+c)^2)}, \quad (7)$$

$$\frac{\partial H}{\partial x} = -\frac{\partial \Omega}{\partial x} = \frac{x^2 - (r+c)^2}{2\pi(x^2 + (r+c)^2)}, \quad (8a)$$

$$\frac{\partial H}{\partial r} = -\frac{\partial \Omega}{\partial r} = \frac{2x(r+c)}{2\pi(x^2 + (r+c)^2)^2}. \quad (8b)$$

The absolute magnetic field is

$$H = \sqrt{\left(\frac{\partial H}{\partial x} \right)^2 + \left(\frac{\partial H}{\partial r} \right)^2}, \quad (9a)$$

where,

$$\frac{\partial H}{\partial x} = \frac{2x}{2\pi(r+c)^4}, \quad (9b)$$

and

$$\frac{\partial H}{\partial r} = \frac{1}{2\pi} \left(\frac{-2}{(r+c)^3} + \frac{4x}{(r+c)^5} \right). \quad (10)$$

The magnetic field became more intense, and a linear link between magnetic and temperature variation was formed as follows :

$$M = K^* (T - T_\infty). \quad (11)$$

Similarity transformation

The similarity variables are (Ahmad et al., 2021)

$$u = U_w f'(\eta), v = -\frac{R}{r} \sqrt{\frac{\nu_f U_0}{l}} f(\eta), \theta(\eta) = \frac{T - T_\infty}{T_w - T_0},$$

$$g(\eta) = \frac{C - C_\infty}{C_w - C_0}, h(\eta) = \frac{N - N_\infty}{N_w - N_0}, \quad \eta = \frac{r^2 - R^2}{2R} \sqrt{\frac{U_w}{\nu_f l}}. \quad (12)$$

By applying the aforementioned similarity transformation, Eq. 1 is identically satisfied while Eqs 2–5 take the form as

$$\begin{aligned} &\left(\frac{1 + \frac{1}{\beta}}{A_1 A_2} \right) \left((1 + 2\alpha\eta) f''' + 2\alpha f'' \right) + f f'' - Fr(f')^2 \\ &- \frac{2M\theta}{(\eta + \gamma_1)^4 A_2} \\ &= 0, \end{aligned} \quad (13)$$

$$\begin{aligned} &\left(\frac{k_{hmf}}{k_f} + \frac{4}{3} Rd \right) \left((1 + 2\alpha\eta) \theta'' + 2\theta' \alpha \right) + Pr \left(f \theta' - S_1 f' - 2f' \theta \right) \\ &+ Ec \left(1 + \frac{1}{\beta} \right) f''^2 - \frac{2\lambda M (\theta - \epsilon) f}{(\gamma_1 + \eta)^3} - 2\lambda f'^2 \\ &= 0, \end{aligned} \quad (14)$$

$$\frac{A_1}{Sc} \left((1 + 2\alpha\eta) g'' + 2\alpha g' \right) + f g' - 2Cr g f' - S_2 f' - \gamma_c (f^2 g'' + f f' g') = 0, \quad (15)$$

$$\begin{aligned} &A_1 \left((1 + 2\alpha\eta) h h'' + 2\alpha h' \right) + L_b (f h' - S_3 f' - 2f' h) - Pe (g' h' + (h + \delta) \\ &((1 + 2\alpha\eta) g'' + 2\alpha g')) = 0. \end{aligned} \quad (16)$$

The reduced boundary conditions are

$$f(0) = 0, f'(0) = 1 + \left(1 + \frac{1}{\beta} \right) \frac{s}{A_1} f''(0), \theta(0) = 1 - S_1,$$

$$\begin{aligned} &g(0) = 1 - S_2, h(0) \\ &= 1 - S_3, f'(\infty) \rightarrow 0, \theta(\infty) \rightarrow 0, h(\infty) \rightarrow 0, g(\infty) \rightarrow 0. \end{aligned} \quad (17)$$

Here, S_3 is the microorganism stratification, α is the curvature term, δ the bio-convection constant, β is the Casson fluid constraints, S_1 is the thermal stratification, M is the ferromagnetic term, S_2 is the concentration stratification, Ec is the Eckert number, s is the velocity slip, Rd is the radiation constant, Pe is the Peclet number, ϵ is the free stream parameter, Lb is the Lewis number, Pr is the Prandtl number, Sc is the Schmidt number, γ_c is the concentration relaxation constraints, Cr is the chemical reaction term, and λ is the viscous dissipation parameter.

These physical terms are expressed as (Ahmad et al., 2021)

$$s = w_1 \left(\frac{U_0 \nu_f}{l} \right), Lb = \frac{\gamma_f}{D_m}, Pr = \frac{\gamma_f}{\alpha_f}, S_1 = \frac{c}{b}, Pe = \frac{bW_c}{D_m},$$

$$S_2 = \frac{e}{d} S_c = \frac{v_f}{D_b}, \alpha = \sqrt{\frac{l v_f}{U_0}}, S_3 = \frac{a_1}{a}, M = \frac{\rho_f \gamma_1 \mu_0 K^* (T_0 - T_w)}{2\pi \mu_f}, Ec = \frac{U_0^2}{c_p (T_w - T_\infty)}, \gamma_1 = \sqrt{\frac{\rho_f U_0 b^2}{\mu_f}}, \delta = \frac{N_\infty}{N_w - N_\infty}, \lambda = \frac{\mu_f^2 U_2}{\rho_f k (T_0 - T_w)} \quad (18)$$

The physical interest quantities derived from the present study are

$$Nn_x = \frac{xq_n}{D_m(n_w - n_\infty)}, Sh_x = \frac{xq_m}{D_B(C_w - C_\infty)}, Nu_x = \frac{xq_w}{k_f(T_w - T_\infty)}, C_f = \frac{2\tau_w}{\rho_f u_w^2} \quad (19)$$

The non-dimensional forms of the physical quantities are

$$Nn_x Re_x^{\frac{1}{2}} = -h'(0), Sh_x Re_x^{\frac{1}{2}} = -g'(0), Nu_x Re_x^{\frac{1}{2}} = -\frac{k_{mf}}{k_f} \theta'(0), C_f Re_x^{\frac{1}{2}} = -\frac{1}{A_1} \left(1 + \frac{1}{\beta}\right) f''(0). \quad (20)$$

Numerical solution

Many researchers have used different numerical, computational, and numerical procedures to solve nonlinear systems of PDEs (Jin et al., 2022; Rashid et al., 2022a; Rashid et al., 2022b; Wang et al., 2022; Zhao et al., 2022). Here, the problem is handled through the PCM methodology, which is operated as follows (Berezowski, 2010; Shuaib et al., 2020; Jin et al., 2022; Rashid et al., 2022a; Rashid et al., 2022b; Sun et al., 2022; Wang et al., 2022; Zhao et al., 2022):

Step 1: Reducing Eqs 13–16 to first order

$$\zeta_1 = f(\eta), \zeta_2 = f'(\eta), \zeta_3 = f''(\eta), \zeta_4 = \theta(\eta), \zeta_5 = \theta'(\eta), \zeta_6 = g(\eta), \zeta_7 = g'(\eta), \zeta_8 = h(\eta), \zeta_9 = h'(\eta). \quad (21)$$

By putting Eqs 21 in Eqs 13–17, we get

$$\left(\frac{1 + \frac{1}{\beta}}{A_1 A_2}\right) (1 + 2\alpha\eta) \zeta_3 + \left(2\alpha \left(\frac{1 + \frac{1}{\beta}}{A_1 A_2}\right) + \zeta_1\right) \zeta_3 - Fr(\zeta_2)^2 - \frac{2M\zeta_4}{(\eta + \gamma_1)^4 A_2} = 0, \quad (22)$$

$$\left(\frac{k_{mf}}{k_f} + \frac{4}{3} Rd\right) (1 + 2\alpha\eta) \zeta_5 + \left(2\alpha \left(\frac{k_{mf}}{k_f} + \frac{4}{3} Rd\right) + Pr\zeta_1\right) \zeta_5 + Pr \left(\frac{-2\zeta_2 \zeta_4 - S_1 \zeta_2}{+Ec \left(1 + \frac{1}{\beta}\right) \zeta_3^2} - \frac{2\lambda M(\zeta_4 - \epsilon) \zeta_1}{(\gamma_1 + \eta)^3} - 2\lambda \zeta_2^2\right) = 0, \quad (23)$$

$$\left(\frac{A_1}{S_c} (1 + 2\alpha\eta) - \gamma_c \zeta_1^2\right) \zeta_7 + \left(\frac{A_1}{S_c} 2\alpha + f - \gamma_c \zeta_1 \zeta_2\right) \zeta_7 - 2Cr\zeta_6 \zeta_2 - S_2 \zeta_2 = 0, \quad (24)$$

$$A_1 (1 + 2\alpha\eta) \zeta_9 + (A_1 2\alpha + L_b \zeta_1 - P_e \zeta_7) \zeta_9 - L_b (2\zeta_2 \zeta_8 - S_3 \zeta_2) - P_e \left((\zeta_8 + \delta) \left(\frac{1 + 2\alpha\eta}{\zeta_7 + 2\alpha \zeta_7}\right)\right) = 0, \quad (25)$$

with the corresponding boundary conditions.

$$\zeta_1(0) = 0, \zeta_2(0) = 1 + \left(1 + \frac{1}{\beta}\right) \frac{s}{A_1} \zeta_3(0), \zeta_4(0) = 1 - S_1,$$

$$\begin{aligned} \zeta_6(0) &= 1 - S_2, \zeta_8(0) = 1 \\ &= 1 \\ -S_3, \zeta_2(\infty) &\rightarrow 0, \zeta_4(\infty) \rightarrow 0, \zeta_6(\infty) \rightarrow 0, \zeta_8(\infty) \rightarrow 0. \end{aligned} \quad (26)$$

Step 2: Familiarizing parameter p in Eqs 22–26:

$$\begin{aligned} &\left(\frac{1 + \frac{1}{\beta}}{A_1 A_2}\right) (1 + 2\alpha\eta) \zeta_3 + \left(2\alpha \left(\frac{1 + \frac{1}{\beta}}{A_1 A_2}\right) + \zeta_1\right) ((\zeta_3 - 1)p \\ &+ 1) - Fr(\zeta_2)^2 - \frac{2M\zeta_4}{(\eta + \gamma_1)^4 A_2} = 0, \end{aligned} \quad (27)$$

$$\begin{aligned} &\left(\frac{k_{mf}}{k_f} + \frac{4}{3} Rd\right) (1 + 2\alpha\eta) \zeta_5 + \left(2\alpha \left(\frac{k_{mf}}{k_f} + \frac{4}{3} Rd\right) + Pr\zeta_1\right) \\ &((\zeta_5 - 1)p + 1) + Pr \left(\frac{-2\zeta_2 \zeta_4 - S_1 \zeta_2}{+Ec \left(1 + \frac{1}{\beta}\right) \zeta_3^2} - \frac{2\lambda M(\zeta_4 - \epsilon) \zeta_1}{(\gamma_1 + \eta)^3} - 2\lambda \zeta_2^2\right) = 0, \end{aligned} \quad (28)$$

$$\begin{aligned} &\left(\frac{A_1}{S_c} (1 + 2\alpha\eta) - \gamma_c \zeta_1^2\right) \zeta_7 + \left(\frac{A_1}{S_c} 2\alpha + f - \gamma_c \zeta_1 \zeta_2\right) ((\zeta_7 - 1)p + 1) \\ &- 2Cr\zeta_6 \zeta_2 - S_2 \zeta_2 = 0, \end{aligned} \quad (29)$$

$$\begin{aligned} &A_1 (1 + 2\alpha\eta) \zeta_9 + (A_1 2\alpha + L_b \zeta_1 - P_e \zeta_7) ((\zeta_9 - 1)p + 1) \\ &- L_b (2\zeta_2 \zeta_8 - S_3 \zeta_2) - P_e ((\zeta_8 + \delta) ((1 + 2\alpha\eta) \zeta_7 + 2\alpha \zeta_7)) = 0. \end{aligned} \quad (30)$$

Step 3: Applying the Cauchy Principal and discretizing Eqs 27–30.

After discretization, the obtained set of equations is computed through Matlab code of PCM.

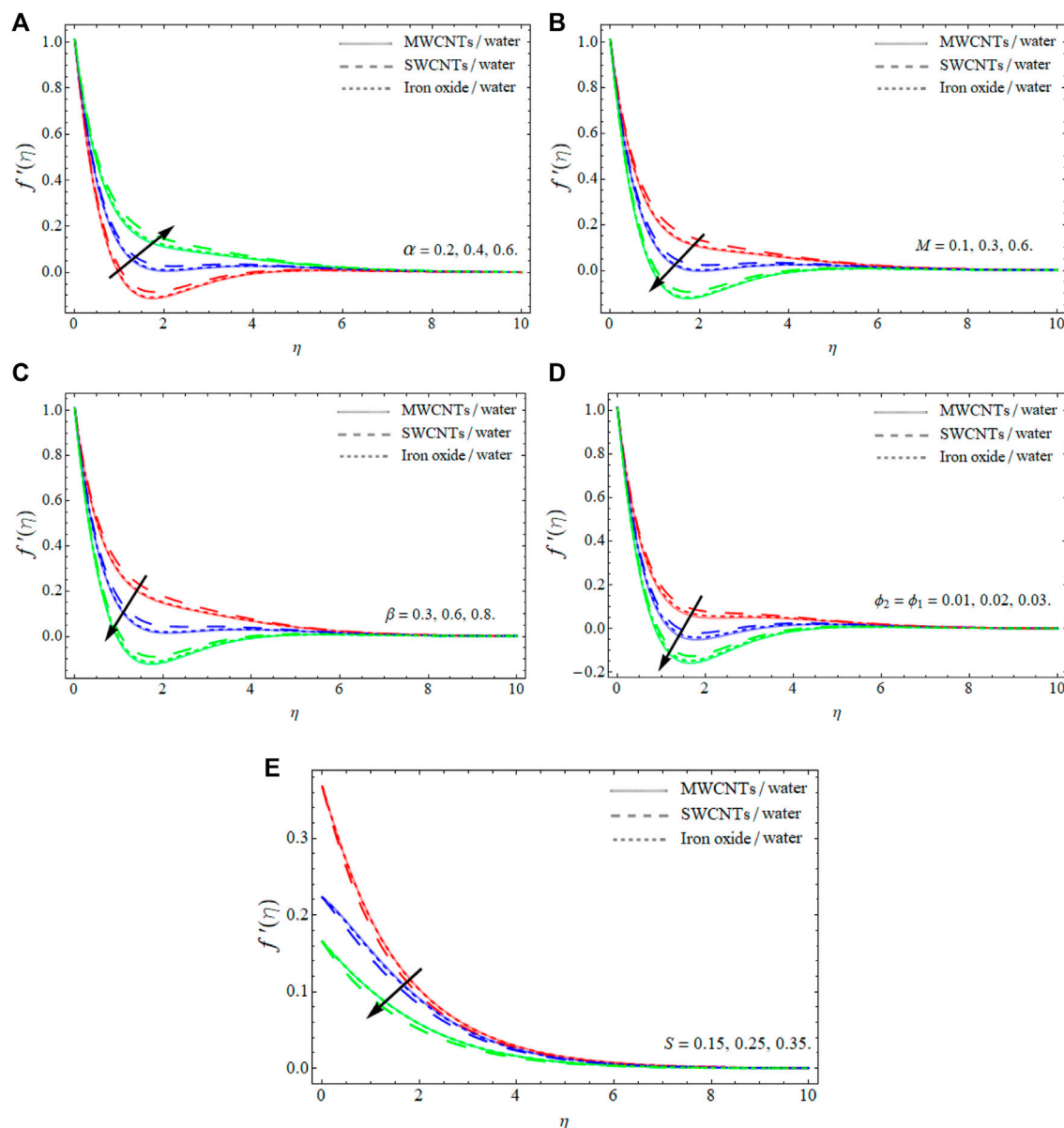


FIGURE 2

Effects of curvature parameter α , ferromagnetic parameter M , fluid parameter β , volume fraction ϕ_1 , and slip parameter S on velocity profile $f'(\eta)$.

Results and discussion

For hybrid NF consisting of CNTs and magnetic ferrite NPs, the discussion section examines the comportment of velocity, energy, and motile microbe profile against the change of numerous physical restrictions. The comparative Figures 2–5 and Tables 2–4 exhibit their outcomes.

Figure 1 illustrates the physical mechanism of fluid flow over a stretching cylinder. Figures 2A–E exemplify the variations in the velocity profile for the curvature parameter α , ferromagnetic

parameter M , fluid parameter β , volume fraction ϕ_1 , and slip parameter S , respectively. The results indicate that the velocity field shows a reducing trend for the enhanced values of the curvature constraint. It is observed in the result that as the curvature factor is increased, the radius of the cylinder shrinks which produces minimal resistance to fluid flow, and therefore, the fluid velocity increases. The decreasing behavior of the velocity profile for the variation of ferromagnetic parameter M can be seen in Figure 2B. The reason for this decline is that when the ferromagnetic

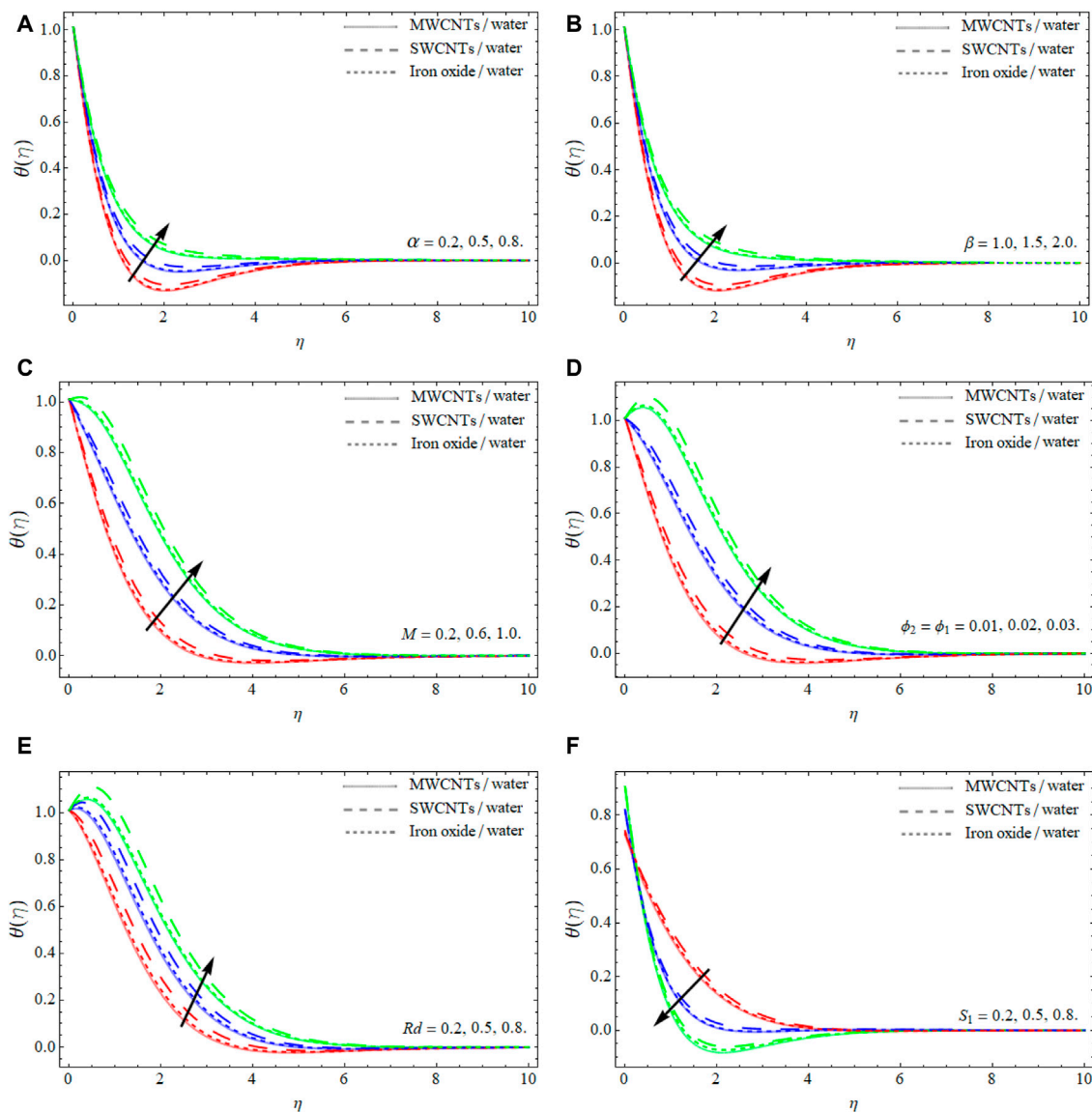


FIGURE 3

Effects of curvature parameter α , fluid parameter β , ferromagnetic M , volume fraction ϕ_1 , thermal radiation Rd , and thermal stratification S_1 on energy profile $\theta(\eta)$.

parameter increases, a stronger resistive force arises known as Lorentz force which decreases the fluid velocity. The velocity profile displays a declining behavior for the rising values of the Casson fluid factor, as shown in Figure 2C. The reason behind this decline is that as the Casson parameter increases, the fluid acts like a Newtonian fluid which reduces the velocity field. Figure 2D shows the upshot of ϕ_1 on $f'(\eta)$. Higher valuation of ϕ_1 diminishes the velocity $f'(\eta)$ field. By expanding the volume percentage, the transit, adhesive force, and excitation energy across CNTs and Fe_3O_4 NF reduce, resulting in a drop in the velocity field. Figure 2E shows the upshot of the velocity slip constraint S on the fluid velocity.

The graph indicates the decrease in the fluid velocity due to growing values of S . It is due to velocity difference between near the surface and away from the cylinder.

The influence of α , β , M , ϕ_1 , Rd , and S_1 on the energy profile is shown in Figures 3A–F. The impact of the curvature on the energy outlines $\theta(\eta)$ is seen in Figure 3A. The heat transfer improves as the values of α improve, as seen in the figures. Physically, as the curvature term upsurges, the radius of the cylinder expands, due to which the maximum number of NPs are attached to the surface of the cylinder, which transmits more heat, so the temperature field improves. Figure 3B shows influence of β (Casson fluid) on the energy contour $\theta(\eta)$. The

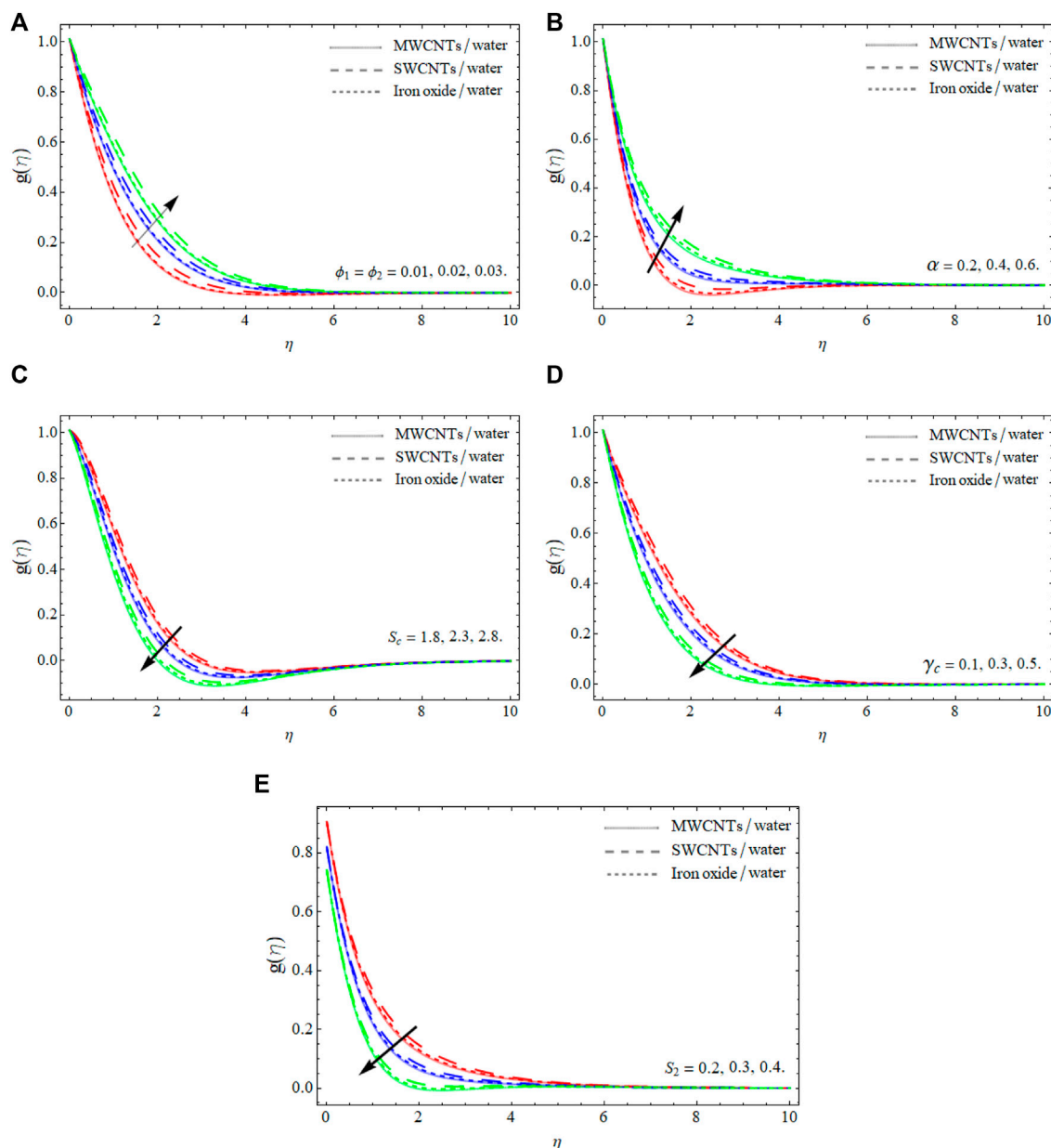


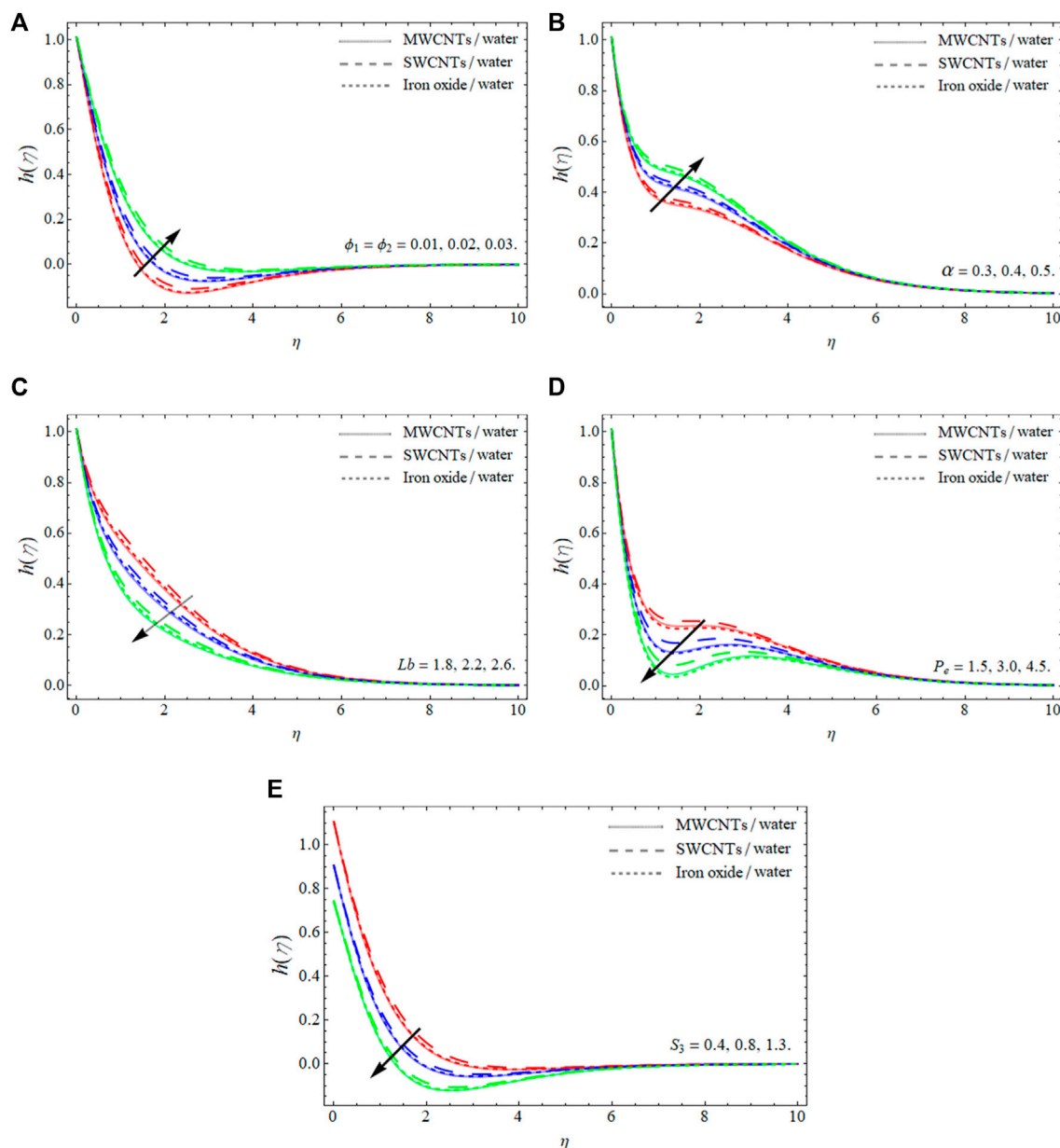
FIGURE 4

Effects of volume fraction ϕ_1 , curvature parameter α , Schmidt number S_c , the concentration relaxation parameter γ_c , and concentration stratification parameter S_2 on concentration profile $g(\eta)$.

temperature distribution improves with improved β values, as shown in the figure. It is shown that the Casson term is in an inverse relation to the yield stress. The influence of the magnetic coefficient M and ϕ_1 on the energy dispersal is seen in Figures 3C,D. Improvement in the fluid temperature corresponded to rises in the magnetic effect M and solid volume fraction parameter ϕ_1 , as seen in the figures. A resistive pressure is created when the magnetic field is improved, which raises the temperature of the fluid. In

Figure 3E, the effect of the radiation term Rd on the fluid's temperature field is investigated. As the radiation number upsurges, the fluid temperature rises. When the radiation term is increased, the fluid absorbs more heat, causing the fluid temperature to rise. The impact of thermal stratification parameter S_1 is shown in Figure 3F. It is to be noted that the energy profile decreases for larger values of S_1 .

The effects ϕ_1 , α , S_c , γ_c , and S_2 on concentration profile $g(\eta)$ are shown in Figures 4A–E. Figure 4A shows the influence of the

**FIGURE 5**

Effects of volume fraction ϕ_1 , curvature parameter α , bio-convection Lewis number Lb , Peclet number Pe , and the microorganism stratification parameter S_3 , on microorganism profile $h(\eta)$.

volume fraction indicator ϕ_1 for both CNTs and iron ferrite NF on the mass profile. Because the fluid average viscosity becomes dense as the quantity of iron oxide NPs and CNTs increases, the mass transfer rate slows. As a result, as credit ϕ_1 grows, the concentration profile decreases. Figure 4B shows that the curvature parameter α is a decreasing function of mass transfer $g(\eta)$. The mass transmission rate reduces with increases in α . Figure 4C indicates the influence of the concentration profile. By increasing the values of S_o the

TABLE 1 Experimental values of water, CNTs, and Fe_3O_4 nanoparticles (Gul et al., 2020).

| | ρ (kg/m ³) | C_p (j/kgK) | k (W/mK) |
|------------|-----------------------------|---------------|------------|
| Pure water | 997.1 | 4,179 | 0.613 |
| SWCNTs | 2,600 | 425 | 6,600 |
| MWCNTs | 1,600 | 796 | 300 |
| Fe_3O_4 | 5,200 | 670 | 6 |

TABLE 2 Thermo-physical relations of hybrid nanofluids (Gul et al., 2020).

Properties

| | |
|-------------------------|--|
| Viscosity | $\mu_{hnf}/\mu_{bf} = 1/(1 - \phi_{Fe_3O_4} - \phi_{CNT})^2$ |
| Density | $\frac{\rho_{hnf}}{\rho_{bf}} = \phi_{Fe_3O_4}(\rho_{Fe_3O_4}/\rho_{bf}) + \phi_{CNT}(\rho_{CNT}/\rho_{bf}) + (1 - \phi_{Fe_3O_4} - \phi_{CNT})$ |
| Thermal capacity | $(\rho C_p)_{hnf}/(\rho C_p)_{bf} = \phi_{Fe_3O_4}((\rho C_p)_{Fe_3O_4}/(\rho C_p)_{bf}) + \phi_{CNT}((\rho C_p)_{CNT}/(\rho C_p)_{bf}) + (1 - \phi_{Fe_3O_4} - \phi_{CNT})$ |
| Thermal conductivity | $\frac{k_{hnf}}{k_{bf}} = [(\phi_{Fe_3O_4}k_{Fe_3O_4} + \phi_{CNT}k_{CNT}/\phi_{Fe_3O_4} + \phi_{Fe_3O_4}) + 2k_{bf} + 2(\phi_{Fe_3O_4}k_{Fe_3O_4} + \phi_{CNT}k_{CNT}) - 2(\phi_{Fe_3O_4} + \phi_{CNT})k_{bf}/(\phi_{Fe_3O_4}k_{Fe_3O_4} + \phi_{CNT}k_{CNT}/\phi_{Fe_3O_4} + \phi_{CNT}) + 2k_{bf} - 2(k_{Fe_3O_4}\phi_{Fe_3O_4} + k_{CNT}\phi_{CNT}) + (\phi_{Fe_3O_4} + \phi_{CNT})2k_{bf}]$ |
| Electrical conductivity | $\frac{\sigma_{hnf}}{\sigma_{bf}} = [(\phi_{Fe_3O_4}\sigma_{Fe_3O_4} + \sigma_{CNT}\phi_{CNT}/\phi_{Fe_3O_4} + \phi_{Fe_3O_4}) + 2\sigma_{bf} + 2(\phi_{Fe_3O_4}\sigma_{Fe_3O_4} + \phi_{CNT}\sigma_{CNT}) - 2(\phi_{Fe_3O_4} + \phi_{CNT})\sigma_{bf}/(\phi_{Fe_3O_4}\sigma_{Fe_3O_4} + \phi_{CNT}\sigma_{CNT}/\phi_{Fe_3O_4} + \phi_{CNT}) + 2\sigma_{bf} - (\phi_{Fe_3O_4}\sigma_{Fe_3O_4} + \phi_{CNT}\sigma_{CNT}) + (\phi_{Fe_3O_4} + \phi_{CNT})\sigma_{bf}]$ |

TABLE 3 Numerical outcomes of $C_f Re_x^{1/2}$, $Sh_x Re_x^{-1/2}$, $Nu_x Re_x^{-1/2}$, and $Nn_x Re_x^{-1/2}$ when $\beta \rightarrow \infty$.

| M | α | ϕ_1 | $C_f Re_x^{1/2}$ | $Sh_x Re_x^{-1/2}$ | $Nu_x Re_x^{-1/2}$ | $Nn_x Re_x^{-1/2}$ |
|-----|----------|----------|------------------|--------------------|--------------------|--------------------|
| 0 | 0.1 | 0.01 | 0.948817 | 1.474229 | 1.392515 | 2.613915 |
| 0.2 | 0.1 | | 1.019293 | 1.472838 | 1.374741 | 2.609771 |
| 0.5 | 0.1 | | 1.114171 | 1.471116 | 1.350623 | 2.604243 |
| 1.0 | 0.1 | | 1.251316 | 1.468902 | 1.315447 | 2.596366 |
| | 0.0 | | 0.951866 | 1.345417 | 1.360632 | 2.589183 |
| | 0.2 | | 1.017015 | 1.500974 | 1.406222 | 2.634011 |
| | 0.5 | | 1.108962 | 1.579961 | 1.474076 | 2.698487 |
| | 0.7 | | 1.251286 | 1.701900 | 1.583912 | 2.799354 |
| | | 0.01 | 0.916480 | 1.456307 | 1.312150 | 2.604988 |
| | | 0.02 | 0.922977 | 1.460090 | 1.328514 | 2.606844 |
| | | 0.03 | 0.984888 | 1.473504 | 1.383434 | 2.611791 |
| | | 0.04 | 1.134798 | 1.487764 | 1.453457 | 2.619460 |

TABLE 4 Statistical outcomes of microorganism transmission rate $-h'(0)$.

| Lb | Pe | α | δ | $-h'(0)$ | |
|------|------|----------|----------|----------|--------|
| | | | | SWCNTs | MWCNTs |
| 0.5 | 0.5 | 0.1 | 0.1 | 1.6591 | 1.6606 |
| 0.6 | | | | 1.7422 | 1.7439 |
| 0.7 | | | | 1.8210 | 1.7227 |
| 0.5 | 0.1 | | | 1.3693 | 1.3707 |
| | 0.2 | | | 1.5329 | 1.5345 |
| | 0.3 | | | 1.6987 | 1.7003 |
| | 0.5 | 0.2 | | 2.0662 | 2.0679 |
| | | 0.3 | | 2.0962 | 2.0978 |
| | | 0.4 | 0.2 | 2.1262 | 2.1278 |
| | | | 0.3 | 2.0996 | 2.1014 |
| | | | 0.4 | 2.1631 | 2.1649 |
| | | | 0.5 | 2.2267 | 2.2285 |

concentration profile decreases. Because increasing the value of Sc lowers the mass permeability, the mass rate falls. Figure 4D depicts the variance in the concentration profile sketch as a

function of various estimations of the concentration relaxation. It is stated that a higher mass relaxation factor approximation lowers the concentration profile. The effect of the

concentration stratification coefficient on the concentration distribution is shown by Figure 4E. The augmentation of the concentration stratification factor results in a diminution in the sketch and the related boundary layer thickness.

Figures 5A,B show the consequences of ϕ_1 and α on the microbial density sketch. The microorganism frequency and corresponding boundary layer thickness show an increasing tendency for larger values of ϕ_1 and α , as shown in Figures 5A,B. Figures 5C–E show that the effect of Lb , P_e , and S_3 on $h(\eta)$ declines the motile microorganism profile. Physically, Lb is in an inverse relation with the mass diffusion and an increase in Lb results in the reduction of $h(\eta)$. Additionally, it is observed that rising values of P_e destabilize the gyrotactic microbes' profile and a higher P_e enhances the progress of NF flow.

Tables 1, 2 revealed the experimental values of base fluid and nanoparticles and the mathematical model used for the proposed model. Table 3 shows the statistical assessments of skin friction $C_f Re_x^{1/2}$, mass transfer $Sh_x Re_x^{-1/2}$, heat transfer rate $Nu_x Re_x^{-1/2}$, and motile microorganism transmission rate $Nn_x Re_x^{-1/2}$. Table 4 shows the comparative analysis between SWCNTs and MWCNTs for the microorganism transfer rate.

Conclusion

We have studied the energy and mass transfer across an expanding cylinder in a water-based Darcy–Forchheimer hybrid nanofluid flow. The influence of a magnetic field, viscous dissipation, heat source, thermal radiation, concentration stratification, and chemical reaction on fluid flow has been investigated. The phenomena are treated as a nonlinear system of PDEs. Using similarity substitution, the modeled equations are further solved through a computational approach PCM. The key findings are:

- The addition of carbon nanotubes (CNTs) and nanocrystals to the base fluid boosts heat and mass conduction remarkably.
- The velocity outlines $f'(\eta)$ significantly lower with the variation of the curvature factor, ferromagnetic effect, Casson fluid constraints, volume fraction, and slip parameter.
- The heat transport rate $\theta(\eta)$ increases with the rising values of curvature parameter, Casson fluid parameter, magnetic effect, and solid nanoparticles volume fraction, while declining with the effect of the thermal stratification parameter
- The mass transfer rate $g(\eta)$ declines with growing credit of nanoparticles, Schmidt number Sc , and concentration

relaxation constraint, while enhances with the effect of the curvature term.

- The motile microorganism propagation rate boosts with variations in ϕ_1 and α , while reduces with the effect of Lb , P_e , and S_3 .

Data availability statement

The original contributions presented in the study are included in the article/Supplementary Material; further inquiries can be directed to the corresponding author.

Author contributions

All authors listed have made a substantial, direct, and intellectual contribution to the work and approved it for publication.

Funding

The authors extend their appreciation to the Deanship of Scientific Research at King Khalid University for funding this work through Large Groups (RGP.2/94/43). The authors would like to thank the Deanship of Scientific Research at Umm Al-Qura University for supporting this work by Grant Code: 22UQU4282396DSR17.

Conflict of interest

The authors declare that the research was conducted in the absence of any commercial or financial relationships that could be construed as a potential conflict of interest.

Publisher's note

All claims expressed in this article are solely those of the authors and do not necessarily represent those of their affiliated organizations, or those of the publisher, the editors, and the reviewers. Any product that may be evaluated in this article, or claim that may be made by its manufacturer, is not guaranteed or endorsed by the publisher.

References

- Ahmad, S., Akhter, S., Shahid, M. I., Ali, K., Akhtar, M., and Ashraf, M. (2022). Novel thermal aspects of hybrid nanofluid flow comprising of manganese zinc ferrite $MnZnFeO$, nickel zinc ferrite $NiZnFeO$ and motile microorganisms. *Ain Shams Eng. J.* 13 (5), 101668. doi:10.1016/j.asej.2021.101668
- Ahmad, S., Naveed Khan, M., Rehman, A., Felemban, B. F., Alqurashi, M. S., Alharbi, F. M., et al. (2021). Analysis of heat and mass transfer features of hybrid casson nanofluid flow with the magnetic dipole past a stretched cylinder. *Appl. Sci.* 11 (23), 11203. doi:10.3390/app112311203

- Al-Mubaddel, F. S., Allehiyany, F. M., Nofal, T. A., Alam, M. M., Ali, A., and Asamoah, J. K. K. (2022). Rheological model for generalized energy and mass transfer through hybrid nanofluid flow comprised of magnetized cobalt ferrite nanoparticles. *J. Nanomater.* 2022, 1–11. doi:10.1155/2022/7120982
- Alharbi, K. A. M., Ahmed, A. E. S., Ould Sidi, M., Ahammad, N. A., Mohamed, A., El-Shorbagy, M. A., et al. (2022). Computational valuation of Darcy ternary-hybrid nanofluid flow across an extending cylinder with induction effects. *Micromachines* 13 (4), 588. doi:10.3390/mi13040588
- Alhowaity, A., Hamam, H., Bilal, M., and Ali, A. Numerical study of Williamson hybrid nanofluid flow with thermal characteristics past over an extending surface. *Heat. Trans.* (2022b). doi:10.1002/htj.22616
- Alsallami, S. A., Zahir, H., Muhammad, T., Hayat, A. U., Khan, M. R., and Ali, A. (2022). Numerical simulation of Marangoni Maxwell nanofluid flow with Arrhenius activation energy and entropy anatomization over a rotating disk. *Waves Random Complex Media*, 1–19. doi:10.1080/17455030.2022.2045385
- Areekara, S., Mabood, F., Sabu, A. S., Mathew, A., and Badruddin, I. A. (2021). Dynamics of water conveying single-wall carbon nanotubes and magnetite nanoparticles subject to induced magnetic field: A bioconvective model for theranostic applications. *Int. Commun. Heat Mass Transf.* 126, 105484. doi:10.1016/j.icheatmasstransfer.2021.105484
- Ashraf, M. Z., Rehman, S. U., Farid, S., Hussein, A. K., Ali, B., Shah, N. A., et al. (2022). Insight into significance of bioconvection on mhd tangent hyperbolic nanofluid flow of irregular thickness across a slender elastic surface. *Mathematics* 10 (15), 2592. doi:10.3390/math10152592
- Benhacine, H., Mahfoud, B., and Salmi, M. (2022). Stability of conducting fluid flow between coaxial cylinders under thermal gradient and axial magnetic field. *Int. J. Thermofluid Sci. Technol.* 9 (2), 090202. doi:10.36963/ijst.2022090202
- Berezowski, M. (2010). The application of the parametric continuation method for determining steady state diagrams in chemical engineering. *Chem. Eng. Sci.* 65 (19), 5411–5414. doi:10.1016/j.ces.2010.07.003
- Bhatti, M. M., Arain, M. B., Zeeshan, A., Ellahi, R., and Doranehgard, M. H. (2022a). Swimming of Gyrotactic Microorganism in MHD Williamson nanofluid flow between rotating circular plates embedded in porous medium: Application of thermal energy storage. *J. Energy Storage* 45 (4), 103511. doi:10.1016/j.est.2021.103511
- Bhatti, M. M., Ellahi, R., and Doranehgard, M. H. (2022b). Numerical study on the hybrid nanofluid ($\text{Co}_3\text{O}_4\text{-Go}/\text{H}_2\text{O}$) flow over a circular elastic surface with non-Darcy medium: Application in solar energy. *J. Mol. Liq.* 361, 119655. doi:10.1016/j.molliq.2022.119655
- Chu, Y. M., Bashir, S., Ramzan, M., and Malik, M. Y. (2022a). Model-based comparative study of magnetohydrodynamics unsteady hybrid nanofluid flow between two infinite parallel plates with particle shape effects. *Math. Methods Appl. Sci.* doi:10.1002/mma.8234
- Chu, Y. M., Nazir, U., Sohail, M., Selim, M. M., and Lee, J. R. (2021). Enhancement in thermal energy and solute particles using hybrid nanoparticles by engaging activation energy and chemical reaction over a parabolic surface via finite element approach. *Fractal Fract.* 5 (3), 119. Article 119. doi:10.3390/fractalfract5030119
- Chu, Y. M., Shankaralingappa, B. M., Gireesha, B. J., Alzahrani, F., Khan, M. I., and Khan, S. U. (2022b). Combined impact of Cattaneo-Christov double diffusion and radiative heat flux on bio-convective flow of Maxwell liquid configured by a stretched nano-material surface. *Appl. Math. Comput.* 419, 126883. doi:10.1016/j.amc.2021.126883
- Dey, D., Borah, R., and Mahanta, B. (2021). “Boundary layer flow and its dual solutions over a stretching cylinder: Stability analysis,” in *Emerging technologies in data mining and information security* (Singapore: Springer), 27–38.
- Dou, H. S. (2022). “Stability of taylor-couette flow between concentric rotating cylinders,” *Origin of turbulence* (Singapore: Springer), 271–304.
- Elattar, S., Helmi, M. M., Elkotb, M. A., El-Shorbagy, M. A., Abdelrahman, A., Bilal, M., et al. (2022). Computational assessment of hybrid nanofluid flow with the influence of hall current and chemical reaction over a slender stretching surface. *Alexandria Eng. J.* 61 (12), 10319–10331. doi:10.1016/j.aej.2022.03.054
- Elayarani, M., Shanmugapriya, M., and Kumar, P. S. (2021). Intensification of heat and mass transfer process in MHD carreau nanofluid flow containing gyrotactic microorganisms. *Chem. Eng. Process. - Process Intensif.* 160, 108299. doi:10.1016/j.ccep.2021.108299
- Gul, T., Rahman, J. U., Bilal, M., Saeed, A., Alghamdi, W., Mukhtar, S., et al. (2020). Viscous dissipated hybrid nanofluid flow with Darcy-Forchheimer and forced convection over a moving thin needle. *AIP Adv.* 10 (10), 105308. doi:10.1063/1.5002210
- Habib, D., Salamat, N., Abdal, S., Siddique, I., Salimi, M., and Ahmadian, A. (2022). On time dependent MHD nanofluid dynamics due to enlarging sheet with bioconvection and two thermal boundary conditions. *Microfluid Nanofluid* 26, 11. doi:10.1007/s10404-021-02514-y
- Hosseinzadeh, K., Roghani, S., Mogharrebi, A. R., Asadi, A., Waqas, M., and Ganji, D. D. (2020). Investigation of cross-fluid flow containing motile gyrotactic microorganisms and nanoparticles over a three-dimensional cylinder. *Alexandria Eng. J.* 59 (5), 3297–3307. doi:10.1016/j.aej.2020.04.037
- Hussain, Z., Hussain, A., Anwar, M. S., and Farooq, M. (2022). Analysis of Cattaneo-Christov heat flux in Jeffery fluid flow with heat source over a stretching cylinder. *Therm. Anal. Calorim.* 147, 3391–3402. doi:10.1007/s10973-021-10573-0
- Jin, F., Qian, Z. S., Chu, Y. M., and ur Rahman, M. (2022). On nonlinear evolution model for drinking behavior under Caputo-Fabrizio derivative. *jaac.* 12 (2), 790–806. doi:10.11948/20210357
- Khan, S. U., Al-Khaled, K., and Bhatti, M. M. (2021). Bioconvection analysis for flow of Oldroyd-B nanofluid configured by a convectively heated surface with partial slip effects. *Surf. Interfaces* 23, 100982. doi:10.1016/j.surf.2021.100982
- Khashi'ie, N. S., Arifin, N. M., and Pop, I. (2022). Magnetohydrodynamics (MHD) boundary layer flow of hybrid nanofluid over a moving plate with Joule heating. *Alex. Eng. J.* 61 (3), 1938–1945. doi:10.1016/j.aej.2021.07.032
- Kumar, D., and Sahu, A. K. (2022). Non-Newtonian fluid flow over a rotating elliptic cylinder in laminar flow regime. *Eur. J. Mech. B Fluids* 93, 117–136. doi:10.1016/j.euromechflu.2022.01.005
- Kumar, L. H., Kazi, S. N., Masjuki, H. H., and Zubir, M. N. M. (2022). A review of recent advances in green nanofluids and their application in thermal systems. *Chem. Eng. J.* 429, 132321. doi:10.1016/j.cej.2021.132321
- Lim, Y. J., Shafie, S., Isa, S. M., Rawi, N. A., and Mohamad, A. Q. (2022). Impact of chemical reaction, thermal radiation and porosity on free convection Carreau fluid flow towards a stretching cylinder. *Alexandria Eng. J.* 61 (6), 4701–4717. doi:10.1016/j.aej.2021.10.023
- Lung, I., Soran, M. L., Stegarescu, A., and Oprea, O. (2021). Devrinol and triadimefon removal from aqueous solutions using CNT-COOH/MnO₂/Fe₃O₄ nanocomposite. *J. Iran. Chem. Soc.* 19, 2031–2039. doi:10.1007/s13738-021-02442-2
- Ma, T., Guo, Z., Lin, M., and Wang, Q. (2021). Recent trends on nanofluid heat transfer machine learning research applied to renewable energy. *Renew. Sustain. Energy Rev.* 138, 110494. doi:10.1016/j.rser.2020.110494
- Ma, Y., Luan, Y., and Xu, W. (2020). Hydrodynamic features of three equally spaced, long flexible cylinders undergoing flow-induced vibration. *Eur. J. Mech. - B/Fluids* 79, 386–400. doi:10.1016/j.euromechflu.2019.09.021
- Mohamed, M. K. A., Yasin, S. H. M., Salleh, M. Z., and Alkasasbeh, H. T. (2021). MHD stagnation point flow and heat transfer over a stretching sheet in a blood-based casson ferrofluid with Newtonian heating. *J. Adv. Res. Fluid Mech. Therm. Sci.* 82 (1), 1–11. doi:10.37934/arfmts.82.1.111
- Muhammad, T., Alamri, S. Z., Waqas, H., Habib, D., and Ellahi, R. (2021). Bioconvection flow of magnetized Carreau nanofluid under the influence of slip over a wedge with motile microorganisms. *J. Therm. Anal. Calorim.* 143 (2), 945–957. doi:10.1007/s10973-020-09580-4
- Muhammad, T., Waqas, H., Manzoor, U., Farooq, U., and Rizvi, Z. F. (2022). On doubly stratified bioconvective transport of Jeffrey nanofluid with gyrotactic motile microorganisms. *Alexandria Eng. J.* 61 (2), 1571–1583. doi:10.1016/j.aej.2021.06.059
- Nazeer, M., Hussain, F., Khan, M. I., El-Zahar, E. R., Chu, Y. M., Malik, M. Y., et al. (2022). Theoretical study of MHD electro-osmotically flow of third-grade fluid in micro channel. *Appl. Math. Comput.* 420, 126868. doi:10.1016/j.amc.2021.126868
- Poply, V. (2021). “Analysis of outer velocity and heat transfer of nanofluid past a stretching cylinder with heat generation and radiation,” in *Proceedings of international conference on trends in computational and cognitive engineering* (Singapore: Springer), 215–234.
- Rafei, A., Loni, R., Mahadzir, S. B., Najafi, G., Sadeghzadeh, M., Mazlan, M., et al. (2022). Hybrid solar desalination system for generation electricity and freshwater with nanofluid application: Energy, exergy, and environmental aspects. *Sustain. Energy Technol. Assess.* 50, 101716. doi:10.1016/j.seta.2021.101716
- Rashid, S., Abouelmagd, E. I., Khalid, A., Farooq, F. B., and Chu, Y. M. (2022). Some recent developments on dynamical h-discrete fractional type inequalities in the frame of nonsingular and nonlocal kernels. *Fractals* 30 (2), 2240110. doi:10.1142/s0218348x22401107
- Rashid, S., Sultana, S., Karaca, Y., Khalid, A., and Chu, Y. M. (2022). Some further extensions considering discrete proportional fractional operators. *Fractals* 30 (01), 2240026. doi:10.1142/s0218348x22400266
- Shruthy, M., and Mahanthesh, B. (2019). Rayleigh-bénard convection in casson and hybrid nanofluids: An analytical investigation. *J. nanofluids* 8 (1), 222–229. doi:10.1166/jon.2019.1571

- Shuaib, M., Shah, R. A., and Bilal, M. (2020). Variable thickness flow over a rotating disk under the influence of variable magnetic field: An application to parametric bcontinuation method. *Adv. Mech. Eng.* 12 (6), 168781402093638. doi:10.1177/1687814020936385
- Sun, T. C., DarAssi, M. H., Bilal, M., and Khan, M. A. (2022). The study of Darcy-Forchheimer hybrid nanofluid flow with the thermal slip and dissipation effect using parametric continuation approach over a rotating disk. *Waves Random Complex Media*, 1–14. doi:10.1080/17455030.2022.2072537
- Syam Sundar, L., Sousa, A. C., and Singh, M. K. (2015). Heat transfer enhancement of low volume concentration of carbon nanotube-Fe₃O₄/water hybrid nanofluids in a tube with twisted tape inserts under turbulent flow. *J. Therm. Sci. Eng. Appl.* 7 (2), 021015. doi:10.1115/1.4029622
- Ullah, I., Hayat, T., Alsaedi, A., and Asghar, S. (2019). Dissipative flow of hybrid nanofluid (H₂O-aluminum alloy nanoparticles) with thermal radiation. *Phys. Scr.* 94 (12), 125708. doi:10.1088/1402-4896/ab31d3
- Ullah, I., Hayat, T., and Alsaedi, A. (2021a). Optimization of entropy production in flow of hybrid nanomaterials through Darcy–Forchheimer porous space. *J. Therm. Anal. Calorim.* 147, 5855–5864. doi:10.1007/s10973-021-10830-2
- Ullah, I., Hayat, T., Aziz, A., and Alsaedi, A. (2022). Significance of entropy generation and the coriolis force on the three-dimensional non-Darcy flow of ethylene-glycol conveying carbon nanotubes (SWCNTs and MWCNTs). *J. Non-Equilibrium Thermodyn.* 47 (1), 61–75. doi:10.1515/jnet-2021-0012
- Ullah, I., Ullah, R., Alqarni, M. S., Xia, W. F., and Muhammad, T. (2021b). Combined heat source and zero mass flux features on magnetized nanofluid flow by radial disk with the applications of Coriolis force and activation energy. *Int. Commun. Heat Mass Transf.* 126, 105416. doi:10.1016/j.icheatmasstransfer.2021.105416
- Varun Kumar, R. S., Punith Gowda, R. J., Naveen Kumar, R., Radhika, M., and Prasannakumara, B. C. (2021). Two-phase flow of dusty fluid with suspended hybrid nanoparticles over a stretching cylinder with modified Fourier heat flux. *SN Appl. Sci.* 3 (3), 384–389. doi:10.1007/s42452-021-04364-3
- Wang, F., Khan, M. N., Ahmad, I., Ahmad, H., Abu-Zinadah, H., and Chu, Y. M. (2022). Numerical solution of traveling waves in chemical kinetics: Time-fractional Fishers equations. *Fractals* 30 (2), 2240051–2240134. doi:10.1142/s0218348x22400515
- Waqas, H., Manzoor, U., Muhammad, T., and Hussain, S. (2021). Thermo-bioconvection transport of nanofluid over an inclined stretching cylinder with Cattaneo–Christov double-diffusion. *Commun. Theor. Phys.* 73 (7), 075006. doi:10.1088/1572-9494/abfcb9
- Zhang, M., Wang, X., and Oiseth, O. (2021). Torsional vibration of a circular cylinder with an attached splitter plate in laminar flow. *Ocean. Eng.* 236, 109514. doi:10.1016/j.oceaneng.2021.109514
- Zhao, T. H., Khan, M. I., and Chu, Y. M. (2021). Artificial neural networking (ANN) analysis for heat and entropy generation in flow of non-Newtonian fluid between two rotating disks. *Math. Methods Appl. Sci.* doi:10.1002/mma.7310
- Zhao, T. H., Wang, M. K., Hai, G. J., and Chu, Y. M. (2022). Landen inequalities for Gaussian hypergeometric function. *Rev. Real Acad. Ciencias Exactas, Físicas Nat. Ser. Matemáticas* 116 (1), 53–23. doi:10.1007/s13398-021-01197-y
- Zhou, J. C., Abidi, A., Shi, Q. H., Khan, M. R., Rehman, A., Issakhov, A., et al. (2021). Unsteady radiative slip flow of MHD Casson fluid over a permeable stretched surface subject to a non-uniform heat source. *Case Stud. Therm. Eng.* 26, 101141. doi:10.1016/j.csite.2021.101141

Nomenclature

u, v Velocity components

α Curvature parameter

ϵ Curie temperature

M Magnetization

k Thermal conductivity [$Wm^{-1}K^{-1}$]

D_m Microorganism diffusivity

Ω Magnetic scalar potential

τ_{xy} Shear stress

β Casson fluid parameter

T_w Temperature at the surface

λ Viscous dissipation parameter

η Scaled boundary-layer coordinate

U_w Stretching velocity

K^* Pyromagnetic co-efficient

W_c Microbe floating speed

D_B Brownian motion

S_2 Concentration stratification

C_f Surface drag force

α_f Modified thermal diffusivity

P_e Bioconvection Peclet number

x, r Coordinate

T_w Temperature at wall

δ Bioconvection constant

H Magnetic field

C_p Specific heat

q_w Surface heat flux

μ_0 Magnetic permeability

w_1 Slip factor

μ Dynamic viscosity

T_∞ Ambient temperature [K]

ϕ_1 Volume fraction of nanoparticles

θ Dimensionless temperature

S_1 Thermal stratification

Pr Prandtl number

Re_x Rayleigh number

S_3 Microorganism stratification

s Velocity slip parameter

λ_c Concentration relaxation time

(ρC_p) Specific heat capacity

Nu_x Nusselt number



OPEN ACCESS

EDITED BY

Umar Khan,
Hazara University, Pakistan

REVIEWED BY

Homan Emadifar,
Islamic Azad University, Iran
Umair Ali,
Universiti Sains Malaysia (USM), Malaysia

*CORRESPONDENCE

I. Rashid,
mehar.irfan014@gmail.com

SPECIALTY SECTION

This article was submitted to Process and Energy Systems Engineering, a section of the journal Frontiers in Energy Research

RECEIVED 01 August 2022

ACCEPTED 05 September 2022

PUBLISHED 07 October 2022

CITATION

Rashid I, Zubair T, Asjad MI and Awrejcewicz J (2022), Entropy generation investigation of MHD Ag– and Au–H₂O nanofluid above an exponential porous stretchable surface with thermal radiation and stagnation point flow. *Front. Energy Res.* 10:1009044. doi: 10.3389/fenrg.2022.1009044

COPYRIGHT

© 2022 Rashid, Zubair, Asjad and Awrejcewicz. This is an open-access article distributed under the terms of the [Creative Commons Attribution License \(CC BY\)](#). The use, distribution or reproduction in other forums is permitted, provided the original author(s) and the copyright owner(s) are credited and that the original publication in this journal is cited, in accordance with accepted academic practice. No use, distribution or reproduction is permitted which does not comply with these terms.

Entropy generation investigation of MHD Ag– and Au–H₂O nanofluid above an exponential porous stretchable surface with thermal radiation and stagnation point flow

I. Rashid^{1*}, T. Zubair², M. I. Asjad³ and J. Awrejcewicz⁴

¹Department of Engineering and Computer Science, National University of Modern Languages, Islamabad, Pakistan, ²School of Mathematical Sciences, Peking University, Beijing, China,

³Department of Mathematics, University of Management and Technology, Lahore, Pakistan,

⁴Department of Automation, Bio-mechanics and Mechatronics, Lodz University of Technology, Łódź, Poland

The current study presents an entropy generation investigation of magnetohydrodynamic Ag- and Au-H₂O nanofluid flows induced by an exponential stretchable sheet implanted in porous media accompanying suction/injection and heat radiation impact. Moreover, the stagnation point flow and silver and gold nanoparticles are considered. The consequences of ohmic heating and thermal radiation are also included as part of the heat transport examination. A physical process is transformed into a set of mathematical expressions using mathematical concepts, which can then be further simplified by using the necessary variables. Considering numerous physiological factors of interest, exact solutions for velocity and temperature profiles are calculated. Graphs and numerical tables are utilized to examine how different physical entities affect the distribution of velocity, temperature, and entropy. It is noted that enhancing the values of Ω reduces entropy inception. It is observed that the entropy inception field gains due to an increment in Ec_{rt} .

KEYWORDS

thermal radiation, entropy inception, ohmic heat, magnetic field, stagnation point flow

1 Introduction

Entropy is defined as a gauge of disorder inside a system and its surroundings or a measure of progress toward thermodynamic equilibrium under the scope of thermodynamics. Working with a thermodynamics process, an entropy generation investigation is essential since entropy calculates the effectiveness of every engineered thermofluid mechanism. The second law of thermodynamics determines the randomness

of any system. According to current research, the second law of thermodynamics is a significant tool for calculating the entropy of any system. Entropy inception has considerable fascinating application in the engineering and chemical industry such as extrusion procedures, lubrication phenomena, and schemes of geothermal energy, thermal mechanisms, heat management, and power production (Abbasi et al., 2021). Bejan (1979) was the first to introduce the concept of entropy production inside the flowing fluid and heat exchange mechanism. Later on, many researchers discussed entropy generation inside fluid and heat transport frameworks. Abbasi et al. (2021) studied the significant entropy inception with ohmic heating and thermal radiation effects of a viscoelastic nanofluid on a lubricated disk. Entropy production inside the MHD flow between porous media was discussed by Rashidi and Freidoonimehr (2014). Hayat et al. (2021) described the entropy in Newtonian nanofluid flow provoked by a curved stretchable sheet. Entropy inception within a Casson nanoliquid by a stretched surface soaked in porous media considering many impacts was investigated by Mahato et al. (2022). Wang et al. (2022) studied the Darcy–Forchheimer nanofluid for irreversibility inception. The entropy production in the Darcy–Forchheimer fluid in the presence of ohmic heat was scrutinized by Khan et al. (2022). Tayebi et al. (2021) examined the entropy and thermo-economics inside a convective nanofluid with the MHD effect. Afridi et al. (2018) analyzed the consequences of frictional and ohmic heating to find the entropy inception inside the used problem. Sithole et al. (2018) investigated the irreversibility of MHD nanofluid flow provoked by a stretchable surface for viscous dissipation influence. The impact of entropy inception inside the nanofluid with several effects is addressed in Noghrehabadi et al. (2013); Bhatti et al. (2017); and Abd El-Aziz and Afify (2019).

Despite the fact that a variety of approaches are used to promote heat transport, low thermal quality is a significant barrier in development of energy-efficient heat transfer fluids, which are in high need for a variety of industrial applications. The thermal capabilities of energy-carrying liquids are accountable for boosting the exchange of heat in a system. As a result, insufficient thermal conductivity is a disadvantage of conventional fluids, such as glycol, oil, water, and ethylene, in promoting the properties and efficiency of various engineered electronic devices. Integrating a fraction of nanometal particles within ordinary fluids is a novel way to improve the thermal conductivity of traditional liquids, which are known as nanofluids. The first time a nanofluid was used by adding nano-sized metallic particles into a conventional fluid was in 1995 by Choi (1995). Such kinds of nanofluids significantly enhance heat transport properties. After that, many scientists investigated the heat exchange rate of a nanofluid with several impacts. Prasannakumara (2021) analyzed the MHD Maxwell nanofluid provoked by a stretched surface

by applying a numerical method. The influence of thermal radiation on the Casson nanofluid by shrinking/stretching walls was observed by Mahabaleshwara et al. (2022). The consequence of dissipation and radiation entities on an MHD bioconvective nanoliquid due to a stretching sheet was discussed by Neethu et al. (2022). B Awati et al. (2021) used the Haar wavelet method to study nanofluid flow with a nonlinear stretchable surface along with mass and energy transport. The impact of nanofluid flow provoked by a stretching sheet along with hydromagnetics is scrutinized by Manzoor et al. (2022). The impact of emerging entities on a nanofluid is presented in Oztop and Abu-Nada (2008); Khan and Pop (2010); Hamad (2011); Yacob et al. (2011); Noghrehabadi et al. (2012); Rohni et al. (2012).

Motivated by the aforementioned studies and interesting applications, entropy inception is calculated inside the magnetohydrodynamic nanofluid flow by incorporating Ag and Au nanoparticles on an exponentially stretchable surface with stagnation point flow, porous wall, and ohmic heating. Furthermore, the Bejan number and energy transport investigation are carried out along with thermal heating. The closed form solutions are acquired by utilizing hypergeometric functions to visualize the impact of numerous emerging parameters on the velocity field, temperature field, local skin friction, Nusselt number, and the chaos due to different effects in the used problem. Additionally, numerical tables and graphs are displayed.

2 Problem statement

A two-dimensional, laminar, incompressible, steady flow of an Ag/Au-water MHD nanofluid provoked by an exponentially stretchable surface immersed in porous media with different body forces has been carried out. The impact of ohmic heating and thermal radiation is also considered part of the heat transfer study. The extending sheet is placed along the x -axis in the flow path, whereas the y -axis is assumed normal to the sheet. Figure 1 shows that the fluid is in the $y \geq 0$ space. Considering a velocity of $u = u_{re}e^{x/L_c}$, the surface is pulled throughout the x dimension. In addition, the magnetic field (B_0) is introduced toward the flowing fluid in a normal direction. The basic equations that regulate the used fluid flow are as shown as follows (Rashidi and Freidoonimehr, 2014):

$$\frac{\partial u}{\partial x} + \frac{\partial v}{\partial y} = 0, \quad (1)$$

$$u \frac{\partial u}{\partial x} + v \frac{\partial v}{\partial y} = \frac{\mu_{sf}}{\rho_{sf}} \frac{\partial^2 u}{\partial y^2} + u_{sp} \frac{\partial u_{sp}}{\partial x} - \frac{\sigma_{sf} B(x)^2}{\rho_{sf}} (u - u_{sp}) - \frac{\mu_{sf}}{\rho_{sf} k} (u - u_{sp}), \quad (2)$$

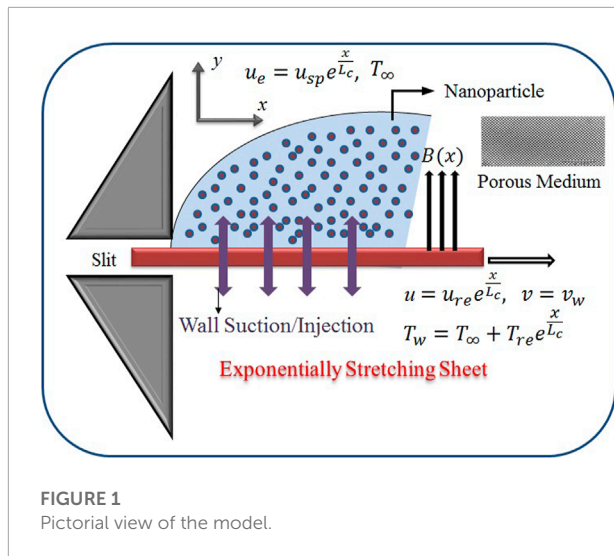


FIGURE 1
Pictorial view of the model.

in which $B(x)$ = magnetic entity; u, v denote the velocity portions in the x and y directions, respectively, ρ_{sf} = density; μ_{sf} is the dynamic viscosity; the thermal diffusivity is expressed by α_{sf} ; the specific heat capacitance is $(\rho c_p)_{sf}$; and ν_{sf} is the kinematic viscosity of the nanofluid. The thermal conductivity can be expressed as follows (Rashid et al., 2017):

$$\left. \begin{aligned} (\rho c_p)_{sf} &= \phi(\rho c_p)_{sf} + ((\rho c_p)_{hf} \cdot 1 - (\rho c_p)_{hf} \phi), \\ \alpha_{sf} &= \frac{k_{sf}}{(\rho c_p)_{sf}}, \quad \mu_{sf} = \frac{\mu_{hf}}{(1 - \phi)^{2.5}}, \\ \rho_{sf} &= \phi(\rho_{sf}) + (1 - \phi)\rho_{hf}, \quad \nu_{sf} = \frac{\mu_{sf}}{\rho_{sf}}, \\ \frac{\sigma_{sf}}{\sigma_{hf}} &= \frac{\left(3 \frac{\sigma_{sf}}{\sigma_{hf}} \phi - 3\phi\right)}{\left(\phi - \frac{\sigma_{sf}}{\sigma_{hf}} \phi\right) + \left(\frac{\sigma_{sf}}{\sigma_{hf}} + 2\right)} + 1, \\ k_{sf} &= \frac{(k_{hf} k_{sf} + 2k_{hf}^2) - 2(k_{hf}^2 \phi - k_{sf} k_{hf} \phi)}{(k_{sf} + 2k_{hf}) + (k_{sf} \phi - k_{sf} \phi)}, \end{aligned} \right\}. \quad (3)$$

In Eq. 5, k_{sf} = thermal conductivity; σ_{sf} = electrical conductivity; $(\rho c_p)_{hf}$ and ρ_{hf} are the effective heat capacity and density, respectively; and ϕ is the nanoparticle volume ratio of the nanofluid. k_{hf} = thermal conductivity and σ_{hf} = electrical conductivity of the host fluid. The appropriate boundary criteria of the aforementioned model are as follows (Bilal et al., 2017):

$$\left. \begin{aligned} u &= u_{re} e^{x/L_c}, \quad v = v_{wmt} \quad \text{at} \quad y = 0, \\ u &\rightarrow u_{sp} = u_{re} e^{x/L_c} \quad \text{as} \quad y \rightarrow \infty. \end{aligned} \right\}. \quad (4)$$

The accompanying similarity variables have been established to non-dimensionalize the basic equations and boundary

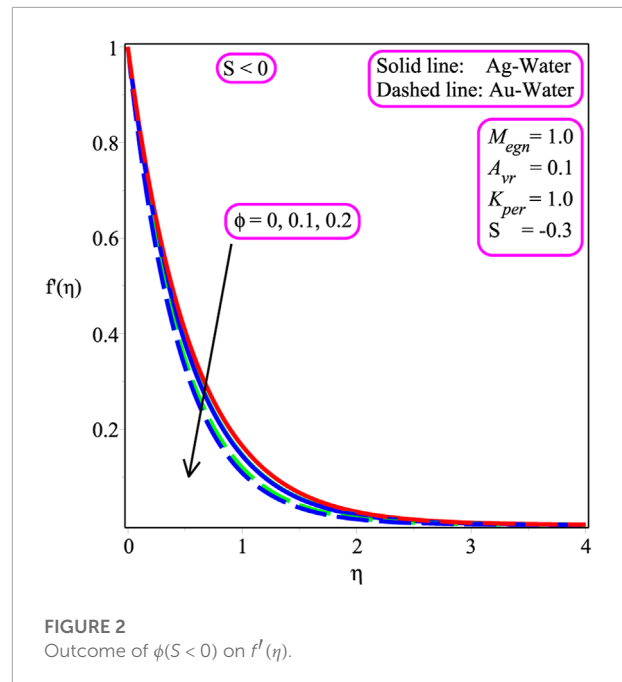


FIGURE 2
Outcome of $\phi(S < 0)$ on $f'(\eta)$.

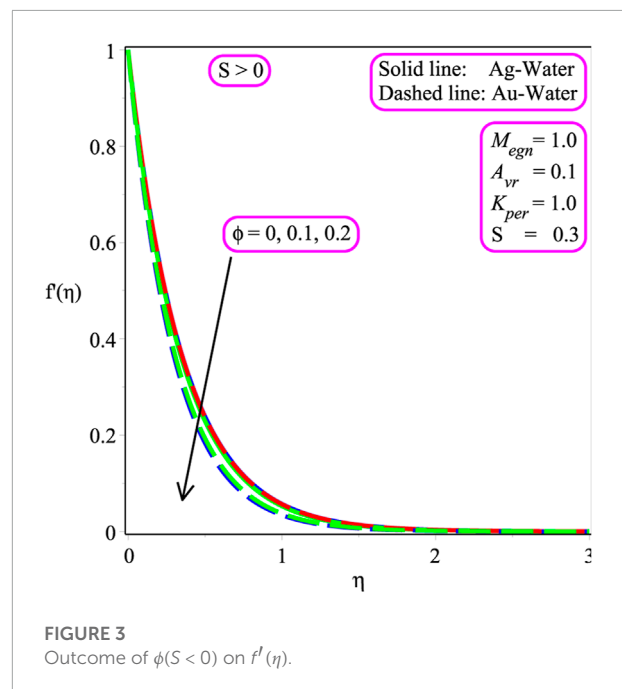


FIGURE 3
Outcome of $\phi(S > 0)$ on $f'(\eta)$.

conditions (Bilal et al., 2017):

$$\left. \begin{aligned} \eta &= y \left(\frac{u_{rf}}{2\nu_{hf} L_c} \right)^{1/2} e^{x/2L_c}, \\ v &= - \left(\frac{u_{rf} \nu_{hf}}{2L_c} \right)^{1/2} e^{x/2L_c} (f + \eta f'), \\ u &= u_{re} e^{x/L_c} f'. \end{aligned} \right\}. \quad (5)$$

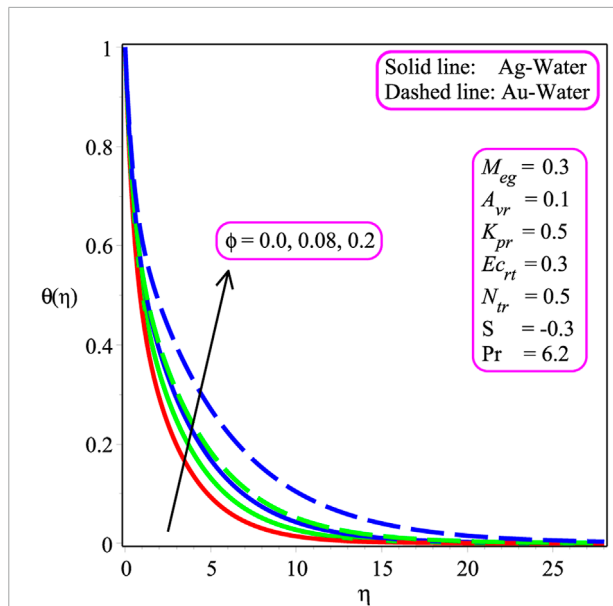


FIGURE 4
Outcome of ϕ on $\theta(\eta)$.

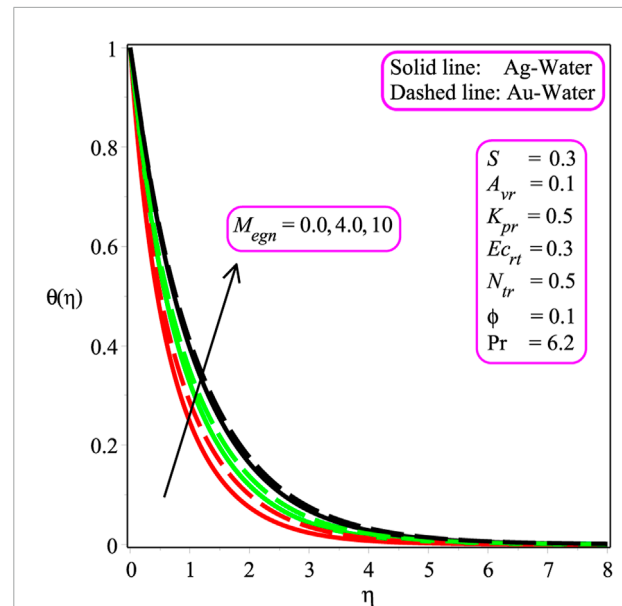


FIGURE 6
Outcome of M_{egn} on $\theta(\eta)$.

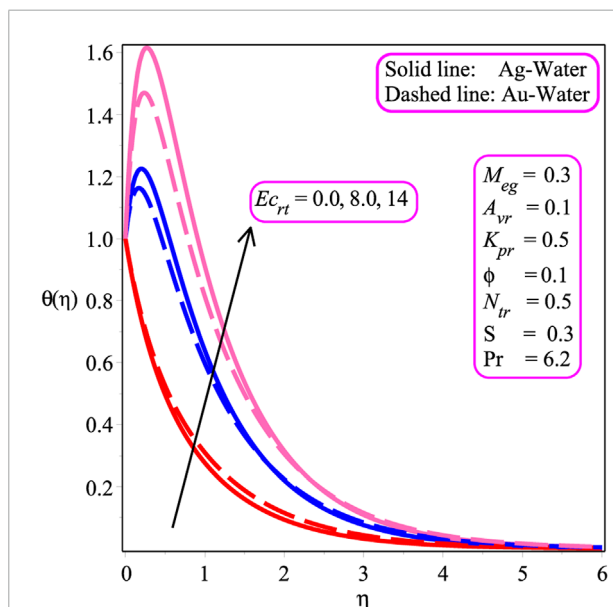


FIGURE 5
Outcome of Ec_{rt} on $\theta(\eta)$.

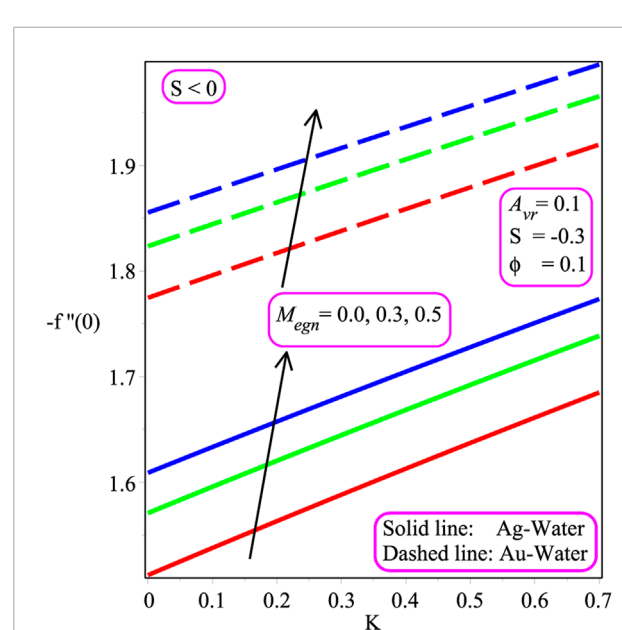


FIGURE 7
Outcome of M_{egn} on $-f'(0)$.

Expression Eq. 5 reduces Eq. 2 into a dimensionless form and is given as

$$f''' + \chi_1 \chi_2 f f'' + 2\chi_1 \chi_2 A_{vr}^2 - 2\chi_1 \chi_2 f'^2 - \chi_1 M_{egn} f' + (K_{pr} A_{vr} - K_{pr} f') = 0, \quad (6)$$

and the boundary conditions are

$$\left. \begin{aligned} f(\eta) = S, \quad f'(\eta) = 1, \quad \text{at} \quad \eta = 0, \\ f'(\eta) \rightarrow \frac{u_{sp}}{u_{re}} = A_{vr} \quad \text{as} \quad \eta \rightarrow \infty. \end{aligned} \right\}. \quad (7)$$

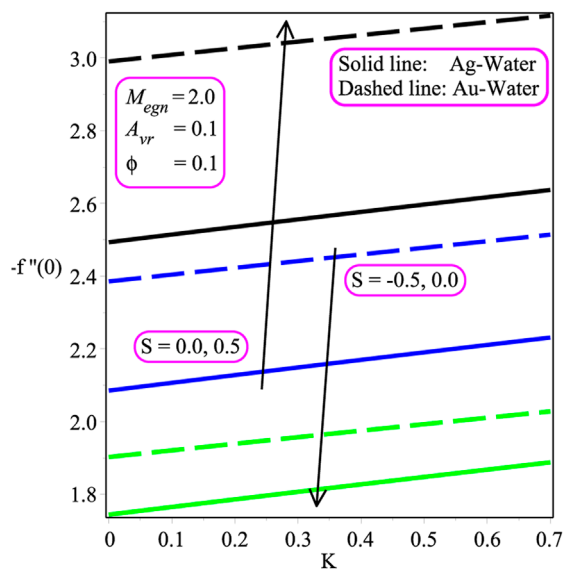


FIGURE 8
Outcome of suction/injection on $-f''(0)$.

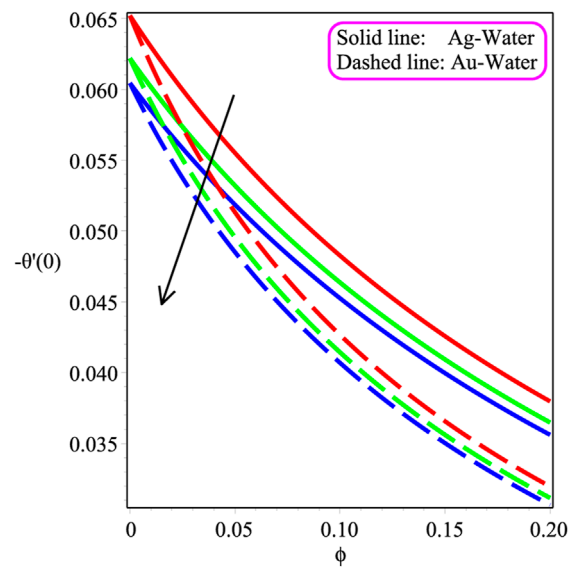


FIGURE 10
Outcome of K_{pr} on $-\theta'(0)$.

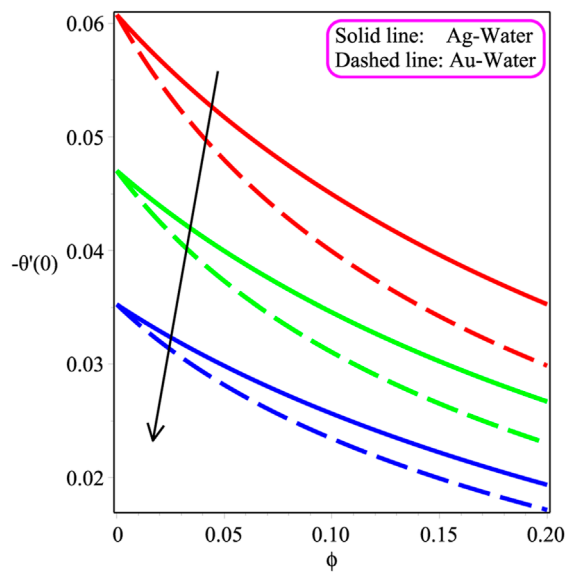


FIGURE 9
Outcome of Ec_{rt} on $-\theta'(0)$.

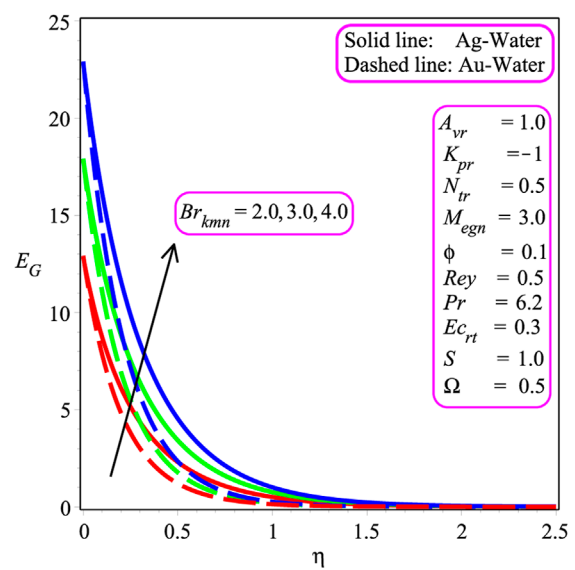


FIGURE 11
Outcome of Br_{kmn} on E_G .

In Eqs. 6, 7,

$$\left. \begin{aligned} \chi_2 &= \left(1 - \phi + \phi \frac{\rho_{sf}}{\rho_{hf}}\right), \quad S = -\left(\frac{2L_c}{u_{re}v_{hf}}\right)^{1/2} e^{-x/2L_c v_w}, \\ M_{egn} &= \frac{2u_{rf}\sigma B_0^2}{\rho}, \\ \chi_1 &= (1 - \phi)^{2.5}, \quad K_{pr} = \frac{u_{re}k_0}{L_c v_{hf}}, \quad u_{sp} \\ &\quad \text{the stagnation - point flow velocity,} \\ &\quad u_{re} \text{ the reference velocity,} \end{aligned} \right\} \quad (8)$$

where K_{pr} is the permeability parameter and M_{egn} is the Hartmann number. The closed form solution of such a kind of equation was introduced by Chakrabarti and Gupta, (1979):

$$f(\eta) = \lambda_1 + \lambda_2 e^{-\Psi\eta}. \quad (9)$$

By solving Eqs. 7, 8,

$$f(\eta) = \left(\frac{1 - e^{-\Psi\eta}}{\Psi}\right) + S. \quad (10)$$

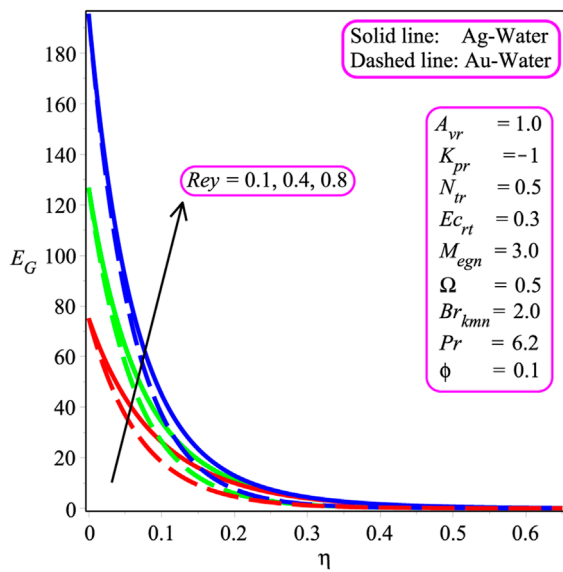


FIGURE 12
Outcome of Re_y on E_G .

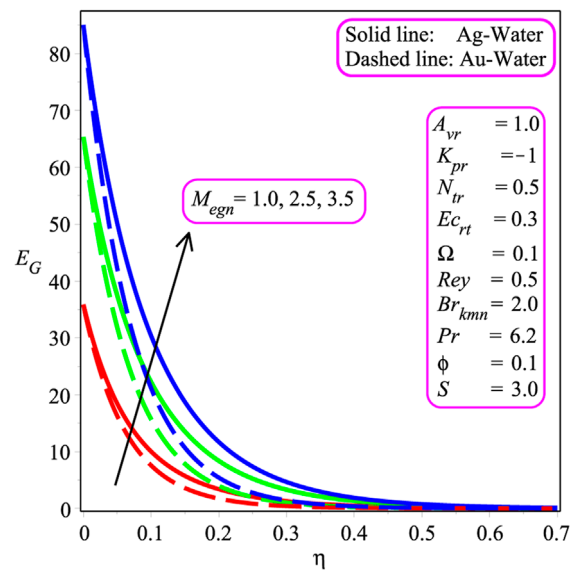


FIGURE 14
Outcome of M_{egn} on E_G .

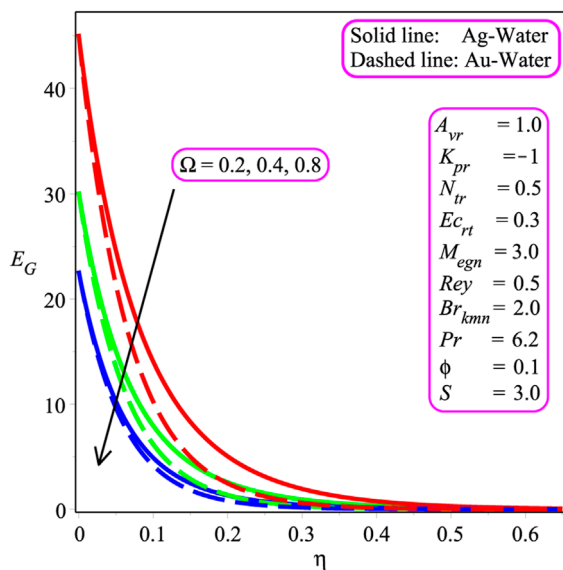


FIGURE 13
Outcome of Ω on E_G .

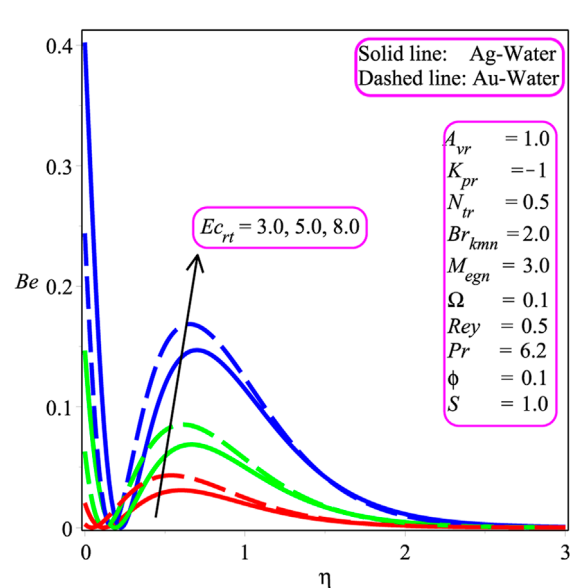


FIGURE 15
Outcome of Ec_{rt} on Be .

To obtain Ψ , λ_1 , and λ_1 , substitute Eq. 9 in Eq. 6:

$$\Psi = \frac{1}{2}\chi_1\chi_2S + \frac{1}{2}\sqrt{\chi_1^2\chi_2^2S^2 - 8A_{vr}^2\chi_1\chi_2 - 4A_{vr}\chi_1M_{egn} + \xi}, \quad (11)$$

$$\lambda_1 = \frac{1}{\frac{1}{2}\chi_1\chi_2S + \frac{1}{2}\sqrt{\chi_1^2\chi_2^2S^2 - 8A_{vr}^2\chi_1\chi_2 - 4A_{vr}\chi_1M_{egn} + \xi}} + S, \quad (12)$$

$$\lambda_2 = -\frac{1}{\frac{1}{2}\chi_1\chi_2S + \frac{1}{2}\sqrt{\chi_1^2\chi_2^2S^2 - 8A_{vr}^2\chi_1\chi_2 - 4A_{vr}\chi_1M_{egn} + \xi}}, \quad (13)$$

$$\xi = -4A_{vr}4K_{pr} + 8\chi_1\chi_2 + 4\chi_1M_{egn} + 4K_{pr}, \quad (14)$$

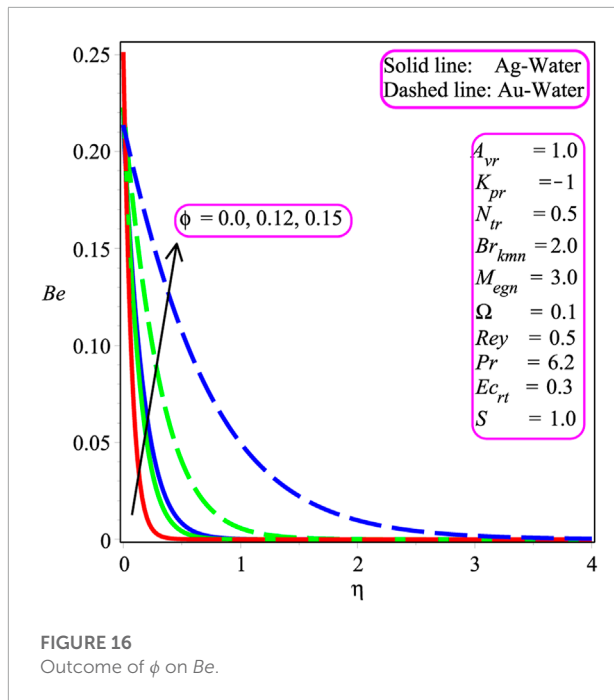


FIGURE 16
Outcome of ϕ on Be.

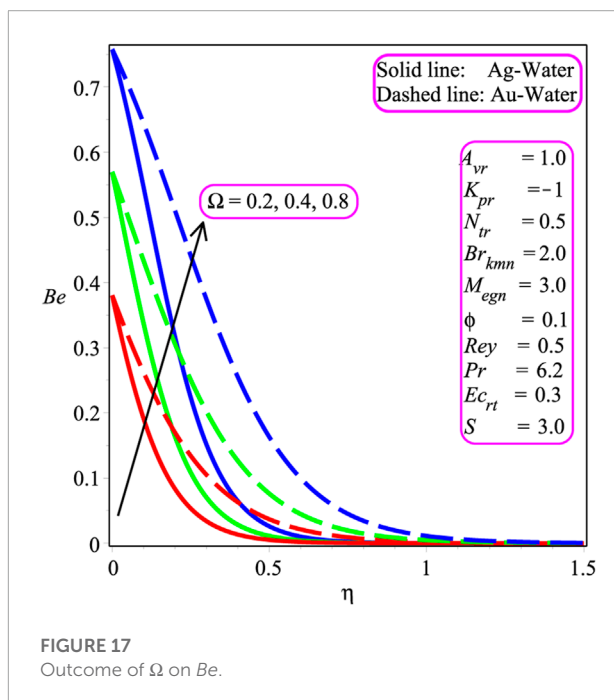


FIGURE 17
Outcome of Ω on Be.

where Ψ , λ_1 , and λ_2 are constants with $\Psi > 0$. After substituting Eqs. 11–13 in Eq. 9, the solution of the velocity field is found as

$$f(\eta) = \left\{ \frac{1}{\frac{1}{2}\chi_1\chi_2S + \frac{1}{2}\sqrt{\chi_1^2\chi_2^2S^2 - 8A_{vr}^2\chi_1\chi_2 - 4A_{vr}\chi_1M_{egn} + \xi}} \left(1 - e^{\frac{1}{2}\chi_1\chi_2S + \frac{1}{2}\sqrt{\chi_1^2\chi_2^2S^2 - 8A_{vr}^2\chi_1\chi_2 - 4A_{vr}\chi_1M_{egn} + \xi}\eta} \right) + S \right\}. \quad (15)$$

The skin friction at the sheet is calculated as follows:

$$C_f = \frac{\tau_w}{\rho u_w^2} = \frac{f''(0)}{Re_x^{1/2}\chi_1}, \quad Re_x^{-1/2}\chi_1 C_f = f''(0). \quad (16)$$

Here, the Reynolds number is shown by $Re_x = \frac{xu_w}{\nu}$, and the stress over the wall = $\tau_w = \mu_w f''(\frac{\partial u}{\partial y})_{y=0}$.

3 Heat transfer analysis

Heat transport analysis is carried out in this portion. Additionally, ohmic heating and thermal radiation are considered, which are presented by the following governing equation:

$$u \frac{\partial T}{\partial x} + v \frac{\partial T}{\partial y} = \alpha_{sf} \frac{\partial^2 T}{\partial y^2} + \frac{\sigma_{sf} B(x)^2}{(\rho C_p)_{sf}} u^2 - \frac{1}{(\rho C_p)_{sf}} \frac{\partial q_{rad}}{\partial y}, \quad (17)$$

where

$$q_{rad} = -\frac{\sigma^*}{3k^*} \frac{\partial T^4}{\partial y}. \quad (18)$$

Here, σ^* is the Stefan–Boltzmann constant, k^* expresses the mass absorption coefficient, and the specific heat = $(C_p)_{sf}$. Expression Eq. 16 takes the following form after substituting Eq. 17 in it (Rashid et al., 2017):

$$u \frac{\partial T}{\partial x} + v \frac{\partial T}{\partial y} = \alpha_{nf} \frac{\partial^2 T}{\partial y^2} + \frac{1}{3(\rho C_p)_{nf}} \frac{16\sigma^* T_\infty^3}{k^*} \frac{\partial^2 T}{\partial y^2} + \frac{\sigma_{nf} B(x)^2}{(\rho C_p)_{nf}} u^2. \quad (19)$$

The suitable boundary conditions are

$$\left. \begin{aligned} T &= T_w = T_\infty + T_{re} e^{x/L_c} & \text{at } y &= 0, \\ T &\rightarrow T_\infty & \text{as } y &\rightarrow \infty, \end{aligned} \right\} \quad (20)$$

where T_w is the temperature of the sheet, the characteristic length = L_c , T_{re} is the reference temperature, and T_∞ is the free stream temperature. The temperature field similarity variable is specified as follows (Rashid et al., 2017):

$$\theta(\eta) = \frac{T - T_\infty}{T_w - T_\infty}. \quad (21)$$

The energy equation takes the following dimensionless form by utilizing Eqs. 5, 20:

$$\kappa \theta'' - 2Pr f' \theta + Pr f \theta' + \frac{Pr M_{egn}}{\chi_4} Ec_{rf} f'^2 = 0, \quad (22)$$

where

$$\begin{aligned} \kappa &= \left(\frac{\chi_3}{\chi_4} \right) \left(1 + \frac{4}{3N_{tr}\chi_3} \right), \quad Ec_{rt} = \frac{u^2}{(T_w - T_\infty)C_p}, \quad Pr = \frac{\nu_{hf}}{\alpha_{hf}}, \\ N_{tr} &= \frac{K^* K_{hf}}{4\sigma^* T_\infty^3}, \\ \chi_3 &= \frac{(k_{sf} + 2k_{hf}) - (k_{hf}2\phi - k_{sf}2\phi)}{(k_{sf} + 2k_{hf}) + (k_{hf}2\phi - k_{sf}2\phi)}, \\ \chi_4 &= \left(\phi \frac{(\rho C_p)_{sf}}{(\rho C_p)_{hf}} - \phi + 1 \right). \end{aligned} \quad (23)$$

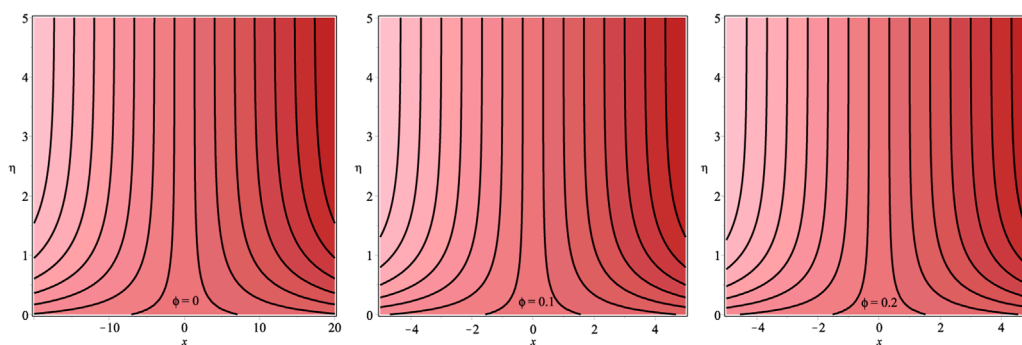


FIGURE 18

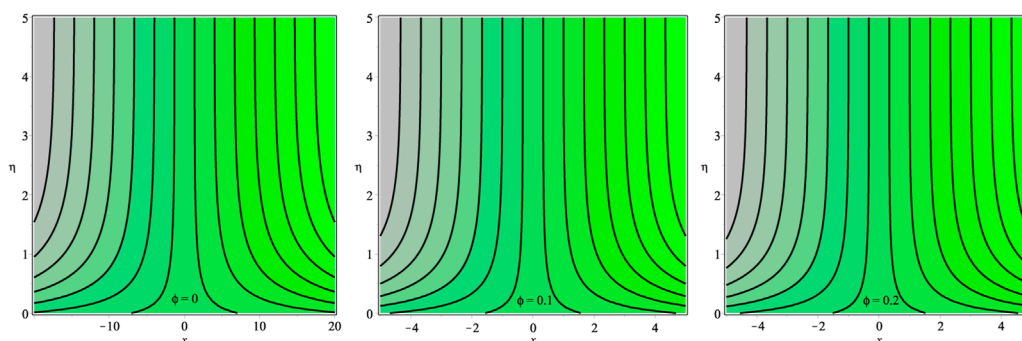
(A–C) Flow pattern of Ag– water for $K_{pr} = 1$, $M_{egn} = 1$, $A_{vr} = 0.8$, and $S = 0.2$.

FIGURE 19

(A–C) Flow pattern of Au– water for $K_{pr} = 1$, $M_{egn} = 1$, $A_{vr} = 0.8$, and $S = 0.2$.

Here, Pr is the Prandtl number, N_{tr} is the radiation parameter, and Ec_{rt} is the Eckert number. The boundary conditions are

$$\left. \begin{aligned} \theta(\eta) &= 1 & \text{at} & \quad \eta = 0, \\ \theta(\eta) &\rightarrow 0 & \text{as} & \quad \eta \rightarrow \infty. \end{aligned} \right\}. \quad (24)$$

Now, using Eq. 9 in Eq. 21,

$$\begin{aligned} \kappa\theta'' - 2Pre^{-\Psi\eta}\theta + Pr\left(S + \frac{1}{\Psi}\left(\frac{1-e^{-\Psi\eta}}{\Psi}\right)\right)\theta' + \frac{PrM_{egn}}{\chi_4} \\ Ec_{rt}(e^{-\Psi\eta})^2 = 0. \end{aligned} \quad (25)$$

introduces the following new variable to convert Eq. 24 into Kummer's ordinary differential equation:

$$\beta = -\frac{Pre^{-\Psi\eta}}{\kappa\Psi^2}. \quad (26)$$

Applying the new variable, Eq. 24 becomes as expressed below:

$$\beta\frac{\partial^2\theta}{\partial\beta^2} + (Q-\beta)\frac{\partial\theta}{\partial\beta} + 2\theta = -\frac{PrM_{egn}}{\chi_4}Ec_{rt}(e^{-\Psi\eta})^2, \quad (27)$$

where $Q = (1-H)$, and $H = \frac{Pr}{\kappa\Psi}\left(\frac{1}{\Psi} + S\right)$.

The boundary conditions are

$$\theta(\beta) = 1, \quad \theta(0) = 0. \quad (28)$$

The closed form solution of Eq. 26 in the form of Kummer's function (Abramowitz and Stegun, 1972) is

$$\theta(\beta) = \left(\frac{M\left(-2 + \frac{Pr}{\kappa\Psi}\left(S + \frac{1}{\Psi}\right), 1 + \frac{Pr}{\kappa\Psi}\left(S + \frac{1}{\Psi}\right), \beta\right)\beta\frac{Pr}{\kappa\Psi}\left(S + \frac{1}{\Psi}\right)}{M\left(-2 + \frac{Pr}{\kappa\Psi}\left(S + \frac{1}{\Psi}\right), 1 + \frac{Pr}{\kappa\Psi}\left(S + \frac{1}{\Psi}\right), -\frac{Pr}{\kappa\Psi^2}\right)2\left(-\frac{Pr}{\kappa\Psi^2}\right)\frac{Pr}{\kappa\Psi}\left(S + \frac{1}{\Psi}\right)} \right) \times \left(\frac{1}{\left(-2 + \frac{Pr}{\kappa\Psi}\left(S + \frac{1}{\Psi}\right)\right)\kappa\Psi^2\chi_4} \right) + \left(\frac{Pr}{\kappa\Psi}\left(S + \frac{1}{\Psi}\right)^2 + (-\beta-3)\frac{Pr}{\kappa\Psi}\left(S + \frac{1}{\Psi}\right) + \beta^2 - 2 \right) \times \left(-M_{egn}Ec_{rt}\kappa\Psi^2\frac{2\xi-1}{2\chi_4Pr}\frac{Pr}{\kappa\Psi}\left(S + \frac{1}{\Psi}\right) + \frac{M_{egn}Ec_{rt}\kappa\Psi^2}{2\chi_4Pr\left(-2 + \frac{Pr}{\kappa\Psi}\left(S + \frac{1}{\Psi}\right)\right)} \right). \quad (29)$$

where M is the confluent hypergeometric function (1st kind). The following is the solution to the energy equation:

TABLE 1 Thermophysical characteristics of water, Ag, and Au (Mahalakshmi and Vennila, 2020).

| | | $P(kgm^{-3})$ | $C_p(Jkg^{-1}K^{-1})$ | $K(Wm^{-1}.K^{-1})$ |
|--------------|-------------|---------------|-----------------------|---------------------|
| Host fluid | Water | 1,000.52 | 4,181.8 | 0.597 |
| Nanoparticle | Silver (Ag) | 10,500 | 235 | 429 |
| | Gold (Au) | 19,320 | 128 | 318 |

TABLE 2 Variation of ϕ , A_{vr} , M_{egn} , and M_{egn} on $-f''(0)$.

| ϕ | A_{vr} | M_{egn} | S | $K_{pr} = 1$ | 2 | 3 | 4 |
|--------|----------|-----------|-----|--------------|-------------|-------------|-------------|
| 0 | 0.5 | 2 | 0.3 | 1.657481343 | 1.815082580 | 1.959005252 | 2.092292460 |
| 0.12 | | | | 1.984443250 | 2.121805427 | 2.249833214 | 2.370204875 |
| 0.19 | | | | 2.035210788 | 2.170034896 | 2.296000878 | 2.414654530 |
| 0.13 | 0.1 | | | 2.333480582 | 2.538101852 | 2.725959990 | 2.900603636 |
| | 0.3 | | | 2.204829536 | 2.375274746 | 2.533104229 | 2.680763159 |
| | 0.4 | | | 2.112178384 | 2.265835379 | 2.408649271 | 2.542635502 |
| | 0.2 | 1 | | 2.345951098 | 2.527749136 | 2.696145995 | 2.853729822 |
| | | 2 | | 2.47583093 | 2.647856384 | 2.808400806 | 2.959495757 |
| | | 3 | | 2.598579716 | 2.762258380 | 2.915956678 | 3.061304242 |

TABLE 3 Numerical values of $-\theta'(0)$ for $Ec_{rt} = 1$, $Pr = 6.2$, and $N_{tr} = 1.5$.

Silver (Ag)

| ϕ | A_{vr} | M_{egn} | S | K_{pr} | 1 | 2 | 3 | 4 |
|--------|----------|-----------|---|----------|-------------|-------------|-------------|-------------|
| 0 | 0.3 | 1 | 1 | | 2.821624541 | 2.815382505 | 2.808359278 | 2.800973518 |
| 0.12 | | | | | 2.396432529 | 2.386817656 | 2.377578170 | 2.368727743 |
| 0.19 | | | | | 2.165174717 | 2.155072352 | 2.145507700 | 2.136449386 |

Gold (Au)

| ϕ | A | M_{egn} | S | K_{pr} | 1 | 2 | 3 | 4 |
|--------|-----|-----------|---|----------|-------------|-------------|-------------|-------------|
| 0 | 0.3 | 1 | 1 | | 2.821624541 | 2.815382505 | 2.808359278 | 2.800973518 |
| 0.12 | | | | | 2.344189203 | 2.335774423 | 2.327801131 | 2.320228978 |
| 0.19 | | | | | 2.096289269 | 2.088535032 | 2.081209005 | 2.074267988 |

$$\theta(\eta) = \left(\frac{e^{-\frac{Pr}{\kappa\Psi}\left(S+\frac{1}{\Psi}\right)} M \left(-2 + \frac{Pr}{\kappa\Psi} \left(S + \frac{1}{\Psi} \right), 1 + \frac{Pr}{\kappa\Psi} \left(S + \frac{1}{\Psi} \right), -\frac{Pr}{\kappa\Psi^2} e^{-\Psi\eta} \right)}{2M \left(-2 + \frac{Pr}{\kappa\Psi} \left(S + \frac{1}{\Psi} \right), 1 + \frac{Pr}{\kappa\Psi} \left(S + \frac{1}{\Psi} \right), -\frac{Pr}{\kappa\Psi^2} \right)} \right) \times \left(\frac{1}{\left(\kappa\Psi^2 \chi_4 \right) \left(-2 + \frac{Pr}{\kappa\Psi} \left(S + \frac{1}{\Psi} \right) \right)} \right) + \left(\frac{Pr}{\kappa\Psi} \left(S + \frac{1}{\Psi} \right)^2 + \left(-\frac{Pr}{\kappa\Psi^2} e^{-\Psi\eta} - 3 \right) \frac{Pr}{\kappa\Psi} \left(S + \frac{1}{\Psi} \right) + \left(\frac{Pr}{\kappa\Psi^2} e^{-\Psi\eta} \right)^2 - 4 \frac{Pr}{\kappa\Psi^2} e^{-\Psi\eta} + 2 \right) \times \left(\frac{M_{egn} Ec_{rt} \kappa\Psi^2}{2\chi_4 Pr \left(-2 + \frac{Pr}{\kappa\Psi} \left(S + \frac{1}{\Psi} \right) \right)} - M_{egn} Ec_{rt} \kappa\Psi^2 \frac{2\xi - 1 + \frac{Pr}{\kappa\Psi} \left(S + \frac{1}{\Psi} \right)}{2\chi_4 Pr} \right). \quad (30)$$

where

$$\lambda_3 = M \left(\frac{Pr}{\kappa\Psi} \left(S + \frac{1}{\Psi} \right) - 2, \frac{Pr}{\kappa\Psi} \left(S + \frac{1}{\Psi} \right) + 1, -\frac{Pr}{\Psi^2 \kappa} \right),$$

$$\lambda_4 = M \left(\frac{Pr}{\kappa\Psi} \left(S + \frac{1}{\Psi} \right) - 1, \frac{Pr}{\kappa\Psi} \left(S + \frac{1}{\Psi} \right) + 1, -\frac{Pr}{\Psi^2 \kappa} \right),$$

$$\lambda_5 = M \left(\frac{Pr}{\kappa\Psi} \left(S + \frac{1}{\Psi} \right), \frac{Pr}{\kappa\Psi} \left(S + \frac{1}{\Psi} \right) + 1, -\frac{Pr}{\Psi^2 \kappa} \right),$$

$$\Psi = \frac{1}{2} \chi_1 \chi_2 S + \frac{1}{2} \sqrt{\chi_1^2 \chi_2^2 S^2 - 8A_{vr}^2 \chi_1 \chi_2 - 4A_{vr} \chi_1 M_{egn} + \xi}.$$

As a result, the non-dimensional wall temperature was generated by the aforementioned equation. The local Nusselt number is as follows:

$$Nu = \frac{-k_{sf} x \left(\frac{\partial T}{\partial y} \right)_{y=0}}{k_{hf} (\Delta T)} = -\frac{k_{sf}}{k_{hf}} Re_x^{1/2} \theta'(0) = \frac{k_{hf}}{k_{sf}} Nu_x Re_x^{-1/2} = -\theta'(0). \quad (32)$$

$$\theta_\eta(0) = \left(\frac{Pr^2 \left(S + \frac{1}{\Psi} \right)^2 \lambda_3 \left(2\chi_4 Pr \Psi \left(S + \frac{1}{\Psi} \right) - 4\chi_4 \Psi^2 \kappa - M_{egn} Ec_{rt} Pr \right)}{2\kappa^2 \chi_4 \Psi^2 (-2 + Pr)} + \left(\frac{Pr \left(S + \frac{1}{\Psi} \right) (\lambda_4 - \lambda_3) \left(2\chi_4 Pr \Psi \left(S + \frac{1}{\Psi} \right) - 4\chi_4 \Psi^2 \kappa - M_{egn} Ec_{rt} Pr \right)}{\kappa^2 \lambda_3 \chi_4 \Psi} \right) - \left(\frac{1}{2\alpha \chi_4 \Psi \kappa} \left(-(\lambda_5 - \lambda_4) \left(-1 + \frac{PrS}{\kappa\Psi} + \frac{Pr}{\kappa\Psi^2} \right) \Psi + (\lambda_4 - \lambda_3) \right) \right) \left(-2\xi + \frac{PrS}{\kappa\Psi} + \frac{Pr}{\kappa\Psi^2} \right) \Psi \times \left(2\chi_4 Pr \Psi \left(S + \frac{1}{\Psi} \right) - 4\chi_4 \Psi^2 \kappa - M_{egn} Pr Ec_{rt} \right) + \left(\frac{-2Pr \left(S + \frac{1}{\Psi} \right) + \frac{4Pr}{\kappa}}{\kappa^2 \Psi} \right) \frac{Ec_{rt} M_{egn} \Psi^2 \kappa}{\chi_4 Pr \left(-2 + \frac{Pr}{\kappa\Psi} \left(S + \frac{1}{\Psi} \right) \right)} + \frac{Ec_{rt} M_{egn} \Psi^2}{\chi_4} \right). \quad (31)$$

4 Second law analysis

The interchange of momentum, temperature, and magnetic effects inside the fluid and at the surfaces generates a continual entropy accumulation, resulting in a non-equilibrium condition. The following formula can be used to compute the volumetric entropy inception factor (S_{Gen}):

$$S_{Gen} = \frac{k_{sf}}{T_\infty^2} \left(1 + \frac{16T^3\sigma^*}{3k^*} \right) \left(\frac{\partial T}{\partial y} \right)^2 + \frac{\mu_{sf}u^2}{T_\infty k} + \frac{\sigma^* B_0^2 u^2}{T_\infty}. \quad (33)$$

The impact of three independent mechanisms generating entropy production is reflected in Eq. 33. The first term of Eq. 33 shows the entropy inception provoked by heat transport along with a thermal impact, which is expressed by (E_{HT}), the second term represents the entropy inception because of a magnetic impact (E_{MGN}), and the entropy inception due to porous (E_{PM}) is described by the third term. Entropy is a measure of disordered in a system and its surroundings. The amount of non-dimensional entropy production $E_G = \frac{S_{Gen}}{S_{gen}}$ is

$$E_G = \chi_3 Re (1 + N_{tr}) \theta'(\eta)^2 + Br_{knn} K_{pr} f'(\eta)^2 + Br_{knn} \frac{M_{egn}}{\Omega} f'(\eta)^2, \quad (34)$$

where

$$S_{gen} = \frac{k_{hf}}{T_\infty^2 \left(\frac{\Delta T}{x} \right)^2}, \quad Br_{knn} = \frac{\mu_{sf} u_{re} x^2}{\Delta T k_{sf}}, \quad \Omega = \frac{T_\infty}{\Delta T}, \quad \text{and} \\ M_{egn} = \frac{\sigma B_0^2 u_{re}}{\mu_{hf}}, \quad (35)$$

where Ω is the ratio of free stream temperature to the change in temperature. Bejan (1979) proposed an additional parameter, the Bejan number (Be), to find out the irreversibility field. The Bejan number (Be) is the ratio of heat exchange irreversibility to the total amount of irreversibility inside the process, expressed as

$$Be = \frac{E_{HT}}{E_{HT} + E_{MGN} + E_{PM}}. \quad (36)$$

5 Results and discussion

The influence of several emerging factors on the velocity, temperature, and entropy inception fields has been demonstrated in the current phase to examine the impact of these parameters. Furthermore, under the effect of suction/injection parameter (S), permeability parameter K_{pr} , and magnetic parameter M_{egn} , Ec_{rt} , ϕ , Br_{knn} , Ω , and Rey , local skin friction, stream line, local Nusselt number, and Bejan (Be) number are presented. In this scenario, Figures 2–18 are plotted and Tables 1, 2, 3 are shown. Figures 2, 3 show the trend of the velocity field as the magnitude

of ϕ is varied. It is to be noted that the velocity field is accelerated due to an increment in the magnitude of the nanoparticle volume friction in the case of Ag– and Au– water with $S > 0$ depicted in Figure 2. Physically, inter-molecular forces are increased in the presence of nanoparticles, which leads to a reduction in the velocity distribution. In the case of both Ag– and Au– water nanofluids with $S < 0$, the velocity distribution decreases due to an increase in ϕ as shown in Figure 3. The variation of nanoparticle friction on the temperature field is shown in Figure 4. An increment is observed in temperature distribution while gaining the magnitude of ϕ . Physically, the friction factor is enhanced with the existence of nanoparticles due to friction, and the overall internal temperature is accelerated in both Ag– and Au– water.

Figure 5 depicts the influence of Ec_{rt} on the temperature profile. As heat energy is produced in Ag– and Au– water nanofluids caused by friction heat, the temperature field is being augmented with an increasing value of Ec_{rt} . The impression of M_{egn} on the temperature field is shown in Figure 6. It is pointed out that the temperature distribution increases with a gain in M_{egn} . In fact, the Lorentz effect has a considerable influence on M_{egn} . A greater Lorentz force is associated with elevated M_{egn} , whereas a smaller Lorentz strength is linked with lower M_{egn} . The larger Lorentz force creates more energy in both Ag– and Au– water, resulting in an increase in temperature change. The consequences of M_{egn} on $-f''(0)$ are plotted in Figure 7. It is perceived that an augmentation in the magnetic entity escalates skin friction at the wall in both Ag– and Au– water. Moreover, Ag– water has a higher rate of skin friction than the Au– water nanofluid. Figure 8 shows the reaction of the wall mass transport entity on $-f''(0)$. The magnitude of $-f''(0)$ is stated to be reduced due to the decreasing amount of the wall mass transport entity (S) for both Ag– and Au– water. Additionally, Ag– water has a higher rate of skin friction than the Au– water nanofluid. The effects of Ec_{rt} and K_{pr} are shown in Figures 9, 10. The heat transport rate is seen to decrease with the magnitude of Ec_{rt} and K_{pr} for both Ag– and Au– water nanofluids. It is also noted that the heat exchange rate rapidly decreases in the occurrence of Au– water than in the Ag– water in Figures 9, 10. Physically, the magnitude of $-\theta'(0)$ decreases as the value of the permeability parameter decelerates. Physically, the existence of a porous structure restricts nanofluid flow, slowing fluid velocity and decreasing the heat transport rate at the wall.

Figures 11, 17 plot the influence of different parameters on the entropy inception E_G and Bejan Be number to visualize the system's chaos. Figure 11 portrays the result of the Br_{knn} number. It is expressed that entropy inception is decreased with an increase in Br_{knn} . Additionally, more chaos is reported in the case of silver–water in the system than the gold–water nanofluid. Similar trends are shown in Figures 12, 14 for Rey and M_{egn} , respectively. The opposite behavior is observed in Figure 13 for Ω . In Figures 15, 17, the variation of Ec_{rt} , ϕ , and Ω is investigated.

It is perceived that Be is increased while increasing the value of Ec_{rt} , ϕ , and Ω . Physically, the Bejan Be number is, indeed, a non-dimensional quantity that shows the proportion of overall entropy creation that is generated by thermal dissipation. As a result, the Bejan number is a description of the entropy created by heat transmission and resistance to flow rather than a heat transport parameter.

Table 1 lists the thermophysical characteristics of H_2O , Ag , and Au . **Tables 2, 3** are constructed for numerical values of $-f''(0)$ and $-\theta'(0)$, respectively. **Figures 18A–C, Figures 19A–C** are plotted to provide insight into the flow pattern in the case of Ag - and Au - water (**Figure 16**).

6 Conclusion

The study presents an entropy inception investigation of magnetohydrodynamic Ag - and Au - H_2O nanofluid flows induced by an exponential stretching surface embedded in a porous medium with suction/injection and thermal conductivity. The investigation's principal conclusions have been summarized as follows:

- In both Ag - and Au - H_2O , the solid volume percentage has an accelerating effect on the velocity profile with suction/injection parameters.
- In both Ag - and Au - H_2O , the Ec_{rt} and M_{egn} have an increasing impact on the temperature profile.
- It is perceived that an augmentation in the magnetic entity escalates skin friction at the wall in both Ag - and Au - water. Moreover, Ag - water has a higher rate of skin friction than the Au - water nanofluid.
- The heat transport rate is a decreasing function of Ec_{rt} and K_{pr} for both Ag - and Au - water nanofluids.
- It is also noted that the heat exchange rate rapidly decreases in the occurrence of Au - water than in Ag - water.
- The entropy inception is an increasing function of Br_{knn} , Re_y , and M_{egn} in both Ag - and Au - water.

References

- Abbasi, A., Farooq, W., Khan, M. I., Khan, S. U., Chu, Y. M., Hussain, Z., et al. (2021). Entropy generation applications in flow of viscoelastic nanofluid past a lubricated disk in presence of nonlinear thermal radiation and Joule heating. *Commun. Theor. Phys.* 73 (9), 095004.
- Abd El-Aziz, M., and Afify, A. A. (2019). MHD Casson fluid flow over a stretching sheet with entropy generation analysis and Hall influence. *Entropy* 21 (6), 592. doi:10.3390/e21060592
- Abramowitz, M., and Stegun, L. A. (1972). *Handbook of Mathematical Functions* 55. Washington, D. C.: National Bureau of Standards/Amer. Math. Soc. Providence.
- Afridi, M., Qasim, M., Khan, I., and Tlili, I. (2018). Entropy generation in MHD mixed convection stagnation-point flow in the presence of Joule and frictional heating. *Case Stud. Therm. Eng.* 12, 292–300. doi:10.1016/j.csste.2018.04.002
- B Awati, V., Kumar, M., and Wakif, A. (2021). Haar wavelet scrutinization of heat and mass transfer features during the convective boundary layer flow of a nanofluid moving over a nonlinearly stretching sheet. *Partial Differ. Equations Appl. Math.* 4, 100192. doi:10.1016/j.padiff.2021.100192
- Bejan, A. (1979). Study of entropy generation in fundamental convective heat transfer. *J. Heat. Transf.* 101 (4), 718–725. doi:10.1115/1.3451063
- Bhatti, M. M., Abbas, T., and Rashidi, M. M. (2017). Entropy generation as a practical tool of optimisation for non-Newtonian nanofluid flow through a

- More chaos is observed in the case of Ag - water in the system than in the Au - water nanofluid.

Data availability statement

The original contributions presented in the study are included in the article/Supplementary Material; further inquiries can be directed to the corresponding author.

Author contributions

IR initiated the fluid model and methodology. TZ, IR, and MA solved the model using software. JA completed the write-up and assisted in fluid model development.

Funding

The work in this study has been supported by the Polish National Science Centre under the grant OPUS 14 No. 2017/27/B/ST8/01330.

Conflict of interest

The authors declare that the research was conducted in the absence of any commercial or financial relationships that could be construed as a potential conflict of interest.

Publisher's note

All claims expressed in this article are solely those of the authors and do not necessarily represent those of their affiliated organizations, or those of the publisher, the editors, and the reviewers. Any product that may be evaluated in this article, or claim that may be made by its manufacturer, is not guaranteed or endorsed by the publisher.

permeable stretching surface using SLM. *J. Comput. Des. Eng.* 4 (11), 21–28. doi:10.1016/j.jcde.2016.08.004

Bilal, S., Malik, M. Y., Awais, M., Rehman, K., Hussain, A., and Khan, I. (2017). Numerical investigation on 2D viscoelastic fluid due to exponentially stretching surface with magnetic effects: An application of non-fourier flux theory. *Neural Comput. Applic.* 30 (9), 2749–2758.

Chakrabarti, A., and Gupta, A. S. (1979). Hydromagnetic flow and heat transfer over a stretching sheet. *Quart. Appl. Math.* 37, 73–78. doi:10.1090/qam/99636

Choi, S. U. S. (1995). “Enhancing thermal conductivity of fluids with nanoparticles,” in *International mechanical engineering congress and exposition* (San Francisco, USA, 99–105. ASME, FED 231/MD, 66.

Hamad, M. (2011). Analytical solution of natural convection flow of a nanofluid over a linearly stretching sheet in the presence of magnetic field. *Int. Commun. Heat Mass Transf.* 38 (4), 487–492. doi:10.1016/j.icheatmasstransfer.2010.12.042

Hayat, T., Shinwari, W., Khan, S. A., and Alsaedi, A. (2021). Entropy optimized dissipative flow of Newtonian nanofluid by a curved stretching surface. *Case Stud. Therm. Eng.* 27, 101263. doi:10.1016/j.csite.2021.101263

Khan, S. A., Khan, M. I., Alsallami, S. A., Alhazmi, S. E., Alharbi, F. M., and El-Zahar, E. R. (2022). Irreversibility analysis in hydromagnetic flow of Newtonian fluid with joule heating: Darcy-forchheimer model. *J. Pet. Sci. Eng.* 212, 110206. doi:10.1016/j.petrol.2022.110206

Khan, W., and Pop, I. (2010). Boundary-layer flow of a nanofluid past a stretching sheet. *Int. J. Heat. Mass Transf.* 53 (11–12), 2477–2483. doi:10.1016/j.ijheatmasstransfer.2010.01.032

Mahabaleshwara, U. S., Aly, H. E., and Anushaa, T. (2022). MHD slip flow of a Casson hybrid nanofluid over a stretching/shrinking sheet with thermal radiation. *Chin. J. Phys.* doi:10.1016/j.cjph.2022

Mahalakshmi, D., and Vennila, B. (2020). Boundary layer flow of silver and gold nanofluids over a flat plate by adomain decomposition method. *AIP Conf. Proc.* 2277 (1), 170002. doi:10.1063/5.0025571

Mahato, R., Das, M., Sen, S. S. S., and Shaw, S. (2022). Entropy generation on unsteady stagnation-point Casson nanofluid flow past a stretching sheet in a porous medium under the influence of an inclined magnetic field with homogeneous and heterogeneous reactions. *Heat. Trans.* 51, 5723–5747. doi:10.1002/htj.22567

Manzoor, U., S Naqvi, S. M. R., Muhammad, T., Naeem, H., Waqas, H., and M Galal, A. (2022). Hydro-magnetic impact on the nanofluid flow over stretching/shrinking sheet using Keller-box method. *Int. Commun. Heat Mass Transf.* 135, 106114. doi:10.1016/j.icheatmasstransfer.2022.106114

Neethu, T. S., Sabu, A. S., Mathew, A., Wakif, A., and Areekara, S. (2022). Multiple linear regression on bioconvective MHD hybrid nanofluid flow past an

exponential stretching sheet with radiation and dissipation effects. *Int. Commun. Heat Mass Transf.* 135, 106115. doi:10.1016/j.icheatmasstransfer.2022.106115

Noghrehabadi, A., Pourrajab, R., and Ghalambaz, M. (2012). Effect of partial slip boundary condition on the flow and heat transfer of nanofluids past stretching sheet prescribed constant wall temperature. *Int. J. Therm. Sci.* 54, 253–261. doi:10.1016/j.ijthermalsci.2011.11.017

Noghrehabadi, A., Saffarian, M. R., Pourrajab, R., and Ghalambaz, M. (2013). Entropy analysis for nanofluid flow over a stretching sheet in the presence of heat generation/absorption and partial slip. *J. Mech. Sci. Technol.* 27 (3), 927–937. doi:10.1007/s12206-013-0104-0

Oztop, H. F., and Abu-Nada, E. (2008). Numerical study of natural convection in partially heated rectangular enclosures filled with nanofluids. *Int. J. Heat. Fluid Flow.* 29 (5), 1326–1336. doi:10.1016/j.ijheatfluidflow.2008.04.009

Prasannakumara, B. C. (2021). Numerical simulation of heat transport in Maxwell nanofluid flow over a stretching sheet considering magnetic dipole effect. *Partial Differ. Equations Appl. Math.* 4, 100064. doi:10.1016/j.padiff.2021.100064

Rashid, I., Haq, R. U., Khan, Z. H., and Al-Mdallal, Q. M. (2017). Flow of water based alumina and copper nanoparticles along a moving surface with variable temperature. *J. Mol. Liq.* 246, 354–362. doi:10.1016/j.molliq.2017.09.089

Rashidi, M. M., and Freidoonimehr, N. (2014). Analysis of entropy generation in MHD stagnation-point flow in porous media with heat transfer. *Int. J. Comput. Methods Eng. Sci. Mech.* 15 (4), 345–355. doi:10.1080/15502287.2014.915248

Rohni, A. M., Ahmad, S., and Pop, I. (2012). Flow and heat transfer over an unsteady shrinking sheet with suction in nanofluids. *Int. J. Heat. Mass Transf.* 55 (7–8), 1888–1895. doi:10.1016/j.ijheatmasstransfer.2011.11.042

Sithole, H., Mondal, H., and Sibanda, P. (2018). Entropy generation in a second grade magnetohydrodynamic nanofluid flow over a convectively heated stretching sheet with nonlinear thermal radiation and viscous dissipation. *Results Phys.* 9, 1077–1085. doi:10.1016/j.rinp.2018.04.003

Tayebi, T., Dogonchi, A. S., Karimi, N., Ge-JiLe, H., Chamkha, A. J., and Elmasry, Y. (2021). Thermo-economic and entropy generation analyses of magnetic natural convective flow in a nanofluid-filled annular enclosure fitted with fins. *Sustain. Energy Technol. Assessments* 46, 101274. doi:10.1016/j.seta.2021.101274

Wang, F., Khan, S. A., Khan, M. I., El-Zahar, E. R., Yasir, M., Nofal, T. A., et al. (2022). Thermal conductivity performance in propylene glycol-based Darcy-Forchheimer nanofluid flow with entropy analysis. *J. Pet. Sci. Eng.* 215, 110612. doi:10.1016/j.petrol.2022.110612

Yacob, N. A., Ishak, A., Pop, I., and Vajravelu, K. (2011). Boundary layer flow past a stretching/shrinking surface beneath an external uniform shear flow with a convective surface boundary condition in a nanofluid. *Nanoscale Res. Lett.* 6 (1), 314. doi:10.1186/1556-276x-6-314



OPEN ACCESS

EDITED BY

Adnan Abbasi,
Mohi-ud-Din Islamic University,
Pakistan

REVIEWED BY

Muhammad Hafeez,
Gdansk University of Technology,
Poland
Ali Akgül,
Siirt University, Turkey

*CORRESPONDENCE

Wasim Jamshed,
wasiktk@hotmail.com

SPECIALTY SECTION

This article was submitted to Process
and Energy Systems Engineering,
a section of the journal
Frontiers in Energy Research

RECEIVED 17 July 2022

ACCEPTED 08 August 2022

PUBLISHED 07 October 2022

CITATION

Rahman MM, Jamshed W, Devi. S SU,
Ibrahim RW, Pasha AA, Souayeh B,
Safdar R, Eid MR, Hussain SM and
Tag El Din ESM (2022), Quadratic
regression estimation of hybridized
nanoliquid flow using Galerkin finite
element technique considering shape
of nano solid particles.
Front. Energy Res. 10:996556.
doi: 10.3389/fenrg.2022.996556

COPYRIGHT

© 2022 Rahman, Jamshed, Devi. S,
Ibrahim, Pasha, Souayeh, Safdar, Eid,
Hussain and Tag El Din. This is an open-
access article distributed under the
terms of the [Creative Commons
Attribution License \(CC BY\)](#). The use,
distribution or reproduction in other
forums is permitted, provided the
original author(s) and the copyright
owner(s) are credited and that the
original publication in this journal is
cited, in accordance with accepted
academic practice. No use, distribution
or reproduction is permitted which does
not comply with these terms.

Quadratic regression estimation of hybridized nanoliquid flow using Galerkin finite element technique considering shape of nano solid particles

Mustafa Mutiur Rahman¹, Wasim Jamshed^{2*},
Suriya Uma Devi. S³, Rabha W. Ibrahim⁴, Amjad Ali Pasha⁵,
Basma Souayeh⁶, Rabia Safdar⁷, Mohamed R. Eid^{8,9},
Syed M. Hussain¹⁰ and El Sayed M. Tag El Din¹¹

¹Department of Mechanical and Mechatronics Engineering, University of Waterloo, Waterloo, ON, Canada, ²Department of Mathematics, Capital University of Science and Technology (CUST), Islamabad, Pakistan, ³Department of Mathematics, KPR Institute of Engineering and Technology, Coimbatore, India, ⁴Mathematics Research Center, Department of Mathematics, Near East University, Mersin, Turkey, ⁵Aerospace Engineering Department, King Abdulaziz University, Jeddah, Saudi Arabia, ⁶Department of Physics, King Faisal University, College of Science, Al-Ahsa, Saudi Arabia, ⁷Department of Mathematics, Lahore College Women University, Lahore, Pakistan, ⁸Department of Mathematics, Faculty of Science, New Valley University, Al-Kharga, Al-Wadi Al-Gadid, Egypt, ⁹Department of Mathematics, Faculty of Science, Northern Border University, Arar, Saudi Arabia, ¹⁰Department of Mathematics, Faculty of Science, Islamic University of Madinah, Medina, Saudi Arabia, ¹¹Electrical Engineering, Faculty of Engineering and Technology, Future University in Egypt, New Cairo, Egypt

Because of its multivariate particle suspension approach, the developing class of fluid has a better level of stability as well as increased heat transfer. In this regard, hybrid nanofluid outperforms ordinary fluid and even well-known nanofluid. In a slick environment, we investigate its fluidity and heat transfer qualities. Nano-leveled particle morphologies, porousness materials, variable thermal conductivity, slippage velocity, and thermal radiative effects are all being studied. The Galerkin finite element method is a numerical methodology for numerically solving the governing equations (G-FEM). For this analysis, a Powell-Eyring hybrid nanofluid (PEHNF) flowing via a permeable stretchable surface is used, which comprises two types of nanoparticles (NP), copper (Cu), and titanium alloy (Ti₆Al₄V) dispersed in sodium alginate (C₆H₉NaO₇). The heat transfer ratio of PEHNF (Ti₆Al₄V-Cu/C₆H₉NaO₇) remained much greater than that of conventional nanofluids (Cu-C₆H₉NaO₇), with a range of 43%–54%. When lamina particles are present, the thermal conductivity of the boundary layer increases dramatically, while spherical nanoparticles have the lowest thermal conductivity. As nanoparticles are added under their fractional sizes, radiative heat conductance, and flexible heat conductance, the system's entropy increases. The flow system's ability to transport mass decreases when molecule diffusivity decreases dramatically. This is theoretically related to a rise in Schmidt number against molecular diffusivity.

KEYWORDS

Powell-Eyring hybridized nanofluid, modified Buongiorno's structure, shape factor, irreversibility analysis, Galerkin finite element technique

Introduction

Different simulations, including the regulator rule scheme, Carreau's scheme, Cross' scheme, and Ellis's scheme, are offered to shed light on the behavior of HNFs, however, few researchers have investigated the Williamson liquid scheme (WLS). Williamson (1929) thought about the flow of hybrid nanofluids (HNFs) such as (pseudo-plastic liquids), proposed an equation system to represent the flow of HNFs, and then empirically verified the results. In an advanced gravitational investigation, researchers proposed that an echoing level of a WLS should movement concluded an inspired superficial. A real fluid has both the lowest and highest operational viscosities that relate to its molecular structure. The WLS measures together the lowest and highest thicknesses. During the attendance of revolution, Said et al. (Said et al., 2021) planned a 3D-class of HNF to additional upsurge the heat transfer (HT) rate completed by widening slip. Mandal et al. (Mandal et al., 2022) exploited an artificial neural network to form investigational statistics. Saha et al. (Saha et al., 2022) described an investigation of HT and rheological possessions of HNFs for refrigeration presentations. Survey studies by Al-Chlahawi et al. (Al-Chlahawi et al., 2022), Kursus et al. (Kursus et al., 2022), Xiong et al. (Xiong et al., 2021), and Muneeshwaran et al. (Muneeshwaran et al., 2021) respectively, can be located in this direction, while Dubey et al. (Dubey and Sharma, 2022) offered a short survey in HNF on mechanics revisions. Syed and Jamshed (Hussain and Jamshed, 2021) considered the movement of MHD tangent HNF *via* a strained slip's boundary layer. In accumulation, the demonstration of the extended HT of tangent hyperbolic fluids crossways a nonlinearly fluctuating slide containing HNFs was tested by Qureshi (Qureshi, 2022), Jamshed et al. (Jamshed et al., 2021a), and Parvin et al. (Parvin et al., 2021).

Puneeth et al. (Shankaralingappa et al., 2021) measured 3D-assorted convection movement of HNFs of a non-linear widening surface using a modified Buongiorno's nanofluids model (MBNM). Rana et al. (Rana et al., 2021) presented a study of HNF movement past a perpendicular platter with nanoparticle aggregation kinematics, the current slide, and important buoyancy force possessions utilizing MBNM. Mahanthesh et al. (Mahanthesh et al., 2021) estimated the HT optimization of HNFs with the help of MBNM. Owhaib and Al-Kouz (Owhaib and Al-Kouz, 2022) and Owhaib et al. (Owhaib et al., 2021) employed the concept of MBNM in 3D systems of movement and HT of bi-directional overextended HNF film showing an exponential heat generation. Hussain et al. (Hussain et al., 2022a) characterized a biochemical response and current of HNFs flow-through solar gatherer as potential solar energy applying the idea of MBNM. Roşca et al. (Roşca et al., 2021) engaged the movement

and HT of a stretching/shrinking slip by the virtue of MBNM. Akram et al. (Akram et al., 2022) analyzed the electroosmotic movement of silver-water HNF controlled by using two altered methods for NF including the MBNM. Areekara et al. (Areekara et al., 2022) suggested a study on NF movement with asymmetrical heat foundation and representative boundary conditions with the application by MBNM.

Nanofluids own the characteristics of the non-Newtonian fluid, together with the viscoelastic properties. Extended experimental work research is required to develop nanofluid viscosity models for use in simulation studies (Wang and Mujumdar, 2008; Bilgili et al., 2021). Therefore, the Powell-Eyring fluid is considered in the current model, together with the significance of non-Newtonian fluid properties. This type of fluid is proposed by Powell and Eyring (Hayat and Nadeem, 2018) in 1944. Moreover, Powell-Eyring fluid is one type of viscoelastic fluid. Eyring-Powell fluid model implements a higher-level complicated mathematical framework, but it is found to be the greater model over previous viscoelastic fluid models. This model is founded on the kinetic theories of liquids, not on empirical expressions. In addition, Eyring-Powell fluid model has Newtonian properties at low and great shear stress. Examples of Powell-Eyring fluids are polymer melts and solids suspended in non-Newtonian liquids. The significant implementations of Powell-Eyring fluid have been observed in engineering, manufacturing, and industrial areas such as polymers, pulp, plasma, and other biological technology. However, several researchers have investigated the properties of non-Newtonian Powell-Eyring nanofluid (Hayat et al., 2015; Malik et al., 2015; Hayat et al., 2017). Aziz and Afy (El-Aziz and Afify, 2019) chose the shooting technique, together with the Buongiorno nanofluid model to obtain the Casson nanofluid's numerical solution over a stretching sheet. At the initial stages of flow (primary and secondary flow), they concluded that the Hall parameter upsurges in the convective rate of heat and mass transfer, together with the drag coefficient. Moreover, the nanoparticle volume concentration parameter increases for increasing velocity slip values. Consequently, the Sherwood number is reduced. Subsequently, the influences on the magnet field and Soret-Dufour have been reportedly on non-rotational Newton's Oldroyd-B nanofluid stream bounded by the stretched sheet (Ali et al., 2021). This model is also being restricted under the modification of Fourier's law. For the step of numerical findings, the Galerkin-Finite element system was developed.

Porous media models (PMMs), frequently referred to as porous materials, have pores (vacuums). The thin part of the material is referred to as the "matrix" or "frame." Typically, a fluid is injected into the pores (fluid or fume). Though the material that makes up the frame is regularly hard, structures

like foams might profit from the idea of PMM. To apply solar heat, Jamshed et al. (Jamshed et al., 2021b) employed PMM in solar aircraft combining tangent HNFs. Using the PMM in HNFs, Shahzad et al. (Shahzad et al., 2021) developed a comparative mathematical study of HT. Numerical conduct of a 2D-Magneto double-diffusive convection flow of HNF over PMM was provided by Parvin et al. (Parvin et al., 2021). Faisal et al. (Shahzad et al., 2022a) reported that using HNFs rather than PMM increased the thermal efficacy of solar water pumps. Banerjee and Paul (Banerjee and Paul, 2021) examined the most recent research and advancements concerning PMM combustion applications. For pebble-bed devices, Zou et al. (Zou et al., 2022) designed an explicit system of stone heat in the PMM. PMM substantiation using stress drip dimensions was suggested by Lee et al. (Lee et al., 2022). On a constructed soaking soil pile model, Cui et al. (Cui et al., 2021) investigated a numerical analysis of the solution for longitudinal quivering of a fluctuating pile based on PMM. A machine learning approach was taken by Alizadeh et al. (Alizadeh et al., 2021) to calculate transference and thermodynamic processes in metaphysical systems HT in HNFs movement in PMM. A non-homogenous HNF was proposed by Rashed et al. (Rashed et al., 2021) for 3D convective movement in enclosures with assorted PMM (AdnanKhan et al., 2021; Adnan and Ashraf, 2022a; Khan et al., 2022a; Alharbi et al., 2022; Ashraf et al., 2022a; Ashraf et al., 2022b; Adnan and Ashraf, 2022b; Khan et al., 2022b; Khan et al., 2022c; Murtaza et al., 2022). presented the latest updating that involves the traditional nanofluids with the features of heat and mass transmission in a different physical situation.

The rate of HT through a component thickness of a material per unit area per temperature variation is known as the variable thermal conductivity (VTC) of that material. Alternatively said, the VTC is inversely proportional to the temperature capacity. Gbadeyan et al. (Olabode et al., 2021) studied the effect of VTC and thickness on Casson NF movement with convective warming and velocity slide. Mabood et al. (Mabood et al., 2021) impacted the Stefan blowing and mass convention on the movement of HNF of VTC in a revolving disk. Abouelregal et al. (Abouelregal et al., 2021) checked the thermo-viscoelastic fractional model of revolving HNFs with VTC owing to mechanical and current loads. Swain et al. (Swain et al., 2021) utilized the HT and stagnation-point movement of influenced HNFs with VTC. Also, Ahmed et al. (Ahmed et al., 2021) considered the HT of MHD movement of HNFs via an exponential penetrable widening arched surface with VTC. Mahdy et al. (Mahdy et al., 2021) employed the VTC and hyperbolic two-temperature philosophy throughout the magneto-photothermal model of semiconductors induced by laser pulses. Hobiny and Ibrahim (Hobiny and Abbas, 2022) analyzed the impacts of VTC in a semiconducting medium utilizing the finite element technique. Ahmad et al. (Ahmad et al., 2022a) studied the unsteady 3D-bio convective movement of HNFs by an exponentially widening sheet with VTC and chemical reaction. Din et al. (Din et al., 2022) assumed the entropy generation from convective released moving exponential porous fins with VTC and

interior temperature compeers. For more details see Refs (Akgül et al., 2022; Attia et al., 2022; Ahmad et al., 2022b; Bilal et al., 2022; Qureshi et al., 2022; Safdar et al., 2022).

A statistical technique called quadratic regression estimation (QRE) is considered to identify the parabola equation that finest fits a given collection of data. Finding the equation of the conventional line that most closely fits a collection of information is the goal of this sort of regression, which is an extension of modest linear regression. Jamei et al. (Jamei et al., 2022) estimated the thickness of HNFs for current energy using the QRE. Nandi et al. (Nandi et al., 2022a; Nandi et al., 2022b) suggested different investigations on HNFs based on QRE. Bhattacharyya et al. (Bhattacharyya et al., 2022) introduced a numerical and statistical method to capture the movement characteristics of HNFs containing copper and grapheme HNs utilizing QRE. Kumbhakar and Nandi (Kumbhakar and Nandi, 2022) presented an unsteady MHD radiative-dissipative movement of HNFs of a widening sheet with slide and convective conditions employing QRE. Said et al. (Said et al., 2022) considered the application of the original outline by collaborative boosted QRE of HNFs. Chen et al. (Chen et al., 2022a; Chen et al., 2022b) gave a long approximation of the physical properties of HNFs.

By focusing on the flowing rapidity of a Powell-Eyring HNFs as well as thermal transmission with changing heat and current conductance flowing through a stretched permeable material, this work intends to bridge a gap in the previous survey and fill a knowledge gap. The flow of nanoliquid was geometrically modeled using a single-phase nanoliquid. The foundation liquid in the investigation of copper (Cu) and titanium alloy (Ti₆Al₄V) hybrid nanoparticles is sodium alginate (C₆H₉NaO₇). The regulatory equations of the Powell-Eyring hybridization nanoliquid are transformed into ordinary differential equations (ODEs). The influences of porous parameters, thermal radiative fluxing, and variable thermal conductance are considered in the examination. Then, the effects of the slippage velocity and nanoparticle shape factors are probed in flowing and entropy aspects. The obtained ODEs are solved numerically using the Galerkin finite element technique and the necessary prevailing parametric parameters. Numerical results are shown graphically, and comments are built upon. In-depth research has been done on the possessions of particle morphologies, the convective slide boundary condition, the thermal energy movement, and the slippery velocity.

Flow examination

Analysis of movement shows how a superficial moves horizontally at an accelerating rate.

$$U_w(x, t) = \frac{ex}{1 - \Omega t}, \quad (1)$$

where e is the preliminary increasing amount. Solitary slip heat is $\Theta_w(x, t) = \Theta_\infty + \frac{e^*x}{1 - \Omega t}$ and based on the suitability, pretend to be

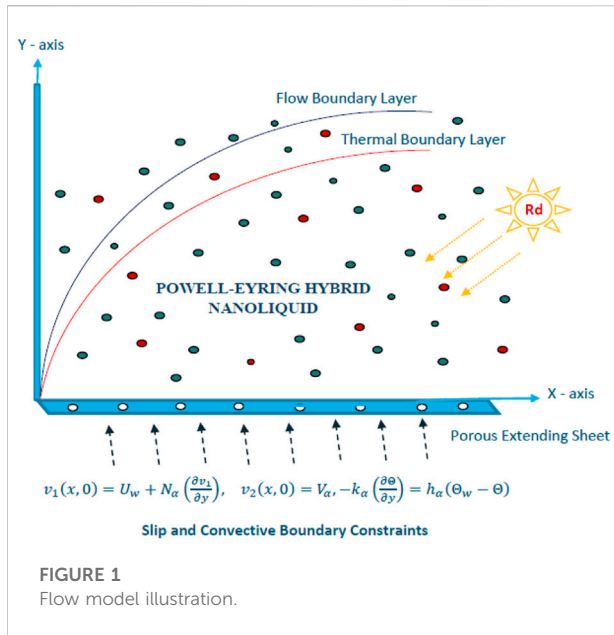


FIGURE 1
Flow model illustration.

stable at $x = 0$, e^* , Θ_w and Θ_∞ let the current difference ratio, surface heat, and free-streaming heat, consistently.

Under the following hypotheses and constraints, the theoretical framework is selected:

- 1) Unsteady two-dimensional laminar flowing.
- 2) Boundary-layer guesstimate.
- 3) Modified Buongiorno's structure.
- 4) Non-Newtonian PEHNFs.
- 5) Different effects i.e., porous medium, variable thermal conductivity, radiative flowing, and nanomolecules shaped influence.
- 6) Penetrable expanding surface.
- 7) Slip and convective boundary constraints.

The exact formulary of the stress tensor of fluid follows the Powell-Eyring relationship is provided as (Aziz et al., 2021):

$$\tau_{ij} = \mu_{mf} \left(\frac{\partial u_i}{\partial x_j} \right) + \frac{1}{\zeta} \sinh^{-1} \left(\frac{1}{\varrho^*} \frac{\partial u_i}{\partial x_j} \right). \quad (2)$$

Here, μ_{mf} is the mechanical viscosity of PEHNF, and ζ and ϱ^* are matter constants. The movement geometric is illuminated in Figure 1.

Framed model

Classic formulas (Aziz et al., 2021) of a viscidness P-EHNF beside with entropy assembly befittingly adapted underneath normal boundary-layer approximations *via* a penetrable substantial, porous medium, variable thermal conductivity, and radiative flowing are

TABLE 1 Thermo-physical properties of PENF.

| Aspect | Nanoliquid |
|-----------------------------------|--|
| Viscid (μ) | $\mu_{nf} = \mu_f (1 - \phi)^{-2.5}$ |
| Density (ρ) | $\rho_{nf} = (1 - \phi)\rho_f - \phi\rho_s$ |
| Heat capacity (ρC_p) | $(\rho C_p)_{nf} = (1 - \phi)(\rho C_p)_f + \phi(\rho C_p)_s$ |
| Thermal conductivity (κ) | $\frac{\kappa_{nf}}{\kappa_f} = \left[\frac{(\kappa_s + (m-1)\kappa_f) - (m-1)\phi(\kappa_f - \kappa_s)}{(\kappa_s + (m-1)\kappa_f) + \phi(\kappa_f - \kappa_s)} \right]$ |

$$\frac{\partial v_1}{\partial x} + \frac{\partial v_2}{\partial y} = 0, \quad (3)$$

$$\frac{\partial v_1}{\partial t} + v_1 \frac{\partial v_1}{\partial x} + v_2 \frac{\partial v_1}{\partial y} = \left(\nu_{mf} + \frac{1}{\rho_{mf} \zeta \varrho^*} \right) \frac{\partial^2 v_1}{\partial y^2} - \frac{1}{2\beta \varrho^{*3} \rho_{mf}} \left(\frac{\partial v_1}{\partial y} \right)^2 \frac{\partial^2 v_1}{\partial y^2} - \frac{\mu_{mf}}{\rho_{mf} k} v_1, \quad (4)$$

$$\frac{\partial \Theta}{\partial t} + v_1 \frac{\partial \Theta}{\partial x} + v_2 \frac{\partial \Theta}{\partial y} = \frac{1}{(\rho C_p)_{mf}} \left[\frac{\partial}{\partial y} \left(\kappa_{mf}^* \frac{\partial \Theta}{\partial y} \right) \right] - \frac{1}{(\rho C_p)_{mf}} \left[\frac{\partial q_r}{\partial y} \right], \quad (5)$$

$$v_1 \frac{\partial C^*}{\partial x} + v_2 \frac{\partial C^*}{\partial y} = D_B \frac{\partial^2 C^*}{\partial y^2} + \frac{D_T}{T_\infty} \frac{\partial^2 \Theta}{\partial y^2} - k_1 (C^* - C_\infty^*). \quad (6)$$

the suitable boundary conditions are (Aziz et al., 2021):

$$v_1(x, 0) = U_w + N_\alpha \left(\frac{\partial v_1}{\partial y} \right), v_2(x, 0) = V_\alpha, -k_\alpha \left(\frac{\partial \Theta}{\partial y} \right) = h_\alpha (\Theta_w - \Theta) C^* = C_w^*, \quad (7)$$

$$v_1 \rightarrow 0, \Theta \rightarrow \Theta_\infty, C^* \rightarrow C_\infty^* \text{ as } y \rightarrow \infty. \quad (8)$$

Where a flow speed is of the structure $\mathbf{v}^* = [v_1(x, y, t), v_2(x, y, t), 0]$. Time is denoted by t , Θ signifies a fluid temperature. The penetrability of an expanding plate is symbolized by V_α . N_α is the slip length. The porousness of NF is characterized by k . The additional parameters like thermal conductivity of nanosolid and heat transmission factor are represented by k_0 and h_f , respectively.

The mongrelized nanoliquid is combined principally with Cu nano molecules in machine grease standard liquid at a constant fractional size (ϕ_{Cu}) and it is put at 0.09 all about the study. $\text{Ti}_6\text{Al}_4\text{V}$ NP were put together into HNFs consuming attentiveness scope (ϕ_{TA}).

The combination of nanomolecules in the basefluid runs to a difference in the characteristics thermophysically. Table 1 summarises the relevant parameters for PENF (Reddy et al., 2014; Din et al., 2022).

ϕ is the nanomolecules fractional volume factor. μ_f , ρ_f , $(C_p)_f$, σ_f and k_f are dynamical viscidness, density, efficient heat capacitance, and the electrical and thermal conductance of the base fluid, correspondingly. The further attributes ρ_s , $(C_p)_s$,

TABLE 2 Thermophysical properties of PEHNF.

| Aspect | Hybrid nanoliquid |
|-----------------------------------|---|
| Viscid (μ) | $\mu_{hnf} = \mu_f (1 - \phi_{Cu})^{-2.5} (1 - \phi_{TA})^{-2.5}$ |
| consistency (ρ) | $\rho_{hnf} = (1 - \phi_{TA}) \{ (1 - \phi_{Cu}) \rho_f + \phi_{Cu} \rho_{p_1} \} + \phi_{TA} \rho_{p_2}$ |
| Heat capacity (ρC_p) | $(\rho C_p)_{hnf} = [(1 - \phi_{TA}) \{ (1 - \phi_{Cu}) (\rho C_p)_f + \phi_{Cu} (\rho C_p)_{p_1} \}]$ |
| $+\phi_z (\rho C_p)_{p_2}$ | |
| Thermal conductivity (κ) | $\frac{\kappa_{hnf}}{\kappa_f} = \left[\frac{(\kappa_{p_1} + (m-1)\kappa_f) - (m-1)\phi_{Cu}(\kappa_f - \kappa_{p_1})}{(\kappa_{p_1} + (m-1)\kappa_f) + \phi_{Cu}(\kappa_f - \kappa_{p_1})} \right]$ |

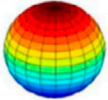


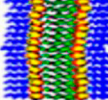

| Nanoparticles Type | Sphere | Hexahedron | Tetrahedron | Column | Lamina |
|--------------------|---|---|---|--|---|
| Shape |  |  |  |  |  |
| m | 3 | 3.7221 | 4.0613 | 6.3698 | 16.1576 |

FIGURE 2

Standards of the practical shaped element for diverse particle shaped. The material possessions of the crucial sodium alginate ($C_6H_9NaO_7$) and the various NP exploited in this research are indicated in Figure 3 (Xu and Chen, 2017; Makinde et al., 2018; Jamshed et al., 2021d).

σ_f and k_s are the density, active heat capacitance, and the electrical and thermal conductance of nanomolecules, correspondingly. The physical properties of PEHNF are defined in Table 2 (Devi and Devi, 2016).

Herein, μ_{hnf} , ρ_{hnf} , $\rho(C_p)_{hnf}$ and κ_{hnf} indicates the dynamic viscous, density, specific temperature capacitor, and current conductivity of HNF. ϕ is a fractional size factor and $\phi_{hnf} = \phi_{Cu} + \phi_{TA}$ is the size parameter of solid-nanoparticle combination. μ_f , ρ_f , $(C_p)_f$ and κ_f are dynamic viscosity, density, specific heat capacity, and the thermal conducting of the ordinary fluid. ρ_{p_1} , ρ_{p_2} , $(C_p)_{p_1}$, $(C_p)_{p_2}$, κ_{p_1} and κ_{p_2} are the density constancy, precise heat competence, and current conducting of the solid-nanoparticle.

Heat conditional of heat conducting for hybrid nanoliquid blend is followed as (Jamshed et al., 2021c):

$$\kappa_{hnf}^*(\Theta) = \kappa_{hnf} [1 + \gamma(\Theta - \Theta_{\infty})(\Theta_w - \Theta_{\infty})^{-1}] \quad (9)$$

The significance of several nanomolecules shaped is identified as the nanomolecules shaped influence. Figure 2 gives the values of the practical shaped component for different element shapes are obtained as (Akgül et al., 2022): Figure 3 demonstrates the themophysical values of the used materials of HNF.




| Thermophysical Properties | ρ (kg/m ³) | C_p (J/kgK) | k (W/m) |
|---|-----------------------------|---------------|-----------|
| Sodium Alginate ($C_6H_9NaO_7$) | | | |
|  | 989 | 4175 | 0.6376 |
| Copper (Cu) | | | |
|  | 8933 | 385 | 401 |
| Titanium Alloy (Ti6Al4V) | | | |
|  | 4420 | 526.3 | 6.7 |

FIGURE 3

Substance effects of $C_6H_9NaO_7$ and NPs at 293 K.

PEHNF radiative flow only travels a little space resulting in the thickener of NF. Because this is happening, Rosseland's guesstimate for radiative fluxing (Shahzad et al., 2022b), is used in Eq. 5 and it is given

$$q_r = -\frac{4\sigma^*}{3k^*} \frac{\partial \Theta^4}{\partial y}, \quad (10)$$

Where σ^* is Stefan-Boltzmann amount and k^* is the absorbing factor.

Model solution

Boundary-value problem (BVP) formulas (3–6) are converted in the definition of the similarity procedure that converts the regulating PDEs to ODEs. Advancing streaming function ψ as the next

$$v_1 = \frac{\partial \psi}{\partial y}, v_2 = -\frac{\partial \psi}{\partial x}. \quad (10a)$$

and similarity transformations are

$$\begin{aligned} \delta(x, y) &= \sqrt{\frac{e}{\nu_f(1-\Omega t)}} y, \psi(x, y) = \sqrt{\frac{\nu_f e}{(1-\Omega t)}} x f(\delta), \theta(\delta) \\ &= (\Theta - \Theta_{\infty})(\Theta_w - \Theta_{\infty})^{-1} h_{\delta}(\Theta - \Theta_{\infty})(\Theta_w - \Theta_{\infty}). \end{aligned} \quad (11)$$

into Eqs. 3–6. We get

$$\begin{aligned} \left(\frac{1}{\phi_{x_1} \phi_{x_2}} + \frac{\beta_1}{\phi_{x_1}} \right) f''' + f f'' - f'^2 - \xi \left(f' + \frac{\delta}{2} f'' \right) - \frac{\beta_1 \beta_2}{\phi_{x_2}} f''^2 f''' \\ - \Gamma f' \\ = 0, \end{aligned} \quad (12)$$

$$\theta'' \left(1 + \gamma \theta + \frac{1}{\phi_{x_4}} P_r N_r \right) + \gamma \theta'^2 + P_r \frac{\phi_{x_3}}{\phi_{x_4}} \left[f \theta' - f' \theta - \xi \left(\theta + \frac{\delta}{2} \theta' \right) \right] = 0. \quad (13)$$

$$h'' + P_r Sc f h' + \frac{Nt}{Nb} \theta'' - Sc \chi h = 0. \quad (14)$$

with

$$\begin{aligned} f(0) = S, f'(0) = 1 + \varepsilon f''(0), \theta'(0) \\ = -B_{\alpha}(1 - \theta(0)) f'(\delta) \rightarrow 0, f''(\delta) \rightarrow 0, \theta(\delta) \rightarrow 0, h(\delta) \rightarrow 0 \text{ as } \delta \rightarrow \infty. \end{aligned} \quad (15)$$

where ϕ'_{is} ; $1 \leq i \leq 4$ in Eqs. 12, 13 establishes the thermophysical characteristics of the Powell-Eyring nanofluid.

$$\begin{aligned} \phi_{x_1} &= (1 - \phi_{Cu})^{2.5} (1 - \phi_{TA})^{2.5}, \phi_{x_2} \\ &= (1 - \phi_{TA}) \left\{ (1 - \phi_{Cu}) + \phi_1 \rho_{p1} / \rho_f \right\} + \phi_{TA} \frac{\rho_{p2}}{\rho_f}, \end{aligned} \quad (16)$$

$$\phi_{x_3} = (1 - \phi_{TA}) \left\{ (1 - \phi_{Cu}) + \phi_{Cu} \frac{(\rho C_p)_{p1}}{(\rho C_p)_f} \right\} + \phi_{TA} \frac{(\rho C_p)_{p2}}{(\rho C_p)_f}, \quad (17)$$

$$\begin{aligned} \phi_{x_4} &= \left[\frac{(\kappa_{p2} + (m-1)\kappa_{nf}) - (m-1)\phi_{TiO_2}(\kappa_{nf} - \kappa_{p2})}{(\kappa_{p2} + (m-1)\kappa_{nf}) + \phi_{TiO_2}(\kappa_{nf} - \kappa_{p2})} \right] \\ &\quad \left[\frac{(\kappa_{p1} + (m-1)\kappa_f) + \phi_{Cu}(\kappa_f - \kappa_{p1})}{(\kappa_{p1} + (m-1)\kappa_f) - (m-1)\phi_{Cu}(\kappa_f - \kappa_{p1})} \right]. \end{aligned} \quad (18)$$

Meticulous authentication is done on Eq. 3. Notation ' is used for the demonstration of derivatives concerning δ . The parametric values were defined in Table 3.

It is noticed a variety of factors depend on the similarity variable " Ω " and unsteadiness. Consequently, to acquire non-

similar solutions for the suggested problematic computational results are processed for local similar considerations.

Drag force and nusselt quantity

The drag force C_f together with a Nusselt amount Nu_x are the physical amounts of importance that dominate the light and can be confirmed as (Aziz et al., 2021)

$$C_f = \frac{\tau_w}{\rho_f U_w^2}, Nu_x = \frac{x q_w}{k_f (\Theta_w - \Theta_{\infty})} \quad (19)$$

where τ_w and q_w correspond to the heating flux revealed by

$$\begin{aligned} \tau_w &= \left(\left(\mu_{mf} + \frac{1}{\zeta \varrho^*} \right) \frac{\partial v_1}{\partial y} - \frac{1}{6 \zeta \varrho^{*3}} \left(\frac{\partial v_1}{\partial y} \right)^3 \right)_{y=0}, q_w \\ &= -k_{mf} \left(1 + \frac{16}{3} \frac{\sigma^* T_{\infty}^3}{\kappa^* \nu_f (\rho C_p)_f} \right) \left(\frac{\partial \Theta}{\partial y} \right)_{y=0}. \end{aligned} \quad (20)$$

Employing the dimensionless makeovers (11), one acquires

$$\begin{aligned} C_f Re_x^{\frac{1}{2}} &= \left[\left(\frac{1}{\phi_{x_1} \phi_{x_2}} + \beta_1 \right) f''(0) - \frac{\beta_1 \beta_2}{3} (f''(0))^3 \right], Nu_x Re_x^{-\frac{1}{2}} \\ &= -\frac{k_{mf}}{k_f} (1 + N_r) \theta'(0). \end{aligned} \quad (21)$$

Where Nu_x signifies Nusselt quantity and C_f specify the skin resistance. $Re_x = \frac{u_w x}{\nu_f}$ signifies $Re_x = \frac{u_w x}{\nu_f}$ signifies local Reynolds amount based on $u_w(x)$.

Numerical implementation: Galerkin finite element method

The relevant constraints of the present system were studied numerically using the finite element technique. The finite element approach is based on the partitioning of the desired domain into elements (finite). The FES (finite element scheme) is covered in this section. Figure 4 depicts the flow chart of the finite element method. This method has been employed in numerous computational fluid dynamics (CFD) problems; the assistances of employing this methodology are discussed further below. II- A Galerkin finite element manner (G-FEM) is utilized to determine the solutions of highly elliptic equations (Brewster, 1992) (non-linear). Using a finite element technique, the domain of the current exemplary is broken into small parts. G-FEM is used in a variety of applications, including electrical systems, solid mechanics, chemical processes, and fluid-related challenges. The phases of the G-FEM strategy are as next:

Phase-I. Weak form is derived from strong form (mentioned ODEs), and residuals are computed.

TABLE 3 Explanation of the entrenched control constraints.

| Symbol | Name | Formula | Default value |
|---------------|--------------------------------|---|---------------|
| β_1 | Non-Newtonian Powell-Eyring-I | $\beta_1 = \frac{1}{\mu_f \zeta_0^*}$ | 0.1 |
| β_2 | Non-Newtonian Powell-Eyring-II | $\beta_2 = \frac{U_w^3}{2\zeta_0^* \nu_f x}$ | 0.1 |
| Γ | Porous media | $\Gamma = \frac{\nu_f (1-\Omega t)}{e k}$ | 0.1 |
| P_r | Prandtl number | $P_r = \frac{\nu_f}{\alpha_f}$ | 6.5 |
| ϕ | Volume fraction | - | 0.18 |
| m | Shape factor | - | 3 |
| S | Suction/injection parameter | $S = -V_a \sqrt{\frac{1}{\nu_f e}}$ | 0.4 |
| N_r | Thermal radiation parameter | $N_r = 5.33 \frac{\sigma^* \Theta_\infty^3}{\kappa^* \nu_f (\rho C_p)_f}$ | 0.3 |
| B_a | Biot number | $B_a = \frac{h_a}{k_a} \sqrt{\frac{\nu_f (1-\Omega t)}{e}}$ | 0.2 |
| Sc | Schmidt number | $Sc = \frac{\nu}{D_b}$ | 0.3 |
| Nb | Brownian motion | $Nb = \frac{\tau D_b (C_w^* - C_\infty^*)}{\nu}$ | 0.1 |
| Nt | Thermophoresis parameter | $Nt = \frac{\tau D_T (\bar{E}_w - \bar{E}_\infty)}{\nu \bar{E}_\infty}$ | 0.3 |
| ε | Velocity slip | $\varepsilon = \sqrt{\frac{e}{\nu_f (1-\Omega t)}} N_a$ | 0.3 |

Phase -II. Shape functions are linearly taken, and G-FEM is used to generate a weak form.

Phase -III. The assembly method is used to build stiffness elements, and a global stiffness matrix is created.

Phase -IV. Using the Picard linearizing technique, an algebraic structure (non-linear equalities) is produced.

Phase -V. Employing the next halting conditions, algebraic equations are simulated using 10⁻⁵ (computational tolerance).

$$\left| \frac{\delta_{i+1} - \delta_i}{\delta^i} \right| < 10^{-5}. \quad (23)$$

Additionally, the Galerkin restricted constituent technique's watercourse summary is represented in Figure 4.

Code authentication

On the one hand, the validity of the computational technique was tested by comparing the current method's performance to the available data on heat transfer rate in Refs. (Hussain et al., 2022b; Bouslimi et al., 2022). Table 3 demonstrates the consistent comparison found across the investigations. The current study's provided results, on the other hand, are quite accurate.

Irreversibility analysis (second law of thermodynamics)

A crucial aspect that interests scientists and researchers is the reduction of energy resource waste. Therefore, these necessary outcomes for researchers are gained by enhancing the functionality of earlier systems. Systems' entropy creation is examined in order

to achieve energy irreversibility and reduce waste. Design is prearranged about entropy generation in NFs (Hussain, 2022)

$$E_G = \frac{k_{mf}}{\Theta_\infty^2} \left\{ \left(\frac{\partial \Theta}{\partial y} \right)^2 + \frac{16}{3} \frac{\sigma^* \Theta_\infty^3}{\kappa^* \nu_f (\rho C_p)_f} \left(\frac{\partial \Theta}{\partial y} \right)^2 \right\} + \frac{\mu_{mf}}{\Theta_\infty} \left(\frac{\partial v_1}{\partial y} \right)^2 + \frac{\mu_{mf} v_1^2}{k \Theta_\infty} \quad (21)$$

The irreversibility of thermal transport is represented by the leading term in the preceding equation, while the frictional and porous media effects are represented by the following terms. The nondimensional entropy establishment is prearranged by N_G [(Jamshed and Nisar, 2021; Jamshed et al., 2022a)].

$$N_G = \frac{\Theta_\infty^2 e^2 E_G}{k_f (\Theta_w - \Theta_\infty)^2}. \quad (22)$$

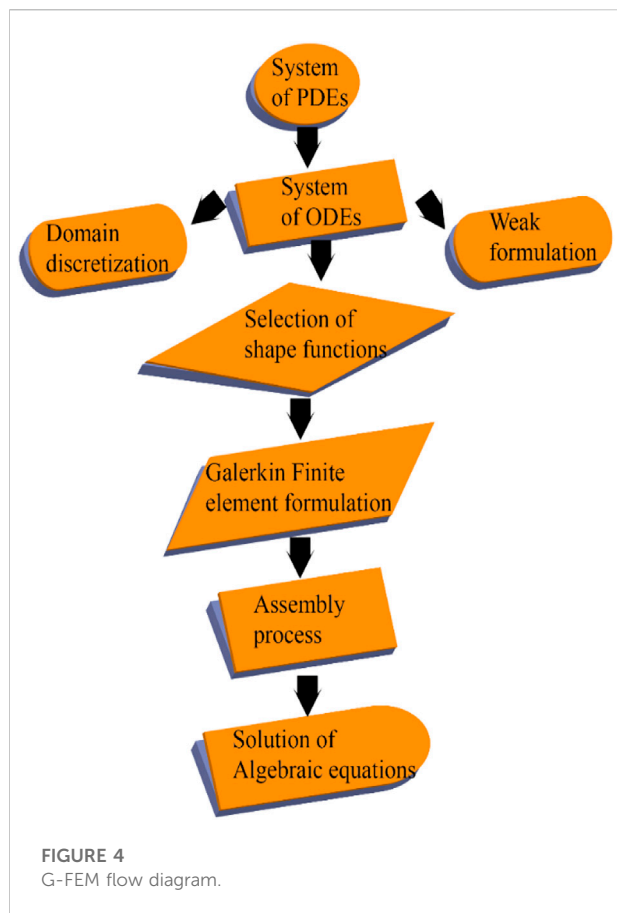
Eq. 11 is utilized to obtain a dimensionless equation regarding entropy formation as follows,

$$N_G = Re \left[\phi_4 (1 + N_r) \theta'^2 + \frac{1}{\phi_{x1}} \frac{B_r}{\Lambda} (f''^2 + \Gamma f'^2) \right], \quad (23)$$

Here, Re and B_r indicate Reynolds and Brinkmann quantities. Λ signs nondimensional current gradient.

Quadratic regression assessment of frictional force and thermal gradients of the surface

Quadratic regression analysis (QRA) is the statistical procedure that was used to test the elements that influence the flow in the



system one at a time. Technically, this process works with the single key aspect and tends to explore its significance over the flow by keeping the other constraints as constants. In this section, the features of frictional force and Nusselt quantity are examined under Quadratic regression analysis (QRA).

Regarding the frictional factor f_x , after testing with 100 combinations of suction (S) and speed slippage constrain (ε) between 0.2 and 1.1, it was noted that those constraints tend to resist frictional factors.

QRA for the predicted Cf_x owed to pressure influence S and speed slippage ε variation is delivered by

$$Cf_{x(est)} = Cf_x + h_1 S + h_1 \varepsilon + h_3 S^2 + h_4 \varepsilon^2 + h_5 S \varepsilon, \quad (24)$$

Likewise, towards the Quadratic regression assessment of Nusselt quantity Nu_x , time-dependent variant ξ and radiative variable N_r were tested under 100 consistent values were presented as

$$Nu_{x(est)} = Nu_x + p_1 \xi + p_1 N_r + p_3 \xi^2 + p_4 (N_r)^2 + p_5 \xi N_r, \quad (25)$$

with h_1, h_2, h_3, h_4, h_5 and are the factors of QRA to guide for the reduced Cf_x and Nu_x , congruently.

Tables 4, 5 illustrate correspondences between the frictional factor (Cf_x) and the Nusselt quantity (Nu_x) under significant constraints for $\beta_1 = 0.1, \beta_2 = 0.3, \xi = 0.2, \Gamma = 0.1, \phi = 0.18, \phi_{Cu} = 0.09, \varepsilon = 0.3, \gamma = 0.2, N_r = 0.3, B_a = 0.3, S = 0.1, m = 3, P_r = 6.5, R_e = 5$ and $B_r = 5$. The ideal relative error limits σ_1 was deduced by the relation $\sigma_1 = |Cf_{x(est)} - Cf_x|/Cf_x$, similarly, $\sigma_2 = |Nu_{x(est)} - Nu_x|/Nu_x$ is employed for the relative error limits σ_2 . It can be evident that for the factors S or N_r , both the frictional factor (Cf_x) and the Nusselt quantity (Nu_x) tends to reduce the higher values of influencing factors. Variations in the velocity slip clarify the dominance of speed slippage ε over the suction factor S in the shear stress manipulations.

Because of the thermal outcome, the thermal slippage constrain plays a vital role in the heat transference rate. The reduced frictionless force mechanisms hold an upper hand over the QRA technique with fast and better convergence when the optimal regression estimate was introduced to the process and the percentage difference tends to be nearly zero.

Outcomes and review

Results of the numerical procedure adapted for the parametrical studies were showcased and discussed in this section. Influence constraints like $\beta_1, \beta_2, \xi, \Gamma, \phi, \varepsilon, N_r, B_a, S, \gamma, R_e$ and B_r were worked over the crucial aspects of flow, thermal, entropy, and concentration dispersion in the system. Plots from 6(a)-11(b) for $C_6H_5NaO_7$ traditional PENF and $Ti_6Al_4V-Cu/C_6H_5NaO_7$ PEHNF tend to visually illustrate the outcomes and significant impact of such parameters.

TABLE 4 Comparing of $-\theta'(0)$ with Pr when $\xi = 0, \phi = 0, \phi_{hnf} = 0, \gamma = 0, \varepsilon = 0, N_r = 0, S = 0$ and $B_a \rightarrow \infty$.

| Pr | Bouslimi et al. (Hussain et al., 2022b) | Hussain (Bouslimi et al., 2022) | Present Results |
|---------------------|---|---------------------------------|-----------------|
| 72×10^{-2} | 0.80876181 | 0.80876181 | 0.80878120 |
| 1×10^0 | 1.00000000 | 1.00000000 | 1.00000000 |
| 3×10^0 | 1.92357420 | 1.92357420 | 1.92357114 |
| 7×10^0 | 3.07314651 | 3.07314651 | 3.07335681 |
| 10×10^0 | 3.72055429 | 3.72055429 | 3.72055845 |

TABLE 5 Frictional factor (Cf_x) and ideal relative error bound (σ_1) for various values of suction (S) and speed slippage constraint (ε).

| S | Cf_x | h_1 | h_2 | h_3 | h_4 | h_5 | σ_1 |
|-----|---------|---------|--------|--------|---------|--------|------------|
| 0.5 | -1.3257 | -0.8022 | 1.6029 | 0.0250 | -1.3232 | 0.9033 | 0.0196 |
| 1.5 | -1.4202 | -0.7394 | 1.7238 | 0.0421 | -1.4197 | 0.7956 | 0.0185 |
| 2.5 | -1.7149 | -0.6527 | 1.9069 | 0.0829 | -1.5819 | 0.6210 | 0.0173 |
| 3.5 | -1.9015 | -0.4951 | 2.2036 | 0.1901 | -1.7452 | 0.3502 | 0.0104 |

Impact of powell-eyring parameter (β_2)

The illustration of the non-Newtonian Powell-Eyring fluid term (β_2) on the model profiles (flow velocity, temperature, and entropy) against a rising stream term (β_2) were depicted in Figures 5A,B,C. The velocity profile (Figure 5A) is decreased as the material term increases due to the material term shear

being induced by infinite fluid viscosity. As a result, yield stress restricts the flow, resulting in a velocity decrement towards the infinite fluid stream. The heat propagation in the Powell-Eyring fluid heat propagation was boosted, as shown in Figure 5B. This effect is caused by the support of the stretching surface in overcoming the material yield stress dominance. In addition, temperature-dependent control fluid viscosity causes the temperature distribution to rise at various levels. As the Powell-Eyring effect is augmented, the molecular bond is disrupted, and the particles are allowed to move freely. As a result, Powell-Eyring 's term has a minimal rising effect Figure 5B. In Figure 5C, the entropy variation is plotted versus the Powell-Eyring term. Under the increment of β_2 , the curves show different patterns. It illustrates an augmentation near the stretching wall, while a modest reduction is detected at a distance from it. The reason for this illustration is that when a large temperature gradient occurs at the surface, more entropy is produced, causing higher oscillations in nanoparticle mobility.

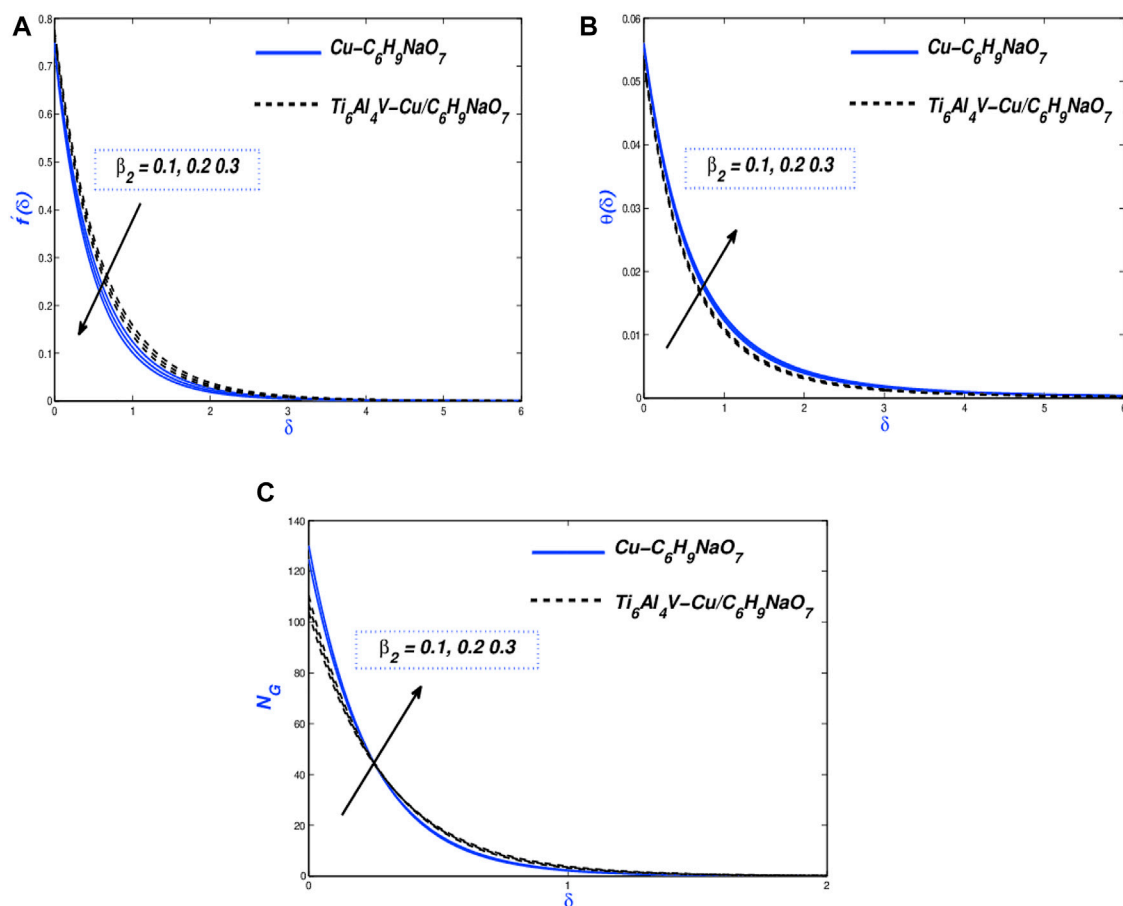


FIGURE 5 (A) $f'(\delta)$, (B) $\theta(\delta)$, and (C) N_G with diverse β_2 values.

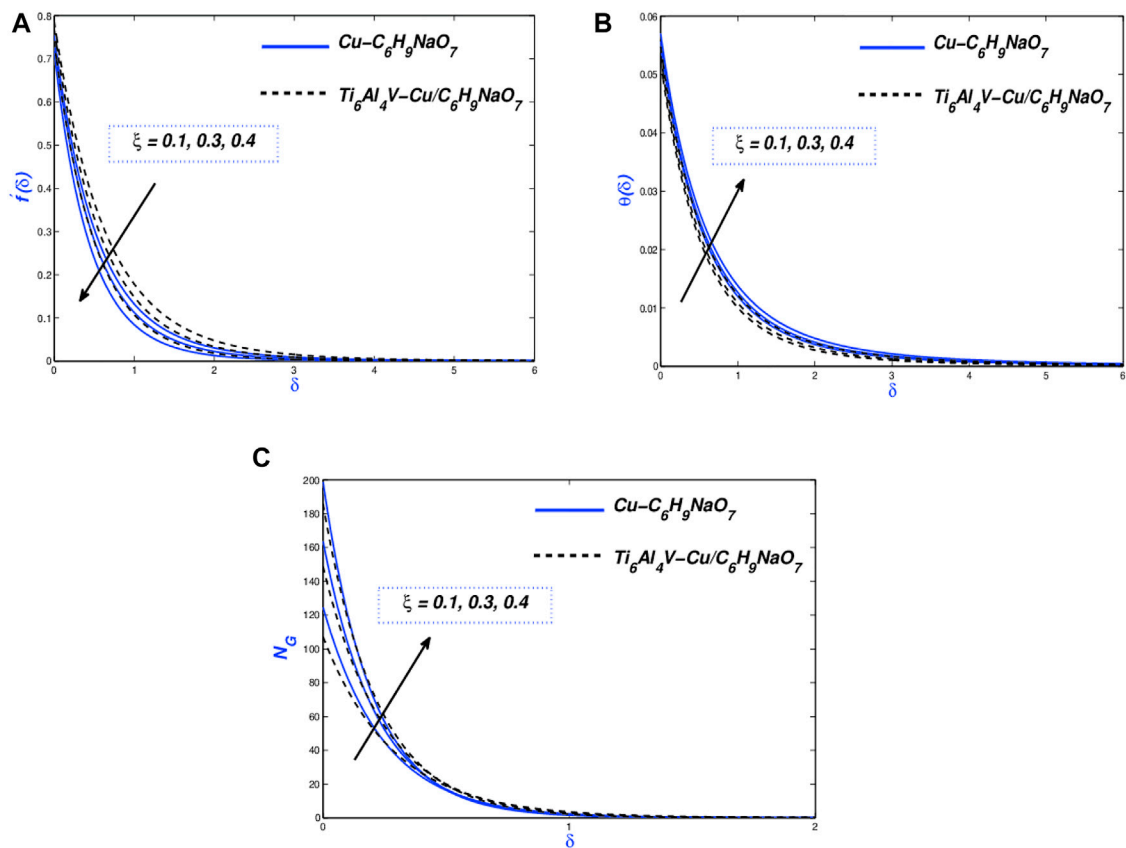


FIGURE 6
(A) $f'(\delta)$, (B) $\theta(\delta)$, and (C) N_G with diverse I values.

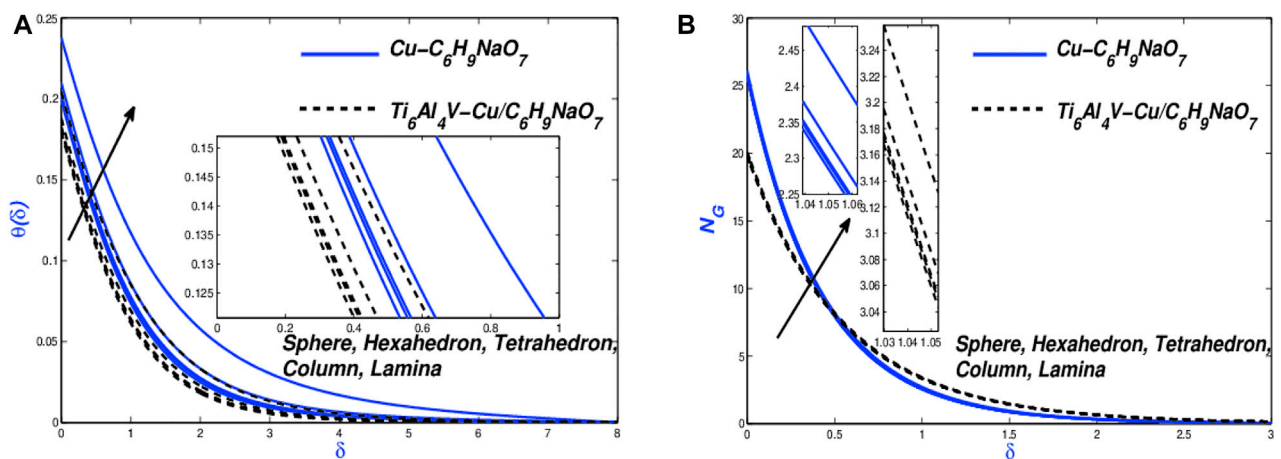
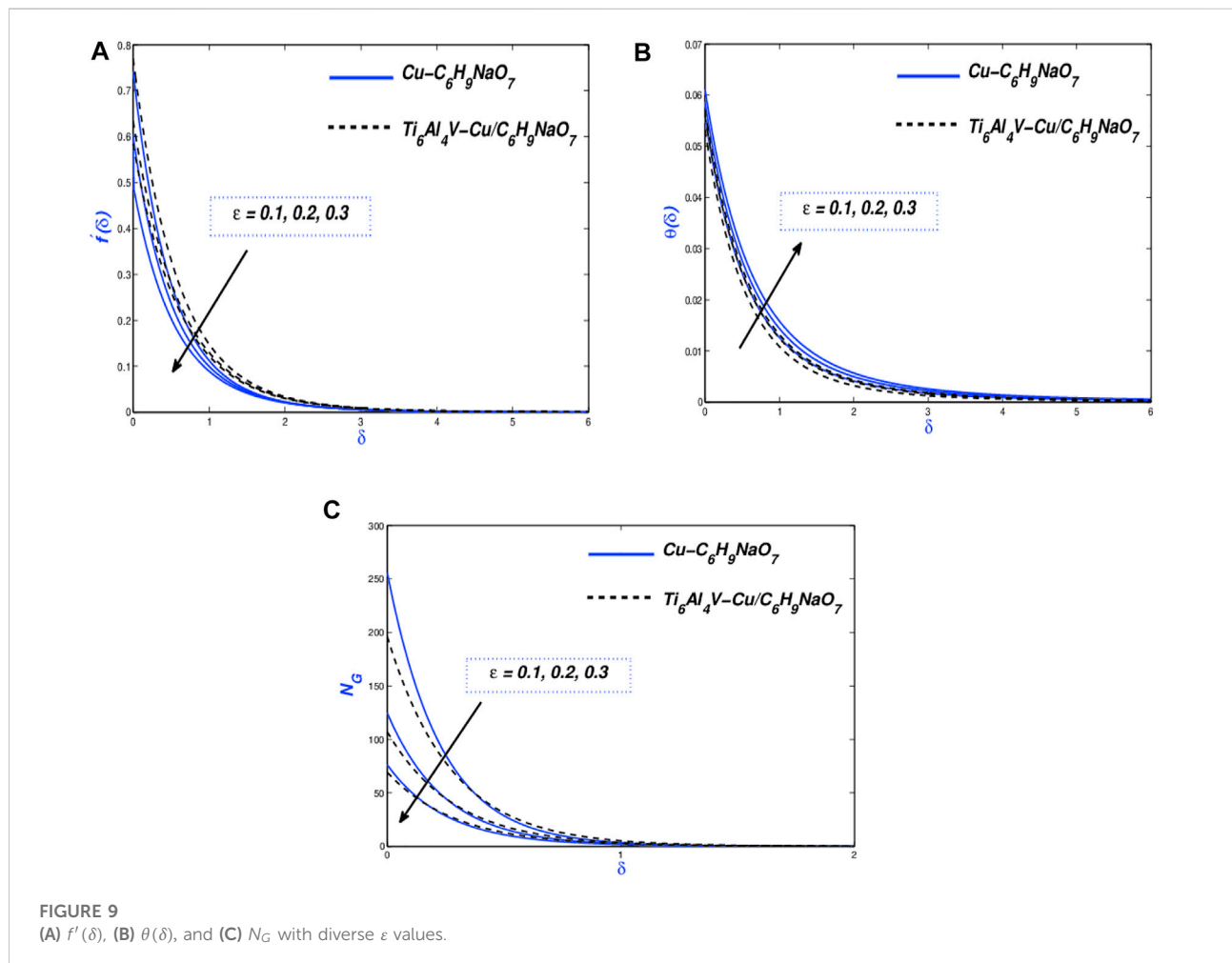
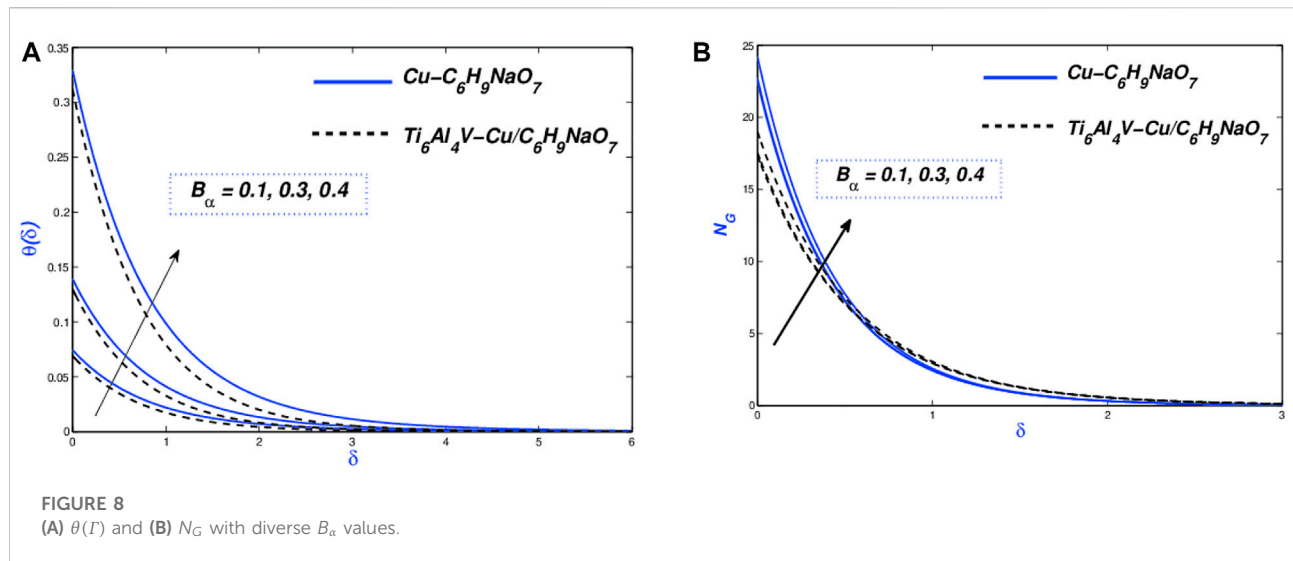


FIGURE 7
(A) $\theta(\delta)$ and (B) N_G with diverse m values.



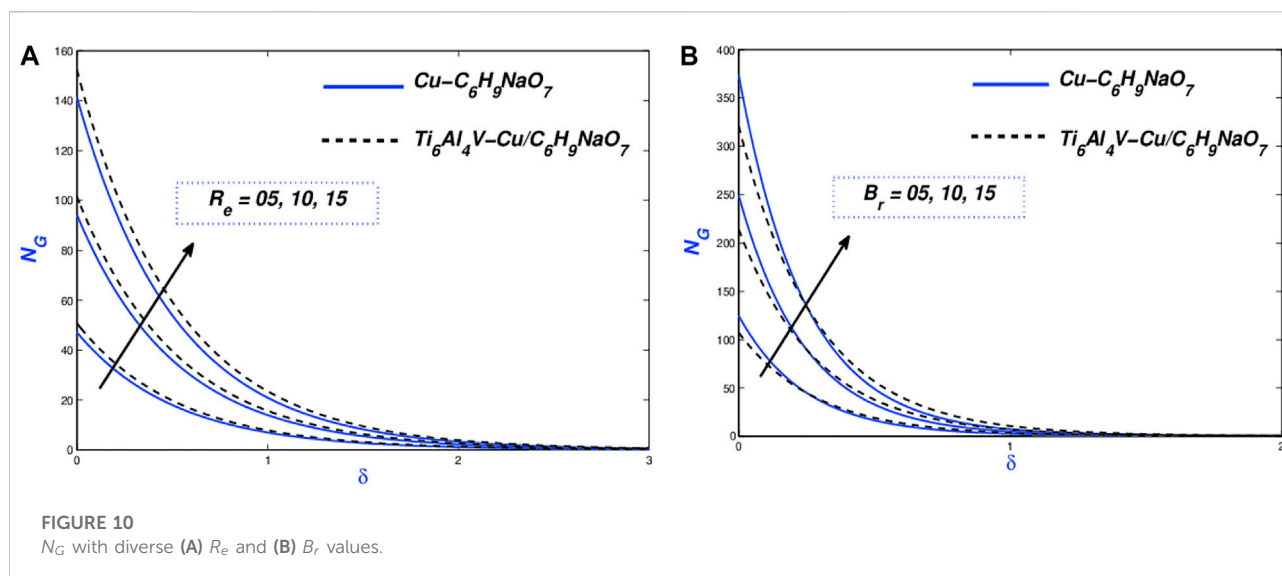


FIGURE 10
 N_G with diverse (A) Re and (B) Br values.

Impact of penetrable material factor (Γ)

The graphical results of permeability parameter (Γ) against the flow, thermal, and entropy distribution of PENF ($\text{Cu-C}_6\text{H}_9\text{NaO}_7$) and PEHNF ($\text{Ti}_6\text{Al}_4\text{V-Cu/C}_6\text{H}_9\text{NaO}_7$) are presented in Figure 6A–C. Figure 6A shows the descending behavior of Powell-Eyring's non-liquid flow curve through the porous medium, resulting in a plate surface while velocity is dragged. In fact, as the porosity effect enhances, the flow pores increase significantly, resulting in fewer nanoparticle collisions and lower heat generation. Viscous force controls buoyancy, thereby slowing the flow rate. The opposite effect is portrayed in Figure 6B. As shown in Figure 6B, increasing the porosity effect enhances the flow temperature. Figure 6C portrayed the entropy generated N_G against (Γ). This shows an increment near the surface, whereas a slight reduction is observed away from the surface. This result is caused by the large temperature difference near the surface, which causes more entropy to be produced. In industrial applications, the contribution of the porous medium permeability is to control the spin coating flow properties. Greater permeability, which can be depicted as bigger pore spaces provide better nanoparticle percolation. Besides, this effect (higher mobility) relates to reduced friction at the sheet surface.

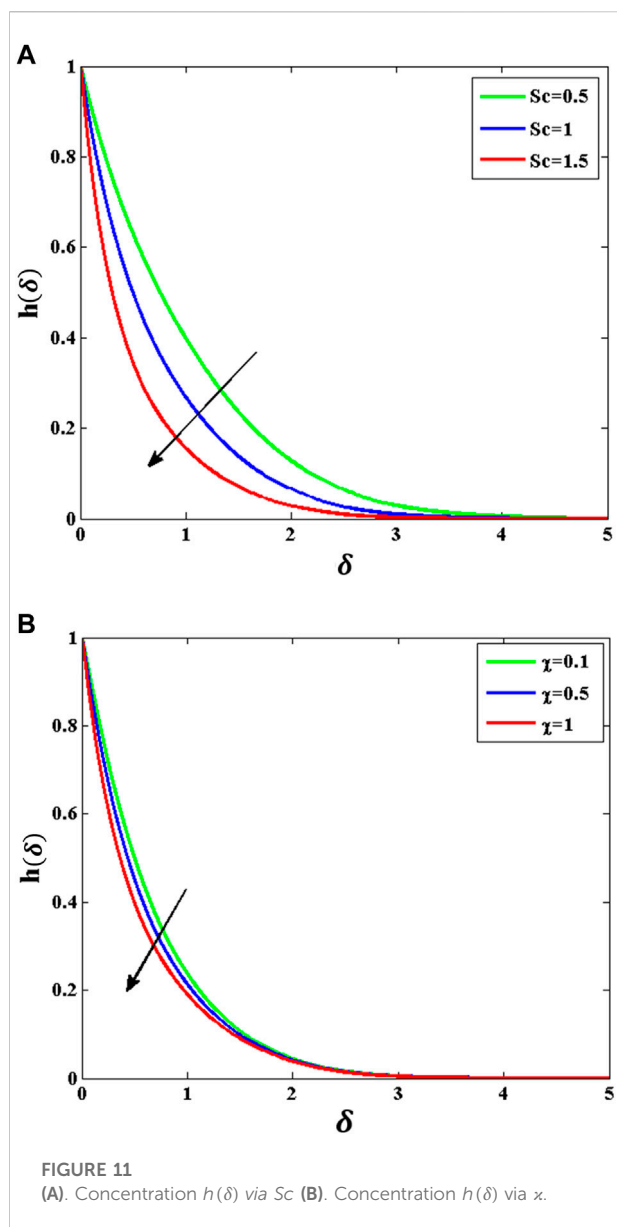
Diverse nanoparticles shaped parameter m trace

Finally, the achieved outcome of the impact of the changes in various parameters and 5 shape nanoparticles by the names of a sphere, hexahedron, tetrahedron, column, and lamina on

the profile of temperature and entropy have been analyzed and investigated in Figure 7A,B. In Figure 7A, the influence of the increment in nanoparticle shape parameter (m) on the profile of temperature has been depicted, observations show that the temperature increment because of the ascent in shape factors. Physically the increment in thermal conductivity and thermal boundary-layer thickener are the main causes of such an outcome. Additionally compared to a sphere, hexahedron, tetrahedron, and column shape nanoparticles, lamina has engendered more enhancement in the temperature (Pasha et al., 2022). Besides, the function of temperature for lamina shape nanoparticles has been continuously more than that of a sphere, hexahedron, tetrahedron, column shape nanoparticles, the temperature range in PEHNF ($\text{Ti}_6\text{Al}_4\text{V-Cu/C}_6\text{H}_9\text{NaO}_7$) case is higher than that of PENF ($\text{Cu-C}_6\text{H}_9\text{NaO}_7$) case. The impact of increasing the nanoparticle shape parameter (m) on the profile of entropy has been presented in Figure 7B, and measurements demonstrate that entropy increases as shape factors increase. It is worth noting that the PEHNF ($\text{Ti}_6\text{Al}_4\text{V-Cu/C}_6\text{H}_9\text{NaO}_7$) nanofluid phase had a higher initial entropy than the PENF ($\text{Cu-C}_6\text{H}_9\text{NaO}_7$) nanofluid phase. Later, when the shape factor is separated from the stream by a sufficient distance, it fiercely behaves in the other direction and influences the entropy rate in the stretching porous device, as observed.

Impact of the biot number (B_α)

The visualization of the temperature profile against Biot numbers (B_α) for PEHNF ($\text{Ti}_6\text{Al}_4\text{V-Cu/C}_6\text{H}_9\text{NaO}_7$) and PENF ($\text{Cu-C}_6\text{H}_9\text{NaO}_7$) nanoparticles is displayed in Figure 8A. Overall,



the enhancing (B_a) rises a temperature. The thermal thin state is regarding the low Biot number: The condition of uniform temperature region within the body (nano-polymer surface). Higher values of B_a indicate the thermal thick state in which non-uniform of temperature domains occur. The plot of N_G against (B_a) as displayed in Figure 8B discovers that the entropy profile is insensitive (only slight changes) with the increasing (B_a) at the stretching surface, compared to the position away from it. It is found that less enhancement in entropy profile is observed near the stretching walls. However, a decline in entropy generation is observed with the growth of (B_a).

TABLE 6 Nusselt quantity (Nu_x) and ideal relative error bound (σ_2) for various values of time-dependent variant (ξ) and radiative variable (N_r).

| γ | Nu_x | p_1 | p_2 | p_3 | p_4 | p_5 | σ_2 |
|----------|---------|--------|---------|---------|--------|---------|------------|
| 0.04 | -1.8017 | 2.1244 | -0.7419 | -2.0179 | 0.1720 | -0.3247 | 0.0043 |
| 0.10 | -1.6956 | 2.0156 | -0.6276 | -1.9856 | 0.1254 | -0.2729 | 0.0054 |
| 0.16 | -1.4209 | 1.8057 | -0.4025 | -1.7514 | 0.0982 | -0.2088 | 0.0079 |
| 0.22 | -1.2023 | 1.6412 | -0.3253 | -1.6049 | 0.0717 | -0.1054 | 0.0090 |

Impact of velocity slip variable (ϵ)

The impacts of velocity slip parameters (ϵ) on the velocity field, temperature field, and entropy generation are plotted in Figure 9A–C, by choosing $C_6H_9NaO_7$ as the base fluid. The effect of the strain parameter is reported from the PENF ($Cu-C_6H_9NaO_7$) and PEHNF ($Ti_6Al_4V-Cu/C_6H_9NaO_7$) momentum distribution (Figure 9A). This parameter is obtained from the boundary conditions of the current model. The gradual increment of the velocity slip enhances the fluid viscosity, thus decreasing the fluid velocity. The higher concentration of slip velocity (ϵ) values lowers the thermal boundary layer thickness (Figure 9B), which the diminution of the profile is associated with the Williamson nanofluids. At the same time, the slip velocity parameter slows the collisions with molecular diffusion. When the concentration of nanoparticles is higher in a system, the system is associated with the instantaneous possessions of thermal convection, transmission, and kinematic viscosity. Figure 9C shows the plot of entropy generated (N_G) versus (ϵ). The plot of N_G shows an effective reduction in this profile because the location is far from the plate. Due to the act of the velocity slip, entropy gradually decreases.

Entropy changes regarding Reynolds (R_e) and brinkman numbers (B_r)

The effect of the Reynolds number (R_e) on the entropy profile is shown in Figure 10A when both types of nanofluids are bounded by the stretching sheet. It is noted that the higher R_e boosts the level of entropy that can be generated in the fluid system. Figure 10B shows the relationship between the entropy generation N_G and the values of the Brinkman number (B_r), showing that increasing Brinkman number (B_r) enhances entropy generation. Brinkman number (B_r) defines the viscous influence of fluid behavior. As a consequence, high Brinkman numbers (B_r) denotes that fluid friction is the utmost factor of entropy generation. In both the Reynolds number and Brinkman number relationship, $Cu-C_6H_9NaO_7$ nanoparticles are found to have higher entropy level, compared to $Ti_6Al_4V-Cu/C_6H_9NaO_7$ nanoparticles.

TABLE 7 $C_f Re_x^{\frac{1}{2}}$ and $Nu Re_x^{\frac{-1}{2}}$ values at $P_r = 6.5$, $\beta_1 = 0.01$ and $m = 3$.

| β_2 | ξ | Γ | ϕ | ϕ_{TA} | ε | γ | N_r | B_α | S | $C_f Re_x^{\frac{1}{2}}$ Cu- C ₆ H ₉ NaO ₇ | $C_f Re_x^{\frac{1}{2}}$ Ti ₆ Al ₄ V -Cu/C ₆ H ₉ NaO ₇ | $Nu Re_x^{\frac{-1}{2}}$ Cu- C ₆ H ₉ NaO ₇ | $Nu Re_x^{\frac{-1}{2}}$ Ti ₆ Al ₄ V -Cu/C ₆ H ₉ NaO ₇ |
|-----------|-------|----------|--------|-------------|---------------|----------|-------|------------|-----|---|--|---|--|
| 0.1 | 0.2 | 0.1 | 0.18 | 0.09 | 0.3 | 0.2 | 0.3 | 0.3 | 0.1 | 1.8921 | 2.1301 | 0.5563 | 1.1216 |
| 0.2 | | | | | | | | | | 1.8562 | 2.0953 | 0.5269 | 1.1033 |
| 0.3 | | | | | | | | | | 1.8134 | 2.0264 | 0.4903 | 1.0761 |
| | 0.2 | | | | | | | | | 1.8921 | 2.1301 | 0.5563 | 1.1216 |
| | 0.6 | | | | | | | | | 1.9309 | 2.1745 | 0.5732 | 1.1905 |
| | 0.8 | | | | | | | | | 1.9647 | 2.2068 | 0.5907 | 1.2351 |
| | | 0.1 | | | | | | | | 1.8921 | 2.1301 | 0.5563 | 1.2516 |
| | | 0.3 | | | | | | | | 1.9163 | 2.1564 | 0.5374 | 1.2167 |
| | | 0.4 | | | | | | | | 1.9357 | 2.1849 | 0.5012 | 1.1856 |
| | | | 0.09 | | | | | | | 1.8089 | - | 0.4718 | - |
| | | | 0.15 | | | | | | | 1.8454 | - | 0.5025 | - |
| | | | 0.18 | | | | | | | 1.8921 | - | 0.5563 | - |
| | | | | 0.0 | | | | | | - | 1.8089 | - | 0.4718 |
| | | | | 0.06 | | | | | | - | 2.0963 | - | 1.1091 |
| | | | | 0.09 | | | | | | - | 2.1301 | - | 1.1216 |
| | | | | | 0.1 | | | | | 1.9728 | 2.2060 | 0.6175 | 1.8116 |
| | | | | | 0.2 | | | | | 1.9359 | 2.1642 | 0.5845 | 1.1520 |
| | | | | | 0.3 | | | | | 1.8921 | 2.1301 | 0.5563 | 1.1216 |
| | | | | | | 0.1 | | | | 1.8921 | 2.1301 | 0.6437 | 1.2372 |
| | | | | | | 0.2 | | | | 1.8921 | 2.1301 | 0.6044 | 1.1530 |
| | | | | | | 0.3 | | | | 1.8921 | 2.1301 | 0.5563 | 1.1216 |
| | | | | | | | 0.1 | | | 1.8921 | 2.1301 | 0.5119 | 1.0906 |
| | | | | | | | 0.3 | | | 1.8921 | 2.1301 | 0.5563 | 1.1216 |
| | | | | | | | 0.5 | | | 1.8921 | 2.1301 | 0.5729 | 1.5238 |
| | | | | | | | | 0.1 | | 1.8921 | 2.1301 | 0.5218 | 1.1016 |
| | | | | | | | | 0.3 | | 1.8921 | 2.1301 | 0.5563 | 1.1216 |
| | | | | | | | | 0.4 | | 1.8921 | 2.1301 | 0.5980 | 1.1464 |
| | | | | | | | | | 0.1 | 1.8921 | 2.1301 | 0.5563 | 1.1216 |
| | | | | | | | | | 0.3 | 1.9127 | 2.1527 | 0.5864 | 1.1504 |
| | | | | | | | | | 0.2 | 1.9432 | 2.1965 | 0.6238 | 1.1714 |

Concentration changes regarding schmidt number (Sc) and chemical reaction parameter (χ)

Figure 11A exhibits dispersal of concentration $h(\delta)$ towards the significant Schmidt number (Sc) which has a vital impact on it. Technically for the higher Schmidt number (Sc), the progress in the molecular diffusion tends to get reduced which restricts the mass transference in the system which can be visualized from Figure 11A. On other hand, Figure 11B discloses the influence of chemical reaction constraints on mass diffusion. The effective chemical reaction process exerts more mass in the system which makes the mass transference process harder and this may lead to the deceleration noted in Figure 11B for the higher values of chemical reaction constraint.

Parametrical study on drag force (C_f) and nusselt number (Nu)

The coefficients in the components of the flow and heat transmission are namely dragged force (C_f) and Nusselt numbers (Nu_x), respectively. These parameters are tabulated in Tables 5, 6 showing their numerical values. Table 7 shows that a frictional force factor has non-uniform changes for both of the nanoparticles with an increasing ε and ξ . Also, it is observed that the drag force coefficient upsurges with an increment of Γ and ϕ . Besides, the reduction is remarked with rising ε for both the case of nanoparticles. Furthermore, the increasing values of B_α and N_r have no impact on drag force coefficient for both PEHNF (Ti₆Al₄V-Cu/C₆H₉NaO₇) and PENF (Cu-

$C_6H_9NaO_7$) nanoparticles. The Nusselt number enhances with an augmentation ξ , whereas an opposite function is remarked with the addition of β_2, γ and N_r for both PEHNF ($Ti_6Al_4V-Cu/C_6H_9NaO_7$) and PENF ($Cu-C_6H_9NaO_7$) nanoparticles (Figure 7).

Concluding consequences and forthcoming course

In this mathematical investigation, the heat transmission in a Powell-Eyring hybrid nanofluid (PEHNF) model bounded by an expanding surface is investigated. This model is implemented in a thermal system, which is inspired by the modified Buongiorno's NF prototype. The presence of nanoparticles such as $Cu-C_6H_9NaO_7$ and $Ti_6Al_4V-Cu/C_6H_9NaO_7$ nanoparticles are implemented in this model. The influences of porous media, thermal radiative flow, and variable thermal conductivity are taken into account in the mathematical model. Furthermore, the effect of the nanoparticles' shape factors is determined, and their impacts can be observed in thermal and entropy aspects. The numerical solutions for the current mathematical model can be achieved by following these steps: 1) Apply similarity solution to convert PDEs to ODEs, and 2) solve the ODEs with Galerkin finite element plan. The primary outcomes from this investigation are listed for the profiles such as velocity, temperature, and concentration, together with the coefficients of drag force and Nusselt number. These outcomes are listed below:

- 1) Along the far stream, the velocity field is reduced for the upsurging Powell-Eyring fluid (β_2), porosity (I), volume fraction (ϕ), and velocity slip (ϵ).
- 2) The temperature profile of Powell-Eyring fluid for both cases of $Cu-C_6H_9NaO_7$ (conventional nanofluid) and $Ti_6Al_4V-Cu/C_6H_9NaO_7$ (hybrid nanofluid) intensifies under the increment of γ, I, ϕ and B_α .
- 3) The temperature distribution is affected by most of the physical quantities, which denotes that nanofluids have a high heat exchange rate. This property helps control the temperature during spin coating processes.
- 4) The entropy profile against Powell-Eyring fluid (β_2), Porosity term (I), volume fraction (ϕ, ϕ_{mf}) and Biot number (B_α) and shape factor (m) explore dual behavior.
- 5) The shape of nanoparticles is namely sphere, hexahedron, tetrahedron, lamina, and column. Among them, lamina has the greatest impact on the function of temperature and entropy.
- 6) The ability of the flow system toward the mass transference gets reduced as the molecular diffusivity drops significantly. This can be technically connected with the increase in Schmidt number versus the molecular diffusivity.
- 7) The remarkable change in frictional force factor for $Ti_6Al_4V-Cu/C_6H_9NaO_7$ and $Cu-C_6H_9NaO_7$ nanofluids can be seen, compared to the Nusselt number coefficient for the porosity and volume fraction.

Future track

These outcomes can be a guideline for the industry and technology, to choose the appropriate working fluid for improved productivity in the associated device or prototype. Subsequently, this research work can be extended by applying the model of rotating disk flow considering ferromagnetic nanoparticles (Jamshed et al., 2021e; Pasha et al., 2022). The FEM could be applied to a variety of physical and technical challenges in the future (Jamshed et al., 2022b; Hussain et al., 2022b; Hussain et al., 2022a).

Data availability statement

The raw data supporting the conclusions of this article will be made available by the authors, without undue reservation.

Author contributions

WJ, MR and SS formulated the problem. WJ and RI solved the problem. WJ, MR, SS, RI, BS, RS, AP, ME, SH and ED computed and scrutinized the results. All the authors equally contributed in writing and proof reading of the paper. All authors reviewed the manuscript.

Acknowledgments

Authors are grateful to the Deanship of Scientific Research, Islamic University of Madinah, Ministry of Education, KSA for supporting this research work through research project grant under Research Group Program/1/804.

Conflict of interest

The authors declare that the research was conducted in the absence of any commercial or financial relationships that could be construed as a potential conflict of interest.

Publisher's note

All claims expressed in this article are solely those of the authors and do not necessarily represent those of their affiliated organizations, or those of the publisher, the editors and the reviewers. Any product that may be evaluated in this article, or claim that may be made by its manufacturer, is not guaranteed or endorsed by the publisher.

References

- Abouelregal, A. E., Ahmad, H., Nofal, T. A., and Abu-Zinadah, H. (2021). Thermo-viscoelastic fractional model of rotating nanobeams with variable thermal conductivity due to mechanical and thermal loads. *Mod. Phys. Lett. B* 35 (18), 2150297. doi:10.1142/s0217984921502973
- Adnanand Ashraf, W. (2022a). Numerical thermal featuring in $\gamma\text{Al}_2\text{O}_3\text{-C}_2\text{H}_6\text{O}_2$ nanofluid under the influence of rotating nanobeams with variable heat condition by inducing novel effects of effective Prandtl number model (EPNM). *Adv. Mech. Eng.*, 14(6), p.168781322211065, doi:10.1177/16878132221106577
- Adnanand Ashraf, W., (2022b). *Thermal efficiency in hybrid ($\text{Al}_2\text{O}_3\text{-CuO/H}_2\text{O}$) and ternary hybrid nanofluids ($\text{Al}_2\text{O}_3\text{-CuO-Cu/H}_2\text{O}$) by considering the novel effects of imposed magnetic field and convective heat condition*. Waves in Random and Complex Media, pp.1–16.
- AdnanKhan, U., Ahmed, N., Manzoor, R., and Mohyud-Din, S. T. (2021). Impacts of various shaped Cu-nanomaterial on the heat transfer over a bilateral stretchable surface: Numerical investigation. *Adv. Mech. Eng.* 13 (12), 168781402110674. doi:10.1177/16878140211067420
- Ahmad, S., Naveed Khan, M., and Nadeem, S. (2022). Unsteady three dimensional bioconvective flow of Maxwell nanofluid over an exponentially stretching sheet with variable thermal conductivity and chemical reaction. *Int. J. Ambient Energy* in press, 1–11. doi:10.1080/01430750.2022.2029765
- Ahmad, N., Mehmood, N., and Akgül, A. (2022). Applications of some new Krasnoselskii-type fixed-point results for generalized expansive and equiexpansive mappings. *Adv. Contin. Discret. Model.* 2022 (1), 30–19. doi:10.1186/s13662-022-03704-w
- Ahmed, K., Akbar, T., Muhammad, T., and Alghamdi, M. (2021). Heat transfer characteristics of MHD flow of Williamson nanofluid over an exponential permeable stretching curved surface with variable thermal conductivity. *Case Stud. Therm. Eng.* 28, 101544. doi:10.1016/j.csite.2021.101544
- Akgül, E. K., Akgül, A., Jamshed, W., Rehman, Z., Nisar, K. S., Alqahtani, M. S., et al. (2022). Analysis of respiratory mechanics models with different kernels. *Open Phys.* 20 (1), 609–615. doi:10.1515/phys-2022-0027
- Akram, J., Akbar, N. S., and Tripathi, D. (2022). Analysis of electroosmotic flow of silver-water nanofluid regulated by peristalsis using two different approaches for nanofluid. *J. Comput. Sci.* 62, 101696. doi:10.1016/j.jocs.2022.101696
- Al-Chalhawi, K. K., Alaydamee, H. H., Faisal, A. E., Al-Farhany, K., and Alomari, M. A. (2022). Newtonian and non-Newtonian nanofluids with entropy generation in conjugate natural convection of hybrid nanofluid-porous enclosures: A review. *Heat. Trans.* 51 (2), 1725–1745. doi:10.1002/htj.22372
- Alharbi, K. A. M., Khan, U., Ahammad, N. A., Ullah, B., Wahab, H. A., Zaib, M., et al. (2022). Heat transport mechanism in Cu/water and (Cu– Al_2O_3)/water under the influence of thermophysical characteristics and non-linear thermal radiation for Blasius/Sakiadis models: Numerical investigation. *J. Indian Chem. Soc.* 99 (8), 100578. doi:10.1016/j.jics.2022.100578
- Ali, B., Hussain, S., Nie, Y., Hussein, A. K., and Habib, D. (2021). Finite element investigation of Dufour and Soret impacts on MHD rotating flow of Oldroyd-B nanofluid over a stretching sheet with double diffusion Cattaneo Christov heat flux model. *Powder Technol.* 377, 439–452. doi:10.1016/j.powtec.2020.09.008
- Alizadeh, R., Abad, J. M. N., Ameri, A., Mohebbi, M. R., Mehdizadeh, A., Zhao, D., et al. (2021). A machine learning approach to the prediction of transport and thermodynamic processes in multiphysics systems-heat transfer in a hybrid nanofluid flow in porous media. *J. Taiwan Inst. Chem. Eng.* 124, 290–306. doi:10.1016/j.jtice.2021.03.043
- Areekara, S., Mackolil, J., Mahanthesh, B., Mathew, A., and Rana, P. (2022). A study on nanoliquid flow with irregular heat source and realistic boundary conditions: A modified buongiorno model for biomedical applications. *Z. Angew. Math. Mech.* 102 (3), e202100167. doi:10.1002/zamm.202100167
- Ashraf, W., Junaid Anjum, H., and Khan, I. (2022a). Energy transformation and entropy investigation in the nanofluid composed by γ -nanomaterial over a permeable convective surface with solar thermal radiation: Numerical analysis. *Front. Energy Res.* 10, 507.
- Ashraf, W., Khan, I., Shemseldin, M. A., and Mousa, A. A. (2022b). Numerical energy storage efficiency of MWCNTs-propylene glycol by inducing thermal radiations and combined convection effects in the constitutive model. *Front. Chem.* 10, 879276. doi:10.3389/fchem.2022.879276
- Attia, N., Akgül, A., Seba, D., Nour, A., and Asad, J. (2022). A novel method for fractal-fractional differential equations. *Alexandria Eng. J.* 61 (12), 9733–9748. doi:10.1016/j.aej.2022.02.004
- Aziz, A., Jamshed, W., Aziz, T., Bahaidarah, H., and Ur Rehman, K. (2021). Entropy analysis of Powell–Eyring hybrid nanofluid including effect of linear thermal radiation and viscous dissipation. *J. Therm. Anal. Calorim.* 143 (2), 1331–1343. doi:10.1007/s10973-020-10210-2
- Banerjee, A., and Paul, D. (2021). Developments and applications of porous medium combustion: A recent review. *Energy* 221, 119868. doi:10.1016/j.energy.2021.119868
- Bhattacharyya, A., Sharma, R., Hussain, S. M., Chamkha, A. J., and Mamatha, E. (2022). A numerical and statistical approach to capture the flow characteristics of Maxwell hybrid nanofluid containing copper and graphene nanoparticles. *Chin. J. Phys.* 77, 1278–1290. doi:10.1016/j.cjph.2021.09.015
- Bilal, S., Shah, I. A., Akgül, A., Tekin, M. T., Botmart, T., Yahia, I. S., et al. (2022). A comprehensive mathematical structuring of magnetically effected Sutterby fluid flow immersed in dually stratified medium under boundary layer approximations over a linearly stretched surface. *Alexandria Eng. J.* 61 (12), 11889–11898. doi:10.1016/j.aej.2022.05.044
- Bilgili, F., Nathaniel, S. P., Kuşkaya, S., and Kassouri, Y. (2021). Environmental pollution and energy research and development: An environmental kuznets curve model through quantile simulation approach. *Environ. Sci. Pollut. Res.* 28 (38), 53712–53727. doi:10.1007/s11356-021-14506-0
- Bouslimi, J., Alkathiri, A. A., Alharbi, A. N., Jamshed, W., Eid, M. R., and Bouazizi, M. L. (2022). Dynamics of convective slippery constraints on hybrid radiative Sutterby nanofluid flow by Galerkin finite element simulation. *Nanotechnol. Rev.* 11 (1), 1219–1236. doi:10.1515/ntrev-2022-0070
- Brewster, M. Q. (1992). *Thermal radiative transfer and properties*. Hoboken, NJ: John Wiley & Sons.
- Chen, T. C., Hammid, A. T., Akbarov, A. N., Shariati, K., Dinari, M., and Ali, M. S. (2022). Estimating the physical properties of nanofluids using a connectionist intelligent model known as gaussian process regression approach. *Int. J. Chem. Eng.* 2022, 1–14. doi:10.1155/2022/1017341
- Chen, T. C., Majdi, H. S., Ismael, A. M., Pouresmi, J., Ahangari, D., and Noori, S. M. (2022). Insights into the estimation of the enhanced thermal conductivity of phase change material-containing oxide nanoparticles using gaussian process regression method. *Int. J. Chem. Eng.* 2022, 1–10. doi:10.1155/2022/7119336
- Cui, C., Meng, K., Xu, C., Liang, Z., Li, H., and Pei, H. (2021). Analytical solution for longitudinal vibration of a floating pile in saturated porous media based on a fictitious saturated soil pile model. *Comput. Geotechnics* 131, 103942. doi:10.1016/j.compgeo.2020.103942
- Devi, S. S. U., and Devi, S. A. (2016). Numerical investigation of three-dimensional hybrid Cu– Al_2O_3 /water nanofluid flow over a stretching sheet with effecting Lorentz force subject to Newtonian heating. *Can. J. Phys.* 94 (5), 490–496. doi:10.1139/cjp-2015-0799
- Din, Z. U., Ali, A., De la Sen, M., and Zaman, G. (2022). Entropy generation from convective–radiative moving exponential porous fins with variable thermal conductivity and internal heat generations. *Sci. Rep.* 12 (1), 1791–1811. doi:10.1038/s41598-022-05507-1
- Dubey, V., and Sharma, A. K. (2022). A short review on hybrid nanofluids in machining processes. *Adv. Mater. Process. Technol.*, 1–14. doi:10.1080/2374068x.2022.2087315
- El-Aziz, M. A., and Afify, A. A. (2019). Effect of Hall current on MHD slip flow of Casson nanofluid over a stretching sheet with zero nanoparticle mass flux. *Thermophys. Aeromech.* 26 (3), 429–443. doi:10.1134/s0869864319030119
- Hayat, T., and Nadeem, S. (2018). Flow of 3D Eyring–Powell fluid by utilizing Cattaneo–Christov heat flux model and chemical processes over an exponentially stretching surface. *Results Phys.* 8, 397–403. doi:10.1016/j.rinp.2017.12.038
- Hayat, T., Ashraf, B., Shehzad, S. A., and Abouelmagd, E. (2015). Three-dimensional flow of Eyring–Powell nanofluid over an exponentially stretching sheet. *Int. J. Numer. Methods Heat Fluid Flow* 25, 593–616. doi:10.1108/hff-05-2014-0118
- Hayat, T., Ullah, I., Alsaedi, A., and Farooq, M. (2017). MHD flow of Powell–Eyring nanofluid over a non-linear stretching sheet with variable thickness. *Results Phys.* 7, 189–196. doi:10.1016/j.rinp.2016.12.008
- Hobiny, A. D., and Abbas, I. (2022). The impacts of variable thermal conductivity in a semiconducting medium using finite element method. *Case Stud. Therm. Eng.* 31, 101773. doi:10.1016/j.csite.2022.101773
- Hussain, S. M., and Jamshed, W. (2021). A comparative entropy based analysis of tangent hyperbolic hybrid nanofluid flow: Implementing finite difference method.

- Int. Commun. Heat Mass Transf. 129, 105671. doi:10.1016/j.icheatmasstransfer.2021.105671
- Hussain, S. M., Jamshed, W., Safdar, R., Shahzad, F., Mohd Nasir, N. A. A., and Ullah, I. (2022). Chemical reaction and thermal characteristics of maxwell nanofluid flow-through solar collector as a potential solar energy cooling application: A modified Buongiorno's model. Energy & Environment, 0958305X221088113. doi:10.1177/0958305X221088113
- Hussain, S. M., Jamshed, W., Pasha, A. A., Adil, M., and Akram, M. (2022b). Galerkin finite element solution for electromagnetic radiative impact on viscous Williamson two-phase nanofluid flow via extendable surface. Int. Commun. Heat Mass Transf. 137, 106243. doi:10.1016/j.icheatmasstransfer.2022.106243
- Hussain, S. M. (2022). Irreversibility analysis of time-dependent magnetically driven flow of sutterby hybrid nanofluid: A thermal mathematical model. Waves in Random and Complex Media, 1. doi:10.1080/17455030.2022.2089369
- Jamei, M., Karbasi, M., Mosharaf-Dehkordi, M., Olumegbon, I. A., Abualigah, L., Said, Z., et al. (2022). Estimating the density of hybrid nanofluids for thermal energy application: Application of non-parametric and evolutionary polynomial regression data-intelligent techniques. Measurement 189, 110524. doi:10.1016/j.measurement.2021.110524
- Jamshed, W., and Nisar, K. S. (2021). Computational single-phase comparative study of a Williamson nanofluid in a parabolic trough solar collector via the Keller box method. Int. J. Energy Res. 45 (7), 10696–10718. doi:10.1002/er.6554
- Jamshed, W., Prakash, M., Devi, S., Ibrahim, R. W., Shahzad, F., Nisar, K. S., et al. (2021). A brief comparative examination of tangent hyperbolic hybrid nanofluid through a extending surface: Numerical keller–box scheme. Sci. Rep. 11 (1), 24032–32. doi:10.1038/s41598-021-03392-8
- Jamshed, W., Nisar, K. S., Ibrahim, R. W., Shahzad, F., and Eid, M. R. (2021). Thermal expansion optimization in solar aircraft using tangent hyperbolic hybrid nanofluid: A solar thermal application. J. Mater. Res. Technol. 14, 985–1006. doi:10.1016/j.jmrt.2021.06.031
- Jamshed, W., Devi, S. U., and Nisar, K. S. (2021). Single phase based study of Ag-Cu/EO Williamson hybrid nanofluid flow over a stretching surface with shape factor. Phys. Screen. 96 (6), 065202. doi:10.1088/1402-4896/abec0
- Jamshed, W., Şirin, C., Selimefendigil, F., Shamshuddin, M. D., Altowairqi, Y., and Eid, M. R. (2021). Thermal characterization of coolant Maxwell type nanofluid flowing in parabolic trough solar collector (PTSC) used inside solar powered ship application. Coatings 11 (12), 1552. doi:10.3390/coatings11121552
- Jamshed, W., Nasir, N. A. A. M., Isa, S. S. P. M., Safdar, R., Shahzad, F., Nisar, K. S., et al. (2021). Thermal growth in solar water pump using Prandtl–Eyring hybrid nanofluid: A solar energy application. Sci. Rep. 11 (1), 18704–18721. doi:10.1038/s41598-021-98103-8
- Jamshed, W., Safdar, R., Rehman, Z., Lashin, M. M., Ehab, M., Moussa, M., et al. (2022). Computational technique of thermal comparative examination of Cu and Au nanoparticles suspended in sodium alginate as Sutterby nanofluid via extending PTSC surface. J. Appl. Biomaterials Funct. Mater. 20, 228080002211040. doi:10.1177/22808000221104004
- Jamshed, W., Eid, M. R., Safdar, R., Pasha, A. A., Isa, S. S. P. M., Adil, M., et al. (2022). Solar energy optimization in solar-HVAC using sutterby hybrid nanofluid with smoluchowski temperature conditions: A solar thermal application. Sci. Rep. 12, 11484. doi:10.1038/s41598-022-15685-7
- Khan, U., Abdul Wahab, H., Syed, H., Ullah, B., and Adnan (2022). Numerical study of heat transport mechanism in hybrid nanofluid [(Cu-Al₂O₃)/water] over a stretching/shrinking porous wedge. Proc. Institution Mech. Eng. Part E J. Process Mech. Eng., 095440892211079. doi:10.1177/09544089221107981
- Khan, U., Ahmed, N., and Khan, I. (2022). Heat transfer evaluation in MgZn₆Zr/C₈H₁₈ [(Magnesium-Zinc-Zirconium)/Engine oil] with non-linear solar thermal radiations and modified slip boundaries over 3-dimensional convectively heated surface. Front. Energy Res., 351.
- Khan, U., Adnan, Ullah, B., Abdul Wahab, H., Ullah, I., Almuqrin, M. A., and Khan, I. (2022). Comparative thermal transport mechanism in Cu-H₂O and Cu-Al₂O₃/H₂O nanofluids: Numerical investigation. Waves in Random and Complex Media, 1–16. doi:10.1080/17455030.2021.2023783
- Kumbhakar, B., and Nandi, S. (2022). Unsteady MHD radiative-dissipative flow of Cu-Al₂O₃/H₂O hybrid nanofluid past a stretching sheet with slip and convective conditions: A regression analysis. Math. Comput. Simul. 194, 563–587. doi:10.1016/j.matcom.2021.12.018
- Kursun, M., Liew, P. J., Che Sidik, N. A., and Wang, J. (2022). Recent progress on the application of nanofluids and hybrid nanofluids in machining: A comprehensive review. Int. J. Adv. Manuf. Technol. 121, 1455–1481. doi:10.1007/s00170-022-09409-4
- Lee, J., King, S., Hassan, Y. A., Nguyen, T., Balestra, P., Schunert, S., et al. (2022). “Pronghorn porous media model validation with pressure drop measurements,” in Paper in the 19th international topical meeting on nuclear reactor thermal hydraulics (NURETH-19), Brussels, Belgium, March 6 - 11.
- Mabood, F., Rauf, A., Prasannakumara, B. C., Izadi, M., and Shehzad, S. A. (2021). Impacts of Stefan blowing and mass convection on flow of Maxwell nanofluid of variable thermal conductivity about a rotating disk. Chin. J. Phys. 71, 260–272. doi:10.1016/j.cjph.2021.03.003
- Mahanthesh, B., Shehzad, S. A., Mackolil, J., and Shashikumar, N. S. (2021). Heat transfer optimization of hybrid nanomaterial using modified buongiorno model: A sensitivity analysis. Int. J. Heat Mass Transf. 171, 121081. doi:10.1016/j.ijheatmasstransfer.2021.121081
- Mahdy, A. M. S., Lotfy, K., El-Bary, A., and Tayel, I. M. (2021). Variable thermal conductivity and hyperbolic two-temperature theory during magneto-photothermal theory of semiconductor induced by laser pulses. Eur. Phys. J. Plus 136 (6). doi:10.1140/epjp/s13360-021-01633-3
- Makinde, O. D., Mahanthesh, B., Gireesha, B. J., Shashikumar, N. S., Monaleli, R. L., and Tshela, M. S. (2018). MHD nanofluid flow past a rotating disk with thermal radiation in the presence of aluminum and titanium alloy nanoparticles. Defect Diffusion Forum 384, 69. doi:10.4028/www.scientific.net/DDF.384.69
- Malik, M. Y., Khan, I., Hussain, A., and Salahuddin, T. (2015). Mixed convection flow of MHD Eyring–Powell nanofluid over a stretching sheet: A numerical study. AIP Adv. 5 (11), 117118. doi:10.1063/1.4935639
- Mandal, D. K., Biswas, N., Manna, N. K., Gayen, D. K., Gorla, R. S. R., and Chamkha, A. J. (2022). Thermo-fluidic transport process in a novel M-shaped cavity packed with non-Darcian porous medium and hybrid nanofluid: Application of artificial neural network (ANN). Phys. Fluids 34 (3), 033608. doi:10.1063/5.0082942
- Muneeshwaran, M., Srinivasan, G., Muthukumar, P., and Wang, C. C. (2021). Role of hybrid-nanofluid in heat transfer enhancement—A review. Int. Commun. Heat Mass Transf. 125, 105341. doi:10.1016/j.icheatmasstransfer.2021.105341
- Murtaza, R., Hussain, I., Rehman, Z., Khan, I., and Andualem, M. (2022). Thermal enhancement in Falkner–Skan flow of the nanofluid by considering molecular diameter and freezing temperature. Sci. Rep. 12 (1), 9415–9514. doi:10.1038/s41598-022-13423-7
- Nandi, S., Kumbhakar, B., and Seth, G. S. (2022). Quadratic regression analysis of unsteady MHD free convective and radiative-dissipative stagnation flow of hybrid nanofluid over an exponentially stretching surface under porous medium. Chin. J. Phys. 77, 2090–2105. doi:10.1016/j.cjph.2021.12.011
- Nandi, S., Kumbhakar, B., and Sarkar, S. (2022). MHD stagnation point flow of Fe₃O₄/Cu/Ag-CH₃OH nanofluid along a convectively heated stretching sheet with partial slip and activation energy: Numerical and statistical approach. Int. Commun. Heat Mass Transf. 130, 105791. doi:10.1016/j.icheatmasstransfer.2021.105791
- Olabode, J. O., Idowu, A. S., Akolade, M. T., and Titiloye, E. O. (2021). Unsteady flow analysis of Maxwell fluid with temperature dependent variable properties and quadratic thermo-solutal convection influence. Partial Differ. Equations Appl. Math. 4, 100078. doi:10.1016/j.padiff.2021.100078
- Owhaib, W., and Al-Kouz, W. (2022). Three-dimensional numerical analysis of flow and heat transfer of bi-directional stretched nanofluid film exposed to an exponential heat generation using modified Buongiorno model. Sci. Rep. 12 (1). doi:10.1038/s41598-022-13351-6
- Owhaib, W., Basavarajappa, M., and Al-Kouz, W. (2021). Radiation effects on 3D rotating flow of Cu-water nanofluid with viscous heating and prescribed heat flux using modified Buongiorno model. Sci. Rep. 11 (1). doi:10.1038/s41598-021-00107-x
- Parvin, S., Isa, S. S. P. M., Jamshed, W., Ibrahim, R. W., and Nisar, K. S. (2021). Numerical treatment of 2D-Magneto double-diffusive convection flow of a Maxwell nanofluid: Heat transport case study. Case Stud. Therm. Eng. 28, 101383. doi:10.1016/j.csite.2021.101383
- Pasha, A. A., Islam, N., Jamshed, W., Alam, M. I., Jameel, A. G. A., Juhany, K. A., et al. (2022). Statistical analysis of viscous hybridized nanofluid flowing via Galerkin finite element technique. Int. Commun. Heat Mass Transf. 137, 106244. doi:10.1016/j.icheatmasstransfer.2022.106244
- Qureshi, Z. A., Bilal, S., Khan, U., Akgül, A., Sultana, M., Botmart, T., et al. (2022). Mathematical analysis about influence of Lorentz force and interfacial nano layers on nanofluids flow through orthogonal porous surfaces with injection of SWCNTs. Alexandria Eng. J. 61 (12), 12925–12941. doi:10.1016/j.aej.2022.07.010
- Qureshi, M. A. (2022). Thermal capability and entropy optimization for Prandtl–Eyring hybrid nanofluid flow in solar aircraft implementation. Alexandria Eng. J. 61 (7), 5295–5307. doi:10.1016/j.aej.2021.10.051
- Rana, P., Mahanthesh, B., Mackolil, J., and Al-Kouz, W. (2021). Nanofluid flow past a vertical plate with nanoparticle aggregation kinematics, thermal slip and significant buoyancy force effects using modified Buongiorno model. Waves in Random and Complex Media, 1. doi:10.1080/17455030.2021.1977416

- Rashed, Z. Z., Alhazmi, M., and Ahmed, S. E. (2021). Non-homogenous nanofluid model for 3D convective flow in enclosures filled with hydrodynamically and thermally heterogeneous porous media. *Alexandria Eng. J.* 60 (3), 3119–3132. doi:10.1016/j.aej.2021.01.049
- Reddy, N. B., Poornima, T., and Sreenivasulu, P. (2014). Influence of variable thermal conductivity on MHD boundary layer slip flow of ethylene-glycol based Cu nanofluids over a stretching sheet with convective boundary condition. *Int. J. Eng. Math.* 2014, 905158. doi:10.1155/2014/905158
- Rosca, N. C., Rosca, A. V., Aly, E. H., and Pop, I. (2021). Flow and heat transfer past a stretching/shrinking sheet using modified buongiorno nanoliquid model. *Mathematics* 9 (23), 3047. doi:10.3390/math9233047
- Safdar, R., Jawad, M., Hussain, S., Imran, M., Akgül, A., and Jamshed, W. (2022). Thermal radiative mixed convection flow of MHD Maxwell nanofluid: Implementation of buongiorno's model. *Chin. J. Phys.* 77, 1465–1478. doi:10.1016/j.cjph.2021.11.022
- Saha, A., Manna, N. K., Ghosh, K., and Biswas, N. (2022). Analysis of geometrical shape impact on thermal management of practical fluids using square and circular cavities. *Eur. Phys. J. Spec. Top.* 231, 2509–2537. doi:10.1140/epjs/s11734-022-00593-8
- Said, Z., Sundar, L. S., Tiwari, A. K., Ali, H. M., Sheikholeslami, M., Bellos, E., et al. (2021). Recent advances on the fundamental physical phenomena behind stability, dynamic motion, thermophysical properties, heat transport, applications, and challenges of nanofluids. *Phys. Rep.* 946, 1–94. doi:10.1016/j.physrep.2021.07.002
- Said, Z., Sharma, P., Tiwari, A. K., Huang, Z., Bui, V. G., Hoang, A. T., et al. (2022). Application of novel framework based on ensemble boosted regression trees and Gaussian process regression in modelling thermal performance of small-scale Organic Rankine Cycle (ORC) using hybrid nanofluid. *J. Clean. Prod.* 360, 132194. doi:10.1016/j.jclepro.2022.132194
- Shahzad, F., Jamshed, W., Ibrahim, R. W., Sooppy Nisar, K., Qureshi, M. A., Hussain, S. M., et al. (2021). Comparative numerical study of thermal features analysis between Oldroyd-B copper and molybdenum disulfide nanoparticles in engine-oil-based nanofluids flow. *Coatings* 11 (10), 1196. doi:10.3390/coatings11101196
- Shahzad, F., Jamshed, W., DeviS, S. U., Safdar, R., Prakash, M., Ibrahim, R. W., et al. (2022). Raising thermal efficiency of solar water-pump using Oldroyd-B nanofluids' flow: An optimal thermal application. *Energy Science & Engineering*. doi:10.1002/ese3.1173
- Shahzad, F., Jamshed, W., Nisar, K. S., Nasir, N. A. A. M., Safdar, R., Abdel-Aty, A. H., et al. (2022). Thermal analysis for Al_2O_3 -sodium alginate magnetized Jeffrey's nanofluid flow past a stretching sheet embedded in a porous medium. *Sci. Rep.* 12 (1), 1. doi:10.1038/s41598-022-06983-1
- Shankaralingappa, B. M., Madhukesh, J. K., Sarris, I. E., Gireesha, B. J., and Prasannakumara, B. C. (2021). Influence of thermophoretic particle deposition on the 3D flow of sodium alginate-based Casson nanofluid over a stretching sheet. *Micromachines* 12 (12), 1474. doi:10.3390/mi12121474
- Swain, K., Mahanthesh, B., and Mebarek-Oudina, F. (2021). Heat transport and stagnation-point flow of magnetized nanoliquid with variable thermal conductivity, Brownian moment, and thermophoresis aspects. *Heat. Transf.* 50 (1), 754–767. doi:10.1002/htj.21902
- Wang, X. Q., and Mujumdar, A. S. (2008). A review on nanofluids-part II: Experiments and applications. *Braz. J. Chem. Eng.* 25, 631–648. doi:10.1590/s0104-66322008000400002
- Xiong, Q., Altnji, S., Tayebi, T., Izadi, M., Hajjar, A., Sundén, B., et al. (2021). A comprehensive review on the application of hybrid nanofluids in solar energy collectors. *Sustain. Energy Technol. Assessments* 47, 101341. doi:10.1016/j.seta.2021.101341
- Xu, X., and Chen, S. (2017). Cattaneo-Christov heat flux model for heat transfer of Marangoni boundary layer flow in a copper–water nanofluid. *Heat. Trans. Asian. Res.* 46 (8), 1281–1293. doi:10.1002/htj.21273
- Zou, L., Hu, G., O'Grady, D., and Hu, R. (2022). Explicit modeling of pebble temperature in the porous-media model for pebble-bed reactors. *Prog. Nucl. Energy* 146, 104175. doi:10.1016/j.pnucene.2022.104175



OPEN ACCESS

EDITED BY

Adnan,
Mohi-ud-Din Islamic University,
Pakistan

REVIEWED BY

B. Shankar Goud,
Jawaharlal Nehru Technological
University, Hyderabad, India
Mohsan Hassan,
COMSATS University Islamabad,
Pakistan

*CORRESPONDENCE

Wasim Jamshed,
wasiktk@hotmail.com

SPECIALTY SECTION

This article was submitted to Process
and Energy Systems Engineering,
a section of the journal
Frontiers in Energy Research

RECEIVED 22 July 2022

ACCEPTED 16 August 2022

PUBLISHED 11 October 2022

CITATION

Bilal Hafeez M, Krawczuk M,
Jamshed W, Tag El Din ESM,
El-Wahed Khalifa HA and
Aziz ElSeabee FA (2022), Thermal
energy development in
magnetohydrodynamic flow utilizing
titanium dioxide, copper oxide and
aluminum oxide nanoparticles: Thermal
dispersion and heat
generating formularization.
Front. Energy Res. 10:1000796.
doi: 10.3389/fenrg.2022.1000796

COPYRIGHT

© 2022 Bilal Hafeez, Krawczuk,
Jamshed, Tag El Din, El-Wahed Khalifa
and Aziz ElSeabee. This is an open-
access article distributed under the
terms of the [Creative Commons
Attribution License \(CC BY\)](https://creativecommons.org/licenses/by/4.0/). The use,
distribution or reproduction in other
forums is permitted, provided the
original author(s) and the copyright
owner(s) are credited and that the
original publication in this journal is
cited, in accordance with accepted
academic practice. No use, distribution
or reproduction is permitted which does
not comply with these terms.

Thermal energy development in magnetohydrodynamic flow utilizing titanium dioxide, copper oxide and aluminum oxide nanoparticles: Thermal dispersion and heat generating formularization

Muhammad Bilal Hafeez¹, Marek Krawczuk¹, Wasim Jamshed^{2*},
El Sayed M. Tag El Din³, Hamiden Abd El-Wahed Khalifa^{4,5} and
Fayza Abdel Aziz ElSeabee^{6,7}

¹Faculty of Mechanical Engineering and Ship Technology, Institute of Mechanics and Machine Design, Gdansk University of Technology, Gdańsk, Poland, ²Department of Mathematics, Capital University of Science and Technology (CUST), Islamabad, Pakistan, ³Department of Electrical Engineering, Faculty of Engineering and Technology, Future University in Egypt, New Cairo, Egypt, ⁴Department of Operations Research, Faculty of Graduate Studies for Statistical Research, Cairo University, Giza, Egypt, ⁵Department of Mathematics, College of Science and Arts, Qassim University, Al-Badaya, Saudi Arabia, ⁶Department of Mathematics, Faculty of Science, Helwan University, Cairo, Egypt, ⁷Department of Mathematics, College of Science and Arts, Qassim University, Alasyah, Saudi Arabia

Background: The main aim of this article heat transfer in thermal engineering deals with the production, use, transformation, and transfer of thermal energy. Engineering and industrial fields including food packaging, the production of food additives, electronic cooling, microturbines, etc. Heavily rely on heat transmission. Due to its intriguing potential in industries like the production of polymers, paper, crystal glass, etc., scientists from all over the world have endeavored to investigate the effect of heat transmission on fluid flows past an expandable surface.

Purpose: The use of a single-phase technique to assess Newtonian nanofluid flow along stretched surfaces with heat transfer convective models is emphasized in this research. A mathematical formulation is used to do the numerical computations for copper oxide (CuO), aluminum oxide (Al₂O₃), and titanium dioxide (TiO₂) nanoparticles using water (H₂O) as the base fluid.

Formulation: The fifth-order Runge-Kutta shooting method procedure with shelling performance are used to solve non-linear ordinary differential equations with boundary conditions numerically. Researched and analyzed for changes in several parameters, plots illustrating the effects of motivated and non-motivated MHD are given to explain the physical values.

Finding: Dispersion of solid items in the working fluid is reported to significantly improve thermal performance. The Biot number determines how convective the border is. With an increase in the Biot number, the fluid's temperature drops

significantly. It has been demonstrated that Copper oxide (CuO), nanoparticles are more efficient than Titanium Dioxide (TiO₂) and Aluminum Oxide for thermal enhancement (Al₂O₃).

Novelty: As far as the authors are aware, no studies have been done on the steady MHD flow and convective heat transfer of nanofluids over a nonuniform stretched surface under the influence of a heat source and viscous dissipation.

KEYWORDS

thermal performance, magnetohydrodynamic flow, porous medium, nanoparticles, thermal jump conditions

Introduction

Many scientists who study the design of thermal systems are continuously thinking of new ways to build thermal systems that are more effective. The recent technique dispersion of metallic nano-structures in base fluid is the most popular and several aspects of this technique have been discussed so far. Using both theory and experiment, it has been demonstrated that a base fluid's thermal properties can be improved by the addition of nanostructures, improving the base fluid's efficiency as a working fluid. Nanofluids are just such fluids. The development of nanofluids has inspired researchers, and as a result, several papers have been published up to this point. As an illustration, [Sheikholeslami et al. \(2019a\)](#) and [Sheikholeslami et al. \(2019b\)](#). The effects of alumina nanoparticle dispersion on momentum and heat energy transfer, as well as an increase in wall heat flux caused by increased thermal conductivity in a magnetohydrodynamic fluid, were all the subjects of investigations. [Li et al. \(2019\)](#) investigated a rising behavior of thermal energy transfer in the fluid which conducts electricity when subjected to a magnetic field and computed the governing issues using the Lattice Boltzmann method to better comprehend the underlying physics (LBM). The effect of metallic nano-structure addition on the working fluid's capacity for thermal conduction was theoretically examined by [Sadiq et al. \(2019\)](#). [Saleem et al. \(2019a\)](#) mathematical models for improving mixed convective heat and mass transmission were based on Water's B rheology. They researched a range of topics using numerical simulations. The working fluid's thermal performance significantly improved as a result of [Ramzan et al. \(2019\)](#) examination of the transport process in a 3D flow of MHD fluid including nanoparticles. [Saleem et al. \(2019b\)](#) discussed the best analytical technique in regard to the thermal performance of nanomaterials. The influence of heat dissipation on the temperature profile in nanoparticle was also examined, and it was discovered that the presence of metallic nanostructures improved the performance of the working fluid. [Dogonchi et al. \(2019a\)](#) looked at natural convection in addition to the impact of nano-solid formations on the working fluid's

thermal effectiveness of an elliptic heater in a cavity. The effects of heat radiation and porous media on momentum and energy transmission in fluids containing solid nanoparticles were examined by [Dogonchi et al. \(2019b\)](#). [Hosseinizadeh et al. \(2019\)](#) investigated instantaneous effects of nonlinear thermal radiation and porous media on thermal characteristics of fluid subjected to dispersion of nano-structures in the presence of mass transport under the influence of chemical reaction. [Gholinia et al. \(2019\)](#) during mass transportation MHD, created mathematical models for homogeneous-heterogeneous chemical interactions over a revolving disk, Eyring-Powell fluid is poured. [Chamkha et al. \(2019\)](#) formulated a mathematical model to investigate the hybridity of metallic nano-particles on the heat transfer properties of the working fluid when provided an external magnetic field. [Afridi et al. \(2018\)](#) used mathematical models to examine how the hybridity of nanoparticles affects the efficiency of fluid thermal conductivity over moving surfaces when there is significant heat dissipation. To investigate an improvement in fluid thermal performance, they solved the developed challenges. [Zangoee et al. \(2019\)](#) performance hydrothermal analysis for magnetohydrodynamic flow over rotating disk subjected to thermal radiations and external magnetic field.

Electrically conducting fluid performs entirely different from electrically nano-conducting fluid, when provided magnetic field, because of the Lorentz effect, which changes the flow and distribution of heat energy. Such magnetic-field-exposed fluid flows are known as MHD flows, and they have been extensively studied. For instance, [Ghadikolaei et al. \(2018a\)](#) and [Ghadikolaei et al. \(2018b\)](#) examined at how the magnetic field affected how heat and velocity were transferred in a convective fluid including nanostructures. [Hatami et al. \(2014\)](#) numerical simulation of two-phase MHD flow between nanoparticle-containing plates was completed. Hall and ion slip effects in three-dimensional flow with a magnetic field and nanoparticles were investigated by [Nawaz et al. \(2018a\)](#). [Nawaz et al. \(2018b\)](#) investigated using computers how to increase heat transmission in MHD flow over a moving surface. [Alharbi et al. \(2019\)](#) investigated heat transfer in an MHD flow of fluid over a cylinder exposed to a magnetic field. In a chamber containing liquid and exposed to an external

magnetic field, Saleem et al. (2019c) looked at heat transport in the liquid.

The flows of fluids in porous medium are encountered in several daily life applications, such as seepages of fluid through sands and rocks, movement of oil in soil etc. Thereby, various studies on the effects of heat transfer and fluid flow have been conducted. For example, Hayat et al. (2017) addressed governing issues for the impact of magnetic and thermal radiation on heat transfer in a Maxwellian fluid under a permeable channel field. Sheikholeslami and Zeeshan (2018) performed numerical simulations to enhance the thermal conduction properties of nanofluids containing iron oxide nanoparticles with a porous medium. Darcy's law is followed by the flow resistance caused by porous media. Maghsoudi and Siavashi (2019) investigated the optimization of pore diameters in a heterogeneous porous media with different convection in a lid-driven cavity with two sides. Vo et al. (2019) investigated the effect of nano-particles on the transmission of heat energy in magnetohydrodynamic flow during convective heat transfer under the influence of sinusoidal resistive force due to porous media. In a cadmium telluride nanofluid, Hanif et al. (2019) examined the effects of a cone inserted into a porous media on MHD natural convection. Khan and Aziz (2011) investigated the impact of nanoparticles and porous media on mass and heat transmission during heterogeneous-homogeneous chemical processes.

The Shooting method RK-5 method is utilized to solve initial value problems Along with the Newton-Raphson approach in the application of nanofluids. The higher order nonlinear ordinary differential equations are resolved by the shooting method (Rohani et al., 2012; Olatundun and Makinde, 2017; Nawaz and Shoaib Arif, 2019). The purpose of this study, which is motivated by the aforementioned sources of inspiration, is to investigate The effects of MHD, porous media, viscosity dissipation, Joule heating, and boundary layer restrictions on the heat flux and flow of Newtonian nanofluid. It was possible to complete the mathematical flow modeling of the nanofluid using a phase flow nanofluid model. It has been suggested that the nanoparticles in water (H_2O) base fluid are comprised of copper oxide (CuO), aluminum oxide (Al_2O_3), and Titanium Dioxide (TiO_2) nanoparticles. A quantitative model is created, which is then transformed into an ODE system by making the necessary similar modifications. The shooting method was used to resolve the nondimensional system of equations. The aftereffects of velocity and temperature distributions are shown and displayed using the MATLAB program for a lengthy period of time. Visual and numerical analyses of drag force and heat transfer rates are performed. The numerical results of the current study are also contrasted with those of earlier studies for comparison's sake. As far as we can tell, there are no other publications in the literature that compare this model to it; it is novel and unique.

The results of this study will be useful for many power production and industries. So, (Hassan, 2018; Goud, 2020;

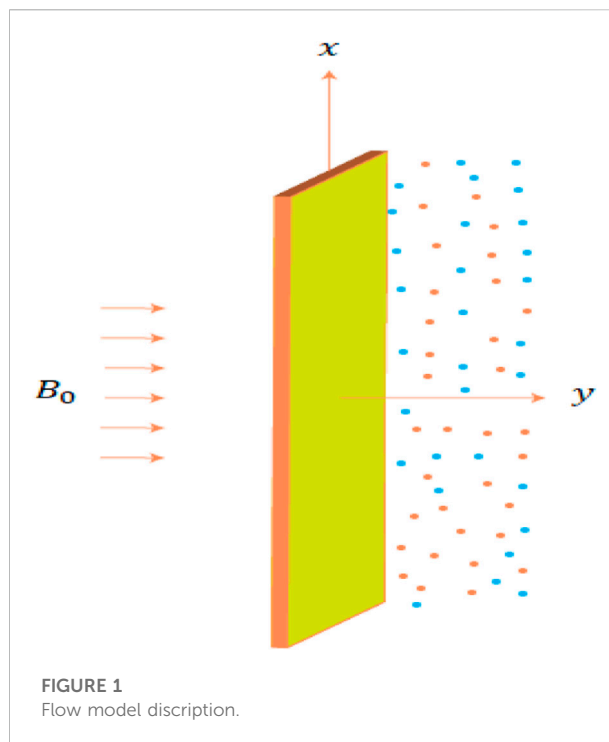


FIGURE 1
Flow model description.

Goud et al., 2020; Pramod Kumar et al., 2020; Hassan et al., 2021a; Kumar et al., 2021a; Bejawada et al., 2021; Hassan et al., 2021b; Kumar et al., 2021b; Goud and Nandeppanavar, 2021; Srinivasulu and Goud, 2021; Zhang et al., 2021; Hassan et al., 2022; Rizwan and Hassan, 2022; Shankar Goud et al., 2022) are a chosen number of the important determinants.

This paper is divided into five parts. The second segment has extensive modeling. Section 3 of the article covers the solution approach. Section 5 presents and discusses the results. The results of this investigation are described near the end.

Description of the physical setup

To investigate the rise in heat conductivity, let's explore how three various nanometallic structures, namely CuO , Al_2O_3 and TiO_2 disperse in water. Nano-water is exposed to a magnetic field. When heated, vertical surfaces are coated with a nano-water mixture, convection happens. Additionally, it is anticipated that this nano-water mixture generates heat. A Boussinesq calculation shows that the buoyancy force is significant.

Research hypothesis for the current model

The ensuing standards, together with the requirements, be relevant to the stream framework:

TABLE 1 Nanofluid thermophysical properties are (Goud, 2020).

| Features | Nanofluid |
|--------------------------------------|--|
| Dynamical viscidness (μ) | $\mu_{nf} = \mu_f (1 - \phi)^{-2.5}$ |
| Density (ρ) | $\rho_{nf} = (1 - \phi)\rho_f + \phi\rho_s$ |
| Thermal expansion (β) | $\beta_{nf} = (1 - \phi)\beta_f + \phi\beta_s$ |
| Heat capacity (ρC_p) | $(\rho C_p)_{nf} = (1 - \phi)(\rho C_p)_f + \phi(\rho C_p)_s$ |
| Thermal conductivity (κ) | $\frac{\kappa_{nf}}{\kappa_f} = \left[\frac{(\kappa_s + 2\kappa_f) - 2\phi(\kappa_s - \kappa_f)}{(\kappa_s + 2\kappa_f) + \phi(\kappa_s - \kappa_f)} \right]$ |
| Electrical conductivity (σ) | $\frac{\sigma_{nf}}{\sigma_f} = \left[1 + \frac{3(r-1)\phi}{(r+2) - (r-1)\phi} \right], r = \frac{\sigma_s}{\sigma_f}$ |

2 – D laminar steady flow, phase flow model,
MHD, permeable medium,
joule heating, viscous dissipation
vertical wall convective boundary conditions.

In Figure 1, the geometry of the flow model is shown as:

Since fluid is moving through a porous media, it is subject to a resistive force. Simplified PDEs are

$$\frac{\partial u}{\partial x} + \frac{\partial v}{\partial y} = 0, \quad (1)$$

$$u \frac{\partial u}{\partial x} + v \frac{\partial u}{\partial y} = \frac{\mu_{nf}}{\rho_{nf}} \frac{\partial^2 u}{\partial y^2} + \beta_{nf} g \left[u \frac{\partial T}{\partial x} - \frac{\partial u}{\partial x} (T_f - T_\infty) + T_f - T_\infty \right] - \frac{\sigma_{nf} B_0^2 u}{\rho_{nf}} - \mu_{nf} \frac{u}{k_1}, \quad (2)$$

$$u \frac{\partial T_f}{\partial x} + v \frac{\partial T_f}{\partial y} = \frac{k_{nf}}{(\rho C_p)_{nf}} \frac{\partial^2 T_f}{\partial y^2} + \frac{\mu_{nf}}{(\rho C_p)_{nf}} \left(\frac{\partial u}{\partial y} \right)^2 + \frac{Q_0}{(\rho C_p)_{nf}} (T_f - T_\infty) + \frac{\sigma_{nf} B_0^2 u^2}{(\rho C_p)_{nf}}, \quad (3)$$

The given BCs are

$$\left. \begin{aligned} u(x, 0) = ax, v(x, 0) = 0, -k_f \frac{\partial T}{\partial y}(x, 0) &= h_f (T_f - T(x, 0)), \\ u(x, \infty) = 0, T_f(x, \infty) &= T_\infty. \end{aligned} \right\} \quad (4)$$

Where,

$$\left. \begin{aligned} \text{flow velocity } (\vec{V} = [u, v, 0]), \text{ temperature } (T), \\ \text{gravitational acceleration } (g), \text{ magnetic field strength } (B), \\ \text{porosity } (k_1), \text{ thermal conductivity of the surface } (k_f), \\ \text{kinematic viscosity } (\mu), \text{ specific heat constant } (c_p), \\ \text{heat transfer coefficient } (h_f), \text{ density } (\rho), \\ \text{thermal conductivity } (k), \text{ electrical conductivity } (\sigma), \\ \text{nanofluid } (nf), \text{ thermal expansion of nanofluid } (\beta_{nf}) \end{aligned} \right\}$$

Table 1 below lists nanoparticle correlations.

Equations 1–4 become dimensionless by adding new variables.

TABLE 2 Overview of the ingrained control restrictions.

| Symbols | Name | Formule |
|-----------|---------------------------|---|
| β^* | heat generation parameter | $\beta^* = \frac{Q}{a(\rho C_p)_{nf}}$ |
| M | magnetic parameter | $M = \frac{\sigma_f B_0^2}{\rho_f a}$ |
| ϕ | Volume fraction | - |
| G | Grashof number | $Gr = \frac{\beta_f g (T_f - T_\infty)}{U_0 a}$ |
| K | porous medium parameter | $K = \frac{\nu_f}{ak_1}$ |
| Ec | Eckert number | $Ec = \frac{U_0^2}{C_p T_0}$ |
| Pr | Prandtl-number | $Pr = \frac{\nu_f}{\alpha_f}$ |

$$\begin{aligned} u &= ax f'(\eta), v = -\sqrt{av_f}, \psi = (av_f)^{\frac{1}{2}} x f(\eta), \eta = \left(\frac{a}{\nu_f} \right)^{\frac{1}{2}} y, \theta(\eta) \\ &= \frac{T - T_\infty}{T_w - T_\infty}, \end{aligned} \quad (5)$$

and as a result, one can

$$\begin{aligned} f''' + \phi_1 [f f'' - f'^2] - [M \phi_2 (1 - \phi)^{2.5} + K] f' + Gr \phi_1 \left(1 - \phi + \phi \frac{\beta_s}{\beta_f} \right) \theta \\ = 0, \end{aligned} \quad (6)$$

$$\theta'' + \frac{k_f}{k_{nf}} Pr \phi_3 \left[f \theta' - f' \theta + \beta^* \theta + \frac{Ec}{\phi_4} f'^2 \right] + \phi_2 \frac{k_f M Ec Pr}{k_{nf}^2}, \quad (7)$$

Dimensionless BCs (boundary conditions) are

$$\left. \begin{aligned} f(0) = 0, f'(0) = 1, \theta'(0) &= Bi[1 - \theta(0)], \\ \theta(\infty) = 0, f'(\infty) &= 0. \end{aligned} \right\} \quad (8)$$

The derivatives mentioned above relate to the variable η . The following Table 2 defines the parameter initial values. Where

ϕ_1, ϕ_2, ϕ_3 and ϕ_4 are

$$\phi_1 = (1 - \phi)^{2.5} \left(1 - \phi + \phi \frac{\rho_s}{\rho_f} \right), \phi_2 = \left(1 + \frac{3(r-1)\phi}{(r+2) - (r-1)\phi} \right), \quad (9)$$

$$\phi_3 = \left(1 - \phi + \phi \frac{(\rho C_p)_s}{(\rho C_p)_f} \right), \phi_4 = (1 - \phi)^{2.5} \left(1 - \phi + \phi \frac{(\rho C_p)_s}{(\rho C_p)_f} \right). \quad (10)$$

Divergent velocity is (Hafeez et al., 2021)

$$C_f = \frac{\tau_{xy}|_{y=0}}{\rho_f U_0^2} = \frac{1}{Re_x^{1/2} (1 - \phi)^{2.5}} f''(0). \quad (11)$$

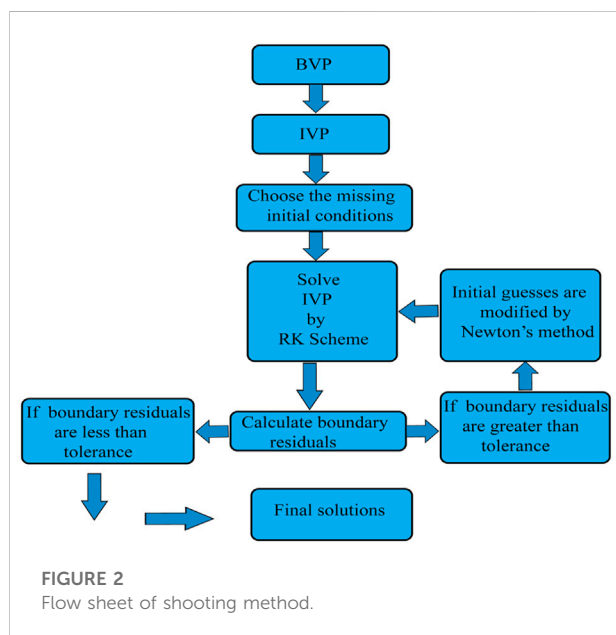
Nusselt number is

TABLE 3 Thermo physical properties water and nanoparticles (Jamshed and Aziz, 2018; Jamshed, 2021; Khashif et al., 2020).

| Materials | ρ (kg/m ³) | c_p (J/kgK) | k (W/mK) | $\beta \times 10^{-6}$ (K ⁻¹) | σ (S/m) |
|-----------------------------------|-----------------------------|---------------|------------|---|----------------------|
| Water (H ₂ O) | 987.4 | 4200 | 0.7 | 22.0 | 0.4×10^{-5} |
| (CuO) | 6209 | 525 | 33.0 | 0.90 | 5.10×10^6 |
| (Al ₂ O ₃) | 3899 | 780 | 39.0 | 0.85 | 53.5×10^6 |
| (TiO ₂) | 4146 | 687 | 9.0 | 1.0 | 238×10^6 |

TABLE 4 Comparing $-\theta'(0)$ with alteration in Prandtl number, and taking $\beta^* = Ec = M = 0$ and $B_1 = 0$.

| P_r | Qureshi (2021) | Jamshed et al. (2021a) | This study |
|-------|----------------|------------------------|------------|
| 0.72 | 0.8087618 | 0.8087618 | 0.8087612 |
| 1.0 | 1.0000000 | 1.0000000 | 1.0000000 |
| 3.0 | 1.9235742 | 1.9235742 | 1.9235720 |
| 7.0 | 3.0731465 | 3.0731465 | 3.0731427 |
| 10 | 3.7205542 | 3.7205542 | 3.7205511 |



$$Nu = \frac{xq_w}{k_f(T_f - T_\infty)} = \frac{Re_x^{1/2} k_{nf}}{k_f} \theta'(0), \quad (12)$$

Local Reynolds number is $Re_x = \frac{ax^2}{\nu_f}$.

Thermo physical properties water and nanoparticles are presented in Table 3.

Numerical approach

Shooting method

Shooting method is used to solve the higher order nonlinear ordinary differential equations (ODEs). It is an iterative technique that transforms the original boundary value problems (BVPs) into initial value problems (IVPs). The differential equations of IVPs are integrated numerically through RK-5 method Table 4. The formulated problem needs the IVP with arbitrarily chosen initial conditions to approximate the boundary conditions. If the boundary conditions are not fulfilled to the required accuracy, with the new set of initial conditions, which are modified by Newton's method. The process of Newton method is repeated until the required accuracy is achieved. The flow chart of the shooting method is as follows in Figure 2.

Algorithm for shooting method

For a structure of two coupled first ODEs.

- $Y_1(X) = Y(X)$ and $Y_2(X) = Y'(X)$.
- $Y(X_s)$ and $Y(X_0)$ are known but $Y'(X_s)$ and $Y'(X_0)$ are unknown.
- Set $Y(X_s)$ and guess $Y'(X_s)$.
- Solve the ODE using IVP technique (RK-5), and compared the result at $X = X_0$ to the target $Y(X_0)$.
- Make another guess.
- If solution at $X = X_0$ bracket the known value, start zooming in.

Runge-Kutta 5 method

Different techniques are used by researchers for solving ordinary differential equations and this always remain area of interest. Linear differential equation is easy

to solve by analytical method but solving non-linear ODEs by systematic method is difficult to solve. So researchers used other techniques to find approximate solutions for these equations. The two most popular Runge-Kutta techniques are Runge-Kutta 4 and Runge-Kutta 5. Runge-Kutta method is also iterative technique and includes well known routine called Euler method. In this thesis we used RK-5 method and algorithm for RK-5 method is given below.

Algorithm for RK-5 method

Suppose the following problem with given initial conditions

$$x = f(t, x) \quad x(t_0) = x_0. \quad (13)$$

Then, RK-5 Method for the above initial valued problem is given by

$$x_{n+1} = x_n + \left(\frac{7K_1 + 32K_3 + 12K_4 + 32K_5 + 7K_6}{90} \right). \quad (14)$$

In above expression, x_{n+1} is the RK-5 calculation of $x(t_{n+1})$ and each K_i , $i = 1, 2, 3, 4, 5$

$$K_1 = f(t_n, x_n), \quad (15)$$

$$K_2 = hf \left(t_n + \frac{h}{2}, x_n + \frac{K_1}{2} \right), \quad (16)$$

$$K_3 = hf \left(t_n + \frac{h}{4}, x_n + \frac{3K_1 + K_2}{16} \right), \quad (17)$$

$$K_4 = hf \left(t_n + \frac{h}{2}, x_n + \frac{K_3}{2} \right), \quad (18)$$

$$K_5 = hf \left(t_n + \frac{3h}{4}, x_n + \frac{-3K_2 + 6K_3 + 9K_4}{16} \right), \quad (19)$$

$$K_6 = hf \left(t_n + h, x_n + \frac{K_1 + 4K_2 + 6K_3 - 12K_4 + 8K_5}{2} \right). \quad (20)$$

Where, h is the size of time interval.

Code-validation

The correctness of the computational strategy was established by comparing the heat transfer magnitude from the current approach with the verified results of prior investigations (Jamshed et al., 2021a; Qureshi, 2021). The results of the current investigation were quite accurate and comparable.

Results and discussion

Initial value problems are built using normalized governing boundary-value problems with correlations for thermally factors. Utilizing starting circumstances, the shooting method with Runge-Kutta 5th order is used to solve problems with changed beginning value. Using parametric simulations, the dynamics of the flow low variables are examined in Table 1. To choose the best nanoparticles from CuO, Al₂O₃ and TiO₂ for the system, simulations are done. When $Gr = 0$ and 2.5, the compression of the velocities of copper, aluminum, and titanium nanofluids is shown in Figure 3. The Grashof number Gr is significant because it measures the relationship between the buoyant force brought on by changes in fluid density over space (resulting from temperature differences) and the restraining force brought on by fluid viscosity. This figure explains that for both scenarios nanofluid has a higher velocity as compared to purefluid. This figure also explains how raising the magnitude of Gr causes, nanofluids to move more quickly. Figure 4 shows that the effects of porosity parameter on velocity for the case of CuO nanofluid. The velocity of the copper nanofluid decreases by increasing the parameter. The effects of Biot number Bi on velocity are depicted in Figure 5. A lower Biot number means that an objects conductive resistance is relatively lower than external resistance. The velocity will decrease as the Biot number is increased. The boundary layer viscosity decreases as the magnetic field parameter on velocity increases in Figure 6, which shows the application of a magnetic field to electrically conducting fluid particles, a Lorentz force in the boundary layer, and boundary layer application. The effect of the heat generating parameter β^* on temperature is seen in Figure 7. It has been observed that when Ec increases, so does the thickness of the boundary layer. Figure 8 shows the effects of parameter Eckert number E_{con} on the temperature of nanofluids. It has been found that as the Eckert number Ec grows, the temperature rises. Because Eckert number has storage of energy in the fluid region and due to the deformation of viscosity and elastic. When compared to the enthalpy difference from across boundary layer, the flow's kinetic energy is measured by the Eckert number. Figure 9 shows that the temperature is increasing by rises the value of magnetic field. When we increased the value of Gr , we saw that the temperature increased (see Figure 10, which depicts the effects of Gr on temperature). We observe that when the amount of nanofluids increases, the viscosity

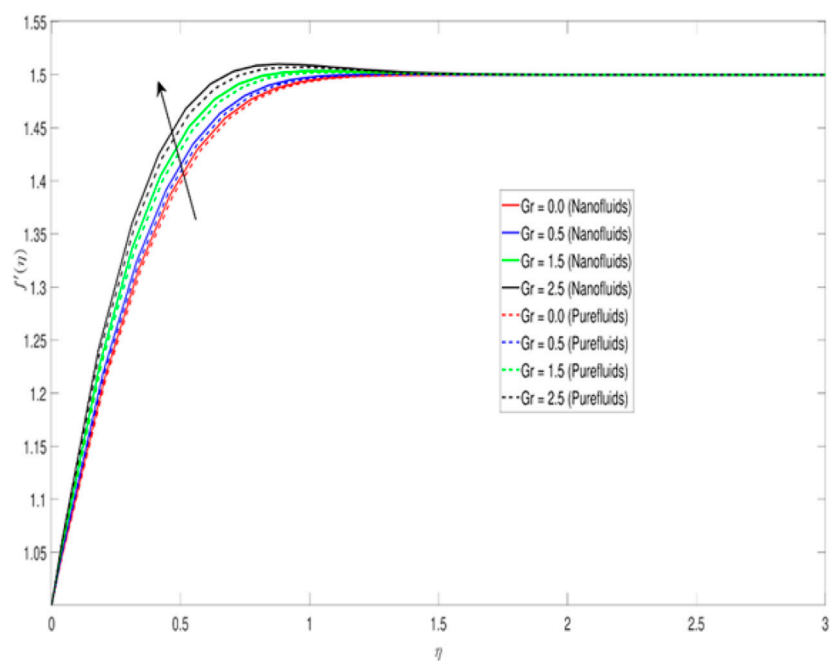


FIGURE 3
Velocity profile in opposition to modifications in the action of the buoyancy force.

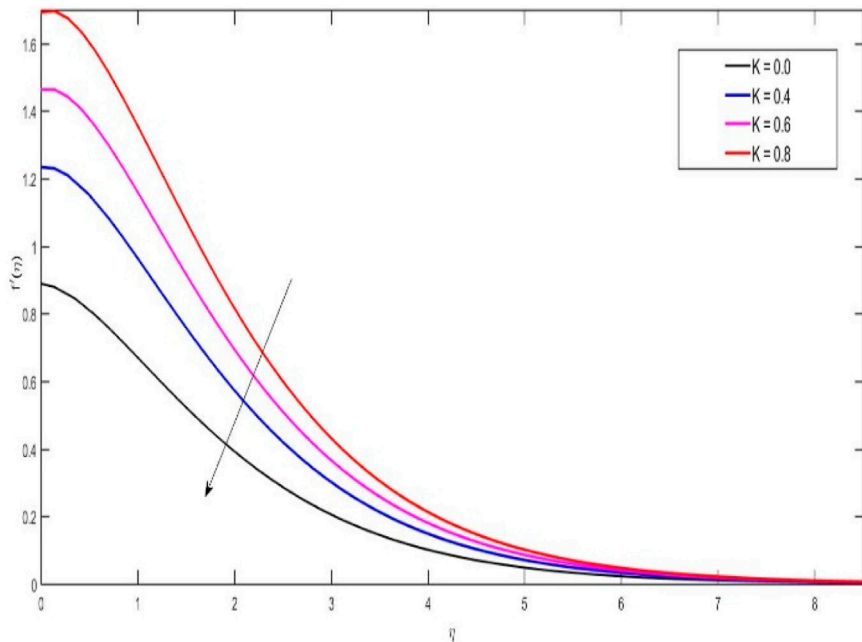


FIGURE 4
Velocity profile against change in porous medium.

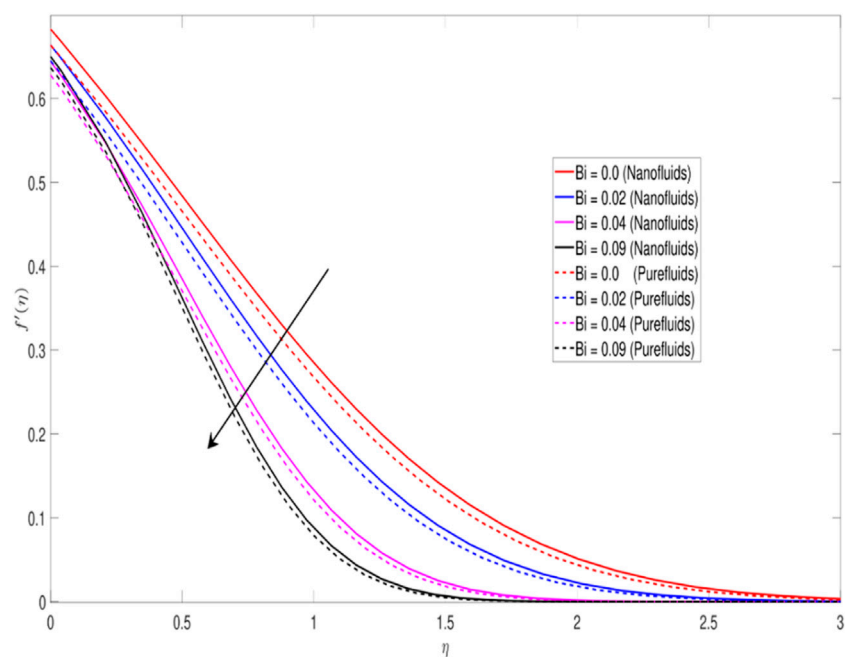


FIGURE 5
Velocity profile in relation to changes in the Biot number.

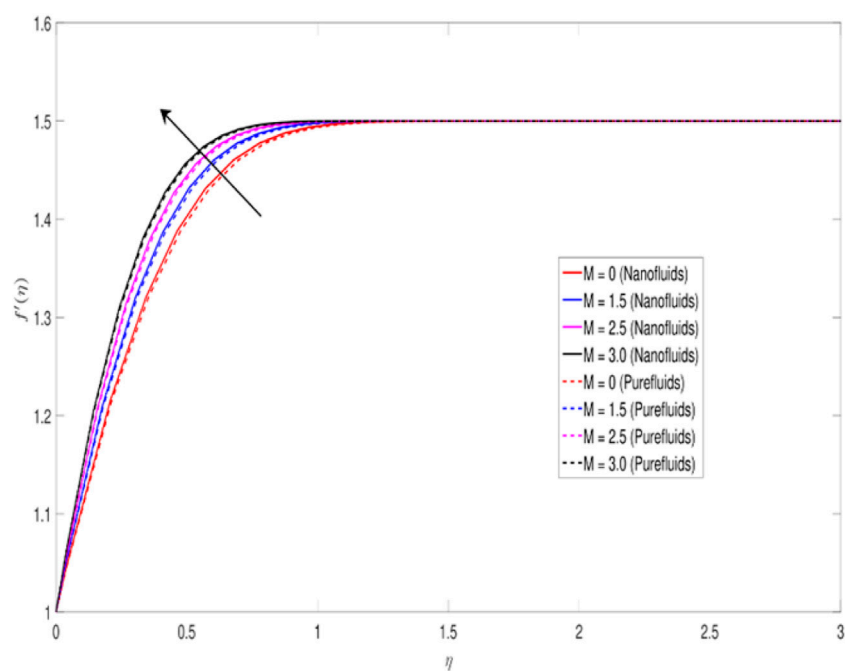


FIGURE 6
Velocity profile in relation to magnetic field change.

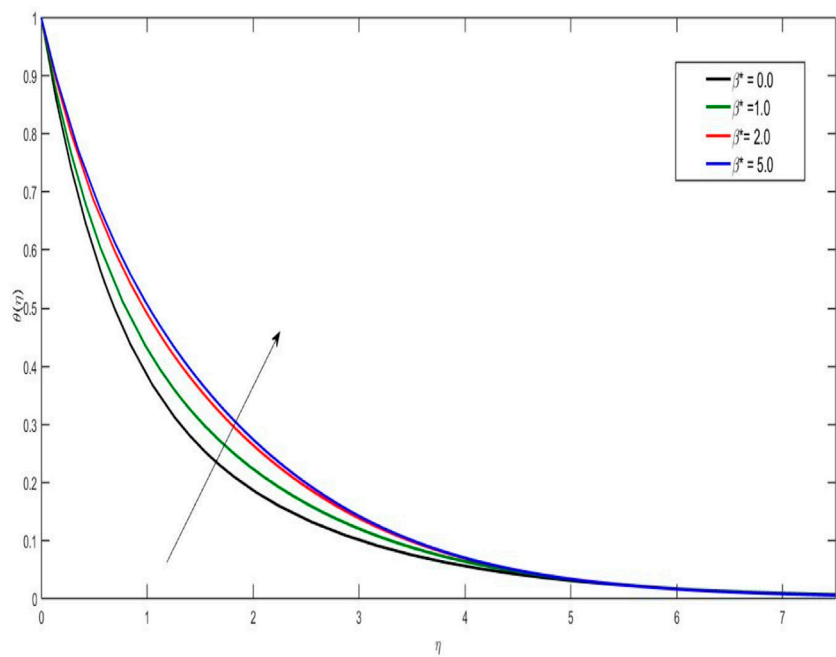


FIGURE 7
Temperature profile as a function of changing heat generation.

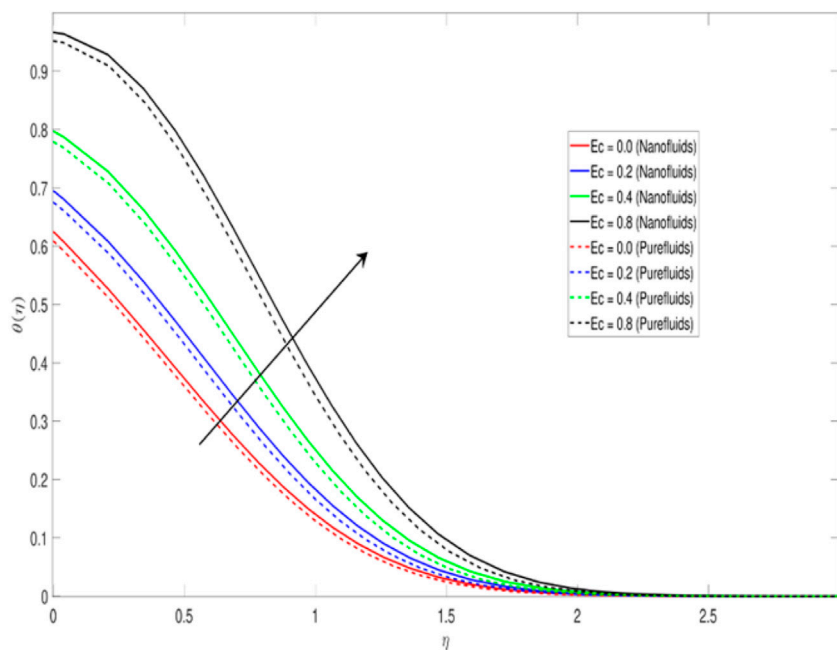


FIGURE 8
Temperature distribution vs. an Eckert number change.

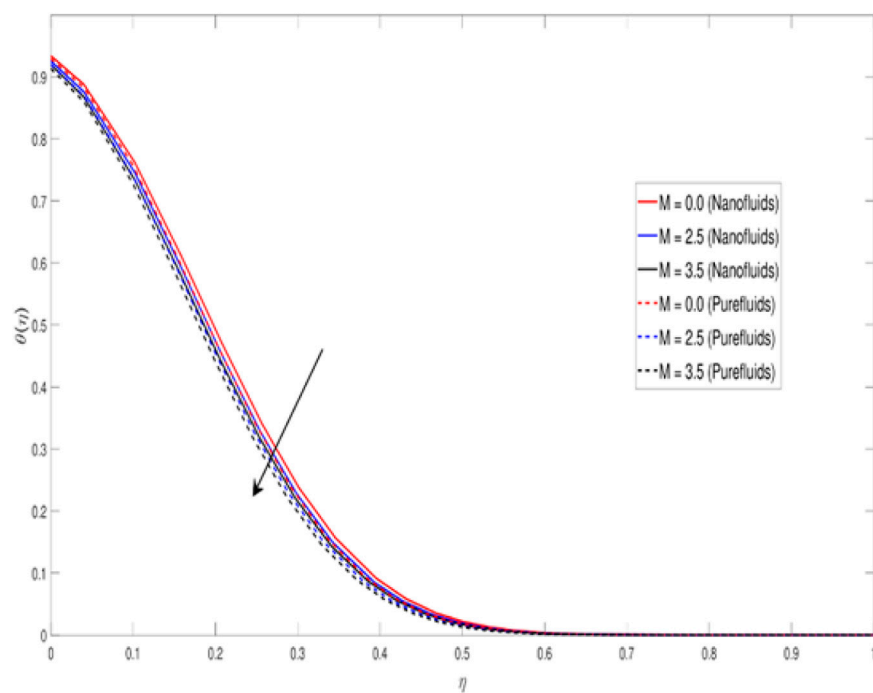


FIGURE 9
Temperature distribution vs. magnetic field variation.

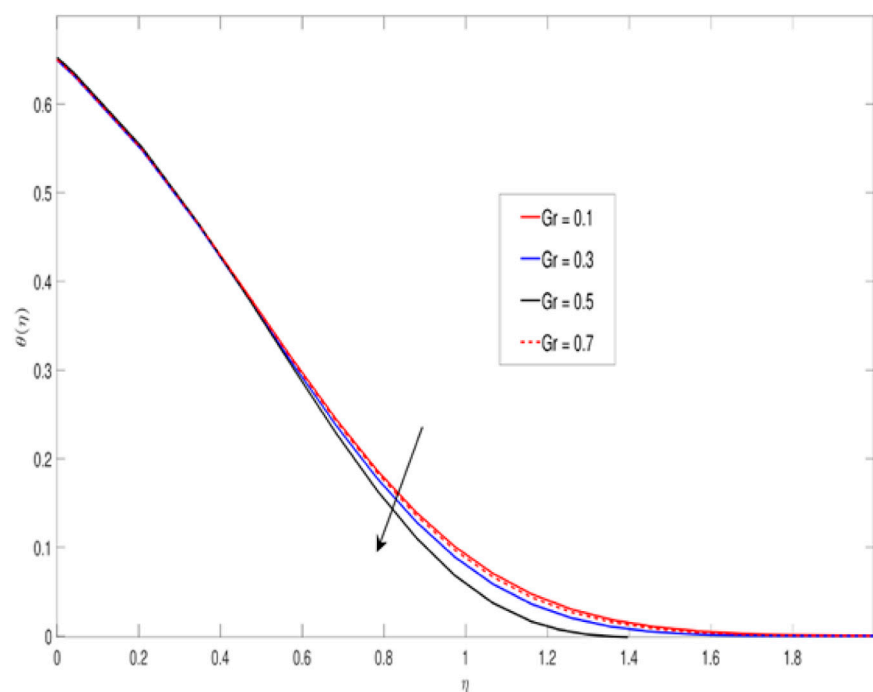


FIGURE 10
Temperature distribution vs. modification of the favored buoyancy force.

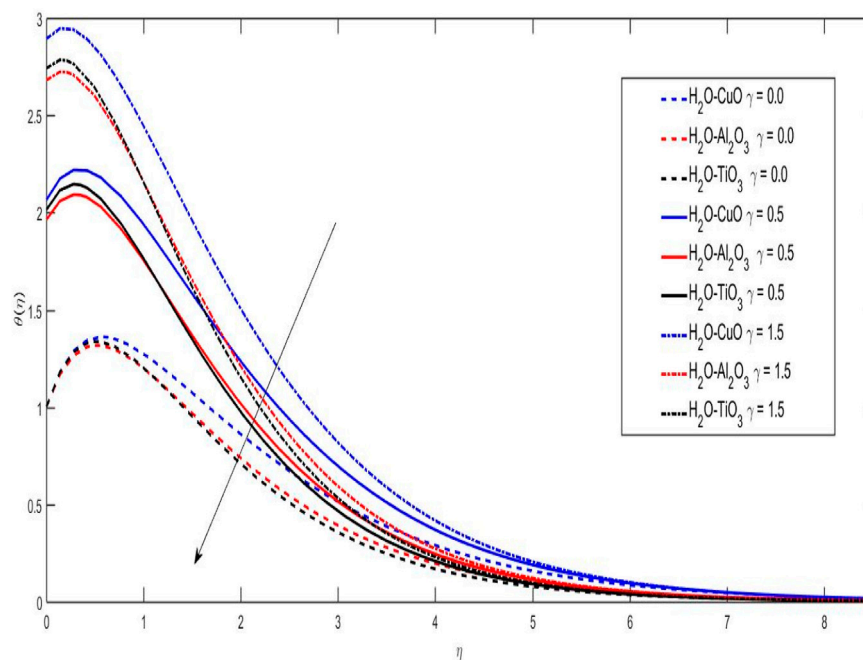


FIGURE 11
Temperature thermal effects alter vs. profile.

TABLE 5 For nanofluid with copper oxide nanoparticles with several nanoparticle factors, Nusselt number and local skin friction coefficient are equal to 0.2.

| k_{nf} | $Re_x^{-1/2}Nu$ | $Re_x^{1/2}Cf$ |
|----------|-----------------|----------------|
| 0.628 | 0.084138154 | 0.993989767 |
| 0.72141 | 0.085608603 | 1.18560452 |
| 0.82458 | 0.086968704 | 1.381935016 |
| 0.9391 | 0.091634371 | 1.58355532 |
| 1.06696 | 0.095644211 | 1.79198143 |
| 0.628 | 0.084138154 | 0.993989767 |

of the boundary layer decreases. The temperature impacts of the thermal slip parameter γ with copper-water, aluminum-water, and titanium-water nanofluids are shown in Figure 11. When the value of γ is increased, a decrease in temperature is seen. In comparison to titanium nanofluid and aluminum nanofluid, the copper nanofluid is more heat-efficient. It has been discovered that as the velocity slip parameter rises, the velocity profile decreases, the skin friction and heat transfer go down, and the mass transfer rises. Mass transport and heat transfer rates decrease when the thermal slip parameter is increased.

Table 5 displays the local friction coefficient and Nusselt number for a nanofluid containing Cu for different nanoparticle factors.

Conclusion

- 1) Convection heat transfer in Newtonian fluid exposed to magnetic field and having nano-solid metallic structures is being explored to look into the improvement in thermal conductivity. Then, for an efficient thermal system like car engines, dispersion of nano-particles among nanofluids CuO, Al_2O_3 and TiO_2 may be suggested. Key studies are listed below, along with the numerical solutions to the governing problems.
- 2) The favorable Buoyancy force assists the flow and magnetohydrodynamic boundary layer thickness has shown a rising trend when Grashof number is increased. This study is noted for all types of nanoparticles;
- 3) The variation of Biot number has shown decreasing trend on the flow of fluid. Hence flow is decelerated when Biot number is increased;

A significant restriction to fluid flow results from increasing the magnetic field's intensity. As a result, as the magnetic field increases, the boundary layer's thickness decreases.

Future applications of the fifth-order Runge-Kutta shooting technique could include a range of physical and technological difficulties (Adnan et al., 2021; Adnan, 2022; Adnan and Ashraf, 2022; Khan et al., 2022a; Khan et al., 2022b). According to (Jamshed et al., 2021b; Jamshed, 2021; Jamshed and Nisar, 2021), there have been several recent advancements that explore the importance of the research domain under consideration.

Data availability statement

The raw data supporting the conclusions of this article will be made available by the authors, without undue reservation.

Author contributions

MB and MK formulated the problem. MB and WJ solved the problem. MB, MK, WJ, ET, HE-W, and FA, computed and scrutinized the results. All the authors equally contributed in writing and proof reading of the paper. All authors reviewed the manuscript.

References

- Adnan, U. K., Ahmed, N., Manzoor, R., Mohyud-Din, S. T., and Mohyud-Din, S. T. (2021). Impacts of various shaped Cu-nanomaterial on the heat transfer over a bilateral stretchable surface: Numerical investigation. *Adv. Mech. Eng.* 13, 168781402110674. doi:10.1177/16878140211067420
- Adnan, W. A., and Ashraf, W. (2022). Numerical thermal featuring in $\gamma\text{Al}_2\text{O}_3\text{-C}_2\text{H}_6\text{O}_2$ nanofluid under the influence of thermal radiation and convective heat condition by inducing novel effects of effective Prandtl number model (EPNM). *Adv. Mech. Eng.* 14 (6), 168781322211065. doi:10.1177/16878132221106577
- Adnan, W. A. (2022). Thermal efficiency in hybrid ($\text{Al}_2\text{O}_3\text{-CuO/H}_2\text{O}$) and ternary hybrid nanofluids ($\text{Al}_2\text{O}_3\text{-CuO-Cu/H}_2\text{O}$) by considering the novel effects of imposed magnetic field and convective heat condition. *Waves in Random and Complex Media*, 1–16.
- Afridi, M. I., Qasim, M., and Saleem, S. (2018). Second law analysis of three dimensional dissipative flow of hybrid nanofluid. *J. nanofluids* 7 (6), 1272–1280. doi:10.1166/jon.2018.1532
- Alharbi, S. O., Nawaz, M., and Nazir, U. (2019). Thermal analysis for hybrid nanofluid past a cylinder exposed to magnetic field. *AIP Adv.* 9 (11), 115022. doi:10.1063/1.5127327
- Bejawada, S. G., Khan, Z. H., and Hamid, M. (2021). Heat generation/absorption on MHD flow of a micropolar fluid over a heated stretching surface in the presence of the boundary parameter. *Heat. Transf.* 50 (6), 6129–6147. doi:10.1002/htj.22165
- Chamkha, A. J., Dogonchi, A. S., and Ganji, D. D. (2019). Magneto-hydrodynamic flow and heat transfer of a hybrid nanofluid in a rotating system among two surfaces in the presence of thermal radiation and Joule heating. *AIP Adv.* 9 (2), 025103. doi:10.1063/1.5086247
- Dogonchi, A. S., Armaghani, T., Chamkha, A. J., and Ganji, D. D. (2019). Natural convection analysis in a cavity with an inclined elliptical heater subject to shape factor of nanoparticles and magnetic field. *Arab. J. Sci. Eng.* 44, 7919–7931. doi:10.1007/s13369-019-03956-x
- Dogonchi, A. S., Waqas, M., Seyyedi, S. M., Hashemi-Tilehnoe, M., and Ganji, D. D. (2019). Numerical simulation for thermal radiation and porous medium characteristics in flow of $\text{CuO-H}_2\text{O}$ nanofluid. *J. Braz. Soc. Mech. Sci. Eng.* 41 (6), 249. doi:10.1007/s40430-019-1752-5
- Ghadikolaei, S. S., Hosseinzadeh, K., and Ganji, D. D. (2018a). RETRACTED: MHD radiative boundary layer analysis of micropolar dusty fluid with graphene oxide (go)- engine oil nanoparticles in a porous medium over a stretching sheet with

Acknowledgments

The researchers would like to thank the Deanship of Scientific Research, Qassim University for funding the publication of this project.

Conflict of interest

The authors declare that the research was conducted in the absence of any commercial or financial relationships that could be construed as a potential conflict of interest.

Publisher's note

All claims expressed in this article are solely those of the authors and do not necessarily represent those of their affiliated organizations, or those of the publisher, the editors and the reviewers. Any product that may be evaluated in this article, or claim that may be made by its manufacturer, is not guaranteed or endorsed by the publisher.

joule heating effect. *Powder Technol.* 338, 425–437. doi:10.1016/j.powtec.2018.07.045

Ghadikolaei, S. S., Hosseinzadeh, K., Ganji, D. D., and Hatami, M. (2018b). $\text{Fe}_3\text{O}_4\text{-(CH}_2\text{OH)}_2$ nanofluid analysis in a porous medium under MHD radiative boundary layer and dusty fluid. *J. Mol. Liq.* 258, 172–185. doi:10.1016/j.molliq.2018.02.106

Gholinia, M., Hosseinzadeh, K., Mehrzadi, H., Ganji, D. D., and Ranjbar, A. A. (2019). Investigation of MHD Eyring–Powell fluid flow over a rotating disk under effect of homogeneous–heterogeneous reactions. *Case Stud. Therm. Eng.* 13, 100356. doi:10.1016/j.csite.2018.11.007

Goud, B. S. (2020). Heat generation/absorption influence on steady stretched permeable surface on MHD flow of a micropolar fluid through a porous medium in the presence of variable suction/injection. *Int. J. Thermofluids* 7, 100044. doi:10.1016/j.ijft.2020.100044

Goud, B. S., and Nandeppanavar, M. M. (2021). Ohmic heating and chemical reaction effect on MHD flow of micropolar fluid past a stretching surface. *Partial Differ. Equations Appl. Math.* 4, 100104. doi:10.1016/j.padiff.2021.100104

Goud, B. S., Srilatha, P., Bindu, P., and Krishna, Y. H. (2020). Radiation effect on MHD boundary layer flow due to an exponentially stretching sheet. *Adv. Math. Sci. J.* 9 (12), 10755–10761. doi:10.37418/amsj.9.12.59

Hafeez, M. B., Amin, R., Nisar, K. S., Jamshed, W., Abdel-Aty, A. H., and Khashan, M. M. (2021). Heat transfer enhancement through nanofluids with applications in automobile radiator. *Case Stud. Therm. Eng.* 27, 101192. doi:10.1016/j.csite.2021.101192

Hanif, H., Khan, I., and Shafie, S. (2019). MHD natural convection in cadmium telluride nanofluid over a vertical cone embedded in a porous medium. *Phys. Scr.* 94 (12), 125208. doi:10.1088/1402-4896/ab36e1

Hassan, M., Ali, S., Aich, W., Khliisa, F., Ayadi, B., and Kolsi, L. (2022). Transport pattern of Non-Newtonian mass and thermal energy under two diverse flow conditions by using modified models for thermodynamics properties. *Case Stud. Therm. Eng.* 29, 101714. doi:10.1016/j.csite.2021.101714

Hassan, M., Al-Khaled, K., Khan, S. U., Tlili, I., and Chammam, W. (2021). Assessment of boundary layer for flow of non-Newtonian material induced by a moving belt with power law viscosity and thermal conductivity models. *Numer. Methods Partial Differ. Equ.*, num.22743. doi:10.1002/num.22743

- Hassan, M., El-Zahar, E. R., Khan, S. U., Rahimi-Gorji, M., and Ahmad, A. (2021). Boundary layer flow pattern of heat and mass for homogenous shear thinning hybrid-nanofluid: An experimental data base modeling. *Numer. Methods Partial Differ. Equ.* 37 (2), 1234–1249. doi:10.1002/num.22575
- Hassan, M. (2018). Impact of iron oxide particles concentration under a highly oscillating magnetic field on ferrofluid flow. *Eur. Phys. J. Plus* 133 (6), 230–234. doi:10.1140/epjp/i2018-12045-7
- Hatami, M., Hosseinzadeh, K., Domairry, G., and Behnamfar, M. T. (2014). Numerical study of MHD two-phase Couette flow analysis for fluid-particle suspension between moving parallel plates. *J. Taiwan Inst. Chem. Eng.* 45 (5), 2238–2245. doi:10.1016/j.jtice.2014.05.018
- Hayat, T., Khan, M. I., Waqas, M., Alsaedi, A., and Farooq, M. (2017). Numerical simulation for melting heat transfer and radiation effects in stagnation point flow of carbon–water nanofluid. *Comput. methods Appl. Mech. Eng.* 315, 1011–1024. doi:10.1016/j.cma.2016.11.033
- Hosseinzadeh, K., Gholinia, M., Jafari, B., Ghanbarpour, A., Olfian, H., and Ganji, D. D. (2019). Nonlinear thermal radiation and chemical reaction effects on Maxwell fluid flow with convectively heated plate in a porous medium. *Heat. Trans. Res.* 48 (2), 744–759. doi:10.1002/htj.21404
- Jamshed, W., and Aziz, A. (2018). Entropy analysis of TiO₂-CuO/EG casson hybrid nanofluid via cattaneo-christov heat flux model. *Appl. Nanosci.* 08, 01–14.
- Jamshed, W., Devi, S. U., and Nisar, K. S. (2021). Single phase-based study of Ag-Cu/EO Williamson hybrid nanofluid flow over a stretching surface with shape factor. *Phys. Scr.* 96, 065202. doi:10.1088/1402-4896/abec0
- Jamshed, W., and Nisar, K. S. (2021). Computational single-phase comparative study of a Williamson nanofluid in a parabolic trough solar collector via the Keller box method. *Int. J. Energy Res.* 45 (7), 10696–10718. doi:10.1002/er.6554
- Jamshed, W., Nisar, K. S., Mohamed Isa, S. S. P., Batool, S., Abdel-Aty, A. H., and Zakarya, M. (2021). Computational case study on tangent hyperbolic hybrid nanofluid flow: Single phase thermal investigation. *Case Stud. Therm. Eng.* 27, 101246. doi:10.1016/j.csite.2021.101246
- Jamshed, W. (2021). Numerical investigation of MHD impact on maxwell nanofluid. *Int. Commun. Heat Mass Transf.* 120, 104973. doi:10.1016/j.icheatmasstransfer.2020.104973
- Khan, U. A., Ullah, B., Abdul Wahab, H., Ullah, I., Almuqrin, M. A., and Khan, I. (2022). Comparative thermal transport mechanism in Cu-H₂O and Cu-Al₂O₃/H₂O nanofluids: Numerical investigation. *Waves in Random and Complex Media*, 1–16.
- Khan, U., Ahmed, N., and Khan, I. (2022). Heat transfer evaluation in MgZn₆Zr/C8H18 [(Magnesium-Zinc-Zirconium)/Engine oil] with non-linear solar thermal radiations and modified slip boundaries over 3-dimensional convectively heated surface. *Front. Energy Res.* 351.
- Khan, W. A., and Aziz, A. (2011). Double-diffusive natural convective boundary layer flow in a porous medium saturated with a nanofluid over a vertical plate: Prescribed surface heat, solute and nanoparticle fluxes. *Int. J. Therm. Sci.* 50 (11), 2154–2160. doi:10.1016/j.jthermalsci.2011.05.022
- Khashi'ie, N. S., Arifin, N. M., Pop, I., and Wahid, N. S. (2020). Flow and heat transfer of hybrid nanofluid over a permeable shrinking cylinder with joule heating: A comparative analysis. *Alexandria Eng. J.* 59 (3), 1787–1798. doi:10.1016/j.aej.2020.04.048
- Kumar, M. A., Reddy, Y. D., Goud, B. S., and Rao, V. S. (2021). Effects of solet, dufour, hall current and rotation on MHD natural convective heat and mass transfer flow past an accelerated vertical plate through a porous medium. *Int. J. Thermofluids* 9, 100061. doi:10.1016/j.ijft.2020.100061
- Kumar, M. A., Reddy, Y. D., Rao, V. S., and Goud, B. S. (2021). Thermal radiation impact on MHD heat transfer natural convective nano fluid flow over an impulsively started vertical plate. *Case Stud. Therm. Eng.* 24, 100826. doi:10.1016/j.csite.2020.100826
- Li, Z., Sheikholeslami, M., Mittal, A. S., Shafee, A., and Haq, R. U. (2019). Nanofluid heat transfer in a porous duct in the presence of Lorentz forces using the lattice Boltzmann method. *Eur. Phys. J. Plus* 134 (1), 30.
- Maghsoodi, P., and Siavashi, M. (2019). Application of nanofluid and optimization of pore size arrangement of heterogeneous porous media to enhance mixed convection inside a two-sided lid-driven cavity. *J. Therm. Anal. Calorim.* 135 (2), 947–961. doi:10.1007/s10973-018-7335-3
- Nawaz, M., Rana, S., and Qureshi, I. H. (2018). Computational fluid dynamic simulations for dispersion of nanoparticles in a magnetohydrodynamic liquid: A galerkin finite element method. *RSC Adv.* 8 (67), 38324–38335. doi:10.1039/c8ra03825b
- Nawaz, M., Rana, S., Qureshi, I. H., and Hayat, T. (2018). Three-dimensional heat transfer in the mixture of nanoparticles and micropolar MHD plasma with Hall and ion slip effects. *AIP Adv.* 8 (10), 105109. doi:10.1063/1.5050670
- Nawaz, Y., and Shoaib Arif, M. (2019). Keller-Box shooting method and its application to nanofluid flow over convectively heated sheet with stability and convergence. *Numer. Heat. Transf. Part B Fundam.* 76 (3), 152–180. doi:10.1080/10407790.2019.1644924
- Olatundun, A. T., and Makinde, O. D. (2017). “Analysis of Blasius flow of hybrid nanofluids over a convectively heated surface,” in *Defect and diffusion forum* (Trans Tech Publications Ltd), 377, 29–41.
- Pramod Kumar, P., Shankar Goud, B., and Malga, B. S. (2020). Finite element study of Soret number effects on MHD flow of Jeffrey fluid through a vertical permeable moving plate. *Partial Differ. Equ. Appl. Math.* 1, 100005. doi:10.1016/j.padiff.2020.100005
- Qureshi, M. A. (2021). Thermal capability and entropy optimization for Prandtl-Eyring hybrid nanofluid flow in solar aircraft implementation. *Alexandria Eng. J.* 61 (7), 5295–5307. doi:10.1016/j.aej.2021.10.051
- Ramzan, M., Sheikholeslami, M., Saeed, M., and Chung, J. D. (2019). On the convective heat and zero nanoparticle mass flux conditions in the flow of 3D MHD Couple Stress nanofluid over an exponentially stretched surface. *Sci. Rep.* 9 (1), 562. doi:10.1038/s41598-018-37267-2
- Rizwan, M., and Hassan, M. (2022). *Feature of metallic oxide nanoparticles in the thermal efficiency and flow structure of non-Newtonian homogeneous nanofluid: Experimental data-based mathematical approach*. *Waves in Random and Complex Media*, 1–20.
- Rohni, A. M., Ahmad, S., and Pop, I. (2012). Flow and heat transfer over an unsteady shrinking sheet with suction in nanofluids. *Int. J. Heat Mass Transf.* 55 (7–8), 1888–1895. doi:10.1016/j.ijheatmasstransfer.2011.11.042
- Sadiq, M. A., Khan, A. U., Saleem, S., and Nadeem, S. (2019). Numerical simulation of oscillatory oblique stagnation point flow of a magneto micropolar nanofluid. *RSC Adv.* 9 (9), 4751–4764. doi:10.1039/c8ra09698h
- Saleem, S., Firdous, H., Nadeem, S., and Khan, A. U. (2019). Convective heat and mass transfer in magneto Walter's B nanofluid flow induced by a rotating cone. *Arab. J. Sci. Eng.* 44 (2), 1515–1523. doi:10.1007/s13369-018-3598-z
- Saleem, S., Nadeem, S., Rashidi, M. M., and Raju, C. S. (2019). An optimal analysis of radiated nanomaterial flow with viscous dissipation and heat source. *Microsyst. Technol.* 25 (2), 683–689. doi:10.1007/s00542-018-3996-x
- Saleem, S., Shafee, A., Nawaz, M., Dara, R. N., Tlili, I., and Bonyah, E. (2019). Heat transfer in a permeable cavity filled with a ferrofluid under electric force and radiation effects. *AIP Adv.* 9 (9), 095107. doi:10.1063/1.5120439
- Shankar Goud, B., Pramod Kumar, P., and Malga, B. S. (2022). Induced magnetic field effect on MHD free convection flow in nonconducting and conducting vertical microchannel walls. *Heat. Trans.* 51 (2), 2201–2218. doi:10.1002/htj.22396
- Sheikholeslami, M., Mehryan, S. A., Shafee, A., and Sheremet, M. A. (2019a). Variable magnetic forces impact on magnetizable hybrid nanofluid heat transfer through a circular cavity. *J. Mol. Liq.* 277, 388–396. doi:10.1016/j.molliq.2018.12.104
- Sheikholeslami, M., Saleem, S., Shafee, A., Li, Z., Hayat, T., Alsaedi, A., et al. (2019b). Mesoscopic investigation for alumina nanofluid heat transfer in permeable medium influenced by Lorentz forces. *Comput. Methods Appl. Mech. Eng.* 349, 839–858.
- Sheikholeslami, M., and Zeeshan, A. (2018). Numerical simulation of Fe₃O₄-water nanofluid flow in a non-Darcy porous media. *Int. J. Numer. Methods Heat. Fluid Flow.* 28 (3), 641–660. doi:10.1108/hff-04-2017-0160
- Srinivasulu, T., and Goud, B. S. (2021). Effect of inclined magnetic field on flow, heat and mass transfer of Williamson nanofluid over a stretching sheet. *Case Stud. Therm. Eng.* 23, 100819. doi:10.1016/j.csite.2020.100819
- Vo, D. D., Hedayat, M., Ambreen, T., Shehzad, S. A., Sheikholeslami, M., Shafee, A., et al. (2019). Effectiveness of various shapes of Al₂O₃ nanoparticles on the MHD convective heat transportation in porous medium. *J. Therm. Anal. Calorim.* 139, 1345–1353. doi:10.1007/s10973-019-08501-4
- Zangooee, M. R., Hosseinzadeh, K., and Ganji, D. D. (2019). Hydrothermal analysis of MHD nanofluid (TiO₂-GO) flow between two radiative stretchable rotating disks using AGM. *Case Stud. Therm. Eng.* 14, 100460. doi:10.1016/j.csite.2019.100460
- Zhang, X. H., Shah, R., Saleem, S., Shah, N. A., Khan, Z. A., and Chung, J. D. (2021). Natural convection flow Maxwell fluids with generalized thermal transport and Newtonian heating. *Case Stud. Therm. Eng.* 27, 101226. doi:10.1016/j.csite.2021.101226



OPEN ACCESS

EDITED BY

Umar Khan,
Hazara University, Pakistan

REVIEWED BY

Abderrahim Wakif,
University of Hassan II Casablanca,
Morocco
Md. Shafiqul Islam,
Dhaka University, Bangladesh

*CORRESPONDENCE

Taza Gul,
tazagul@cusit.edu.pk
ElSayed Tag ElDin,
elsayed.tageldin@fue.edu.eg

SPECIALTY SECTION

This article was submitted to Process
and Energy Systems Engineering,
a section of the journal
Frontiers in Energy Research

RECEIVED 09 June 2022

ACCEPTED 22 August 2022

PUBLISHED 14 October 2022

CITATION

Gul T, Mukhtar S, Alghamdi W, Raizah Z,
Alhazmi SE and ElDin ET (2022),
Radiative couple stress Casson hybrid
nanofluid flow over an inclined
stretching surface due to nonlinear
convection and slip boundaries.
Front. Energy Res. 10:965309.
doi: 10.3389/fenrg.2022.965309

COPYRIGHT

© 2022 Gul, Mukhtar, Alghamdi, Raizah,
Alhazmi and ElDin. This is an open-
access article distributed under the
terms of the [Creative Commons
Attribution License \(CC BY\)](#). The use,
distribution or reproduction in other
forums is permitted, provided the
original author(s) and the copyright
owner(s) are credited and that the
original publication in this journal is
cited, in accordance with accepted
academic practice. No use, distribution
or reproduction is permitted which does
not comply with these terms.

Radiative couple stress Casson hybrid nanofluid flow over an inclined stretching surface due to nonlinear convection and slip boundaries

Taza Gul^{1*}, Safyan Mukhtar², Wajdi Alghamdi³, Zehba Raizah^{4,5},
Sharifah E. Alhazmi⁶ and ElSayed Tag ElDin^{7*}

¹Department of Mathematics, City University of Science and Information Technology, Peshawar, Pakistan, ²Department of Basic Sciences, Preparatory Year Deanship King Faisal University, Al-Ahsa, Saudi Arabia, ³Department of Information Technology, Faculty of Computing and Information Technology, King Abdulaziz University, Jeddah, Saudi Arabia, ⁴Department of Mathematics, College of Science, King Khalid University, Abha, Saudi Arabia, ⁵Research Center for Advanced Materials Science (RCAMS), King Khalid University, Abha, Saudi Arabia, ⁶Mathematics Department, Al-Qunfudah University College, Umm Al-Qura University, Mecca, Saudi Arabia, ⁷Faculty of Engineering and Technology, Future University in Egypt New Cairo, New Cairo, Egypt

The study of fluid dynamics due to the stretching surface is one of the most eminent topics due to its potential industrial applications viz. drawing wire and plastic films, metal and polymer extrusion, fiber and glass production. In the present article, the author is going to study the effects of hybrid nanofluids flow on an inclined plate including CuO (Copper Oxide), and Cu (Copper). The Casson fluid with a couple-stress term has been used in the flow analysis. The surface of the plate is considered slippery. The convection has been taken nonlinear with thermal radiation. The governing equation of the flow of hybrid nanofluids with energy equation has been transformed into highly nonlinear ODEs through similarity transformation. The proposed model has been solved through a numerical RK-4 method. Significant variables of the physical process such as solar radiation, nonlinear convection parameters, heat transfer rates, and their effect on the solar power plant have been noticed.

KEYWORDS

(Cu, CuO)₂ nanoparticles, thermal radiations, inclined plate, nonlinear convection, numerical RK-4 method

Introduction

Rising energy needs around the world, including irreversible means of energy such as natural fuels, energy storage, heat exchangers, and thermal resources. The production of these real resources, the result in huge detrimental effects on the environment, such as air pollution and global warming. To mitigate these losses, scientists have focused on techniques that improve renewable energy skills, like the production of solar energy. The spotless and cheapest renewable source of energy is solar energy, which may be

converted into environmentally sociable thermal energy. These kinds of energies can be found in the shape of (solar collectors) and heat-changing liquids.

The collectors acquire solar rays by an absorbent plate and convey heat further to the absorbent solution such as water, water mixture). Nevertheless, their significant loss is the lower thermal capability of these conventional fluids, as they reveal low thermal efficiency in the alteration development. Converting conventional working liquids into nanofluids is one of the initiatives that has received much attention over the past few years to enhance the thermal efficiency of this technology. Nanofluids refer to a stable dispersion of solid particles of sizes between 1 and 100 nm (Choi, 1995). Nanofluids are widely used in various physical processes such as energy storage (Gul et al., 2019). Mebarek-Oudina (Mebarek-Oudina, 2019) studied the flow of nanofluids using different base liquids Sheikhholeslami et al. (2014) presented a complete numerical simulation of nanofluid flow with magnetic and viscous dissipation effects. Because of the excellent use of nano liquid, Li et al. (2019) studied the flow of nano liquid within a porous duct by using external power in the form of the Buongiorno model. The impacts of magnetic hydrodynamics (MHD) on the heat trade-off dynamics of chemically reactive water base nano-liquids containing Cu/Ag in a rotating disk inside the permeable channel have been investigated by Reddy et al. (2017). Many recent studies have been conducted in the area of energy and thermal environments using analytical and numerical methods for handling heat exchange and nano-fluids. For instance, Zaim et al. (2020) and Khan et al. (2019), Hybrid nanofluid is obtained by combining two types of nanomaterials, which are added to conventional liquids, and are used in many heat exchange areas. Khan et al. (2017a) and Khan et al. (2020a) formulated and analyzed the transient flow of $(Cu - Al_2O_3/H_2O)$, and concluded that the Nusselt number performance improved considerably through the addition of 5% nanomaterials. Hayat and Nadeem (Hayat and Nadeem, 2017) investigated the inspiration of energy exchange through the increasing surface of hybrid nanofluids $(Cu - Ag/H_2O)$. Ali Lunda et al. (2020) studied the impacts of viscous dissipation on the flow of hybrid nano liquid $(Cu - Al_2O_3/H_2O)$ by analyzing the stability of the shrinking plate. Aziz et al. (2020) and Khan et al. (2017b) considered the flow of hybrid nano-fluids on an extended plate. Sundar et al. (2020) has been examined the resistive aspect and energy transport phenomenon of $(MWCNT - Fe_3O_4/H_2O)$ hybrid nano liquid. Sohail et al. (2020) examined the three-dimensional movement of nanofluid in a flexible medium along with thermal radiation. Besides the aforementioned research papers, the following current articles can also be cited for getting more knowledge on the hybrid nano liquid process in various geometries. For example, Khan et al. (2021), Tahir et al. (2017), Khan et al. (2020b).

Recently, particles of different shapes on a closed porous surface and liquid moving in the permeable medium have attracted the attention of scientists. Their use can be measured in various fields such as nuclear engineering, and environmental sciences. Various physical processes that require the liquid movement on a porous medium include the use of blood flow in the veins or lungs,

chemically catalysts connectors, geothermal energy, porous heat pipes, and porous heat pipes. As a Forchheimer term, it was introduced in Forchheimer (1901). Many researchers have used Darcy-Forchheimer concepts in various geometries for the study of fluid flow in a porous space. We are going to mention a few of them. Saif et al. (2019) discussed the movement of nano-fluids through a porous space. The variation in the motion of a liquid was created an expandable curved surface. Rasool et al. (2019) reported the flow of Darcy-Forchheimer nano-fluids produced by the stretching medium. The Darcy-Forchheimer liquid that flows through a spinning disc was discovered by Sadiq et al. (2020). Sheikhholeslami et al. (2020) (Rasool et al., 2022) observed the behavior of non-Darcy liquid within a clear cavity. Hayat et al. (2020b), Sheikhholeslami et al. (2020) examined the influence of Darcy-Forchheimer and EMHD on the flow of viscous liquids with joule heating and thermal flux over an extending surface. The numerical outcomes of CNTs nano-liquid flow across the divergent and convergent channels with thermal radiation have been calculated by Kumar et al. (2020) (Hayat et al., 2020a). There are various technical methods available for estimating temperature. The significance of radiation for heat and flow transmission is understood, especially in the fields of glass manufacturing, rocket engineering, furnace construction, nuclear plant, solar farms, physical science, and manufacturing, etc. Of such importance, the imposition of thermal radiation for heat transport is shown in Kumar et al. (2020). The different properties of such fluids were further studied by many researchers. Nanofluid flow reduces (Bilal, 2020; Khan et al., 2020c; Algehyne et al., 2022) the resistance to heat transfer for different flow systems. With the passage of time researchers came to know that the spread of two different types of nanoparticles in a pure fluid further augment the thermal flow characteristics. They termed such fluid as hybrid nanofluid. Rasool et al. (2022) and Wakif et al. (2022) have inspected the dynamics of hybrid nanofluid flow with the influence of thermal radiations and viscous dissipation past a stretching surface and have determined the influence of various parameters. It has been observed by the authors that the upper branch of the solution has been highlighted to be more applicable due to its stable nature (Alghamdi et al., 2021; Xia et al., 2021; Shah et al., 2022). have deliberated an incredible work to discuss the thermal flow improvement for hybrid nanofluid flow by means of different flow geometries and flow conditions. Recently, it has been noticed by researchers that the suspension of three different types of nanoparticles in a pure fluid can enhance the thermal conductivity of such fluid to the best possible limit. Such fluids are termed tri-hybrid nanofluids.

The main aim of the ongoing study is to observe the impact of (Cu, CuO) nano-components on the flow and heat transmission of water as a base fluid. Such formulation of fluid is used further on the inclined plate to improve the efficiency of solar collectors. Thermal radiation, nonlinear convection, and slip conditions are considered while formulating basic equations. The flow-related issues were formulated via differential equations which were solved numerically using the BVP-4 technique. Different significant quantities are discussed in terms of temperature and velocity.

Model analysis

The flow of the hybrid nanofluids containing (Cu – CuO) nanoparticles is considered over an inclined plate that makes an angle ψ with the upright axis as shown in the. [Figure 1](#). The surface of the plate is considered slippery to reduce the stability of the external dust particles. The thermal convection is expanded and taking nonlinear. The basic equations in the presence of thermal radiation and Couple stress are displayed as.

$$\frac{\partial u}{\partial x} + \frac{\partial v}{\partial y} = 0, \quad (1)$$

$$\rho_{hmf} \left(u \frac{\partial u}{\partial x} + v \frac{\partial u}{\partial y} \right) = \left(1 + \frac{1}{\beta} \right) \mu_{hmf} \left(\frac{\partial^2 u}{\partial y^2} \right) \pm g(\rho)_{hmf} \left[(\beta_T)_{hmf} (T - T_\infty) + (\beta_T)_{hmf}^2 (T - T_\infty)^2 \right] \cos \psi - \eta^* \frac{\partial^4 u}{\partial y^4}, \quad (2)$$

$$(\rho c_p)_{hmf} \left(u \frac{\partial T}{\partial x} + v \frac{\partial T}{\partial y} \right) = k_{hmf} \frac{\partial^2 T}{\partial y^2} + \frac{16}{3} \left(\frac{\sigma^* T_\infty^3}{k^*} \frac{\partial^2 T}{\partial y^2} \right), \quad (3)$$

Acceptable boundary conditions are

$$u = u_w + \mu_{hmf} \frac{\partial u}{\partial y}, \quad v = 0, \quad -k_{hmf} \frac{\partial T}{\partial y} = (T_w - T), \quad \text{at } y = 0, \quad (4)$$

$$u = 0 = v, \quad T \rightarrow T_\infty, \quad \text{at } y \rightarrow \infty.$$

The velocity components u and v in the x and y -direction,

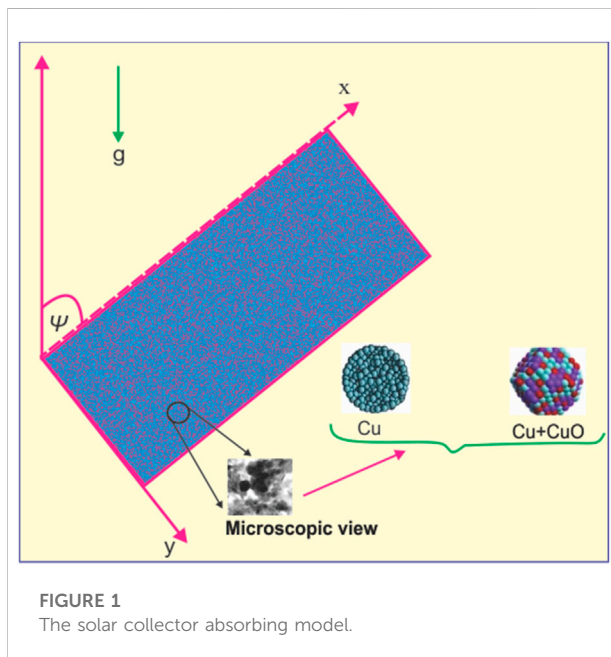


FIGURE 1
The solar collector absorbing model.

Mathematical formulation of thermos-physical properties HNF

$$\frac{\mu_{hmf}}{\mu_f} = \frac{1}{(1 - \phi_1)^{2.5} (1 - \phi_2)^{2.5}}, \quad (5)$$

$$\frac{\rho_{hmf}}{\rho_f} = \left[(1 - \phi_2) \left\{ 1 - \left(1 - \frac{\rho_{Cu}}{\rho_f} \right) \phi_1 \right\} + \phi_2 \frac{\rho_{CuO}}{\rho_f} \right], \quad (6)$$

$$\frac{k_{hmf}}{k_{nf}} = \frac{k_{CuO} + (n - 1)k_{nf} - (n - 1)\phi_2(k_{nf} - k_{CuO})}{k_{CuO} + (n - 1)k_{nf} + \phi_2(k_{nf} - k_{CuO})}, \quad (7)$$

$$\frac{k_{nf}}{k_f} = \frac{k_{Cu} + (n - 1)k_f - (n - 1)\phi_1(k_f - k_{Cu})}{k_{Cu} + (n - 1)k_f + \phi_1(k_f - k_{Cu})},$$

$$\frac{(\rho c_p)_{hmf}}{(\rho c_p)_f} = \left[(1 - \phi_2) \left\{ 1 - \left(1 - \frac{(\rho c_p)_{Cu}}{(\rho c_p)_f} \right) \phi_1 \right\} + \phi_2 \frac{(\rho c_p)_{CuO}}{(\rho c_p)_f} \right], \quad (8)$$

In the above mathematical expression, ϕ_1 denotes the nanomaterials (Cu) volume fraction whereas ϕ_2 denotes the volume fraction of (CuO) nanocomponents.

Introduction to useful similarity transformation variables as follows:

$$u = f'(\eta) b x, \quad v = -\sqrt{b \nu_f} f(\eta), \quad (T_w - T_\infty) \theta(\eta) = T - T_\infty, \quad \eta = y \sqrt{\frac{b}{\nu_f}}, \quad (9)$$

In the light of [Eq.11](#), the [Eqs 1–5](#) become

$$\left(1 + \frac{1}{\beta} \right) f''' + \frac{\rho_{hmf}}{\rho_f} \frac{\mu_f}{\mu_{hmf}} \left[f f'' - (f')^2 \right] \pm \frac{\mu_f}{\mu_{hmf}} [Gr \theta + Gr^* (\theta)^2] \cos \psi - k f' v = 0, \quad (10)$$

$$\left(\frac{k_{hmf}}{k_f} + Rd \right) \theta'' + Pr \frac{(\rho c_p)_{hmf}}{(\rho c_p)_f} f \theta' = 0, \quad (11)$$

$$f(0) = 0, \quad f'(0) = 1 + \frac{\Lambda}{(1 - \phi_1)(1 - \phi_2)} f''(0), \quad \theta'(0) = -Bi(1 - \theta(0)), \quad f(\infty) = \theta(\infty) \rightarrow 0. \quad (12)$$

In terms of mutual boundary conditions:

$$Gr = \frac{g \beta_T (T_w - T_\infty)}{b \nu_w}, \quad Gr^* = \frac{g \beta_T^2 (T_w - T_\infty)^2}{b \nu_w}, \quad Rd = \frac{16}{3} \frac{\sigma^* T_\infty^3}{k^* k},$$

$$= \frac{\eta^* b}{\nu_f^2 \rho_f}, \quad Pr = \frac{\nu_f}{\alpha_f}, \quad \Lambda = \mu_f \sqrt{\frac{b}{\nu_f}}. \quad (13)$$

The above-mentioned physical numbers are Grashof numbers, Couple stress term, Radiation factor, Slip velocity, parameter, and Prandtl number, Velocity slip, and Biot number.

In addition, some of the most useful physical numbers are, as, (Sherwood number), Skin friction coefficient (C_{fx}), and Nusselt number (Nu_x).

$$C_{fx} = \frac{\tau_w}{\frac{1}{2}\rho_{hmf}(u_w)^2}, Nu_x = \frac{xq_w}{k_{hmf}(T_w - T_{\infty})}. \quad (14)$$

Where q_w represents heat flux close to the surface, and τ_w denotes shear stress, employing Eqs. 9 and Eq. 14 gives,

$$C_{fx}Re_x^{0.5} = \frac{2}{(1-\phi_1)^{2.5}(1-\phi_2)^{2.5}}f''(0),$$

$$Nu_xRe_x^{-0.5} = -\left(\frac{k_{hmf}}{k_f} + Rd\right)\Theta'(0). \quad (15)$$

Numerical method

The RK-4 numerical method has been used. The modeled Eqs 10, 11 are transformed to the first order by considering,

$$x_1 = \eta, x_2 = f, x_3 = f', x_4 = f'', x_5 = f''', x_6 = f^{iv}, \quad (16)$$

$$x_7 = \theta, x_8 = \theta'.$$

The first order ODEs system (Zaydan et al., 2022) has been solved with the efforts of the projected variables as shown in Eq. 16. The first order system using the RK4 method has been obtained as:

$$D_\eta x_1 = 1, D_\eta x_2 = x_3, D_\eta x_3 = x_4, D_\eta x_5 = x_6, D_\eta x_7 = x_8$$

$$D_\eta x_6 = \frac{1}{k} \left[\left(1 + \frac{1}{\beta} \right) x_5 + \frac{\rho_{hmf}}{\rho_f} \frac{\mu_f}{\mu_{hmf}} (x_2 x_4 - (x_3)^2) \pm \frac{\mu_f}{\mu_{hmf}} (Gr x_7 + Gr^* x_7 x_7) \cos \psi \right],$$

$$D_\eta x_8 = -\left(\frac{k_{hmf}}{k_f} + Rd\right)^{-1} \Pr \frac{(\rho C p)_{hmf}}{(\rho C p)_f} x_2 x_8. \quad (17)$$

The first order system solution obtained and the results are analyzed for various embedded parameters.

Results and discussion

The hybrid nanofluid flow over a slippery surface of an inclined plane is considered for the applications of heat transfer. The impact of $f'(\eta)$ (velocity profile) and $\Theta(\eta)$ (temperature profile) quantitatively *via* different tables and graphs for various active variables such as Λ (slip parameter), Gr, Gr^* (Gravitational parameters), B_i (Biot number), ϕ_1, ϕ_2 (Volume fractions), and Rd (Radiation factor) while considering (Cu + Water), (CuO + Water) nano liquid and hybrid nanofluid. The schematic diagram of the flow field is shown in Figure 1. Figure 2 The flow of fluid is increases over the slippery surface and this increase is more effective due to the larger values of the slip parameter Λ . As the fluid moves over the surface, it traps more heat from the sheet, causing significant thermal dispersion. Intriguingly, even under favorable thermal transmission conditions, the entropy rate decreases to improve the quality of the slow-moving barrier. This can improve the slip to influence the suspended components and consequently the

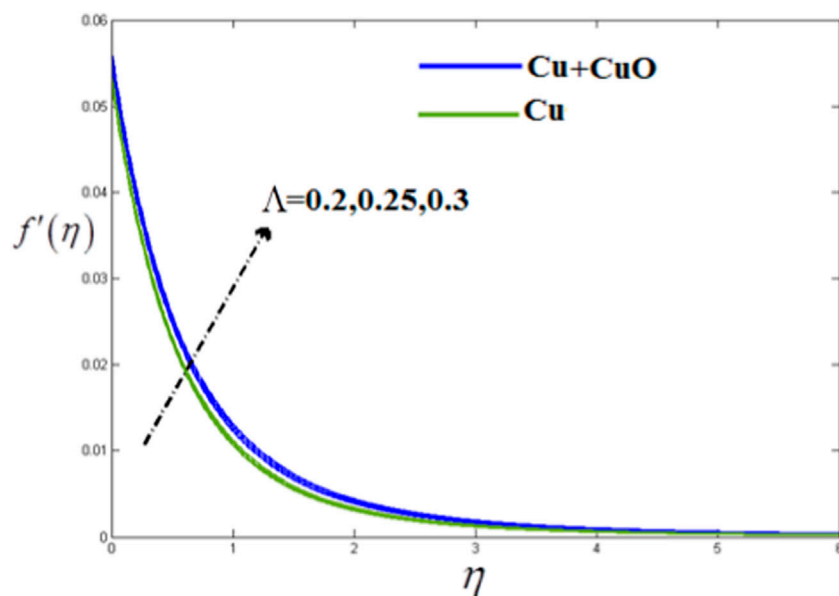


FIGURE 2

Λ versus $f'(\eta)$. When, $\phi_1, \phi_2 = 0.02, k = 0.2, Gr = Gr^* = Rd = 0.3, B_i = 0.1, Pr = 6.2$.

fluid motion is increases. **Figure 3** The influence of the couple stress parameter versus velocity profile is shown in **Figure 3**. It is perceived that the development in couple stress terms results, decreases in the fluid motion at all locations. The rise in the couple stress parameter values improves the resistance force, to decline the velocity of the fluid. **Figure 4** Incremented fractional volume through particle strength in porosity, hybrid nano-fluids also affects the flow rate. As a result, it increases the production of thermal transport and entropy in both types of flowing fluids and reduces the velocity profile by incrementing the volume fraction. **Figure 5** Incremented Casson fluid parameter, increasing the resistive force and declining the fluid motion. The decline effect is compared for both Cu and CuO hybrid nano-fluids (**Figures 6, 7**). The increment in the positive value of the gravity parameters Gr, Gr^* will raise the velocity profile and the velocity of the liquid is improved by the positive value of the gravity parameter. The opposite impact declines the fluid motion. The comparative analysis for both Cu and Cu-CuO shown has been displayed in **Figures 6, 7** which signifies that the velocity profile decrement due to the negative value of the gravity parameter.

Figure 8 Biot number B_i denotes an incremental convectively thermal rates that can affect the area of interest related to temperature. According to the limitation to heat production, the Biot number B_i tends to increase the current thermal rates in the flow region but makes the lower portion of the sheet. According to previous entropy and thermal plots, the Biot number B_i is also a factor in the elevation of the thermal diffusion, which

simultaneously increases the rate of entropy. **Figure 9** As the volume friction value rises which reduces the temperature profile. will decrease. This is because when nanoparticles are put in the conventional fluid, the nanoparticles increase in temperature, which will increase the temperature profile.

Figure 10 illustrates the state of thermal radiation sequentially, for the growing values of the thermal radiation barrier. Radiation heat raises the thermal state of the environment of interest, which places a greater thermal transfer load on the passing fluid, which increases the thermal conductivity to the radiation barriers. The thermal properties of the solid materials and base fluid are displayed in **Table 1**. The skin friction improved with the increasing values of the parameters $\phi_1, \phi_2, k, Gr, Gr^*$ as displayed in **Table 2**. Physically, the greater values of these factors enrich the resistance force and subsequently skin friction enhancing. The heat transfer rate grows with the cumulative values of the nanoparticle volume fraction and Radiation factors as displayed in **Table 3**. The heat transfer rate enhancing for the nanofluids Cu up to 8.1501% using $\phi_1 = 0.01$ and 8.473% increases for Cu + CuO hybrid nanofluids using $\phi_1, \phi_2 = 0.01$. Similarly, the rate of heat transfer escalates gradually with the growing amount of nanoparticle volume fraction. From **Table 4** it has been detected that hybrid nanofluids are more proficient for heat transfer enhancement. The comparison of the current results is compared with the existing literature considering base fluid only and shown in **Table 4**.

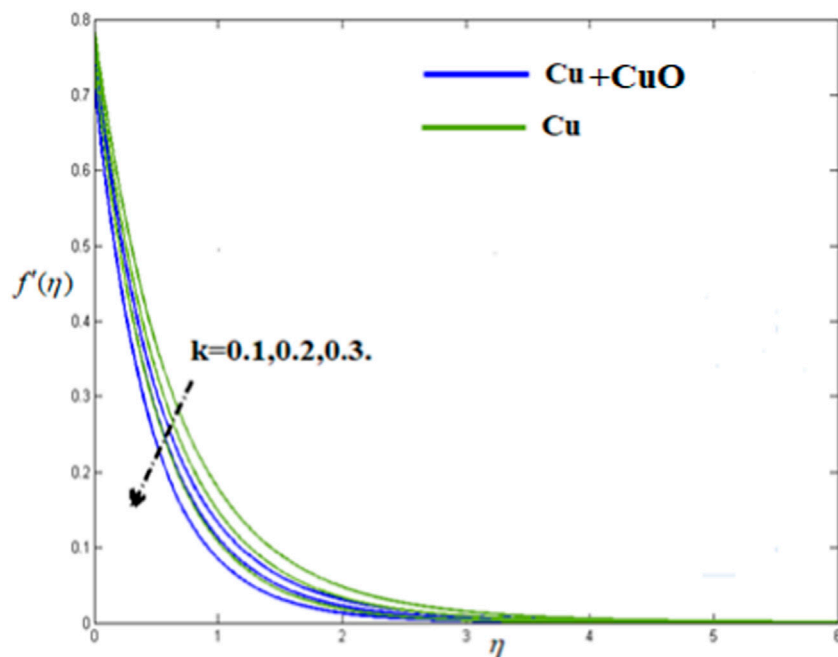


FIGURE 3

k versus $f'(\eta)$. When, $\phi_1, \phi_2 = 0.02, \Lambda = 0.4, Gr = Gr^* = Rd = 0.3, B_i = 0.1, Pr = 6.2$.

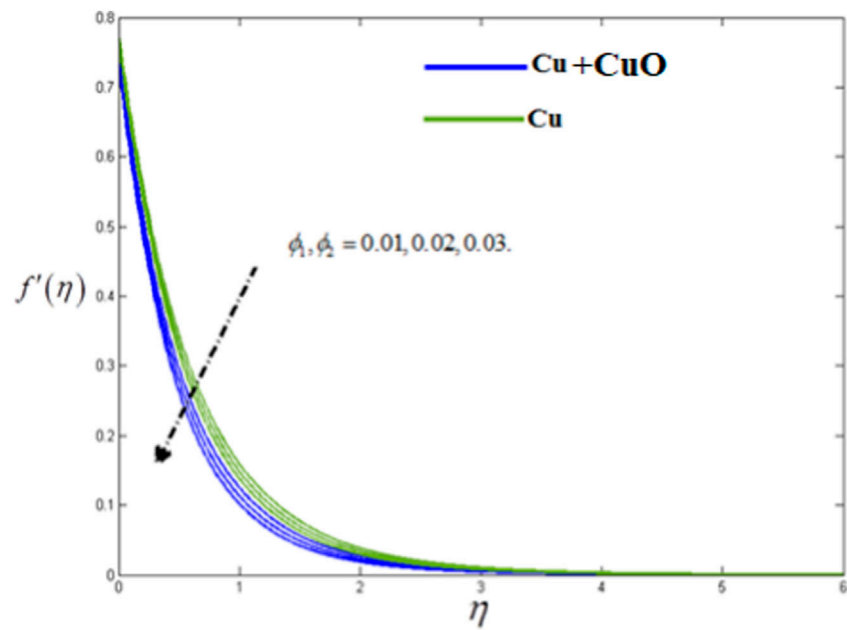


FIGURE 4

ϕ_1, ϕ_2 versus $(f'(\eta))$. When, $k = 0.2, \Lambda = 0.4, Gr = Gr^* = Rd = 0.3, B_l = 0.1, Pr = 6.2$.

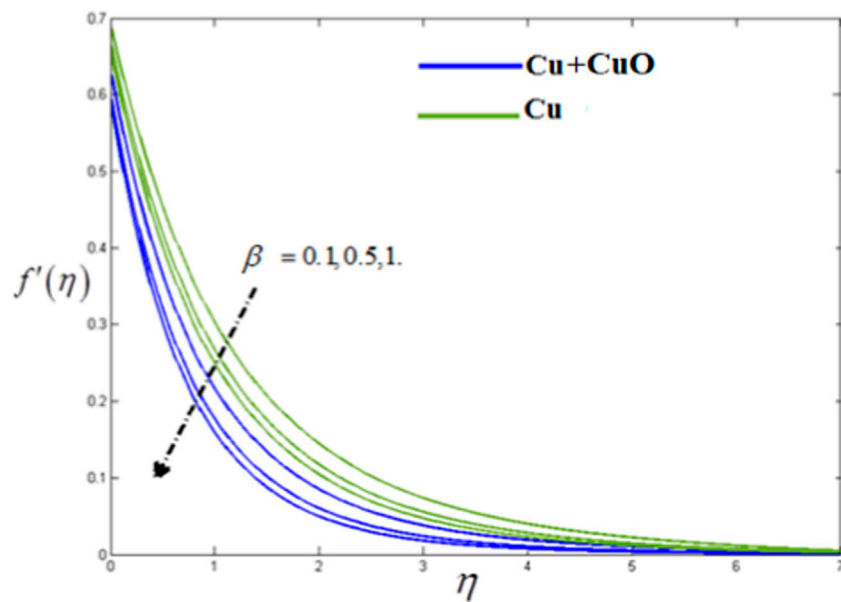


FIGURE 5

β versus $(f'(\eta))$. When, $k = 0.2, \Lambda = 0.4, \phi_1, \phi_2 = 0.02, Rd = 0.3, B_l = 0.1, Pr = 6.2$.

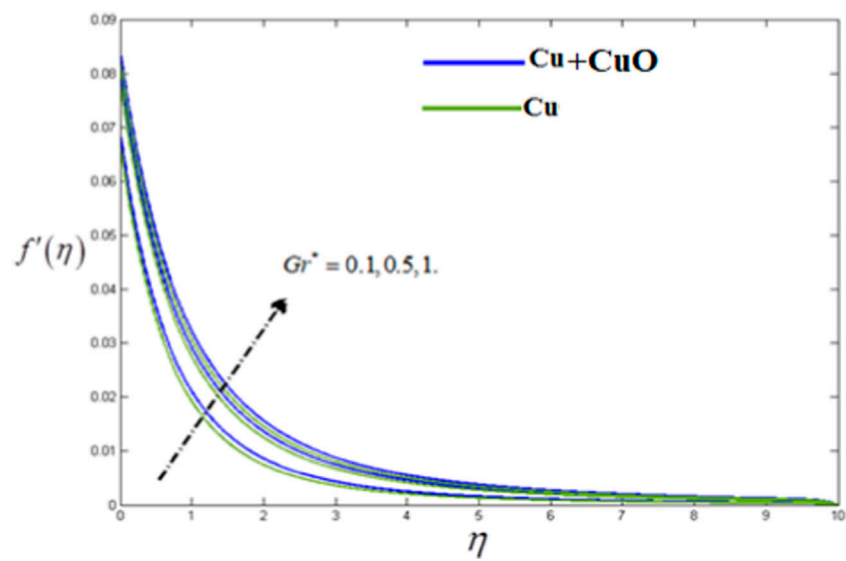


FIGURE 6

Gr^* versus $f'(\eta)$. When, $k = 0.2, \Lambda = 0.4, \phi_1, \phi_2 = 0.02, Rd = 0.3, B_j = 0.1, Pr = 6.2$.

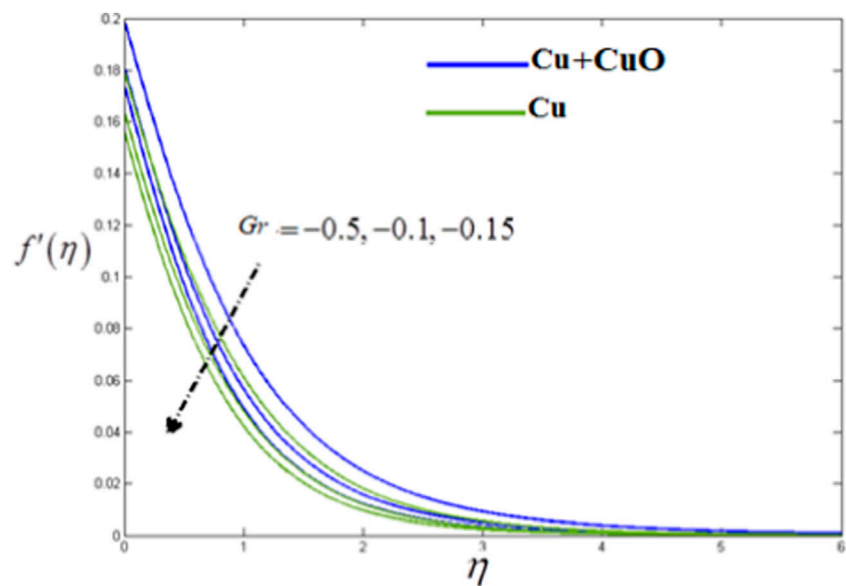


FIGURE 7

Gr versus $f'(\eta)$. When, $k = 0.2, \Lambda = 0.4, \phi_1, \phi_2 = 0.02, Rd = 0.3, B_j = 0.1, Pr = 6.2$.

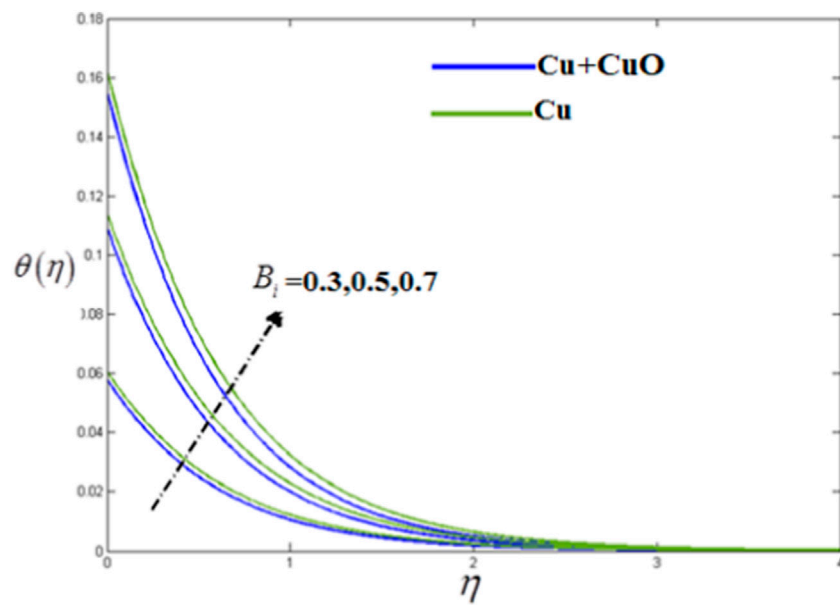


FIGURE 8

B_i versus $\theta(\eta)$. When, $k = 0.2$, $\Lambda = 0.4$, $\phi_1, \phi_2 = 0.02$, $Rd = 0.3$, $Gr = 0.1$, $Pr = 6.2$.

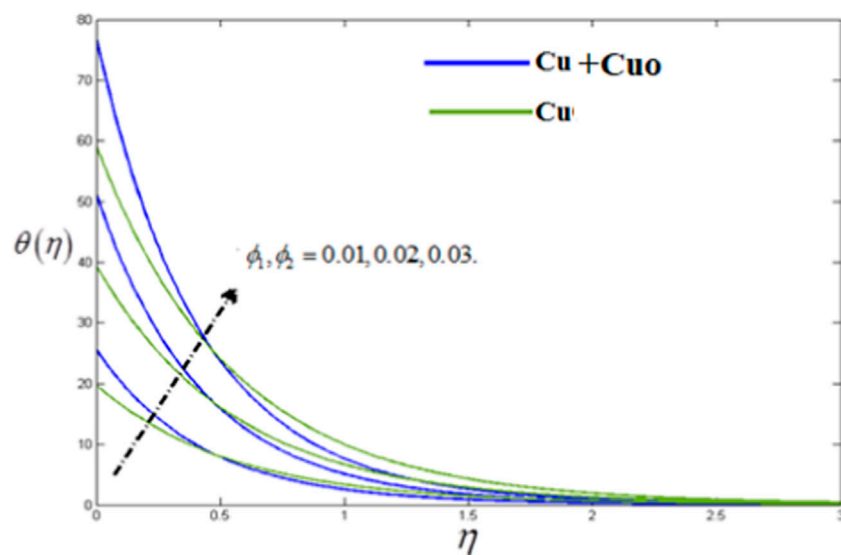


FIGURE 9

ϕ_1, ϕ_2 versus $\theta(\eta)$. When, $k = 0.2$, $\Lambda = 0.4$, $B_i = 0.2$, $Rd = 0.3$, $Gr = 0.1$, $Pr = 6.2$.

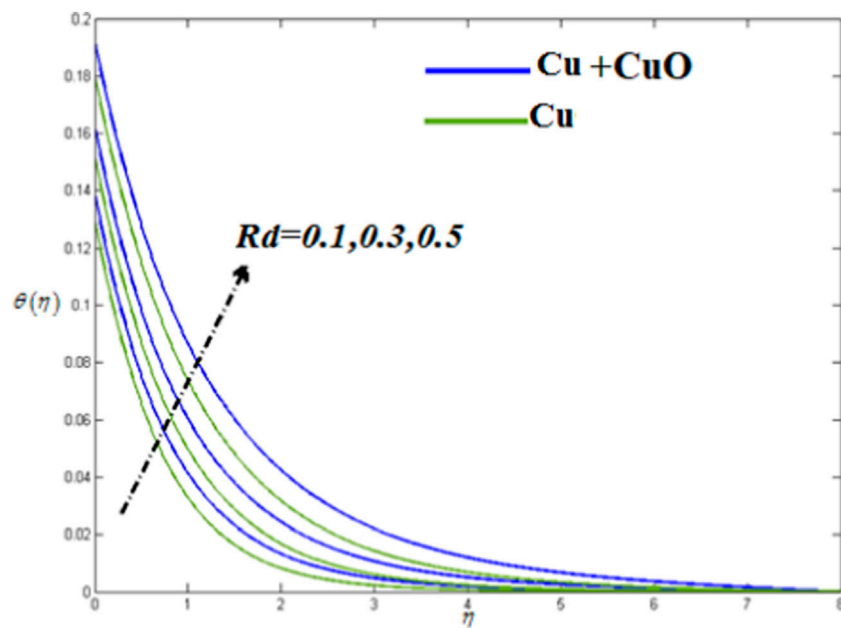


FIGURE 10

Rd versus $\theta(\eta)$. When, $k = 0.2, \Lambda = 0.4, B_l = 0.2, \phi_1, \phi_2 = 0.02, Gr = 0.1, Pr = 6.2$.

TABLE 1 Cu & CuO thermo-physical properties.

| Property | Cu | CuO |
|-------------------------|-------|------|
| $\rho (Kg m^{-3})$ | 6320 | 3580 |
| $c_p (K g^{-1} K^{-1})$ | 531.8 | 960 |
| $k (W m^{-1} K^{-1})$ | 76.5 | 48.4 |

TABLE 2 $C_{fx} Re_x^{0.5}$ numerical outcomes versus different values of emerging parameters.

| Gr | ϕ_1, ϕ_2 | k | Gr^* | $C_{fx} - Cu$ | $C_{fx} - Cu \& CuO$ |
|------|------------------|-----|--------|---------------|----------------------|
| 0.2 | 0.0 | 0.2 | 0.2 | 0.472836 | 0.473952 |
| 0.3 | | | | 1.473962 | 1.4745742 |
| 0.4 | | | | 1.4749321 | 1.47575322 |
| | 0.01 | | | 1.4735318 | 1.474421331 |
| | 0.02 | | | 1.4744321 | 1.47538012 |
| | | 0.4 | | 1.483120 | 1.4846352 |
| | | 0.6 | | 1.49431275 | 1.49532125 |
| | | | 0.4 | 1.47343546 | 1.47446874 |
| | | | 0.6 | 1.47412023 | 1.4753214091 |

TABLE 3 $Nu_x Re_x^{-0.5}$ numerical outcomes versus different values of emerging parameters and % enhancement in heat transfer rate.

| ϕ_1, ϕ_2 | Rd | $Nu_x - Cu$ | $Nu_x - Cu \& CuO$ |
|------------------|------|-------------|--------------------|
| 0.0 | 0.1 | 0.132421 | 0.132421 |
| 0.01 | | 0.143214 | 0.1436422 |
| | | 8.1501% | 8.473% |
| 0.02 | | 0.14491 | 0.146474 |
| | | 9.431% | 10.612 |
| 0.03 | | 0.1458321 | 0.147623 |
| | | 10.127% | 11.48% |
| | 0.2 | 0.523416 | 0.5243215 |
| | 0.3 | 0.621571 | 0.6223532 |
| | 0.5 | 0.62314 | 0.6243212 |

TABLE 4 Quantitative analogy with [39], [40] using $Nu_x Re_x^{-0.5}$.

| Pr | Wang Wang (1989) | Golra and sidawi Golra and Sidawi (1994) | Recent |
|-----|------------------|--|----------|
| 6.3 | 0.24532 | 0.24545 | 0.24548 |
| 6.5 | 0.194522 | 0.194642 | 0.194653 |
| 6.7 | 0.135281 | 0.135393 | 0.135412 |

Conclusion

The impact of the Cu and CuO hybrid nanofluid flow for the enhancement of heat transfer rate has been examined through a slippery surface of the inclined plate. The convection is taken quadratic and due to the stretching of the plate, the gravity force is assumed negative and positive. The significant physical characteristics of Nusselt number versus radiation and other physical constraints have been noticed. In this article, some significant points present our conclusion in the following remarks. For Gr , Gr^* impact have been analyzed and the comparative results for the Cu & CuO hybrid nanofluid are observed. The higher value of the nanoparticle volume fractions ϕ_1, ϕ_2 incremented the temperature distribution $\Theta(\eta)$. The heat transfer rate enhancing for Cu up to 10.127% using $\phi_1 = 0.01, 0.02, 0.03$ and 11.48% increases for Cu + CuO hybrid nanofluids using $\phi_1, \phi_2 = 0.01, 0.02, 0.03$. The Biot number increases the temperature distribution for its larger amount. The larger value of the parameter Rd enhances the rate of heat transfer and, as a result, the Nusselt number rises. Nanoliquids are more viscous than ordinary liquids, which reflects that the boiling point of nanoliquids is more than that of conventional base liquids. This would improve the heat transfer power of the solar collectors.

Data availability statement

The raw data supporting the conclusion of this article will be made available by the authors, without undue reservation.

References

- Algehyne, E. A., Wakif, A., Rasool, G., Saeed, A., and Ghoul, Z. (2022). Significance of Darcy-forchheimer and Lorentz forces on radiative alumina-water nanofluid flows over a slippery curved geometry under multiple convective constraints: A renovated Buongiorno's model with validated thermophysical correlations. *Waves Random Complex Media* 2022, 1–30. doi:10.1080/17455030.2022.2074570
- Alghamdi, M., Wakif, A., Thumma, T., Khan, U., Baleanu, D., and Rasool, G. (2021). Significance of variability in magnetic field strength and heat source on the radiative-convective motion of sodium alginate-based nanofluid within a Darcy-Brinkman porous structure bounded vertically by an irregular slender surface. *Case Stud. Therm. Eng.* 28, 101428. doi:10.1016/j.csite.2021.101428
- Ali Lunda, L., Omara, Z., Khan, I., Seikh, A., El-Sayed, H., Sherif, M., et al. (2020). Stability analysis and multiple solution of Cu–Al₂O₃/H₂O nanofluid contains hybrid nanomaterials over a shrinking surface in the presence of viscous dissipation. *J. Mat. Res. Technol.* 9 (1), 421–432. doi:10.1016/j.jmrt.2019.10.071
- Aziz, A., Jamshed, W., Ali, Y., and Shams, M. (2020). Heat transfer and entropy analysis of Maxwell hybrid nanofluid including effects of inclined magnetic field, Joule heating and thermal radiation. *Discrete Contin. Dyn. Syst. Ser. S* 13 (10), 101428. doi:10.3934/dcdss.2020142
- Bilal, M. (2020). Micropolar flow of EMHD nanofluid with nonlinear thermal radiation and slip effects. *Alexandria Eng. J.* 59 (2), 965–976. doi:10.1016/j.aej.2020.03.023
- Choi, U. S. (1995). Enhancing thermal conductivity of fluids with nanoparticles. *AS-MEFED* 231, 99–103.
- Forchheimer, P. (1901). Wasserbewegung durch boden. *Z. Des. Vereins Dtsch. Ingenieure* 45, 1782–1788.
- Gorla, R. S. R., and Sidawi, I. (1994). Free convection on a vertical stretching surface with suction and blowing. *Appl. Sci. Res.* 52 (3), 247–257. doi:10.1007/bf00853952
- Gul, T., Noman, W., Sohail, M., and Khan, M. A. (2019). Impact of the Marangoni and thermal radiation convection on the graphene-oxide-water-based and ethylene-glycol-based nanofluids. *Adv. Mech. Eng.* 11 (6), 1687814019856773. doi:10.1177/1687814019856
- Hayat, T., Haider, F., and Alsaedi, A. (2020a). Darcy-Forchheimer flow with nonlinear mixed convection. *Appl. Math. Mech.* 41 (11), 1685–1696. doi:10.1007/s10483-020-2680-8
- Hayat, T., Khan, S. A., Alsaedi, A., and Fardoun, H. M. (2020b). Heat transportation in electro-magnetohydrodynamic flow of Darcy-Forchheimer viscous fluid with irreversibility analysis. *Phys. Scr.* 95 (10), 105214. doi:10.1088/1402-4896/abb7aa
- Hayat, T., and Nadeem, S. (2017). Heat transfer enhancement with Ag–CuO/water hybrid nanofluid. *Results Phys.* 7, 2317–2324. doi:10.1016/j.rinp.2017.06.034
- Khan, A., Saeed, A., Tassaddiq, A., Gul, T., Mukhtar, S., Kumam, P., et al. (2021). Bio-convective micropolar nanofluid flow over thin moving needle subject to Arrhenius activation energy, viscous dissipation and binary chemical reaction. *Case Stud. Therm. Eng.* 25, 100989. doi:10.1016/j.csite.2021.100989
- Khan, S. U., Tlili, I., Waqas, H., and Imran, M. (2020). Effects of nonlinear thermal radiation and activation energy on modified second-grade nanofluid with Cattaneo–Christov expressions. *J. Therm. Anal. Calorim.* 143 (2), 1175–1186. doi:10.1007/s10973-020-09392-6

Author contributions

TG, modeling and solution; SM, writing draft WA, editing. ZR, Validated, SEA and ETE, participated in revision and provide funding source.

Acknowledgments

This work was supported by the King Khalid University through a grant KKU/RCAMS/22 under the Research Center for Advance Materials (RCAMS) at King Khalid University, Saudi Arabia. The author Sharifah E. Alhazmi sehazmi@uqu.edu.sa would like to thank the Deanship of Scientific Research at Umm Al-Qura University for supporting this work by Grant Code: (22UQU4282396DSR24).

Conflict of interest

The authors declare that the research was conducted in the absence of any commercial or financial relationships that could be construed as a potential conflict of interest.

Publisher's note

All claims expressed in this article are solely those of the authors and do not necessarily represent those of their affiliated organizations, or those of the publisher, the editors and the reviewers. Any product that may be evaluated in this article, or claim that may be made by its manufacturer, is not guaranteed or endorsed by the publisher.

- Khan, U., Zaib, A., and Mebarek-Oudina, F. (2020). Mixed convective magneto flow of $\text{SiO}_2\text{-MoS}_2/\text{C}_2\text{H}_6\text{O}_2$ hybrid nanoliquids through a vertical stretching/shrinking wedge: Stability analysis. *Arab. J. Sci. Eng.* 45 (11), 9061–9073. doi:10.1007/s13369-020-04680-7
- Khan, U., Ahmed, N., and Mohyud-Din, S. T. (2017). Influence of the shape factor on the flow and heat transfer of a water-based nanofluid in a rotating system. *Eur. Phys. J. Plus* 132 (4), 166–211. doi:10.1140/epjp/i2017-11410-4
- Khan, U., Ahmed, N., and Mohyud-Din, S. T. (2020). Surface thermal investigation in water functionalized Al_2O_3 and $\gamma\text{-Al}_2\text{O}_3$ nanomaterials-based nanofluid over a sensor surface. *Appl. Nanosci.*, 1–11. doi:10.1007/s13204-020-01527-3
- Khan, U., Alkanhal, T. A., Ahmed, N., Khan, I., and Mohyud-Din, S. T. (2019). Stimulations of thermophysical characteristics of nano-diamond and silver nanoparticles for nonlinear radiative curved surface flow. *IEEE Access* 7, 55509–55517. doi:10.1109/access.2019.2907304
- Khan, U., Asadullah, M., Ahmed, N., and Mohyud-Din, S. T. (2017). Influence of Joule heating and viscous dissipation on MHD flow and heat transfer of viscous fluid in converging/diverging stretchable channels. *J. nanofluids* 6 (2), 254–263. doi:10.1166/jon.2017.1327
- Kumar, K. G., Rahimi-Gorji, M., Reddy, M. G., Chamkha, A. J., and Alarifi, I. M. (2020). Enhancement of heat transfer in a convergent/divergent channel by using carbon nanotubes in the presence of a Darcy–Forchheimer medium. *Microsyst. Technol.* 26 (2), 323–332. doi:10.1007/s00542-019-04489-x
- Li, Z., Saleem, S., Shafee, A., Chamkha, A. J., and Du, S. (2019). Analytical investigation of nanoparticle migration in a duct considering thermal radiation. *J. Therm. Anal. Calorim.* 135 (3), 1629–1641. doi:10.1007/s10973-018-7517-z
- Mebarek-Oudina, F. (2019). Convective heat transfer of Titania nanofluids of different base fluids in cylindrical annulus with discrete heat source. *Heat. Trans. Res.* 48 (1), 135–147. doi:10.1002/htj.21375
- Rasool, G., Shafiq, A., Khaliq, C. M., and Zhang, T. (2019). Magnetohydrodynamic Darcy–Forchheimer nanofluid flow over a nonlinear stretching sheet. *Phys. Scr.* 94, 105221. doi:10.1088/1402-4896/ab18c8
- Rasool, G., Shah, N. A., El-Zahar, E. R., and Wakif, A. (2022). Numerical investigation of EMHD nanofluid flows over a convectively heated riga pattern positioned horizontally in a Darcy–forchheimer porous medium: Application of passive control strategy and generalized transfer laws. *Waves Random Complex Media* 2022, 1–20. doi:10.1080/17455030.2022.2074571
- Reddy, P. S., Sreedevi, P., and Chamkha, A. J. (2017). MHD boundary layer flow, heat and mass transfer analysis over a rotating disk through porous medium saturated by Cu-water and Ag-water nanofluid with chemical reaction. *Powder Technol.* 307, 46–55. doi:10.1016/j.powtec.2016.11.017
- Sadiq, M. A., Haider, F., Hayat, T., and Alsaedi, A. (2020). Partial slip in Darcy–Forchheimer carbon nanotubes flow by rotating disk. *Int. Commun. Heat Mass Transf.* 116, 104641. doi:10.1016/j.icheatmasstransfer.2020.104641
- Saif, R. S., Hayat, T., Ellahi, R., Muhammad, T., and Alsaedi, A. (2019). Darcy–Forchheimer flow of nanofluid due to a curved stretching surface. *Int. J. Numer. Methods Heat. Fluid Flow* 29, 2–20. doi:10.1108/hff-08-2017-0301
- Shah, N. A., Wakif, A., El-Zahar, E. R., Ahmad, S., and Yook, S. J. (2022). Numerical simulation of a thermally enhanced EMHD flow of a heterogeneous micropolar mixture comprising (60%)-ethylene glycol (EG), (40%)-water (W), and copper oxide nanomaterials (CuO). *Case Stud. Therm. Eng.* 35, 102046. doi:10.1016/j.csite.2022.102046
- Sheikholeslami, M., Abelman, S., and Ganji, D. D. (2014). Numerical simulation of MHD nanofluid flow and heat transfer considering viscous dissipation. *Int. J. Heat. Mass Transf.* 79, 212–222. doi:10.1016/j.ijheatmasstransfer.2014.08.004
- Sheikholeslami, M., Arabkoohsar, A., and Ismail, K. A. R. (2020). Entropy analysis for a nanofluid within a porous media with magnetic force impact using non-Darcy model. *Int. Commun. Heat Mass Transf.* 112, 104488. doi:10.1016/j.icheatmasstransfer.2020.104488
- Sohail, M., Naz, R., and Abdelsalam, S. I. (2020). On the onset of entropy generation for a nanofluid with thermal radiation and gyrotactic microorganisms through 3D flows. *Phys. Scr.* 95, 045206. doi:10.1088/1402-4896/ab3c3f
- Sundar, L. S., Singh, M. K., and Sousa, A. C. M. (2020). Enhanced heat transfer and friction factor of MWCNT– Fe_3O_4 /water hybrid nanofluids. *Int. Commun. Heat Mass Transf.* 52, 73–83. doi:10.1016/j.icheatmasstransfer.2014.01.012
- Tahir, F., Gul, T., Islam, S., Shah, Z., Khan, A., Khan, W., et al. (2017). Flow of a nano-liquid film of Maxwell fluid with thermal radiation and magneto hydrodynamic properties on an unstable stretching sheet. *J. nanofluids* 6 (6), 1021–1030. doi:10.1166/jon.2017.1400
- Wakif, A., Zaydan, M., Alshomrani, A. S., Muhammad, T., and Sehaqui, R. (2022). New insights into the dynamics of alumina-(60% ethylene glycol+ 40% water) over an isothermal stretching sheet using a renovated buongiorno's approach: A numerical gdqllm analysis. *Int. Commun. Heat Mass Transf.* 133, 105937. doi:10.1016/j.icheatmasstransfer.2022.105937
- Wang, C. Y. (1989). Free convection on a vertical stretching surface. *Z. Angew. Math. Mech.* 69 (11), 418–420. doi:10.1002/zamm.19890691115
- Xia, W. F., Animasaun, I. L., Wakif, A., Shah, N. A., and Yook, S. J. (2021). Gear-generalized differential quadrature analysis of oscillatory convective Taylor–Couette flows of second-grade fluids subject to Lorentz and Darcy–Forchheimer quadratic drag forces. *Int. Commun. Heat Mass Transf.* 126, 105395. doi:10.1016/j.icheatmasstransfer.2021.105395
- Zaim, A., Aissa, A., Mebarek-Oudina, F., Mahanthesh, B., Lorenzini, G., Sahnoun, M., et al. (2020). Galerkin finite element analysis of magneto-hydrodynamic natural convection of Cu-water nanoliquid in a baffled U-shaped enclosure. *Propuls. Power Res.* 9 (4), 383–393. doi:10.1016/j.jprr.2020.10.002
- Zaydan, M., Hamad, N. H., Wakif, A., Dawar, A., and Sehaqui, R. (2022). Generalized differential quadrature analysis of electro-magneto-hydrodynamic dissipative flows over a heated riga plate in the presence of a space-dependent heat source: The case for strong suction effect. *Heat. Trans.* 51 (2), 2063–2078. doi:10.1002/htj.22388

Nomenclature

Greek symbols

u, v Velocities components (ms^{-1})
 μ_{nf} Dynamic viscosity of nanofluid (mPa)
 f Dimensional velocity profiles
 μ_f Dynamic viscosity of base fluid (mPa)
 T Fluid temperature (K)
 ρ_{nf} Nanofluid density (Kgm^{-3})
 T_w Wall surface temperature (K)
 ρ_f Base fluid density (Kgm^{-3})
 T_∞ Free surface temperature (K)
 ξ Similarity variable
 f Dimensional velocity profiles Dimensional
 ϕ volume fraction of CuO , TiO_2 and Al_2O_3 nanoparticles
 B_i Biot number
 θ Dimensional heat profiles
 P Pressure

σ_{nf} electrical conductivity of nanofluid Sm^{-1}
 Pr Prandtl number
 η Couple stress parameter
 Re Local Reynolds number
 σ^* Stefan Boltzmann constant
 ψ Stream function
 a_k Coefficient of mean absorption
 Nu Nusselt number
 C_f Skin friction coefficient
 $(C_p)_f$ Specific heat of base fluid (J/kgK)
 k_{nf} Thermal conductivity ($Wm^{-1}K^{-1}$)

Subscripts

Thnf Tri-hybrid Nanofluid
nf Nanofluid
f Base fluid



OPEN ACCESS

EDITED BY

Umar Khan,
Hazara University, Pakistan

REVIEWED BY

Kasra Ghasemi,
University of Guelph, Canada
Najma Saleem,
Prince Mohammad bin Fahd University,
Saudi Arabia
Saranya Shekar,
United Arab Emirates University, United
Arab Emirates

*CORRESPONDENCE

Zahoor Iqbal,
izahoor@math.qau.edu.pk
Elsayed Tag-eldin,
elsayed.tageldin@fue.edu.eg

SPECIALTY SECTION

This article was submitted to Process and
Energy Systems Engineering,
a section of the journal Frontiers in Energy
Research

RECEIVED 03 July 2022

ACCEPTED 08 August 2022

PUBLISHED 21 October 2022

CITATION

Hussain A, Iqbal Z, Abdelmohimen MAH,
Guedri K, Tag-eldin E and Yassen MF
(2022), Energy transport features of
Oldroyd-B nanofluid flow over bidirectional
stretching surface subject to
Cattaneo–Christov heat and mass fluxes.
Front. Energy Res. 10:985146.
doi: 10.3389/fenrg.2022.985146

COPYRIGHT

© 2022 Hussain, Iqbal, Abdelmohimen,
Guedri, Tag-eldin and Yassen. This is an
open-access article distributed under the
terms of the [Creative Commons Attribution
License \(CC BY\)](#). The use, distribution or
reproduction in other forums is permitted,
provided the original author(s) and the
copyright owner(s) are credited and that
the original publication in this journal is
cited, in accordance with accepted
academic practice. No use, distribution or
reproduction is permitted which does not
comply with these terms.

Energy transport features of Oldroyd-B nanofluid flow over bidirectional stretching surface subject to Cattaneo–Christov heat and mass fluxes

Arafat Hussain¹, Zahoor Iqbal^{2*},
Mostafa A. H. Abdelmohimen^{3,4}, Kamel Guedri⁵,
Elsayed Tag-eldin^{6*} and Mansour F. Yassen^{7,8}

¹Institute of Applied System Analysis, Jiangsu University, Zhenjiang, China, ²Department of Mathematics, Quaid-i-Azam University, Islamabad, Pakistan, ³Mechanical Engineering Department, College of Engineering, King Khalid University, Abha, Saudi Arabia, ⁴Shoubra Faculty of Engineering, Benha University, Cairo, Egypt, ⁵Mechanical Engineering Department, College of Engineering and Islamic Architecture, Umm Al-Qura University, Makkah, Saudi Arabia, ⁶Faculty of Engineering and Technology, Future University in Egypt New Cairo, Cairo, Egypt, ⁷Department of Mathematics, College of Science and Humanities in Al-Aflaj, Prince Sattam Bin Abdulaziz University, Al-Aflaj, Saudi Arabia, ⁸Department of Mathematics, Faculty of Science, Damietta University, New Damietta, Egypt

By considering the Cattaneo–Christov approach and Buongiorno's model, the thermal transport model is formulated for the flow of Oldroyd-B nanofluid over a bidirectional stretching surface. The flow profile of Oldroyd-B nanofluid is examined for various physical parameters, and the effects of heat source/sink are also utilized to explore the thermal transport properties subject to thermal relaxation time. Governing mathematical models are developed on the basis of basic laws and presented in the form of Partial differential equations (PDEs). The governing partial differential equations are transformed into ordinary differential equations considering suitable dimensionless transformations. The homotopic method is applied to study the feature of heat and velocity components in fluid flow. The influence of each physical parameter over the thermal and concentration profile is displayed graphemically. It is noticed that thermal transport is decreasing with increment in thermal relaxation time. The mass transfer becomes weak with magnifying values of the stretching strength parameter. Moreover, the larger thermophoretic parameter regulates the heat transfer during fluid flow.

KEYWORDS

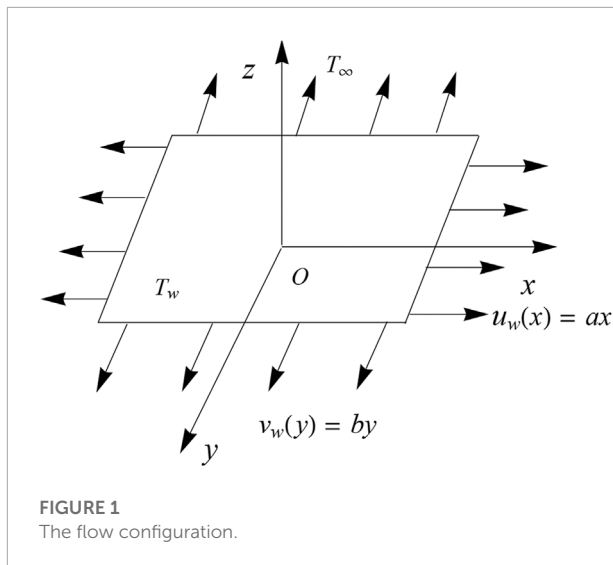
energy transport, Oldroyd-B nanofluid, heat source/sink, bidirectional stretching, Cattaneo–Christov theory, Buongiorno's model for nanofluids

1 Introduction

The heating and cooling fluids play a significant role in the advancement and development of engineering and industries. In general, usual fluids such as water, glycol, and ethylene have the incompetent ability of thermal conduction. However, metals possess a three-time greater ability of thermal transport compared to usual fluids. Therefore, it was required to make the mixture of a usual fluid and metal particle to enhance the thermal conductivity of the fluid. This mixture is called nanofluid. This concept of nanoparticle addition in a based fluid was introduced by Choi (1995). Choi et al. (2001) experimentally proved that the thermal transport of nanofluid is high, followed by a base fluid. Due to their high thermal conductivity, nanofluids have numerous applications in, for example, the advancement of thermal machines and the microelectromechanical system. The influence of the Brownian motion parameter on the heat transfer of nanofluid is studied by Evans et al. (2006). Sheikholeslami and Ganji (2013) investigated the flow of Cu-H₂O nanofluid between flat surfaces and concluded that the concentration of nanoparticles was enhanced by magnifying the Nusselt number. Sheikholeslami et al. (2014) examined the effect of magnetic force over the convective energy transport during nanofluid flow and noticed that, by increasing the Hartmann number, the heat diffusion in the system rises. The flow of Burgers nanofluid under the influence of stretching surface is examined by Khan et al. (2016a). For a greater radiation parameter, the heat profile of the Burgers nanofluid is ascending. Earlier research (Hayat et al., 2016; Hayat et al., 2017a; Hayat et al., 2018; Hayat et al., 2019) studied the convective transport of nanofluid by considering slip mechanism over a surface. Moreover, it analyzed the ferromagnetic and cross nanofluid flows considering various physical influences. The thermal transport rate magnifies for a greater ratio of velocity. Hayat et al. (2017b) discussed the two-dimensional flow of the Burgers nanofluid with a modified heat and mass flux approach. They concluded that an increment in thermal relaxation time sufficiently decreases the thermal transport. Some studies (Khan et al., 2019; Khan et al., 2020a; Khan and Alzahrani, 2020) analyzed the transport of nanofluid considering porous media; the magnifying influence of the Eckert number gives strength to the heat conduction of the nanofluid. Bhattacharyya et al. (2019) considered the flow of nanofluid over the rotating and stretchable surface. Based on this study, the higher Reynolds number minimizes the magnitude of radial velocity. Sher et al. (2019) explored the features of the Burgers nanofluid model formulation for nanofluid with a stretching surface with an improved thermal flux theory, which was investigated by Ahmad et al. (2019). Khan et al. (2020b) proposed a new flow model for the Burgers nanofluid and investigated the thermal transport. They summarized that, for increasing magnitudes of stagnation, the parameter flow velocity

of nanofluid is improved. Amjid et al. (2020) approximated the transport of Casson nanofluid over a curve surface. They examined that flow is decreasing because of magnifying the Casson constant. Muhammad et al. (2020) computed the bidirectional flow of nanofluid applying thermal radiation and concluded that the increment in thermophoresis force increases the heat conduction in the nanofluid flow. Khan and Alzahrani (2021), Khan et al. (2021), and Khan and Puneeth (2021) presented some current significant studies about nanofluids.

Thermal transport is a significant natural phenomenon with multiple applications in industries. The theory of heat transport was firstly introduced by Fourier (Grattan-Guinness, 2005) and introduced Fourier's law of thermal transport. Laterally, based on Fourier's law, numerous researchers studied the features of thermal transformation in different fluid flow phenomena (Rashidi et al., 2014; Ahmed et al., 2019; Nadeem and Khan, 2019; Khan et al., 2020; Khan et al., 2022; Raza et al., 2022). Cattaneo (1948) made amendments to Fourier's law and stated that thermal transport depends on the time called the thermal relaxation time. Christov (2009) introduced further modifications to the Cattaneo model. The Cattaneo–Christov approach is proposed to investigate heat transformation using familiarizing thermal relaxation time. After that, researchers applied this Cattaneo–Christov approach to study the thermal transformation phenomena in different kinds of fluid flows. Straughan (2010) presented a study based on the Cattaneo–Christov theory. Haddad (2014) applied the Cattaneo–Christov thermal transport theory to examine the instability. Shehzad et al. (2016) applied Cattaneo–Christov to study the Darcy flow of viscoelastic fluid and concluded that the flow profile of such fluid changes by varying the values of the Forchheimer parameter. Saleem et al. (2017) employed Cattaneo–Christov approach to investigate the Maxwell fluid flow and found that thermal conduction decreased with ascending thermal relaxation time. Waqas et al. (2018) applied the Cattaneo–Christov approach to inquire the thermal conduction in Burgers fluid and reported that a greater thermal relaxation time constant reduced the thermal flow of the fluid. Rasool and Zhang (2019) examined the Darcy flow of nanofluid over the surface by applying the Cattaneo–Christov approach. Shehzad et al. (2019) studied the fluid flow by applying the Cattaneo–Christov approach of thermal and mass transfer and investigated that the ascending values of the Prandtl parameter enhanced the thermal curve. Hafeez et al. (2020) investigated chemical reactions, applied the Cattaneo–Christov approach to study the fluid flow using rotating surfaces, and used the Midrich technique to examine the influence of different parameters. Ahmed et al. (2020) applied the Cattaneo–Christov approach to analyze fluid transport over a stretching sheet. Recently, Iqbal et al. (2020) analyzed the heat transfer while the Burgers nanofluid flow based on the Cattaneo–Christov



approach. They found that the magnifying values of the thermal relaxation constant results minimized the thermal flow rate. Rehman et al. (2016) constructed the solution of the set of equations to study the heat transfer phenomena. Currently, Ali et al. (2021) applied a finite differencing approach to analyze the heat transfer. Some other studies are carried out to solve such problems for examining thermal transport (Kamran et al., 2015; Kamran et al., 2016a; Kamran et al., 2016b; Rehman and Kamran, 2019).

The heat transport during the nanofluid flow using stretched surfaces has been examined by numerous researchers (Khan et al., 2016a; Hayat et al., 2019; Khan et al., 2020b). The Cattaneo–Christov approach has been applied by researchers to study heat transfer in the Burgers fluid (Khan et al., 2016b; Khan and Khan, 2016). Still, no mathematical formulation has been developed to analyze the thermal transport by applying the Cattaneo–Christov theory for the flow of the Oldroyd-B nanofluid and Buongiorno’s model. In this article, we proposed a new model of heat transport applying the Cattaneo–Christov approach and Buongiorno’s model to investigate the thermal transport in the Burgers nanofluid under the influence of a stretching sheet. The homotopic algorithm is applied to solve governing problems.

2 Mathematical formulation

This section presents a mathematical formulation for three-dimensional convective transport of Oldroyd-B nanofluid employed by a bidirectional stretching sheet. In-compressible and steady flow phenomena are studied in this article. A model combining the Cattaneo–Christov approach with Buongiorno’s model is employed to present a mathematical formulation for

solutal and thermal conduction in the flow of the Oldroyd-B nanofluid. A cartesian coordinate system was applied to formulate the proposed model. Axial velocities in the x and y direction are $u = ax$ and $v = by$, where a and b denote constants. The flow region is taken as $z > 0$. The velocity vector is $\mathbf{V} = [u, v, w]$, T_w denotes temperature, and C_w represents concentration, respectively. The flow pattern is presented in Figure 1.

The rheology of Oldroyd-B fluid is represented by the following equation:

$$\left(1 + \lambda_1 \frac{D}{Dt}\right) \mathbf{S} = \mu \left(1 + \lambda_2 \frac{D}{Dt}\right) \mathbf{A}_1, \quad (1)$$

where \mathbf{S} is tensor representing the extra stress, μ is dynamic viscosity, $\mathbf{A}_1 = (\nabla \mathbf{V}) + (\nabla \mathbf{V})^T$ denotes the Rivlin–Ericksen tensor, and $\frac{D}{Dt}$ is upper convective derivative.

The continuity and momentum governing model by neglecting pressure are given as follows (khan et al., 2020; Iqbal et al., 2020):

$$\nabla \cdot \mathbf{V} = 0, \quad (2)$$

$$\rho_f \frac{d\mathbf{V}}{dt} = \text{div} \mathbf{S}. \quad (3)$$

For the current problem, the law of energy conservation is (Iqbal et al., 2020)

$$\frac{dT}{dt} - \left[D_B \nabla C \cdot \nabla T + \frac{D_T}{D_\infty} (\nabla T)^2 \right] = -\frac{1}{(\rho c_p)} (\nabla \cdot \mathbf{q}), \quad (4)$$

where \mathbf{q} denotes the thermal flux and satisfies the equation

$$\mathbf{q} + \left[\frac{\partial \mathbf{q}}{\partial t} + (\nabla \cdot \mathbf{V}) \mathbf{q} + \mathbf{V} \cdot \nabla \mathbf{q} - \mathbf{q} \cdot \nabla \mathbf{V} \right] \lambda_t = -k \nabla T. \quad (5)$$

The mass transfer model is as follows (Iqbal et al., 2020; Iqbal et al., 2021)

$$\frac{dC}{dt} - \frac{D_T}{D_\infty} \nabla^2 T = -\nabla \cdot \mathbf{J}, \quad (6)$$

where \mathbf{J} indicates mass flux and satisfies the following relation:

$$\mathbf{J} + \lambda_c \left[\frac{\partial \mathbf{J}}{\partial t} + \mathbf{V} \cdot \nabla \mathbf{J} - \mathbf{J} \cdot \nabla \mathbf{V} + (\nabla \cdot \mathbf{V}) \mathbf{J} \right] = -D_B \nabla C. \quad (7)$$

Here, λ_t , λ_c , and λ_1 denote the thermal and the mass and fluid relaxation time, respectively. λ_2 is the Oldroyd-B fluid parameter, ν denotes kinematics viscosity, T denotes temperature, and C represents the concentration, respectively. D_B denotes diffusion coefficient, whereas \mathbf{q} is thermal flux and \mathbf{J} represents mass flux, respectively.

Eliminating \mathbf{S} from (1) and (3), \mathbf{q} from Eqs. (4) and (5) and \mathbf{J} between Eqs. (6) and (7), we arrive at following governing PDEs:

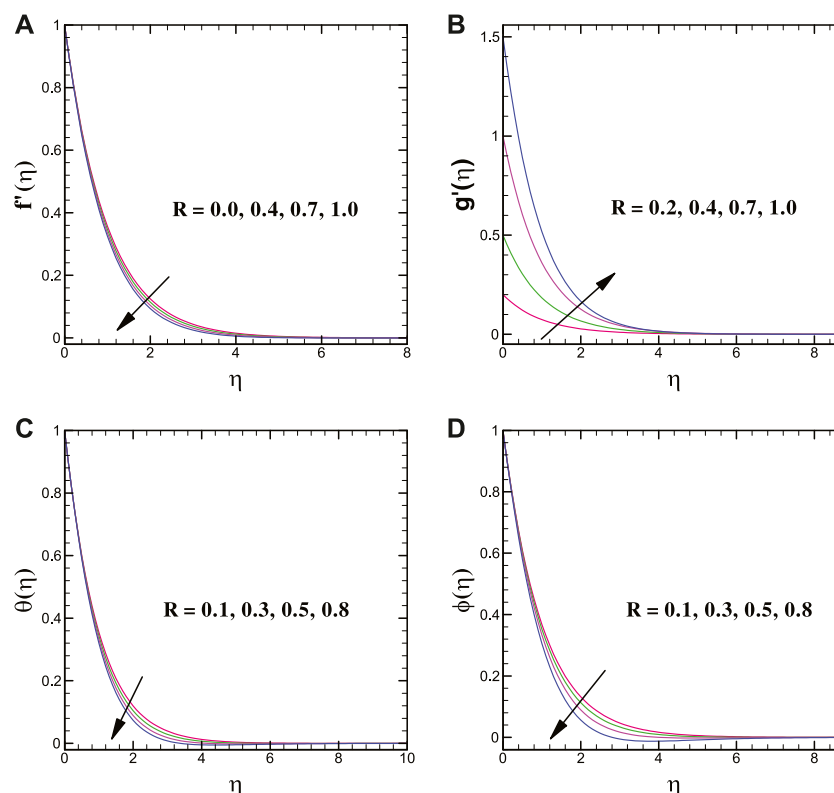


FIGURE 2

(A–D) Impact of R on f' , g' , θ , and ϕ .

$$\frac{\partial u}{\partial x} + \frac{\partial v}{\partial y} + \frac{\partial w}{\partial z} = 0, \quad (8)$$

$$\begin{aligned} u \frac{\partial u}{\partial x} + v \frac{\partial u}{\partial y} + w \frac{\partial u}{\partial z} + \lambda_1 \left[2uv \frac{\partial^2 u}{\partial x \partial y} + 2wv \frac{\partial^2 u}{\partial y \partial z} + 2wu \frac{\partial^2 u}{\partial x \partial z} \right. \\ \left. + u^2 \frac{\partial^2 u}{\partial x^2} + v^2 \frac{\partial^2 u}{\partial y^2} + w^2 \frac{\partial^2 u}{\partial z^2} \right] = v \frac{\partial^2 u}{\partial z^2} - \frac{\sigma B_0^2}{\rho} \left(u + \lambda_1 w \frac{\partial u}{\partial z} \right) \\ + \nu \lambda_2 \left[u \frac{\partial^3 u}{\partial x \partial z^2} + v \frac{\partial^3 u}{\partial y \partial z^2} + w \frac{\partial^3 u}{\partial z^3} - \frac{\partial u}{\partial x} \frac{\partial^2 u}{\partial z^2} \right. \\ \left. - \frac{\partial u}{\partial z} \frac{\partial^2 w}{\partial z^2} - \frac{\partial u}{\partial y} \frac{\partial^2 v}{\partial z^2} \right], \end{aligned} \quad (9)$$

$$\begin{aligned} u \frac{\partial v}{\partial x} + v \frac{\partial v}{\partial y} + w \frac{\partial v}{\partial z} + \lambda_1 \left[2uv \frac{\partial^2 v}{\partial x \partial y} + 2wu \frac{\partial^2 v}{\partial x \partial z} + 2wv \frac{\partial^2 v}{\partial y \partial z} \right. \\ \left. + w^2 \frac{\partial^2 v}{\partial z^2} + u^2 \frac{\partial^2 v}{\partial x^2} + v^2 \frac{\partial^2 v}{\partial y^2} \right] = v \frac{\partial^2 v}{\partial z^2} - \frac{\sigma B_0^2}{\rho} \left(v + \lambda_1 w \frac{\partial v}{\partial z} \right) \\ + \nu \lambda_2 \left[u \frac{\partial^3 v}{\partial x \partial z^2} + v \frac{\partial^3 v}{\partial y \partial z^2} + w \frac{\partial^3 v}{\partial z^3} - \frac{\partial v}{\partial z} \frac{\partial^2 w}{\partial z^2} - \frac{\partial v}{\partial x} \frac{\partial^2 u}{\partial z^2} - \frac{\partial v}{\partial y} \frac{\partial^2 v}{\partial z^2} \right], \end{aligned} \quad (10)$$

$$\begin{aligned} u \frac{\partial T}{\partial x} + v \frac{\partial T}{\partial y} + w \frac{\partial T}{\partial z} - \tau \left[D_B \left(\frac{\partial C}{\partial z} \frac{\partial T}{\partial z} \right) + \frac{D_T}{T_\infty} \left(\frac{\partial T}{\partial z} \right)^2 \right] \\ + \lambda_t \left[u^2 \frac{\partial^2 T}{\partial x^2} + v^2 \frac{\partial^2 T}{\partial y^2} + w^2 \frac{\partial^2 T}{\partial z^2} + 2uv \frac{\partial^2 T}{\partial x \partial y} + 2vw \frac{\partial^2 T}{\partial y \partial z} + 2uw \frac{\partial^2 T}{\partial x \partial z} + u \frac{\partial u}{\partial x} \frac{\partial T}{\partial x} + u \frac{\partial v}{\partial x} \frac{\partial T}{\partial y} \right. \\ \left. + u \frac{\partial w}{\partial x} \frac{\partial T}{\partial z} + v \frac{\partial u}{\partial y} \frac{\partial T}{\partial x} + v \frac{\partial v}{\partial y} \frac{\partial T}{\partial y} + u \frac{\partial w}{\partial y} \frac{\partial T}{\partial z} + w \frac{\partial u}{\partial z} \frac{\partial T}{\partial x} + w \frac{\partial v}{\partial z} \frac{\partial T}{\partial y} + w \frac{\partial w}{\partial z} \frac{\partial T}{\partial z} \right] \\ - \lambda_t \tau D_B \left[u \frac{\partial^2 C}{\partial x \partial z} \frac{\partial T}{\partial z} + u \frac{\partial C}{\partial z} \frac{\partial^2 T}{\partial x \partial z} + v \frac{\partial^2 C}{\partial y \partial z} \frac{\partial T}{\partial z} + v \frac{\partial C}{\partial z} \frac{\partial^2 T}{\partial y \partial z} + w \frac{\partial^2 C}{\partial z^2} \frac{\partial T}{\partial z} + w \frac{\partial C}{\partial z} \frac{\partial^2 T}{\partial z^2} \right] \\ - 2\lambda_t \tau \frac{D_T}{T_\infty} \left[u \frac{\partial T}{\partial z} \frac{\partial^2 T}{\partial x \partial z} + v \frac{\partial T}{\partial z} \frac{\partial^2 T}{\partial y \partial z} + w \frac{\partial T}{\partial z} \frac{\partial^2 T}{\partial z^2} \right] = \alpha_1 \left[\frac{\partial^2 T}{\partial z^2} \right] \\ + \lambda_t \frac{Q_0}{\rho c_p} \left(u \frac{\partial T}{\partial x} + v \frac{\partial T}{\partial y} + w \frac{\partial T}{\partial z} \right) + Q_0 (T - T_w) \end{aligned} \quad (11)$$

$$\begin{aligned} u \frac{\partial C}{\partial x} + v \frac{\partial C}{\partial y} + w \frac{\partial C}{\partial z} + \lambda_c \\ \left[w^2 \frac{\partial^2 C}{\partial z^2} + u^2 \frac{\partial^2 C}{\partial x^2} + v^2 \frac{\partial^2 C}{\partial y^2} + 2uv \frac{\partial^2 C}{\partial x \partial y} + 2uw \frac{\partial^2 C}{\partial x \partial z} + 2vw \frac{\partial^2 C}{\partial y \partial z} \right. \\ \left. + u \frac{\partial u}{\partial x} \frac{\partial C}{\partial x} + u \frac{\partial w}{\partial x} \frac{\partial C}{\partial z} + v \frac{\partial u}{\partial y} \frac{\partial C}{\partial x} + u \frac{\partial v}{\partial x} \frac{\partial C}{\partial y} + v \frac{\partial v}{\partial y} \frac{\partial C}{\partial y} \right. \\ \left. + v \frac{\partial w}{\partial y} \frac{\partial C}{\partial z} + w \frac{\partial v}{\partial z} \frac{\partial C}{\partial y} + w \frac{\partial u}{\partial z} \frac{\partial C}{\partial x} + w \frac{\partial w}{\partial z} \frac{\partial C}{\partial z} \right] \\ - \frac{D_T}{T_\infty} \lambda_c \left[w \frac{\partial^3 T}{\partial z^3} + v \frac{\partial^3 T}{\partial y \partial z^2} + u \frac{\partial^3 T}{\partial x \partial z^2} \right] = \frac{D_T}{T_\infty} \left(\frac{\partial^2 T}{\partial z^2} \right) + D_B \left[\frac{\partial^2 C}{\partial z^2} \right], \end{aligned} \quad (12)$$

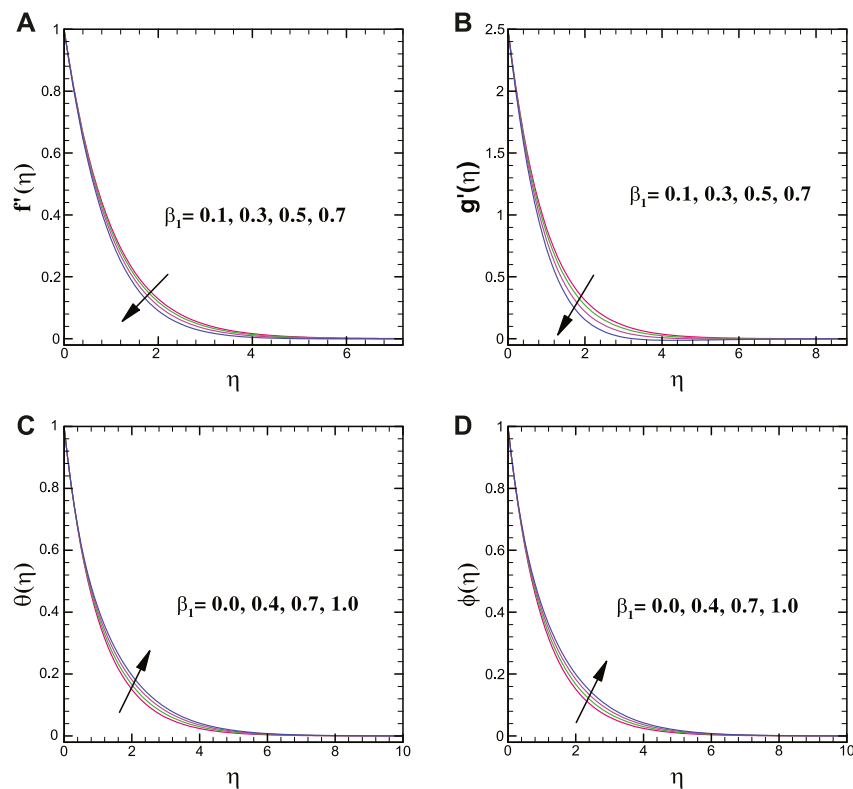


FIGURE 3
(A–D) Impact of β_1 on f' , g' , θ , and ϕ .

with the boundary conditions

$$u = u_w = ax, v = v_w = by, w = 0, T = T_w, C = C_w \text{ at } z = 0, \quad (13)$$

$$u \rightarrow 0, v \rightarrow 0, T \rightarrow T_\infty, C \rightarrow C_\infty \text{ as } z \rightarrow \infty. \quad (14)$$

Here, $\alpha_1 = \left(\frac{k}{\rho c_p}\right)$ indicates thermal diffusivity, p and ρ denote pressure and density, respectively, c_p is the specific heat capacity, k is thermal conductivity, and C_∞ and T_∞ denote the ambient concentration and temperature, respectively.

See the following transformations (Ahmad et al., 2019; Iqbal et al., 2021):

$$u = axf'(\eta), v = ayf'(\eta), w = -\sqrt{av}(f+g), \eta = z\sqrt{\frac{a}{v}} \\ \phi(\eta) = \frac{C - C_\infty}{C_w - C_\infty}, \theta(\eta) = \frac{T - T_\infty}{T_w - T_\infty}, \quad (15)$$

By invoking these transformations, Eq. 8 is satisfied and Eqs. (9)–(12) take the following forms:

$$f''' + (1 + M^2\beta_1)(f+g)f'' - (f')^2 + \beta_1[2(f+g)f'f'' - (f+g)^2f'''] + \beta_2[(f'' + g'')f'' - (f+g)f^{iv}] - M^2f' = 0, \quad (16)$$

$$g''' + (1 + M^2\beta_1)(f+g)g'' - (g')^2 + \beta_1[2(f+g)g'g'' - (f+g)^2g'''] + \beta_2[(f'' + g'')g'' - (f+g)g^{iv}] = 0, \quad (17)$$

$$\theta'' + \text{Pr}(f+g)\theta' + \text{Pr}(N_b\phi'\theta' + N_t\theta'^2) - \text{Pr}\beta_t[(f' + g')(f+g)\theta' + (f+g)^2\theta''] - \beta_t N_b \text{Pr}[(f+g)\theta''\phi' + (f+g)\phi''\theta'] - 2N_t\beta_t \text{Pr}(f+g)\theta''\theta' + \text{Pr}\delta[\theta + \beta_t(f+g)\theta'] = 0, \quad (18)$$

$$\phi'' + \text{Le Pr}(f+g)\phi' + \frac{N_t}{N_b}\text{Le Pr}\theta'' - \text{Le Pr}\beta_c[(f+g)(f' + g')\phi' + (f+g)^2\phi''] - \text{Le Pr}\frac{N_t}{N_b}(f+g)\theta''' = 0, \quad (19)$$

with transformed boundary conditions are follows:

$$f(0) = 0, g(0) = 0, f'(0) = 1, g'(0) = R, \theta(0) = 1, \phi(0) = 1, \quad (20)$$

$$f'(\infty) = 0, g'(\infty) = 0, \theta(\infty) = 0, \phi(\infty) = 0. \quad (21)$$

Here, β_1 is the relaxation time, β_2 the Oldroyd-B fluid material parameter, Pr the Prandtl number, Le the Lewis number, β_t the thermal relaxation time constraint, and β_c the mass relaxation time. Thermophoresis, Brownian motion, and ratio of

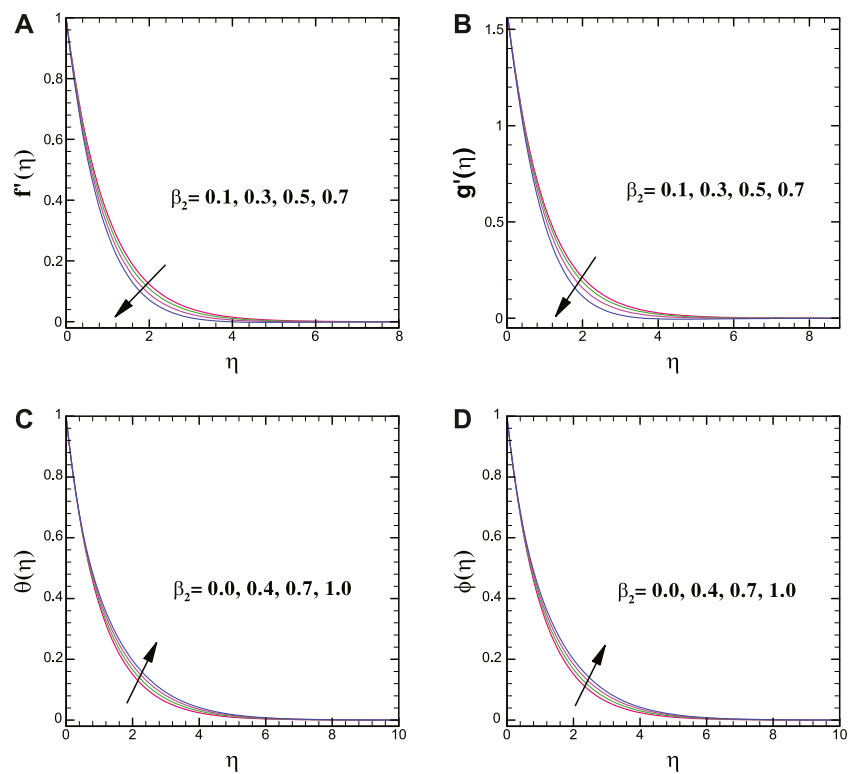


FIGURE 4
(A–D) Impact of β_2 on f_l , g_l , θ , and ϕ .

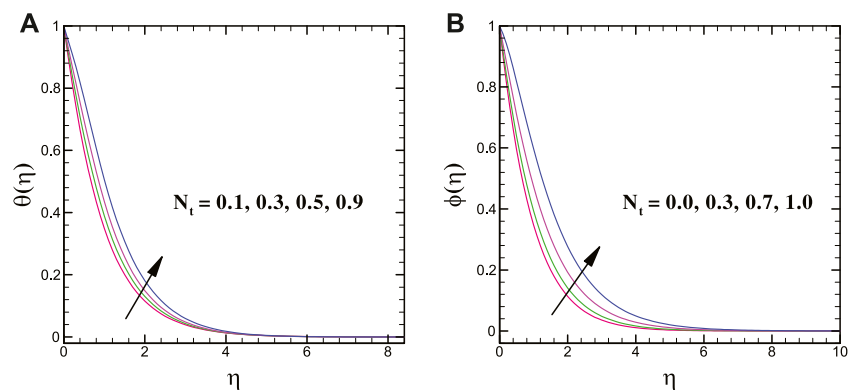


FIGURE 5
(A,B) Effect of N_t on θ and ϕ .

stretching rates are (N_t) , (N_b) , and (R) , respectively, are define as follows:

$$\beta_1 = \lambda_1 \frac{U_0}{l}, \beta_2 = \lambda_2 \frac{U_0}{l}, \beta_t = \lambda_t \frac{U_0}{l}, \beta_c = \lambda_c \frac{U_0}{l}, R = \frac{b}{a}$$

$$Le = \frac{\alpha_1}{D_B}, Pr = \frac{\nu}{\alpha_1}, N_t = \frac{\tau D_T (T_w - T_\infty)}{\nu T_\infty}, N_b = \frac{\tau D_B (C_w - C_\infty)}{\nu} \quad (22)$$

3 Homotopic solution approach

In this manuscript, the homotopic analysis approach (Hayat et al., 2017b; Khan et al., 2020b; Khan et al., 2020) is applied to solve the Eqs 16–19 with boundary conditions defined in Eqs 20, 21. Initial guess and linear operators are

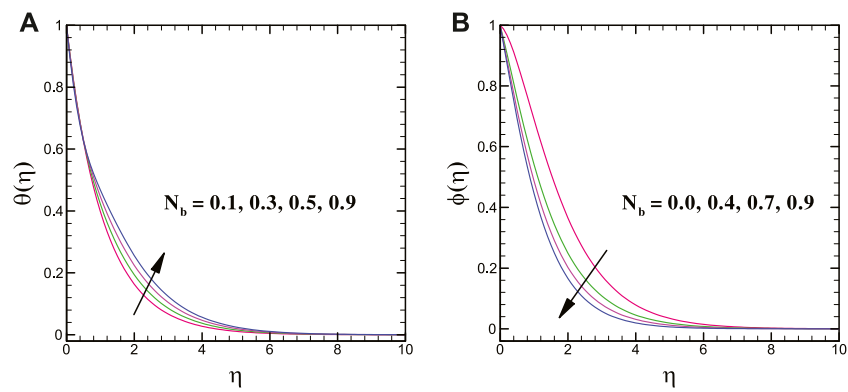


FIGURE 6
(A,B) Effect of N_b on θ and ϕ .

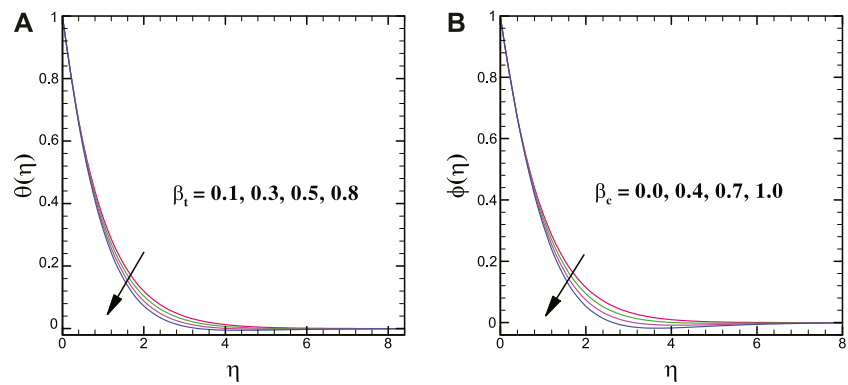


FIGURE 7
(A,B) Effect of β_t and β_c on θ and ϕ .

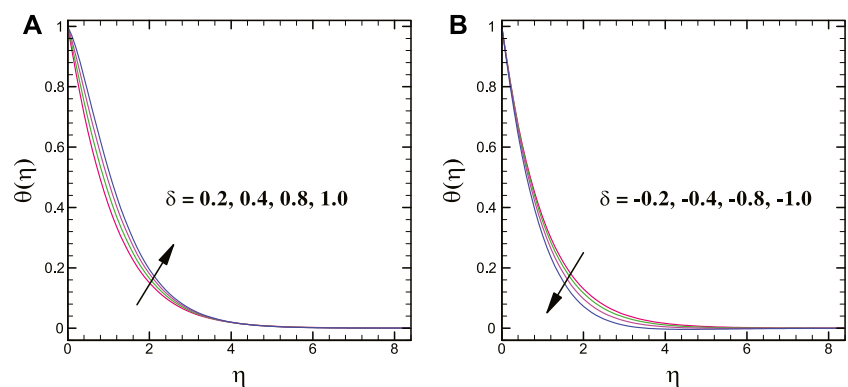


FIGURE 8
(A,B) Impact of δ on θ .

TABLE 1 An evaluation table for $-f''(0)$ and $-g''(0)$ for several magnitudes of R in reduced case when $\beta_1 = \beta_2 = M = 0$.

| R | Khan et al. (2016c) | | Present study | |
|-----|---------------------|-----------|---------------|-----------|
| | $-f''(0)$ | $-g''(0)$ | $-f''(0)$ | $-g''(0)$ |
| 0.0 | 1.0 | 0.0 | 0.0 | 0.0 |
| 0.1 | 1.02026 | 0.06685 | 1.02019 | 0.06669 |
| 0.2 | 1.03949 | 0.14874 | 1.03937 | 0.14863 |
| 0.3 | 1.05795 | 0.24336 | 1.05789 | 0.24312 |
| 0.4 | 1.07578 | 0.34921 | 1.07567 | 0.34901 |
| 0.5 | 1.09309 | 0.46521 | 1.09302 | 0.46509 |
| 0.6 | 1.10994 | 0.59053 | 1.10913 | 0.59048 |
| 0.7 | 1.12639 | 0.72453 | 1.12618 | 0.72438 |
| 0.8 | 1.14249 | 0.86668 | 1.14229 | 0.86654 |
| 0.9 | 1.15826 | 1.016538 | 1.15811 | 1.016539 |
| 1.0 | 1.17372 | 1.17372 | 1.17121 | 1.17361 |

needed to proceed with this approach. Hence, for analytic solutions' linear operators $(\mathcal{E}_f, \mathcal{E}_\theta, \mathcal{E}_\phi)$ and the initial guesses (f_0, θ_0, ϕ_0) used, the models of energy and the concentration diffusion are

$$f_0(\eta) = 1 - e^{-\eta}, \quad g_0(\eta) = \alpha(1 - e^{-\eta}), \quad \theta_0(\eta) = e^{-\eta}, \quad \phi_0(\eta) = e^{-\eta}, \quad (23)$$

$$\mathcal{E}_f[f(\eta)] = f''' - f', \quad \mathcal{E}_\theta[\theta(\eta)] = \theta'' - \theta, \quad \mathcal{E}_\phi[\phi(\eta)] = \phi'' - \phi. \quad (24)$$

4 Physical analysis of results

The three-dimensional steady-state thermal transfer phenomena of nanofluid by a bidirectional stretching surface is analyzed. For the Oldroyd-B nanofluid flow features, the Cattaneo–Christov approach and Buongiorno's model are employed together. The homotopic approach is used to analyze the impact of various physical parameters involved in Eqs. (16–(19) with boundary conditions (20) and (21).

The axial velocity components $f'(\eta)$, $g'(\eta)$, thermal distribution $\theta(\eta)$, and solutal distribution $\phi(\eta)$ are examined under the impact of physical parameters such as relaxation timer (β_1), Oldroyd B fluid (β_2), thermophoresis (N_t), thermal relaxation (β_t), and Brownian motion (N_b), mass relaxation (β_c) and explained through Figs. 2–8. Moreover, for leading constraints, magnitudes are fixed as $R = 0.2$, $\beta_1 = 0.5$, $\beta_2 = 0.15$, $Pr = 5.0$, $M = 1.5$, $\beta_t = 0.3$, $\beta_c = 0.5$, $Le = 4.5$, $N_b = 0.5$, and $N_t = 0.7$. The influence of physical parameters is graphemically presented and also theoretically discussed.

$f'(\eta)$ and $g'(\eta)$ represent the x -axis and y -axis, respectively. $\theta(\eta)$ is the thermal profile and $\phi(\eta)$ denotes solutal curve of nanofluid.

Figures 2A–D represent the effect of stretching strength (R) over $f'(\eta)$, $g'(\eta)$, thermal profile $\theta(\eta)$, and solutal profile $\phi(\eta)$ of the Oldroyd-B nanofluid. It is clear that the $f'(\eta)$ is falling for magnifying magnitudes of R but the magnitude of the normal velocity component $g'(\eta)$ is increasing for larger R . As R denotes stretching ratio defined as $R = \frac{b}{a}$, where a and b represent stretching rate along x -direction and y -direction, respectively. This implies that, for higher R , the stretching strength along the y -axis is greater than stretching in the x -direction. Therefore, the flow velocity $f'(\eta)$ is decreasing, whereas the curves for $g'(\eta)$ are escalating for greater values of R . The impact of the Deborah parameter β_1 (relaxation time) over the axial-velocity components $f'(\eta)$, $g'(\eta)$, thermal profile $\theta(\eta)$, and solutal profile $\phi(\eta)$ of the Oldroyd-B nanofluid is represented in **Figures 3A–D**. The graphs in **Figures 3A–D** indicate that the flow profiles of the Oldroyd-B nanofluid are showing a falling behavior for increasing values of β_1 , whereas the heat and solutal energy profile during flow are growing for magnifying values of β_1 . The increment in the relaxation time constraint physically increases resistance to flow, so the velocity profiles decrease. However, because the resistance collision of particles increases, it directly increases the thermal energy of the system. Hence, resistance results in additional heat generation, which increases the thermal transport and solutal profile. The influence of thermal source/sink constraint (δ) over the thermal and solutal profiles is presented in **Figures 3A,B**. The increment in the source parameter ($\delta > 0$) increases the thermal profile, but it falls for heat sink constraint ($\delta < 0$). The magnification of the source parameter ($\delta > 0$) generates extra heat, which magnifies the heat transport, whereas the increment in sink parameter ($\delta < 0$) absorbs heat which obviously refers to minimizing the heat transfer. **Figures 4A–D** shows the influence of the Oldroyd-B fluid parameter (β_2) over velocity components $f'(\eta)$, $g'(\eta)$, thermal transport $\theta(\eta)$, and solutal transport $\phi(\eta)$. These graphs indicate that $f'(\eta)$ and $g'(\eta)$ fall for greater values of β_2 , whereas the thermal and solutal profiles of nanofluid are growing. The impact of the thermophoretic force parameter (N_t) heat and concentration profile of the nanofluid is presented in **Figures 5A,B**. Graphical results indicate that heat and concentration profiles of the nanofluid are showing a growth trend for magnifying values of N_t and the thermal thickness of the boundary also magnifies for greater N_t . In

TABLE 2 An assessment table for $-\theta'(0)$ for pertinent ranges of R in reducing case when $\beta_1 = \beta_2 = \delta = \beta_t = N_t = N_b = 0$ and $Pr = 1$.

| R | Liu and Andersson (2008) | Hayat et al. (2014) | Present study |
|------|--------------------------|---------------------|---------------|
| 0.25 | −0.665933 | −0.66593 | −0.665929 |
| 0.50 | −0.735334 | −0.73533 | −0.735326 |
| 0.75 | −0.796472 | −0.79472 | −0.796469 |

the thermophoresis process, fluid particles move from a warm to a cool region. This particle motion produces extra heat, due to which the solutal profile of the Oldroyd-B nanofluid escalates. **Figures 6A,B** represents the effect of (N_b) over the thermal and solutal distributions of the Oldroyd-B nanofluid. These graphs show that the thermal transport magnifies, whereas the solutal transport de-escalates for magnifying values of N_b . Basically, the Brownian motion parameter controls the motion of fluid particles. For high values of parameter N_b , the random motion of fluid particles is high and increases the kinetic energy, and particles collide with each other, due to which the thermal energy also increases. Due to this collision, fluid particles' mass transport profile decays. The influence of parameters (β_t) and (β_c) over the heat and mass transport profile is presented in **Figures 7A,B**. The thermal and concentration distributions represent the decaying trend for magnifying values of β_t and β_c , respectively. The thermal relaxation time parameter represents the time duration required by a particle to transfer heat from one part to another. As known physically, with the passage of time, thermal transport becomes slow due to the decrease in the thermal gradient. Therefore, magnifying thermal relaxation time implies that the thermal transport slows down, and the heat transport profile is falling. Similarly, the mass profile also decreases for ascending solutal relaxation time parameter.

5 Validation of homotopic outcomes

In this section, approximated $-f''(0)$, $-g''(0)$, and $-\theta'(0)$ for different α are displayed in **Tables 1, 2**, and the obtained values are compared with other studies. This comparison indicates that our approximations are accurate and the adopted homotopic technique is a valid approach.

Concluding remarks

The Cattaneo–Christov approach and Buongiorno's model were employed together to investigate the momentum and energy transport features of the three-dimensional flow of the Oldroyd-B nanofluid over a bidirectional stretched sheet. After utilizing the homotopy analysis method on the governing equation to solve them, we found some important results, which are noted here.

We found that, for magnifying stretching strength R , the vertical velocity in the y -direction magnifies, but it decreases in the x -direction. The flow curves of the Oldroyd-B nanofluid for the relaxation time parameter show an opposite behavior compared to the Oldroyd-B material parameter.

For varying values of the Brownian motion parameter, the solutal transport decays, whereas the thermal conduction shows

enhancing trend for it. Moreover, the thermal and concentration transport = escalates for larger magnitudes of the thermophoretic force parameter. In addition, a larger thermal relaxation time parameter deteriorates the thermal transport. The mass transfer profile decreases for a greater solutal relaxation time parameter. The larger stretching strength decreases the thermal energy transport of the nanoliquid. **Figures 8A,B** clearly elucidate that the thermal profile is augmented for larger heat source parameter while it declines for heat sink parameter.

Data availability statement

The original contributions presented in the study are included in the article/supplementary materials. Further inquiries can be directed to the corresponding authors.

Author contributions

All authors listed have made a substantial, direct, and intellectual contribution to the work and approved it for publication.

Funding

This work is supported by National Natural Science Foundation of China (12071408), Natural Science foundation of Jiangsu (BK20201149) and Jiangsu Funding Program for excellent Postdoctoral Talent, Grant No: 2022ZB675. The authors would like to thank the Deanship of Scientific Research at Umm Al-Qura University for supporting this work by Grant Code:22UQU4331317DSR67.

Acknowledgments

The authors extend their appreciation to the Deanship of Scientific Research at King Khalid University for funding this work through Large Groups (RGP.2/94/43). The authors would like to thank the Deanship of Scientific Research at Umm Al-Qura University for supporting this work by Grant Code: 22UQU4331317DSR67.

Conflict of interest

The authors declare that the research was conducted in the absence of any commercial or financial relationships that could be construed as a potential conflict of interest.

Publisher's note

All claims expressed in this article are solely those of the authors and do not necessarily represent those of their affiliated

organizations or those of the publisher, the editors, and the reviewers. Any product that may be evaluated in this article, or claim that may be made by its manufacturer, is not guaranteed or endorsed by the publisher.

References

- Ahmad, I., Faisal, M., and Javed, T. (2019). Bi-directional stretched nanofluid flow with Cattaneo-Christov double diffusion. *Results Phys.* 15, 102581. doi:10.1016/j.rinp.2019.102581
- Ahmed, J., Khan, M., and Ahmad, L. (2019). MHD swirling flow and heat transfer in Maxwell fluid driven by two coaxially rotating disks with variable thermal conductivity. *Chin. J. Phys.* 60, 22–34. doi:10.1016/j.cjph.2019.02.010
- Ahmed, S., Nadeem, S., Muhammad, N., and Khan, M. N. (2020). Cattaneo-Christov heat flux model for stagnation point flow of micropolar nanofluid toward a nonlinear stretching surface with slip effects. *J. Therm. Anal. Calorim.* 143, 1187. doi:10.1007/s10973-020-09504-2
- Ali, B., Raju, C. S. K., Ali, L., Hussain, S., and Kamran, T. (2021). G-Jitter impact on magnetohydrodynamic non-Newtonian fluid over an inclined surface: Finite element simulation. *Chin. J. Phys.* 71, 479–491. doi:10.1016/j.cjph.2021.03.020
- Amjid, M., Zehra, I., Nadeem, S., and Abbas, N. (2020). Thermal analysis of Casson micropolar nanofluid flow over a permeable curved stretching surface under the stagnation region. *J. Therm. Anal. Calorim.* 143, 2485–2497. doi:10.1007/s10973-020-10127-w
- Bhattacharyya, A., Seth, G. S., Kumar, R., and Chamkha, A. J. (2019). Simulation of Cattaneo-Christov heat flux on the flow of single and multi-walled carbon nanotubes between two stretchable coaxial rotating disks. *J. Therm. Anal. Calorim.* 139, 1655–1670. doi:10.1007/s10973-019-08644-4
- Cattaneo, C. (1948). Sulla conduzione del calore. *Atti Semin. Mat. Fis. Univ. Modena Reggio Emilia* 3, 83–101.
- Choi, S. U. S. (1995). "Enhancing thermal conductivity of fluids with nanoparticles, the proceedings of the 1995," in *ASME international mechanical engineering congress and exposition* (San Francisco, USA: ASME), 99–105.
- Choi, S. U. S., Zhang, Z. G., Yu, W., Lockwood, F. E., and Grulke, E. A. (2001). Anomalous thermal conductivity enhancement in nanotube suspensions. *Appl. Phys. Lett.* 4, 2252–2254. doi:10.1063/1.1408272
- Christov, C. I. (2009). On frame indifferent formulation of the Maxwell-Cattaneo model of finite-speed heat conduction. *Mech. Res. Commun.* 36, 481–486. doi:10.1016/j.mechrescom.2008.11.003
- Evans, W., Fish, J., and Keblinski, P. (2006). Role of Brownian motion hydrodynamics on nanofluid thermal conductivity. *Appl. Phys. Lett.* 88, 093116. doi:10.1063/1.2179118
- Grattan-Guinness, I. (2005). Chapter 26 – Joseph Fourier, Théorie analytique de la chaleur (1822). *Landmark Writings West. Math. 1640-1940*. 2005. 354. doi:10.1016/B978-0-444-50871-3/50107-8
- Haddad, S. A. M. (2014). Thermal instability in Brinkman porous media with Cattaneo-Christov heat flux. *Int. J. Heat. Mass Transf.* 68, 659–668. doi:10.1016/j.jheatmasstransfer.2013.09.039
- Hafeez, A., Khan, M., and Ahmed, J. (2020). Thermal aspects of chemically reactive Oldroyd-B fluid flow over a rotating disk with Cattaneo-Christov heat flux theory. *J. Therm. Anal. Calorim.* 144, 793–803. doi:10.1007/s10973-020-09421-4
- Hayat, T., Ahmed, S., Khan, M. I., and Alsaedi, A. (2018). Simulation of ferromagnetic nanomaterial flow of Maxwell fluid. *Results Phys.* 8, 34–40. doi:10.1016/j.rinp.2017.11.021
- Hayat, T., Aslam, N., Khan, M. I., Khan, M. I., and Alsaedi, A. (2019). Physical significance of heat generation/absorption and Soret effects on peristalsis flow of pseudoplastic fluid in an inclined channel. *J. Mol. Liq.* 275, 599–615. doi:10.1016/j.molliq.2018.11.055
- Hayat, T., Aziz, A., Muhammad, T., and Alsaedi, A. (2017). On model for flow of Burgers nanofluid with Cattaneo-Christov double diffusion. *Chin. J. Phys.* 55, 916–929. doi:10.1016/j.cjph.2017.02.017
- Hayat, T., Khan, M. I., Tamoor, M., Waqas, M., and Alsaedi, A. (2017). Numerical simulation of heat transfer in MHD stagnation point flow of Cross fluid model towards a stretched surface. *Results Phys.* 7, 1824–1827. doi:10.1016/j.rinp.2017.05.022
- Hayat, T., Shehzad, S. A., and Alsaedi, A. (2014). Three-dimensional flow of an Oldroyd-B fluid over a bidirectional stretching surface with prescribed surface temperature and prescribed surface heat flux. *J. Hydrology Hydromechanics* 62, 117–125. doi:10.2478/johh-2014-0016
- Hayat, T., Tamoor, M., Khan, M. I., and Alsaedi, A. (2016). Numerical simulation for nonlinear radiative flow by convective cylinder. *Results Phys.* 6, 1031–1035. doi:10.1016/j.rinp.2016.11.026
- Iqbal, Z., Khan, M., Ahmed, A., Ahmed, J., and Hafeez, A. (2020). Thermal energy transport in Burgers nanofluid flow featuring the Cattaneo-Christov double diffusion theory. *Appl. Nanosci.* 10, 5331–5342. doi:10.1007/s13204-020-01386-y
- Iqbal, Z., Khan, M., Ahmed, M. A., and Ullah, M. Z. (2021). The mechanical aspects of bidirectional stretching on thermal performance in Burgers nanofluid flow subject to ohmic heating and chemical reaction. *Proc. Inst. Mech. Eng. Part E J. Proc. Mech. Eng.* 2021, 0954408921999613. doi:10.1177/0954408921999613
- Kamran, T., Amir, M. J., and Rehman, M. S. (2015). Solution of Eigen value problems by using new iterative method. *Int. J. Sci. Eng. Res.* 11, 1355–1361.
- Kamran, T., Rehman, M. S., and Amir, M. J. (2016). Using new iterative method to find the exact s for a class of stiff systems of equations. *Int. J. Math. Phys. Sci. Res.* 3, 60–65.
- Kamran, T., Yaseen, M., and Rehman, M. S. (2016). Solution of variational problems using new iterative method. *Int. J. Sci. Eng. Res.* 7, 1619–1624.
- Khan, M. I., Alsaedi, A., Hayat, T., and Khan, N. B. (2019). Modeling and computational analysis of hybrid class nanomaterials subject to entropy generation. *Comput. Methods Programs Biomed.* 179, 104973. doi:10.1016/j.cmpb.2019.07.001
- Khan, M. I., and Alzahrani, F. (2020). Binary chemical reaction with activation energy in dissipative flow of non-Newtonian nanomaterial. *J. Theor. Comput. Chem.* 19, 2040006. doi:10.1142/s0219633620400064
- Khan, M. I., Alzahrani, F., and Hobiny, A. (2020). Simulation and modeling of second order velocity slip flow of micropolar ferrofluid with Darcy-Forchheimer porous medium. *J. Mat. Res. Technol.* 9, 7335–7340. doi:10.1016/j.jmrt.2020.04.079
- Khan, M. I., and Alzahrani, F. (2021). Physical impact of double stratification in Darcy-Forchheimer hybrid nanofluid (Al_2O_3 -Cu- H_2O) subject to Arrhenius pre-exponential factor law and entropy generation. *Waves Random Complex Media* 1, 22. doi:10.1080/17455030.2021.2011985
- Khan, M. I., Malik, M. Y., Chaudhry, F., Khan, S. U., and El-Zahar, E. R. (2021). Transportation of Marangoni convection with dust particles random motion in flow of hybrid nanomaterials. *Waves Random Complex Media* 1, 14. doi:10.1080/17455030.2021.2017072
- Khan, M. I., and Puneeth, V. (2021). Isothermal autocatalysis of homogeneous-heterogeneous chemical reaction in the nanofluid flowing in a diverging channel in the presence of bioconvection. *Waves Random Complex Media* 1, 21. doi:10.1080/17455030.2021.2008547
- Khan, M., Iqbal, Z., and Ahmed, A. (2020). A mathematical model to examine the heat transport features in Burgers fluid flow due to stretching cylinder. *J. Therm. Anal. Calorim.* 147, 827–841. doi:10.1007/s10973-020-10224-w
- Khan, M., Iqbal, Z., and Ahmed, A. (2020). Stagnation point flow of magnetized Burgers' nanofluid subject to thermal radiation. *Appl. Nanosci.* 10, 5233–5246. doi:10.1007/s13204-020-01360-8
- Khan, M., Khan, W. A., and Alshomrani, A. S. (2016). Non-linear radiative flow of three-dimensional Burgers nanofluid with new mass flux effect. *Int. J. Heat. Mass Transf.* 101, 570–576. doi:10.1016/j.jheatmasstransfer.2016.05.056
- Khan, M., and Khan, W. A. (2016). Three-dimensional flow and heat transfer to Burgers fluid using Cattaneo-Christov heat flux model. *J. Mol. Liq.* 221, 651–657. doi:10.1016/j.molliq.2016.06.041
- Khan, M. R., Mao, S., Deebani, W., and Elsiddeeg, A. M. (2022). Numerical analysis of heat transfer and friction drag relating to the effect of Joule heating, viscous dissipation and heat generation/absorption in aligned MHD slip flow of a nanofluid. *Int. Commun. Heat Mass Transf.* 131, 105843. doi:10.1016/j.icheatmasstransfer.2021.105843

- Khan, W. A., Alshomrani, A. S., and Khan, M. (2016). Assessment on characteristics of heterogeneous-homogenous processes in three-dimensional flow of Burgers fluid. *Results Phys.* 6, 772–779. doi:10.1016/j.rinp.2016.09.019
- Khan, W. A., Khan, M., and Alshomrani, A. S. (2016). Impact of chemical processes on 3D Burgers fluid utilizing Cattaneo-Christov double-diffusion: Applications of non-Fourier's heat and non-Fick's mass flux models. *J. Mol. Liq.* 223, 1039–1047. doi:10.1016/j.molliq.2016.09.027
- Liu, I. C., and Andersson, H. I. (2008). Heat transfer over a bidirectional stretching sheet with variable thermal conditions. *Int. J. Heat. Mass Transf.* 51, 4018–4024. doi:10.1016/j.ijheatmasstransfer.2007.10.041
- Muhammad, T., Waqas, H., Khan, S. A., Ellahi, R., and Sait, S. M. (2020). Significance of nonlinear thermal radiation in 3D Eyring-Powell nanofluid flow with Arrhenius activation energy. *J. Therm. Anal. Calorim.* 143, 929–944. doi:10.1007/s10973-020-09459-4
- Nadeem, S., and Khan, A. U. (2019). MHD oblique stagnation point flow of nanofluid over an oscillatory stretching/shrinking sheet: Existence of dual solutions. *Phys. Screen.* 94, 075204. doi:10.1088/1402-4896/ab0973
- Rashidi, M. M., Rostami, B., Freidoonimehr, N., and Abbasbandy, S. (2014). Free convective heat and mass transfer for MHD fluid flow over a permeable vertical stretching sheet in the presence of the radiation and buoyancy effects. *Ain Shams Eng. J.* 5, 901–912. doi:10.1016/j.asej.2014.02.007
- Rasool, G., and Zhang, T. (2019). Darcy-Forchheimer nanofluidic flow manifested with Cattaneo-Christov theory of heat and mass flux over non-linearly stretching surface. *PLoS ONE* 14, e0221302. doi:10.1371/journal.pone.0221302
- Raza, A., Ghaffari, A., Khan, S. U., Haq, A. U., Khan, M. I., and Khan, M. R. (2022). Non-singular fractional computations for the radiative heat and mass transfer phenomenon subject to mixed convection and slip boundary effects. *Chaos, Solit. Fractals* 155, 111708. doi:10.1016/j.chaos.2021.111708
- Rehman, M. S., and Kamran, T. (2019). Solution of nonlinear Riccati differential equations using new iterative method. *Int. J. Eng. Fut. Tech.* 16.
- Rehman, M. S., Yaseen, M., and Kamran, T. (2016). New iterative method for solution of system of linear differential equations. *Int. J. Sci. Res.* 5.
- Saleem, S., Awais, M., Nadeem, S., Sandeep, N., and Mustafa, M. T. (2017). Theoretical analysis of upper-convected Maxwell fluid flow with Cattaneo-Christov heat flux model. *Chin. J. Phys.* 55, 1615–1625. doi:10.1016/j.cjph.2017.04.005
- Shehzad, S. A., Abbasi, F. M., Hayat, T., and Alsaedi, A. (2016). Cattaneo-Christov heat flux model for Darcy-Forchheimer flow of an Oldroyd-B fluid with variable conductivity and non-linear convection. *J. Mol. Liq.* 224, 274–278. doi:10.1016/j.molliq.2016.09.109
- Shehzad, S. A., Mushtaq, T., Abbas, Z., and Rauf, A. (2019). Double-diffusive Cattaneo-Christov squeezing flow of micropolar fluid. *J. Therm. Anal. Calorim.* 143, 445–454. doi:10.1007/s10973-019-09183-8
- Sheikholeslami, M., Bandpy, M. D., Ellahi, R., and Zeeshan, A. (2014). Simulation of MHD CuO-water nanofluid flow and convective heat transfer considering Lorentz forces. *J. Magn. Magn. Mat.* 369, 69–80. doi:10.1016/j.jmmm.2014.06.017
- Sheikholeslami, M., and Ganji, D. D. (2013). Heat transfer of Cu-water nanofluid flow between parallel plates. *Powder Technol.* 235, 873–879. doi:10.1016/j.powtec.2012.11.030
- Sher, M., Muhammad, I., Asif, H. S., Muhammad, T., Muhammad, T., Muhammad, N., et al. (2019). Semi analytical solution of steady Burgers' nanofluid flow between parallel channels with heat generation/absorption under the influence of thermal radiation. *J. Nanofluids* 8, 1468–1478. doi:10.1166/jon.2019.1706
- Straughan, B. (2010). Thermal convection with the cattaneo-christov model. *Int. J. Heat. Mass Transf.* 53, 95–98. doi:10.1016/j.ijheatmasstransfer.2009.10.001
- Waqas, M., Hayat, T., Shehzad, S. A., and Alsaedi, A. (2018). Analysis of forced convective modified Burgers liquid flow considering Cattaneo-Christov double diffusion. *Results Phys.* 8, 908–913. doi:10.1016/j.rinp.2017.12.069

Nomenclature

u, v, w Velocity components (ms^{-1})

μ Dynamic viscosity ($\text{kg m}^{-1} \text{s}^{-1}$)

x, y, z Cartesian coordinates (ms^{-1})

N_b Brownian motion parameter

α_1 Thermal diffusivity ($\text{m}^2 \text{s}^{-1}$)

β_1 Fluid relaxation time parameter

k Thermal conductivity ($\frac{\text{W}}{\text{MK}}$)

C_w Concentration at surface

l Specific length (m)

D_B The mass diffusion coefficient ($\text{m}^2 \text{s}^{-1}$)

q Heat flux

σ Fluid electric conductivity (Sm^{-1})

C_∞ Ambient concentration

c_p Specific heat capacity ($\text{JK}^{-1} \text{kg}^{-1}$)

C Concentration

S Extra stress tensor

ν Kinematic viscosity ($\text{m}^2 \text{s}^{-1}$)

U_0 Reference velocity (ms^{-1})

Le Lewis number

λ_1 Fluid relaxation time (s)

λ_2 The material parameter of Oldroyd-B fluid (s^2)

ρ Fluid density (kg m^{-3})

θ Dimensionless temperature

J Mass flux

T_w Surface temperature (K)

T_∞ Ambient temperature (K)

D_T Thermophoresis coefficient ($\text{m}^2 \text{s}^{-1}$)

β_t Thermal relaxation time parameter (s)

h_f Heat convection coefficient ($\frac{\text{W}}{\text{KM}^2}$)

η Dimensionless similarity variable

ax, by linear stretching velocities (ms^{-1})

T Fluid temperature (K)

A_1 First Rivlin–Ericksen tensor

f' Dimensionless fluid velocity component

Pr Prandtl number

β_c Solutal relaxation time parameter (s)

ϕ Dimensionless concentration



OPEN ACCESS

EDITED BY

Adnan,
Mohi-ud-Din Islamic University,
Pakistan

REVIEWED BY

Esra Karatas Akgül,
Siirt University, Turkey
Muhammad Farooq,
University of Engineering and
Technology, Pakistan

*CORRESPONDENCE

Wasim Jamshed,
wasiktk@hotmail.com

SPECIALTY SECTION

This article was submitted to Process
and Energy Systems Engineering,
a section of the journal
Frontiers in Energy Research

RECEIVED 27 June 2022

ACCEPTED 09 August 2022

PUBLISHED 03 November 2022

CITATION

Zada L, Ali N, Nawaz R, Jamshed W,
Eid MR, Tag El Din ESM, Khalifa HAEW
and ElSeabee FAA (2022), Applying the
natural transform iterative technique for
fractional high-dimension equations of
acoustic waves.
Front. Energy Res. 10:979773.
doi: 10.3389/fenrg.2022.979773

COPYRIGHT

© 2022 Zada, Ali, Nawaz, Jamshed, Eid,
Tag El Din, Khalifa and ElSeabee. This is
an open-access article distributed
under the terms of the [Creative
Commons Attribution License \(CC BY\)](#).
The use, distribution or reproduction in
other forums is permitted, provided the
original author(s) and the copyright
owner(s) are credited and that the
original publication in this journal is
cited, in accordance with accepted
academic practice. No use, distribution
or reproduction is permitted which does
not comply with these terms.

Applying the natural transform iterative technique for fractional high-dimension equations of acoustic waves

Laiq Zada¹, Nasir Ali¹, Rashid Nawaz¹, Wasim Jamshed^{2*},
Mohamed R. Eid^{3,4}, El Sayed M. Tag El Din⁵,
Hamiden Abd El- Wahed Khalifa^{6,7} and
Fayza Abdel Aziz ElSeabee^{8,9}

¹Department of Mathematics, Abdul Wali Khan University Mardan, Mardan, Pakistan, ²Department of Mathematics, Capital University of Science and Technology (CUST), Islamabad, Pakistan, ³Department of Mathematics, Faculty of Science, New Valley University, Al-Kharga, Al-Wadi Al-Gadid, Egypt, ⁴Department of Mathematics, Faculty of Science, Northern Border University, Arar, Saudi Arabia, ⁵Electrical Engineering, Faculty of Engineering and Technology, Future University in Egypt, New Cairo, Egypt, ⁶Department of Operations Research, Faculty of Graduate Studies for Statistical Research, Cairo University, Giza, Egypt, ⁷Department of Mathematics, College of Science and Arts, Qassim University, Al-Badaya, Saudi Arabia, ⁸Mathematics Department, Faculty of Science, Helwan University, Cairo, Egypt, ⁹Department of Mathematics, College of Science and Arts, Qassim University, Alasyah, Saudi Arabia

In the present study, the natural transform iterative method (NTIM) has been implemented for the solution of a fractional Zakharov–Kuznetsov (FZK) equation. NTIM is a relatively new technique for handling non-linear fractional differential equations. The method is tested upon the two non-linear FZK equalities. The solution of the proposed technique has been compared with the existing perturbation–iteration algorithm (PIA) method and residual power series method (RPSM). From the numerical results, it is clear that the method handles non-linear differential equations very suitably and provides the results in very closed accord with the accurate solution. As a result, the NTIM approach is regarded as one of the finest analytical techniques for solving fractional-order linear and non-linear problems.

KEYWORDS

natural transform method, fractional order differential equations (FDEs), approximate solution, acoustic waves, perturbation-iteration algorithm

1 Introduction

Entropy and fractional calculus are appealing concepts that are increasingly being used to investigate the dynamics of complicated systems. Fractional calculus (FC) has been increasingly used in numerous sectors of research in recent years. Fractional differential equalities (FDEs) efficiently depict the natural evolution associated with viscoelasticity, models of porous electrodes, thermal stresses, electromagnetism, energy transmission in viscous dissipation systems, relaxing oscillations, and thermoelasticity.

Most of the mathematical models are obtained through real-world problems which can be modeled *via* differential equations of the integer order or of the fractional order. The differential equations may arise in diverse areas of technological sciences and biological sciences. In engineering sciences, they may be in the field of fluid dynamics, aerodynamics, the nuclear decay, climate changes, electronic circuits, etc. In biosciences, these models may be of the blood flow, population growth, and decay problems of some kind of species of organisms like bacteria or virus and may be the study of some rate of flow of some gas models or may be the concentration control of some liquids in some other liquids. Similarly, differential equations may also model some problems related to social sciences as in the fields of banking and finance. The customer may be satisfied by preparing a fractional model of interest or premium according to the required efforts of a person. Fractional calculus plays an essential role in these kinds of problems.

Fractional calculation is the generalization of the classical calculus which is an ancient branch of mathematics. The fractional calculus received much more attention of researchers during the last few decades. Fractional calculus has great achievements in the fields of physics, engineering, biology, medicine, hydrology, economics, and finance [1–5]. The models of differential equations may be linear or nonlinear; linear models can be solved easily by different methods and do not require too much difficulty for obtaining the exact solution. But most of the problems of the real world occur non-linearly and cannot be solved easily. They are very hard to solve by simple methods. Most of the non-linear problems do not have exact solutions. Therefore, researchers use different approaches to solve them.

Researchers use numerical methods to solve non-linear problems, but they have discretization issue, are costly, and time-consuming. The famous numerical methods are the following: the collocation method, finite difference technique, finite element procedure, and radial basis function technique [6–8]. Similarly, perturbation methods need small or large parameter assumptions which are very difficult [9, 10]. Non-perturbation methods are the Adomian decomposition methodology (ADM) and differential transformation methodology (DTM). These methods work on repetition and that is why these types of problems can be solved with the help of computer software easily. Some well-known iterative methods are the variational iterating methodology (VIM), new iterating methodology, modified variational iteration method (MVIM), etc. [11, 12]. The Zakharov–Kuznetsov (ZK) equation is an enticing modeling formula for studying vortices in geophysics flows. The ZK difficulties appear in many areas of material sciences, implemented arithmetic, and design. It occurs particularly in the realm of physical sciences. The ZK issues govern the behavior of weak non-linear particle acoustic plasma waves, such as cold nanoparticles and hot adiabatic electrons, in the presence of smooth magnetism. The non-direct higher order

of the expanded KdV criteria for geometrical removal was used to generate solitary wave configurations. The accurate expository structures of various non-linear advancement equations in numerical materials engineering, namely, space time-fractional Zakharov–Kuznetsov and altered Zakharov–Kuznetsov formulas, were found using a fractional technique. Many approaches, including the new iterating Sumudu understanding of the complex, homotopy perturbation transform method, expanded direct algebra methodology, natural decomposition technique, and q-homotopy analysis transform methodology, have been used to examine it during the last few decades. In this research work, we will find the approximate solution to the fractional order of the Zakharova–Kuznetsova FZK equation (13). The general form of the FZK equation is

$$D_t^\beta \varphi + a(\varphi^p)_x + b(\varphi^q)_{xxx} + c(\varphi^r)_{yyx} = 0, \quad 0 \leq t, \quad 0 < \beta \leq 1, \quad (1)$$

where $\varphi = \varphi(x, y, t)$, $0 < \beta \leq 1$ signifies an order of the fractional derivative, and a, b and c are optional fixed factors. The integers p, q, r control the behavior of weak non-linear ion acoustical waves in hemoglobin-containing coolant ions and hotness isotherm electrons in the existence of a consistent magneto force. Numerous researchers have tried to solve the FZK equation by using different approaches such as VIM, OHAM, PIA method, and RPSM [14]. We have obtained the solution of the FZK equation by NTIM which is an extension of the natural iterating methodology NIM presented by Gejji and Jafari [15, 16] to obtain the estimated solution of linear and non-linear differential equalities. NTIM was recently applied by Nawaz et al. [17] for solving the fractional order differential equation. In the proposed methodology, NIM is combined with the natural transform for the solution of the FZK equation. We observed that the proposed method was easy to implement and provide an encouraging approximate solution for the linear and non-linear differential equalities of fractional- and integer-order derivatives.

2 Basic definitions

Definition 2.1 [14]: The fractional integral operator I^α of order $\alpha \geq 0$ in the Riemann–Liouville idea of a function is described as

$$I^\alpha f(\chi) = \frac{1}{\Gamma(\alpha)} \int_0^\chi (\chi - s)^{\alpha-1} f(s) ds, \quad \alpha, \chi > 0, \quad (2)$$

where $I^0 f(\chi) = f(\chi)$ and Γ is the well-known function.

Definition 2.2 [14]: Riemann–Liouville fractional derivative can be defined if $g(r) \in C[a, b]$ then

$$I_a^\alpha = \frac{1}{\Gamma(\alpha)} \int_a^r \frac{g(\chi)}{(r - \chi)^{1-\alpha}} d\chi. \quad (3)$$

Some properties of the fractional derivative and integral are given as $f \in C_\mu, \mu \geq 1, \alpha, \beta \geq 0$ and $\lambda > -1$ then

$$\begin{aligned} \bullet I^\alpha I^\beta &= I^{\alpha+\beta} f(\chi), \\ \bullet I^\beta I^\alpha &= I^{\alpha+\beta} f(\chi), \\ \bullet I^\alpha \chi^\lambda &= \frac{\Gamma(\lambda+1)}{\Gamma(\lambda+1+\alpha)} \chi^{\lambda+\alpha}. \end{aligned}$$

Definition 2.3: Natural transubstantiate is specified as [18]

$$N^+[\phi(t)] = \mathfrak{R}(s, u) = \frac{1}{u} \int_0^\infty e^{-\frac{st}{u}} (\phi(t)) dt, \quad s, u > 0. \quad (4)$$

u and s are the transformation variables.

Definition 2.4 [18]: The inverse of the natural transubstantiate $\mathfrak{R}(s, u)$ is defined as

$$N^-[\mathfrak{R}(s, u)] = \phi(t) = \frac{1}{2\pi i} \int_{c-i\infty}^{c+i\infty} e^{\frac{st}{u}} (\mathfrak{R}(s, u)) ds. \quad (5)$$

$s = a + bi$ is the complex plan for executing the integral along $s = c$, where $c \in \mathbb{R}$.

Definition 2.5 [18]: If $\phi(t)$ is a function and $\phi^n(t)$ is its n th derivative, then the natural transubstantiate of $\phi(t)$ is

$$\begin{aligned} N^+(\phi^n(t)) &= \mathfrak{R}_n(s, u) = \frac{s^n}{u^n} \mathfrak{R}(s, u) - \sum_{k=0}^{n-1} \frac{s^{n-(k+1)}}{u^{n-k}} (\phi^n(0)), \\ n &\geq 1. \end{aligned} \quad (6)$$

Theorem 2.6: If $k(t)$ and $h(t)$ are defined on a set A and have the natural transforms $K(s, u)$ and $H(s, u)$, respectively, then

$$N[k^*h] = u K(s, u) H(s, u),$$

where $[h^*k]$ is the convolution of h and k .

2.1 Natural Transform Iterative Method (NTIM)

Consider the fractional order PDE in the manner

$$D_t^\beta [\varphi(y, t)] = g(y, t) + L[\varphi(y, t)] + N[\varphi(y, t)], \quad n-1 < \beta \leq n, \quad (7)$$

where D_t^β is the Caputo's fractional derivative operator of order β , $k \in \mathbb{N}$, and $y = y_1 + y_2 + \dots + y_k$. L and N represent the non-linear function. $g(y, t)$ is the resource bound. The initialization constraint is

$$\varphi(y, 0) = f(y). \quad (8)$$

Taking the natural transform of (7), we have

$$\begin{aligned} N^+[D_t^\beta (\varphi(y, t))] &= N^+[g(y, t)] + N^+[L(\varphi(y, t))] \\ &+ N(\varphi(y, t)). \end{aligned} \quad (9)$$

By employing the differentiate characteristic of the natural conversion to Eq. (9), we have

$$\begin{aligned} \frac{s^\beta}{u^\beta} N^+[\varphi(y, t)] - \frac{s^{\beta-1}}{u^\beta} \varphi(y, 0) &= N^+[g(y, t)] + N^+[L(\varphi(y, t))] \\ &+ N(\varphi(y, t)). \end{aligned} \quad (10)$$

Using the initial condition and rearranging Eq. (10), we obtain

$$\begin{aligned} N^+[\varphi(y, t)] &= \frac{f(y)}{s} + \frac{u^\beta}{s^\beta} (N^+[g(y, t)] + \frac{u^\beta}{s^\beta} (N^+[L(\varphi(y, t))] \\ &+ N(\varphi(y, t)))). \end{aligned} \quad (11)$$

As the linear term $L(\varphi(y, t))$ can be created in the structure of infinite series as

$$L(\sum_{m=0}^\infty \varphi_m(y, t)) = \sum_{m=0}^\infty L(\varphi_m(y, t)) \quad (12)$$

and $N(\varphi(y, t))$, the non-linear term is proposed as

$$\begin{aligned} N(\sum_{m=0}^\infty \varphi_m(y, t)) &= N(\varphi_0(y, t)) + \sum_{m=1}^\infty \left\{ N\left(\sum_{j=0}^i \varphi_j(y, t)\right) \right. \\ &\left. - N\left(\sum_{j=0}^{m-1} \varphi_j(y, t)\right) \right\}. \end{aligned} \quad (13)$$

Applying Eq. (13) in Eq. (11), we obtain

$$\begin{aligned} 0.9! N^+[\sum_{i=1}^\infty \varphi_i] &= \frac{f}{s} + \frac{u^\beta}{s^\beta} (N^+[g]) + \frac{u^\beta}{s^\beta} \left[N^+ \left[\sum_{m=0}^\infty L(\varphi_m) \right] \right. \\ &+ N(\varphi_0) + \sum_{m=1}^\infty \left\{ N\left(\sum_{j=0}^m \varphi_j\right) \right. \\ &\left. \left. - N\left(\sum_{j=0}^{m-1} \varphi_j\right) \right\} \right]. \end{aligned} \quad (14)$$

The recursive relation of Eq. (14) by the use of natural transform is

$$0.9! \begin{cases} N^+[\varphi_0(y, t)] = \frac{g(y)}{s} + \frac{u^\beta}{s^\beta} N^+[g(y, t)], \\ N^+[\varphi_1(y, t)] = \frac{u^\beta}{s^\beta} N^+[\mathfrak{F}(\varphi_0) + N(\varphi_0)], \\ N^+[\varphi_2(y, t)] = \frac{u^\beta}{s^\beta} N^+[L(\varphi_1) + N(\varphi_0 + \varphi_1) - N(\varphi_0)] \\ \vdots \\ N^+[\varphi_{i+1}(y, t)] = \frac{u^\beta}{s^\beta} N^+ \left[L(\varphi_i) + N(\varphi_0 + \varphi_1 + \dots + \varphi_i) \right. \\ \left. - N(\varphi_0 + \varphi_1 + \dots + \varphi_{i-1}) \right], \quad i \geq 0. \end{cases} \quad (15)$$

Utilizing the inverted natural transmute to Eq. (15), the solution component can be obtained as

$$0.9! \begin{cases} \varphi_0(y, t) = N^{-1} \left[\frac{g(x)}{s} + \frac{u^\beta}{s^\beta} N^+ [g] \right], \\ \varphi_0(y, t) = N^{-1} \left[\frac{u^\beta}{s^\beta} N^+ [L(\varphi_0) + N(\varphi_0)] \right], \\ \varphi_0(y, t) = N^{-1} \left[\frac{u^\beta}{s^\beta} N^+ [L(\varphi_1) + N(\varphi_0 + \varphi_1) - N(\varphi_0)] \right], \\ \vdots \\ \varphi_{i+1}(y, t) = N^{-1} \left[\frac{u^\beta}{s^\beta} N^+ \left[L(\varphi_0 + \varphi_1 + \dots + \varphi_i) \right. \right. \\ \left. \left. - N(\varphi_0 + \varphi_1 + \dots + \varphi_{i-1}) \right] \right], i \geq 0. \end{cases} \quad (16)$$

The n bounds approximated the solution of Eqs. 7 and 8 by the proposed method, which is obtained by adding the components as

$$\tilde{\varphi}(y, t) = \varphi_0(y, t) + \varphi_1(y, t) + \dots + \varphi_{n-1}(y, t). \quad (17)$$

2.2 Convergence of the NTIM

Theorem 2.7 [18]: If N is analytic in a neighborhood of ϕ_0 and

$$\|N^m(\phi_0)\| = \sup\{N^m(\phi_0)(b_1, b_2, \dots, b_n) / \|b_k\| \leq 1, 1 \leq k \leq m\} \leq l$$

for any m and for certain real $l > 0$ & $\|\phi_k\| \leq M < \frac{1}{e}$, $k = 1, 2, \dots$, then the series $\sum_{m=0}^{\infty} G_m$ is absolutely convergent and more over

$$\|G_m\| \leq l M^m e^{m-1} (e - 1), m = 1, 2, \dots$$

To appear in the boundaries of $\|\phi_k\|$, for every k , the conditions on $N^{(j)}(\phi_0)$ are provided which are appropriate to assure convergence of the sequence. The satisfactory constraint for the convergent is provided in the subsequent theory.

Theorem 2.8: If N is C^∞ and $\|N^m(\phi_0)\| \leq M \leq e^{-1} \forall m$, then the sequence $\sum_{m=0}^{\infty} G_m$ is absolutely convergent. These are the required conditions for the convergence of the series $\sum \varphi_j$.

3 Implementation of the NTIM to the FZK equation

Example 3.1. Consider the FZK equation in the following form [13]:

$$D_t^\beta \varphi + (\varphi^k)_x + \frac{1}{8}(\varphi^k)_{xxx} + \frac{1}{8}(\varphi^k)_{yyx} = 0, \quad 0 \leq t, \quad 0 < \beta \leq 1. \quad (18)$$

Together, the initial condition is

$$\varphi(x, y, 0) = f(x, y). \quad (19)$$

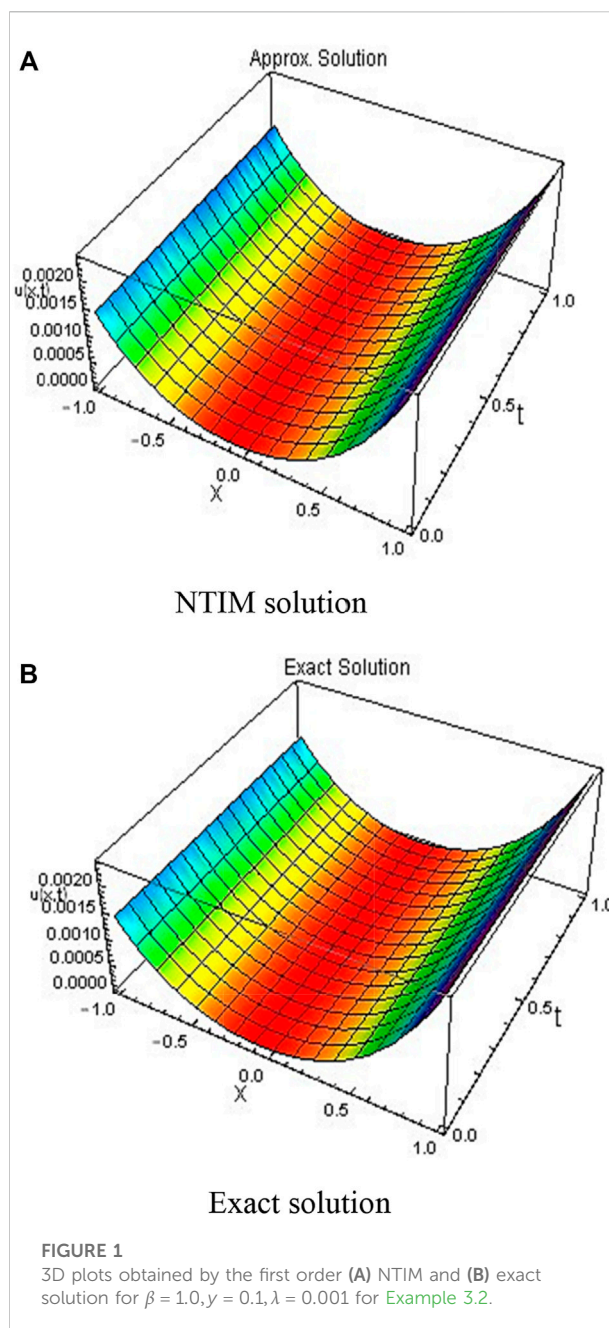


FIGURE 1
3D plots obtained by the first order (A) NTIM and (B) exact solution for $\beta = 1.0, y = 0.1, \lambda = 0.001$ for Example 3.2.

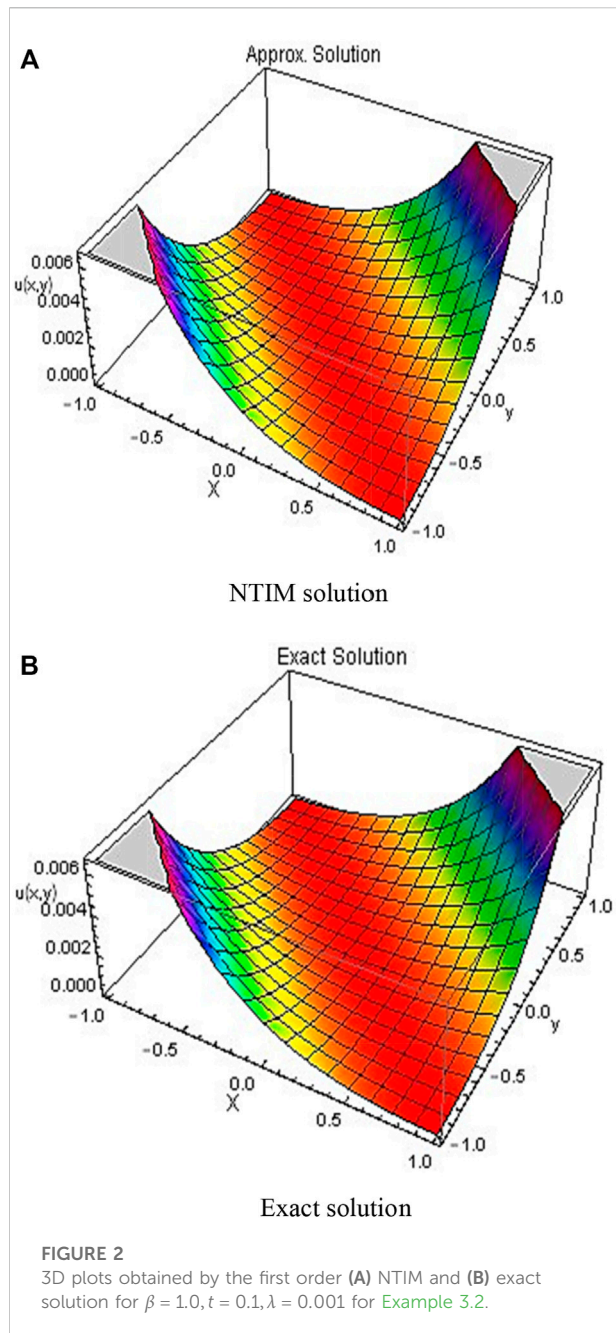
Eq. (18) is written in the implicit form as

$$D_t^\beta \varphi = -(\varphi^k)_x - \frac{1}{8}(\varphi^k)_{xxx} - \frac{1}{8}(\varphi^k)_{yyx}. \quad (20)$$

Using natural conversion to Eq. (20), we get

$$N^+ [D^\beta(\varphi)] = N^+ \left[-(\varphi^k)_x - \frac{1}{8}(\varphi^k)_{xxx} - \frac{1}{8}(\varphi^k)_{yyx} \right]. \quad (21)$$

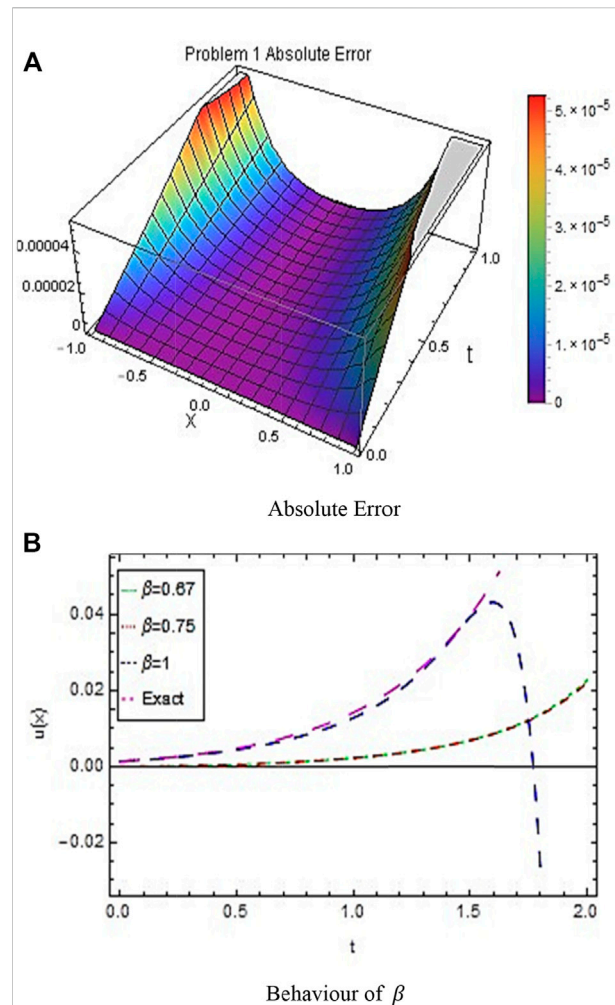
Utilize the differentiation characteristic of the natural convert as



$$\frac{s^\beta}{u^\beta} N^+[\varphi] - \frac{s^{\beta-1}}{u^\beta} \varphi(x, y, 0) = N^+ \left[-(\varphi^k)_x - \frac{1}{8} (\varphi^k)_{xxx} - \frac{1}{8} (\varphi^k)_{yyx} \right]. \quad (22)$$

Using the initial condition in Eq. (20) and rearranging, we have

$$N^+[\varphi] = \frac{f(x, y)}{s} + \frac{u^\beta}{s^\beta} N^+ \left[-(\varphi^k)_x - \frac{1}{8} (\varphi^k)_{xxx} - \frac{1}{8} (\varphi^k)_{yyx} \right]. \quad (23)$$



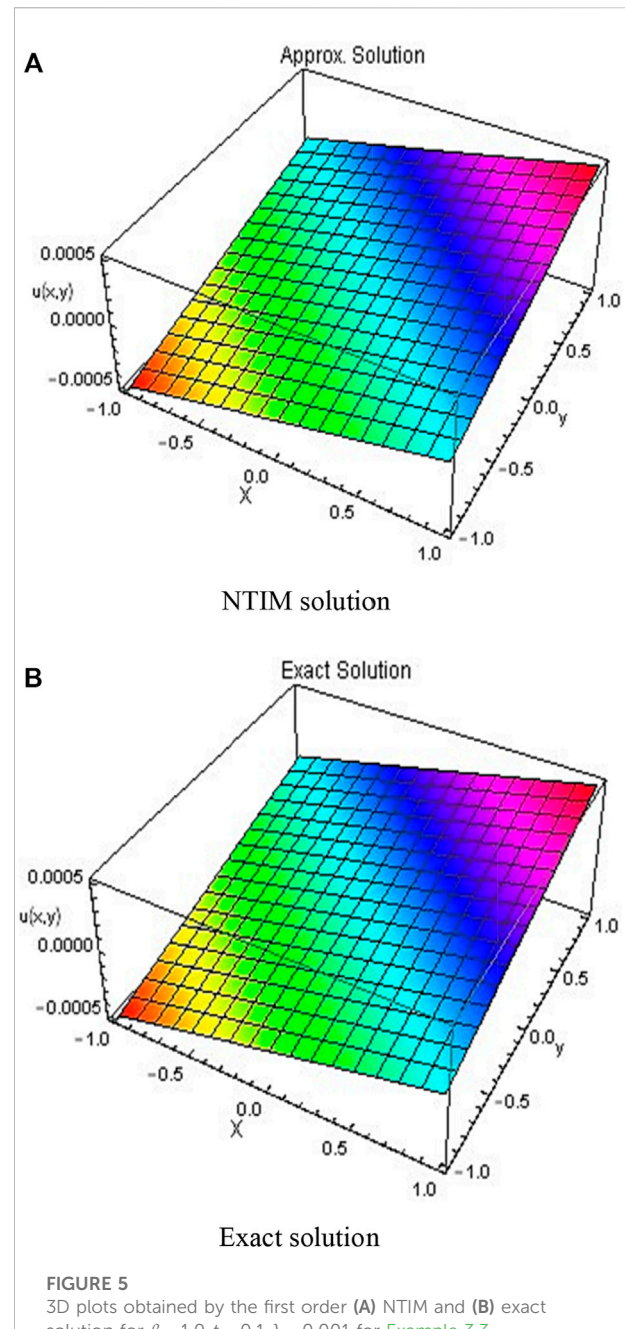
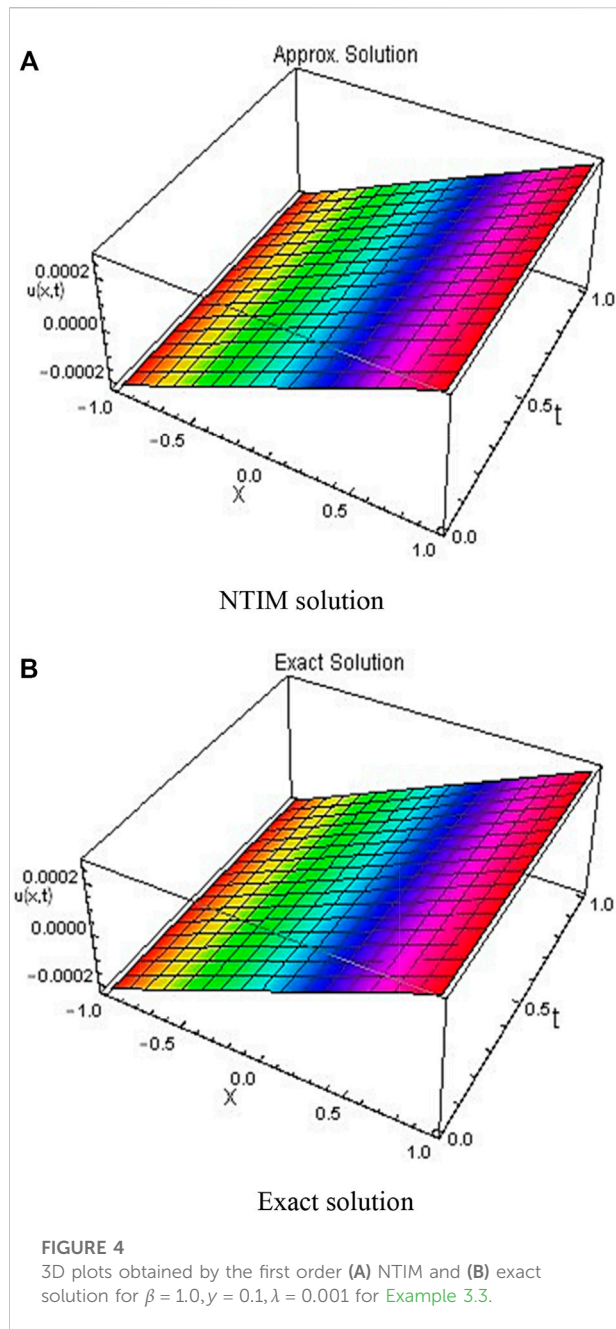
As $\varphi(x, y, t)$ is the infinite series given as

$$\sum_{m=0}^{\infty} \varphi_m(x, y, t), \quad (24)$$

applying natural transform to Eq. (25) and using the idea explained in the method

$$\begin{cases} N^+[\varphi_0(x, y, t)] = \frac{f(x, y)}{s}, \\ N^+[\varphi_1(x, y, t)] = \frac{u^\beta}{s^\beta} N^+ \left[-(\varphi_0^k)_x - \frac{1}{8} (\varphi_0^k)_{xxx} - \frac{1}{8} (\varphi_0^k)_{yyx} \right], \\ N^+[\varphi_2(x, y, t)] = \frac{u^\beta}{s^\beta} N^+ \left[-((\varphi_0 + \varphi_1)^k)_x - \frac{1}{8} ((\varphi_0 + \varphi_1)^k)_{xxx} - \frac{1}{8} ((\varphi_0 + \varphi_1)^k)_{yyx} \right], \\ \vdots \end{cases} \quad (25)$$

Now, by taking the inverted natural transmute of Eq. 25, we obtain the solution elements as



$$\begin{cases} \varphi_0(x, y, t) = N^{-1} \left[\frac{f(x, y)}{s} \right], \\ \varphi_1(x, y, t) = N^{-1} \left[\frac{t^\beta}{s^\beta} N^+ \left[-(\varphi_0^k)_x - \frac{1}{8}(\varphi_0^k)_{xxx} - \frac{1}{8}(\varphi_0^k)_{yyx} \right] \right], \\ \varphi_2(x, y, t) = N^{-1} \left[\frac{t^\beta}{s^\beta} N^+ \left[-((\varphi_0 + \varphi_1)^k)_x - \frac{1}{8}((\varphi_0 + \varphi_1)^k)_{xxx} - \frac{1}{8}((\varphi_0 + \varphi_1)^k)_{yyx} \right] \right], \\ \vdots \end{cases} \quad (26)$$

The n – terms approximate solution of Eqs. 18 and 19 by NTIM is presented as

$$\varphi(x, y, t) = \varphi_0 + \varphi_1 + \dots + \varphi_{m-1}. \quad (27)$$

Example 3.2. Regarding the FZK (2, 2, 2) equality of the structure [13]

$${}^c D_t^\beta \varphi + (\varphi^2)_x + \frac{1}{8}(\varphi^2)_{xxx} + \frac{1}{8}(\varphi^2)_{yyx} = 0, \quad 0 < \beta \leq 1. \quad (28)$$

With preliminary conditions

$$\varphi(x, y, 0) = \frac{4}{3} \lambda \sinh^2(x + y). \quad (29)$$

Here, λ is an optional fixed value. The accurate solution for $\beta = 1.0$ is given by

$$\varphi(x, y, t) = \frac{4}{3} \lambda \sinh^2(x + y - \lambda t). \quad (30)$$

Utilizing the procedure of NTIM, we obtain the solution components for Eq. (28) as

$$\varphi_0(x, y, t) = \frac{4}{3} \lambda \sinh^2(x + y), \quad (31)$$

$$\varphi_1(x, y, t) = \frac{8\lambda^2 t^\beta (4 \sinh(2(x + y)) - 5 \sinh(4(x + y)))}{9\Gamma(\beta + 1)}, \quad (32)$$

$$\varphi_2(x, y, t) = \frac{64\lambda^3 t^{2\beta} \left(\begin{aligned} &3\Gamma(\beta + 1)^2 \Gamma(3\beta + 1) (13 \cosh(2(x + y)) \\ &- 70 \cosh(4(x + y)) + 75 \cosh(6(x + y))) \\ &- 20\lambda \Gamma(2\beta + 1)^2 t^\beta (4 \sinh(2(x + y)) \\ &+ 8 \sinh(4(x + y)) - 60 \sinh(6(x + y))) \\ &+ 85 \sinh(8(x + y))) \end{aligned} \right)}{81\Gamma(\beta + 1)^2 \Gamma(2\beta + 1) \Gamma(3\beta + 1)}. \quad (33)$$

Adding the elements, the second-order approximated solution can be written as

$$\tilde{\varphi}(x, y, t) = \varphi_0 + \varphi_1 + \varphi_2.$$

Example 3.3. Consider the FZK (3, 3, 3) equation of the structure [13]

$${}^c D_t^\beta \varphi + (\varphi^3)_x + 2(\varphi^3)_{xxx} + 2(\varphi^3)_{yyx} = 0. \quad (34)$$

Together with initial conditions

$$\varphi(x, y, 0) = \frac{3}{2} \lambda \sinh\left(\frac{x + y}{6}\right). \quad (35)$$

Here, λ is an optional fixed amount. The exact solution for $\beta = 1.0$ is given by

$$\varphi(x, y, t) = \frac{3}{2} \lambda \sinh\left(\frac{1}{6}(x + y - \lambda t)\right). \quad (36)$$

Using the procedure of the NTIM, the solution elements can be acquired as

$$\varphi_0(x, y, t) = \frac{3}{2} \lambda \sinh\left(\frac{1}{6}(x + y)\right), \quad (37)$$

$$\varphi_1(x, y, t) = \frac{3\lambda^3 t^\beta \cosh\left(\frac{x+y}{6}\right) \left(7 - 9 \cosh\left(\frac{x+y}{3}\right)\right)}{16\Gamma(\beta + 1)}, \quad (38)$$

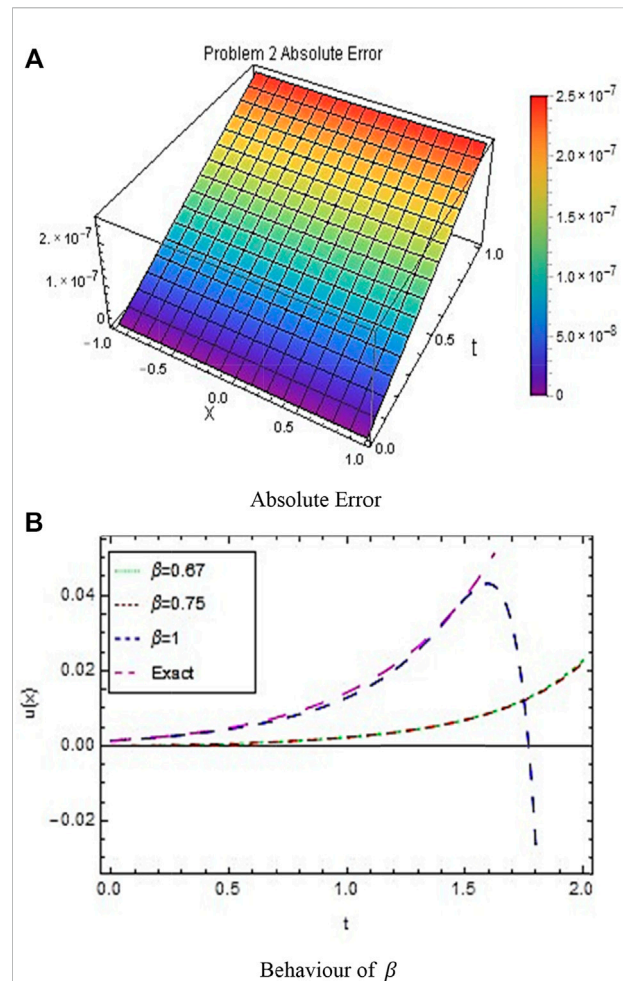


FIGURE 6

(A) shows the absolute error and (B) shows the behavior of β on the solution of the NTIM for diverse amounts of β when $x = 0.1, \lambda = 0.001$ for Example 3.3.

TABLE 1 Few important expressions and their natural transubstantiates.

| Function | Natural transformation | Function | Natural transformation |
|---------------------------------------|-----------------------------------|---------------------------------------|-----------------------------------|
| 1 | $\frac{1}{s}$ | e^{kt} | $\frac{1}{s - ku}$ |
| t | $\frac{u}{s}$ | $\sin(t)$ | $\frac{u}{s^2 + u^2}$ |
| $\frac{t^{k-1}}{\Gamma(k)}$ | $\frac{u^{k-1}}{s^k}$ | $\cos(t)$ | $\frac{s}{s^2 + u^2}$ |
| $\frac{t^{k\beta}}{\Gamma(k\beta+1)}$ | $\frac{u^{k\beta}}{s^{k\beta+1}}$ | $\frac{t^{k\beta-1}}{\Gamma(k\beta)}$ | $\frac{u^{k\beta-1}}{s^{k\beta}}$ |

TABLE 2 Comparison of the second-order NTIM with the third-order RPSM and PIA method for diverse amounts of β .

| $\beta = 0.67$ | | | | | | $\beta = 0.75$ | | |
|----------------|-----|-----|------------|---------------|--------------|----------------|---------------|--------------|
| x | y | t | PIA [13] | R (E)PSM [13] | N (E)TIM (E) | PIA [13] | R (E)PSM [13] | N (E)TIM (E) |
| 0.1 | 0.1 | 0.2 | 5.31854-5 | 5.31244-5 | 5.3124653-5 | 5.32747-5 | 5.32479-5 | 5.32479992-5 |
| | | 0.3 | 5.28631-5 | 5.28410-5 | 5.28415918-5 | 5.29757-5 | 5.29675-5 | 5.29678730-5 |
| | | 0.4 | 5.25777-5 | 5.25897-5 | 5.25907412-5 | 5.27039-5 | 5.27119-5 | 5.27125824-5 |
| 0.6 | 0.6 | 0.2 | 2.95493-3 | 2.95185-3 | 7.56548023-4 | 2.96356-3 | 2.96251-3 | 7.57930078-4 |
| | | 0.3 | 2.92662-3 | 2.92709-3 | 7.53381879-4 | 2.93717-3 | 2.93780-3 | 7.54759291-4 |
| | | 0.4 | 2.90307-3 | 2.90522-3 | 7.50623656-4 | 2.91448-3 | 2.91561-3 | 7.51914369-4 |
| 0.9 | 0.9 | 0.2 | 1.068220-2 | 1.055060-2 | 1.80363649-3 | 1.077160-2 | 1.071430-2 | 1.80827769-3 |
| | | 0.3 | 1.044870-2 | 1.011990-2 | 1.79302639-3 | 1.054880-2 | 1.036950-2 | 1.79746844-3 |
| | | 0.4 | 1.027770-2 | 9.606060-3 | 1.78401363-3 | 1.037360-2 | 9.96743-3 | 1.78798550-3 |

$$\varphi_2(x, y, t) = \left[\begin{aligned} & \frac{3\lambda^5 t^{2\beta}}{131072\Gamma(\beta+1)^3\Gamma(2\beta+1)\Gamma(3\beta+1)\Gamma(4\beta+1)} \times \\ & \lambda^4\Gamma(2\beta+1)\Gamma(3\beta+1)^2 t^{2\beta} \left(9 \left(\frac{1700}{6} \sinh(5(x+y)) + \frac{9135}{6} \sinh(7(x+y)) \right) \right. \\ & \quad \left. - \frac{3412}{2} (\sinh(x+y)) - \frac{10935}{2} (\sinh(3(x+y))) \right) \\ & \quad + \frac{3550}{6} \sinh(x+y) \\ & + 16\lambda^2\Gamma(\beta+1)\Gamma(2\beta+1)^2\Gamma(4\beta+1) t^\beta \left(9 \left(\frac{75}{2} \cosh(x+y) + \frac{1827}{6} \cosh \right. \right. \\ & \quad \left. \left. (7(x+y)) - \frac{1615}{6} (\cosh(5(x+y))) \right) \right) \\ & \quad + \frac{1385}{6} \cosh(x+y) \\ & - 256\Gamma(\beta+1)^3\Gamma(3\beta+1)\Gamma(4\beta+1) \left(\frac{70}{6} \sinh(x+y) + \frac{765}{6} \sinh(5(x+y)) \right) \\ & \quad \left. - \frac{621}{2} (\sinh(x+y)) \right) \end{aligned} \right] \quad (39)$$

Adding the components, the second-order series solution can be written as

$$\tilde{\varphi}(x, y, t) = \varphi_0(x, y, t) + \varphi_1(x, y, t) + \varphi_2(x, y, t). \quad (40)$$

4 Results and discussion

In this work, two problems of the FZK equation have been tested by the new developed methodology NTIM. The obtained results are assessed by diverse plots and tabulated data for testing the reliability of the proposed method. Figure 1 shows the 3D surfaces obtained by the NTIM and the accurate result correspondingly for Example 3.2 in the 3D graph by keeping the y parameter constant. By keeping the time parameter constant, the approximate and accurate results are shown in Figure 2 respectively, for problem 3.2. In Figure 3, the absolute error is shown by a 3D plot by the variation of x and y parameters while time is kept constant. A comparison for the variation of the fractional value β is shown by 2D plots for

Example 3.2 which shows the consistency of the method by agreeing to the amount of β tactics to the standard amount 1 of a differential equation; the approximated result converges to the accurate solution of the problem. Similarly, Figure 4 shows the approximates and exacted solution by variation of the x and t components, while Figure 5 shows the 3D graphs of the approximated solution and exacted solution by keeping the time parameter constant for problem 3.3. Figure 6 shows the absolute error of the NTIM result and the exacted solution for problem 2. Table 1 shows the comparison of data on the computational amounts of the approximated solution of the PIA and RPS methods for diverse amounts of β , while in Table 2, the absolute errors of our suggested methodology have been matched with the absolute errors of the PIA and RPS methods. Similarly, in Table 3, the fractional value of NTIM has been compared with the third-order RPSM and PIA methods. In Table 4, the absolute errors of NTIM, RPSM, and PIA methods have been compared. The approximate solution in this article is executed up to second order for both problems. The accuracy may be increased by obtaining a higher order of the approximate solution. From the tables and graphs, it is so far clear that the NTIM reveals encouraging approximated results as evaluated with other existing methodologies in the previously published works Table 5.

5. Conclusion

In the current investigation, the NTIM has been applied successfully to the FZK equations. Two problems have been tested. The proposed results reveal that the method handles the non-linear equations in a good way and provides an efficient approximate solution to non-linear PDEs. The numerical values of approximate and exact solutions through tables show the efficiency and reliability of the

TABLE 3 Comparison of the second-order NTIM with the third-order RPSM and PIA method.

| $\beta = 1.0$ | | | | | | $\beta = 1.0$ | | |
|---------------|-----|-----|--------------|-------------------|-------------------|----------------|---------------------|--------------------|
| x | y | t | PIA sol [13] | R (E)PSM sol [13] | N (E)TIM sol. (E) | PIA error [13] | R (E)PSM error [13] | N (E)TIM error (E) |
| 0.1 | 0.1 | 0.2 | 5.35536-5 | 5.355360-5 | 5.3553572-5 | 3.85217-7 | 3.852170-7 | 3.8520-7 |
| | | 0.3 | 5.33082-5 | 5.330820-5 | 5.3308223-5 | 5.75911-7 | 5.759120-7 | 5.75853-7 |
| | | 0.4 | 5.30641-5 | 5.306410-5 | 5.3064197-5 | 7.65350-7 | 7.653520-7 | 7.65214-7 |
| 0.6 | 0.6 | 0.2 | 2.98987-3 | 2.989870-3 | 2.9900091-3 | 4.66337-5 | 4.66389-5 | 4.64983-5 |
| | | 0.3 | 2.96717-3 | 2.96715-3 | 2.9676221-3 | 6.86056-5 | 6.86314-5 | 6.81568-5 |
| | | 0.4 | 2.94523-3 | 2.94515-3 | 2.9462709-3 | 8.98243-5 | 8.99046-5 | 8.87798-5 |
| 0.9 | 0.9 | 0.2 | 1.10248-2 | 1.10227-2 | 1.1041339-2 | 5.12131-4 | 5.14241-4 | 4.95639-4 |
| | | 0.3 | 1.07964-2 | 1.07861-2 | 1.0848876-2 | 7.38186-4 | 7.48450-4 | 6.85665-4 |
| | | 0.4 | 1.05742-2 | 1.05429-2 | 1.0691791-2 | 9.57942-4 | 9.89139-4 | 8.40313-4 |

TABLE 4 Comparison of the second-order NTIM with the third-order RPSM and PIA method.

| $\beta = 1.0$ | | | | | | $\beta = 1.0$ | | |
|---------------|-----|-----|--------------|-------------------|-------------------|----------------|---------------------|--------------------|
| x | y | t | PIA sol [13] | R (E)PSM sol [13] | N (E)TIM sol. (E) | PIA error [13] | R (E)PSM error [13] | N (E)TIM error (E) |
| 0.1 | 0.1 | 0.2 | 5.00091-5 | 5.00091-5 | 5.00091-5 | 5.00091-5 | 5.00091-5 | 5.00091-5 |
| | | 0.3 | 5.00090-5 | 5.00091-5 | 5.00091-5 | 5.00090-5 | 5.00091-5 | 5.00090-5 |
| | | 0.4 | 5.00090-5 | 5.0009-5 | 5.00091-5 | 5.00090-5 | 5.00091-5 | 5.00090-5 |
| 0.6 | 0.6 | 0.2 | 3.02003-4 | 3.02004-4 | 1.75397-4 | 3.02003-4 | 3.02004-4 | 3.02003-4 |
| | | 0.3 | 3.02003-4 | 3.02004-4 | 1.75397-4 | 3.02003-4 | 3.02004-4 | 3.02003-4 |
| | | 0.4 | 3.02003-4 | 3.02004-4 | 1.75397-4 | 3.02003-4 | 3.02004-4 | 3.02003-4 |
| 0.9 | 0.9 | 0.2 | 4.56780-4 | 4.5678-4 | 2.51159-4 | 4.5678-4 | 4.56780-4 | 4.56780-4 |
| | | 0.3 | 4.56780-4 | 4.5678-4 | 2.51159-4 | 4.56780-4 | 4.56780-4 | 4.56780-4 |
| | | 0.4 | 4.56780-4 | 4.5678-4 | 2.51159-4 | 4.56780-4 | 4.56780-4 | 4.56780-4 |

TABLE 5 Comparison of the second-order NTIM with the third-order RPSM and PIA method.

| $\beta = 1.0$ | | | | | | $\beta = 1.0$ | | |
|---------------|-----|-----|--------------|-------------------|-------------------|----------------|---------------------|--------------------|
| x | y | t | PIA sol [13] | R (E)PSM sol [13] | N (E)TIM sol. (E) | PIA error [13] | R (E)PSM error [13] | N (E)TIM error (E) |
| 0.1 | 0.1 | 0.2 | 5.00091-5 | 5.00092-5 | 5.00092-5 | 4.99592-5 | 4.99519-8 | 5.00091-5 |
| | | 0.3 | 5.00091-5 | 5.00091-5 | 5.00091-5 | 4.99342-5 | 7.49278-8 | 5.00091-5 |
| | | 0.4 | 5.00091-5 | 5.00091-5 | 5.00091-5 | 4.99092-5 | 9.99037-8 | 5.00091-5 |
| 0.6 | 0.6 | 0.2 | 3.02003-4 | 3.02004-4 | 3.02004-4 | 3.01953-4 | 5.08987-8 | 3.02003-4 |
| | | 0.3 | 3.02003-4 | 3.02004-4 | 3.02004-4 | 3.01927-4 | 7.63479-8 | 3.02003-4 |
| | | 0.4 | 3.02003-4 | 3.02004-4 | 3.02004-4 | 3.01902-4 | 1.01797-7 | 3.02003-4 |
| 0.9 | 0.9 | 0.2 | 4.56780-4 | 4.5678-4 | 4.5678-4 | 4.56728-4 | 5.21227-8 | 4.56780-4 |
| | | 0.3 | 4.56780-4 | 4.5678-4 | 4.5678-4 | 4.56702-4 | 7.81839-8 | 4.56780-4 |
| | | 0.4 | 4.56780-4 | 4.5678-4 | 4.5678-4 | 4.56676-4 | 1.04245-7 | 4.56780-4 |

method. Also, the graphs verify the efficiency of the proposed method through 3D and 2D plots. The fractional approximation through 2D graphs also shows the consistency of the method by approaching the fractional value β of the equation to the conventional amount 1, so an approximate result converges to the exact result of the problems. This strategy is also effective when the answer to the integer order model is unknown. As a result, we decided that the current technique is trustworthy and effective in obtaining estimated solutions for various classes of linear and non-linear fractional formulations of ordinary and partial differential equations.

Data availability statement

The original contributions presented in the study are included in the article/supplementary material; further inquiries can be directed to the corresponding author.

Author contributions

LZ and RN formulated the problem. NA and WJ solved the problem. LZ, NA, RN, WJ, MRE, ESMTED, HAEWK, and FAAE, computed and scrutinized the results. All the authors equally

contributed in writing and proof reading of the paper. All authors reviewed the manuscript.

Acknowledgments

The researchers would like to thank the Deanship of Scientific Research, Qassim University for funding the publication of this project.

Conflict of interest

The authors declare that the research was conducted in the absence of any commercial or financial relationships that could be construed as a potential conflict of interest.

Publisher's note

All claims expressed in this article are solely those of the authors and do not necessarily represent those of their affiliated organizations, or those of the publisher, the editors, and the reviewers. Any product that may be evaluated in this article, or claim that may be made by its manufacturer, is not guaranteed or endorsed by the publisher.

References

- Gorenflo, R., and Mainardi, F. (2005). Simply and multiply scaled diffusion limits for continuous time random walks. *J. Phys. Conf. Ser.* 7, 1–16. doi:10.1088/1742-6596/7/1/001
- Barkai, E., Metzler, R., and Klafter, J. (2000). From continuous time random walks to the fractional Fokker-Planck equation. *Phys. Rev. E* 61 (1), 132–138. doi:10.1103/physreve.61.132
- Benson, D.A., Wheatcraft, S.W., and Meerschaert, M.M. (2000). Application of a fractional advection-dispersion equation. *Water Resour. Res.* 36 (6), 1403–1412.
- Almeida, R. (2017). A caputo fractional derivative of a function with respect to another function. *Commun. Nonlinear Sci. Numer. Simul.* 44, 460–481. doi:10.1016/j.cnsns.2016.09.006
- Muslih, S., Baleanu, D., and Rabei, E. (2007). Gravitational potential in fractional space. *Open Physics* 5 (3), 285–292. doi:10.2478/s11534-007-0014-9
- Hu, H.Y., Chen, J.S., and Hu, W. (2007). Weighted radial basis collocation method for boundary value problems. *Int. J. Numer. Methods Eng.* 69 (13), 2736–2757. doi:10.1002/nme.1877
- Zhao, E., Shi, B., Qu, K., Dong, W., and Zhang, J. (2018). Experimental and numerical investigation of local scour around submarine piggyback pipeline under steady current. *J. Ocean Univ. China* 17 (2), 244–256. doi:10.1007/s11802-018-3290-7
- Kwon, Y.W., and Bang, H. (2018). *The finite element method using MATLAB*. Florida: CRC, press.
- D.S. Carter (1965). *Perturbation techniques in mathematics, physics and engineering*. New York: Richard bellman.
- Benabidallah, M., and Cherruault, Y. (2004). Application of the adomian method for solving a class of boundary problems. *Kybernetes* 33, 118–132. doi:10.1108/03684920410514553
- Abassy, T.A. (2010). Modified variational iteration method (nonlinear homogeneous initial value problem). *Comput. Math. Appl.* 59 (2), 912–918. doi:10.1016/j.camwa.2009.10.002
- Molliq, R.Y., Noorani, M.S.M., Hashim, I., and Ahmad, R.R. (2009). Approximate solutions of fractional zakharov-kuznetsov equations by vim. *J. Comput. Appl. Math.* 233 (2), 103–108. doi:10.1016/j.cam.2009.03.010
- Senol, M., Alquran, M., and Kasmaei, H.D. (2018). On the comparison of perturbation-iteration algorithm and residual power series method to solve fractional zakharov-kuznetsov equation. *Results Phys.* 9, 321–327. doi:10.1016/j.rinp.2018.02.056
- Nawaz, R., Zada, L., Khattak, A., Jibran, M., and Khan, A. (2019). Optimum solutions of fractional order Zakharov-Kuznetsov equations. *Complexity* 2019, 1–9. doi:10.1155/2019/1741958
- Daftardar-Gejji, V., and Bhalekar, S. (2008). Solving fractional diffusion-wave equations using a new iterative method. *Fract. Calc. Appl. Anal.* 11 (2), 193–202.
- Bhalekar, S., and Daftardar-Gejji, V. (2011). Convergence of the new iterative method. *International Journal of Differential Equations* 2011, 1–10. doi:10.1155/2011/989065
- Nawaz, R., Ali, N., Zada, L., Nisar, K.S., Alharthi, M.R., and Jamshed, W. (2021). Extension of natural transform method with daftardar-jafari polynomials for fractional order differential equations. *Alexandria Engineering Journal* 60 (3), 3205–3217. doi:10.1016/j.aej.2021.01.051
- Nawaz, R., Ali, N., Zada, L., Shah, Z., Tassaddiq, A., and Alreshidi, N.A. (2020). Comparative analysis of natural transform decomposition method and new iterative method for fractional foam drainage problem and fractional order modified regularized long-wave equation. *Fractals* 28 (07), 2050124. doi:10.1142/s0218348x20501248

Frontiers in Energy Research

Advances and innovation in sustainable, reliable
and affordable energy

Explores sustainable and environmental
developments in energy. It focuses on
technological advances supporting Sustainable
Development Goal 7: access to affordable,
reliable, sustainable and modern energy for all.

Discover the latest Research Topics

[See more →](#)

Frontiers

Avenue du Tribunal-Fédéral 34
1005 Lausanne, Switzerland
frontiersin.org

Contact us

+41 (0)21 510 17 00
frontiersin.org/about/contact



Frontiers in Energy Research

